



HAL
open science

Exploring cell polarity and motility of the protozoan *Toxoplasma gondii* in an innovative biological and biophysical coupled framework

Luis Miguel Vigetti

► **To cite this version:**

Luis Miguel Vigetti. Exploring cell polarity and motility of the protozoan *Toxoplasma gondii* in an innovative biological and biophysical coupled framework. Structural Biology [q-bio.BM]. Université Grenoble Alpes [2020-..], 2023. English. NNT : 2023GRALV055 . tel-04434520

HAL Id: tel-04434520

<https://theses.hal.science/tel-04434520v1>

Submitted on 2 Feb 2024

HAL is a multi-disciplinary open access archive for the deposit and dissemination of scientific research documents, whether they are published or not. The documents may come from teaching and research institutions in France or abroad, or from public or private research centers.

L'archive ouverte pluridisciplinaire **HAL**, est destinée au dépôt et à la diffusion de documents scientifiques de niveau recherche, publiés ou non, émanant des établissements d'enseignement et de recherche français ou étrangers, des laboratoires publics ou privés.

THÈSE

Pour obtenir le grade de

DOCTEUR DE L'UNIVERSITÉ GRENOBLE ALPES

École doctorale : CSV- Chimie et Sciences du Vivant

Spécialité : Biologie Structurale et Nanobiologie

Unité de recherche : IAB : Epigenetics, Environment, Cell Plasticity, Cancer (UGA / Inserm U1209 / CNRS UMR 5309)

**Etude de la polarité cellulaire et de la motilité du protozoaire
Toxoplasma gondii par une approche biologique et biophysique
combinée**

**Exploring cell polarity and motility of the protozoan Toxoplasma
gondii in an innovative biological and biophysical coupled framework**

Présentée par :

Luis Miguel VIGETTI

Direction de thèse :

Isabelle TARDIEUX
Directeur de Recherche, cnrs

Directrice de thèse

Rapporteurs :

Delphine DELACOUR
DIRECTRICE DE RECHERCHE, CNRS délégation Provence et Corse

Catherine LAVAZEC
DIRECTRICE DE RECHERCHE, CNRS délégation Ile-de-France Villejuif

Thèse soutenue publiquement le **16 octobre 2023**, devant le jury composé de :

Isabelle TARDIEUX Directrice de thèse
DIRECTRICE DE RECHERCHE, CNRS délégation Alpes

Delphine DELACOUR Rapporteuse
DIRECTRICE DE RECHERCHE, CNRS délégation Provence et Corse

Catherine LAVAZEC Rapporteuse
DIRECTRICE DE RECHERCHE, CNRS délégation Ile-de-France
Villejuif

Markus MEISSNER Examineur
FULL PROFESSOR, Ludwig-Maximilians- Universität München

Isabelle FLORENT Examinatrice
PROFESSEURE DES UNIVERSITES, Muséum national d'Histoire
naturelle

Guy ROYAL Président
PROFESSEUR DES UNIVERSITES, Université Grenoble Alpes

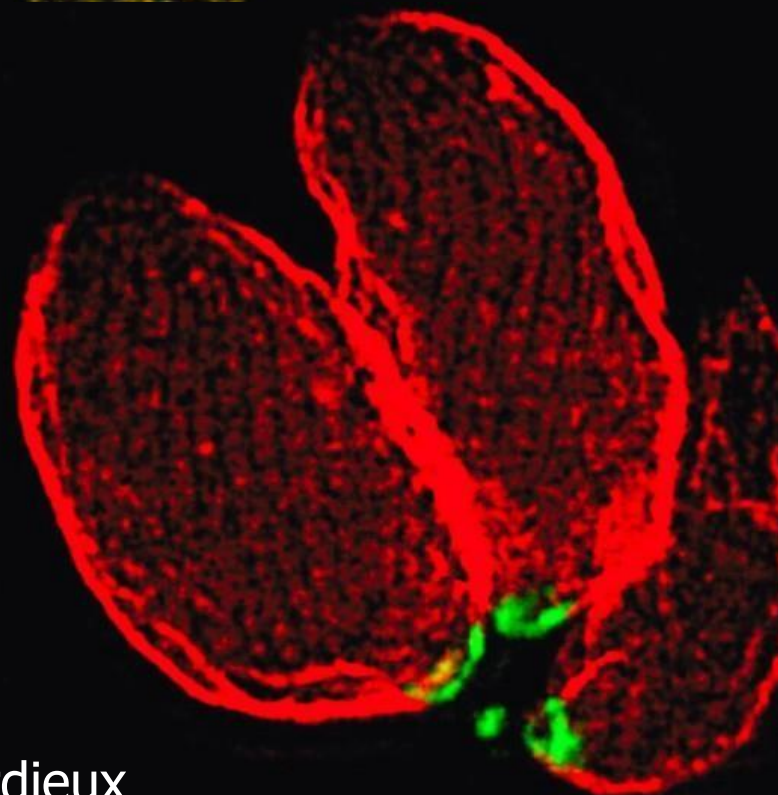
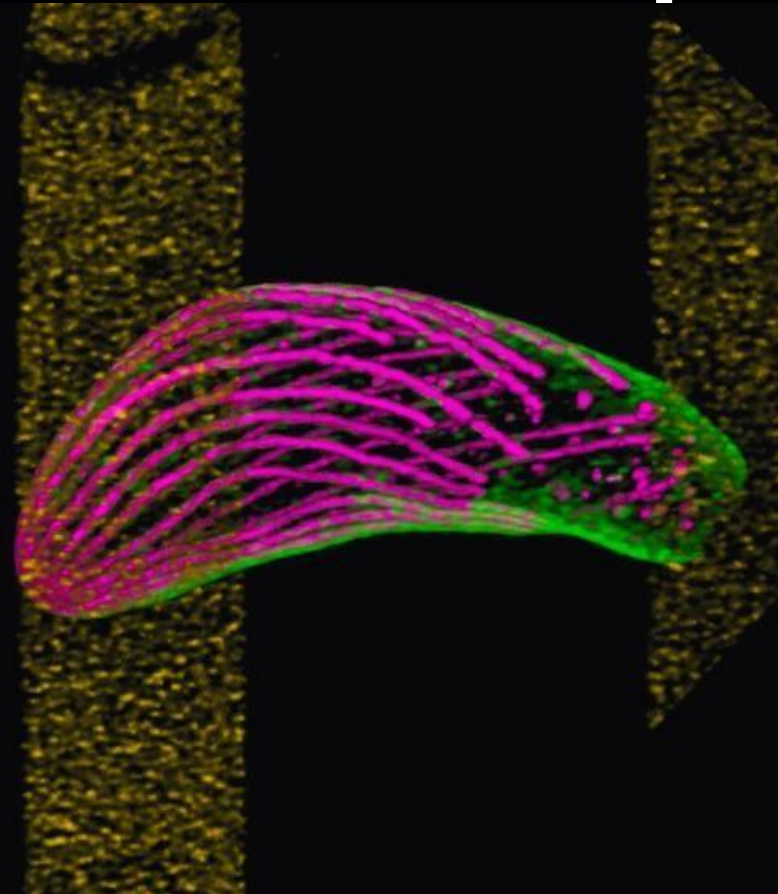


Exploring cell
polarity and motility
of the protozoan
Toxoplasma gondii
in an innovative
biological and
biophysical coupled
framework

Luis Vigetti

Ph.D. Thesis

Supervisor: Dr. Isabelle Tardieux
Institute for Advanced Biosciences
Grenoble, France



2023

Summary

Toxoplasma gondii is a single-celled eukaryotic microbe that belongs to the large and ancient phylum of Apicomplexan parasites, and strictly depends on cells from a wide range of homeothermic metazoan hosts, human included, to achieve a complex life cycle. To succeed, *T. gondii* has evolved infectious developmental stages called zoites. Here, we focus on the fast-cycling tachyzoite, a several-micron-sized cell, with a strong arc-shape silhouette featured by an apical and a basal pole of distinctive architecture and functions. The tachyzoite mechanical properties determine gliding and invasive capacities and largely arise from an outlying three-layered membrane or pellicle together with the underneath basket of stable but flexible cortical microtubules. Indeed, the tachyzoite encounters extracellular compartments of various mechanical properties before invading cells within which it expands population. The tachyzoite undergoes helical gliding thanks to two sub-membranous multimolecular machineries called glideosomes which rely on class XIV myosins (A and H) to translocate newly nucleated and dynamic actin filaments in a rearward direction along the parasite length. Gliding proceeds with a focal adhesion built through the capture of an extracellular ligand by a parasite surface-exposed adhesin that bridges the former with the actin cytoskeleton. Traction force is applied at this site, thus enabling the parasite to glide over it while posteriorly disengaging from the substrate along with dragging forces. Nevertheless, how cell adhesion couples with force production during gliding or how the polar architecture contributes to these forces remain unclear. Accordingly, the Ph.D. research focused on the biomechanical singularities of the tachyzoite and brought new insights on (i) the extracellular ligand requirements beneath productive helical movement, and (ii) the structural and functional contribution of a still uncharacterized 500 kDa basal pole protein named BCC7. In the first part, we combined high-resolution micropatterns with confocal video-microscopy and expansion microscopy and found that only one apical anchoring contact built by the tachyzoite with the substrate is sufficient to assemble a force transmission platform compatible with gliding. Next, we developed tunable surface chemistry based on PLL-PEG coupled with streptavidin/biotin platforms, which we biochemically and biophysically controlled by Quartz Crystal Microbalance with Dissipation monitoring to screen for minimal ligands of parasite adhesins. Using these combinatorial approaches, we highlighted the sufficiency of glycosaminoglycan species as substrates for productive interaction and helical gliding. We also demonstrated that the anteroposterior

membrane flow occurs in the absence of cell adhesion, taking advantage of anti-fouling surfaces. The second part combined biochemistry, mass spectrometry-based proteomics, with live and super-resolution microscopy to accurately position BCC7 at the interface between the Inner Membrane Complex (IMC) and myosinC, a motor typifying the basal pole of mature tachyzoites. These approaches also allowed monitoring of the anteroposterior trafficking of the protein as patches along with daughter cell assembly before the maternal material recycles into the newborn progeny. In addition, thirteen BCC7 partners were identified, several of which cluster in the IMC-like family. Two new IMC proteins, IMC35 and IMC36, were also described and shown to be differently expressed during the cell cycle. Therefore, this Ph.D. offers an unprecedented biophysical toolkit to interrogate the molecular mechanisms of cell-cell or cell-surface interfaces including beyond the *T. gondii* parasite which has proved promising for refining the gliding mechanistic model.

Keywords: *Toxoplasma gondii*, cell migration, live and super resolution microscopy, quantitative analysis, surface chemistry, cytoskeleton, cell biogenesis, cell polarity.

Résumé

Toxoplasma gondii est un microbe eucaryote unicellulaire du phylum des parasites Apicomplexa, qui dépend strictement de cellules pour son cycle de vie chez un large spectre d'hôtes homéothermes, dont l'homme. *T. gondii* a développé différents stades de développement infectieux appelés zoïtes parmi lesquels le tachyzoïte. Cette cellule polarisée de quelques microns possède une forme arquée dont les deux pôles ont une organisation structurale et fonctionnelle distincte. Le tachyzoïte navigue au sein des matrices extracellulaires et envahit activement les cellules hôtes permissives à la prolifération, en exécutant un mouvement par glissement hélicoïdal. Ce glissement est sous le contrôle de machines supramoléculaires appelées « glideosomes » qui, en position sous membranaire, utilisent des myosines de la classe XIV pour déplacer des filaments d'actine néoformés et dynamiques dans un mouvement antéro-rétrograde sur la longueur du parasite. Quand le flux rétrograde d'actine est couplé à celui d'adhésines ayant capturé le ligand présenté par la matrice extracellulaire, il entraîne le glissement du parasite vers l'avant. Cependant, la compréhension du couplage moléculaire entre la formation d'une adhésion et la production de force comme celle de la contribution du pôle basal aux forces de mouvement reste incomplète. Le projet de thèse a porté sur l'étude des singularités biomécaniques du tachyzoïte afin de caractériser (i)

les ligands extracellulaires minimaux requis pour un glissement hélicoïdal, et (ii) la contribution structurelle et fonctionnelle de la protéine BCC7 localisée au pôle basal. Dans la première partie, nous avons combiné des micropatterns à haute résolution avec la vidéo-microscopie et la microscopie d'expansion, et mis en évidence qu'un seul site d'ancrage sur le substrat initié par l'apex du parasite et sur lequel ce dernier progresse représente une plateforme de transmission de force suffisante pour permettre un glissement hélicoïdal. Ensuite, nous avons développé une chimie de surface ajustable basée sur des PLL-PEG couplés à des plateformes de streptavidine/biotine, que nous avons contrôlées à l'aide de la technique de microbalance à cristal de quartz avec mesure de la dissipation. En criblant les ligands minimaux candidats des adhésines parasitaires requis pour le glissement, nous avons établi que la présentation de glycosaminoglycanes sulfatés sur le substrat suffit pour une interaction productive avec la surface du parasite. Nous avons également démontré que le flux membranaire antéro-postérieur se produit en l'absence d'adhésion cellulaire, en tirant parti des surfaces contrôlées comme anti-adhésives. La deuxième partie de la thèse a combiné les approches de biochimie et de protéomique quantitative par spectrométrie de masse avec les microscopies dynamique et à super-résolution pour positionner la protéine BCC7 à l'extrémité de complexe de membrane interne (IMC) de la pellicule et le moteur myosine C, strictement associé au pôle basal des tachyzoïtes matures. Ces approches ont également permis de suivre le trafic antéro-postérieur de la protéine sous forme de patchs avant que le matériel maternel ne soit recyclé au sein des cellules filles naissantes. De plus, treize partenaires de BCC7 ont été identifiés, dont plusieurs font partie de la famille IMC. Deux nouvelles protéines IMC, IMC35 et IMC36, ont également été décrites ainsi que leur profil d'expression différentielle au cours du cycle cellulaire. En conclusion, ce doctorat a permis de développer une nouvelle boîte à outils biophysique d'intérêt pour étudier les mécanismes moléculaires des interfaces cellule-cellule ou cellule-surface, y compris au-delà du parasite *T. gondii*. Chez le parasite, il devrait permettre d'affiner le modèle mécanistique de la mobilité par glissement.

Mots-clés : *Toxoplasma gondii*, migration cellulaire, microscopie en temps réel et à super résolution, analyse quantitative, chimie de surface, cytosquelette, biogenèse cellulaire, polarité cellulaire.

Preamble

This Ph.D. work is structured into two separate but related chapters, each of them comprising a research article regarding the single-celled eukaryotic microbe *Toxoplasma gondii*.

The document begins with an **Introduction** providing the context of the evolutionary path of the Apicomplexa phylum which *T. gondii* belongs to, and the particularities of a group that has adopted a parasitic lifestyle. Then, the focus will rely on *T. gondii*, introducing its life cycle and main structural characteristics, with a zoom on the tachyzoite, the fast and motile developmental stage.

On **Chapter 1**, the attention is set on the characteristic motile behavior the tachyzoite presents, and the questions regarding the minimal requirements needed in order to generate movement, exploring the delicate interplay between adhesive forces and chemical surface ligands. Next, on **Chapter 2**, the focus shifts to the basal pole of the tachyzoite, with a newly characterized protein named BCC7. In each of these divisions, a dedicated background will guide the way that led to our research questions, followed by the main points of the work to introduce the corresponding research articles published or under peer evaluation. Both chapters also describe the wide set of biophysical technical developments that were implemented, which include among others, micropatterning, high-speed and super-resolution microscopy, expansion microscopy, quartz crystal microbalance with dissipation and mass-spectrometry based proteomics.

Finally, the **Conclusion** presents the complementation between the two main projects, and debate on the outlooks of the research, opening the gate, as usually happens in science, for even more interesting research and innovative techniques.

Lastly, in the **Annex** section there are listed the research articles resulted from different collaborative works, including a background and main highlights of each study.

List of abbreviations

| | |
|---------|---|
| AFM | Atomic Force Microscopy |
| AID | Auxin Inducible Degron |
| AIDS | Acquired Immunodeficiency Syndrome |
| AMA1 | Apical Membrane Antigen 1 |
| ATP | Adenosine triphosphate |
| BC | Basal Complex |
| BCC | Basal Complex Component |
| BIC | Basal Inner Complex |
| BIR | Basal Inner Ring |
| BSA | Bovine Serum Albumin |
| CDC | Center for Disease Control |
| cGMP | cyclic guanosine monophosphate |
| CMC | critical micelle concentration |
| CNA | Collagen-binding adhesion protein |
| Cryo ET | Cryo-electron tomography |
| DAG | Diacylglycerol |
| DDM | n-Dodecyl- β -D-maltoside |
| DNA | Deoxyribonucleic acid |
| ECM | Extracellular Matrix |
| EDC | 1-ethyl-3- [3-dimethylaminopropyl] carbodiimide |
| EGF | Epidermal growth factor |
| ELC | Essential light chain |
| ER | Endoplasmic reticulum |
| EV | Entry vesicle |
| F-actin | Filamentous actin |
| FCS | Fetal Calf Serum |
| FITC | Fluorescein isothiocyanate |
| FUSE | Far upstream element |
| GAC | Glideosome-associated connector |
| GAG | Glycosaminoglycans |
| GAP | Glideosome-associated protein |
| GFP | Green Fluorescent Protein |
| GPI | Glycosylphosphatidylinositol |
| GRA | Granule Proteins |
| HA | Hemagglutinin |
| HIV | Human immunodeficiency virus |
| HS | Heparan Sulfate |
| HAS | Human Serum Albumin |
| IAA | Indole-3-acetic acid |
| ICAM-1 | Intercellular adhesion molecule 1 |
| IEE | Ionophore induced egress |
| IMC | Inner Membrane Complex |
| IP3 | Inositol trisphosphate |
| kDa | kiloDalton |

| | |
|-------|--|
| KO | Knock-Out |
| LIC | Ligation Independent Cloning |
| MIC | Microneme protein |
| MLC | Myosin light chain |
| MRS | Multiple resistance sequence |
| MS | Mass spectrometry |
| MT | Microtubule |
| MTOC | Microtubule organizing center |
| Myo | Myosin |
| NA | Numerical aperture |
| NHS | N-Hydroxysuccinimide |
| NMT | N-Myristolytransferase |
| NP | Nonyl phenoxyethoxyethanol |
| OT | Optical tweezers |
| PA | Phosphatidic acid |
| PBS | Phosphate-buffered saline |
| PCR | Polymerase Chain Reaction |
| PDMS | Polydimethylsiloxane |
| PEG | Polyethylene glycol |
| PEST | Proline- glutamic acid – serine - threonine |
| PKG | Protein kinase G |
| PLL | Poly-L-Lysine |
| PM | Plasma membrane |
| POI | Protein of interest |
| PPM | Peripheral plasma membrane |
| PTM | Post-translational modification |
| PV | Parasitophorous vacuole |
| PVM | Parasitophorous vacuole membrane |
| QCM-D | Quartz Crystal Microbalance with Dissipation |
| RICM | Reflection Interference Contrast Microscopy |
| RON | RhOpry Neck protein |
| ROP | RhOpry Protein |
| SAG | Surface Antigen |
| SAR | Stramenopila, Alveolata, Rhizaria |
| SAv | Streptavidin |
| SDS | Sodium dodecyl sulfate |
| SEM | Scanning Electron Microscopy |
| SPN | Subpellicular Network |
| STED | Stimulated Emission Depletion |
| TFM | Traction Force Microscopy |
| TSR | Thrombospondin-1 type |
| TX | Triton-X |
| UTR | Untranslated Region |
| UV | Ultraviolet |
| VPV | Valine-Proline-Valine |
| WT | Wild-Type |
| ZCJ | Zoite-Cell Junction |

Contents

| | |
|--|----|
| Summary | 1 |
| Résumé | 2 |
| Preamble | 4 |
| List of abbreviations | 5 |
| 1. Introduction | |
| 1.1 When it started: Apicomplexan parasites phylogeny | 10 |
| 1.2 <i>Toxoplasma gondii</i>: here, there and everywhere | 13 |
| 1.2.1 <i>Toxoplasma gondii</i> life cycle | 13 |
| 1.3 <i>Toxoplasma gondii</i> infection and host immune control | 16 |
| 1.4 The <i>Toxoplasma gondii</i> tachyzoite stage | 17 |
| 1.5 The <i>Toxoplasma gondii</i> tachyzoite lytic cycle | 19 |
| 2. Chapter 1 | |
| Probing the <i>T. gondii</i>-substrate adhesion minimal requirement for gliding motility through live and super resolution imaging coupled with micropatterns and tunable surface chemistry | 24 |
| 2.1 Rationale and main objectives of the study | 24 |
| 2.2 Context and state-of-the-art | 25 |
| 2.2.1 The main mode of Eukaryotic cell migration | 25 |
| 2.2.2 Outside from the typical motility modes: Apicomplexa gliding motility | 28 |
| 2.3 Technical developments | 36 |
| 2.3.1 Designing controlled cell adhesive and cell repellent areas using micropatterning techniques | 36 |
| 2.3.2 Combining photolithography micropattern and live video-microscopy to monitor tachyzoite gliding behavior | 44 |
| 2.3.3 Coupling photolithography micropattern with Ultrastructure Expansion Microscopy for super resolution imaging of tachyzoites in contact with micropatterned areas | 46 |

| | |
|---|------------|
| 2.3.4 Designing specific tunable model surfaces for monitoring tachyzoite adhesive and motile capacities | 47 |
| 2.3.5 Implementing microbeads covalent bound for decoupling adhesion and membrane flow | 51 |
| 2.4 Main highlights of the study | 53 |
| 2.5 Publication - Vigetti et al., 2023 | 54 |
| 2.6 Discussion and perspectives | 108 |
| 2.7 Review - Vigetti and Tardieux, <i>Biol. Cel.</i>, 2023 | 113 |
| | |
| 3. Highlighting the apico-basal bipolarity of the <i>T. gondii</i> tachyzoite..... | 130 |
| | |
| 4. Chapter 2 | |
| Towards a better understanding of the <i>T. gondii</i> tachyzoite basal pole ... | 132 |
| | |
| 4.1 Rationale and main objectives of the study | 132 |
| 4.2 Context and state-of-the-art..... | 133 |
| 4.2.1 The <i>Toxoplasma gondii</i> tachyzoite division | 133 |
| 4.2.2 The IMC system assembles as the core of the tri-layered pellicle that delineates the tachyzoite and compartmentalize specific glideosomes | 135 |
| 4.2.3 A basal pole dynamically assembles below the IMC during endodyogeny with recruitment of specific components including myosin motors | 137 |
| | |
| 4.3 Implemented techniques to study the basal pole candidate BCC7 protein | 139 |
| 4.3.1 Bioinformatic analysis | 139 |
| 4.3.2 Engineering of tachyzoite lines expressing different reporters of interest. | 139 |
| 4.3.3 Biochemical characterization | 141 |
| 4.3.4 Mass-spectrometry based proteomics | 142 |
| 4.3.5 Scanning Electron Microscopy | 143 |
| 4.3.6 Coupling microfluidics and micropattern for long-recording videomicroscopy | 144 |
| | |
| 4.4 Main highlights of the study | 146 |
| 4.5 Publication – Vigetti et al., <i>Int. J. Mol. Sci.</i>, 2022 | 147 |
| 4.6 Discussion and perspectives | 170 |
| | |
| 5. Conclusion..... | 174 |
| | |
| 6. Annex..... | 176 |
| | |
| 6.1 Broncel et al., <i>eLife</i>, 2020 | 176 |
| 6.1.1 Context and questions | 176 |
| 6.1.2 Contributions to the publication | 177 |
| 6.1.3 Main highlights of the study | 177 |

CONTENTS

| | |
|---|------------|
| 6.1.4 Publication | 178 |
| 6.2 Pavlou et al., <i>ACS Nano</i>, 2020 | 217 |
| 6.2.1 Context and questions..... | 217 |
| 6.2.2 Contributions to the publication: technical innovations | 217 |
| 6.2.3 Main highlights of the study | 218 |
| 6.2.4 Publication..... | 219 |
| | |
| 7. References | 239 |
| | |
| 8. Acknowledgements..... | 254 |

1. Introduction

1.1 When it started: Apicomplexan parasites phylogeny

Approximately 1.500 million years ago, during the Proterozoic era, an evolutionary event took place: an endosymbiosis between a single-celled eukaryotic protist and a photosynthetic cyanobacterium. This process gave rise to several photosynthetic eukaryotic organisms including plants, green algae, and red algae (McCourt, 2016). Specifically for the last one, a second endosymbiotic event of red algae being engulfed by a heterotrophic eukaryotic protist created the SAR supergroup, named due to the initials of the clades Stramenopila, Alveolata, and Rhizaria (Adl et al., 2019; Cavalier-Smith, 1999). All these unicellular organisms have a membrane-based structure in common known as alveoli, made of flattened membranous vesicle-like sacs present beneath the plasma membrane, and which collectively form the pellicle (Gould et al., 2008).

Digging deeper into the Alveolata group, it is comprised of three eukaryotic phyla: Apicomplexa, Ciliata, and Dinoflagellata (Adl et al., 2019). The alveolates are present in a variety of ecosystems, and their lifestyle ranges from free-living for the micro-predators exemplified with ciliates and some phytoplankton dinoflagellates to parasitic with the majority of obligate intracellular apicomplexa. The Apicomplexa phylum, which encompasses more than six thousand species, relying on a variety of metazoan hosts to produce progeny (Levine, 1988). Apicomplexa are divided into four subgroups: Coccidia, Cryptosporidia, Gregarina, and Haematoxoa (Adl et al., 2019). Several members of these groups have been studied given their wide range of invertebrate and vertebrate hosts, and a handful of them are intensively investigated due to their medical and veterinary importance. **Figure 1** shows a representation of the phylogenetic tree displaying the evolutionary relationship between the subgroups.

First, the Coccidia group encompasses the likes of *Eimeria sp.*, *Neospora caninum*, *Sarcocystis sp.*, and most importantly, *Toxoplasma gondii*. The first three are mostly restricted to livestock, hence their veterinary importance and economic impact. *T. gondii*, on its part, is the causative agent of toxoplasmosis and one of the most prevalent and successful Apicomplexan parasites.

The group Cryptosporidia is known for the relation of its members as causative agents of diarrhea and gastrointestinal illnesses in several mammal species, including humans. Their most studied organism, *Cryptosporidium parvum*, distinguishes itself from other members of the Apicomplexa group as it lacks the second endosymbiotic acquired structure, the apicoplast, and also displays a reduced mitochondrion (Abrahamsen et al., 2004).

The Gregarina members are able to infect the intestine of several invertebrates, both aquatic and terrestrial. Unlike other parasites mentioned in this section, gregarines are almost exclusively restricted to invertebrates, with a few exceptions (Leander, 2008).

The Haematoxoa group can be further divided into Haemosporidia (with *Plasmodium spp.* the most prominent member) and Piroplasmida (*Babesia sp.* and *Theileria sp.* are examples of the members of the group). *Plasmodium spp.* are the causative agents of malaria in humans, causing approximately 600.000 deaths a year and being highly prevalent in tropical and subtropical regions, mostly in sub-Saharan Africa (*World Health Organization Malaria Report, 2022*). The number of cases and deaths have remained stable in the last years, mostly due to limited healthcare outreach in low-income countries, limiting the goal of achieving its eradication (Phillips et al., 2017). There are five species that cause malaria in humans: *P. falciparum*, *P. knowlesi*, *P. malariae*, *P. ovale* and *P. vivax*. Most of the scientific research is performed on *P. falciparum*, due to being the most deadly of the five, and on *P. berghei*, an easier culture species that causes malaria in rodents.

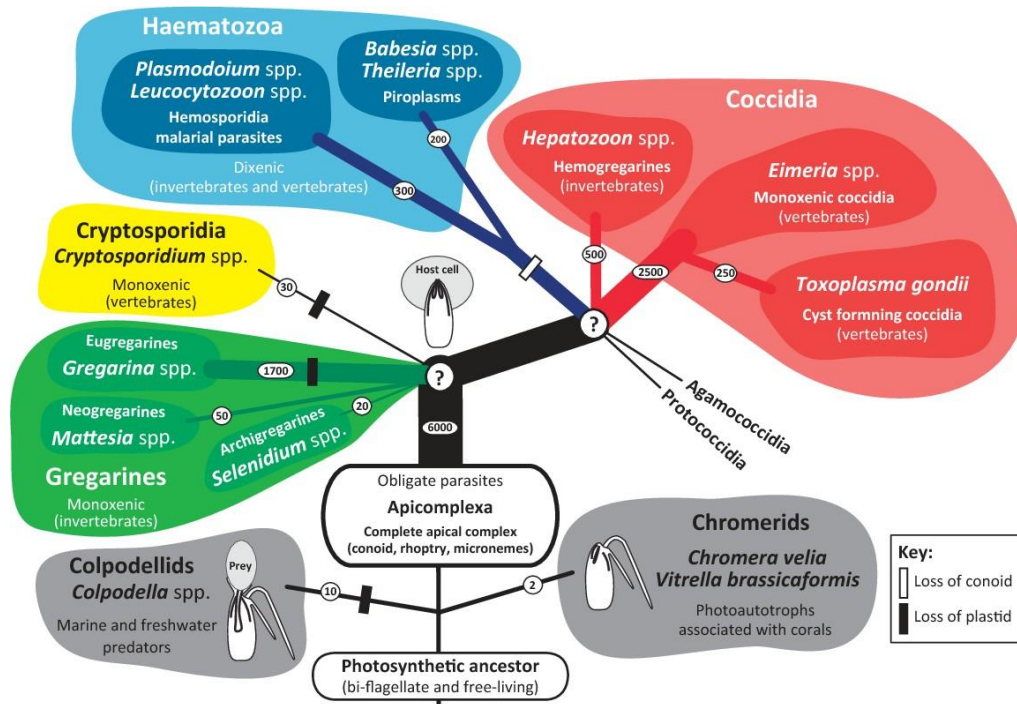


Figure 1 - Schematic representation of the Apicomplexan phylogenetic tree. The two closest non-obligatory parasites groups are also depicted. For the apicomplexan groups, the host organisms are indicated between parentheses. The thickness of the branches represent the diversity of organisms inside each group. Adapted from (Portman & Šlapeta, 2014).

Apicomplexa are a very diverse group, but nevertheless they all share some key characteristics:

- An apical complex, a structure featuring the apical pole of the infectious stages called zoites which determines their motile and cell invasive skills. The name Apicomplexa is in reference to this prominent complex in zoites (Levine, 1971).
- A complex life cycle that differentiates between sexual and asexual stages, also causing a difference in cataloging the hosts: the ones where parasites are able to sexually reproduce are classified as definitive hosts, while those where only asexual reproduction occurs are qualified as intermediate hosts.
- The apicoplast, a non-photosynthetic plastid with metabolic functions (with the exception of Cryptosporidia, as mentioned earlier) (McFadden & Yeh, 2017)

The work on this thesis is focused on one Apicomplexan responsible for major sanitary and economic impact, *Toxoplasma gondii*. Nevertheless, when discussing major findings in the studies for this parasite, comparisons with other Apicomplexans, mainly *Plasmodium*, will be addressed.

1.2 *Toxoplasma gondii*: here, there and everywhere

When the first years of the XX century were starting, two independent but related discoveries started the research on *Toxoplasma gondii*, which would span more than 110 years until our days. In Tunisia, Louis Manceux and future Nobel winner Charles Nicolle described a new protozoan organism in tissues of a small rodent common in the North of Africa, the gundis (*Ctenodactylidae gundi*), while conducting leishmaniasis research. They assigned it to this genus and named it *Leishmania gondii* (Nicolle & Manceaux, 1908). One year later, they would correctly separate it into a different genre, and they gave it the name *Toxoplasma*, derived from the Greek *toxon* ('arc') and *plasma* ('shape') (Nicolle & Manceaux, 1909). At the same time, in Brazil, Alfonso Splendore was describing a new protozoan inhabiting rabbits in Sao Paulo, which turned out to be *T. gondii* too (Splendore, 1909). These two discoveries were later deepened by the first description of human infection and congenital transmission (Wolf & Cowen, 1937). The understanding of the parasite life cycle together with the fine characterization of the host(s)-parasite interplay, which will be detailed below, took even more time, spanning into the 1970s (Dubey & Frenkel, 1973).

1.2.1 *Toxoplasma gondii* life cycle

Among the members of the Apicomplexa phylum, *Toxoplasma gondii* is generally seen as one of the most successful parasites on Earth, given its ability to infect virtually all homeothermic metazoan in order to achieve its complex life cycle (Dubey, 1998). *T. gondii* is able to infect and multiply in most nucleated cells. In humans, its ubiquitous presence is reflected in the high serological prevalence, which indicates that one-third of the world's population has been exposed to this parasite (Robert-Gangneux & Darde, 2012).

T. gondii's complex life cycle includes both sexual and asexual stages. The sexual stage occurs only within felids (*i.e.* the definitive hosts), while the asexual stages occur in all kinds of warm-blooded animals (*i.e.* the intermediate hosts) (Dubey & Frenkel, 1972). Along with the two types of hosts, *T. gondii* displays several developmental stages or morphotypes depending on the environmental context, among them the bradyzoite, sporozoite, and tachyzoite stages (Dubey & Frenkel, 1972).

We can start the description *T. gondii*'s life cycle by the common processes occurring in both the definitive and intermediate host (Hunter & Sibley, 2012). A host can get infected by two major means: the ingestion of (i) preys infected with the *T. gondii*'s cyst stage (*i.e.* bradyzoite) or (ii) water or food contaminated by sporulated oocysts containing sporozoites released in the environment through felid's feces. When in the gastrointestinal tract, the cysts are disintegrated by mechanical and enzymatic reaction, and either of the free developmental stages (*i.e.* bradyzoites or sporozoites) travel to eventually invade and infect the enterocytes of the small intestine tract. Once intracellular, they differentiate into tachyzoites, the rapidly dividing stage, that proliferates in the intestinal mucosa hence causing inflammatory foci that can lead to ileitis. Using their motile or invasive skills, tachyzoites leave the infection site as free cells or cargoes of immune cells through the lymphatic and blood vasculatures to eventually reach distant tissues, particularly more immunotolerant ones (*i.e.* central nervous system, striated muscles, testis, eye's retina). In these immune-privileged sites tachyzoites undergo bradygenesis, a cell differentiation process that converts them into bradyzoites enclosed within a protective cyst envelope/ wall inside host cells. Bradyzoites are slow-dividing zoites and support a semi-dormant or subclinical infection, accounting for the long-term parasitism phase.

As a difference to the previously described process, and occurring only on the gastrointestinal system of the definitive host, *T. gondii* bradyzoites can transform into merozoites, which penetrates the epithelial cells and start an asexual development of five morphologically different types, named A to E. This last one can produce male microgametes and female macrogametes, and their fusion produce millions of diploid zygotes that transform into oocysts (Dubey & Frenkel, 1972). Oocysts are released in the environment present in the felid feces, where they sporulate. The ingestion of contaminated food sources by these feces lets the cycle restart (Sena et al., 2023) (**Figure 2**).

T. gondii has evolved a dissemination strategy with a low rate sexual recombination (since only occurs in felids) and a widely spread clonal dissemination (occurring in all metazoans). Interestingly, the fusion of the gametes in the felids represents the only moment in the entire cycle of *T. gondii* with a diploid state, undergoing further meiotic division (D. J. Ferguson et al., 1974). Remaining in a haploid configuration would suggest some advantages for parasite dissemination as a beneficial mutation can be more easily spread to the offspring with a clonal multiplication.

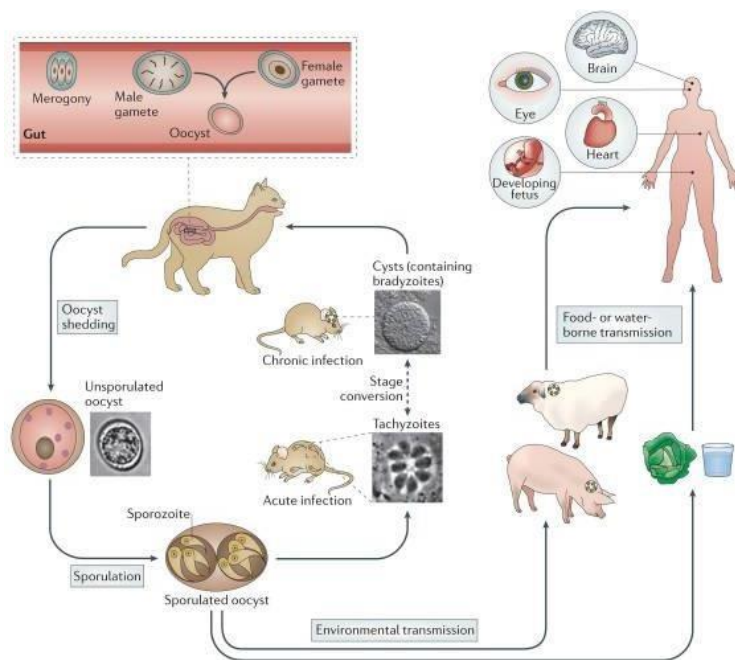


Figure 2 - Schematic of the complex life cycle of *T. gondii*. The life cycle starts with the ingestion of the encysted bradyzoites or sporozoites by virtually all warm-blooded animals. Both morphotypes can be removed of their cystic envelopes in the gastric tract and further infect the enterocytes of the small intestinal system. Then, they rapidly transform into the fast-replicating tachyzoite, a step coinciding with the start of the initial acute phase of the disease. As the innate immune system controls the expansion of the parasite population in the intestinal mucosa, it also promotes the dissemination towards distant tissues, where the conversion to the slow replicating bradyzoites occurs, a process culminating with the formation of intracellular parasite-loaded cysts. These cysts can be ingested by carnivorous or omnivorous animals, repeating the asexual cycle of *T. gondii*. In the case the new host is a felid, the cycle diverges with the formation of female and male gametes in the intestinal cells, whose fusion leads to the formation of a diploid zygote further shed into the environment as an oocyst with the felid's feces. Once sporulated, oocysts can survive in the environment for long periods of time, and contaminate water and food sources for other intermediate hosts. Adapted from Hunter & Sibley, 2012.

1.3 *Toxoplasma gondii* infection and host immune control

In humans, toxoplasmosis is one of the most common food-borne parasitic infection (J. L. Jones & Dubey, 2012), and a leading cause of food-borne illnesses in the US (*CDC - Toxoplasmosis*, 2021). Toxoplasmosis is usually clinically asymptomatic or mild in the acute phase of the infection since the innate immune system rapidly controls the expansion of the parasite-replicating population in the intestinal mucosa while promoting the persistence of cryptic parasites in deep tissues.

The acute phase of the infection starts with the early amplification of the tachyzoite population in the enterocytes of the small intestine. The dissemination of the tachyzoite population occurs via the draining lymph nodes and the lymphatics and is relayed by the bloodstream, allowing the tachyzoite to colonize intestine-distant tissues (Dubey, 1997). On immunocompetent hosts however, only a small fraction of tachyzoites is able to reach further tissues away from the initial site of infection, to differentiate into bradyzoites and persist long-termed. This persistent stage, supports the so-called chronic phase which is clinically sub-silent and was not considered as a direct threat to public health in immunocompetent humans (Courret et al., 2006). Indeed, a causal relationship between the presence of cyst in the host brain and a dopamine increase with consequences on cerebral disorders or behavioral changes in humans is currently investigated (Prandovszky et al., 2011).

However, in the case of immunocompromised people, both in transient or prolonged cases of immune system debilitation, several life-threatening toxoplasmosis-related diseases may emerge. In the case of immunosuppressive treatments such as chemotherapy, graft rejection protocols, organ transplants, or anti-autoimmune therapies, the bradyzoites can reactivate to the tachyzoite stage and produce severe damages (Dubey, 1998). As a clear example, during the 1980s and the HIV spread, *T. gondii* was a present opportunistic parasite, being the leading cause of AIDS-related encephalitis in HIV-immunocompromised people (Luft & Remington, 1992). Nowadays, even after the development of antiretroviral therapies, there is still a high prevalence of co-infection of *T. gondii* infection and HIV, especially in Sub-Saharan Africa and Middle East (Wang et al., 2017).

It is important to note that in tissue dissemination, the tachyzoite is able to cross the maternal-fetal placenta interface and infect the fetus during pregnancy (*i.e.* vertical transmission). Fetuses have no mature immune system and develop within the immunotolerant mother's uterus, being protected by the maternal's antibodies that cross through the umbilical cord. Tachyzoites are shown to use this path as well. In seronegative pregnant females, the tachyzoites colonize the placenta and spread in the fetus where they can cause developmental issues, the severity of which depends on the time of fetal infection (Montoya & Remington, 2008). The first trimester of pregnancy is usually associated with a lower mother-fetus transmission rate, but a higher probability of severe outcomes, such as hydrocephaly or mental retardation of the unborn child, and more prevalent pregnancy interruptions due to spontaneous abortions (J. Jones et al., 2003). Most of the consequences for early-stage primo infections impact the fetus's brain over time (D. J. P. Ferguson et al., 2013). As the pregnancy continues, the transmission rate augments, but the fetal development is less compromised, and often associated with vision impediments such as recurrent chorioretinitis and uveitis in children that can lead to blindness (Weiss & Dubey, 2009).

Taking into consideration the impact of *T. gondii* on human health, serological essays are routinely performed especially for pregnant people. Serological markers are mostly informative of the population which has been in contact with the tachyzoite stage, and considered to be a good indicator of the bradyzoite presence as well (Pappas et al., 2009). These tests are of prime importance to detect maternal infection during pregnancy and assess the relevance of prenatal and postnatal treatments (Sawers et al., 2022)

1.4 The *Toxoplasma gondii* tachyzoite stage

1.4.1 Main structures

The tachyzoite morphotype was the first zoite described by Nicolle and Manceaux, and named by Dubey and Frenkel in 1973 according to its high-replicative status (derived from the Greek '*tachos*' - fast,) (Dubey & Frenkel, 1972). The tachyzoite displays a bow or ellipsoid shape, and measures about 5-8 μm in the major axis and 1-2 μm in the minor one. It displays a strong polar architecture, with two distinctive apical and basal poles.

The apical pole is the morphological feature that gives the name to the Apicomplexa phylum and encompasses a particular cytoskeletal structure called the conoid, and two secretory organelles (*i.e.* micronemes and rhoptries). These appendage and organelles are critically required for the motile and invasive capacities of the tachyzoite, and are common to all apicomplexans (Harding & Frischknecht, 2020). The conoid is an appendage composed by tubulin fibers, two preconoidal rings and two intraconoidal microtubules (Haase et al., 2022). At the conoid base, the apical polar ring serves as a microtubule organizing center from which emerge 22 subpellicular microtubules (MTs) organized as a basket. The MTs elongate in a spiral configuration until approximately two-thirds of the tachyzoite, and are stabilized by interactions with the Inner Membrane Complex (IMC) (Liu et al., 2016). Both the conoid structure and the alveolar stabilization of the MTs contribute to the arc-shape of the tachyzoite (Harding et al., 2019) and support motility behavior and cell invasiveness (Barkhuff et al., 2011). More basally located is the rather spherical nucleus that encloses about 63 Mb of DNA surrounded by the endoplasmic reticulum (ER), both in its rough and smooth compositions due to the presence of ribosomes while a typical Golgi apparatus, is usually adjacent to the nucleus in an apical orientation. A single mitochondrion that contains 6 kb of DNA populates the cytoplasm along with the heterogenous population of secretory organelles known as dense granules and lipid droplets. A third genome made of a 35kb circle characterizes the plastid-derived apicoplast which most proteins are nuclear encoded control a variety of biochemical and metabolic pathways that are absent from host species, making it a promising drug target (Fichera & Roos, 1997; Sanchez et al., 2023). Other major compartments of the tachyzoite such as the IMC and the basal pole components will be provided a specific attention in the ‘Context’ section of **Chapter 2**, and a schematic representation of their localization can be seen on **Figure 3**.

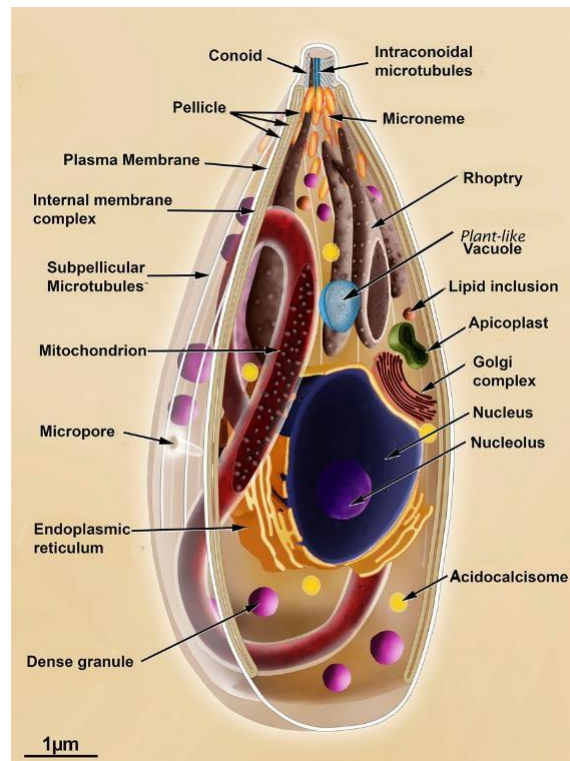


Figure 3 – Schematic representation of *T. gondii* tachyzoite displaying its organelles and structural elements. Adapted from Attias et al., 2020.

1.5 The *Toxoplasma gondii* tachyzoite lytic cycle

The tachyzoite follows a life cycle itself, once it emerges from the enterocytes from the small intestine, in order to expand its population. The lytic cycle consists of four steps: (i) the tachyzoite attaches its apical pole in the membrane of the host cell, and actively invades it, (ii) divides asexually by endodyogeny to proliferate within a concomitantly enlarging vacuole, (iii) egresses from the host cell, and lastly (iv) navigates through the extracellular matrix until reaches the next target host cell (**Figure 4**). The repetition of this lytic cycle leads to irreversible tissue damages that sign for the acute phases (initial or chronic) of the toxoplasmosis set of diseases.

Considering that the tachyzoite is the only *T. gondii* stage that (i) can be massively produced *in vitro*, therefore, enabling a panel of biochemical/ proteomics and cell biology approaches and (ii) is genetically tractable with the most advanced molecular genetic approaches, it is unambiguously the most relevant model to interrogate the mechanisms underlying high-performance motile, proliferative and invasive skills, major assets for the *T. gondii* expansion in the host.

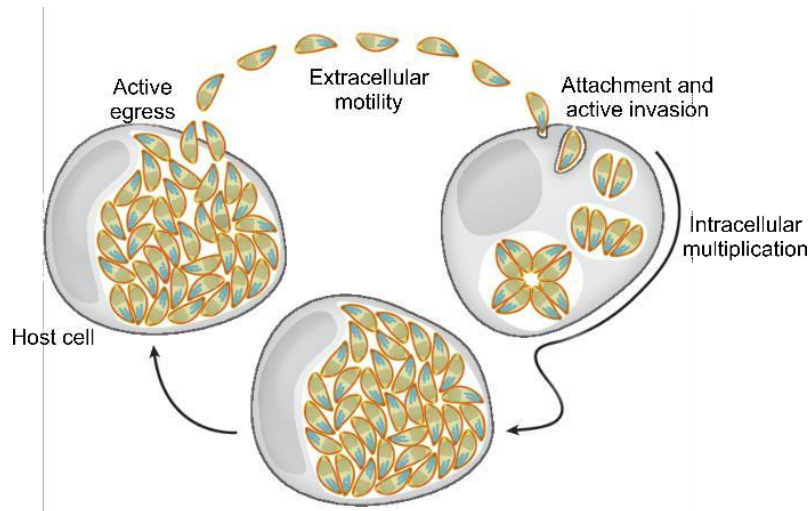


Figure 4 – Schematic representation of the *T. gondii* lytic cycle. The lytic cycle starts with the attachment of the apical pole of the tachyzoite to the host cell’s membrane, followed by active entry into the hosting cell within a budding entry vesicle that evolves as a cytoplasmic parasitophorous vacuole (PV). The PV serves as a niche for massive multiplication and once the progeny fills up the host cell, it actively egresses out of the dying host cell and repeats the cycle. Adapted from Blader et al., 2015.

The tachyzoite actively invades any nucleated cell from homeotherm metazoans, in a process which commonly proceeds after a minimal forward motion referred to as “minimal impulse”, or less frequently following substantial displacement (Bichet et al., 2014; Meissner, et al., 2002). First, the tachyzoite attaches to the host cell membrane using microneme-secreted adhesins, known as MICs, which form complexes and bind to different extracellular domains of transmembrane proteins at the host cell surface (Carruthers & Tomley, 2008).

After attachment, the invasion sequence *per se* starts with the secretion of a parasite protein complex, the so-called RhOptry Neck (RON) complex into the target cell Plasma membrane (PM), composed of the proteins RON2, RON4, RON5, and RON8. This complex tightly teams up with the micronemal protein Apical Membrane Antigen 1 (AMA1), and the two together can be seen as a multi-unit invasive nanodevice (Bichet et al., 2014; Pavlou et al., 2018). Once bridging the two cells, the multi-unit complex defines a torus-shaped Zoite-Cell Junction (ZCJ) (Gonzalez et al., 2009), where the structure of the RON2-AMA1 bridge shows its function in the force transmission process (Tonkin et al., 2011). Indeed, by pulling onto the torus, the tachyzoite forces the host cell PM to invaginate in a budding entry vesicle, which evolves as the parasitophorous vacuole (PV). The traction force comes from the Myosin H (MyoH) at the apical pole of the tachyzoite, later taking the relay up to the basal pole by Myosin A (MyoA)

(Bichet et al., 2016; Graindorge et al., 2016). In contrast with other types of intracellular protozoan ways of entry (*i.e.* phagocytosis, macropinocytosis, or endocytosis), it is the parasite that provides the force for budding and folding the PM in the entry vesicle. Importantly, as it is anchored into the host cell cortical cytoskeleton, the toroidal nanodevice withstands the parasite invasive and bridges the parasite's peculiar actomyosin motor to the host cell cortical actin cytoskeleton (Bichet et al., 2014; Pavlou et al., 2018). Specifically, the detection of a ring of F-actin coinciding with the recruitment of the Arp2/3 complex at the junction site suggests a *de novo* actin polymerization event while the functional contribution of cortactin, the actin-Arp2/3 regulatory protein, reinforces the view that the process is regulated by Arp2/3 complex (Gonzalez et al., 2009). In addition, the actin reaction could be fueled by the release of host cell actin monomers through the activity of toxofilin, a rhoptry-secreted actin-binding protein that promotes actin turnover as a cofilin homologue (Delorme-Walker et al., 2012; Poupel et al., 2000).

Once driven by the tachyzoite torque onto the nanodevice, the budding vesicle pinches off from the PM, giving birth to a parasitophorous vacuole (PV). To cope with the transition from an extracellular to an intracellular lifestyle, the tachyzoite rapidly remodels the vacuolar compartment as a niche sustaining progeny production (Pavlou et al., 2018). In the absence of the proper MyosinA motor, the tachyzoite retains only residual invasive capacity (Egarter et al., 2014). Also, once motorless tachyzoites have injected the RON-AMA1 invasive nanodevice in the target cell PM, there is a several-minute long process through which actin-driven membrane projections from the cell membrane form and push the tachyzoite through the ZCJ, thereby providing an alternative invasive force for entering the host cell (Bichet et al., 2016).

The invasion event lasts 20 to 30 seconds from the tachyzoite attachment in the host cell PM and the end of the process, which is led by a parasite's twisting motion that constricts and fissions the PM upstream of the junction, freeing the PV into the cytoplasm (Pavlou et al., 2018). **Figure 5** provides a schematic representation of both the invasion and membrane fission process.

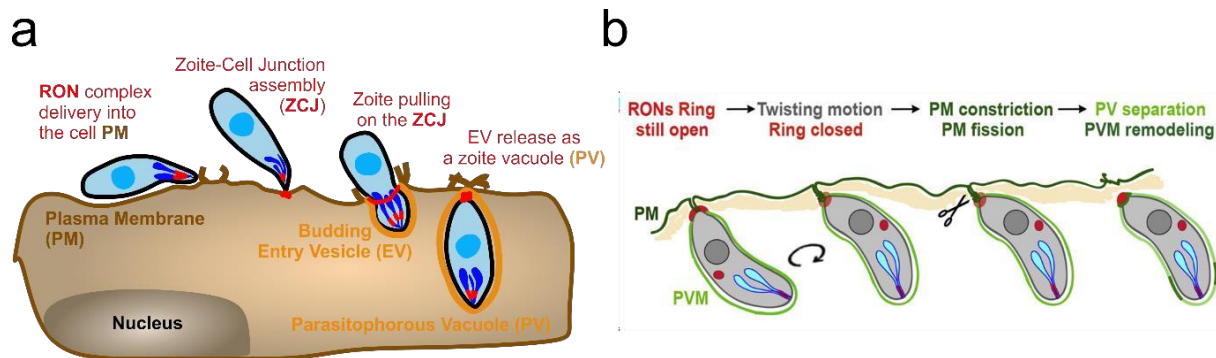


Figure 5 – (a) The tachyzoite invasion starts with the injection of the RON nanodevice complex, stored in the rhoptries, in to the host cell's plasma membrane (PM). The complex forms a ring-like shape connecting the parasite and the cell, known as Zoite-Cell Junction (ZCJ). Then, the tachyzoite pulls on the ZCJ to pass through, while creating the budding of an entry vesicle (EV). The EV, composed by host cell PM, matures onto a parasitophorous vacuole (PV) once the tachyzoite is fully internalized. (b) The excision from the host PM occurs after a rotational twisting motion from the tachyzoite, in an independent process from host cell dynamics. This twisting forces the two edges of the PM to constrict upstream the ZCJ thereby promoting local fusion and fission. Once the PV has separated from the PM, a signal is probably given for rapid and remodeling in the PV membrane, to generate the environment for parasite growth and multiplication. Adapted from Pavlou et al., 2018.

Once intracellular the asexual reproduction takes place inside the PV in a process called endodyogeny: two daughter cells are gradually formed by budding within the mother cell, which maintains its shape and polarity throughout the process. The endodyogeny features are refined on **Chapter 2**.

After six to seven rounds of endodyogeny multiplication, in an approximate timespan of 40 hours at laboratory conditions (*i.e.* 37°C, 5% CO₂), the vacuole containing the tachyzoites takes up most of the cytoplasmic space of the host cell. The egress from the PV is tightly regulated by signaling pathways requiring the activation of the cyclic guanosine monophosphate (cGMP)-dependent protein kinase G (PKG). This activation promotes the secretion of a set of micronemal perforins and proteases, as perforin-like protein 1 (TgPLP1), that create holes in the PV membrane (Arrizabalaga & Boothroyd, 2004; Kafsack et al., 2009). The microneme secretion is a calcium-dependent event, derived from the calcium ions mobilization from several tachyzoite sources, such as the ER, acidocalcisome or the IMC (Bonhomme et al., 1992). Several external stimuli associated with changes on host cell membrane homeostasis have been identified as microneme release triggers, such as a diminish in the potassium concentration, entry of sodium ions, changes on the external pH or the presence of serum

albumin (K. M. Brown et al., 2016; Moudy et al., 2001; Roiko et al., 2014). Furthermore, the tachyzoite uses the cysteine protease calpain to cleave and remodel the host cell cytoskeleton network, facilitating the parasite egress (Chandramohanadas et al., 2009); a similar process is used by *P. falciparum* merozoites to egress from red blood cells (Callan-Jones et al., 2012). Just before egress, the actin filaments present at the center of the rosette break in a calcium-dependent manner, with some remaining present at the residual body (Periz et al., 2017).

Once the tachyzoites are released from the host cell, they display high-speed migratory skills through many different extracellular matrices prior to invading the next target cell. As the *T. gondii*'s tachyzoite motility is a fundamental aspect that runs through the experimental approach of the articles in the thesis, it will be expanded in detail on **Chapter 1**.

2. Chapter 1

Probing the *T. gondii*-substrate adhesion minimal requirement for gliding motility through live and super resolution imaging coupled with micropatterns and tunable surface chemistry

2.1 Rationale and main objectives of the study

The tachyzoite has evolved peculiar motile skills, defined by a typical **gliding** mode of motility, that play a pivotal role during the active invasion of host cells, a critical event to escape from the host immune innate killing activities and to exploit the host resources for its perpetuation. In addition, tachyzoites also glide across cellular barriers, hence colonize deep tissues in which they can further transform into bradyzoites, a process which enhances chance of parasite transmission, hence parasitic sustainability (see *Section 1.2.1*).

Gliding is usually defined as an adhesion-dependent mode of cell motility that does not rely on external appendages such as flagella or cilia and support movement in the direction of the main axis of the cell through a diversity of force generating mechanisms. In the case of the *T. gondii* Apicomplexan, the current mechanistic model of gliding - which is commonly shared with other Apicomplexan zoites- is based on a unidirectional linear motor that lies beneath the zoite's membrane, and that is linked to an adhesive molecular system expressed at the cell surface. This adhesin-motor coupling is believed to be responsible for generating continuous unidirectional forces along the length of the tachyzoite, which in turn drives the cell body forward.

However, several studies from different labs using different approaches have recently highlighted the oversimplification of such model which, indeed does not fit with major datasets. Especially, main knowledge gaps remain among which:

- The contribution of localized periodic forces along the tachyzoite's body in the generation of productive movement, thereby questioning the unidirectionality of movement and linear motor as it currently stands.
- The required substrate-presented molecules to engage into intermolecular interactions with appropriate strength and dynamics for the timely adhesion-deadhesion coupling that drives the tachyzoite's displacement.
- The contribution and engagement of the antero-posterior membrane flow to gliding.
- The 3D organization of F-actin at the force productive adhesion site(s).

Based on our previous work, our hypothesis is that the tachyzoite interacts with the substrate to create a spatially defined discrete adhesion site on the substrate, which would be not only necessary *but also* sufficient for force generation and subsequent gliding. To test this hypothesis, we chose to deconstruct the contribution of parasite-substrate adhesion by using a minimalistic work frame. In addition to identifying the minimal substrate area to accommodate productive adhesion for force generation, we also investigated what would be the minimal adhesin ligand that would be required for such productive anchoring platform. To this end, we implemented and coupled several biophysical and biochemical methods like (i) micropattern to create high-resolution distinctive adhesion areas, (ii) expansion microscopy and high-resolution imaging to resolve at a high-spatiotemporal scale the gliding process on complex surfaces, and (iii) tunable surface layer constructions to characterize given molecules that account for the tachyzoite's locomotion.

As the project encouraged the innovation in several biophysical technologies, in the following *Section 2.3* we have highlighted the technical challenges we had to solve in this study (Vigetti et al., 2023, advanced draft unpublished). Also, as the Apicomplexan community should benefit greatly from different biochemical and physical synergies on state-of-the-art technologies, we discuss the utilization of them in a recently published review article (Vigetti & Tardieux, 2023).

2.2 Context and state-of-the-art

2.2.1 The main mode of Eukaryotic cell migration

In the late XVII century, the Scientific Revolution was taking place in several countries in Europe, and with it, one invention that would (literally) illuminate our understanding of the world that goes beyond what our eyes are capable of perceive. It was during this time that Antoine van Leeuwenhoek and Robert Hooke first designed and tested several lens-based apparatuses that would pave the way to centuries of microscope development and applications until the current generation of practical far-field and real-time super-resolution imaging devices. These devices are nowadays widely used in optics, biology, medical science, nanotechnology, and other related interdisciplinary fields.

Van Leeuwenhoek and his crafted lenses provided the first sight of microorganisms, today named protists, which were swimming and meandering on aqueous solutions. Across the English Channel, Hooke proposed that the individuals observed in these specimens were the smallest building blocks of the living organisms, and coined the term ‘cell’. The convergence of both observations was the foundation for two nascent fields, one of the studies of microscopic organisms, microbiology, and the technical complementation to study those objects, microscopy. What van Leeuwenhoek realized when observing for the first time the spermatozoids under a lens, is that these types of cells and many others don’t just randomly vague in their environment, but rather have a directed type of movement. Indeed, cell motility dictates physiological processes as diverse as tissue formation during embryogenesis, tissue healing and renewal, immune surveillance among others, and in the case of physio-pathological disorders many cerebral diseases, as well tumor metastasis to cite only a few (Dupré et al., 2015; Paluch & Raz, 2013; Reig et al., 2014).

Non-swimming cell motility is commonly categorized into two main modes: crawling, also known as mesenchymal, and blebbing or amoeboid motility. From a biomechanics point of view, these two types of locomotion require different cytoskeleton dynamics for force generation, and accordingly they also differ on the changes on cell protrusion they produce. Here, we also need to differentiate between motility and migration: motility denotes spontaneous non-directional movement, whereas migration entails a directional movement as a response to a cell attractant or repellent; cell adhesion can lead the directionality of the migration, through the formation of stabilizing protrusions (Petrie et al., 2009).

Crawling across and between solid surfaces was the first mode to be described. It proceeds through the formation of a thin protrusion of the plasma membrane and cytoplasmic content at

the cell leading edge, known as lamellipodia, powered by the polymerization of new branched actin networks (Bershadsky & Kozlov, 2011). To ensure proper lamellipodia formation, nascent focal adhesions form being mediated by the cell surface transmembrane integrins that cluster, and bridge the cell cytoskeleton with the substrate. Some of these focal adhesions mature and recruits the myosin contractile molecular motor which controls the development of traction force to pull the cell forward. Once new adhesions assemble at the protruding edge, the older ones are located at the cell trailing edge and must disassemble to enable net forward translocation of the cell body. Nevertheless, in more constraint environments and in particular in 3D, cells can also display a different type of migration, first observed on Amoeba, that proceeds through the protrusion and retraction of a membrane bleb structure known as pseudopods (Lämmermann & Sixt, 2009).

Both of these types of movements are intertwined as cells can adapt and commit to one or the other in response to physical and chemical properties of the surrounding extracellular matrix (*i.e.* stiffness, confinement, viscosity) (Ghosh et al., 2021; Gupta et al., 2016; Yamada & Sixt, 2019). Mesenchymal locomotion is usually preferred by cells when the surroundings permit the creation of strong focal adhesions, through the bridge that integrins create between the internal cytoskeleton and external elements such as ECM ligands or cell surface-exposed ligands. Amoeboid locomotion, on the other hand, involves weaker interactions and lower traction forces, with a more significant cell body deformation. This type of movement differs as there is no need to disassemble complex adhesive platforms like crawling cells do (Paluch & Raz, 2013); for instance, this blebbing mode allows neutrophils to move at speeds up to 19 $\mu\text{m}/\text{min}$ during chemotaxis assays (Hoang et al., 2013).

Briefly, the molecular structure behind the cell contraction and motility is the actomyosin system. Actin can exist as globular monomers (G-actin) or polymerize as filaments (F-actin); myosin II, on its part, is composed by a head/ neck region that is attached to the actin filaments, and a tail that connects to other filaments. Myosin motors hydrolyze ATP slide backwards on the actin filaments, in a three-step process: binding, power stroke and unbinding (Pollard, 2016). The continuous repetition of this process guides the cell forward, showing that the cell movement is tightly spatiotemporally coordinated, as mechanical changes on different proteins in the cytoskeleton change the force production center.

2.2.2 Outside from the typical motility modes: Apicomplexa gliding motility

If now we refer to peculiar types of locomotion that can't be assigned to the previous categories, we can consider the *T. gondii* tachyzoite as a very interesting model to decipher cell motility. While displaying a high speed motile behavior (up to 3 $\mu\text{m/s}$), the tachyzoite always maintains its apicobasal polarity, and doesn't create any lamellipodia or blebbing while propelling forward.

The first observations of how the zoites move outside the host cells were performed in the early 1960s with *Plasmodium* sporozoites (Vanderberg, 1974; Yoeli, 1964), coining the term gliding for their peculiar motility. In the next decades, videomicroscopy essays for *T. gondii* tachyzoites performed on 2D surfaces allowed the categorization of the types of movement the tachyzoite performs, and the major characteristics (Frixione et al., 1996; Håkansson et al., 1999). On a 2D surface, the tachyzoite only possess three types of movement: (i) twirling, consisting in the basal pole attached to the surface and the rest of the body rotating axially in a vertical plane, (ii) circular, a clockwise movement of the tachyzoite lying down on its major axis, and (iii) helical, a counterclockwise complex adhesion/ deadhesion steps from both poles, that propels the tachyzoite apically forward. The most common 2D surfaces used on *in vitro* studies include coating glass coverslips coated with fibronectin, PLL, heparin, FCS or BSA (*i.e.* Carruthers et al., 2000; Gras et al., 2019; Håkansson et al., 1999; Pavlou et al., 2020). Of note, the helical movement is the only one present in the locomotion of the tachyzoite *in vitro* using extracellular matrix components (*i.e.* Matrigel or collagen fibers) or *ex vivo* (*i.e.* using a mouse earflap as a model) (Leung et al., 2014), and it is suspected *in vivo* too similarly to what has been reported for *Plasmodium* sporozoites (De Niz et al., 2017). This corkscrew-like behavior is also observed for *Plasmodium* sporozoites when they migrate on hepatocytes or dermis, even though they typically move in circles on hard 2D surfaces *in vitro* (Amino et al., 2006; Frevert et al., 2005).

Helical and circular types of gliding are considered 'productive' types of movement, since the zoite displaces forward, unlike the 'unproductive' twirling which maintains the tachyzoite attached to the same adhesion point. As a result, both types can be seen in the tachyzoite navigation prior to a host cell invasion *in vitro*, in addition to another type of short displacement referred to as a 'minimal impulse', which includes a sudden conoid extrusion associated with body elongation before an apical contact with the host cell membrane and the typical release

of the invasive nanodevice (Bichet et al., 2014). Helical and circular movements have in common characteristics that (i) they are most often unidirectional and apically directed, (ii) they require dynamic and periodic attachment to the substrate coinciding with the stop-and-go attributes, (iii) they support speeds ranging in the 2-3 $\mu\text{m/s}$, and (iv) they proceed without marked changes in cell shape, in particular without the formation of membrane protrusions along the process.

One additional hallmark of gliding is the trail left by the tachyzoite which reflects the composition of the parasite surface i.e. a mix of membrane lipids and surface proteins. This material is shed at the basal pole of the tachyzoite, in the posterior end of the cell once it glides (Håkansson et al., 1999). The most common strategy to visualize them *a posteriori* using immunofluorescent staining of the GPI-linked surface antigen 1, TgSAG1, which is abundantly present in the surface of the tachyzoite (Carey et al., 2004; Dobrowolski & Sibley, 1996); this shed trail can also be seen on 3D matrices (Leung et al., 2014). Most studies use this shed trail as an evidence of gliding, and use it to study, for example, the impact of inhibitors for motility (Carruthers et al., 2000). Although it is known that the shedding occurs due to proteolysis action from a set of proteolytic enzymes (*i.e.* subtilisins, rhomboid proteins) in the membrane (Dowse & Soldati, 2005), the functional contribution of this trail to movement remains elusive. It was proposed that it could be due to a leftover in the endocytic recycling system, as a critical process for homeostatic maintenance (Gras et al., 2019; Koreny et al., 2023).

2.2.2.1 The tachyzoite gliding machinery

As mentioned in *Section 1.5*, tachyzoite is a morphotype highly specialized for locomotion and replication.

The glideosome, a hallmark force machinery of the Apicomplexa zoite

To understand how forces are generated during gliding, it is important to analyze the organization and function of the different components that assemble as a supra-molecular sub-membranous machinery which powers movement. Accordingly, this composite structure was defined as glideosome, and was first identified and characterized beneath the length of the tachyzoite body but excluding the two polar regions. A major breakthrough came with the discovery of TgMyoA, which belongs to the unconventional class XIV of myosins and was

shown *quasi* essential for parasite survival (Meissner, Schlüter, et al., 2002). With the advances in molecular genetic tools and techniques, and the success of conditional gene silencing, it was then confirmed that MyoA has a prominent but not essential role during gliding motility *in vitro* (Egarter et al., 2014) while a poorly efficient alternative mode of entry was highlighted when looking at the residual cell invasive capacity of MyoA motorless tachyzoites *in vitro* (Bichet et al., 2016).

Structurally, the MyoA that is composed by a single head with the actin binding motor domain and a neck domain which interacts with the light chains: myosin light chain 1 (TgMLC1) and the essential light chains (TgELC1 and TgELC2) (Bookwalter et al., 2014; Meissner et al., 2002; Williams et al., 2015) (**Figure 6**). TgMyoA is much smaller than myosin II, resembling more to the ones present in the fast skeletal muscles. In fact, TgMyoA was initially shown to move at about 3 $\mu\text{m/s}$ on mammalian actin, which matches the speed of the tachyzoite gliding (Herm-Götz et al., 2002.)

Additionally, three gliding-associated proteins (TgGAP40, TgGAP45 and TgGAP50) whose function is the anchoring between the IMC and the PM were identified (Fréchal et al., 2010; Gaskins et al., 2004). TgGAP45 fills the entire space between the PM and the IMC, while the other two are shorter and remain in the IMC side of the TgMyoA. The anchoring of the glideosome in the parasite cytoskeleton is the docking source for the force generation; deletion of the associated proteins such as TgGAP45 result in deficiencies in motility, invasion and egress (Fréchal et al., 2010).

Aside from this MyoA-based , two variations of glideosomes were next identified in the *T. gondii* tachyzoite, one in the apical complex and other in the basal one (Fréchal et al., 2014). At the conoid, the myosin present is TgMyoH, and GAP70 is the linker of the glideosome with the PM whereas in the basal pole, TgMyoC and TgGAP80 take the relay from TgMyoA and TgGAP45 respectively (Fréchal et al., 2014).

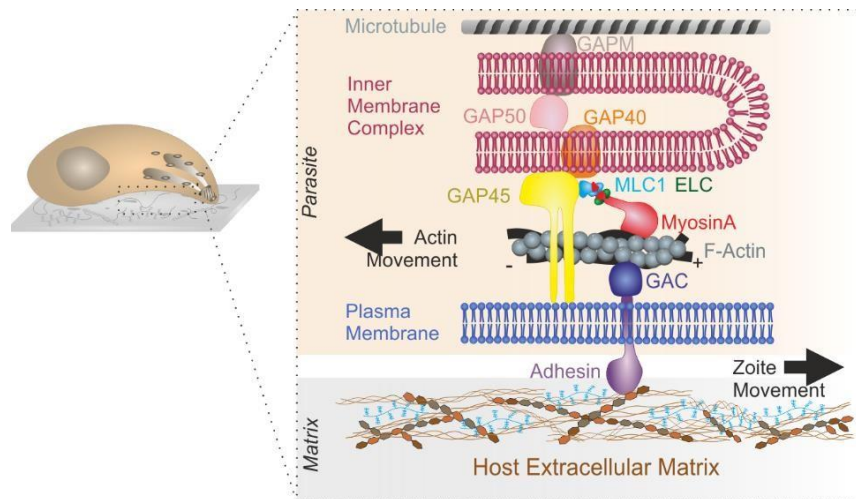


Figure 6 – (a) The glideosome main component is the class XIV myosin A, which is anchored in the outer membrane of the IMC and interacts with the actin filaments in the space within the outer PM. Several glideosome elements bridge and regulate MyoA, such as GAP45, MLC1 and ELC.

Besides the myosins previously mentioned, eight additional myosins that belong to 5 of the 31 eukaryote family classes (*i.e.* classes VI, XIV, XXII, XXII, XXIV) are expressed in *T. gondii* and differentially located from the plasma membrane (MyoD and MyoG) to the centrosome (MyoK) and the maternal residual body (MyoI) (Mueller et al., 2017). Only MyoA and MyoF are conserved across the entire phylum with the latter involved in apicoplast division (Jacot et al., 2013).

Different components of the glideosome have been identified as druggable targets. As example, the actin polymerization inhibitor Cytochalasin D has been demonstrated as motile and invasive blocker (Dobrowolski & Sibley, 1996). For MyoA, in contrast, it has been only recently identified compound named KNX-002, which targets this unusual myosin and inhibits parasite motility and growth (Kelsen et al., 2023); similar studies have also been performed for *P. falciparum* (Trivedi et al., 2022). Before these studies, the blocking effects towards MyoA were indirect, targeting the myosin light chain kinase or the myosin ATPase activity (Dobrowolski, Carruthers, et al., 1997).

An unusual actin and actin dynamics

Apicomplexan parasites have divergent actins with respect to the ‘conventional’ actins present in yeast or mammalian cells. *T. gondii* possess a single copy actin gene (ACT I), sharing ~80% sequence identity with the mammalian isoform, and is present mostly in globular form (97%)

(Dobrowolski, Niesman, et al., 1997). *Plasmodium spp.*, on its side, carries two actin genes: PfACT I has a 97% similarity with the *T. gondii* ACTI, but also carries a second isoform, PfACT II (Dobrowolski, Niesman, et al., 1997; Wesseling et al., 1988). The parasite's actin also differs from other eukaryotic actins as they form short (~100 nm) and unstable filaments (Sahoo et al., 2006; Skillman et al., 2013).

In eukaryotes, actin polymerization starts with an energetically unfavorable step where monomers nucleate into a trimer, followed by an elongation step with a lower equilibrium constant. This type of polymerization is called cooperative, and as a result the polymer formation occurs only above a critical monomer concentration (Smulders et al., 2010). On the other hand, actin polymerization dynamics on *T. gondii* has been proposed to follow an isodesmic model, which would allow nucleation and elongation as equally energetically favorable, and which could explain the short filaments (Skillman et al., 2013). Nevertheless, this model lacks validation.

Moreover, from the actin regulatory factors that eukaryotes usually express to control actin dynamics, exemplified with the Arp actin nucleating complex and the formin family, there are only three formin members present, all from the formin family: formin1 is an essential protein and in combination with formin 2 are required for actin filaments elongation during gliding motility and invasion (Daher et al., 2010); formin3, on the other hand, is much less abundant and dispensable, and is localized in the residual body with intravacuolar cell-cell communication (Daher et al., 2012; Tosetti et al., 2019). Actin polymerization is also regulated by the protein coronin, which binds to F-actin barbed-ends and promoting the branches expansion, creating actin bundles, especially at the posterior end of the parasite (Salamun et al., 2014). The tachyzoite actin filaments were difficult to visualize *in vivo* due to their short and rapid-turnover rate, and since actin labelling techniques (*i.e.* LifeAct, phalloidin) don't mark F-actin inside the parasites. Nevertheless, a new method using a line that expresses a chromobody fused-actin showed an actin bundle concentration that goes in the vacuole and connects the tachyzoites (Periz et al., 2017). Unfortunately, it is still not resolute enough to discriminate single actin filaments, which could be possibly achieved in the near future using super-resolution microscopy techniques.

The tachyzoite adhesins as bridges between the extracellular world and the force powering machinery

In order to move forward the tachyzoite needs to interact with the surroundings and create an anchoring point, in either extracellular matrix components, adhesive substrates or extracellular host cell receptors. To generate this attachment, the tachyzoites rely on the secretion of adhesins, mainly micronemal proteins (TgMICs), which need to be secreted in a timely manner by complex signaling cascades (Bullen et al., 2019). The MIC protein family includes around 20 different types of proteins, termed MIC1 to 20 (Carruthers & Tomley, 2008). The major part of them exhibits multiple copies of different domains known crucial for interacting with molecules from the extracellular matrix or exposed at the cell surface. These adhesive domains include the thrombospondin-1 type (TSR), EGF-like and lectins (Carruthers & Tomley, 2008). Many MICs are anchored to the PM by transmembrane domains after they are secreted, as several are categorized as type I transmembrane proteins with short cytoplasmic tails (*e.g.* MICs 2, 6, 7, 8, 9, 12, 14, 15 and 16). The membrane anchored MICs can work as binding partners for other secreted adhesins, such as MIC6 for MIC1 and MIC4, and MIC2 for the MIC2 associated protein (MIC2AP) (Huynh et al., 2015).

The exocytosis of proteins from micronemes and rhoptries occurs at the apical tip of the tachyzoite where the canals of both types of vesicles are opened (Mageswaran et al., 2021). Because micronemes undergo regulated secretion to timely release their products, a number of studies have interrogated the upstream signaling pathway that could direct the secretion process. Briefly, secretion is switched following cGMP production that in turn activates the protein kinase G (PKG) and eventually promotes the membrane phospholipid phosphatidylinositol-4, 5-bisphosphate (PIP₂) production (Bullen et al., 2019). The latter is further cleaved by the phospholipase C activity into diacylglycerol (DAG) and inositol trisphosphate (IP₃). IP₃ promotes calcium efflux from the endoplasmic reticulum (a usual Ca²⁺ intracellular store) or other stores and calcium binds to calcium-dependent protein kinases (CDPKs) which phosphorylate numbers of substrates involved in microneme exocytosis (Carruthers & Sibley, 1999). DAG is also involved through the production of phosphatidic acid and the acylation of microneme surface-exposed proteins. Extracellular parasites can be treated with a variety of compounds to stimulate microneme secretion, as (i) A23187, which acts by elevating the cytosolic Ca²⁺ concentrations (Carruthers & Sibley, 1999); (ii) ethanol, acting by elevating IP₃ and phosphatidic acid (PA) concentrations (Carruthers et al., 1999); (iii) zaprinast, an inhibitor of cGMP phosphodiesterase (K. M. Brown et al., 2016); or (iv) bovine serum albumin(BSA), by elevating the concentration of cGMP (K. M. Brown et al., 2016).

The ligands of the different MIC proteins remain largely unknown, although the ectodomains in their structure suggest different motifs for substrate binding. MIC2 is reported to be the adhesin that binds to the intercellular adhesion molecule 1 (ICAM-1) when the tachyzoite crosses cellular barriers through a paracellular route (Barragan et al., 2005). Whether they actually use this route to cross barriers in particular *in vivo* is still unclear. Instead, multiphoton *in vivo* imaging has enabled to monitor free tachyzoites in the bloodstream and revealed these can attach to central nervous system (CNS) endothelial cells, invade and replicate, and eventually egress from these cells, potentially depositing these egressing parasites into the CNS parenchyma (Konradt et al., 2016).

MIC2 is also the major adhesin candidate during gliding in an acellular context as it is shown to bridge with the *de novo* formed actin filaments through the glideosomes-associated connector (GAC) (Jacot et al., 2016; Kumar et al., 2023). Several direct and indirect pieces of evidence unambiguously argue for a prominent MIC2 contribution to gliding. Using viable MIC2 knock-out strains, live imaging in 2D conditions show that parasites lacking MIC2 have significant attachment impairments and affects helical gliding by reducing the initiation and movement duration (Gras et al., 2017; Meissner, Reiss, et al., 2002); in 3D conditions, the absence of MIC2 also reduces the capacities to exert forces on the ECM (Stadler et al., 2022). Furthermore, to disengage the adhesion points and create new focal points, proteases located inside the membrane like subtilisins and rhomboid protease 4 (TgROM4) are responsible for this cleavage (Buguliskis et al., 2010). When TgROM4 is removed, TgMIC2 could not be cleaved and accumulated in the outside of the tachyzoites, impairing their gliding and invasive capabilities (Huynh & Carruthers, 2006; Shen et al., 2014).

Implementing force measurement to mechanistically decode zoite gliding

If we dig deeper into the helical type of gliding on a flat surface, the Tardieux lab has recently detailed the mechanics of force generation and the poles' coordination for engaging in locomotion (Pavlou et al., 2020). First, the tachyzoite needs to establish a necessary apical adhesion with the substrate; without this starting point, there is no beginning of helical gliding. This apical anchoring applies the traction force momentum for a tachyzoite's deformation, termed 'kink', measured using Traction Force Microscopy (TFM). This traction force coincides with a bending behavior in the subpellicular MTs; from these measures and observations we

proposed that this angled conformation is the energy accumulation step coming from the MyoA displacement, and when released it concurs with the maximal forward acceleration. After, the basal pole displays a dragging force up to the point where the apical anchoring was established, and the cycle is able to repeat to guarantee forward locomotion (**Figure 7**).

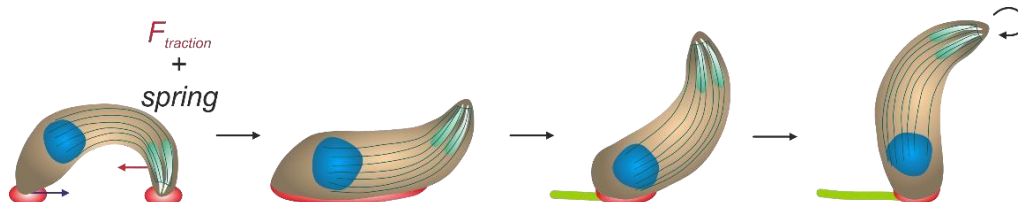


Figure 7 – Schematic of the tachyzoite helical gliding on 2D surfaces. First, the apical adhesion site creates a firm anchoring point, and a subsequent deformation that generates an apical traction force and a spring-like force sustained by the microtubule contraction. The release of this contraction propels the tachyzoite forward, with a spread of the contact points and promoting a dragging force in the basal pole. After the basal pole reaches the location of the first apical anchoring, the apex lifts and the tachyzoite performs a body rotation, liberating the apical pole to create a new anchoring and repeat the cycle. Adapted from (Pavlou et al., 2020).

Correlating with the *Plasmodium* sporozoite, motility is also limited by the creation and turnover of discrete adhesion sites, on a stick-and-slip repeated process (Münter et al., 2009). On 2D surfaces, sporozoites first attach to the substrate at both poles, measured by Reflection Interference Contrast Microscopy (RICM). Then, a larger adhesive patch towards the anterior pole appears, subsequently disengaging the front pole. This new central adhesion site is the force anchoring site to pull forward the cell's body. After, TFM showed stalling forces from the basal pole, up to the site of the new central anchoring.

In the case of 3D environments, different live imaging studies show that the *T. gondii* tachyzoite only moves in a locomotive path that closely resembles the helical gliding, in a corkscrew-like trajectory. First, *in vitro* videomicroscopy experiments using Matrigel (Leung et al., 2014) or fibrillary collagen (Pavlou et al., 2020) environments, show that the tachyzoite propels forward by velocity peaks as it releases its body curvature in the gel's spaces, or by pulling on the fibers to generate their acceleration, respectively. Recently, it has been shown using 3D TFM that the tachyzoite creates a circular zone of attachment within the extracellular matrix, through which the tachyzoite squeezes leading to a visible constriction in its body in the focalized point of attachment (Stadler et al., 2022).

2.3 Technical developments

2.3.1 Designing controlled cell adhesive and cell repellent areas using micropatterning techniques

The first step was to find the appropriate experimental setup to generate differential adhesive and anti-adhesive surfaces, to confine the tachyzoite movement possibilities, and restrict its body's contact points with the substrate. To create the microfabrication of differential 2D surfaces we employed a technique known as micropattern.

Micropatterns have multiple applications in the different fields of cell biology, *i.e.* to study cell-cell interaction (Dow et al., 2022), cell interactions in tissue-like constructions (Rim et al., 2018), cell-substrate interaction (Ermiş et al., 2018), F-actin stress fiber formation and morphogenesis (Théry, 2010; Théry et al., 2007), force generation and migration (Brückner et al., 2021) among other fields. As a result of its diverse application, several protocols have risen and can be divided into three categories: photolithography based patterning, microcontact or stencil microprinting, and microchannel printing. A schematic of them can be seen on **Figure 8**; the three main categories have a common step that first the anti-adhesive surface is formed, followed by a disruption of it in some patches to create the second type of surface, the adhesive one. The methods tested in this work were both from the photolithography based category, and as such they are first introduced to later discuss the reasons behind the choice made.

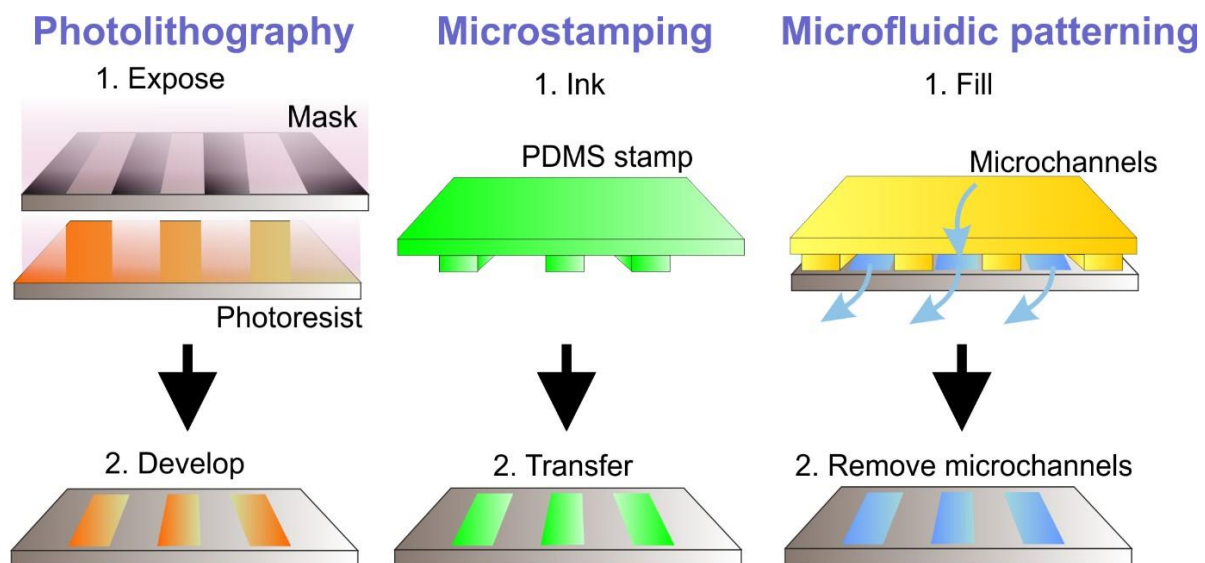


Figure 8 – Schematic of the three main strategies for micropattern fabrication. (1) Photolithography micropattern uses a mask to protect selected areas of a passivated surface, and then expose it to UV light. The areas that were exposed to the UV will be destroyed, leaving the place for adding a second biomolecule. This protocol will be detailed in Section 2.2.1.1 (2) Microstamping, also known as micro-contact printing, involves the creation of an elastic polydimethylsiloxane (PDMS) stamp, which is embedded on different types of biomolecules and transferred to silanised substrates. (3) Microfluidic micropattern also uses a PDMS mold, but in this case to generate microchannels that will delimit the inflow of biomolecules on the surface. As different tubes can be connected to the different channels, this technique allows the creation of micropatterns with different molecules at the same time. Figure adapted from Folch & Toner, 2000.

2.3.1.1 Photolithography micropattern

The general concept of photolithography micropattern is to coat uniformly a glass coverslip with the polymer layer used as anti-adherent for protein attachment. Usually, poly-L-lysine grafted with polyethylene glycol (PLL-PEG) is used as the repellent agent; this first step is known as the passivation of the surface, and assures that the cells do not adhere to undesired areas of the coverslip. Once this first layer is created, there is selective destruction of the layer by UV light illumination; the polymer is burnt where the light reaches the surface and the glass is again exposed. The remaining areas are then filled by a second compound, most commonly ECM proteins known for cell-protein interaction (Azioune et al., 2010). The selective destruction of the layer is performed by passing the UV light through a quartz mask that has holes with the shape of the desired patterns, protecting the areas to conserve the anti-fouling material and letting it pass into the areas that will delineate the designed patterns (**Figure 9**).

The possibility of performing several coverslips at the same time with high-reproducibility between each other is a big advantage of this technique, as well as the time to finish the preparation (~3 hours) for later combining with videomicroscopy. Nevertheless, it has a high-starting cost, as the UV-ozone and photomask are expensive materials, but the rest of the materials are easily accessible; this provides a low-cost scenario for routinely performing micropattern once the initial machines are amortized. Every mask containing the designs of choice, although highly resilient and with the possibility to be reused forever, has the limitation that every new type of pattern or improvement in the design needs a new mask production and purchase.

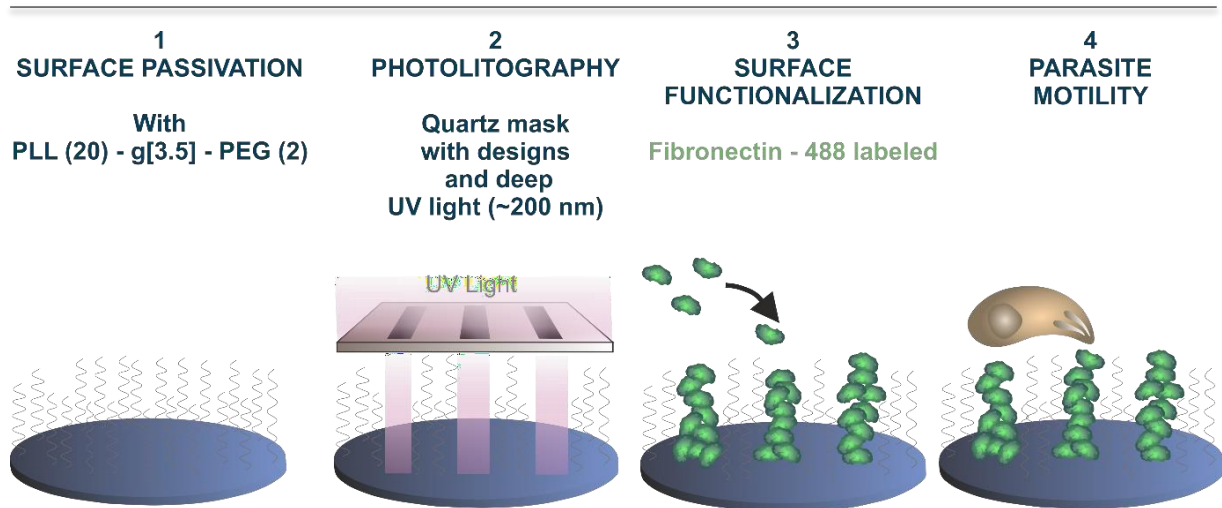


Figure 9 - Schematic of the main steps for micropatterning glass coverslips using the photolithography technique.

2.3.1.2 Alvéole PRIMO Micropattern

In order to overcome this limitation, a variation of the protocol was proposed by (Strale et al., 2016), in a photo patterning technique that relies on precise UV laser to remove the anti-fouling polymers for specific areas and then apply the desired protein or binding agent. Basically, all the micropattern process is performed directly inside the microscope chamber. First, the coverslip is functionalized with the anti-fouling polymer, in this case mixed with a photoinitiator compound; as a result, by using specific wavelength coming from a module adjusted to a regular confocal microscope, it is possible to etch directly in the microscope chamber the areas of interest. After that, the resulting patches can be selectively filled with several proteins for *in vitro* experiments, such as fibronectin or collagen (Khan et al., 2019; Pasturel et al., 2020), or diverse ECM proteins (Engel et al., 2019; Zhang et al., 2020). In principle, any type of biomolecule can be used, provided it adsorbs to the glass surface exposed after the etching process (**Figure 10**).

The advantages offered by this technique are (i) the polyvalence in the micropattern design: as no masks are needed to be made in advance, new patterns can be designed at will by loading an image of the micropattern in the connected software, hence allowing direct adjustment on a try-and-error approach, and the possibility to prepare multiprotein micropatterns. Nevertheless, as the process is performed in the area of the focal plane of the microscope, the worked field is quite small (~200 μm) and several patterns need to be juxtaposed to create the entire coverslip,

augmenting the experimental time (~ 6-8 hours), hence limiting the percentage of surface that can be patterned in a reasonable timeframe.

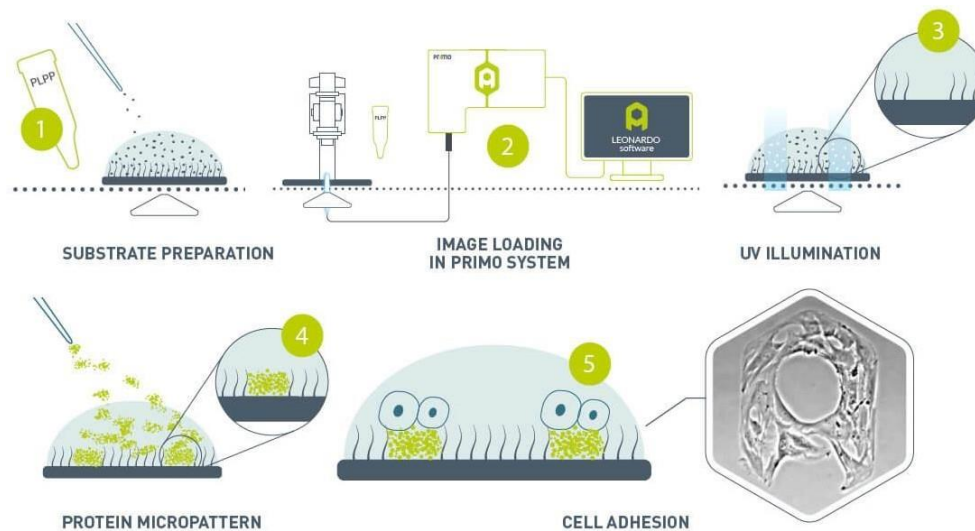


Figure 10 – Schematics of the step-by-step process of Alvéole PRIMO micropatterning. (1) The first layer of the anti-fouling polymer is set on the coverslip, and mixed with the photoinitiator compound to create a photosensitive hydrogel. (2) A design of the areas to keep intact and the surface to etch is loaded into the corresponding software. (3) The photoinitiator combined with the microscope laser ($\lambda \sim 350$ nm) degrades the layer. (4) The adhesive protein of interest is added (*i.e.* fibronectin, lamin). (5) Cells can be seeded on the micropatterned coverslip and they will be restricted to the adhesive areas and hence adapt their shape to it. Adapted from Alvéole website

2.3.1.3 Choosing the go-to micropattern technique

For our choice, there were several criteria to fulfill:

- High resolution adhesive/ anti-adhesive interphases, with micrometer discrimination in the frontier between both.
- The quality of the patterns should be reproducible between experiments.
- The experimental cost should be reasonable.
- Ability to be combined in the workflow of live videomicroscopy experiments.

Given the above criteria, the method chosen was photolithography micropattern using a photomask. Overall, it had a good compromise in the high-resolution achieved ($\pm 1 \mu\text{m}$), providing a low-cost and reproducible approach, as several coverslips can be prepared together, and easily combined with videomicroscopy as it takes less than 3 hours to finish the preparation. Alvéole PRIMO micropattern was preliminary tested, and as it works one field-of-view at the time, making very large areas can take several hours to be finished, being incompatible with videomicroscopy at the same time. Moreover, as the photo-initiator used in

combination with the antifouling polymer in the Alvéole PRIMO at that time was not shown to be totally repellent for tachyzoite activity, this patterning was not further considered in our experimental approach.

Photolithography micropattern also provided us with versatility in the desired adherent component in the micropattern. After the etching process, any type of biomolecule that interacts with the exposed glass can fill the area. As a result, several proteins like fibronectin or PLL in their fluorescent versions were utilized, but also glycosaminoglycans like heparin, also coupled to an FITC fluorophore. As heparin is heavily charged, it can electrostatically interact with glass and be restricted to the designed areas. Similar approaches could be found (Park & Ito, 2000), but none that use a PLL-PEG/ Heparin-FITC combination were reported so far.

Furthermore, it is important to note that the mechanical properties of the micropatterned surfaces and the resolution in high-precision areas tend to decrease over time. This relatively short shelf life also impacts on the planning of producing and transporting from a different lab site. As such, the final decision was to setup the photolithography micropattern technique in-house. In the next section, and in the process of setting up the technique, it was necessary to understand the relative errors and optimal distances between the UV lamp and the quartz mask, and also between the mask and the coverslip to be patterned, in order to detail the possible aberrations in the pattern creation and have an estimation of the error carried.

2.3.1.4 Photopatterning setup: a technical study

The photolithography micropattern technique was developed in-house using a UV-ozone cleaner, a quartz-chromium photomask and glass coverslips. As the UV-ozone cleaner could have several uses, we needed to calibrate the system in order to calculate the magnification of the patterns from the theoretical to the experimental one. To do so, we modeled the process and reduced it to the properties of the materials involved, and the distances and angles in the system that will generate our patterns.

Once the light leaves the UV lamp, it transverses through air until it reaches the quartz mask, and later passes onto the coverslip that is attached by capillarity of a water drop. This journey that the UV light does can be simplified as shown in **Figure 11**.

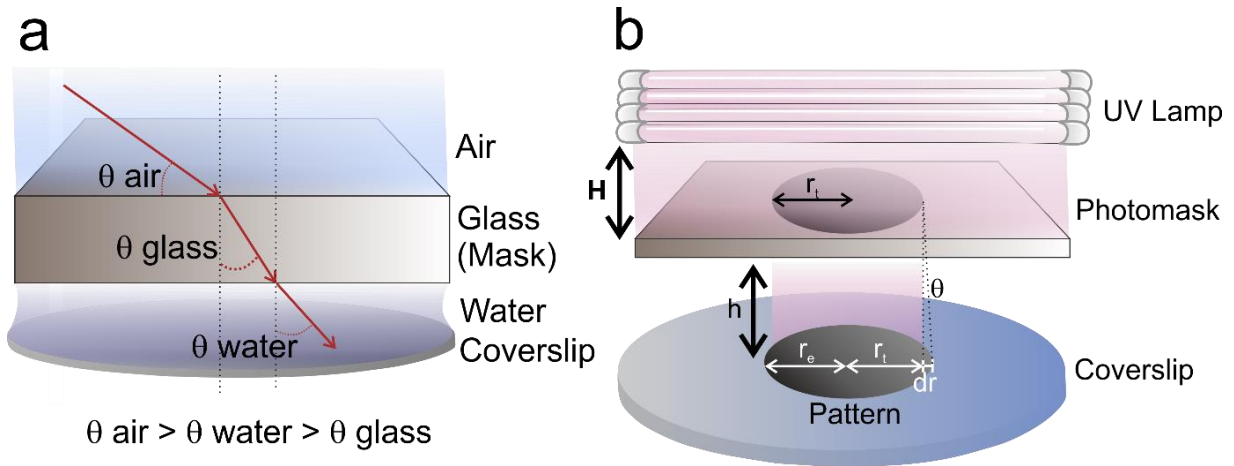


Figure 11 – (a) Schematic representation of the light pathway (red arrows), as it transverses from the air medium to the glass photomask and then the water drop holding the coverslip. The refraction angles for each of the respective media are noted as Θ , and their relationship is shown in the bottom of the design. The dashed lines represent the center of the light cross from one media to the other. (b) Design of the elements organization for photomask lithography. Top to bottom: the UV lamp, quartz photomask, and glass coverslip; the black circle represents the created pattern. The following parameters were considered for calculating the theoretical magnification of the patterns: H represents the distance from the lamp to the quartz mask; r_t the theoretical radius of the pattern; h the distance from the mask to the coverslip as a result of the water capillarity; Θ the angle formed between the edge of the pattern in the mask and the pattern created in the coverslip, r_e the experimental radius of the pattern formed, δr the difference between the theoretical radius and the experimental radius. Distances and sizes are not to scale.

There are several distances in our setting that we need to take into account, comprising all the components, to account in the calculations of the resulted pattern magnification. As can be seen in **Figure 11b**, there are:

- H is the distance between the UV-ozone lamp and the quartz photomask.
- h is the distance between the quartz mask and the glass coverslip.
- r_t is the theoretical radius of the pattern in the quartz mask.
- Θ is the angle formed between the edge of the quartz mask pattern and the end of the pattern formed in the glass coverslip.
- r_e is the experimental radius of the formed pattern.
- δr is the difference between r_t and r_e .

The starting point for the approximation is the optical principle stating that the numerical aperture (NA) of air is equal to that of the glass component of the mask:

$$n_{air} * \sin(\theta_{air}) = n_{glass} * \sin(\theta_{glass}) \text{ (Equation 1)}$$

The same relation can be stated for the passing of light from glass to water, thus:

$$n_{air} * \sin(\theta_{glass}) = n_{water} * \sin(\theta_{water}) \text{ (Equation 2)}$$

From Equations 1 and 2 and considering the angle amplitude relationship depicted in **Figure 11a** derived from the Snell Law, it is possible to postulate the following relation:

$$n_{air} * \sin(\theta_{air}) = n_{water} * \sin(\theta_{water}) \text{ (Equation 3)}$$

Furthermore, we can reorganize the Equation 3 into:

$$\sin \theta_{air} = \frac{n_{air}}{n_{water}} * \sin(\theta_{water}) \text{ (Equation 4)}$$

As stated that the distance between the UV lamp and the quartz is H , and rt the radius of the quartz crystal pattern, for that relationship we can say:

$$0 < \tan (\theta_{air}) < \frac{rt}{H} \text{ (Equation 5)}$$

To move forward in the model construction, we can take a first approximation of the distances involved based on the size of the UV-ozone machine and the photolithography mask:

$$rt \approx 10^{-6} \text{ m}$$

$$H \approx 10^{-2} \text{ m}$$

The ratio will follow an estimated:

$$\frac{rt}{H} \approx 10^{-4}$$

Having set that first estimation, we can also postulate that:

$$\tan (\theta_{air}) \approx \tan (\theta_{water})$$

Using this to create a relationship between Equations 4 and 5, we can reformulate it as:

$$0 < \sin (\theta_{water}) < \frac{rt}{H} * \frac{n_{air}}{n_{water}} \text{ (Equation 6)}$$

By applying trigonometric relations, we can derive as:

$$\sin (\theta_{water}) = \frac{\delta r}{\sqrt{\delta r^2 + h^2}} \text{ (Equation 7)}$$

where h is the height of water drop between the coverslip and the formed micropattern.

From **Figure 11b**, we can also see that

$$dr = re - rt$$

and also due to Pythagoras's theorem of triangles, that:

$$\text{Hypotenuse} = \sqrt{\delta r^2 + h^2}$$

Arriving at this point, we can add the definition for the magnification, which is the parameter we want to calculate, and that can be expressed as the ratio of the experimental radius and the theoretical radius

$$M = re - rt$$

From the two previous statements, we can reformulate as:

$$\delta r = re - rt = rt (M - 1) \quad (\text{Equation 8})$$

By approximating the relationship shown in Equation 6 to its maximum and combining it to the relationship shown in Equation 7, continue:

$$\sin (\theta_{\text{water}}) \approx \frac{t}{H} * \frac{n_{\text{air}}}{n_{\text{water}}} \quad (\text{Equation 9a})$$

$$\frac{1}{\sqrt{1 + (\frac{h}{\delta r})^2}} \approx \frac{t}{H} * \frac{n_{\text{air}}}{n_{\text{water}}} \quad (\text{Equation 9b})$$

$$\frac{\sqrt{1 - (\frac{h}{\delta r})^2}}{1 + (\frac{h}{\delta r})^2} \approx \frac{H}{rt} * \frac{n_{\text{water}}}{n_{\text{air}}} \quad (\text{Equation 9c})$$

$$1 + (\frac{h}{\delta r})^2 \approx (\frac{H}{rt} * \frac{n_{\text{water}}}{n_{\text{air}}})^2 \quad (\text{Equation 9d})$$

$$\frac{h}{\delta r} \approx \sqrt{(\frac{H}{rt} * \frac{n_{\text{water}}}{n_{\text{air}}})^2 - 1} \quad (\text{Equation 9d})$$

Using the relationships in Equation 8 and 9e, we further postulate that:

$$h \approx \delta r \sqrt{(\frac{H}{rt} * \frac{n_{\text{water}}}{n_{\text{air}}})^2 - 1} \quad (\text{Equation 10a})$$

$$h \approx rt * (M - 1) \sqrt{(\frac{H}{rt} * \frac{n_{\text{water}}}{n_{\text{air}}})^2 - 1} \quad (\text{Equation 10b})$$

If we factorize rt on the right hand on the Equation 10b, we arrive:

$$h \approx (M - 1) \sqrt{(\frac{n_{\text{water}}}{n_{\text{air}}})^2 * H^2 - rt^2} \quad (\text{Equation 11})$$

If we want to approximate even further, since

$$rt \approx 10^{-6} \text{ m}$$

$$H \approx 10^{-2} \text{ m}$$

We can deduce that

$$\frac{H^2}{rt^2} \approx 10^8$$

So we can neglect rt^2 due to the small size, thus transforming Equation 11 into

$$h \approx (M - 1) * (\frac{n_{\text{water}}}{n_{\text{air}}}) * H \quad (\text{Equation 12})$$

In order to be able to calculate the correct amount of water needed to form our patterns, we can use:

$$V_{\text{water}} = h * S_{\text{coverslip}} \quad (\text{Equation 13})$$

where V_{water} is the volume of water needed and $S_{\text{coverslip}}$ the surface of the coverslip, whatever the shape may be.

If we combine *Equations 12* and *13*, we then get:

$$V_{water} \approx (M - 1) * \left(\frac{n_{water}}{n_{air}}\right) * H * S_{coverslip} \quad (\text{Equation 14})$$

We can also express the magnification in itself from the relation designed on Equation 14 as follows:

$$M \approx \frac{V_{water}}{\left(\frac{n_{water}}{n_{air}}\right) * H * S_{coverslip}} + 1 \quad (\text{Equation 15})$$

In order to verify if these relationships are experimentally reliable, we replaced the coefficients with the measures used in the first micropattern tests for an 18 mm diameter coverslip, the size fitting our microscope chamber:

$$V_{water} \approx 4 \text{ mm}^3$$

$$r_{coverslip} \approx 9 \text{ mm}$$

$$S_{coverslip} \approx 254.5 \text{ mm}^2$$

$$H \approx 20 \text{ mm}$$

$$n_{water} / n_{air} = 1.33$$

By replacing everything on *Equation 15*, we get that our magnification $M \approx 1.0005$. This means that the magnification between the sample and the micropattern on the coverslip is negligible mainly due to the volume of water being small enough. In contrast, H is the crucial element, as a bigger distance between the UV lamp and the quartz pattern provokes a smaller magnification.

From this theoretical analysis, we can conclude:

- The height between the UV lamp and the quartz photomask, H in the equation, is the most important criteria. As a result, in our new micropattern setup, the distance between the lamp and the plate holding the photomask was adjusted at the longest possible.
- The volume of water to stick the coverslips on the photomask can be easily adjustable if it is needed to vary the coverslip size, independently from its shape (*i.e.* circular, square) and get the minimum distance possible while still attached by capillarity.

2.3.2 Combining photolithography micropattern and live video-microscopy to monitor tachyzoite gliding behavior

We previously referred to the speed of the gliding tachyzoites as being in the second scale for moving its entire body but it most often moves forward intermittently. As a result, the main challenge is to capture in detail the fast stop-and-go action that can span from seconds to a few

minutes. Thus, it was necessary to use a camera with a recording speed of 1 frame/ second or better to fully catch the displacement of the tachyzoite on the micropatterned surfaces. We built a protocol to acquire images from brightfield (for imaging the tachyzoite body) and one laser corresponding to the micropattern excitation wavelength. For some of our experiments, we also used a tachyzoite expressing a fluorescent version of the protein BCC7 (detailed in **Chapter 2**) to follow the basal pole at the recording. With our current live imaging platform, if we acquired images using a third wavelength (for a marker for the apical pole, for example), the tachyzoite's speed surpassed the recording capabilities of the camera and resulted in losing vital information frames. Nevertheless, even when using only two channels, there is a compromise to be achieved: the faster the recording, the lower the quality, as the exposure time and the number of lasers used in the acquisition need to decrease.

The second aspect to note was the on-focus plane, as the tachyzoite's body is slightly off-focus from the surface focal plane. For that, the piezo objective offered a steady focus adjustment, with an easy Z-plane change if needed. As a result, the focal plane used was a compromise between both; in all recordings, there was a previous set of images of the micropattern field in case the focus was slightly off and the signal became faded.

For the full recording process, we applied the acquisition parameters of at least one frame per second for at least 5 minutes, dividing each coverslip for at least three fields of study. This resulted in a large number of tachyzoites recorded (in the range of the hundreds, as can be seen in each of the corresponding figures of the publication). For the resulting dataset, ImageJ and Icy (de Chaumont et al., 2012; Schneider et al., 2012) were used for manually tracking of each individual tachyzoite, and obtaining information about the active state of each (active/ inactive), the type of movement for the active ones (twirling/ circular/ helical in the micropattern line an helical crossing lines), and the main properties of the displacement:

- Total distance traveled: by tracking the basal pole of the tachyzoite, we sum the displacement between the starting and finishing point for each parasite performing helical gliding.
- Duration of the movement: time length of the helical gliding performed.
- Average speed: we computed the mean speed of the tachyzoite in the entire helical process as a ratio of the two parameters mentioned before. As helical gliding can take different routes, we differentiated from the velocity which includes the vectorial direction into account.

- Geometry of the displacement: we used the linearity coefficient, a unitless parameter which assigns a 0 value to a perfect circle shape and a 1 to a straight line, to characterize the polygonal geometry of the helical crossing paths.

2.3.3 Coupling photolithography micropattern with Ultrastructure Expansion Microscopy for super resolution imaging of tachyzoites in contact with micropatterned areas

For solving the (ii) objective stated in *Section 2.1*, regarding the mechanical production for helical gliding, we had to implement a technique that allowed us to visualize the step-by-step adhesion contact sites of the parasite when is gliding on micropattern surfaces. The lab has pioneered Ultrastructure Expansion Microscopy (U-ExM) in the past in the field of *T. gondii*, to detect at ~30 nm resolution cytoskeleton elements (*i.e.* cortical microtubules and myosin A motors) involved in gliding in both motile and immotile conditions (Pavlou et al., 2020). U-ExM allows the physical enlargement of samples in order to surpass the ~250 nm resolution limitation existing in light microscopy (Chen et al., 2015). Briefly, it functions by embedding the samples in a polymer solution, which is turned into a hydrogel that will swell in presence of water or shrink in a high osmolarity solution (*i.e.* PBS). The sample is subsequently treated in a denaturation step including a proteinase K digestion to allow the physical expansion of the specimen. Adding water to the hydrogel then increases the size of it, isotropically expanding the distance between biomolecules that are covalently attached to the gel (Wassie et al., 2019). After it has been enlarged, the specimen can be stained with a variety of fluorophore conjugated antibodies which resist the denaturation step (Chozinski et al., 2016). At the end of these steps, the sample is enlarged between 4 to 10 times, depending on the protocol followed (Damstra, Mohar, et al., 2022; Gambarotto et al., 2019).

Nevertheless, here we added an extra complexity layer, as the micropattern in the surface of the coverslip needs to be conserved as well in the expansion process. As a result and for the first time reported, we combined our PPL-PEG/ fibronectin micropatterns with U-ExM and successfully retrieved both the surface polymers and the tachyzoites on top. Previous reports (Damstra, Passmore, et al., 2022) only used glass/ fibronectin micropatterns as a method to localize and retrieve the same cell before and after expansion process, but none so far used micropatterns to circumscribe the cell's movement.

As a difference from the photolithography micropatterns described in *Section 2.2*, we had to overcome the loss of fluorescence of the fibronectin HiLyte 488 used in the videomicroscopy experiments, as the fluorophore did not sustain the denaturalization process in the U-ExM process. As a result, we performed a coupling of bovine plasma fibronectin with an N-Hydroxysuccinimide (NHS) ester-dye conjugate, that supports well the gelation and expansion process (M'Saad & Bewersdorf, 2020). NHS based-dyes work by reacting with primary or secondary amines present in proteins (*i.e.* on residues of lysine, arginine, asparagine and glutamine aminoacids) (Nanda & Lorsch, 2014), and resist well the denaturation process in the U-ExM methodology.

2.3.4 Designing specific tunable model surfaces for monitoring tachyzoite adhesive and motile capacities

With the question in mind of tackling which are the molecular moieties that serve as receptors for the tachyzoite to promote the required apical anchoring adhesion for helical displacement, we aimed to produce well-controlled surfaces with a modifiable chemistry. To do so, we had to confront two different challenges, as (i) the need to find a technique that allowed high-resolution characterization of the physicochemical properties of the surfaces to test for tachyzoite motility; and (ii) a model to construct surfaces with similar physical properties but different chemical exposed moieties.

As a result, we chose to implement the highly sensitive acoustic-based technique Quartz Crystal Microbalance with Dissipation (QCM-D); we also introduced a PLL-PEG chemistry combined with streptavidin-biotin interactions to create modular complex surface layers, to test the parasite's activity on them.

2.3.4.1 Characterization of surfaces using Quartz Crystal Microbalance with Dissipation (QCM-D)

To characterize the physicochemical characteristic of the different coatings, the ones used for micropattern assay (*i.e.* PLL-PEG and fibronectin) and the ones created using a tunable layer construction (which will be described later), we used Quartz Crystal Microbalance with Dissipation (QCM-D). This instrument is ideal for studying surfaces in solution, as can monitor film formation and interaction with the solution in real time, and without the need of labels (Schumacher, 1990; Ward & Buttry, 1990).

The heart of QCM relies on a quartz crystal, which has a gold electrode. As the majority of crystalline materials, when we apply a voltage in it the material suffers a mechanical deformation, due to the inverse piezoelectric effect. We can then alternate the application of the voltage, and as a result the crystal will suffer an oscillatory motion. Moreover, we can tune the frequency of the voltage to make it match the crystal's resonance frequency, and we will get a stable oscillator circuit (Cady, 1946). This oscillation is very important, since the top and the bottom of the crystal will move in antiparallel directions; as such, any interaction of the crystal with a solvent or compound will modify the shear-waves of the oscillation frequency, and we can measure that change as a function of the mass in contact. Making a broad comparison, the crystal works as a balance that senses not weight differences, but frequency changes. Indeed, depositing a film on the surface of the crystal increases its thickness and also the wavelength of the oscillatory frequency, resulting in a more precise way we can measure extremely small masses (up to 10^{-9} grams) and liquid interfaces as well (Ward & Buttry, 1990) (**Figure 12**).

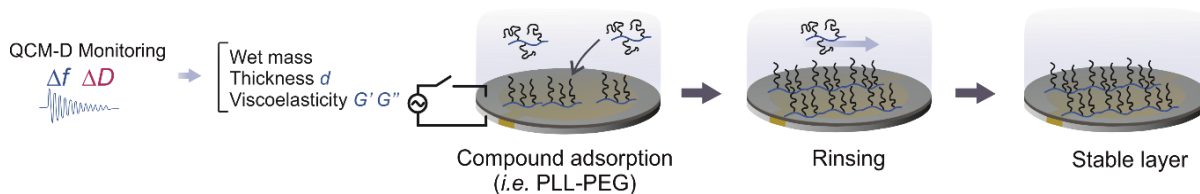


Figure 12 – Schematic of the main steps of QCM-D measurements. The silica-coated quartz sensor oscillates at a resonance frequency, allowing to monitor shifts in frequency (Δf) and dissipation (ΔD) upon binding of a compound to its surface. Measurements are performed in solution, and the stability of molecules attachment is verified upon rinsing with working buffer.

In this study, we used a variation which adds the Dissipation term in the name, and its characterized by the intermittently turning off the voltage source, leaving the oscillations to decay freely (Rodahl et al., 1995). Again due to the piezoelectric characteristic of the quartz, during the decay there is a voltage generated in the material that can be measured, resulting in yielding two main parameters that are going to be extremely used: the resonance frequency f and the dissipation D . The frequency shift, or Δf , is proportional to the mass density of the film on top of the crystal; while the dissipation shift ΔD is a measure of the solvation of the layer. Both parameters allow real time monitoring of surface binding kinetics, adsorption efficiency, stability of the layers created and interaction with the solution buffers. As all measures are done in solution, we can control the formation of the surface layers and their reaction to different buffer changes over time (Domack et al., 1997; Marx, 2003). Consequently, we were able to

verify surface functionalization protocols (*i.e.* incubation times, polymers concentration) and observe the buffers interaction (or lack of) with our layers.

Furthermore, using viscoelastic modeling, QCM-D is extremely useful as we can determine layer thickness and its main viscoelastic properties, named storage modulus (G') and loss modulus (G'') (Eisele et al., 2012). Both are important rheological parameters that allow understanding how materials behave under deformation. To illustrate how these parameters work, let's take an example of a sponge. If the sponge is completely soaked with water until saturation, the overall mass of the sponge has certain resistance to deformation. The sponge itself has a certain rigidity, which we can describe as the storage modulus G' , also known as elastic modulus. The water in the sponge also contributes to the overall resistance to deformation, and because water is inelastic or viscous, this input to the total resistance is called loss modulus G'' or viscous modulus. If instead we change the type of sponge and we use a stiffer one, the storage modulus will change independently of the loss modulus; the same situation will happen with a thicker liquid, like syrup or honey, as the loss modulus will increase.

The modeling allowed us to quantitatively determine the thickness of all our coatings, as well as the viscoelastic properties G' and G'' . As such, we were able to discriminate which properties were contributing more for explaining differences in the tachyzoite active phenotype.

2.3.4.2 Development of tunable complex layer systems

For the second part of the objective, we aimed to screen the molecular determinants that act as surface receptors to promote an apical anchoring and stimulate tachyzoite motility. To do so, we had to construct surfaces with similar components and physicochemical characteristics but with controlled and modifiable chemical differences. As a result, we developed a tunable model system, combining PLL-PEG surface coatings and streptavidin/biotin chemistry. This last layer will allow us the versatility of different biotinylated compounds to test, and at the same time control the amount of residual groups exposed for adjusting the layer density (Dubacheva et al., 2017).

Briefly, the tunable layer system created consisted on a first layer of PLL-PEG-biotin (PLL-PEG-b) adsorbed on the surface, and then a second layer complex of streptavidin:biotin-X (SAv:b-X), where X is the tunable compound that can be different molecules of interest as (i)

PEG with either a terminal hydroxyl group (-OH), amine group (-NH₂) or carboxylic group (-COOH); (ii) human serum albumin (HSA); or (iii) heparan sulfate (HS) (**Figure 13**).

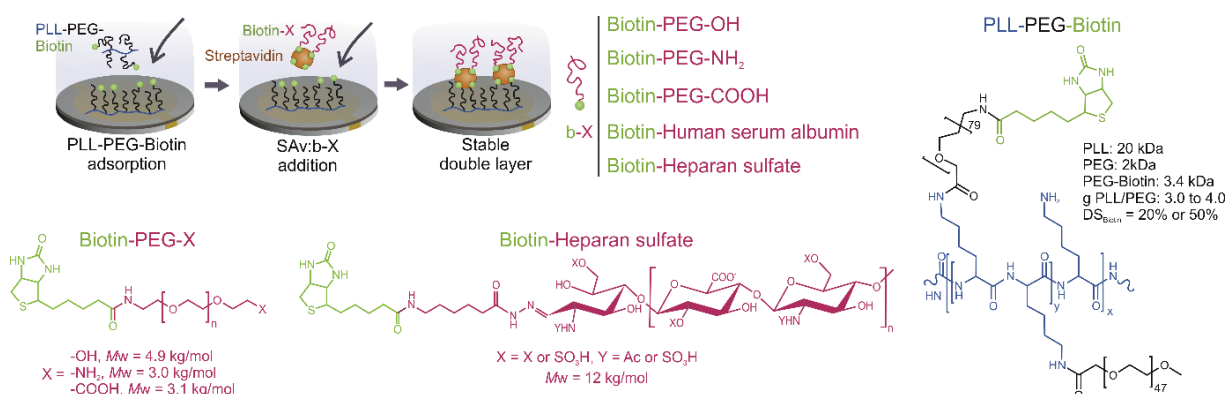


Figure 13 – Schematic of the main steps of the tunable model construction, allowing to change the terminal molecule while using the same surface chemistry. First, PLL-PEG-biotin (PLL-PEG-b) is adsorbed on the silica-coated sensor, followed by the injection of streptavidin/biotin-X (SAv:b-X) complex, being X the tunable terminal group. It is also mentioned the chemical structure, molecular weight and ratios of the main compounds used in the construction.

This new tunable layers construction has the advantages of (i) proposing a variety of specific chemical determinants, with the ability to modulate their ratio in a quantitative manner to test tachyzoite motility; (ii) keeping the core layer (PLL-PEG-biotin/SAv) constant for all the coatings, isolating the cause of any tachyzoite active response to the last layer only; and (iii) being compatible for buildup on glass coverslips to perform live videomicroscopy experiments, but also on quartz crystals compatible with QCM-D, to monitor and characterize the complex layers formation and to prove the inertness with the tachyzoite's motility buffer.

To create the first layer, we used a commercially available PLL-PEG-b (*e.g.* PLL (20kDa)-PEG(2kDa)/PEG(3.4kDa)-biotin(20%)), which proved to bind efficiently to both glass and quartz crystals. The PLL-PEG-b molecule provided the grafting sites for the SAv; after controlling the binding by QCM-D, we realized that all the SAv sites were occupied in this first interaction, as the flexibility of the PEG-b chains saturated the binding sites and didn't leave any empty for forming the second layer. As a result, our strategy was to 'pre-form' the complex of SAv/b-X first, controlling the amount of free binding sites available, and then put in contact with the first layer of PLL-PEG-b. This strategy required the use of biotinylated constructs with only one biotin group per molecule, in order to avoid aggregation with the SAv in solution.

For the second layer, the choices of mono-biotinylated compounds were selected based on different aspects of tachyzoite-surface interactions to investigate:

- Electrostatic interactions: several mono-biotinylated versions of b-PEG-X with different terminal groups (*i.e.* OH, NH₂, and COOH). These variations as charges have long been linked with contributing in host-parasite interactions (Akaki et al., 2001).
- Proteins involved in adhesins secretion: a biotinylated version of human serum albumin was commercially obtained. Albumin has been shown to be involved in microneme secretion, key aspect in motility, through activation of the protein kinase G; (K. M. Brown et al., 2016; Dubois & Soldati-Favre, 2019).
- Glycosaminoglycans: heparan sulfate has been linked with the adhesive capabilities of the tachyzoite (Carruthers et al., 2000). To investigate if a single GAG exposed moiety was enough to promote gliding, a mono-biotinylated version of heparan sulfate was synthesized at the collaborators lab (Dr. Galina Dubacheva, DCM, Université Grenoble Alpes).

2.3.5 Implementing microbeads covalent bound for decoupling adhesion and membrane flow

Microneme secretion is necessarily required for triggering tachyzoite motility, and the exocytosis process occurs through the apical complex, in a tightly regulated discharge process (Bullen et al., 2019). Microneme proteins exhibit adhesive domains, which interact with extracellular host cell receptors or adhesive substrates and bridge with the glideosome. These adhesins are translocated to the basal part of the tachyzoite the action of the glideosome as the MyoA contracts the filaments, and the ones that are not disconnected by proteases and shed are recycled by the endocytic system (Koreny et al., 2023). Recently, the Meissner lab has proposed a contribution for the current tachyzoite motility mechanism, named the ‘fountain flow’ model, where they postulate that the endocytic-secretory pathway that generates an antero-posterior translocation of adhesins contributes to generate productive movement forward (Gras et al., 2019). Nevertheless, there is still a major issue in the dissociation in the speed of both processes; the rate in which membrane flow backwards occurs is significantly faster than the speed of the movement forward of the parasite, suggesting that as for the malaria parasite *P. falciparum* both process could be related but uncoupled (Quadt et al., 2016). Furthermore, in agreement with the Meissner lab data, we already evidenced that the membrane

retrograde flow occurs in tachyzoites adhering on their basal pole and ready to propel but still immotile (Pavlou et al., 2020).

As a result, we aimed to investigate the coordination of the antero-posterior translocation and tachyzoite motility. Taking into consideration that gliding is an adhesion-dependent type of motility, we proposed to study membrane flow under well characterized non-adhesive conditions. To observe the membrane flow backwards, we coupled covalently-activated microbeads to the surface of the tachyzoite, and observed their movement backwards while it was on the non-adhesive surface PLL-PEG. If active tachyzoites with surface-attached beads are exposed to the anti-fouling surface PLL-PEG, we expected that the tachyzoite would be able to translocate the attached beads from its apical pole to its basal pole if the membrane flow is a continuous process, independently of any adhesion event.

To this end, we used commercially available microbeads with carboxylate surface groups, which were activated using 1-ethyl-3-[3-dimethylaminopropyl] carbodiimide, known as EDC, a process that led to a reactive intermediate O-acylisourea product. The latter can react with primary amines to form a stable covalent amide bond. As a result, if we mix activated beads with a population of tachyzoites in solution, the O-acylisourea can react with the largely present amines in the parasite's PM, mostly from membrane proteins and glycoproteins, and form a covalent bound. Once interacting with the parasite surface, the microbeads engage in an antero-posterior capping process, in particular when parasites are settled on a fibronectin-coated surface (Pavlou et al., 2020) (**Figure 14**).

To succeed in the experimental process we adjusted the beads quantity to the minimum to avoid having the interaction of the tachyzoite with some bead sediment in the surface, as a possible adhesion site. Also, even if the carboxylate beads were also fluorescent, we refrained from using a second laser in the video-recording process to obtain at least a 3 frames/ second quality and improve the detail resolution of the translocation process.

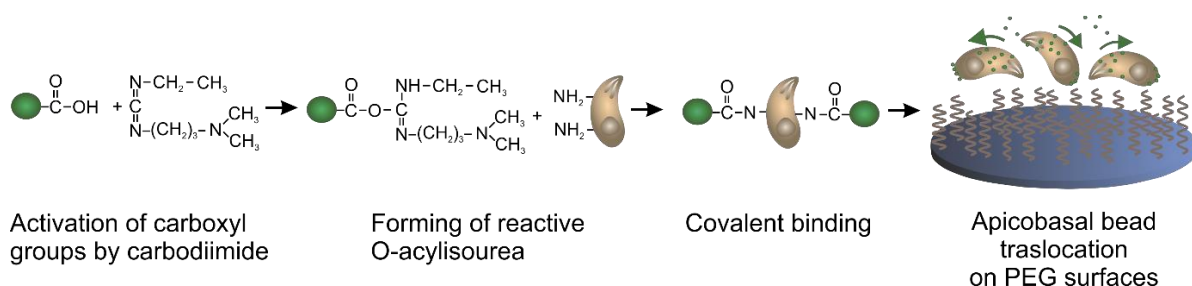


Figure 14 - Schematic representation of carboxylic beads activation with EDC, creating a reactive O-acylisourea to generate a covalent binding between the carboxylic group at the bead surface and the amine groups present on the tachyzoite's membrane proteins.

2.4 Main highlights of the study

In the research article that composes this Chapter, we combined high-resolution micropattern, live and Expansion microscopy, with biochemically controlled tunable surfaces to interrogate the minimal adhesion sites the tachyzoite requires to perform productive movement and understanding the contribution of retrograde membrane flow for helical gliding. The main results of this article are listed below:

- The tachyzoite apical adhesion is both necessary and sufficient to initiate the proper traction force for productive helical gliding forward.
- Glycosaminoglycan molecules (GAG) exposed on the micropatterned surface are sufficient to promote productive adhesion for helical gliding.
- Development and biochemical and biomechanical characterization of tunable surface coatings to present to parasites.
- Screening of chemical groups suggest that negative charge alone and HS are efficient ligand for the parasite adhesin to engage in a helical gliding sequence.
- Apicobasal membrane flow on the tachyzoite occurs in absence of surface adhesion but contributes to basal attachment and twirling.

2.5 Vigetti et al., 2023

Publication

Vigetti L, Touquet B, Rose T, Dubacheva GV, Tardieux I. Coupling tunable surface chemistry with cell imaging identify GAG as sufficient ligand to guarantee minimal focal adhesion for high-speed gliding of the *Toxoplasma* parasite. 2023.

Coupling tunable surface chemistry with cell imaging identify GAG as sufficient ligand to guarantee minimal focal adhesion for high-speed gliding of the *Toxoplasma* parasite

Luis Vigetti¹, Bastien Touquet¹, Thierry Rose², Galina Dubacheva^{3*}, Isabelle Tardieux^{1*}

¹*Institute for Advanced Biosciences (IAB), Team Biomechanics of Parasite–Host Cell Interactions, CNRS UMR5309, INSERM U1209, Université Grenoble Alpes, 38700 Grenoble, France,*

²*Institute Pasteur, Diagnostic Tests Innovation & Development core facility, 75724 PARIS cedex 15, France,*

³*Département de Chimie Moléculaire (DCM), UMR 5250, Université Grenoble Alpes, CNRS, 38000 Grenoble, France*

* email: Isabelle.tardieux@inserm.fr ; galina.dubacheva@univ-grenoble-alpes.fr

KEYWORDS

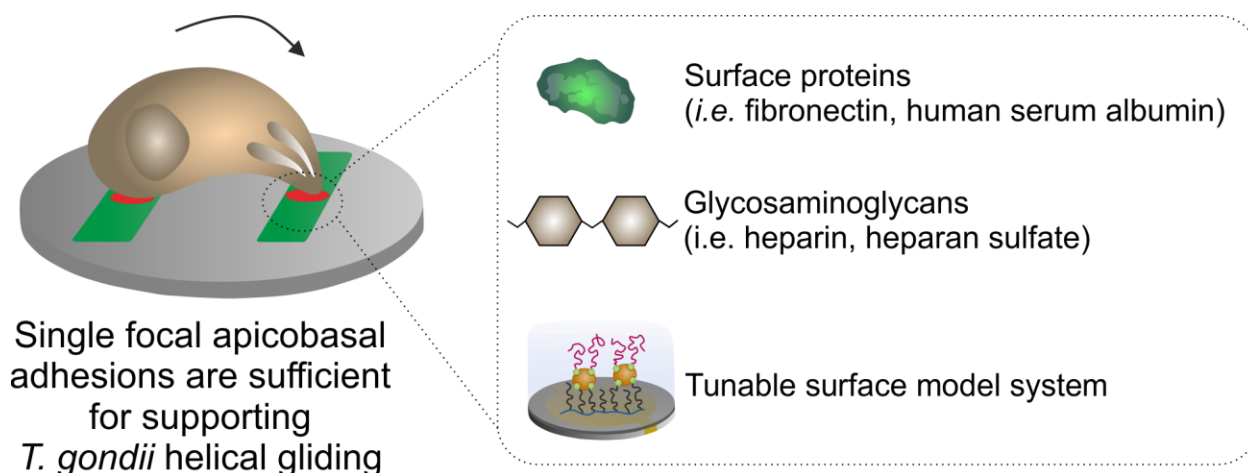
Toxoplasma gondii, cell migration, live and super resolution microscopy, quartz crystal microbalance with dissipation, surface chemistry.

ABSTRACT

Toxoplasma gondii is a protozoan parasite evolved with a developmental morphotype called tachyzoite that navigates between cells, crosses cellular barriers and moves in and out of permissive cells in a wide repertoire of homeothermic hosts. Relying on a uniquely constant apicobasal bipolarity coupled to an actomyosin-driven retrograde membrane flow, the tachyzoite has elaborated a molecular machinery to assemble short-life anchoring contacts with the environment, which support the proper magnitude of traction force that powers a typical helical gliding motility mode. Using micropatterning, live and expansion microscopy, we bring definitive

evidence that the tachyzoite needs to build only one anchoring contact with the substrate which spatially defines a force transmission platform over which it moves with a helical trajectory. Furthermore, we developed biochemical and biophysical quantitative assays using tunable surface chemistry approaches and quartz crystal microbalance with dissipation monitoring to screen for the essential adhesion requirements for optimal helical gliding, in absence of molecule absorption from the medium to the substrate. These sensitive approaches have highlighted the sufficiency of glycosaminoglycan (GAG)-parasite interaction to promote productive contact and helical gliding. Such a combinatorial biochemical-biophysical-cell imaging toolkit implemented with GAG glycomimetics should serve as an advanced resource for future studies of cell-surface interactions, including the characterization of the structure and density of the molecules that must be functionally engaged at this unique parasite-substrate mechanosensitive interface.

GRAPHICAL ABSTRACT



INTRODUCTION

Cell locomotion achieved by eukaryotic individual cells and collectives has been phenomenologically categorized in a spectrum of modes from crawling or mesenchymal to amoeboid-like or bleb-based movements. Although the actomyosin contractile system is generally involved in all modes, it performs either through or independently of a range of dedicated dynamic adhesive structures with the microenvironment (Bershady & Kozlov, 2011; Paluch et al., 2016),

which reflects distinct mechanisms of force generation. Furthermore, many protozoan and metazoan cells adjust to the fluctuating biochemical and biophysical environmental cues by switching from one mode to the others (Lämmermann & Sixt, 2009; Liu et al., 2015; Yamada & Sixt, 2019) (**Supplementary Figure 1a**). Indeed, there is a renewed interest for theoretical and experimental studies on how eukaryotic cells integrate extracellular and intracellular variable inputs to tune their interactions with the extracellular matrices (ECMs) and adapt their migration strategies to fulfill specialized functions.

In this context, the protozoan *Toxoplasma gondii* is an experimentally accessible and simple model system to interrogate the spatiotemporal coupling between cell-substrate adhesion and the contractile machinery required for cell movement. *T. gondii* is one of the most prevalent parasitic microbes of warm-blooded animals which might colonize about a third of the human population (Montoya & Liesenfeld, 2004). It is the etiological agent of toxoplasmosis, a set of potentially life-threatening or debilitating pathologies mostly in immunocompromised hosts (Milne et al., 2020). Tissue damages are primarily caused by the motile and fast-cycling developmental morphotype called tachyzoite, which locomotes between cells in various ECMs and moves in and out of host cells in which it produces progeny (Fréchal et al., 2017; Hu et al., 2002; Leung et al., 2014; Pavlou et al., 2019). Using a peculiar adhesion-dependent motility mode referred as to gliding, the tachyzoite displaces its roughly seven micron-long body in just a handful of seconds, a performance for non-swimming eukaryotic cells (Philips & Milo, 2015).

The main simplifying feature of the tachyzoite model comes from the permanent apicobasal cell polarity, which defines one constant symmetry axis as early as biogenesis starts within the mother cell (Hu et al., 2002). In particular, the apical pole is specified by a conic appendage known as conoid and houses secretory vesicles, in particular the micronemes, as well as an actin nucleation center (Daher et al., 2010; Dos Santos Pacheco et al., 2022). Together, these attributes instruct a unidirectional "apex first" movement of the mature tachyzoite when it egresses out from the host cell and glides further. Therefore, there is no need for the usual macroscopic symmetry breaking step and indeed, no membrane protrusions dictate the direction of parasite locomotion. Moreover, the curved tachyzoite follows prominently or exclusively a helical path in 2 and 3D conditions, respectively (Leung et al., 2014) which reduces the significant cell-to-cell variability in motile movements observed for most populations under study.

To undergo helical gliding on a flat surface, the tachyzoite progresses about one body length with a 180° rotation along the major axis, while lifting the apex, and then completes a 360° rotation before the next move forward (Håkansson et al., 1999; Pavlou et al., 2020) (**Supplementary Figure 1b**). The prevalent mechanistic gliding model is centered around a series of stationary MyosinA (MyoA) motors aligned between the plasma membrane and the beneath inner membrane complex (IMC), ready to pull short actin filaments in a fixed rearward orientation along the parasite length (**Supplementary Figure 1c**). Force is transmitted to the ECM across molecular anchoring platforms that are primarily shaped around ECM ligands and parasite-derived transmembrane adhesin receptors. The so-called MIC adhesins are exclusively released at the apical tip of the parasite through regulated secretion, and MIC2 has been acknowledged as the mechano-transducer MIC prototype (Brown et al., 2016; Bullen et al., 2016). Indeed, the dysregulation of MIC2 expression drastically alters the tachyzoite helical gliding skills in 2D and 3D conditions (Gras et al., 2017; Huynh & Carruthers, 2006; Shen et al., 2014; Stadler et al., 2022). Upon release, MIC2 exposes an ectodomain featured by an integrin-like A/I-domain and an M domain encompassing six thrombospondin-like repeats. The model stipulates that the engagement of the ECM ligand-MIC2 complexes with the sub-membranous F-actin through a specific actin bridging molecule provides the transient mechanical link required for force transmission (Jacot et al., 2016; Kumar et al., 2023). Moreover, along with the MIC2-F-actin complex retrograde translocation, the MIC2 ectodomain is enzymatically released in the medium through a multistep process of elusive kinetics which prevents excessive molecular interaction with the ECM ligands while permitting proper MIC2 disengagement from the ECM ligand, a strict condition for forward displacement (Carruthers et al., 2000).

Recently, using force microscopy and live imaging, we uncovered a privileged contact site which must be initiated by the tachyzoite through its apical region and that remains stationary on the flat surface while the parasite moves over in a twisting motion. This longer-lived contact site serves as an anchor point across which a tachyzoite MyoA-based traction force is transmitted to drag the cell body forward (Pavlou et al., 2020). In a related scheme, when the *T. gondii* tachyzoite glides within Matrigel or an elastic fibrin-based hydrogel, it must build an adhesive ring-shaped platform which critically supports the transmission of inward-directed forces generated by the parasite to squeeze through, as retrieved from a challenging 3D TFM analysis (Stadler et al., 2022). Therefore,

identifying the composition and architecture of these pivotal adhesion platforms is key to solve the spatiotemporal force transmission requirements for helical gliding.

To investigate how the gliding tachyzoite interacts with the ECM components, we combined micropatterning, flow force and live or super resolution imaging with tunable surface chemistry. Specifically, we used PLL-PEG coupled to SAV/biotin chemistry, which allowed to build well-defined, highly specific adaptable model surfaces to tune the nature and density of ligands and to study effects on parasite motility. We complemented our study with a quartz crystal microbalance with dissipation monitoring (QCM-D) technique and viscoelastic modeling for biophysical characterization of the tunable surface, and started screening for the pro-gliding molecular ligand species. Collectively, this work offers a combinatorial framework to experimentally decode the interplay between cell adhesion and force generation behind the high-speed gliding skills of the *Toxoplasma* eukaryote.

RESULTS

The tachyzoite substrate adhesion force is independent from molecular components in the surface

Using high-speed Reflection Interference Microscopy (RICM), we previously mapped at the sub-micrometer scale the substrate site where the motile parasite must first engage apically to generate a traction force (Pavlou et al., 2020). But it is not clear if the ECM ligand species encountered by the parasite during this contact can modulate force generation, hence motility. Indeed, no major phenotypic differences in the parasite performance when settled on glass surfaces coated with either protein (*i.e.*, fibronectin) or complex polysaccharides such as glycosaminoglycans (GAGs) have been reported (Carruthers et al., 2000; Gras et al., 2017; Håkansson et al., 1999; Pavlou et al., 2020). To characterize the overall tachyzoite adhesiveness on biomaterial surfaces, we performed adhesion rupture assays on large samples of newly egressed parasites deposited on either the positively charged high molecular weight plasma fibronectin (M_w from ~ 400 to 550 kg/mol) or the negatively charged low molecular weight heparin ($M_w \sim 18$ kg/mol) immobilized on functionalized glass surfaces. We included in the assay the synthetic Poly-L-Lysine/Poly (EthyleneGlycol) (PLL/PEG) uncharged and hydrophilic polymer which prevents tachyzoite adhesion and the cationic pro-adhesive PLL bio-homo-polymer (Pavlou et al., 2020). Using

brightfield live-cell imaging (3,3 frames/second) of parasites under a controlled flow gradient rate (from a 0.05 $\mu\text{l}/\text{min}$ to 50 $\mu\text{l}/\text{min}$) in a microfluidic chip (Ibidi), it was possible to extrapolate the tachyzoite stalling forces for each surface (see Methods). The stalling force values represent a mix of tachyzoite behaviors including adherent motile and resting stages but they were not statistically different for the fibronectin and heparin surfaces (unpaired t test, $p=0.5647$) since 50% loss of parasites was observed when flow forces reached 105,8 pN and 103,7 pN, respectively (N= 5). In addition, 50% of parasites detached from the pro-gliding PLL substrate for lower forces (70,4 pN, N= 4) as compared to fibronectin or heparin coatings ($p=0.9407$, one way ANOVA followed by Dunnet's multiple comparisons) while for the PLL-PEG substrate, 50% parasites were lost for stalling forces more than 30 times lower (3,16 pN force, N= 4), in agreement with the protein repellent PEG feature (**Figure 1a and 1b**). Therefore, parasite adhesiveness on stiff substrates does not depend on specific molecular requirements.

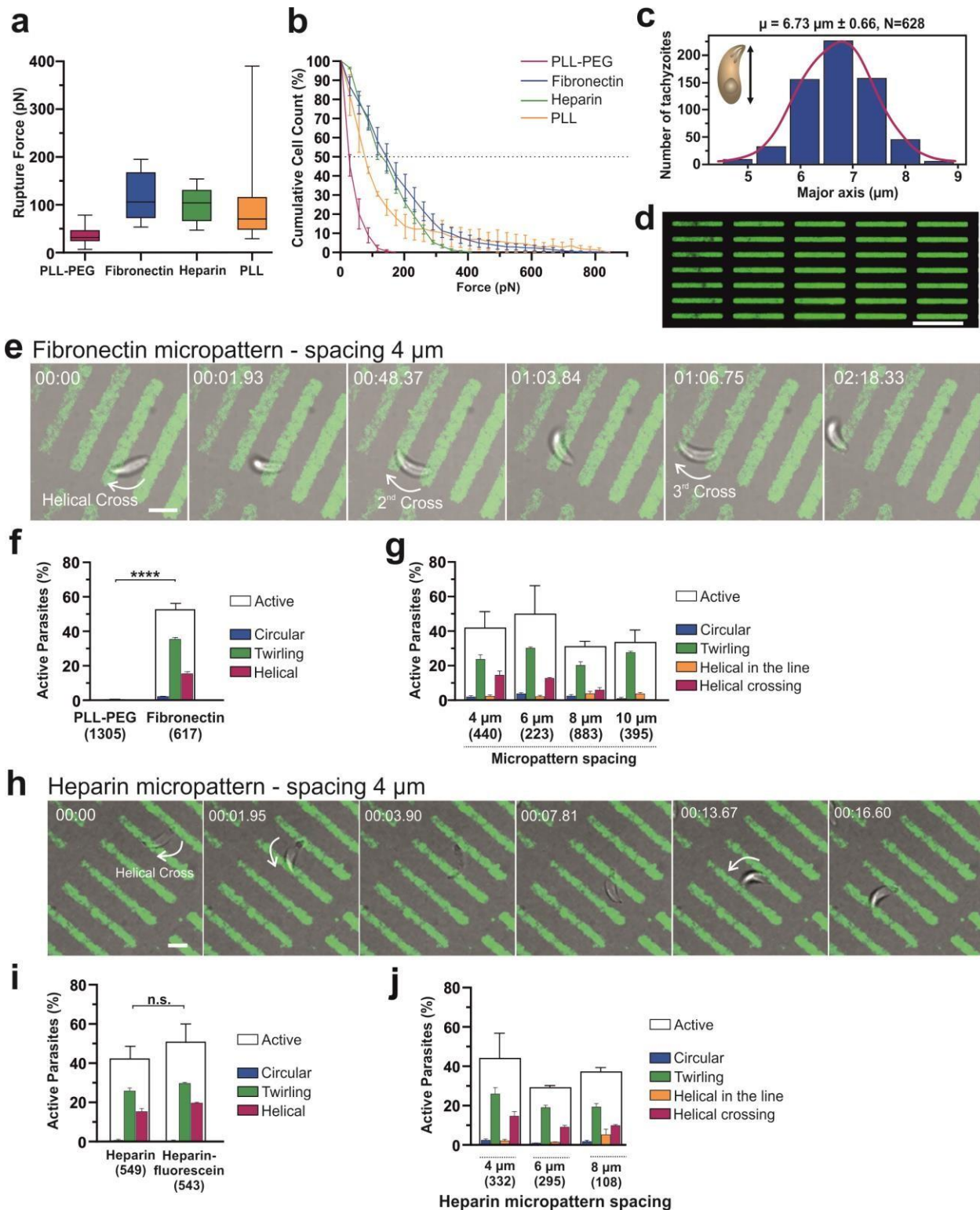


Figure 1 – Tachyzoite-substrate minimal surface requirements for providing an anchoring point. (a) Rupture-force distribution of tachyzoites on the PLL-PEG, fibronectin, heparin and

PLL-functionalized surface. Whiskers are maximum and minimum, and boxes indicate second and third quartiles framing the median. Medians for PLL-PEG, fibronectin, heparin and PLL are 3.17 pN (n = 2761 cells), 106 pN (n = 13148 cells), 104 pN (n = 4471 cells) and 70.4 pN (n = 2405 cells) respectively. **(b)** Cell -cumulative probability distribution plot of the rupture forces for PLL-PEG, fibronectin, heparin and PLL-surfaces. The horizontal black dashed line indicates 50% of the cell subset. **(c)** Histogram for the major axis length ($6.73 \mu\text{m} \pm 0.66$, n = 628 individual cells) for SAG1 stained tachyzoites, support the choice for the fibronectin lines width in the micropattern design and the increasing distances for the PLL-PEG antiadhesive zones. **(d)** Micropattern confocal image: fluorescently labeled fibronectin lanes of $2 \mu\text{m}$ (green) separated by non-adhesive PLL-PEG of $4 \mu\text{m}$ (black). Scale bar: $20 \mu\text{m}$. **(e)** Videomicroscopy timelapse showing a tachyzoite performing helical gliding on a micropattern spaced by $4 \mu\text{m}$. The tachyzoite performed three crossing movements attaching its apical pole in the next line. Time is in minutes: seconds, scale bar: $5 \mu\text{m}$. Video of this timelapse can be seen in Supplementary Video 1. **(f)** Percentage of active tachyzoites on PLL-PEG and fibronectin. (**** $p < 0.0001$, unpaired t Student's test). The active tachyzoites on fibronectin are further subcategorized between the three types of movement: circular, twirling and helical gliding. **(g)** Percentages of active tachyzoites on fibronectin micropatterns with regard to each typical movement (twirling, circular and helical, both in the line and crossing between lines, n = 223-883 parasites from at least 3 experiments). For the $10 \mu\text{m}$ spacing, note the absence of helical crossing. **(h)** Videomicroscopy timelapse showing a tachyzoite attached by the base in the line and performing twirling, the most common type of activity on the micropatterns spaced by $10 \mu\text{m}$. Time is in minutes: seconds, scale bar: $5 \mu\text{m}$. Video of this timelapse can be seen in Supplementary Video 2. **(i)** Percentage of motile tachyzoites on heparin ($M_w \sim 15 \text{ kg/mol}$) and heparin-fluorescein ($M_w \sim 18 \text{ kg/mol}$) surfaces (n.s., $p = 0.4951$, unpaired t Student's test). **(j)** Percentages on heparin-fluorescein micropatterns with regard to each typical movement (twirling, circular and helical, n = 108-332 parasites from at least 3 experiments).

Apicobasal focal adhesions are sufficient to promote tachyzoite helical gliding

Since live imaging and RICM studies have also demonstrated that the parasite moves over the initial anchoring site, we next interrogated whether this stationary site would be sufficient for sustained productive adhesion during parasite helical displacement, and this with either fibronectin or heparin coatings. Addressing this point allowed revisiting the contribution of the full body

adhesiveness during gliding. To this end, we used deep UV printing (Azioune et al., 2010) to design repetitive rectangle patterns coated with pro-adhesive material (*i.e.*, fibronectin or heparin) each separated by increasing widths of PEG lanes. The pro-adhesive rectangles measured 20 μm in length to restrict the chance of helical gliding within the rectangle while serving as good control for the active status of the parasites. The 2 μm width value of these micropatterns, which was close to the resolution limit of our printing method, was selected as it corresponds to slightly less than a third of the parasite length. Indeed, to adjust the pro-adhesive-PEG surface size, we determined the distribution of the tachyzoite length by imaging in real time 628 parasites post-labeling of their plasma membrane with the lipid PKH26 lipophilic membrane dye (**Figure 1c and 1d**). Given the $6,73 \pm 0,66 \mu\text{m}$ average length, we designed anti-adhesive PEG lanes of either 4, 6, 8 or 10 μm width (**Supplementary Figure 2c**). Videorecording sequences (15 min) of tachyzoites settled on these micropatterns but also on non-micropatterned fibronectin, heparin or PLL-PEG coatings were analyzed allowing to discriminate and quantify distinct behaviors among the active tachyzoite fraction. Of note, when adhesion was prevented on PLL-PEG surface for 15 minutes prior to providing a pro-adhesion surface to tachyzoites, no adverse effect on motility was observed (**** $p < 0.0001$, unpaired t Student's test, $n = 739-775$ parasites from at least 3 experiments) (**Supplementary Figure 2b**). In all “motility on micropattern assays” the fraction of active tachyzoites varied between 40 to 60 %, but did not statistically differ from the motility on homogenous fibronectin or heparin surfaces (**Figure 1f, 1i**) or fibronectin-based micropatterns: $p = 0.2015$, ANOVA followed by Dunnet's multiple comparisons. N full coated fibronectin = 617 tachyzoites; N micropattern spaced 4 μm = 440; N micropattern spaced 6 μm = 223 tachyzoites; N micropattern spaced 8 μm = 883 tachyzoites; N micropattern spaced 10 μm = 395 tachyzoites. For heparin-based micropatterns: $p = 0.7767$, ANOVA followed by Dunnet's multiple comparisons. N full coated heparin = 543 tachyzoites; N micropattern spaced 4 μm = 332; N micropattern spaced 6 μm = 295; N micropattern spaced 8 μm = 108 tachyzoites). In all cases the predominant fraction of tachyzoites twirled around their main axis with the basal pole attached to the substrate and in a rather upright position (Fibronectin full coat = $67.3\% \pm 3.4$; micropattern spaced 4 μm = $54.9\% \pm 15.1$; micropattern spaced 6 μm = $60.8\% \pm 2.1$; micropattern spaced 8 μm = $58.6\% \pm 15.9$; micropattern spaced 10 μm = $83.9\% \pm 3.9$) whereas less than ~8% underwent circular trajectory (Fibronectin full coat: $3.7\% \pm 0.6$; micropattern spaced 4 μm = $5.1\% \pm 2.6$; micropattern spaced 6 μm = $8.2\% \pm 1.6$; micropattern spaced 8 μm = $5.1\% \pm 3.1$; micropattern spaced 10 μm = $3.7\% \pm$

2.1). Most importantly, a fraction (for micropattern spaced 4 μm = 33.5% \pm 13.3, micropattern spaced 6 μm = 26.1% \pm 1.4; micropattern spaced 6 μm = 20.6% \pm 8.4; micropattern spaced 10 μm = 0%) of parasites could cross from one permissive rectangle to the next, provided the width of the PLL-PEG lane remained below 10 μm (**Figure 1e, 1h**). The frequency of crossing events decreased with the increasing width of the PEG lanes, which is consistent with the distribution of parasite length in the sample since shorter parasites could only grab the closest pro-adhesive area (**Figure 1g, 1j**). In addition to the cell-repellent PLL-PEG brush copolymer, we also used the poly(N-isopropylacrylamide) (PNIPAM) brushes to generate similar micropatterns with lanes of 4 and 6 μm of width. These PNIPAM micropatterns allow high density brushes with accurate micrometer resolution and showed superior stability and resistance than the PLL-PEG micropatterns due to the covalent chemistry on the substrate PNIPAM brushes (Mandal et al., 2012). PNIPAM uniform brushes prevented tachyzoite adhesion but tachyzoite adhere and twirl readily on the fibronectin rectangles and were able to undergo helical crossing over the PNIPAM area of 4 and 6 μm of width. Therefore, these qualitative and quantitative analyses confirm that once attached from their basal pole, the tachyzoite must slide over only one new site of adhesion on the substrate which position corresponds to the initial molecular anchor built by the parasite through an apical contact.

To discriminate potential differences in the modalities of gliding when parasites performed on top of a rectangles coated with fibronectin or when they crossed over the PEG area, hence were restricted in their adhesive behavior, we analyzed main parameters of the gliding performance. First; tracking the gliding trajectories of parasites did not allow detecting a significant difference in total displacement (n.s., $p=0.1169$, ANOVA followed by Dunnet's multiple comparisons, N Fibronectin = 90 tachyzoites; N micropattern spaced 4 μm = 51; micropattern spaced 6 μm = 31; micropattern spaced 8 μm = 52) while the mean velocity of parasites crossing PEG was significantly faster (**** $p<0.0001$, ANOVA followed by Dunnet's multiple comparisons) (**Figure 2a**), an observation which was not recapitulated when parasites glided on heparin (ANOVA result: $p=0.4282$, followed by Dunnet's multiple comparisons, **Figure 2b**). The observed increase in velocity when parasites crossed micropatterns could indicate higher traction force or a lower resistance to movement due to reduced area of friction.

Ultrastructure-Expansion Microscopy reveals anchoring localization on helical gliding across intermittent adhesive surfaces

To interrogate whether the increased velocity of parasites gliding over the fibronectin micropatterns might arise from a decrease in resistance of motion when compared to parasites moving on uniform fibronectin coat, we analyzed *in situ* at about 50-70 nm nanoscale resolution how the parasite coped with composite or uniform substrates using expansion microscopy. When parasites were caught in their move across PEG or within the pro-adhesive rectangle micropatterns and stained to visualize their contours as well as their cortical spiral microtubules, we noticed a difference between the two situations. Tachyzoites that crossed over PEG made only polar contacts with the two successive fibronectin area and kept their natural curvature as highlighted with the 3D reconstruction of the helical sequence (**Figure 2c**). The tachyzoite extended its body to reach the next fibronectin area, deformed apically and lifted up while dragging its body forward but could not flatten on the substrate as much as did those that glide on non-patterned fibronectin (**Figure 2d**). There is also a considerable microtubule torsion in the pre-kink and kink stages of the crossing helical gliding, which accounts for the spring-like mechanism for displacement and correlates with observations on fully coated 2D surfaces.

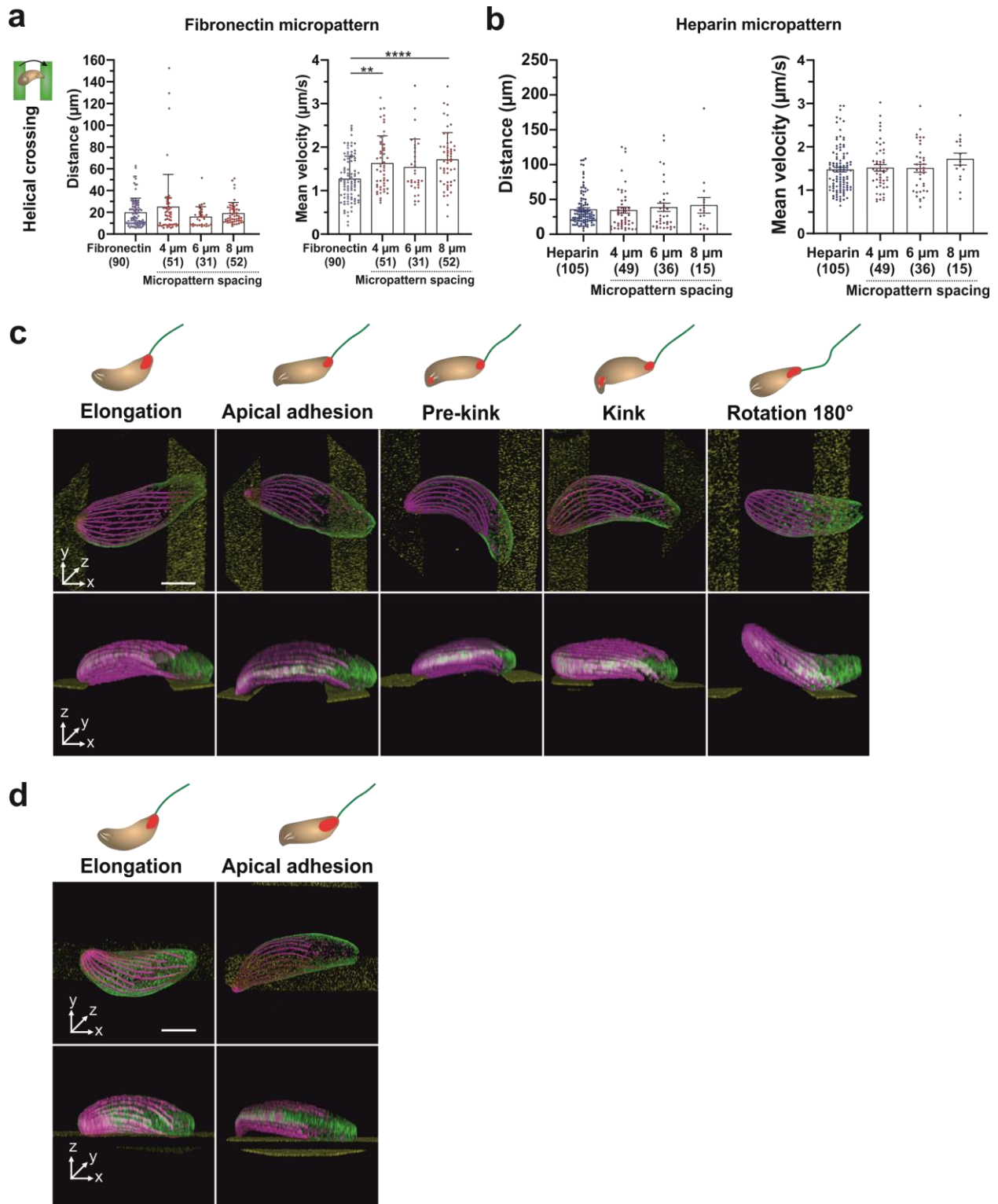


Figure 2 – Dynamics and anchoring traction force localization on crossing helical gliding. (a) Results for total displacement and mean velocity of the crossing helical gliding on fibronectin

micropatterns. Crossing helical gliding does not differ from gliding on a full coated fibronectin coverslip in total displacement (n.s., $p=0.1169$, ANOVA followed by Dunnet's multiple comparisons). Nevertheless, crossing helical gliding displays a faster behavior (4 μm : ** $p<0.01$, 8 μm : **** $p<0.0001$, both ANOVA followed by Dunnet's multiple comparisons). **(b)** On heparin-fluorescein micropatterned surfaces, tachyzoites display a similar total displacement and mean velocity while performing crossing helical gliding, in all types of line distances (n=15-105 parasites from at least three independent essays, n.s., one-way ANOVA followed by Dunnet's multiple comparisons). **(c)** U-ExM confocal images showing representative tachyzoites immunolabeled for the GAP45 protein (green) delineating the parasite periphery, alfa-tubulin (magenta) and the micropatterned fibronectin surface (yellow). During the apical adhesion, the two poles are clearly in contact with the micropatterned surface (white arrowhead: apical pole, white arrow: basal pole) while the rest of the body is not in contact with the anti-adhesive PLL-PEG. Note the pronounced microtubule torsion in the pre-kink and kink stages followed by the extension in the rotation stage, accounting for the functional contribution of the microtubule contraction as spring-like mechanism in the crossing gliding. Scale bar: 2 μm . **(c)** The helical gliding performed in the line shows the same microtubule behavior, with only the two poles attached at the moment before contraction (white arrowhead: apical pole, white arrow: basal pole). Scale bar: 2 μm .

Designing specific tunable model surfaces with physicochemical properties characterized by QCM-D for monitoring tachyzoite motility on single molecule surfaces

Pro-motile conditions for *T. gondii* tachyzoites include a pro-adhesive substrate as illustrated with micropatterns, but also proper trigger(s) for the secretion of MIC adhesins (Brown et al., 2016; Bullen et al., 2016). Indeed, most if not all parasite motility assays have been carried in presence of serum albumin (SA) in the medium or/and adsorbed on glass surfaces provided either through heat inactivated fetal serum or purified plasma-derived protein. In addition, both lipid-bound or lipid-free SA molecules have been characterized as equally highly potent and selective segretagogues of soluble and transmembrane MIC proteins, including MIC2 (Brown et al., 2016). With the goal of identifying the minimal interaction between the ECM and an adhesin ligand that would support helical motility, it was crucial to design an assay in which we could control that

only a given molecular species would be proposed to the parasite, thus preventing adsorption of SA or other serum components to the surface. To this purpose, we used an acoustic surface-sensitive technique, quartz-crystal microbalance with dissipation monitoring (QCM-D) which allows highly sensitive real-time monitoring of the adsorption kinetics, binding stability and specificity through measuring the resonance frequency (Δf) and dissipation (ΔD) shifts of the silica-coated piezoelectric sensor (**Figure 3a**). QCM-D analysis confirmed strong adsorption of the motility buffer components on the widely used bare and PLL coated silica (**Supplementary Figure 3**). In contrast, no binding from the components of the tachyzoite motility buffer (*e.g.* fetal calf serum, glucose) was observed on the PLL-PEG surface (**Figure 3b**). Specifically, QCMD data and viscoelastic modeling showed that PLL-PEG saturation was achieved in less than 5 min and resulted in a stable and soft ($\Delta D > 0$) coating of 5.0 ± 0.8 nm in thickness (**Figure 3b**). We could also perform QCM-D measurement on fibronectin coatings, where binding is observed after ~1 hour, with a soft ($\Delta D > 0$) coating being stable in the studied media and forming a layer of 12.4 ± 0.9 nm in thickness (**Figure 3c**).

Furthermore, to compare physicochemical parameters of the anti-adhesive PLL-PEG and adhesive fibronectin, we used viscoelastic modeling with QCM-D, which allowed us to determine film thickness d and viscoelastic properties (storage modulus G' and loss modulus G''). The results showed that the two layers have similar storage moduli, while the thickness and loss modulus of fibronectin are 2.5- and 1.8-times higher than that of PLL-PEG (inset tables in **Figure 3b, 3c**). It is thus possible that in the case of fibronectin sufficient thickness and viscosity contribute to the enhanced parasites motility. Furthermore, the Δf and ΔD shifts curve behaviors as well as the viscoelastic modeling performed were consistent with the ones previously reported (Hemmersam et al., 2008; Perry et al., 2009; Saftics et al., 2018).

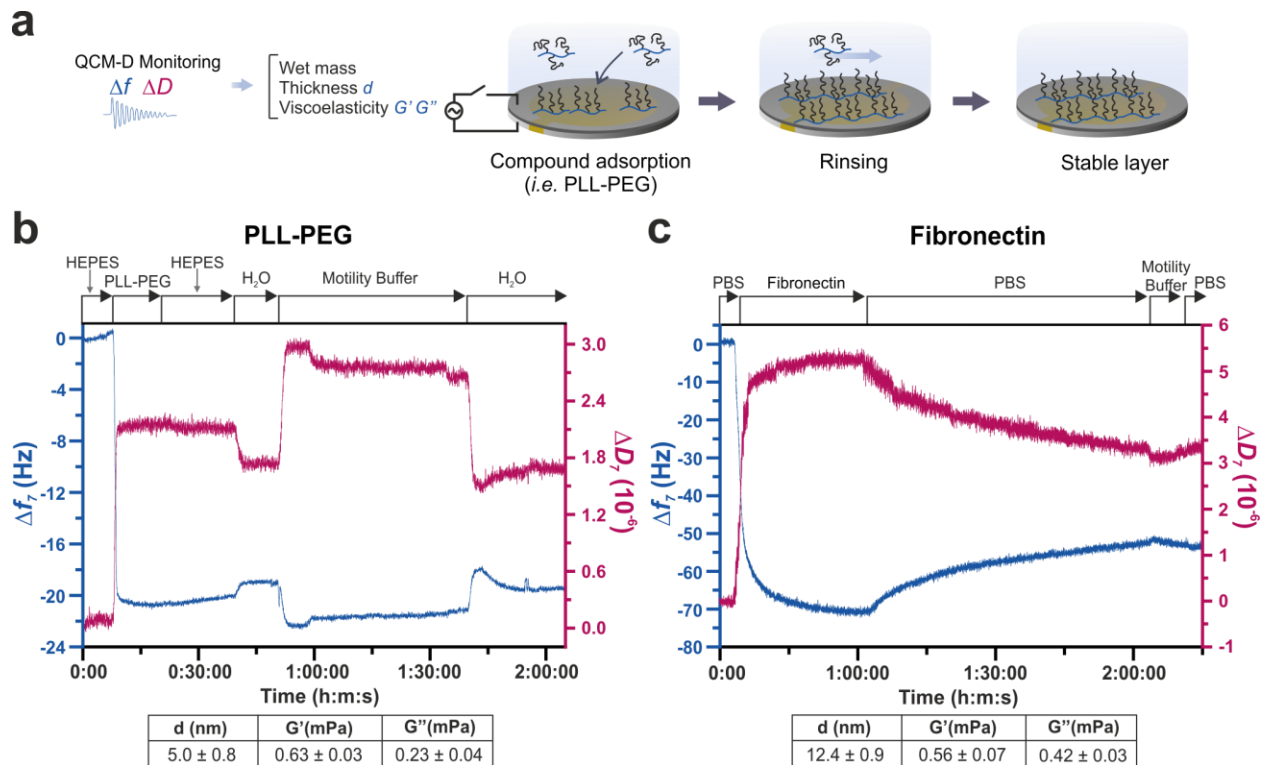


Figure 3 - Characterization of molecular coatings used in micropatterns (a) Main steps of QCM-D measurements. The silica-coated quartz sensor oscillates at a resonance frequency, allowing to monitor shifts in frequency (Δf) and dissipation (ΔD) upon binding to its surface. Measurements are performed in solution, and the stability of molecules attachment is verified upon rinsing with working buffer. (b) Characteristic Δf and ΔD shifts (7th overtone) obtained for PLL-PEG binding to silica. QCM-D shows fast binding of PLL-PEG resulting in a stable and soft ($\Delta D > 0$) coating. (c) Somewhat slower binding observed in the case of fibronectin (saturation in 1 h), with the major part of the soft ($\Delta D > 0$) coating being stable in studied media. Importantly, in both cases, the components of the tachyzoite motility buffer do not attach to the formed layers as evidence by the lack of Δf and ΔD shifts once the motile buffer is injected.

Capitalizing on the PLL-PEG surface results, we next developed a tunable model system based on the streptavidin/biotin chemistry and for which the bottom layer would be kept constant, hence enabling to compare the specific effects of the top layer's determinants on tachyzoite adhesiveness and motility (**Figure 4a**). The model surfaces consisted on a first layer of PLL-PEG-biotin (PPL-PEG-b) adsorbed on silica surfaces combined with a second layer of streptavidin:biotin-X (SAv:b-

X) complex, where X represents different functional groups or molecules. To compare different functional groups, we selected mono-biotinylated versions of PEG with a single terminal hydroxyl group (-OH), amine group (-NH₂) or carboxylic group (-COOH). All b-PEG-X compounds present the same chain length and similar molecular weight (3-5 kg/mol). We also included mono-biotinylated versions of molecules with reported interaction on tachyzoite motility, such as human serum albumin (HSA) and heparan sulfate (HS).

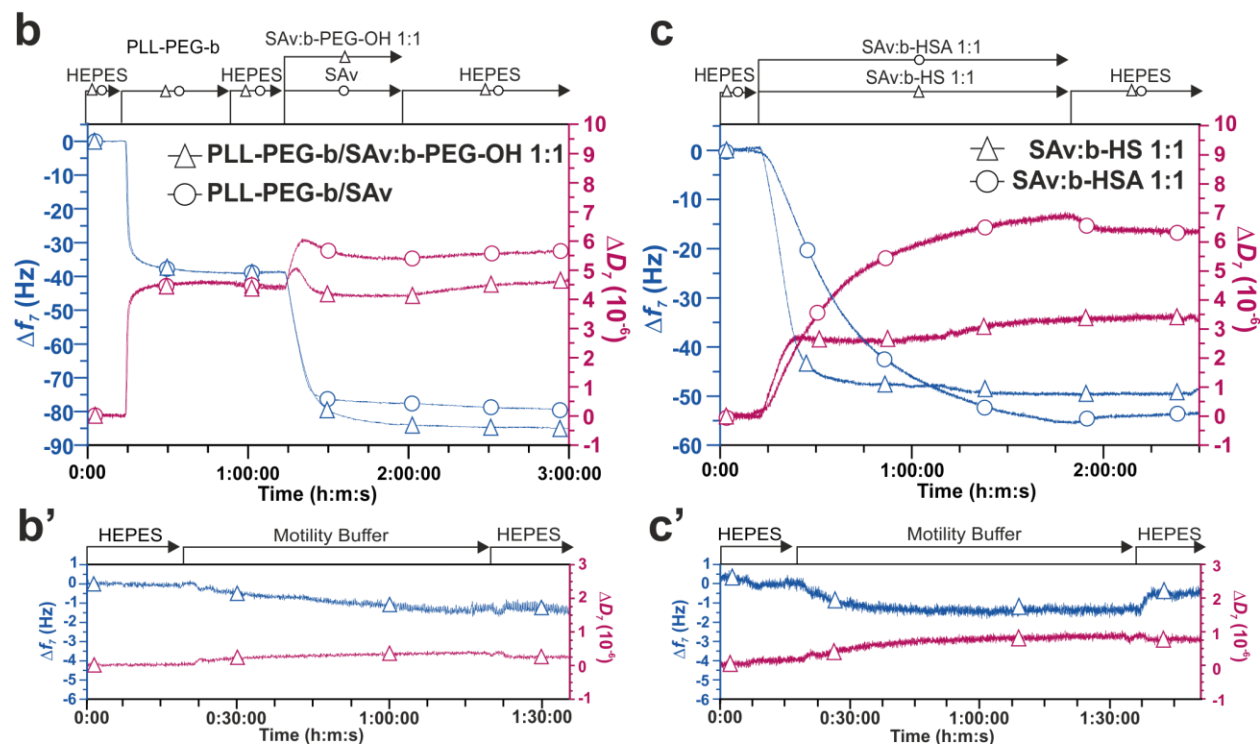
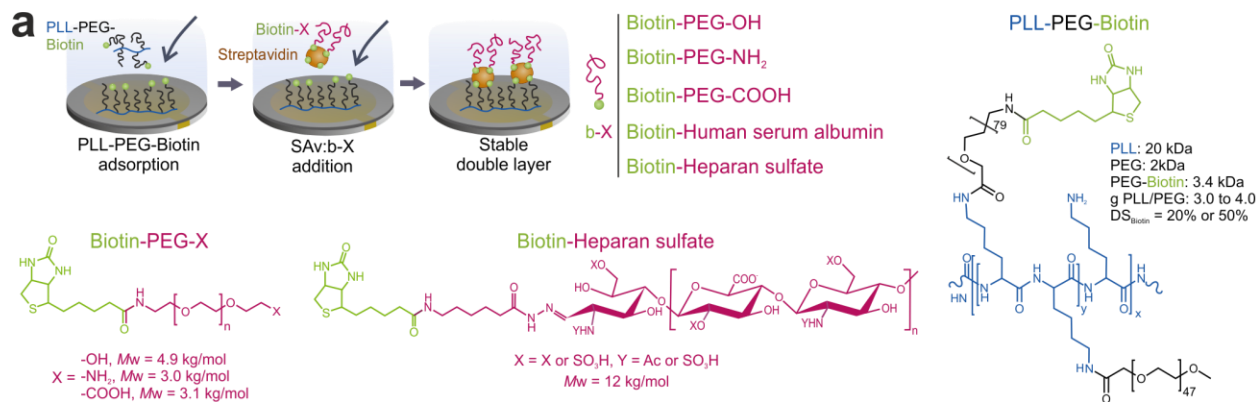
To validate the specific requirements of the tunable systems, we tested two strategies for production with either a two-step or a three-step building process. When PLL-PEG-b was first adsorbed, then SA_v and b-X sequentially added (i.e., three step addition), QCM-D showed a fast binding of SA_v to the PLL-PEG-b layer prior b-X addition with a saturation achieved within a few min, and a resulting stable and hard ($\Delta D \sim 0$) coating. Of note, the SA_v Δf observed in our system is comparable with the ones previously reported for SA_v binding to self-assembled monolayers (SAMs) and supported-lipid bilayers (SLBs) (Dubacheva et al., 2017). However, this step led to the saturation of all SA_v binding pockets, thereby leaving no available site for the subsequent b-X binding (**Supplementary Figure 5a**). In contrast, when the SA_v was first combined with the b-X, and the complex added to the PLL-PEG-b layer, we obtained the specific binding desired (Figure 4b). Furthermore, we checked that the b-X molecules did not interact with the PLL-PEG-b layer in absence of SA_v, as strong indication that the attachment of the SA_v:b-X complex with PLL-PEG-b was specific. Lastly, the ΔD and Δf observed for all the b-X complexes were higher than the ones for SA_v alone, arguing for a stable attachment from the second layer and an absence of SA_v alone binding (**Supplementary Figure 4f**).

Therefore, we continued with the two-step strategy coupled to QCM-D, and first established that the PLL-PEG-b layer common to all constructions bound within 5 minutes to the silica surface, resulting in a stable and soft ($\Delta D > 0$) coating (**Figure 4b**) of 8.4 ± 0.6 nm in thickness (**Figure 4d**). Secondly, we documented that the binding of all SA_v:b-X complexes screened including small and larger biotinylated ligands, occurred in several minutes (~15 minutes for the b-PEG-X compounds, ~20 minutes for b-HS and ~45 minutes for b-HSA) resulting in stable and soft ($\Delta D > 0$) coatings and comparable ΔD and Δf responses (illustrated for SA_v:b-PEG-OH and the bHSA and b-HS in Figure 4b,c and for -NH₂ and -COOH terminal groups in **Supplementary Figure 4a, 4b, 4f**).

A significant benefit of the tunable approach is that it also allows modulating the ratio of the top layer ligands to test different surface densities. By tuning the b-X concentration while maintaining the SA_v concentration fixed, we can vary the b-X per SA_v ratios in 1:1, 1:2 and 1:3 proportions. When increasing the ratios, we observed a proportional increase in ΔD while maintaining similar Δf for all our complexes (**Supplementary Figure 4f**); the comparable Δf signals show a correct formation of our complexes in solution, while the ΔD shifts illustrate the density increase as a result of our second layer. All the ΔD for our b-X showed a soft layer formation as expected, in contrast with the hard coating observed for SA_v alone (**Supplementary Figure 4f**).

To explore further the physicochemical properties of the tunable constructions, we determined thickness and viscoelastic properties (loss modulus G' and storage modulus G'') of the formed layers. Comparing the biophysical characteristics of SA_v:b-PEG-X coatings (X= -OH, -NH₂ and -COOH) at the same stoichiometry (1:2) reveals similar thickness, storage and loss modulus for all of them (**Figure 4d**, **Supplementary Figure 4f** for Δf and ΔD shifts). These results are expected, considering similar sized of PEG chains in these constructs. Moreover, the comparison of the parameters upon increasing the number of b-X ligands per SA_v shows that the thickness of the coating increases, while G' and G'' decrease. These results are expected, indicating that the number of adsorbed b-PEG-X molecules increases with the complex stoichiometry, contributing into the resulting thickness and softness of the bound later (**Figure 4d**).

Finally, it was critical that the buffer components used on the gliding assays (glucose, FCS, salts) did not interact with any of the PLL-PEG-b/SA_v:b-X layers built. Indeed QCM-D indicated that no there is negligible attachment to the PLL-PEG-b/SA_v:b-X coatings, as represented by the lack of Δf and ΔD shifts (**Figure 4b'** and **4c'**, **Supplementary Figure 4 c**, **4d**, **4e**), which validated the model system to study tachyzoite interaction and motility .



d

| Surface | d (nm) | G' (MPa) | G'' (MPa) |
|--|------------|-------------|-------------|
| PLL-PEG-Biotin | 8.4 ± 0.6 | 0.32 ± 0.01 | 0.21 ± 0.01 |
| PLL-PEG-Biotin / SAV:b-PEG-OH 1:1 | 17.5 ± 0.5 | 0.51 ± 0.10 | 0.39 ± 0.01 |
| PLL-PEG-Biotin / SAV:b-PEG-OH 1:2 | 17.9 ± 0.2 | 0.44 ± 0.01 | 0.31 ± 0.03 |
| PLL-PEG-Biotin / SAV:b-PEG-OH 1:3 | 19.3 ± 1.9 | 0.25 ± 0.01 | 0.22 ± 0.01 |
| PLL-PEG-Biotin / SAV:b-PEG-NH ₂ 1:2 | 17.0 ± 2.7 | 0.43 ± 0.02 | 0.32 ± 0.03 |
| PLL-PEG-Biotin / SAV:b-PEG-COOH 1:2 | 16.6 ± 1.6 | 0.43 ± 0.12 | 0.33 ± 0.06 |
| PLL-PEG-Biotin / SAV:b-Human Serum Albumin 1:2 | 20.1 ± 1.7 | 0.29 ± 0.07 | 0.22 ± 0.01 |
| PLL-PEG-Biotin / SAV:b-Heparan Sulfate 1:1 | 17.2 ± 2.6 | 0.44 ± 0.01 | 0.32 ± 0.05 |
| PLL-PEG-Biotin / SAV:b-Heparan Sulfate 1:2 | 20.9 ± 0.7 | 0.27 ± 0.02 | 0.21 ± 0.01 |

Figure 4 - Conceptualization and characterization of tunable surface system (a) Main steps schematic of the model construction, allowing tuning the terminal molecule while using the same

surface chemistry. First, PLL-PEG-biotin (PLL-PEG-b) is adsorbed on the silica-coated sensor, followed by the injection of streptavidin/biotin-X (SAv:b-X) complex, being X the tunable terminal group. Structure and molecular weight of the main components are shown. **(b)** QCM-D shows fast binding of PLL-PEG-b resulting in a stable and soft ($\Delta D > 0$) coating, same as for the SAv:b-PEG-OH (1:1) complex. **(b')** The components of the tachyzoite motility buffer (i.e., glucose, fetal calf serum) do not show strong attachment to the PLL-PEG-b/SAv:b-PEG-OH (1:1) complex. **(c)** QCM-D shows fast binding of SAv:b-HS (1:1) on the PLL-PEG-b layer resulting in a stable and soft ($\Delta D > 0$) coating. **(c')** The components of the tachyzoite motility buffer (i.e., glucose, fetal calf serum) do not show strong attachment to the PLL-PEG-b/SAv:b-HS complex. **(d)** Thickness (d), storage modulus (G') and loss modulus (G'') determined using viscoelastic modeling. Values shown represent mean \pm SEM from at $n = 2-17$ independent QCM-D experiments.

HS presentation to *T. gondii* tachyzoite is sufficient for quasi optimal gliding capacities

First, we tested the tachyzoite motile activity on the bottom layer components PLL-PEG-b and PLL-PEG-b/SAv, and observed tachyzoite did not adhere, hence did not show any motile capacity motility on either similarly to what we reported for PLL-PEG ($p=0.133$, Mann-Whitney test) (**Figure 5a**). Next, we analyzed the effect of the bX molecules exposed to the parasite in the PLL-PEG-b/SAv:b-(PEG)-X coatings. When the tachyzoite was solely exposed to the -OH terminal group, no gliding activity was observed, hence this permissiveness of the substrate was not statistically different from that of PLL-PEG ($p=0.6571$, Mann-Whitney test). In contrast, the presence of -NH₂ and -COOH terminal groups allowed less than 10% of the tachyzoites to exhibit some gliding motile but the reduced motile activity recorded appeared statistically different from the anti-adhesive PLL-PEG (**** $p<0.0001$, Fisher's exact test). Furthermore, increasing the ratio of SAv:b-PEG-NH₂ from 1:2 to 1:3 did not improve gliding capacity ($p=0.4687$, Fisher's exact test), whereas the same change did increase motility for the COOH terminal group (**, $p=0.0091$, Fisher's exact test) (**Figure 5b**). Therefore, exposed negative charges favored motility but these interaction were far less efficient than when parasites settled on the typical fibronectin coat (**** $p<0.0001$, Fisher's exact test) (**Figure 5b**).

Furthermore, we tested the tachyzoite motile response on human serum albumin (HSA) and heparan sulfate (HS), both with a bigger molecular weight than the previous PEG complexes and shown to be relevant molecules for *T. gondii* motility (Brown et al., 2016; Carruthers et al., 2000). For HSA, we observe a restoration in the tachyzoite active phenotype in comparison with PLL-PEG (**** $p < 0.0001$, Fisher's exact test). Interestingly, an increase in the HSA surface density increases the activity even further (*, $p = 0.0306$, Fisher's exact test, Figure 5c). In the case of HS, the activity also increases from the PLL-PEG (**** $p < 0.0001$, Fisher's exact test) (Figure 5d), and even further by doubling the amount of exposed HS in the surface (**, $p = 0.0055$, Fisher's exact test). Consequently, the attached to PLL-PEG-b SA v :b-HS complex at a ratio 1:2 does not differ from the HS coating directly bound to glass ($p = 0.3937$, Fisher's exact test). Interestingly, this last result shows that presence of HS is enough to promote an active phenotype. Taking all together, and combining with the results of similar viscoelastic properties from our tunable model system, we show that *T. gondii* motile activity depends on the chemical nature of the terminal molecular ligands and their density.

More importantly, the thickness and viscoelastic properties of PLL-PEG-b/SA v :b-PEG-OH (1:3), PLL-PEG-b/SA v :b-HS (1:2) and PLL-PEG-b/SA v :b-HSA (1:2) are found to be very similar (**Figure 4d**), while motile responses on them are significantly different (**** $p < 0.0001$, Fisher's exact test) (**Figure 5b, 5c and 5d**). This allows us to conclude on the importance of the chemical nature of surface ligands for the parasite's motility.

Next, we analyzed the main parameters of tachyzoite motile behavior to further discriminate potential differences in the tunable surfaces. First, we tracked the trajectories and observed that tachyzoites displayed similar displacement lengths in all of the cases (n.s., $p > 0.05$, ANOVA followed by Dunnet's multiple comparisons). For some surfaces, the duration of the movement was decreased (b-PEG-NH₂ ratio 1:3, b-PEG-COOH ratio 1:3, b-HSA ratios 1:2 and 1:3, b-HS ratio 1:1), causing the mean velocities in most of the surfaces to be higher than the full coated fibronectin control (**** $p < 0.001$, one-way ANOVA followed by Dunnet's multiple comparisons) (**Supplementary Figure 6**).

Additionally, to pinpoint key properties on chemical structure responsible for parasite motility, we hypothesized that the increased active response from HS was related to the charges present on this proteoglycan, distributed along the HS molecule. To further investigate the relevance of terminal

charge, we neutralized a HS-coated glass surface using surfen (*bis-2-methyl-4-amino-quinolyl-6-carbamide*), which is thought to bind to the sulfated disaccharide units of HS through the interaction of its protonated quinolone rings with the uronic acid's sulfate and carboxyl groups (Schuksz et al., 2008). This neutralization resulted in a reduced tachyzoite motility (**, $p=0.0016$, one-way ANOVA) (**Figure 5e**), pointing towards the importance of negative charge as a key element in the chemical structure of the surface coating among other biophysical properties important for parasite adhesion and motility.

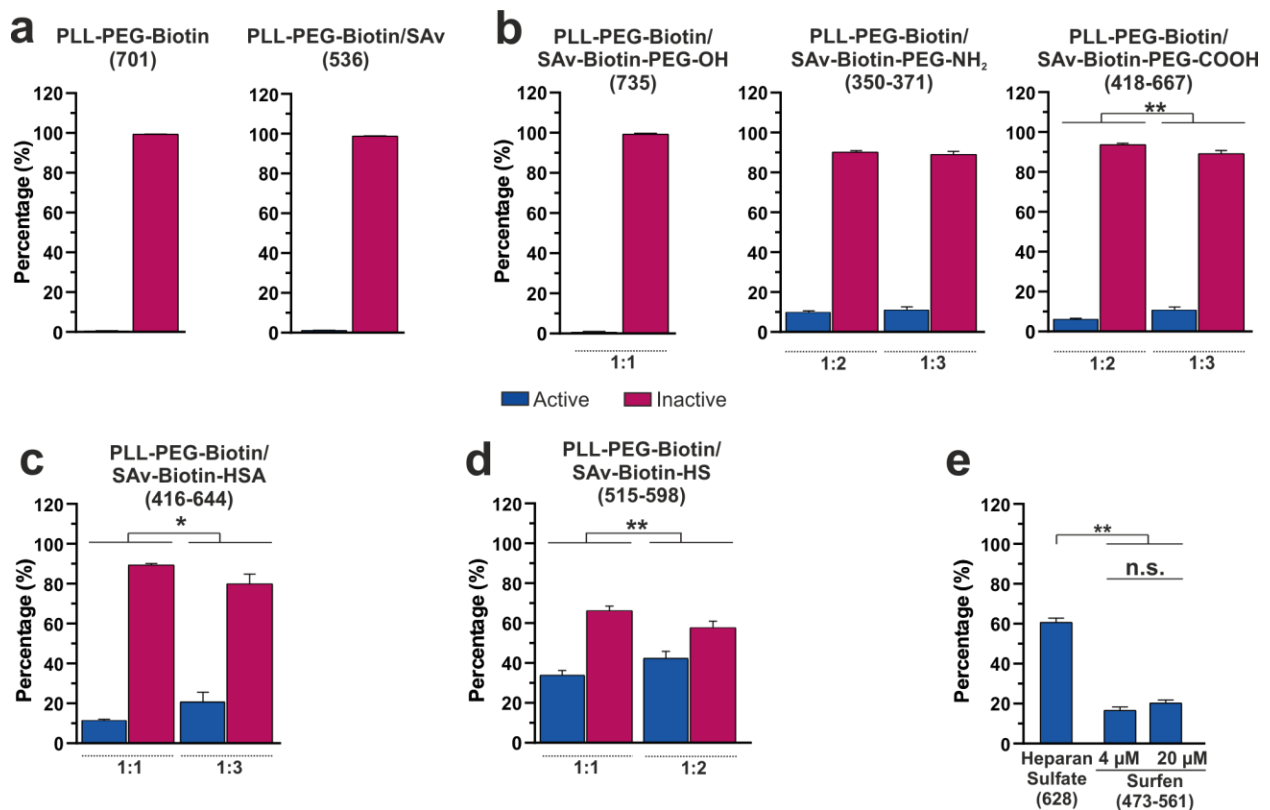


Figure 5 - Tachyzoite activity on tunable surface coatings. (a) Tachyzoites show no activity on the first layer of the tunable system (PLL-PEG-b and PLL-PEG-b/SAv). (b) For the PEG terminal groups, the -OH terminal group shows no increase on the active phenotype, while -COOH and -NH₂ show a significant increase in the activity percentage with respect to PLL-PEG (**** $p<0.0001$, Fisher's exact test). Increasing the ratio of exposed -COOH increases even further tachyzoite motility (**, $p=0.0091$, Fisher's exact test). (c) Terminal layer of HSA increases the activity with respect with PLL-PEG (**** $p<0.0001$, Fisher's exact test). Increasing the ratio of

exposed moieties also increases activity (*, $p=0.0306$, Fisher's exact test). **(d)** HS also show a significant activity difference with the non-adhesive PLL-PEG (**** $p<0.0001$, Fisher's exact test). Doubling the amount of exposed HS in the surface increases even further the activity (**, $p=0.0055$, Fisher's exact test). **(e)** Charge neutralization of HS 12 kg/mol with surfen decreases the tachyzoite activity (**, $p=0.0016$, one-way ANOVA). Increase of surfen concentration from 4 μM to 20 μM doesn't bring a further activity decrease (n.s., $p=0.1804$, unpaired t test). For all graphs, bars represent mean \pm SEM from at least three independent experiments, number of parasites is noted between parentheses.

Apicobasal membrane flow is an independent process from tachyzoite adhesion

Because the anteroposterior membrane flow has been shown tightly associated with the tachyzoite motility through different mechanisms, we used the anti-adhesive substrate properties of PEG to decouple membrane flow and productive adhesion for motility. It was recently proposed a 'fountain flow' model where the adhesins translocated to the posterior pole contribute to generate productive movement forward for the tachyzoite. To monitor membrane translocation, we coupled 0.2 μm microbeads, activated using 1-ethyl-3- [3-dimethylaminopropyl] carbodiimide (EDC), and covalently bound to the amine terminal groups present in the tachyzoite's membrane. Once interacting with the parasite surface, the microbeads engage in an antero-posterior capping process, in particular when actin competent parasites are settled on a fibronectin-coated surface (Pavlou et al., 2020). Using PLL-PEG coated coverslips, we observed using STED microscopy, at a 40 nm xy resolution, that tachyzoites present an accumulation of microbeads in the basal pole 10 minutes after being in contact with the surface (**Figure 6a**). Furthermore, high-speed confocal microscopy at 3 frames/ second showed that tachyzoites were able to translocate beads despite they did not adhere to the PLL-PEG surface and appeared as "floating" objects (**Figure 6b**). These assays brought definitive evidence that membrane flow is a process functionally independent from the adhesive behavior that determine motile capacity. Quantitative analysis of bead translocation efficiencies for parasites on pro-motile (fibronectin) and anti-fouling (PLL-PEG) surfaces showed that the percentage of tachyzoites with basally translocated beads between both surfaces was comparable, and the process followed the same actomyosin-dependent rules in either surface conditions. On both surface conditions, bead translocation was similarly inhibited when parasites

were exposed to the actin polymerization inhibitor Cytochalasin D (**** $p < 0.0001$, unpaired t test) (**Figure 6c and 6d**) and tachyzoites lacking the MyoA-motor required for motility were also unable to translocate beads (**Figure 6f**). In addition, wildtype tachyzoites were unable to translocate beads when exposed to the intracellular mimicking conditions (**** $p < 0.0001$, unpaired t test). They responded to 100 μM zaprinast, a stimulator of microneme secretion, since an increase in the numbers of tachyzoites associated with posteriorly positioned beads was observed on PLL-PEG surface (* $p = 0.0212$, unpaired t test), and to a less extent on fibronectin (n.s., $p = 0.3842$, unpaired t test). Additionally, we explored the possibility of maintaining the tachyzoites in suspension by mechanically periodically resuspending them using a pipette, and fixing directly in solution; this parasite population also showed basally translocated beads (**Figure 6e**). Taking together, these results strengthen the view that membrane flow is switched on upon stimulation of microneme secretion, when tachyzoites sense extracellular chemical, but must operate even in absence of motile behavior to ensure cell size homeostasis.

We analyzed the MIC2 distribution on extracellular tachyzoites expressing the MIC2-HaloTag fusion protein (Gras et al., 2017). Using fluorescent conjugated ligand for HaloTag and super resolution STED microscopy, images with a 40 nm xy resolution show the MIC2 distribution of tachyzoites exposed to non-adhesive surfaces, with an expected accumulation in the apical pole but also a patch distribution in a more basal position of the body (**Figure 6g**). Furthermore, we also observed a colocalization of some of these patches with microbeads, suggesting that MIC2 could be among the adhesins responsible for the translocation process. To test it, we investigated the impact of the deletion of MIC2 for membrane flow, evidenced by the bead translocation. Using mutant tachyzoites lines knock-out for MIC2 (MIC2 KO), we observed that parasites lacking MIC2 are able to translocate beads as the control genotype, both in adhesive and anti-adhesive surfaces (**Figure 6h**). Furthermore, the addition of zaprinast causes an increase of bead translocation (* $p < 0.05$ for PLL-PEG and *** $p < 0.001$ for fibronectin, unpaired t test). These results suggest that even as an accumulation of MIC2 was spotted in the position of the bead, possibly there are other MIC adhesins involved in the translocation process as well besides MIC2.

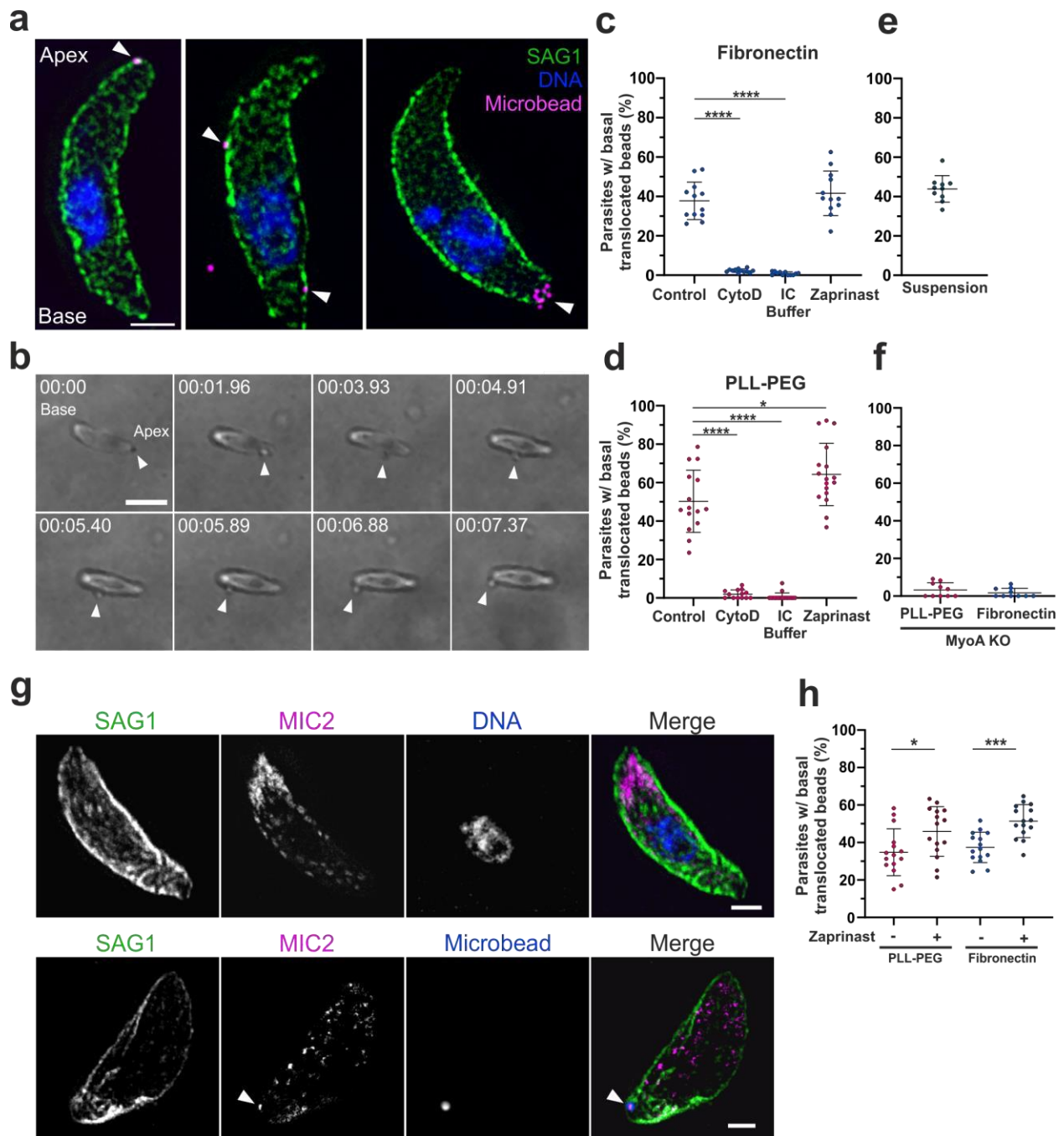


Figure 6 – Tachyzoite apicobasal membrane flow on anti-adhesive surfaces (a) Super-resolution STED images showing beads (magenta, white arrowheads) attached to the apical part of the tachyzoite’s surface (SAG1, in green) (left), in the middle part of the cell (center) and in the basal pole of the tachyzoite (right). Scale bar: 1 μ m. **(b)** Videomicroscopy timelapse showing a tachyzoite on a PLL-PEG surface translocating an apically attached bead (white arrowhead) to its basal pole while being in suspension as a result of the non-adhesiveness of the surface. Time is in

minutes: seconds, scale bar: 5 μm . Video of this timelapse can be seen on Supplementary Video 4. (c) Percentages of tachyzoites on a fibronectin surface with basally translocated beads after 10 minutes, in normal motility buffer (control), with the addition of the actin blocker cytochalasinD (CytoD), in the presence of intracellular buffer conditions (IC Buffer) and with the addition of zaprinast 250 μM , a drug which exacerbates microneme secretion (zaprinast). *** $p < 0.001$ and **** $p < 0.0001$, unpaired t test. $n = 153\text{-}209$ parasites from at least 3 experiments. (d) Percentages of tachyzoites in the same conditions as (c) but with the difference of being on top of the non-adhesive surface PLL-PEG. * $p < 0.05$, *** $p < 0.001$ and **** $p < 0.0001$, unpaired t test. $n = 181\text{-}351$ parasites from at least 3 experiments. (e) Percentages of tachyzoites with basally translocated beads after 10 minutes, without being in contact with any surface during that time and fully in suspension. $n = 342$ parasites from 5 experiments. (f) Percentages of tachyzoites deficient in MyosinA with basally translocated beads after 10 minutes, both in PLL-PEG and fibronectin surfaces. $n = 469\text{-}2149$ parasites from at least 3 experiments. (g) Super-resolution STED images showing beads (blue) colocalizing with extracellular MIC2 (magenta, white arrowhead) in the tachyzoite's surface (SAG1, in green). Scale bar: 1 μm . (h) Percentages of tachyzoites deficient in MIC2 with basally translocated beads after 10 minutes, both in PLL-PEG and fibronectin surfaces. Increase of microneme secretion by addition of 250 μM zaprinast cause an increase in basally translocated beads. * $p < 0.05$, *** $p < 0.001$, $n = 478\text{-}993$ parasites from at least 3 experiments.

Microneme protein MIC2 is necessary for apical anchoring on discontinued surfaces

Several studies report the importance of the microneme protein MIC2 as an adhesin involved in attachment and motility, as it is seen as the bridge between the tachyzoite acto-myosin motor system and ECM ligands (Gras et al., 2017; Huynh & Carruthers, 2006). To gain insights on the interaction between MIC2 and the different surfaces tested on our micropattern setting, we evaluated its effect on the generation of an anchoring point and subsequent traction force compatible with helical gliding. Comparing the active behavior with wild-type parasites, MIC2 KO tachyzoites show significantly less activity than control parasites (**, $p = 0.0016$, unpaired t test), in both fibronectin and heparin full coated coverslips. For the MIC2 KO strain, the activity in these surfaces didn't differ between both surfaces (n.s., $p = 0.3041$, unpaired t test, $n = 455\text{-}795$ tachyzoites) (**Figure 7a**). MIC2 KO tachyzoites placed on our discontinued micropattern showed

an incapacity to cross further spacing distances than 4 μm on fibronectin-based micropattern (Figure 7b). A similar behavior was observed on heparin-FITC based micropatterns, were tachyzoites were unable to cross further spacing of 6 μm (Figure 7c). Taking together, these results support the contribution of MIC2 as key adhesin to build the apical anchoring compatible with the traction force for helical crossing over PEG surfaces.

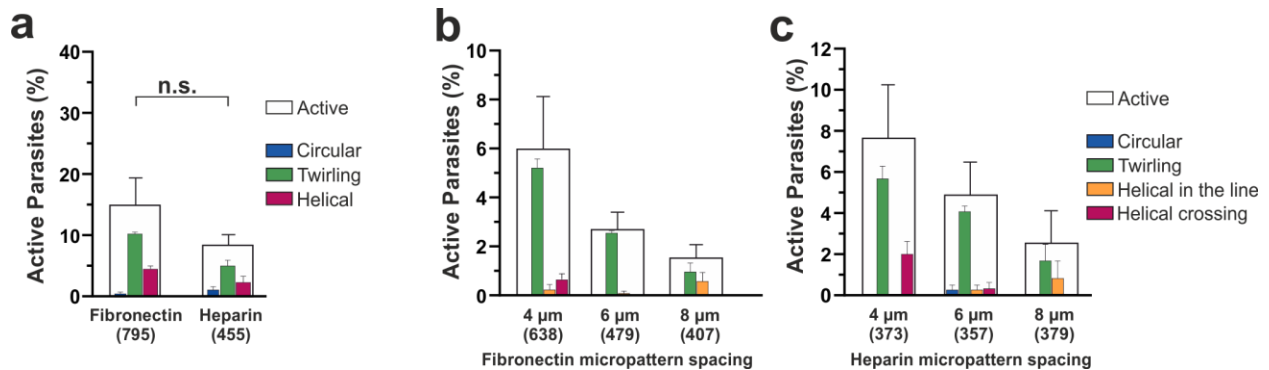


Figure 7 - Microneme protein MIC2 is necessary for apical adhesion in helical gliding. (a) Activity percentages of MIC2 KO tachyzoites on full coated fibronectin and heparin coverslips. (b) Percentages on Fibronectin micropatterns with regard to each typical movement (twirling, circular and helical, n = 407-638 parasites from at least 3 experiments), showing that MIC2 KO tachyzoites are unable to cross at further distances than 4 μm . (c) Percentages on Heparin-FITC micropatterns with regard to each typical movement (twirling, circular and helical, n = 357-379 parasites from at least 3 experiments), showing that MIC2 KO tachyzoites are unable to cross at further distances than 6 μm .

DISCUSSION

When gliding on top of surfaces, the *T. gondii* tachyzoite progresses with a 360° helical forward movement in an iterative few-second lasting sequence. Each sequence includes an obligatory focal engagement of the parasite apex with the substrate to initiate the generation of an actomyosin traction force that tightly coordinates with adhesion disassembly at the rear pole (Pavlou et al., 2020). However, quantitative information on the adhesive requirements for successful gliding is missing. In this study, we first quantified the overall adhesive properties of large tachyzoite

samples (i.e., a mix of active and resting cells) on molecular targets immobilized on glass surfaces and under gradient flow rate by retrieving their stalling forces. While we confirmed that tachyzoites are basically non adherent on PEG, we found they display similar stall forces of about 100 pN on both fibronectin protein and heparin sulfate polysaccharide coatings. If we compare tachyzoites with other cells qualified as “glider”, but displaying different gliding strategies, the adhesive forces of tachyzoites are in the range of those of submicron-scale cell glider such as the bacteria *Mycoplasma mobile* which translocates three to seven times the body length per second (Mizutani et al., 2018) thereby faster than the tachyzoite. For larger gliding cells such as fish keratocyte, stalling forces peak at two to three nN with gliding speed exceeds several tens of micron per minute but these cells typically display a large flat wingspan of 30 μm at the leading edge enriched of focal adhesion and a longitudinal dimension of 10 μm (Heinemann et al., 2011; Herant & Dembo, 2010).

Although resting and active tachyzoites do not strongly adhere to the substratum, their ability to build contact with the substrate is required to resist the environmental fluid flow in particular when they glide. In order to better understand what is minimally required for productive adhesion (i.e., which would support helical gliding), we designed rectangle micropatterns designed to expose alternating non adhesive PEG and pro-adhesive molecular coatings and tested the capacity of the tachyzoite to perform helical gliding while crossing non adhesive surface. We found that if attached to one adhesive area, the tachyzoite can glide onto the next adhesive area just by engaging the apex with the substrate in a specific interaction site and then slip on it through additional transient interaction. Neither the descriptive features nor the paths followed by the gliding parasites over the PEG-fibronectin micropatterns were modified when compared to those moving on top of a homogeneous pro-adhesive fibronectin surface, yet the first displayed faster thrust when they propelled forward. In the same line, comparing 3D images at ~ 40 to 50 nm of parasites either crossing over the non-adhesive PEG or gliding on top of fibronectin highlighted for the latter an increased slippage interface that is likely due to the extended contact of the zoite membrane with the substrate and the myosin-driven actin retrograde flow. Therefore, lowering to a certain extent the overall frictional interaction zone between the cell membrane and the surface which directs de-adhesion of the rear pole and dragging of the cell body forward would benefit to the tachyzoite in

terms of speed performance without compromising motile skills. However, this “molecular clutch” site must be maintained in the substrate to modulate force transmission.

It is well known that tuning the cell surface adhesiveness to the surrounding ECM, controlling ECM geometry or the magnitude and localization of the actomyosin-based contractility are as many ways to modulate cell locomotion (Lämmermann & Sixt, 2009). Engineering substrates with sparse molecular ligands for the major family of cell surface-exposed adhesins (i.e., integrins) impose low adhesion conditions. Alone or in combination with high confinement, low adhesion leads to a speed increase of crawling dermal fibroblasts which switch to fast amoeboid motility under the dual setting (Liu et al., 2015). Moreover, slow crawling fibroblasts form nascent adhesions at the leading edge, a few of which cluster upon ECM-exposed ligand engagement and further evolve as longer-lived, (i.e., stabilized) myosin II positive mature Focal Adhesions (FAs) equipped for traction force transmission (Yamaguchi & Knaut, 2022). In contrast, leucocytes which only build the shortest-lived FA class, hence are exposed to small forces, crawl typically two orders of magnitude faster (Kameritsch & Renkawitz, 2020). Much less has been documented for protozoan parasites but a decrease in adhesion of the motile sporozoite morphotype from the *T. gondii* closely related *Plasmodium* has also been reported to strongly correlate with an increase in speed (Münter et al., 2009).

Another peculiarity of the motile *T. gondii* tachyzoite is the site where the MIC adhesin are released, which is exclusively restricted at the apical tip of the parasite (i.e., at the cell leading edge) and occurs upon a complex signaling cascade induced when tachyzoites sense the extracellular conditions and gain motile proficiency (Bullen et al., 2019). In 2D and 3D conditions, the lack of MIC2 is enough to significantly impact on the tachyzoite capacity to exert forces on the ECM (Gras et al., 2017; Stadler et al., 2022). By monitoring the apicobasal translocation of MIC2 with super resolution imaging, we could now ascertain that an actomyosin-dependent and -driven flow occurs even in absence of any parasite-substrate adhesion. As expected, the membrane flow is independent of MIC2 but dependent of the bulk microneme secretion since mutants translocate microbeads as efficiently as their counterparts in non-adhesive conditions, and respond identically to microneme secretagogue. When excess microneme secretion is triggered by addition of zaprinast, the majority of tachyzoites quickly engage in a twirling behavior before some continue with helical or circular motility suggesting that the excess of membrane material which

cannot be recycled or enzymatically processed trigger a specific actin-dependent machinery. Collectively the data support that MIC2 is a major mechano-transducer candidate once engaged locally with ECM ligands (i.e., fibronectin on the micropattern), and that bulk secreted MIC2 pools, with other MICs must be captured in the membrane flow process and rapidly removed from the parasite surface. This scheme fits with the detection of the two MIC2 populations during gliding, first the soluble products raised from enzymatic processing and, secondly the insoluble population that compose the trails in near contact with the substrate.

How does the MIC2 adhesin engage with their ligands? several early structural studies of MIC2 have established that the MIC2 A domain binds heparin provided the former is presented as large, multimeric complexes (Harper et al., 2004; Tonkin et al., 2010). In the same line, MIC2 was reported to be expressed as a hetero-hexamer comprised of three MIC2-MIC2-Associated Proteins (MIC2AP) and three MIC2 molecules on the surface of *T. gondii* with the idea that multivalent interaction would enhance ligand-adhesin binding efficiency (Jewett & Sibley, 2004). However, whether MIC protein multimeric complexes are released as individuals or clusters, through pulsatile or continuous secretion has never been figure out yet. Similarly, whether the MICs rearrange post-secretion with an individual MIC-ligand bond responding to force loading by recruiting unengaged MICs as elegantly proposed for Integrins in the human breast myoepithelial cell model (Oria et al., 2017) remain unknown. To get insights on the minimal ligand requirement for MIC2 productive engagement, we introduced tunable surface chemistry and quartz crystal microbalance with dissipation monitoring (QCM-D). We observed that negative charges favor productive contact through electrostatic interactions, and these are likely driving the adhesin coupling with GAGs. HS in particular was also shown to be density dependent, as a bigger ratio of exposed moieties increase the frequency of motile parasites. Besides its chemical tunability, QCM-D also inform on the biophysical nanoscale properties of the ligand-presenting layer. Indeed, by modeling the thickness and viscoelasticity of the different layers, we brought evidence that in the range of variation used in the study, ligand chemistry had a superior influence on the capacity of tachyzoite to glide, as surfaces with the same viscoelastic parameters but with different second layers (i.e. -OH vs HS) show significant different phenotypes.

This study demonstrates that the parasite has evolved a unique adhesion system with a fixed position on the surface that is sufficient to timely achieve enough stability for withstanding traction

forces but also enough dynamics to permit gliding. To fulfil its function, these adhesion platforms are expected to show a distinct turnover with a peculiar actin dynamics and organization, yet this scenario has been partly validated for the *Plasmodium* sporozoite (Münter et al., 2009). One challenge remains in developing image-based assays to visualize and measure at the nanometer scale not only the MIC-HS bridge, but also the F-actin flow velocity with the aim to detect any modification at the parasite-substrate interface. Indeed, the fluorescent chromobody actin tool which has been stably introduced in parasites has allowed to uncovering an intravacuolar F-actin bundles and its function (Periz et al., 2017) whereas it does not permit to reliably detect the fast dynamics of sub-membranous F actin. Finally, in vivo, both HSs that typify the glycocalyx and fibronectin that is secreted by cells populate the dynamic 3D ECM network in which the parasite glides. HS and fibronectin bind to each other can cooperate with HS could serving as a tether. The technology we have developed here can allow dissecting the single interaction of a variety of proteoglycans or glycoproteins which form the ECM and their contribution for *T. gondii* host cell invasion and motility.

MATERIALS AND METHODS

Parasite strain and host cell maintenance

All reagents used were from Gibco - Life Technologies (St Aubin, France) unless specified. *T. gondii* strains were propagated on *Mycoplasma*-free human foreskin fibroblasts (HFFs, ATCC CCL-171) at 37 °C and in 5% CO₂ atmosphere in Dulbecco's modified Eagle's medium (DMEM) supplemented with 10% heat-inactivated fetal bovine serum (Invitrogen), 10 mM HEPES buffer pH 7.2, 2 mM L-Glutamine, 100 U/mL penicillin, and 50 µg/mL streptomycin. The laboratory type 1 RH DKU80 strain was provided by V. Carruthers (University of Michigan, USA). RH Δku80: DiCre ΔMyoA and RH DKU80: MIC2 HaloTag were provided by M. Meissner (MLU Munich University, Germany). RH DKU80: diCre/ MIC2 KO YFP and M2AP-SF-TAP HXGPRT lines were provided by C. Tonkin (University of Melbourne).

Micropatterning

18 mm diameter glass coverslips (Knittel) were exposed to UV light ($\lambda=230$ nm, UVO Cleaner, Jelight) for 10 minutes and later exposed for 40 minutes at room temperature to 0.1 mg/mL poly-L-lysine-grafted-polyethylene glycol (PLL (20 kDa) - g[3.5] - PEG (2 kDa), SuSoS) diluted in 10mM HEPES buffer pH 7.4 (Sigma-Aldrich). After incubation, the coverslips were washed using deionized distilled water (dH₂O) and placed onto the chrome side of a patterned quartz photomask (UXM1, Toppan), using a 6 µl drop of dH₂O as capillary contact. The coverslips adhered to the photomask were placed for photolithography treatment inside the UVO cleaner for 10 minutes. The coverslips were removed from the photomask using dH₂O and coated for 40 minutes with either fibronectin HiLyte 488 (10 µg/ml diluted in sodium bicarbonate 0.1 M, FNR02, Cytoskeleton) or heparin-fluorescein conjugate (10 µg/ml diluted in PBS, H7482, *Mw* ~18 kg/mol, ThermoFisher). After incubation, coverslips were rinsed 3 times with PBS and left in PBS until their use. For the micropattern resolution calculation, 5 fields of each micropattern spacing were imaged, and the fluorescence intensity of 20 pairs of fibronectin HiLyte 488 lines with the corresponding PLL-PEG spacing were averaged.

Immunofluorescence

Tachyzoites in intracellular (in HFF cells) or in extracellular conditions were fixed with 4% paraformaldehyde (PFA, Electron Microscopy) diluted in PHEM pH 7.5 and dH₂O for 20 minutes at room temperature, followed by 10 minutes quenching of free aldehyde groups using 50 mM NH₄Cl. The permeabilization step was performed using Triton X-100 (0.1% v/v, Sigma) for 10 min, followed by the saturation of non-specific sites using PBS-BSA (2% w/v, Sigma). First and secondary antibodies described in Table S1 were incubated for 1 hour and nucleic acids were stained for 10 min at room temperature with DAPI (500 nM from 14.3 mM stock, Invitrogen). Coverslips were mounted using Mowiol mounting medium (475904, Merck Millipore).

Table S1

| Primary antibodies | Dilution | Application | Source | Identifier |
|--|-----------------|--------------------|-----------------|------------------------|
| rabbit α -GAP45 | 1:600 | Immunofluorescence | Soldati Lab | |
| rat α -HA | 1:600 | Immunofluorescence | Roche | 3F10 1867 423 50 |
| mouse α -SAG1 | 1:1000 | Immunofluorescence | NovoCastra | clone TP3 |
| α -MIC2 | 1:600 | Immunofluorescence | Sibley Lab | |
| α -FLAG | 1:600 | Immunofluorescence | Cell Signalling | |
| Secondary antibodies | | | | |
| AlexaFluor TM 488 goat α -rabbit IgG (H+L) | 1:600 | Immunofluorescence | Invitrogen | A11034 Lot: 1073084 |

| | | | | |
|--|----------------|----------------------------|------------|------------------------------------|
| AlexaFluor™ 488 goat α -rat IgG (H+L) | 1:600 | Immunofluorescence | Invitrogen | A21208 Lot: 20922 |
| AlexaFluor™ 594 donkey α -rat IgG (H+L) | 1:600 1:400 | Immunofluorescence STED | Invitrogen | A21209 Lot: 22737689 |
| goat α -mouse IgG STAR Orange | 1:400 | STED | Abberior | STORAGE-1001-20UG Lot 10423PK-3 |
| goat α -mouse STAR Red | 1:400 | STED | Abberior | STRED-1001-20UG Lot: 10601PK-4 |
| goat α -rabbit STAR Orange | 1:400 | STED | Abberior | STORAGE-1002-20UG |
| goat α -rabbit STAR Red | 1:400 | STED | Abberior | STRED-1002-20UG Lot: 10614PK-3 |

Image acquisition

Epifluorescence images were acquired using a 63 \times Plan-Apotome oil immersion objective (1.46 NA, Zeiss) in a Zeiss AxioImager M2 fluorescence upright microscope equipped with ApoTome 2 module (Carl Zeiss, Inc., Oberkochen, Germany). For confocal images, samples were imaged

using a 60× Plan-neofluor oil immersion objective (1.46 NA, Zeiss) in a Nikon Ti-Eclipse inverted confocal microscope, coupled with an sCMOS prime camera (Photometrics) camera and a CSU X1 Spinning Disk (Yokogawa, Roper Scientific, Lisses, France). For STimulated Emission Depletion (STED) microscopy, image acquisition was performed using a 100× Plan-Apotome oil immersion objective (1.46 NA, Zeiss) in an Abberior 2D-STEDYCON module on an upright Zeiss Axio Observer Z1 confocal microscope.

Videomicroscopy

Timelapse videomicroscopy was performed in Chamlide chambers (Live Cell Instruments, Seoul, Korea) accommodating 18 mm diameter coverslips, installed on an Eclipse Ti inverted confocal microscope (Nikon France Instruments, Champigny sur Marne France) at 37°C and 5% CO₂ environment (chamber and controllers are from LCI, Seoul, Korea). The microscope was equipped with an sCMOS prime camera (Photometrics) camera, a 60X objective, CSU X1 spinning disk (Yokogawa, Roper Scientific, Lisses, France). Metamorph software (Universal Imaging Corporation, Roper Scientific, Lisses, France) was used for performing videomicroscopy.

Tachyzoite 2D gliding assays

Approximately 10⁵ tachyzoites were collected within a few hours of spontaneous egress from the HFF monolayers and centrifuged at 900g for 7 minutes in *Washing Buffer* (HBSS⁺⁺ buffer with 0.2% Fetal Calf Serum (FCS)). The resulting pellet containing the tachyzoites was resuspended in 500 µl of *Motility Buffer* (HBSS⁺⁺ supplemented with 1% FCS and 1.6 mM CaCl₂) and filtered through a 5 µm membrane (Fisher Scientific) to remove any existing host-cell debris. For an 18 mm diameter glass coverslip placed inside the microscope chamber, 100 µl of the tachyzoite suspension was added to 150 µl of *Motility Buffer* covering the coverslip. Once tachyzoites sedimented on the coverslip plane, images were captured at 1 frame/s or less. At least 3 videos of 5 min each were taken for each surface/condition, coming from 3 independent coverslips and tachyzoite culture. Image analysis for characterizing tachyzoite activity (active/inactive), type of movement (twirling, circular and helical; and helical crossing and in the line for micropatterns), and tracking displacement, duration and velocity of gliding were done using Icy (de Chaumont *et al*, 2012), with plugins “Manual tracking” and “Motion profiler” to extract the *x-y* positions and time.

Functionalization of coverslips with PLL-PEG-b/SAv:b-X model coatings

18 mm glass coverslips were cleaned under UV-ozone for 20 minutes, then rinsed with dH₂O and air gun-dried. For all coverslips, they were first exposed to 500 μ L of 0.1 mg/mL PLL-PEG-b (PLL (20 kDa) - g[3.5] - PEG (2 kDa) / PEG (3.4 kDa) - biotin (20% for QCM-D experiments, 50% for videomicroscopy experiments), SuSoS) in *HEPES dilution buffer* (HEPES 10 mM, 150 mM NaCl, pH 7.4) for 1 hour. Next, coverslips were rinsed with *HEPES dilution buffer* 5 times, using two pipettes to avoid drying. After that they were exposed to the SAv:b-X complexes at given stoichiometry (1:1, 1:2 or 1:3) in *HEPES dilution buffer*. After incubation for 1 h, coverslips were rinsed with *HEPES dilution buffer* 5 times, using two pipettes to avoid drying, and then rinsed with *Motility Buffer*, in which they were kept until motility studies.

Several biotinylated ligands (b-X) were studied: b-PEG-OH (PEG1207.0100, Iris Biotech, 4847 g/mol), b-PEG-NH₂ (PEG1046, Iris Biotech, 2996 g/mol), b-PEG-COOH (PEG1053, Iris Biotech, 3145 g/mol), b-HSA (0.2 kg/mol, biotin grafting efficiency 60%), b-HS (synthesized using oxime ligation on HS 12 kg/mol from porcine intestinal mucosa, Celsius Laboratories, as described previously in Thakar et al., 2014)

The SAv:b-X mixtures were prepared as follows. Stock solutions of b-X were diluted in *HEPES dilution buffer* and then injected into the streptavidin (SAv, S4762 Sigma, ~60 kg/mol) solution prepared in the same buffer. SAv final concentration was fixed to 10 μ g/mL (except SAv:b-HSA samples, where SAv concentration was decreased to 5-6 μ g/mL due to the limited amount of HSA). The final concentration of b-X ligands varied according to the desired stoichiometry (1:1, 1:2 or 1:3). The mixture was vortexed for 20 s and kept in ice for 30 min before placing it on the top of the PLL-PEG-b-functionalized glass coverslips.

Heparan sulfate coatings and neutralization assays

Heparan sulfate sodium salt from bovine kidney (H7640, Sigma Aldrich) was diluted at 5 μ g/mL in 10 mM HEPES buffer pH 7.4 and placed for 45 minutes on an 18 mm glass coverslip previously cleaned using UV-ozone. After incubation, coverslips were rinsed with 10 mM HEPES buffer. In the case of neutralization, they were then exposed for 45 minutes to 4 or 20 μ M surfen solution (S6951, Sigma Aldrich) (Schuksz et al, 2008) diluted in the same buffer. Next, coverslips were

rinsed with 10 mM HEPES buffer and left in it until motility studies. Tachyzoites were then prepared and placed on each of the surfaces and the neutralized versions to perform video recording as described in the *Tachyzoite 2D gliding assays* section.

Quartz crystal microbalance with dissipation monitoring (QCM-D) measurements and viscoelastic modeling

CM-D measurements were performed using a Q-Sense E4 system equipped with four Q-Sense flow modules (Biolin Scientific). The measurements were done at $T = 24$ °C and in a flow mode (flow rate = 20-50 $\mu\text{L}/\text{min}$). Silica-coated quartz sensors (Biolin Scientific) were used as substrates. The sensors were cleaned using UV-ozone for 20 minutes, followed by rinsing with water and ethanol and air gun-dried before installing them into the QCM-D modules. The normalized frequency ($\Delta f = \Delta f_j/j$) and dissipation (ΔD) shifts were recorded for six overtones ($j = 3, 5, 7, 9, 11, \text{ and } 13$), in addition to the fundamental resonance frequency (4.95 MHz), using the QTools software. Changes in Δf and ΔD for $j = 7$ are presented, while other overtones showing similar trends.

For all coatings, QCM-D measurements started with a dH₂O baseline. For simple coatings, QCM-D measurements were prepared as follows. For PLL-PEG, first injection consisted on *HEPES dilution buffer* (HEPES 10 mM, 150 mM NaCl, pH 7.4), followed by injection of PLL-PEG (0.1 mg/ml diluted in *HEPES dilution buffer*), and rinsed using the same buffer. For PLL, after dH₂O baseline, PLL 0.1% w/v diluted in water (P8920, Sigma Aldrich) was injected, rinsed using also with dH₂O. For fibronectin, baseline was PBS (dPBS 1X without calcium and magnesium, 14190-144, Gibco), followed by injection of fibronectin 50 $\mu\text{g}/\text{ml}$ diluted in PBS and rinsed in the same buffer.

For the tunable surfaces, QCM-D measurements started with dH₂O injection until signal stabilization, followed by injection of *HEPES dilution buffer* (HEPES 10 mM, 150 mM NaCl, pH 7.4). First layer injection consisted in 0.1 mg/ml PLL-PEG-Biotin (PLL (20 kDa) - g[3.5] - PEG (2 kDa) / PEG (3.4 kDa) - biotin (50%), SuSoS) diluted in *HEPES dilution buffer*, and rinsed in the same buffer. SAV:b-X mixtures were prepared as described before, and injected for 1 hour. Final concentration for b-X ligands was as follows. For b-PEG OH 1:1 2.42 $\mu\text{g}/\text{ml}$; for b-PEG-NH₂, 1 $\mu\text{g}/\text{ml}$ for 1:2 ratio and 1.51 $\mu\text{g}/\text{ml}$ for 1:3 ratio; for b-PEG-COOH, 1 $\mu\text{g}/\text{ml}$ for 1:2 ratio

and 1.59 $\mu\text{g/ml}$ for 1:3 ratio; for b-HSA, 9.91 $\mu\text{g/ml}$ for 1:1 ratio and 23.4 $\mu\text{g/ml}$ for 1:3 ratio; for b-HS, 8 $\mu\text{g/ml}$ for 1:1 ratio and 120 $\mu\text{g/ml}$ for 1:2 ratio. Final concentration of SAV was 10 $\mu\text{g/ml}$ for all samples except 5-6 $\mu\text{g/ml}$ for b-HSA as described before. All mixtures were rinsed with *HEPES dilution buffer*.

The thickness (d) and viscoelastic properties of the adsorbed layers were determined by fitting the QCM-D data to a continuum viscoelastic model (Johannsmann, 1999) implemented in the QTM software (D. Johannsmann, Technical University of Clausthal, Clausthal-Zellerfeld, Germany). The fitting procedure was described in detail previously (Eisele *et al*, 2012). Viscoelastic properties were parameterized in terms of the shear storage modulus $G'(f)$ and the shear loss modulus $G''(f)$. The frequency dependencies of the storage and loss moduli were assumed to follow power laws within the measured range of 15 to 65 MHz, with exponents α' and α'' , such that $G(f) = G_0 (f/f_0)^\alpha$, with f_0 set to 15 MHz. The data were fitted using a small load approximation (SLA), using a fundamental frequency of 4.95 MHz and a crystal impedance Z_q of 8.769382×10^{-6} $\text{kg/m}^2/\text{s}^1$. The bulk properties of the water or buffer solution were fixed at density $\rho=1.0$ g/cm^3 and viscosity $\eta=0.89$ mPa. The film density was assumed to be 1.0 g/cm^3 . Reduced χ^2 -values were verified to be close to 1.0 (confirming a good fit), and the presented errors correspond to a confidence level of a standard deviation.

MIC2 staining

For tachyzoite preparation, HFF monolayer cells with 24-hour vacuoles of tachyzoites were first rinsed 3 times with PBS, and then with *Intracellular Buffer* (145 mM KCl, 5 mM NaCl, 1 mM MgCl₂, 15 mM MES, 15 mM HEPES, pH 8.3). The monolayer was then scrapped in *Intracellular Buffer*, collected, and passed through a 25G syringe to release the intracellular tachyzoites. The parasite suspension was centrifuged for 7 minutes at 900g, and the resulting pellet was resuspended in 500 μl of *Intracellular Buffer* with the addition of 1 μM final of Janelia Flour HaloTag 646 (GA112A, Promega) and incubated for 15 minutes at 37C, 5% CO₂. For mimicking intracellular conditions of MIC2 expression, tachyzoites were then centrifuged in *Intracellular Buffer* at 900g for 7 min and resuspended in the same buffer, before placing them on a PLL-PEG coated coverslip containing the same buffer. For motile conditions, tachyzoites were centrifuged in *Washing Buffer* at 900g for 7 min and resuspended in *Motility Buffer*, before placing them on a fibronectin or PLL-

PEG coated coverslip containing *Motility Buffer*. In all cases, tachyzoites were centrifuged at 300g for 3 min to sediment them, and left for 15 min at 37 °C, 5% CO₂. Next, they were fixed using 3.2% PFA solution as described before, washed 3 times with PBS and left in this buffer for immunostaining.

Ultrastructure Expansion microscopy (U-ExM) of micropatterned surfaces

12 mm glass coverslips were prepared for micropattern with the passivation photolithography steps as described in the *Micropattern* section. After detachment from the quartz mask, the coverslips were placed for 1 h in a solution of 20 µg/mL fibronectin (F1141, Sigma Aldrich) and 0.1 mg/mL ATTO 488 NHS ester (#41698 Sigma Aldrich) diluted in 0.1 M sodium bicarbonate buffer pH 7.4. After incubation under agitation, coverslips were rinsed 10 min with PBS 3 times and left in PBS until their use.

Approximately 10⁵ freshly egressed tachyzoites were collected and centrifuged at 900g for 7 min in HBSS⁺⁺, and the pellet was resuspended in 500 µL of *Motility Buffer*. The 12 mm diameter glass coverslip was placed inside a 4-well plate and gently covered by a mixture of 100 µL of the tachyzoite suspension with 700 µL of *Motility Buffer*. The plate was centrifuged at 500g for 1 min to synchronize the tachyzoite's sedimentation and left to glide for 2 min. The *Motility Buffer* present in the well was removed and fixation was performed using 3.6% Formaldehyde (#252549, Sigma Aldrich) diluted in PBS for 10 min, followed by aspiration and the addition of cold methanol for 1 minute. After removing methanol, 1 mL of a mixture of 1.9% formaldehyde 2.5% acrylamide (#01697, Sigma Aldrich) diluted in PBS was added for overnight incubation at 37 °C.

For U-ExM, the protocol developed by the Guichard laboratory was followed (Gambiarotto et al 2019). Briefly, after fixation, the samples were prepared for gelation for 1 h at 37 °C. The coverslips with the newly formed gels were incubated in denaturation buffer (0.5% Triton X-100, 8 units/mL Proteinase K) in a 6-well plate for 15 min at room temperature. Gels were removed from the coverslips and transferred to an Eppendorf tube with fresh denaturation buffer and incubated at 95 °C for 1 h. Gels were then placed for 30 min on a 6-well plate with dH₂O for the first round of expansion at room temperature, and water was exchanged two more times for 30 minutes of incubation. After a shrinkage step with PBS, several pieces of ~4 mm diameter were cut and deposited on a 24-well plate. Gels were then incubated for 3 h under shaking for primary

antibodies: anti tubulin, mAb, rabbit anti-GAP45, rat anti-HA (mAb, clone 3F10). Gels were washed in PBS-Tween 0.1 % prior to incubation with the secondary antibodies for 2 h at 37 °C. After incubation, gels were washed with PBS-Tween 0.1 % and re-expanded with three baths of 20 min of dH₂O. Next, the piece of gel was gently transferred to a PLL-coated glass coverslip fitting the microscope chamber, and the excess liquid in the gel was removed with a tissue. The 0.2 μm Z-image stacks were captured using confocal microscopy as described in the Imaging section.

Microbead coupling

0.2 μm diameter FluoSpheres carboxylate-modified polystyrene microspheres (λ: 660/680, 2% solids diluted in water, F8807, ThermoFisher Scientific) were activated using the two-step 1-ethyl-3-[3-dimethylaminopropyl] carbodiimide (EDC)/sulfo NHS covalent coupling (Estopor carboxyl-modified dyed microspheres protocol, MerckMillipore). This process leads to the formation of a reactive intermediate O-acylisourea product, which can react with the primary amines present in the tachyzoite's whole surface. Following the activation, 50 μL of the bead suspension was diluted by 150 μL of 50 mM MES buffer pH 6.

For tachyzoite preparation, HFF monolayer cells with 24-hour vacuoles of tachyzoites were first rinsed 3 times with PBS, and then with *Intracellular Buffer*. Host cells were scrapped in the intracellular buffer, collected, and passed through a 25G syringe to release the intracellular tachyzoites. The parasite suspension was centrifuged for 7 min at 900g, and the resulting pellet was resuspended in 200 μL of *Motility Buffer*, to which and 10 μL of the activated bead suspension was then added. 100 μL of the final suspension was deposited on a glass coverslip coated with either fibronectin or PLL-PEG and already filled with 200 μL of *Motility Buffer*. In some experiments, tachyzoites were incubated in the *Motility Buffer* supplemented with either 1 μM cytochalasin D (C8273, Sigma) or 250 μM zaprinast (Z0878, Sigma) and video-recorded in the presence of these compounds. The suspension of the tachyzoites was let on top of the surfaces for 5 minutes to allow sedimentation and to assess the membrane flow process. Later, samples were fixed using 3.2% PFA diluted in PHEM pH 7.5 and dH₂O for 20 minutes at room temperature. Samples were washed 3 times with PBS before mounting for imaging.

For the group labeled as “in suspension”, tachyzoites were resuspended in *Motility Buffer* and kept in the Eppendorf tube with continuous mechanical resuspension with the pipette for 5 minutes, before placing them on a PLL-PEG coated coverslip, centrifugation for 30 seconds at 500g to quickly sediment them, and immediately fix as before. In all cases, to calculate the number of tachyzoites with basally translocated beads, 10 fields from at least 3 replicates were taken using a confocal microscope as described in the Imaging section, and the total number of tachyzoites with beads present only in the basal pole were quantified.

Acoustic Force Microscopy

The AFS chip consisted on an Ibidi flow chamber equipped with 0.1 mm micro-slides (#80666, Ibidi) and a piezoelectric element (Lumicks). The functionalization of the flow chamber was performed by injecting into the chamber 50 μ l of either PLL-PEG (0.1 mg/mL diluted in 10mM HEPES buffer pH 7.4, SuSoS), fibronectin (10 μ g/ml diluted in sodium bicarbonate 0.1 M, F1141, Sigma), heparin-FITC (10 μ g/ml diluted in PBS, H7482, ThermoFisher) or PLL (50 μ g/ml diluted in H₂O, P4832, Sigma) using a 60 ml Omnifix Braun syringe connected to a KDS410 syringe pump. After incubation for 1-3 hours at room temperature, the chambers were rinsed with 200 μ l of PBS, followed by an equilibration step with *Motility Buffer*. Next, 50 μ l of a solution of freshly egressed tachyzoites in *Motility Buffer* were injected in the chamber, and let to sediment for 5 minutes. The piezoelectric element attached to the flow chamber was driven with a function generator (SDG830; Siglent Technologies), providing oscillating current amplified by a radiofrequency (RF) amplifier (SCD, ARS 2_30_30, 50 Ω impedance, 10 W maximum output power). Data was acquired using a Lumicks AFS stand-alone instrument, along with images acquired with a bright-field inverted microscopy Observer D1 (Zeiss) equipped with an ORCA camera (Hamamatsu), at 0.3125 seconds per image rate. xy -cell positions along time were determined using ImageJ, and cells were counted every 10 images to extrapolate the dragging force vs flow rate. The rupture forces were calculated as described previously (Kamsma et al., 2018).

Image processing

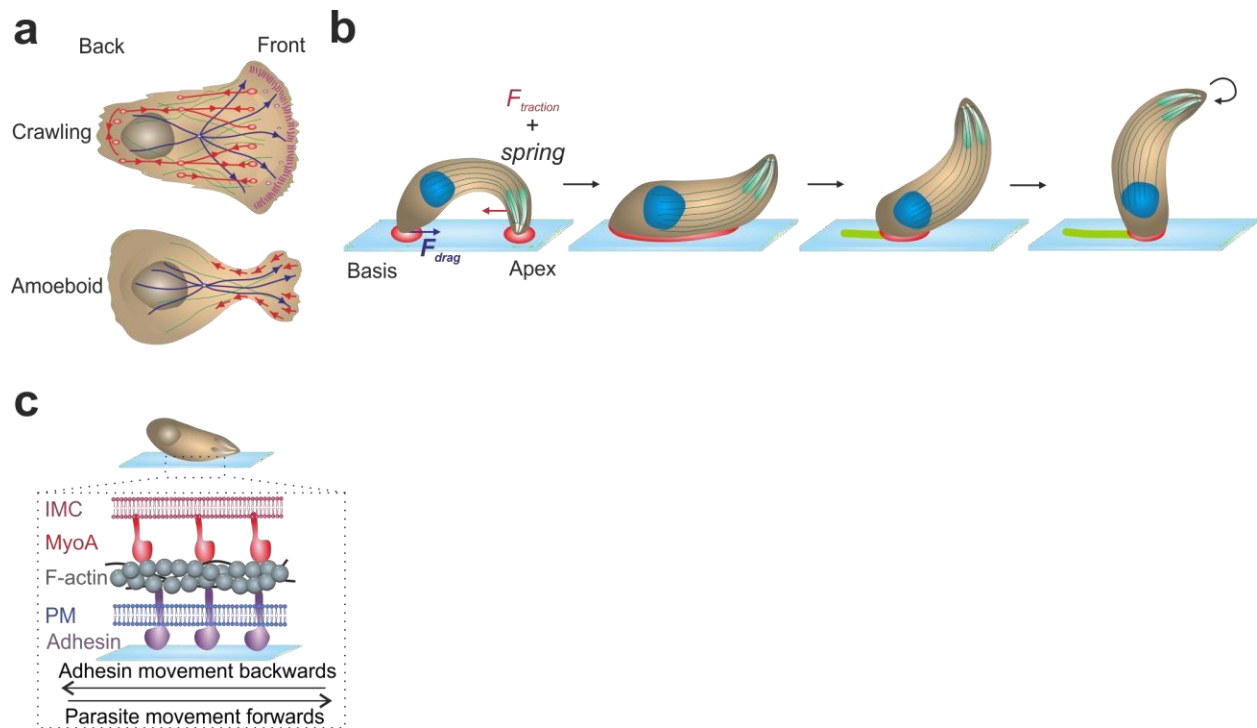
Images for the events of interest were processed using Metamorph (Molecular Devices), ImageJ (Schneider et al 2012), and Icy from the raw x,y,z,t stacks. Photocompositions were made using

ImageJ and CorelDraw 6.0. 3D Slicer (Fedorov et al 2012) and Blender were used for 3D reconstructions. All images are representative of independent replicates.

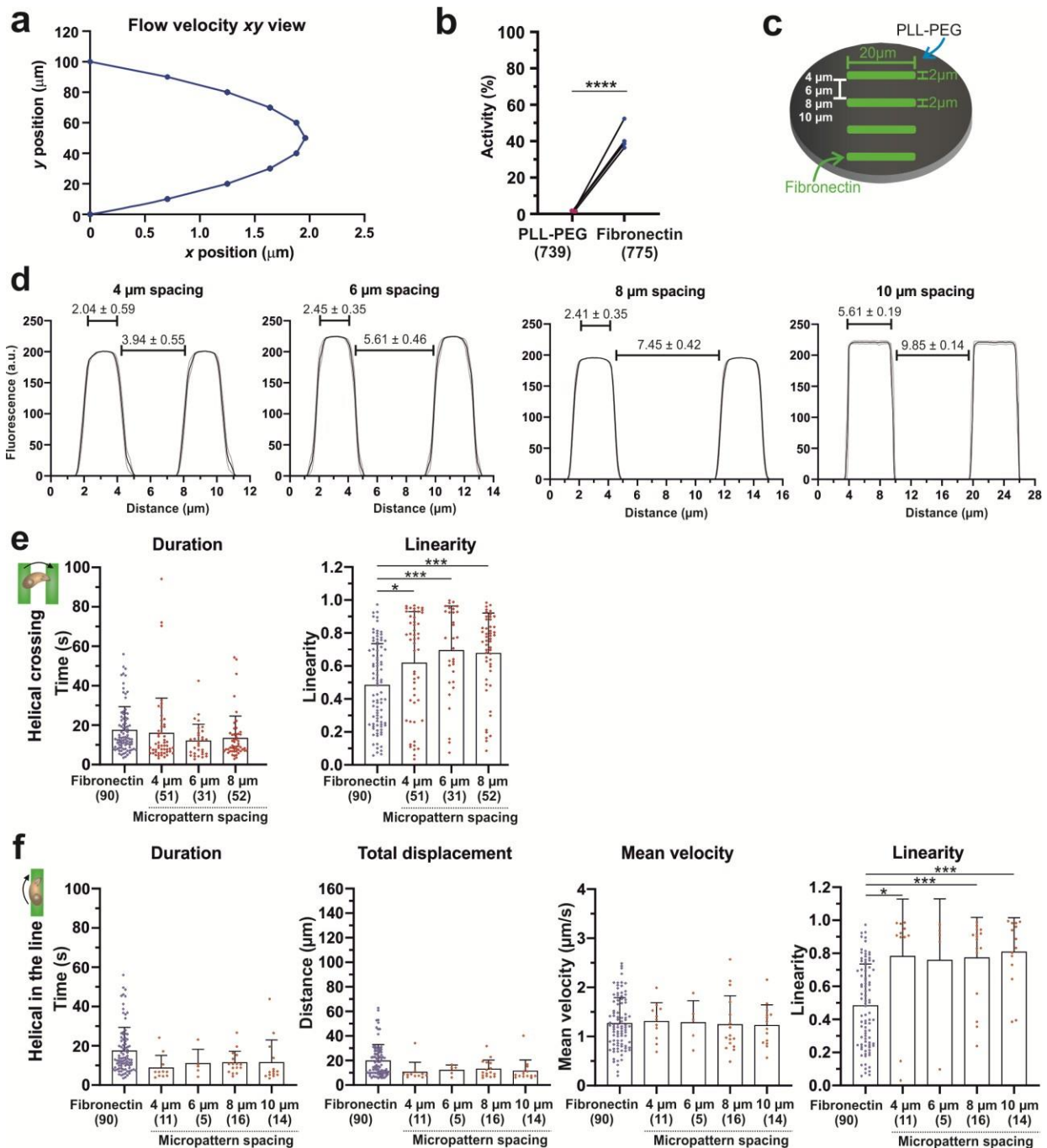
Statistical analysis

Data were statistically analyzed using GraphPad Prism 8.0 software for Windows (La Jolla, CA, USA). Plots were made using the same software, and data are presented as mean \pm standard deviation if not indicated otherwise. Statistical tests and exact p-values are provided in the corresponding captions.

SUPPLEMENTARY FIGURES

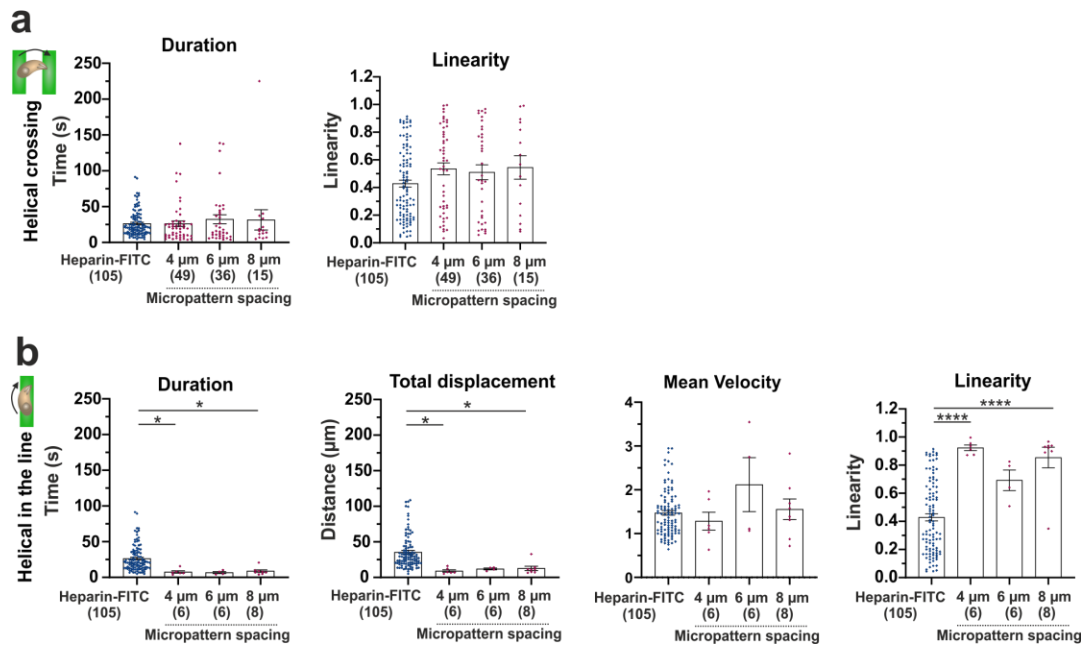


Supplementary Figure 1 - (a) Schematic of the two main locomotion systems used by the majority of eukaryotic cells: crawling and amoeboid movements. Both depend on actin filaments polymerization on the leading edge (blue lines), followed by a contraction of the stress fibers connecting the focal adhesions (red lines). (b) Schematic of tachyzoite helical gliding, showing the two necessary apical and basal contacts and the forces involved. Helical gliding on 2D surfaces starts with an apical contact, followed by a pause and deformation (known as the kink). The body contact then spreads from the back and the apical pole lifts, leaving only the basal pole attached to twirl and repeat the cycle. (c) Simplified schematic of the *T. gondii* glideosome machinery components, centered on the myosin A motor, anchored to the outer membrane of the Inner Membrane Complex and providing the traction force for the actin filaments pulling backwards, establishing the forward motion of the tachyzoite.



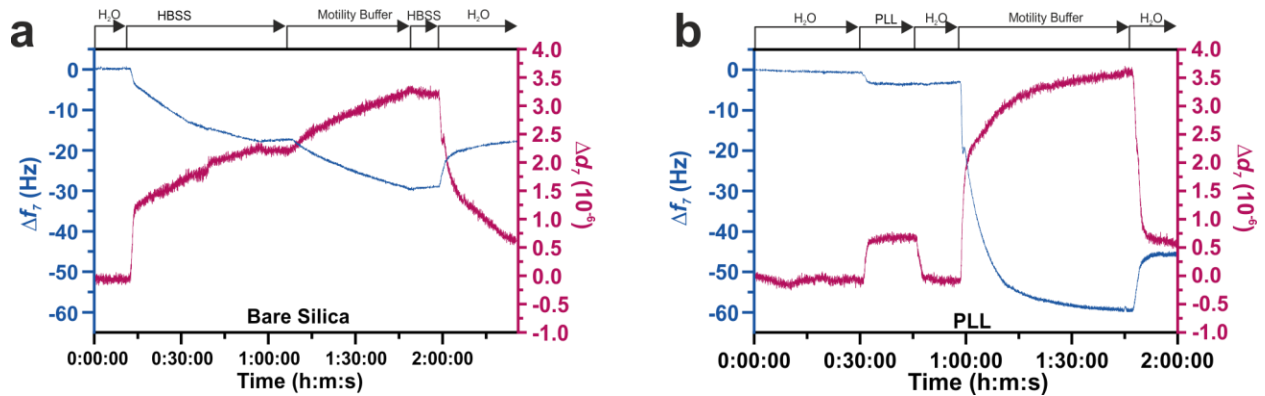
Supplementary Figure 2 - (a) Flow configuration inside the chamber, showing the xy positioning of the liquid run front. **(b)** Tachyzoite motile activity is restored when the inactive population on the PLL-PEG surface is transferred to the fibronectin surface and let to glide (**** $p < 0.0001$, unpaired t Student's test, $n = 739-775$ parasites from at least 3 experiments). **(c)** Schematic of the surface design for photolithography micropattern, with fibronectin lines of 2 µm of width by 20

μm of length separated by 4 μm , 6 μm , 8 μm or 10 μm of the antiadhesive PLL-PEG, that also covers the totality of the coverslip. **(d)** Fibronectin micropattern resolution, as a result of the fluorescence intensity mean of 20 pairs of fibronectin HiLyte 488 lines with the corresponding PLL-PEG spacing. **(e)** Results for duration and linearity of the crossing helical gliding. Crossing helical gliding does not differ from gliding on a full coated fibronectin coverslip in duration (n.s., $p=0.1298$, ANOVA followed by Dunnet's multiple comparisons). Nevertheless, crossing helical gliding produces a more linear direction compared to a full coated surface (4 μm : * $p<0.05$, 6 μm : *** $p<0.001$, 8 μm : *** $p<0.001$, all ANOVA followed by Dunnet's multiple comparisons). **(f)** Helical gliding in the line does not produce any difference in the movement duration, total displacement and mean velocity of the tachyzoite with comparison to a full coated surface (n.s., ANOVA followed by Dunnet's multiple comparisons). However, it does produce a more linear direction compared to a fully coated surface for some distances (4 μm : * $p<0.05$, 8 μm : *** $p<0.001$, 10 μm : *** $p<0.001$, all ANOVA followed by Dunnet's multiple comparisons).

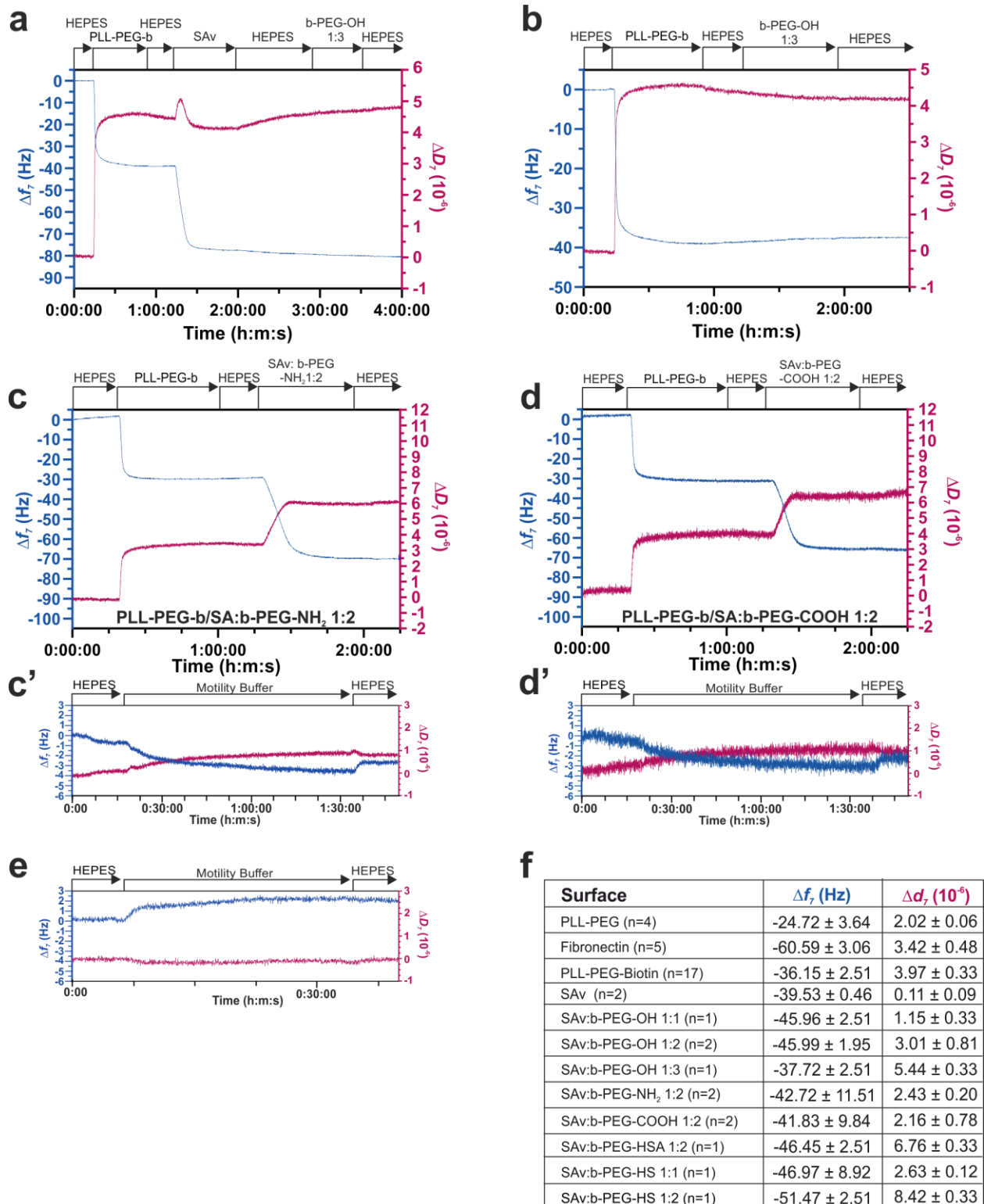


Supplementary Figure 3 - (a) Tachyzoites display a similar displacement duration and linear shape of movement while performing crossing helical gliding on Heparin-fluorescein micropatterned surfaces, in all types of line distances (n=15-105 parasites from at least three independent essays, n.s., one-way ANOVA followed by Dunnet's multiple comparisons). **(b)** Helical gliding in the line is reduced in duration and total displacement for heparin-FITC

micropatterns spaced by 4 μm and 8 μm , while displaying a similar mean velocity in all cases (n=15-105 parasites from at least three independent essays, * $p < 0.05$, one-way ANOVA followed by Dunnet's multiple comparisons). As expected by being circumscribed in moving in only a line direction, the linearity of helical gliding on the line for the 4 μm and 8 μm is significantly higher compared to the control full-coated Heparin-FITC surface (n=15-105 parasites from at least three independent essays, **** $p < 0.0001$, one-way ANOVA followed by Dunnet's multiple comparisons).

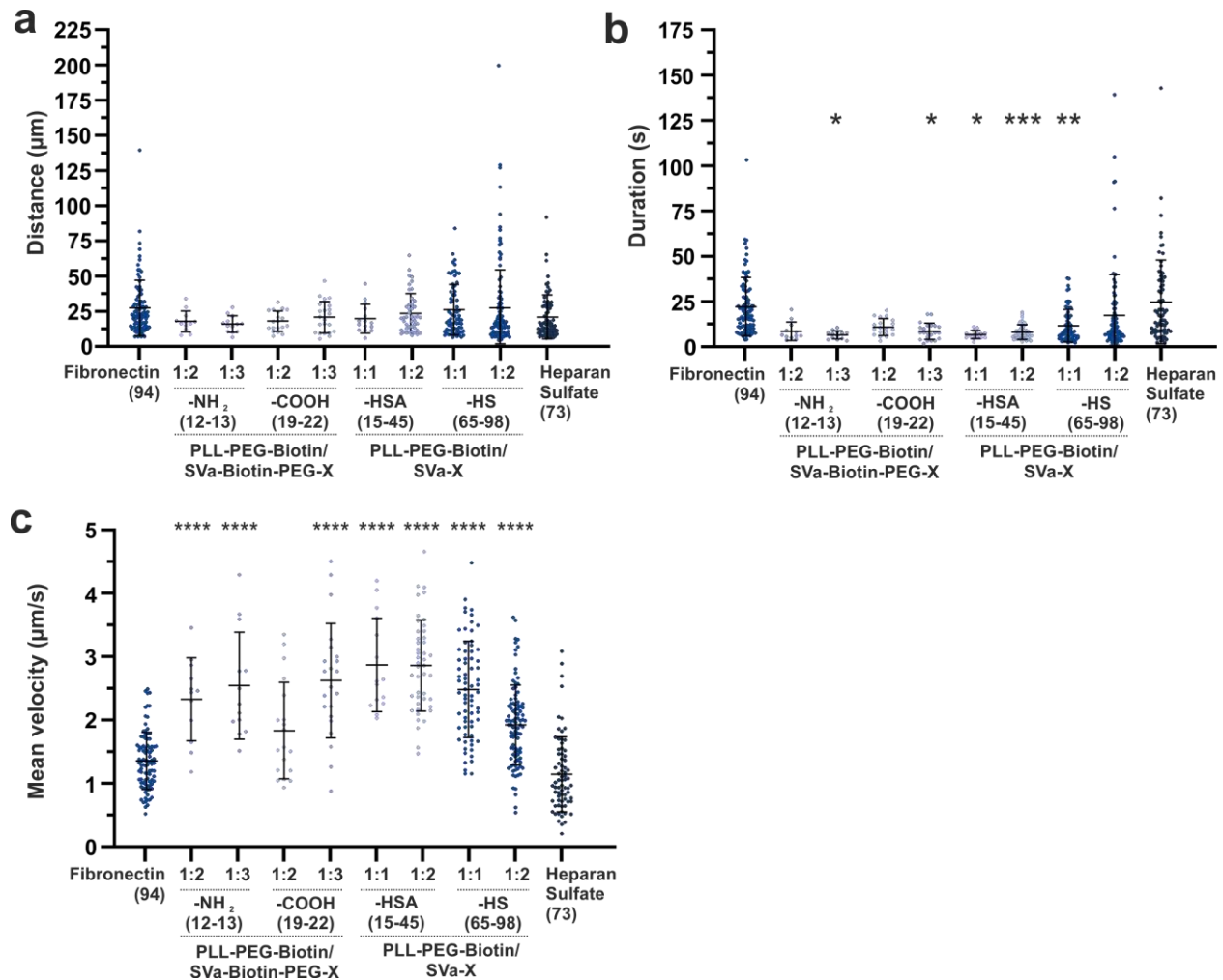


Supplementary Figure 4 - (a) QCM-D shows the presence of non-specific adsorption between the components of the tachyzoite motility buffer (composed of HBSS, fetal calf serum and CaCl_2) and the bare silica surface, showing a strong frequency and dissipation shift at its injection. The unspecific interaction is probably due to the electrostatic interaction of the fetal calf serum with the bare silica surface. **(b)** QCM-D shows fast binding of PLL to the silica surface, resulting in a rigid ($\Delta D \approx 0$) coating, stable in water. The components of the tachyzoite motility buffer (most probably fetal calf serum) show strong attachment to the PLL layer, evidenced by the steep change in Δf and ΔD after injection.

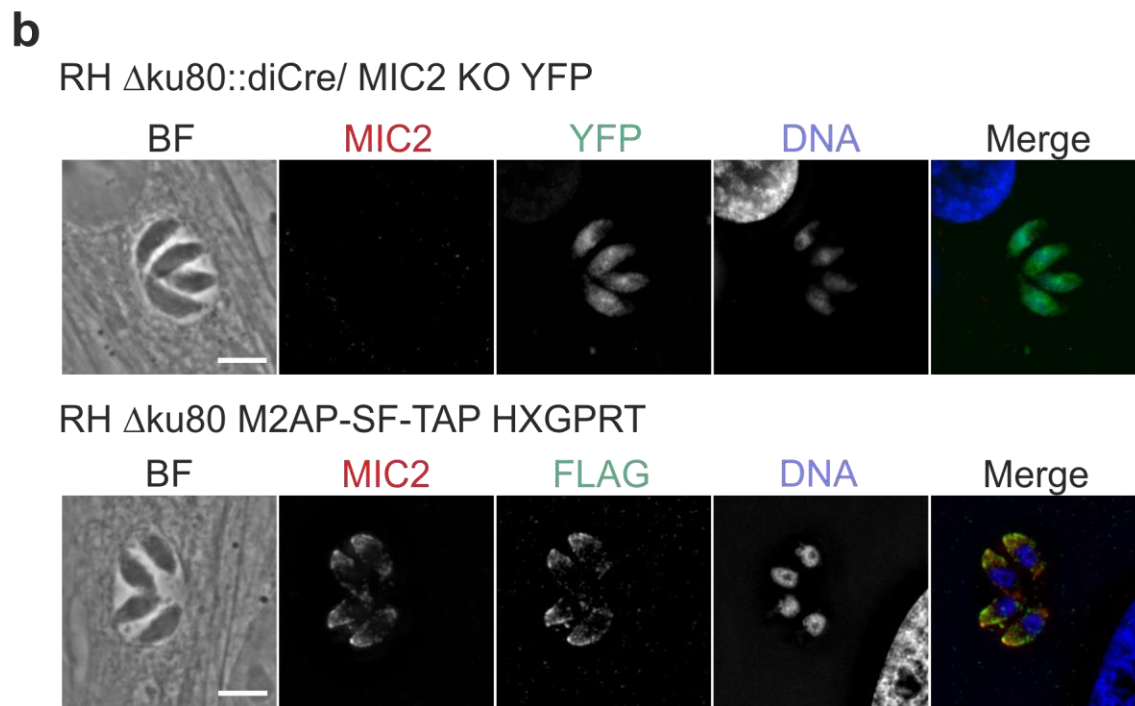
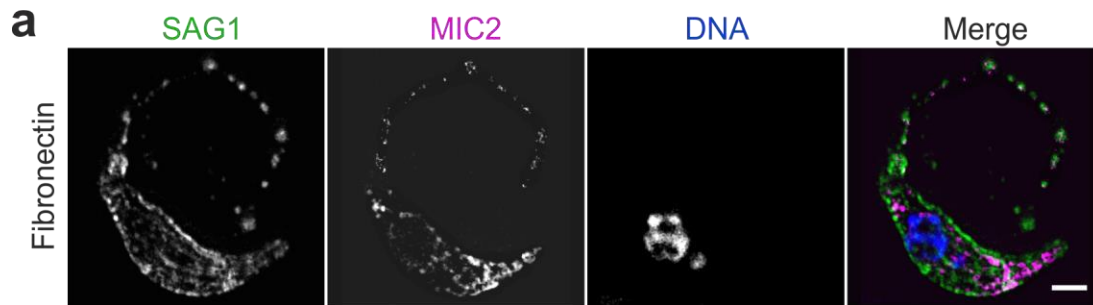


Supplementary Figure 5 - (a) QCM-D shows fast binding of SAV to the PLL-PEG-b layer resulting in a stable and hard ($\Delta D \sim 0$) coating. After stabilization of the layer, all SAV binding

pockets are saturated with the biotin molecules present in the first layer, showed by the lack of Δf and ΔD responses when adding b-PEG-OH. This result led to the construction of our tunable surface model as a two-step process with the binding of the SAV:b-X complex first and a later injection into the PLL-PEG-biotin layer. **(b)** QCM-D shows no interaction of b-PEG-OH with the first layer of PLL-PEG-biotin in absence of SAV. **(c)** QCM-D shows fast binding of SAV:b-PEG-NH₂ (1:2) complex to the PLL-PEG-b layer (saturation < 5 min) resulting in a stable and soft ($\Delta D > 0$) coating. **(c')** In the continuation of the injection in (c), the components of the tachyzoite motility buffer (*i.e.*, glucose, fetal calf serum) do not show strong attachment to the PLL-PEG-b/SAV:b-PEG-NH₂ coating. **(d)** QCM-D shows fast binding of SAV:b-PEG-COOH (1:2) complex to the PLL-PEG-b layer resulting in a stable and soft ($\Delta D > 0$) coating. **(d')** The components of the tachyzoite motility buffer do not show strong attachment to the PLL-PEG-b/SAV:b-PEG-COOH coating in the continuation of the injection in (d). **(e)** Summary of Δf and ΔD shifts for the 7th overtone after formation of PLL-PEG-b/SAV:b-X coatings. Values shown represent mean \pm SEM from at n = 1-17 independent QCM-D experiments. For the SAV:b-X coatings that had one QCM-D run, the SEM corresponds to the one from the PLL-PEG-b first layer.



Supplementary Figure 6 - (a) Tachyzoites display a similar displacement length disregarding the type of surface on the tunable model system (n=12-98 parasites from at least three independent essays, n.s., one-way ANOVA followed by Dunnet's multiple comparisons). **(b)** Helical gliding is reduced in duration for b-PEG-NH₂ ratio 1:3, b-PEG-COOH ratio 1:3, b-HSA ratios 1:2 and 1:3, b-HS ratio 1:1 (n=12-98 parasites from at least three independent essays, * p<0.05, **p<0.01, *** p<0.001, one-way ANOVA followed by Dunnet's multiple comparisons). **(c)** Tachyzoites display a higher mean velocity in several types of surfaces on the tunable system (**** p<0.001, one-way ANOVA followed by Dunnet's multiple comparisons).



Supplementary Figure 7 – Top row: Immunofluorescence images for control of MIC2 deletion of RH $\Delta ku80::diCre/ MIC2 KO YFP$ parasites. **Bottom row:** comparison immunofluorescence for MIC2 presence on a line expressing a FLAG tagged MIC2 associated protein (M2AP). Scale bars: 5 μm .

SUPPLEMENTARY VIDEOS

Supplementary Video 1 – Tachyzoite achieving five crossing helical gliding movements on a fibronectin micropattern spaced 4 μm . Time is in minutes: seconds, scale bar: 5 μm .

Supplementary Video 2 - Tachyzoite carrying out crossing helical gliding across five lines on a Heparin-FITC micropattern with lines spaced 4 μm . At the end of the crossing process the

tachyzoite engages in non-productive twirling in the line. Time is in minutes: seconds, scale bar: 5 μm .

Supplementary Video 3 - Tachyzoite performing twirling on the fibronectin line of a micropattern spaced 10 μm , as a result of being unable to cross the space in between lines. Time is in minutes: seconds, scale bar: 5 μm .

Supplementary Video 4 – Tachyzoite translocating a carboxylated bead from its apical pole to the basal pole, while being on an anti-adhesive PLL-PEG surface. Time is in minutes: seconds, scale bar: 5 μm .

REFERENCES

- Azioune, A., Carpi, N., Tseng, Q., Théry, M., & Piel, M. (2010). Protein Micropatterns. In *Methods in Cell Biology* (Vol. 97, pp. 133–146). Elsevier. [https://doi.org/10.1016/S0091-679X\(10\)97008-8](https://doi.org/10.1016/S0091-679X(10)97008-8)
- Bershadsky, A. D., & Kozlov, M. M. (2011). Crawling cell locomotion revisited. *Proceedings of the National Academy of Sciences*, *108*(51), 20275–20276. <https://doi.org/10.1073/pnas.1116814108>
- Brown, K. M., Lourido, S., & Sibley, L. D. (2016). Serum Albumin Stimulates Protein Kinase G-dependent Microneme Secretion in *Toxoplasma gondii*. *The Journal of Biological Chemistry*, *291*(18), 9554–9565. <https://doi.org/10.1074/jbc.M115.700518>
- Bullen, H. E., Bisio, H., & Soldati-Favre, D. (2019). The triumvirate of signaling molecules controlling *Toxoplasma* microneme exocytosis: Cyclic GMP, calcium, and phosphatidic acid. *PLoS Pathogens*, *15*(5), e1007670. <https://doi.org/10.1371/journal.ppat.1007670>
- Bullen, H. E., Jia, Y., Yamaro-Botté, Y., Bisio, H., Zhang, O., Jemelin, N. K., Marq, J.-B., Carruthers, V., Botté, C. Y., & Soldati-Favre, D. (2016). Phosphatidic Acid-Mediated Signaling Regulates Microneme Secretion in *Toxoplasma*. *Cell Host & Microbe*, *19*(3), 349–360. <https://doi.org/10.1016/j.chom.2016.02.006>
- Carruthers, V. B., Hakansson, S., Giddings, O. K., & Sibley, L. D. (2000). *Toxoplasma gondii* Uses Sulfated Proteoglycans for Substrate and Host Cell Attachment. *Infection and Immunity*, *68*(7), 4005–4011. <https://doi.org/10.1128/IAI.68.7.4005-4011.2000>
- Daher, W., Plattner, F., Carlier, M.-F., & Soldati-Favre, D. (2010). Concerted Action of Two Formins in Gliding Motility and Host Cell Invasion by *Toxoplasma gondii*. *PLoS Pathogens*, *6*(10), e1001132. <https://doi.org/10.1371/journal.ppat.1001132>
- Dos Santos Pacheco, N., Brusini, L., Haase, R., Tosetti, N., Maco, B., Brochet, M., Vadas, O., & Soldati-Favre, D. (2022). Conoid extrusion regulates glideosome assembly to control motility and invasion in Apicomplexa. *Nature Microbiology*, *7*(11), 1777–1790. <https://doi.org/10.1038/s41564-022-01212-x>
- Dubacheva, G. V., Araya-Callis, C., Geert Volbeda, A., Fairhead, M., Codée, J., Howarth, M., & Richter, R. P. (2017). Controlling Multivalent Binding through Surface Chemistry: Model Study on

Streptavidin. *Journal of the American Chemical Society*, 139(11), 4157–4167. <https://doi.org/10.1021/jacs.7b00540>

Frénel, K., Dubremetz, J.-F., Lebrun, M., & Soldati-Favre, D. (2017). Gliding motility powers invasion and egress in Apicomplexa. *Nature Reviews Microbiology*, 15(11), 645–660. <https://doi.org/10.1038/nrmicro.2017.86>

Gras, S., Jackson, A., Woods, S., Pall, G., Whitelaw, J., Leung, J. M., Ward, G. E., Roberts, C. W., & Meissner, M. (2017). Parasites lacking the micronemal protein MIC2 are deficient in surface attachment and host cell egress, but remain virulent in vivo. *Wellcome Open Research*, 2, 32. <https://doi.org/10.12688/wellcomeopenres.11594.2>

Håkansson, S., Morisaki, H., Heuser, J., & Sibley, L. D. (1999). Time-lapse video microscopy of gliding motility in *Toxoplasma gondii* reveals a novel, biphasic mechanism of cell locomotion. *Molecular Biology of the Cell*, 10(11), 3539–3547. <https://doi.org/10.1091/mbc.10.11.3539>

Harper, J. M., Hoff, E. F., & Carruthers, V. B. (2004). Multimerization of the *Toxoplasma gondii* MIC2 integrin-like A-domain is required for binding to heparin and human cells. *Molecular and Biochemical Parasitology*, 134(2), 201–212. <https://doi.org/10.1016/j.molbiopara.2003.12.001>

Heinemann, F., Doschke, H., & Radmacher, M. (2011). Keratocyte Lamellipodial Protrusion Is Characterized by a Concave Force-Velocity Relation. *Biophysical Journal*, 100(6), 1420–1427. <https://doi.org/10.1016/j.bpj.2011.01.063>

Hemmersam, A. G., Rechendorff, K., Foss, M., Sutherland, D. S., & Besenbacher, F. (2008). Fibronectin adsorption on gold, Ti-, and Ta-oxide investigated by QCM-D and RSA modelling. *Journal of Colloid and Interface Science*, 320(1), 110–116. <https://doi.org/10.1016/j.jcis.2007.11.047>

Herant, M., & Dembo, M. (2010). Form and function in cell motility: From fibroblasts to keratocytes. *Biophysical Journal*, 98(8), 1408–1417. <https://doi.org/10.1016/j.bpj.2009.12.4303>

Hu, K., Mann, T., Striepen, B., Beckers, C. J. M., Roos, D. S., & Murray, J. M. (2002). Daughter cell assembly in the protozoan parasite *Toxoplasma gondii*. *Molecular Biology of the Cell*, 13(2), 593–606. <https://doi.org/10.1091/mbc.01-06-0309>

Huynh, M.-H., & Carruthers, V. B. (2006). *Toxoplasma* MIC2 Is a Major Determinant of Invasion and Virulence. *PLOS Pathogens*, 2(8), e84. <https://doi.org/10.1371/journal.ppat.0020084>

Jacot, D., Tosetti, N., Pires, I., Stock, J., Graindorge, A., Hung, Y.-F., Han, H., Tewari, R., Kursula, I., & Soldati-Favre, D. (2016). An Apicomplexan Actin-Binding Protein Serves as a Connector and Lipid Sensor to Coordinate Motility and Invasion. *Cell Host & Microbe*, 20(6), 731–743. <https://doi.org/10.1016/j.chom.2016.10.020>

Jewett, T. J., & Sibley, L. D. (2004). The *toxoplasma* proteins MIC2 and M2AP form a hexameric complex necessary for intracellular survival. *The Journal of Biological Chemistry*, 279(10), 9362–9369. <https://doi.org/10.1074/jbc.M312590200>

Johannsmann, D. (1999). Viscoelastic analysis of organic thin films on quartz resonators. *Macromolecular Chemistry and Physics*, 200(3), 501–516. [https://doi.org/10.1002/\(SICI\)1521-3935\(19990301\)200:3<501::AID-MACP501>3.0.CO;2-W](https://doi.org/10.1002/(SICI)1521-3935(19990301)200:3<501::AID-MACP501>3.0.CO;2-W)

Kameritsch, P., & Renkawitz, J. (2020). Principles of Leukocyte Migration Strategies. *Trends in Cell Biology*, 30(10), 818–832. <https://doi.org/10.1016/j.tcb.2020.06.007>

Kamsma, D., Bochet, P., Oswald, F., Alblas, N., Goyard, S., Wuite, G. J. L., Peterman, E. J. G., & Rose, T. (2018). Single-Cell Acoustic Force Spectroscopy: Resolving Kinetics and Strength of T Cell Adhesion to Fibronectin. *Cell Reports*, 24(11), 3008–3016. <https://doi.org/10.1016/j.celrep.2018.08.034>

- Kumar, A., Vadas, O., Dos Santos Pacheco, N., Zhang, X., Chao, K., Darvill, N., Rasmussen, H. Ø., Xu, Y., Lin, G. M.-H., Stylianou, F. A., Pedersen, J. S., Rouse, S. L., Morgan, M. L., Soldati-Favre, D., & Matthews, S. (2023). Structural and regulatory insights into the glideosome-associated connector from *Toxoplasma gondii*. *ELife*, *12*, e86049. <https://doi.org/10.7554/eLife.86049>
- Lämmermann, T., & Sixt, M. (2009). Mechanical modes of ‘amoeboid’ cell migration. *Current Opinion in Cell Biology*, *21*(5), 636–644. <https://doi.org/10.1016/j.ceb.2009.05.003>
- Leung, J. M., Rould, M. A., Konradt, C., Hunter, C. A., & Ward, G. E. (2014). Disruption of TgPHIL1 Alters Specific Parameters of *Toxoplasma gondii* Motility Measured in a Quantitative, Three-Dimensional Live Motility Assay. *PLoS ONE*, *9*(1), e85763. <https://doi.org/10.1371/journal.pone.0085763>
- Liu, Y.-J., Le Berre, M., Lautenschlaeger, F., Maiuri, P., Callan-Jones, A., Heuzé, M., Takaki, T., Voituriez, R., & Piel, M. (2015). Confinement and low adhesion induce fast amoeboid migration of slow mesenchymal cells. *Cell*, *160*(4), 659–672. <https://doi.org/10.1016/j.cell.2015.01.007>
- Mandal, K., Balland, M., & Bureau, L. (2012). Thermoresponsive Micropatterned Substrates for Single Cell Studies. *PLoS ONE*, *7*(5), e37548. <https://doi.org/10.1371/journal.pone.0037548>
- Mizutani, M., Tulum, I., Kinoshita, Y., Nishizaka, T., & Miyata, M. (2018). Detailed Analyses of Stall Force Generation in *Mycoplasma mobile* Gliding. *Biophysical Journal*, *114*(6), 1411–1419. <https://doi.org/10.1016/j.bpj.2018.01.029>
- Montoya, J., & Liesenfeld, O. (2004). Toxoplasmosis. *The Lancet*, *363*(9425), Article 9425. [https://doi.org/10.1016/S0140-6736\(04\)16412-X](https://doi.org/10.1016/S0140-6736(04)16412-X)
- Münter, S., Sabass, B., Selhuber-Unkel, C., Kudryashev, M., Hegge, S., Engel, U., Spatz, J. P., Matuschewski, K., Schwarz, U. S., & Frischknecht, F. (2009). Plasmodium Sporozoite Motility Is Modulated by the Turnover of Discrete Adhesion Sites. *Cell Host & Microbe*, *6*(6), 551–562. <https://doi.org/10.1016/j.chom.2009.11.007>
- Oria, R., Wiegand, T., Escribano, J., Elosegui-Artola, A., Uriarte, J. J., Moreno-Pulido, C., Platzman, I., Delcanale, P., Albertazzi, L., Navajas, D., Trepast, X., García-Aznar, J. M., Cavalcanti-Adam, E. A., & Roca-Cusachs, P. (2017). Force loading explains spatial sensing of ligands by cells. *Nature*, *552*(7684), 219–224. <https://doi.org/10.1038/nature24662>
- Paluch, E. K., Aspalter, I. M., & Sixt, M. (2016). Focal Adhesion-Independent Cell Migration. *Annual Review of Cell and Developmental Biology*, *32*, 469–490. <https://doi.org/10.1146/annurev-cellbio-111315-125341>
- Pavlou, G., Milon, G., & Tardieux, I. (2019). Intracellular protozoan parasites: Living probes of the host cell surface molecular repertoire. *Current Opinion in Microbiology*, *52*, 116–123. <https://doi.org/10.1016/j.mib.2019.06.007>
- Pavlou, G., Touquet, B., Vigetti, L., Renesto, P., Bougdour, A., Debarre, D., Balland, M., & Tardieux, I. (2020). Coupling Polar Adhesion with Traction, Spring and Torque Forces Allows High Speed Helical Migration of the Protozoan Parasite *Toxoplasma*. *ACS Nano*. <https://doi.org/10.1021/acsnano.0c01893>
- Periz, J., Whitelaw, J., Harding, C., Gras, S., Del Rosario Minina, M. I., Latorre-Barragan, F., Lemgruber, L., Reimer, M. A., Insall, R., Heaslip, A., & Meissner, M. (2017). *Toxoplasma gondii* F-actin forms an extensive filamentous network required for material exchange and parasite maturation. *ELife*, *6*, e24119. <https://doi.org/10.7554/eLife.24119>
- Perry, S. S., Yan, X., Limpoco, F. T., Lee, S., Müller, M., & Spencer, N. D. (2009). Tribological properties of poly(L-lysine)-graft-poly(ethylene glycol) films: Influence of polymer architecture and adsorbed conformation. *ACS Applied Materials & Interfaces*, *1*(6), 1224–1230. <https://doi.org/10.1021/am900101m>

Philips, R., & Milo, R. (2015). *Cell Biology by the numbers*. <http://book.bionumbers.org/how-fast-do-cells-move/>

Saftics, A., Prószyński, G. A., Türk, B., Peter, B., Kurunczi, S., & Horvath, R. (2018). In situ viscoelastic properties and chain conformations of heavily hydrated carboxymethyl dextran layers: A comparative study using OWLS and QCM-I chips coated with waveguide material. *Scientific Reports*, 8(1), 11840. <https://doi.org/10.1038/s41598-018-30201-6>

Schuksz, M., Fuster, M. M., Brown, J. R., Crawford, B. E., Ditto, D. P., Lawrence, R., Glass, C. A., Wang, L., Tor, Y., & Esko, J. D. (2008). Surfen, a small molecule antagonist of heparan sulfate. *Proceedings of the National Academy of Sciences*, 105(35), 13075–13080. <https://doi.org/10.1073/pnas.0805862105>

Shen, B., Buguliskis, J. S., Lee, T. D., & Sibley, L. D. (2014). Functional analysis of rhomboid proteases during *Toxoplasma* invasion. *MBio*, 5(5), e01795-01714. <https://doi.org/10.1128/mBio.01795-14>

Stadler, R. V., Nelson, S. R., Warshaw, D. M., & Ward, G. E. (2022). A circular zone of attachment to the extracellular matrix provides directionality to the motility of *Toxoplasma gondii* in 3D. *ELife*, 11, e85171. <https://doi.org/10.7554/eLife.85171>

Thakar, D., Migliorini, E., Coche-Guerente, L., Sadir, R., Lortat-Jacob, H., Boturyn, D., Renaudet, O., Labbe, P., & Richter, R. P. (2014). A quartz crystal microbalance method to study the terminal functionalization of glycosaminoglycans. *Chemical Communications (Cambridge, England)*, 50(96), 15148–15151. <https://doi.org/10.1039/c4cc06905f>

Tonkin, M. L., Grujic, O., Pearce, M., Crawford, J., & Boulanger, M. J. (2010). Structure of the micronemal protein 2 A/I domain from *Toxoplasma gondii*. *Protein Science: A Publication of the Protein Society*, 19(10), 1985–1990. <https://doi.org/10.1002/pro.477>

Yamada, K. M., & Sixt, M. (2019). Mechanisms of 3D cell migration. *Nature Reviews. Molecular Cell Biology*, 20(12), 738–752. <https://doi.org/10.1038/s41580-019-0172-9>

Yamaguchi, N., & Knaut, H. (2022). Focal adhesion-mediated cell anchoring and migration: From in vitro to in vivo. *Development (Cambridge, England)*, 149(10), dev200647. <https://doi.org/10.1242/dev.200647>

2.6 Discussion and perspectives

In this work, we report in a minimalistic work frame the requirements for productive force during helical gliding, tackling from a mechanics and chemistry point of view. First, using a combinatorial of high-resolution micropatterns with alternating adhesive and non-adhesive surface coating areas and high-speed confocal microscopy, we analyzed the tachyzoite motile capabilities. As a result, we found that the tachyzoite performs equally well on discontinuous substrates compares to continuous ones, demonstrating that the parasite has evolved a unique adhesion system with a fixed position on the surface that is sufficient to timely achieve enough stability for withstanding traction forces but also enough dynamics to permit gliding when the rest of the body is in a non-adhering condition. This single focal adhesion point that the tachyzoite creates in the subsequent adhesive area in our intermittent micropatterned surfaces relate not only to the necessity of the apical anchoring that is needed for helical gliding (Pavlou et al., 2020) but also to the specific spots observed ones on *Plasmodium* (Hegge et al., 2010) affording the parasite-surface generation and transmission of force. On a 3D environment mimicking ECM conditions, this single anchoring sufficiency was observed as a circular zone of attachment from where the parasite squeezes and directs it movement (Stadler et al., 2022). Our photolithography micropattern setting allow variety of adhesive compounds in the permissive areas, and in that spirit we constructed for the first time a heparin-based micropattern surface. The tachyzoite's attachment to heparin, a sulfated glycosaminoglycan, occurs through sugar-binding lectin receptors, playing a role in host cell invasion as tachyzoites showed a reduced infection ratio of cells deficient in the biosynthesis of surface proteoglycans (Ortega-Barria & Boothroyd, 1999). The presence of soluble heparin in the medium has been shown to decrease tachyzoite motility, as it disrupts the parasite attachment on the surface (Carruthers et al., 2000). Here, we show that the local interaction between the apex of the parasite and heparin is sufficient to support helical displacement similarly to fibronectin.

Continuing this work frame, in this study we combined for the first reported time the use of micropattern with Expansion microscopy. By enlarging isotropically our sample, we were able to observe that on alternating adhesive/non-adhesive areas the tachyzoite diminishes its contact zones compared to when moving on a fully adhesive one, restricting to only the apicobasal points of attachment. This is likely due to a combination of reduced membrane-substrate interaction which doesn't impact the overall motility; the discrete adhesion points as a 'patch

gliding' scenario correlate with a similar behavior observed in the *Plasmodium* sporozoite (Münter et al., 2009). The scenario on which the tachyzoite performs as well as in homogeneous surfaces as in discontinuous ones could be related to the persistence needed to avoid staying for long periods of time within the ECM, at the reach of the patrolling immune system's cells, and propel forward with the minimum anchoring site available.

Next, we built biochemical tunable surfaces with quantitatively controlled exposed moieties, in a new SAV/biotin based surface building approach; all was biophysically characterized using the sensitive Quartz Crystal Microbalance with Dissipation technique. Our workflow, given that the SAV-biotin binding stoichiometry varies between 1 and 3 binding sites, allowed a finer control of exposed moieties ratios than performing it over the base of a Self-Assembled Monolayers (SAMs) (Dubacheva et al., 2017). All these surfaces were well characterized, based on our rigorous control of solvent interaction and adsorption as well as the thickness and viscoelasticity by QCM-D. Most importantly, as the surface modeling concluded on their similar softness and elastic properties, the tunable ligands and density variation allowed us to isolate the effect of chemistry on tachyzoite motility. First, we observed that negative charge plays a role in tachyzoite motility, as the highest restoration was observed for Heparan Sulfate. This result would be in coordination with the presence of positive charges in the apical pole of the tachyzoites as observed with Atomic Force Microscopy and surface potential spectroscopy (Akaki et al., 2001). Although the parasite's cell receptors are yet under debate with the possibility that the nanodevice serve as a *bona fide* receptor, these electrostatic forces interactions would play a significant role in motility. Charges aside, sulfated proteoglycans such as HS were shown to interact with the parasites for motility and cell invasion (Carruthers et al., 2000). Next, we observed that ligand chemistry also plays a bigger role in motility than biophysical properties, as surfaces with the same viscoelastic parameters but with different second layers (*i.e.* -OH vs HS) show significant different phenotypes.

Zooming out of the *T. gondii* field, these tunable surface building approach we developed in this study can be scalable for different biological models work lines. Just as an example, in our surface we are able to modulate the storage and loss modulus, two important biophysical properties that regulate bacterial biofilms attachment (Kretschmer et al., 2021) and could provide a complementation to the current flow chamber studies, important for their biomedical applications (Gomes & Mergulhão, 2021).

Coming back to our parasite and its peculiar locomotion, in this work we focused on another point at play for motility too, the presence of the apicobasal retrograde membrane flow observed on extracellular tachyzoites. On motile parasites, there is a secretory cycle that starts at the apical pole with the release of adhesins, which are tightly regulated by complex signaling cascades upon sensing of extracellular conditions (Bullen et al., 2019). These adhesins are linked to the glideosome machinery and translocate backwards powered by the MyoH (in the apical pole) and MyoA (in the rest of the body) motors, in an actin-dependent manner (Graindorge et al., 2016; Jacot et al., 2016; Long et al., 2017). At the basal part of the tachyzoite, adhesins are either recycled through the endocytic pathway or/ and cleaved to shed their ectodomain from the tachyzoite surface (Koreny et al., 2023). Alternatively, it was proposed a model named the ‘fountain flow’ (Gras et al., 2019), where the secretion at the apical pole and the endocytosis at the basal pole creates a membrane flow which contributes to helical gliding in a similar fashion to what occurs in the eukaryote *Dictyostelium* (Tanaka et al., 2017). Now, we add to the model by showing that this retrograde flow is present also on PLL-PEG surfaces, in the absence of parasite-surface adhesion and motility. The bead translocation experiments performed by our team show that the process is MyoA and actin dependent, results which in combination with the observation that retrograde flow is 50% faster than gliding motility on *Plasmodium* (Quadt et al., 2016), would suggest that the membrane translocation is a component of the extracellular lifestyle, independent from adhesion, and contributes in a synergic manner with the actomyosin system and rearward translocation of adhesion for motility, as alongside mechanisms. As such, it is possible that the tachyzoite displays more than one exclusive motile mechanism, where the combination of force generation on highly-focalized attachment areas and retrograde translocation of adhesins propel motility. This would relate to the recent studies on 3D traction force (Stadler et al., 2022) where the parasite creates a localized ring-shaped attachment zone to produce force, and without this area the tachyzoite is still able to move but without the same directionality.

Lastly, we further analyzed the role of the adhesin MIC2 for both retrograde membrane flow and motility in our micropatterned surfaces. In normal 2D and 3D environments, MIC2 is necessary for full phenotypic motile capabilities (Gras et al., 2019; Stadler et al., 2022) and we show the same observation for intermittent surfaces, where the lack of MIC2 impairs crossing. Furthermore, we now display that MIC2 also is also present on the translocation of microbeads in non-adhesive surfaces.

Moving forward, there are several interesting questions that arise in order to further pursue the research line exposed in this work:

- What are the molecular components of the platform required for the tachyzoite adhesion? It still remains largely unknown the ligands and adhesins required in the apical anchoring to generate the productive force. There are several studies showing that these *T. gondii* ligands could be partially mediated by surface antigens responsible for the interaction with sulfate proteoglycans, as for example surface antigen 3 (SAG3) interacting with cell-surface proteoglycans (Jacquet et al., 2001), or the integrin-like A-domain of MIC2 for binding to heparin on host cells (Harper et al., 2004).
- What is the role of the combination of different extracellular matrix (ECM) components in motility and does it exist a precise preferred ligand density? For this, in our tunable system we are able to present a variety of proteoglycans or glycoproteins which form the extracellular matrix (ECM), and vary the ratios exposed, with the only requirement that they are mono-biotinylated. There are several studies showing their contribution for *T. gondii* host cell invasion, *i.e.* for sialic acid (Monteiro et al., 1998), laminin (Furtado et al., 1992) or dextran sulfate (Ortega-Barria & Boothroyd, 1999), but their contribution to parasite motility when it navigates through the ECM is still unclear.

2.7 Vigetti and Tardieux, *Biol. Cell.*, 2023

Several biophysical methods were applied in recent years with the objective to understand the adhesion strength and real-time force measurements on microbe-host cell or microbe-extracellular matrix interactions. As several of these techniques were not applied during the course of the studies presented, we aimed to discuss in this review the importance of understanding the biomechanical interaction between Apicomplexan zoites and their hosts, with a special focus on how quantitative biophysical methods can solve the mechanical challenges that are faced by these eukaryotic parasites during their developmental stages, and discussing future synergies between different techniques will allow retrieving a more complete picture at the dynamic host-parasite interface.

Publication

Vigetti, L. & Tardieux, I. (2023) Fostering innovation to solve the biomechanics of microbe–host interactions: Focus on the adhesive forces underlying Apicomplexa parasite biology. *Biology of the Cell*, 00, 1– 17. <https://doi.org/10.1111/boc.202300016>

REVIEW

Fostering innovation to solve the biomechanics of microbe–host interactions: Focus on the adhesive forces underlying Apicomplexa parasite biology

Luis Vigetti  | Isabelle Tardieux 

Team Biomechanics of Host-Parasite Interactions, Institute for Advanced Biosciences, CNRS UMR5309, INSERM U1209, University of Grenoble Alpes, Grenoble, France

Correspondence

Isabelle Tardieux and Luis Vigetti, Team Biomechanics of Host-Parasite Interactions, Institute for Advanced Biosciences, CNRS UMR5309, INSERM U1209, University of Grenoble Alpes, Grenoble, France
Email: isabelle.tardieux@inserm.fr and luis.vigetti@univ-grenoble-alpes.fr

Abstract

The protozoa, *Toxoplasma gondii* and *Plasmodium* spp., are preeminent members of the Apicomplexa parasitic phylum in large part due to their public health and economic impact. Hence, they serve as model unicellular eukaryotes with which to explore the repertoire of molecular and cellular strategies that specific developmental morphotypes deploy to timely adjust to their host(s) in order to perpetuate. In particular, host tissue- and cell-invasive morphotypes termed zoites alternate extracellular and intracellular lifestyles, thereby sensing and reacting to a wealth of host-derived biomechanical cues over their partnership. In the recent years, biophysical tools especially related to real time force measurement have been introduced, teaching us how creative are these microbes to shape a unique motility system that powers fast gliding through a variety of extracellular matrices, across cellular barriers, in vascular systems or into host cells. Equally performant was this toolkit to start illuminating how parasites manipulate their hosting cell adhesive and rheological properties to their advantage. In this review, besides highlighting major discoveries along the way, we discuss the most promising development, synergy, and multimodal integration in active noninvasive force microscopy methods. These should in the near future unlock current limitations and allow capturing, from molecules to tissues, the many biomechanical and biophysical interplays over the dynamic host and microbe partnership.

KEYWORDS

adhesive strength, Apicomplexa, force microscopy, live imaging, mechanobiology, parasitism, technical synergy

Abbreviations: AFM, Atomic Force Microscopy; EMP1, Erythrocyte Membrane Protein 1; ECL, Essential Light Chains; ECM, Extracellular Matrix; FluidFM, Fluid Force Microscopy; GAC, Glideosome-Associated Connector Protein; GAPs, Glideosome Associated Proteins; GAPMs, Glideosome-Associated Protein with Multiple-membrane Spans; HS-AFM, High-Speed Atomic Force Microscopy; IMC, Inner Membrane Complex; KAHRP, Knob-Associated Histidine Protein; MTs, Magnetic Tweezers; MZLE, Merozoite-Loaded-Erythrocytes; MLC1, Myosin Light Chain 1; MyoA, Myosin A; nN, NanoNewtons; OFTs, Optical Fiber Tweezers; OS, Optical Stretchers; OTs, Optical Tweezers; PV, Parasitophorous Vacuole; pN, PicoNewtons; PM, Plasma Membrane; SGs, Salivary Glands; SECM, Scanning Electrochemical Microscopy; SEM, Scanning Electron Microscopy; SFM, Scanning Force Microscopy; SBATs, Single-Beam Acoustic Tweezers; SMFS, Single Molecule Force Spectroscopy; STED, Stimulated Emission Depletion; STORM, Stochastic Optical Reconstruction; TRAP, Thrombospondin-Related Anonymous Protein; TFM, Traction Force Microscopy; TEM, Transmission Electron Microscopy.

This is an open access article under the terms of the Creative Commons Attribution-NonCommercial-NoDerivs License, which permits use and distribution in any medium, provided the original work is properly cited, the use is non-commercial and no modifications or adaptations are made.

© 2023 The Authors. *Biology of the Cell* published by Wiley-VCH GmbH on behalf of Société Française des Microscopies and Société de Biologie Cellulaire de France.

INTRODUCTION

In the wide context of microbe–host interaction studies, the microbe being considered as living organism per se, two of the predominant and long-lasting challenges are (i) to capture and recapitulate, through the best-suited experimental settings, the main parameters that operate along the stepwise microbe–host partnership, and (ii) to retrieve across multiple scales, through biologically-biophysically-biomechanically-relevant approaches, quantitative spatiotemporal information that features the uniqueness of the relationships between the two partners.

Reaping the benefits of genomics, proteomics, and metabolomics-based research developments throughout the last two decades, an impressive gain of knowledge has been achieved on biomolecules from both microbe and host origins together with structural and functional characterization of dynamic and complex molecular machineries. Aside from those sensitive multi-omics methodologies simultaneously applied to each partner, other challenges remain or even emerge lately. For instance, we need to better integrate the 3D acellular microenvironment and the cell populations in the host as mechanically responsive interdependent compartments that are imposed to the microbe but also potentially modified by the latter in ways that could result in either local and/or systemic damages to the host.

How the microbe and the host use and adjust their own biomechanical properties over their partnership is a key interrogation to which quantitative biophysical methods can provide answers and complement the more classical cell biology approaches. Specifically, adhesive strength and real time force measurements would help to understand how microbes timely interact with a broad or limited molecular repertoire featuring the extracellular matrices (ECMs) or the targeted cells, and consequently experience and respond to forces in these fluctuating microenvironments. Equally important but also quite elusive is the transduction of the mechanical cues into biochemical signals and their biological downstream responses. Indeed, biophysical tools using a force field would allow to probe subcellular mechanotransduction and to manipulate cell signaling in a quantitatively controlled way.

In this review, we begin by introducing a few Apicomplexa zoites that serve as main prototypes to explore the mechanical challenges these eukaryotic parasitic microbes face over highly diversified developmental programs. We select prime studies for which the implementation of biophysical methods, alone or in combination, has helped to clarify the adhesion strength of the parasite–cell or parasite–ECM interfaces in the context of force generation during cell anchoring or/and migratory responses. The first focus concerns the dynamic

coupling between adhesion and motile functions of parasites and starts with a brief overview on the molecular motor machines and motile behaviors of few zoite prototypes. The second focus concerns the changes in the host cell adhesive properties driven by intracellular developing zoites, with major outputs on zoite and host biology, and thus emphasize to the remodeling of the host cell surface and periphery. We provide information on the biophysical methods used to measure force at appropriate scales, their advantages, and current limitations. We outline recent technical development and implementation for a valuable exploration of the multiple adhesion dynamic interfaces built by the zoite to timely cope with the host microenvironments and ensure perpetuation.

A VARIETY OF BIO-MECHANICAL CHALLENGES FOR APICOMPLEXA ZOITES OVER THEIR HIGHLY DIVERSIFIED LIFE CYCLES

Parasitism is a prevalent lifestyle on Earth being interspersed throughout much of the tree of life, and in this regard, the Apicomplexa appears as an exemplary parasitic phylum by gathering more than half of a million unicellular species known to perpetuate through a diversified repertoire of metazoan hosts in aquatic and terrestrial ecosystems. Many Apicomplexa species co-sculpt with their hosts-successive protective niches, each niche accounting for the transition from one to another developmental morphotype (from now on referred to as morphotype) through mono- or heteroxenous complex life cycles. Yet, only a tiny number of species and even a more limited number of species morphotypes have benefited from refined investigations so far. At the top of the list are Apicomplexa species prioritized in scientific research programs either because they presently perpetuate in human beings—the most recent homeotherm metazoan genus to have populated the Earth—or because they colonize non-human animals of social and economic values, hence they represent public health or/and social issues. Other applicable and relevant model hosts include metazoans such as blood-feeding insects reared in insectarium and homeotherm metazoans such as laboratory rodents reared in controlled animal facilities. Leader in the first category is *Plasmodium/P. falciparum* which is the deadliest out of the five *Plasmodium* species responsible for malaria in humans, a disease affecting about 250 million people mainly in Africa and associated with 619.000 deaths among which about 80% are children under 5 years old (World Health Organization, 2021). For the second category, *P. berghei*, one of the *Plasmodium* species isolated from wild rodents and adapted to laboratory mice and insectarium-reared anopheline mosquitoes which

requires only biosafety level 1 conditions. Aside from *Plasmodium* spp., a long-standing interest for the cosmopolitan apicomplexan *Toxoplasma gondii* stems from its ability to (i) persist in its hosts where it poses a threat for cerebral toxoplasmosis illnesses mostly but not exclusively in case of immune dysfunction—still a major concern for AIDS patients deprived of appropriate therapy (Ayoade and Chandranesan, 2023), (ii) cross the placenta and colonize fetuses, thereby putting at risk of human and other animal stillbirth—a significant economic issue for livestock—but also of high morbidity in newborns and children as they progress into adulthood (European Centre for Disease Report, 2019; Kim and Weiss, 2004; Stelzer et al., 2019), and (iii) colonize a spectacularly wide range of natural homeotherm hosts (Dubey et al., 1998).

Unified with the suffix “zoite” the between hosts’ transmissible and host cells’ invasive morphotypes are typically defined by a sustained apicobasal polarity (Dubey et al., 1998) a variable shape from roughly spherical to elliptical or elongated crescent, and a 1–2 μm size in diameter (Dubey et al., 1998). In addition to significant variation in shape and in structural elements, the tubulin cytoskeleton also differs from one zoite morphotype to the other in particular with respect to the number and arrangement of cortical microtubules. These microtubules are nucleated at the apical pole and strikingly stable, and likely in concert with other sub membranous structures they provide main shape and flexibility features, hence they primary determine the zoite ability to squeeze in various environments (for a review, see Harding and Frischknecht, 2020). Indeed, Hosts’ and cells’ invasive zoites have to face various extracellular environments made of viscoelastic complex biomaterials that specify tissues while, once intracellular, these zoites must manage the heterogeneously and cell-specific viscous cytoplasm (Figure 1). For instance, *Toxoplasma* produces a progeny of tachyzoites within a membrane-bound compartment defined as the parasitophorous vacuole (PV) in the “feeding and protective” nucleated host cells it eventually egresses from. The free mature tachyzoites navigate in between cells embedded within tissue-specific scaffolding ECMs or across the ECM specialized form termed basal lamina which borders all basolateral epithelia and endothelia prior to repeat the invasive-replicative processes. Free or loaded onto host leukocytic shuttles, *T. gondii* tachyzoites also translocate across endothelia, including the brain blood endothelial barrier, when the *T. gondii* transmissible morphotype is delivered to laboratory mice through the natural oral route (Courret et al., 2006). In the case of *Plasmodium*, collectives of tens to hundreds merozoites emerge from hepatocyte-derived vesicles known as merozoites which, owing to their striking deformability, can squeeze through the

liver endothelium and reach the blood stream. Once in the capillaries, merozoites liberate individual merozoites (Baer et al., 2007; Burda et al., 2017; Sturm et al., 2006) which subsequently invade and proliferate as erythrocytic merozoites within a PV dynamic compartment. While healthy erythrocytes are biconcave discoid cells that markedly deform through acute membrane folding and cytoplasmic reorganization in response to shearing flow, the repeated passages through the microcapillaries as well as through the narrow inter-endothelial slits of splenic and marrow sinuses, result in the cumulative loss of deformability which compromise their lifespan (Tomaiuolo, 2014). Similarly, a significant alteration in rheological properties correlates with the intraerythrocytic development of *Plasmodium* spp. parasites (i.e., a process referred to as “rheopathobiology”) and leads to a progressive loss of the erythrocyte deformability (Russell and Cooke, 2017) acknowledged as a consequence of the presence of the parasite material and the cytoskeletal rearrangement (Nash et al., 1989). These changes in biomechanical properties differentially induced by *Plasmodium* species and how they translate in a gain of adhesiveness to endothelia as well as the clinical impact have and continue to be intensively investigated through a combination of modeling and biophysical approaches which are detailed below. Moreover, once released in the lumen of blood micro-vessels, the merozoite progeny directly copes with mechanical loads from fluid pressure and flow. Other *Plasmodium* developmental morphotypes are experiencing acute changes of biomechanical conditions since the same individuals alternate intracellular and extracellular movements. It is the case for *Plasmodium* spp. sporozoites which egress from the oocyst lying beneath the midgut epithelium and basal lamina. Upon oocyst rupture, the sporozoites travel with the hemolymph flow toward the insect salivary glands (SGs) of which they successively traverse the basement membrane and cells. Once in the SG cavities, sporozoites can establish peculiar homotypic interactions to slide on each other as unique circling collectives (Patra et al., 2022; Tolić and Tardieux, 2022; Wells and Andrew, 2019). In contrast, the hematophagous insect delivers only individual mature sporozoites along with saliva into the mammalian host dermis. Sporozoites further move in between and through cells prior to access the blood stream and pass the liver sinusoids (Amino et al., 2006; Douglas et al., 2015; Thiberge et al., 2007). There they again migrate through cells (resident macrophages known as Kupffer cells and possibly hepatocytes) using versatile membrane breaching strategies (Ejigiri and Sinnis, 2009; Risco-Castillo et al., 2015) to finally settle within hepatocytes and produce thousands of merozoites ready to initiate the iterative invasive/replicative cycle in erythrocytes.

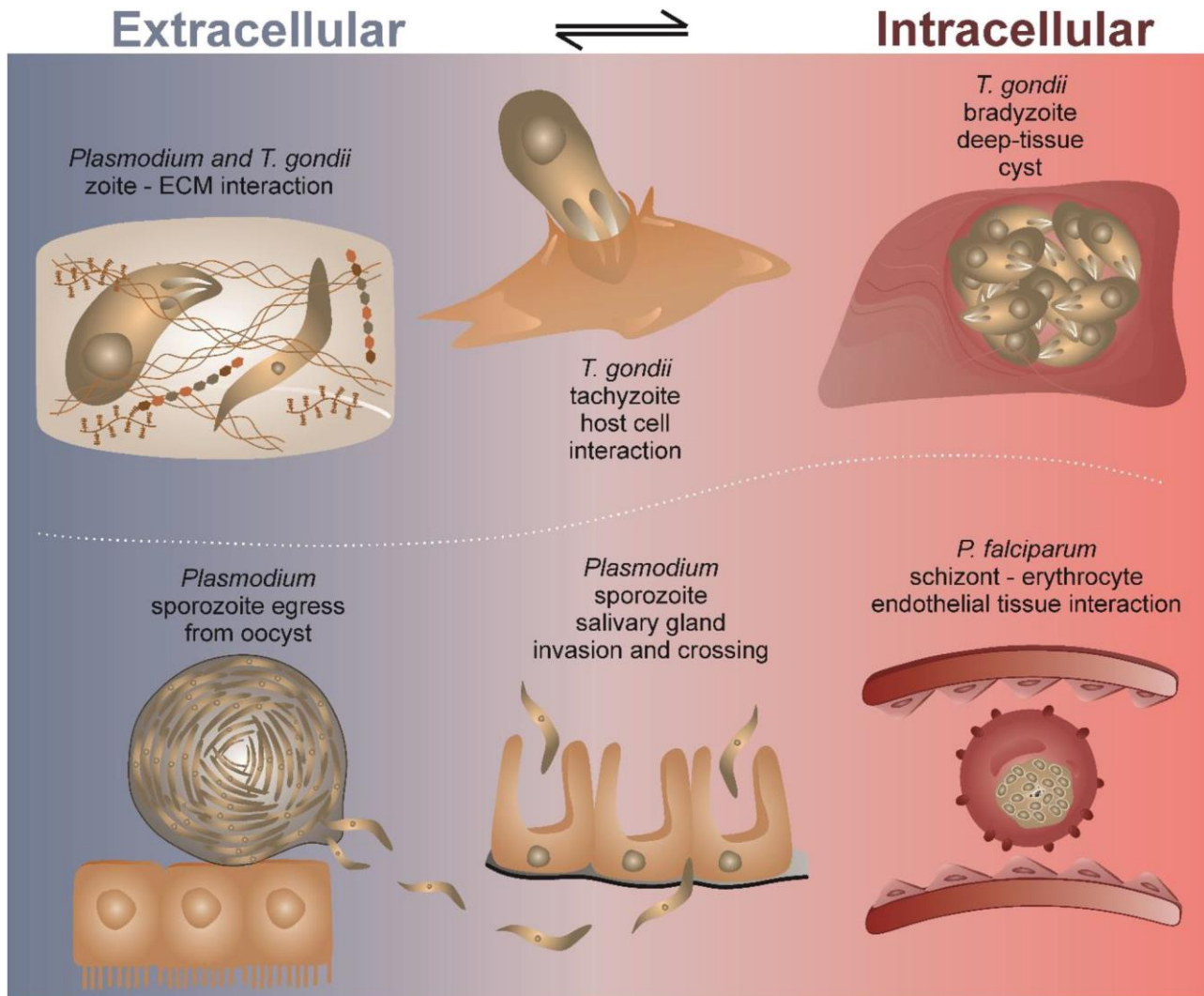


FIGURE 1 Apicomplexan model parasites: on the verge of extracellular and intracellular lifestyle. Along their complex life cycle, *Plasmodium* spp. and *T. gondii* have evolved zoite morphotypes that cycle from host to host and experience a large range of mechanical stimuli. In each host, zoites adjust to immediate extracellular and intracellular cues when they navigate throughout and across a variety of ECMs, enter host blood and lymphatic vascular beds, settle and traverse a restricted or broad host cell spectrum. As an example, *Plasmodium* spp. colonize anopheline mosquito tissues from the intestinal portal of entry to the SGs and gain competency for a long migratory journey in the vertebrate tissues and vasculature once delivered in the skin by the hematophagous host. Once delivered in the digestive tract of homeotherm metazoans, *T. gondii* zoites cross the ileum and newly differentiated tachyzoites emerge in the ab-luminal mucosa, a compartment from which they disseminated in ileum-distant tissues prior to establishing long-term intracellular parasitism in deep tissues.

IDENTIFYING MOTILITY HALLMARKS AND MOLECULAR POWER ENGINES IS NOT SUFFICIENT TO MECHANISTICALLY DECODING THE ZOITE' MOTILE FORCES

First descriptive hallmarks of the ex vivo motile zoite behaviors were reported in the early 1960s in non-viscous media (Freyvogel, 1966; Vanderberg, 1974; Yoeli, 1964) and led to the qualifying term of “gliding” mode of motility. Over the 1980–2000 decades, the ex vivo kinematic pioneering studies performed with either *Plasmodium* or *Eimeria* sporozoites as well as with *T. gondii* tachyzoites allowed characterizing the

zoite' gliding motility mode by (i) a quasi-systematic unidirectional—front first—movement of the zoite, (ii) the strict requirement of highly transient adhesion formation and breakage between the zoite surface and the 2D substrate, (iii) the high-speed (HS) nature of the displacement that ranges around a few microns per second, exceeding by far the speed of the fastest immune patrolling cells in metazoans, and (iv) the maintenance of zoite shape and polarity since no membrane deformations or protrusions were detected in locomoting zoites. Early kinematic studies of zoites moving on surfaces documented typical trajectories showing circular patterns for the *P. berghei* sporozoites (Stewart and

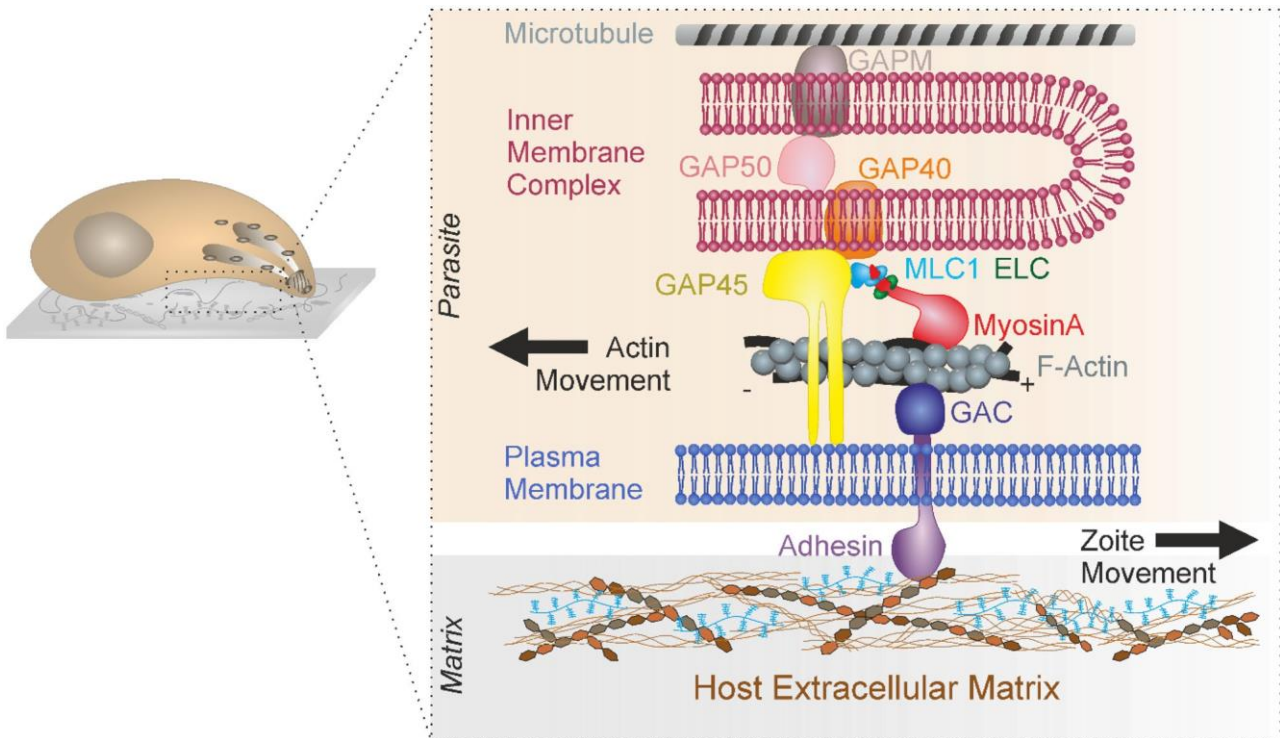


FIGURE 2 The glideosome: the Apicomplexan unidirectional linear acto-myosin motor model. The glideosome is centered on the class XIV MyoA motor which is anchored to the outer membrane of the double layered IMC, in the space between the outer PM. MyoA anchoring is achieved by several glideosome elements, such as the GAPs and GAPMs, and its activity regulated by partners known as the ECLs and the MLC1 partners. MyoA also provides the sub-membranous traction force that powers forward motion of the zoite.

Vanderberg, 1988), and circular and helical ones for the tachyzoite (Håkansson et al., 1999). The helical movement which proceeds with the zoite rotation along its main axis is solely responsible for the locomotion of *Plasmodium* sporozoites and *T. gondii* tachyzoites when maneuvering in vitro within a reconstituted ECM (usually extracted from murine sarcoma, i.e., Matrigel) or ex vivo (Leung et al., 2014a). In line with these observations, a related helical motile behavior of *Plasmodium* sporozoites has been reported in vivo using challenging intra-vital confocal microscopy post-surgery of organ “imaging windows” (De Niz et al., 2017).

To initiate and sustain a motile behavior, the zoite relies on a multi-component machinery called the glideosome (Opitz and Soldati, 2002) which several appear significantly conserved among the few Apicomplexa for which genomes are sequenced (see the Database collection “The VEukaryotic Pathogen, Vector and Host informatics Resource”: (Amos et al., 2022; Aurcochea et al., 2017; Baum et al., 2006) (Figure 2). Centered around the Apicomplexa-specific unconventional class XIV myosin A (MyoA) motor, these power generator units are positioned within the roughly 30 nm space between the outer plasma membrane (PM) and the double layered inner membrane complex (IMC) that hallmarks Apicomplexan cells (Anderson-White et al., 2012; Blader et al., 2015; Gubbels et al., 2004). To

fulfill their force-generating function, the MyoA motor molecules are connected to the IMC outer membrane through specific interactions with scaffolding and bridging glideosome elements, the so-called glideosome associated proteins (GAPs) and glideosome-associated protein with multiple-membrane spans (GAPMs) (Bullen et al., 2009; Frénil et al., 2017; Gaskins et al., 2004; Heintzelman, 2015). In this regard, the MyoA-IMC continuity relies on the myosin light chain 1 (MLC1) which binds both to the neck of MyoA, as a regulatory partner, and to GAP45, the latter ensuring the anchorage to both the IMC and the PM in a series of intermolecular interactions that involve protein lipidation (Frénil et al., 2010; Green et al., 2017; Rompikuntal et al., 2021). Aside from MLC1, other important MyoA regulatory partners have been structurally and functionally identified as the essential light chains (ECLs, ECL1 and ECL2 in *T. gondii*, ELC and MTIP in *Plasmodium*) which are cooperatively recruited to the MyoA neck by MLC 1. Together MLC1 and a given ELC ensure optimal MyoA performance (Leung et al., 2014b; Moussaoui et al., 2020; Pazicky et al., 2020; Powell et al., 2017a, 2017b; Robert-Paganin et al., 2019; Williams et al., 2015). In addition, post-translational modifications also occur on MyoA and regulate motor activity. Most notably, refined structural analysis brought evidence that the phosphorylation of a serine present at a peculiar N terminal extension of the

MyoA motor domain controls the MyoA motor properties in vitro (Moussaoui et al., 2020). In the same line, the use of site-specific *P. berghei* sporozoite mutants combined with ex vivo and in vivo studies has documented the significant contribution of phosphate flux on this serine to the speed and force development performance achieved by different zoite morphotypes along with their respective migratory and invasive needs in the insect and mice hosts (Ripp et al., 2022). This scheme has also been validated for motile *T. gondii* tachyzoites through a combination of biochemical and genetic approaches leading to the view that the phosphorylation of the orthologous serine, likely in conjunction with two other close serine residues is an important determinant for optimal gliding and cell invasiveness (Tang et al., 2014).

In addition to MyoA being anchored to the IMC, productive force transmission at the zoite-substrate interface also implies that MyoA concomitantly connects to some adhesive systems exposed at the zoite surface. Indeed, free zoites secrete transmembrane spanning adhesin receptors at their apex which can engage with the extracellular ligand present at the ECM or the host cell surface. The missing element in this continuous multimodule system was the molecular connector between the cytoplasmic tail of engaged adhesins and the beneath actin filaments. Such player has recently been identified as the glideosome-associated connector protein (GAC) (Jacot et al., 2016). Recent atomic-resolution crystal structure of this giant Armadillo repeat phylum-restricted protein has revealed a spring-like architecture, leading the authors to suggest that the GAC may act as an elastic element during force generation (Hung et al., 2022).

Collectively these structure-function studies have highlighted a physical and mechanical continuity between the extracellular microenvironment and the cell interior and support a common linear motor mechanism *T. gondii* and *Plasmodium* spp. zoites gliding in and out their host cells. To promote HS forward displacement of the zoites relative to the substrate, the anchored MyoA motor would critically pull backward the apically forminucleated actin filaments (Tosetti et al., 2019) which are engaged in adhesive contacts with the ECM or cell surface components through dedicated adhesin molecules (for review see Boucher and Bosch, 2015; Fréchal et al., 2017). Indeed, even the *Plasmodium* merozoites which were thought not to glide in the vascular compartment were in the last years convincingly shown to express an actomyosin-based short duration gliding capacity in vitro (Yahata et al., 2021). However, first deviations from the linear motor model have emerged about a decade ago (see the review Tardieux and Baum, 2016), and they further grow with the studies performed to assess (i) force generation (i.e., motile behavior) of zoite mutants engineered to disrupt the continuity between the actomyosin and glideosome/glideosome associated elements or their functionality (Andenmatten et al.,

2013; Rompikuntal et al., 2021) or (ii) the adhesion-force coupling in space and time during motility and in the context of membrane flow (Hegge et al., 2012; Pavlou et al., 2020; Quadt et al., 2016) do not fit with the currently accepted architecture and linear unidirectional activity of the motor machinery at work during gliding. They inevitably point to the need of digging deeper the relationships between selective intermolecular interaction (throughout the adhesin to IMC modules) and force generation and transmission during motility. In particular, must be addressed the question of how the cell-substrate contacts timely achieve enough stability to withstand traction forces and enough dynamics to permit gliding. With the introduction of more biophysical approaches to enlarge our current theoretical and experimental frameworks while providing quantitative, the expected robust datasets have started and will continue filling the knowledge gaps.

CHARACTERIZING HOW INTRACELLULAR ZOITES DIFFERENTIALLY REMODEL THE HOST CELL SURFACE IS NOT SUFFICIENT TO DECODE CLINICALLY RELEVANT CHANGES IN HOST CELL BIOMECHANICAL PROPERTIES

Along with their intracellular life, zoites extensively remodel the host cell, in particular shaping a growth-permissive PV. To this purpose, they target host signaling pathways and networks primarily related to post-translational mechanisms. Such molecular changes can drive microstructural remodeling at the host cell surface which promote cell rheological modifications as exemplified by the “paramount” case of human erythrocytes hosting human *Plasmodium* species. Indeed, along with a complex ~48 h-lasting phase of asexual multiplication and differentiation that produce merozoites, the host erythrocyte membrane and cortical cytoskeleton are markedly reorganized with the emergence of thousands of protrusive bud-like microstructures termed knobs (Quadt et al., 2012). These knobs were found in the early 1980s to display selective adhesive properties toward endothelial and erythrocytic cells (Udeinya et al., 1981) and further recognized as independent clustering sites for specific zoite-derived molecules post their export to the erythrocyte periphery. Although the critical contribution of the knob-associated histidine protein (KAHRP) to knob formation was genetically established before the 2000s (Crabb et al., 1997), the precise localization and function of KAHRP have long been debated. Most advanced super-resolution imaging approaches (scanning electron microscopy [SEM], tomography, STochastic Optical Reconstruction [STORM], and stimulated emission depletion [STED] microscopy) have allowed positioning of KAHRP at the spiral scaffold featuring the knob (Looker et al.,

2019) and proposing a bridge function in the assembly of the knob molecular puzzle (Sanchez et al., 2022). The delivery of other parasite-exported products at the knob surface, most critically the erythrocyte membrane protein 1 (PfEMP1), correlates with the enhanced Merozoite-Loaded-Erythrocytes (MZLE) cyto-adhesive properties toward both endothelial cells and placental syncytiotrophoblasts (Wichers et al., 2019). Importantly, these punctate adhesive spots counteract the otherwise typical electric repulsion between erythrocytes and account for the aggregative properties to healthy erythrocytes, which cause the vascular obstructions commonly associated with the most severe forms of cerebral (Crabb et al., 1997) and placental (Jensen et al., 2020; Zhang et al., 2017) malaria. However, cytoadherence does not systematically require the shaping of typical knob-like platforms as reported for (i) human young erythrocytes where are niched other human *Plasmodium* species (i.e., *P. vivax*, for a review see Totino and Lopes, 2017) and (ii) model *Plasmodium* species adapted to laboratory-reared hosts (Kirkman and Deitsch, 2020). Altogether, these features allow suggesting distinctive molecular and force modalities at the cell–cell adhesion interface that deserve to be further unveiled and characterized through a combination of high-resolution biochemical and biophysical methods.

Besides, modifications in the molecular composition and mechanical behavior also characterize the erythrocyte hosting a sexually committed female or male *Plasmodium* zoite. This peculiar ZLE displays enhanced cyto-adhesiveness at the onset of gametocytogenesis but only within the extra-vascular compartments of tissues, and primarily for human bone marrow mesenchymal cells (Farfour et al., 2012; Messina et al., 2018). Therefore, immature gametocyte-hosting erythrocytes use different molecular interactions than those identified in the MZLE sequestration process (Neveu and Lavazec, 2019; Silvestrini et al., 2012). Of note, the enhanced cyto-adhesiveness of the host erythrocytes in this case is reversible since along with gametocyte maturation, the deformable erythrocytes de-sequester, ultimately reentering the host's bloodstream, hence ready to be taken-up by any blood-feeding anopheline mosquito females that sample their blood meal.

Therefore, over years of research, the identification and characterization of key force components powering zoite motility or unique focal contacts with peculiar high-adhesive strength of the zoite-hosting cells have benefited from the continuous advances in proteomics, genomics, and epigenomics-based approaches, as well as stunning progress in genome editing and super resolution imaging (Barylyuk et al., 2020; Frénel et al., 2020; Heaslip et al., 2011; Sidik et al., 2016; Treeck et al., 2011). The repertoire might not be complete yet but more than the discovery of missing accessory molecules, there is

a need to interrogate the following questions: how forces are generated in situ and coordinate each other, and how they relate to the zoites' capacities to adhere ultimately translating into zoite movement at the macro- to micro-scales. Moreover, given (i) the stiffening impact of the zoite sexual and asexual developmental morphotypes, on the hosting erythrocytic cells which translate into impaired mechanical properties (Hosseini and Feng, 2011), (ii) the proposed mechanical bridge function of the knob spiral in MZLE (Watermeyer et al., 2016), there has been an obvious interest for a more detailed understanding of the biochemical and biophysical interplays that regulate adhesion strength of the zoite-hosting cells to various host tissues (Helms et al., 2016). With the concern of instigating a more biophysical conceptual and experimental framework, it is crucial to introduce force mapping and quantification in physiologically relevant microenvironments.

INTRODUCING FORCE MAPPING AND MEASURE TO STUDY HOW APICOMPLEXA ZOITE INTERACT WITH THE HOST MICROENVIRONMENTS AND BEYOND

The introduction of techniques for measuring forces including at the single-molecule level has greatly improved our understanding of how molecules, alone or upon homo/heterotypic interaction, functionally operate and coordinate in space and time to deliver forces powering multiple cell behaviors (i.e., motile; anchoring, dividing, feeding...). While techniques referred to as active methods rely on applying forces in order to deform the object/cell or to hold it in a particular manner, the passive methods proceed through the retrieval of mechanical forces such as traction forces exerted by the object/cell. In the present review, we restrict to the first category with their application to the two issues related to adhesion forces. Among others, let us cite atomic force microscopy (AFM), optical tweezers (OTs), and magnetic tweezers (MTs) each having its own advantages and limits but they provide a repertoire of tools to measure and characterize forces and torques ranging from sub-pico-Newtons (pN) to hundreds of pN. While AFM, also known as Scanning Force microscopy (SFM) is limited to systems where forces lie in the nano-Newtons (nN) scale, OTs can afford forces at the pN range and prove therefore suited for analyzing forces derived from weak non-covalent bonds that hold biomolecules or whole cells together. MTs have been invented soon after OTs in 1996 and first used to probe the elasticity of supercoiled DNA using simultaneous and independent force and torque control but are largely applied to study DNA and DNA-protein interactions as they can apply forces in the 0.1–100 pN range.

While MTs are more resolutive and offer to simultaneously probe sub-pN forces exerted by several molecules for example at the cell surface, their application is hampered by a lower spatial and temporal resolution when compared with OTs (Neuman and Nagy, 2008). Another restriction is the need to manipulate objects in magnetic fields which require other particles to be pre-tagged with magnetic compounds. Of note, ongoing development includes the replacement of DNA by proteins as tethers (for a detailed review on MT advances, see Sarkar and Rybenkov, 2016). Although successfully used in combination with millisecond-scale imaging and a microfluidics platform to measure the propulsion force of swimming flagellated *Trypanosoma* protozoan parasite (Stellamanns et al., 2014), the MTs have not yet been applied to Apicomplexa-related motility studies but should definitively be introduced in the field.

Accordingly, these approaches proceed through distinct principles (see Figure 3) and are differentially suited for measuring forces on biological systems predominantly recorded in liquid medium. Thanks to the adjunction of other force spectroscopy approaches, the implementation of imaging modalities, and the help of nano-fluidics devices and micro-robotics, these instrumentations have greatly enlarged the versatility of these approaches opening new avenues to assess the tunable mechanical properties of cells and molecules, under various controllable external stimuli among which temperature, light, ionic strength but also under dynamic flows using microfluidic devices or upon different values of normoxia.

AFM-BASED COMBINATORIAL STRATEGIES TO CHARACTERIZE ADHESIVE PROPERTIES OF THE FREE ZOITE AND THE HOST CELL LOADED WITH ZOITE ALONG WITH CELL SURFACE MICROTOPOGRAPHY

Pioneered by Nobel Prize G. Binnig and H. Rohrer in 1986, AFM works through surface sensing on live samples thanks to an ultra-sharp (nanoscale) tip attached to a flexible micromachined silicon-based cantilever that acts as a spring. Therefore, AFM can provide true quantitative 3D native topography unlike the SEM and transmission electron microscopy (TEM) techniques which require pre-processed samples. Under the control of a piezoelectric ceramic scanner the AFM tip is positioned close enough to sense the interactive atomic forces with the sample surface, which induces bending of the cantilever. The bending amplitude is measured by recording the deflection of a laser beam reflected off the end of the cantilever using a photodetector device. A feed-back system allows to maintain near constant the interaction force. As the tip moves over a surface with

micro-heterogenous texture, the deflection profile provides the line-by-line atomic resolution 3D mapping of the surface microtopography. While in this case, the tip-sample interactive forces are retrieved from continuous contact of the probe onto the sample, other less or non-invasive regimes referred as to dynamic modes minimize or bypass the need for tip-sample contact over the entire scanning. In addition to better preserving both the AFM probe tip and the sample from friction-induced damages, and to avoid surface-contaminating debris to stick to the tip, the dynamic modes allow to probe soft samples or loosely attached ones. Consequently, these modes provide better force control and higher resolution images under biologically compatible conditions: the cantilever is vibrated near its resonance frequency using piezoelectric actuators to either promote intermittent close tip-sample surface contact (i.e., tapping mode) or to keep the tip several nanometers away from the sample (i.e., non-contact mode).

Besides providing topographic data, AFM can adjust to different regimes and scales of cell mechanics by accommodating different geometry and size of the sensor pieces: cantilevers can be shortened and tips can be modified in different ways to fit specific purposes. Moreover, major still going AFM developments have improved the AFM speed capacities with new settings to implement on the HS-AFM existing systems and that sustain even faster scanning/imaging speeds (up to 25–30 frames per second (Fukuda and Ando, 2021) while keeping disturbance of the biological function to almost zero. More specifically, the tip replacement by an electrode has opened ways for localized electrochemical experiments (scanning electrochemical microscopy [SECM]) while the tip functionalization with a specific molecule (i.e., lectin, biotin, streptavidin, antibodies, and any proteins and even lipids) has permitted to map local chemical interactions at the single molecule (SM) level (SM force spectroscopy [SMFS]). However, while AFM-based techniques can measure adhesion strength between individual cells and a given substrate, they can neither provide a kinetic view of the adhesion force over a time scale of hours, nor achieve the high throughput level for retrieving large samples.

A revolutionary step introduced by Meister et al., 2009 has been achieved by combining AFM with nanofluidics through the design of micro-channeled tips which allow applying reversible sucking pressure to a cell/particle. This setting bypasses the need of bio-molecular functionalization that potentially can affect the functional state of the object under study. In contrast, it is also possible to repeatedly deliver particles/compounds/parasite to the cell surface by gentle contact but also to the interior (including directly to the nucleus) by gentle membrane perforation and to then measure how the “functionalized or not” particles/cell/parasite behave (Meister et al., 2009). Indeed, how particles would move

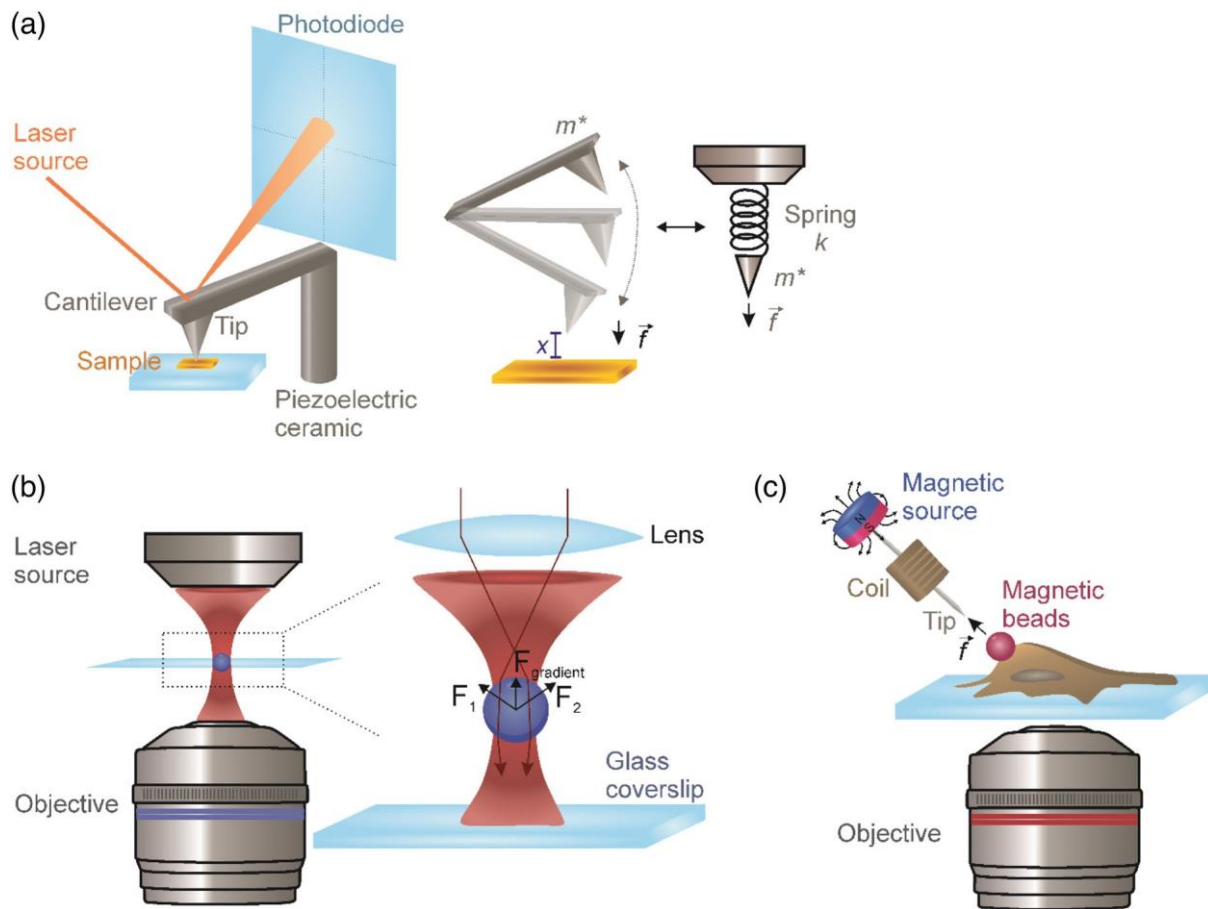


FIGURE 3 Schematic of the working principle of atomic force microscopy (AFM), optical tweezer (OT), and magnetic tweezer (MT). Main active approaches to measure the adhesive strength and mechanical properties across scales. The AFM cantilever tip scans the overall of the sample and probes the attractive or repulsive interaction field. The tip-sample distance can be calculated based on the deflection of a laser source on the cantilever. Knowing that the cantilever follows a spring-mass equation $x = f/k$, where interaction depth x is equal to the division of the force of the tip–surface interaction f and the cantilever spring constant k . The tip geometry and functionalization and the tapping/scanning mode of the cantilever confer attractive versatility to AFM. OT allows the trapping of a nanoscopic to microscopic object using a focused ion beam. The laser provides an attractive force to the bead, which sustains a force to be kept in the center of the laser (F_1 , F_2). This momentum change can be used to measure the reaction of an object to the interaction with the laser beam, or be used to move biocompatible functionalized molecules to probe adhesive interactions. MT relies on the attraction of a magnetic object which attached to the sample toward the source of the magnetic field.

inside the targeted compartment would support studies addressing viscoelastic properties of given cell compartments. The so-called fluid force microscopy (FluidFM) rapidly provides force–distance curves, and in turn direct force measurements between the objects and any substrate of interest including cell monolayers (Sancho et al., 2017). Since the probe is reusable, FluidFM is ideal for fast serial measurements following overpressure pulses to release undamaged objects, while being also quite efficient for quick nano-aspiration/deposition of a range of particles, thereby holding promise for improved throughput analyses (Anderson, 2019; Guillaume-Gentil et al., 2014).

AFM application to the Apicomplexa study was quasi simultaneously pioneered in Japan and the US in the early 2000s and was early on combined with surface potential spectroscopy to probe the electric charge

distribution at the surface of free *Plasmodium* spp. merozoites. Aikawa et al., 1996 reported a positive charge restricted to the parasite apical pole, the region that must closely contact the negatively charged erythrocyte surface when starting to penetrate into the cell, and further propose that electrostatic forces contribute to the ligand–receptor binding efficiency required for entry into erythrocytes. Of note, a similar scheme was extended to *T. gondii* tachyzoite-host cell invasion event (Akaki et al., 2002) but the characterization of these electrostatic forces still remains incomplete. A remarkable era of AFM-based studies in Apicomplexa emerged with the will to quantify the rheological changes of erythrocytes presenting knobs (Helms et al., 2016). The authors found these knobs to be selectively positively charged when compared to the knob-free red cell PM area and the endothelium surface. Therefore, the favored scenario

supports the contribution of local electrostatic attraction between the ZLE and the vascular endothelium to prepare for firm chemical bonds between knobs ligands and endothelial receptors that would withstand the physiological hemodynamic forces. The same rationale would support the aggregative properties between ZLE and erythrocytes, a process reported to involve interaction forces three to four times higher than between ZLE and endothelial cells (Cooke et al., 2002; Nash et al., 1992). AFM brought evidence for the elastic properties of knobs and outlined the key mechanical contribution of KAHRP protein (Rug et al., 2006). Besides, AFM was also used to explore the mechanical and adhesive surface properties of the understudied oocyst stage of *T. gondii* and *Cryptosporidium* spp. which are found in soil and water supplies, where they represent major long-term transmissible threats. Indeed, the *T. gondii* and *Cryptosporidium* oocysts enclose a few sporozoites in a bi-layered and tri-layered wall, respectively. The oocyst walls provide resistance to harsh environmental conditions but also to physical or chemical disinfection procedures, a serious concern in the perspective of transmission control strategies against these parasites. In addition to quantifying stiffness of *T. gondii* oocysts treated or not to selectively remove the outer wall layer, AFM scanning also enabled to probe the non-specific adhesive properties of each layer. While they showed fairly similar high stiffness (i.e., they mechanically resist to forces up to 120 nN), the layers significantly differ in terms of adhesion strengths with much lower values characterizing the outer layer (~100 pN). Collectively, the highly negative charge and low adhesive properties of the oocyst surface likely facilitate their dispersion in the microenvironment (Dumètre et al., 2013). How much this type of analysis could be extended to high throughput quality control procedures for water supplies is still under examination. With this concern, it is worth mentioning the significant gain in accuracy obtained using the FluidFM AFM to measure oocyst-surface forces, thereby allowing not only to better characterize the elastic deformable properties of *Cryptosporidium* oocyst but also to discriminate one species from the other (*C. parvum* vs. *C. muris*), thereby potentially offering a strategy for rapid microbe identification in the course of sanitation procedures (McGrath et al., 2016).

OPTICAL TWEEZER COMBINATORIAL STRATEGIES TO PROBE CELL–CELL OR MOLECULE–MOLECULE ADHESIVE MECHANISMS ALONG WITH CELL SURFACE MICROTOPOGRAPHY

Aside from AFM, a powerful noninvasive way of measuring force was invented in 1986 by Nobel Prize A.

Ashkin (2018, Physics), and refers to OTs. OTs allow to hold (i.e., trap), move and apply calibrated forces including torques to microscopic refractive objects with sizes ranging from micrometers to nanometers (i.e., protein and DNA molecules) and even subnanometer (i.e., atom) in the so-called an optical trap (Ashkin, 1997), and have now been largely introduced to biological systems. The optical trap proceeds through a continuous beam of light—most usually with infrared laser to reduce optical damages—that is forced to focus down to the smallest focal point possible prior to spreading out using a high-numerical aperture objective. When a laser beam passes through a micro-sized particle, it concomitantly exerts on the latter the gradient force and the scattering counteracting force, so the particle can somehow levitate when at the focal center. The gradient force tends to attract the object toward the focus point, whereas the scattering force directs the object toward the light propagation (Figure 3b). It is the measure of object displacement, from the focal region, that provides accurate quantification of the external force applied on the former. Although a tedious trap calibration must be performed prior to each force measurement by determining the force versus displacement for given values of laser light intensities, particle sizes and shapes and refraction index relative to medium, OTs are ideally suited for calculating interaction and adhesion forces in the pN ranges that typify micrometer-sized living organisms. Following the same logic than for the AFM tips, microbeads can be functionalized with a variety of molecular ligands (e.g., fibronectin, RGD peptide, and antibodies) in a quantitative controlled way while the OTs multi-trap mode offers to trap simultaneously several beads for instances on a cell and thereby enabling the force measurement at distinct locations in one individual cell. A significant advantage over AFM is that the trapping force can be changed instantaneously by adjusting the laser beam intensity. Another advantage of OT over classical AFM is the possibility to analyze a larger number of cells/parasites, enhancing statistical analysis and in mimicking physiological conditions. However, as previously mentioned, recent adjunction of modules in AFM with for instances FluidFM have started to overcome this sample size limitation and might be adjusted in the future for temperature or other parameter control to recapitulate physiological conditions. On the other hand, for biological samples the well-known OTs limitations include the size of the biological structures or biomolecules which can be stably trapped (due to the limitation of the lens to focus the trapping beam) and the photothermal (i.e., overheating effect) as well as photochemical (i.e., production of reactive oxygen species) damages (Blázquez-Castro, 2019) which can impact on the mechanical responses of living cells to the applied forces. To solve these issues, a variety of instruments derived from OTs and often coupled

with other methods have been created. Among these, the plasmonic nano-tweezers create strong forces that can trap nanoscale particles and integrate a “heat sink” in the device (Zhang et al., 2021) or the holographic optical stretchers (OSs) (Guck et al., 2001) well suited to study elastic properties of a rather large sample of cells under ECM or vascular flow mechanical constraints, using microfluidic automated flow chambers microfabricated with soft-lithography that guide the cells through the detector (Yang et al., 2016). However, OTs have been mostly used to probe objects in suspension so far and must be adapted if one wants to monitor zoite gliding motility mode. Finally, a major advance in terms of versatile manipulation of nanoscale size objects was accomplished with the optical fiber tweezers (OFTs) for which the fiber(s) can be inserted into thick samples and turbid media (for a review see Zhao et al., 2020).

A great deal of information on the forces exerted by the power engines of motile zoites has already been obtained with the first challenging OTs applications in the 2010s. OTs has allowed to probe adhesion formation and to measure cortical forces from free *Plasmodium* or *T. gondii* zoites under slightly different contexts. A pioneering study was carried on hemolymph-derived *P. berghei* wild type sporozoites or genetically deficient for either of two adhesins from the thrombospondin-related anonymous protein (TRAP) known to contribute to substrate-cell adhesion (i.e., from TRAP and S6) (Hegge et al., 2012). The authors were able to trap zoites in the beam when they formed a first polar contact with the substrate and to force them to build a second adhesion site at the other pole, a situation typically followed by the formation of a tertiary median contact site and gliding per se. Quantitative force measurements unveiled differences in the adhesion capacity between wild type sporozoites and each adhesin mutants, and between the TRAP and S6 mutants thereby establishing (i) the selective contribution of both adhesins to distinct contacts and to capture newly assembled actin filaments (ii) the primary adhesion as the site of highest strength (≈ 25 pN). Next, the introduction of microbeads trapped by OTs in conjunction with very fast live imaging has provided unprecedented opportunities to measure the rate of membrane rearward flow in the case of gliding *P. berghei* sporozoites, hence directly testing whether the retrograde flow directly translates to productive force (see below). Secondly, OTs assays also brought values ranging from ~ 70 to 190 pN for the adhesion forces exerted by the parasite on nonspecific ligands such as naked or streptavidin-coated polystyrene ~ 1.5 – $2 \mu\text{m}$ microbeads (i.e., negatively charged or near neutral particles at physiological pH, respectively). When comparing wild type sporozoites with mutants engineered to lack a TRAP-related adhesin, the authors observed that

the beads translocated faster for the mutants whereas the force produced to pull the microsphere out of the trap was significantly weaker. Those findings definitively argue for a more complex interplay between membrane flow and productive force than the model predicts. Since then, dual beam OT was also used in in vitro reconstitution assay to probe the ability of *P. falciparum* MyoA to bind a filament of actin held between two neutravidin-coated beads, hence providing first chemophysical characterization of the actomyosin power stroke cycle in Apicomplexa zoites (Green et al., 2017). More recently, OTs independent force microscopy analyses performed with the noninvasive “passive” traction force microscopy (TFM) on motile *T. gondii* tachyzoites in both 2D and 3D conditions unveiled peculiar sites of adhesion at the zoite apical pole. These adhesion platforms were shown to account for force production and motion directionality, yet it remains to ascertain the adhesion strength of these focal adhesion platforms relative to other adhesion sites and to qualitatively and quantitatively identify their molecular components (Pavlou et al., 2020; Stadler et al., 2022). OTs applied to *T. gondii* tachyzoites allowed to retrieve cortical forces but also to document new mechanistic features underlying bead posterior capping. The authors monitored the displacement of serum coated microbeads held in contact with the zoite surface by the trap upon release from it (i.e., laser trap off) (Stadler et al., 2017). When released from the trap, the beads underwent transient random motion that was interpreted as the time required for full functionality of the motile machinery prior to position roughly perpendicular to the cell main axis and to be transported by a functional actomyosin motor in a typical antero-posterior direction. Interestingly, the cortical forces were found identical all along the parasite surface until the beads hit the substrate, most often ahead from the zoite basal pole, at a location matching the distal end of the microtubule cytoskeleton. This scheme supports an active guidance of the beads by the cortical helical microtubules, a mechanism which is consistent with the microtubule-based spring contribution proposed to direct helical propelling (Pavlou et al., 2020). For technical reasons, OTs pioneering assays were performed with microbeads positioned on immobilized tachyzoites adherent to a poly-lysine-coated surface and were incubated at room temperature, a suboptimal setting to model in vivo conditions. Of note, OTs were also used to assess the knob-driven adhesive properties and the reduced deformability of infected erythrocytes, highlighting the correlation between loss of cell deformability and impaired release of ATP (Paul et al., 2019), although AFM has been preferred so far (for a more complete list of techniques applied to the study of rheological changes of *Plasmodium* infected erythrocytes, see Depond et al., 2019).

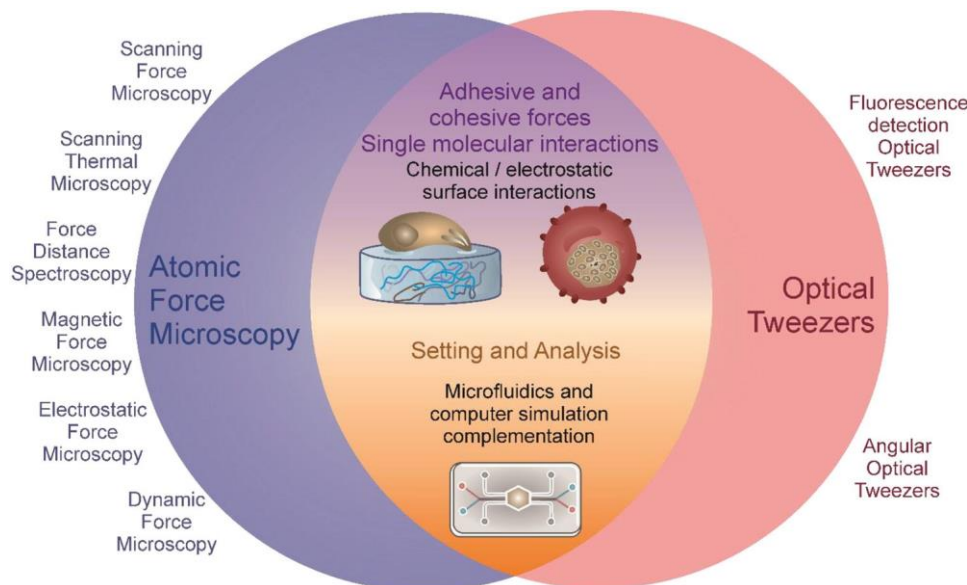


FIGURE 4 Derived techniques from atomic force microscopy (AFM) and optical tweezers (OTs) and future perspectives of their complementation. Since it was first introduced, AFM is in the center of several technical developments, with a special focus on the possibility of adding force spectroscopy measurements (i.e., scanning force microscopy and force distance spectroscopy) to complete the mapping of living samples. In the case of OTs, their derived techniques (i.e., fluorescence detection optical tweezers and angular optical tweezers) mostly involve the use of single-molecule fluorescence spectroscopy allow the further retrieve of biophysical properties such as a molecule twist and torque. AFM and OTs share the common quality of performing in noninvasive manner, facilitating their implementation in a wide range of biological systems, covering from SM analysis to individual cells and tissues. Combining the information of the adhesive properties provided by OTs and the chemical surface interactions by AFM could illuminate, for example, the zotes' capabilities for extracellular navigation through ECM. Moreover, missing information; at the SM level (i.e., the cyto-adhesiveness of human erythrocytes that host the *P. falciparum* merozoites progeny and adhere endothelial cells of micro vessels) could be provided. The integration of microfluidics, robotics and sensor-like chips to the AFM-OTs mix setting should allow recapitulating relevant physiological/ physiopathological environments and thus support high throughput analysis. Finally, the era of computer simulation and machine learning has only started and will greatly assist single molecule to whole cell and tissues analysis, thereby overcoming the low throughput of OTs and AFM limitation.

BUILDING ON AN ENLARGING BIOPHYSICAL TOOLSET TO PROBE ADHESION STRENGTH AND FORCE IN LIVING CELLS AND LIVING ORGANISMS ACROSS SCALES

It is clear that characterizing adhesive forces has become a major challenge for researchers interested in retrieving the biophysical and biomechanical features of the motile zoite morphotypes across nano- to macroscales. How Apicomplexa zoites establish multifaceted parasitism in their host repertoire, whether they move as individuals or collectives or whether they modify, as intracellular cargoes the cell-cell biomechanical behaviors of their hosting “feeding and protective” cells. Although not broadly used yet to study the biology of parasitism, several force microscopy-based approaches have already brought unprecedented opportunities to revisit and document major molecular to cellular mechanistic features underlying critical stages of the zoite's journeys in their hosts as illustrated in this review. The acceleration of technical changes on these versatile instruments which can work synergistically, and support multimodal integration from advanced imag-

ing, nanofabrication and nanotechnology represents a major asset in particular with regard to spatiotemporal resolution of force measurements, assay flexibility, and reproducibility (Figure 4). For example, ongoing developments have allowed combining the surface force measurement and imaging capabilities of AFM with the ability of OTs to apply and measure smallest forces (<500 fN) in 2 and 3D settings. These improvements open a new spectrum of studies in particular related to cell–cell or cell–matrix local interaction. In addition, the adjunction of simultaneous, automated, and artificial intelligence-inspired multi-trap systems hold promise for effective high throughput strategies. In the same line, this biophysical quantitative toolset fits with a larger set of questions spanning from molecular, structural to pharmacological interests by solving the dynamics and strength of biomolecule–biomolecule, biomolecule–inorganic molecule, or molecule–nucleic acid interactions, major asset for therapeutic discoveries. Remarkably, to overcome the challenging applicability of force-measurement approaches in vivo, single-beam acoustic tweezers (SBATs) that rely on the harmless ultrasounds and are driven by a voltage signal generator have been designed: they enable probing forces in deep

intact tissues without inducing damages. Once miniaturized, SBATs have been used to probe human breast cancer cells' mechanical features applying forces up to 200 pN, a value which exceeds by one order of magnitude the maximal forces applied with OTs, and this with one order of magnitude less wave power. Last but not least, the SBATs offer 3D trapping abilities of great value for analyzing in the future parasite mechanical properties in the *in vivo* context (Baudoin et al., 2020). As a common feature for most techniques mentioned in this review which all measure rheological properties, the first application of acoustic tweezers has aimed at trapping the highly deformable erythrocytes with ultrasounds in a microfluidic device that allows mimicking arterioles' or venules' physiological flow speeds (Liu et al., 2017).

In conclusion, the huge phylogenetic complexity of the prevalent Apicomplexa phylum provides true opportunity to witness the many subtleties of permanently ongoing co-adaptive processes between parasitic microbes and their host range. Therefore, one can only advocate for diversifying the biological model systems and experimental contexts to study biology of parasitism within a more biomechanical concern, in order to better recapitulate physiological and pathophysiological conditions. Expertise and techniques continuously evolve forenabling applications on living objects across scales of study, including in combination with omics analysis as a promise to provide "global responses and variations" under controlled mechanical stimuli.

ACKNOWLEDGMENTS

The authors thank Dr. G. Milon (Emeritus professor, Institut Pasteur, Paris, France) for fruitful discussion and comments on the manuscript.

CONFLICT OF INTEREST STATEMENT


Authors declare no competing interests.

DATA AVAILABILITY STATEMENT

Data sharing is not applicable to this article as no new data were created or analyzed in this study.

ORCID

Luis Vigetti  <https://orcid.org/0000-0001-9733-2770>

Isabelle Tardieux  <https://orcid.org/0000-0002-5677-7463>

REFERENCES

- Aikawa, M., Kamanura, K., Shiraishi, S., Matsumoto, Y., Arwati, H., Torii, M. et al. (1996). Membrane knobs of unfixed *Plasmodium falciparum* infected erythrocytes: new findings as revealed by atomic force microscopy and surface potential spectroscopy. *Experimental Parasitology*, 84, 339–343. Available from: <https://doi.org/10.1006/expr.1996.0122>
- Akaki, M., Nagayasu, E., Nakano, Y. & Aikawa, M. (2002). Surface charge of *Plasmodium falciparum* merozoites as revealed by atomic force microscopy with surface potential spectroscopy. *Parasitology Research*, 88, 16–20. Available from: <https://doi.org/10.1007/s004360100485>
- Amino, R., Thiberge, S., Martin, B., Celli, S., Shorte, S., Frischknecht, F. et al. (2006). Quantitative imaging of *Plasmodium* transmission from mosquito to mammal. *Nature Medicine*, 12, 220–224. Available from: <https://doi.org/10.1038/nm1350>
- Amos, B., Aurrecochea, C., Barba, M., Barreto, A., Basenko, E.Y., Bazant, W. et al. (2022). VEuPathDB: the eukaryotic pathogen, vector and host bioinformatics resource center. *Nucleic Acids Research*, 50, D898–D911. Available from: <https://doi.org/10.1093/nar/gkab929>
- Andenmatten, N., Egarter, S., Jackson, A.J., Jullien, N., Herman, J.-P. & Meissner, M. (2013). Conditional genome engineering in *Toxoplasma gondii* uncovers alternative invasion mechanisms. *Nature Methods*, 10, 125–127. Available from: <https://doi.org/10.1038/nmeth.2301>
- Anderson, M.S. (2019). The detection of long-chain bio-markers using atomic force microscopy. *Applied Sciences*, 9, 1280. Available from: <https://doi.org/10.3390/app9071280>
- Anderson-White, B., Beck, J.R., Chen, C.-T., Meissner, M., Bradley, P.J. & Gubbels, M.-J. (2012). Cytoskeleton assembly in *Toxoplasma gondii* cell division. *International review of cell and molecular biology*. 298, 1–31. Available from: <https://doi.org/10.1016/B978-0-12-394309-5.00001-8>
- Ashkin, A. (1997). Optical trapping and manipulation of neutral particles using lasers | PNAS. Available from: <https://www.pnas.org/doi/10.1073/pnas.94.10.4853> [Accessed 15th February 2023].
- Aurrecochea, C., Barreto, A., Basenko, E.Y., Brestelli, J., Brunk, B.P., Cade, S. et al. (2017). EuPathDB: the eukaryotic pathogen genomics database resource. *Nucleic Acids Research*, 45, D581–D591. Available from: <https://doi.org/10.1093/nar/gkw1105>
- Ayoade, F. & Chandranesan, A.S.J. (2023). HIV-1 associated toxoplasmosis. In: *StatPearls*. Treasure Island (FL): StatPearls Publishing. Available from: <http://www.ncbi.nlm.nih.gov/books/NBK441877/> [Accessed 10th May 2023].
- Baer, K., Klotz, C., Kappe, S.H.I., Schnieder, T. & Frevort, U. (2007). Release of hepatic *Plasmodium yoelii* merozoites into the pulmonary microvasculature. *PLoS Pathogens*, 3, e171. Available from: <https://doi.org/10.1371/journal.ppat.0030171>
- Barylyuk, K., Koreny, L., Ke, H., Butterworth, S., Crook, O.M., Lassadi, I. et al. (2020). A comprehensive subcellular atlas of the *Toxoplasma* proteome via hyperLOPIT provides spatial context for protein functions. *Cell Host & Microbe*, 28, 752–766.e9. Available from: <https://doi.org/10.1016/j.chom.2020.09.011>
- Baudoin, M., Thomas, J.-L., Sahely, R.A., Gerbedoen, J.-C., Gong, Z., Sivery, A. et al. (2020). Spatially selective manipulation of cells with single-beam acoustical tweezers. *Nature Communications*, 11, 4244. Available from: <https://doi.org/10.1038/s41467-020-18000-y>
- Baum, J., Richard, D., Healer, J., Rug, M., Krnjanski, Z., Gilberger, T.-W. et al. (2006). A conserved molecular motor drives cell invasion and gliding motility across malaria life cycle stages and other apicomplexan parasites. *Journal of Biological Chemistry*, 281, 5197–5208. Available from: <https://doi.org/10.1074/jbc.M509807200>
- Blader, I., Coleman, B., Chen, C.-T. & Gubbels, M.-J. (2015). The lytic cycle of *Toxoplasma gondii*: 15 years later. *Annual Review of Microbiology*, 69, 463–485. Available from: <https://doi.org/10.1146/annurev-micro-091014-104100>
- Blázquez-Castro, A. (2019). Optical tweezers: phototoxicity and thermal stress in cells and biomolecules. *Micromachines*, 10, 507. Available from: <https://doi.org/10.3390/mi10080507>
- Boucher, L.E. & Bosch, J. (2015). The apicomplexan glideosome and adhesins – structures and function. *Journal of Structural Biology*, 190, 93–114. Available from: <https://doi.org/10.1016/j.jsb.2015.02.008>

- Bullen, H.E., Tonkin, C.J., O'Donnell, R.A., Tham, W.-H., Papenfuss, A.T., Gould, S. et al. (2009). A novel family of Apicomplexan glideosome-associated proteins with an inner membrane-anchoring role. *Journal of Biological Chemistry*, 284, 25353–25363. Available from: <https://doi.org/10.1074/jbc.M109.036772>
- Burda, P.-C., Caldelari, R. & Heussler, V.T. (2017). Manipulation of the host cell membrane during Plasmodium liver stage egress. *mBio*, 8, e00139-17. Available from: <https://doi.org/10.1128/mBio.00139-17>
- Cooke, B.M., Glenister, F.K., Mohandas, N. & Coppel, R.L. (2002). Assignment of functional roles to parasite proteins in malaria-infected red blood cells by competitive flow-based adhesion assay. *British Journal of Haematology*, 117, 203–211. Available from: <https://doi.org/10.1046/j.1365-2141.2002.03404.x>
- Courret, N., Darche, S., Sonigo, P., Milon, G., Buzoni-Gâtél, D. & Tardieux, I. (2006). CD11c- and CD11b-expressing mouse leukocytes transport single Toxoplasma gondii tachyzoites to the brain. *Blood*, 107, 309–316. Available from: <https://doi.org/10.1182/blood-2005-02-0666>
- Crabb, B.S., Cooke, B.M., Reeder, J.C., Waller, R.F., Caruana, S.R., Davern, K.M. et al. (1997). Targeted gene disruption shows that knobs enable malaria-infected red cells to cytoadhere under physiological shear stress. *Cell*, 89, 287–296. Available from: [https://doi.org/10.1016/s0092-8674\(00\)80207-x](https://doi.org/10.1016/s0092-8674(00)80207-x)
- De Niz, M., Burda, P.-C., Kaiser, G., Del Portillo, H. A., Spielmann, T., Frischknecht, F., et al. (2017). Progress in imaging methods: insights gained into Plasmodium biology. *Nature Reviews Microbiology*, 15, 37–54. Available from: <https://doi.org/10.1038/nrmicro.2016.158>
- Depond, M., Henry, B., Buffet, P. & Ndour, P.A. (2019). Methods to Investigate the deformability of RBC during malaria. *Frontiers in Physiology*, 10, 1613. Available from: <https://doi.org/10.3389/fphys.2019.01613>
- Douglas, R.G., Amino, R., Sinnis, P. & Frischknecht, F. (2015). Active migration and passive transport of malaria parasites. *Trends in Parasitology*, 31, 357–362. Available from: <https://doi.org/10.1016/j.pt.2015.04.010>
- Dubey, J.P., Lindsay, D.S. & Speer, C.A. (1998). Structures of Toxoplasma gondii tachyzoites, bradyzoites, and sporozoites and biology and development of tissue cysts. *Clinical Microbiology Reviews*, 11, 267–299.
- Dumètre, A., Dubey, J.P., Ferguson, D.J.P., Bongrand, P., Azas, N. & Puech, P.-H. (2013). Mechanics of the Toxoplasma gondii oocyst wall. *Proceedings of the National Academy of Sciences of the United States of America*, 110, 11535–11540. Available from: <https://doi.org/10.1073/pnas.1308425110>
- Ejigiri, I. & Sinnis, P. (2009). Plasmodium sporozoite-host interactions from the dermis to the hepatocyte. *Current Opinion in Microbiology*, 12, 401–407. Available from: <https://doi.org/10.1016/j.mib.2009.06.006>
- European Centre for Disease Report. (2019). European Centre for Disease Report, 2019. Available from: <https://www.ecdc.europa.eu/en/publications-data/congenital-toxoplasmosis-annual-epidemiological-report-2019> [Accessed 10th May 2023].
- Farfour, E., Charlotte, F., Settegrana, C., Miyara, M. & Buffet, P. (2012). The extravascular compartment of the bone marrow: a niche for Plasmodium falciparum gametocyte maturation? *Malaria Journal*, 11, 285. Available from: <https://doi.org/10.1186/1475-2875-11-285>
- Frénal, K., Jacot, D., Hammoudi, P.-M., Graindorge, A., Maco, B. & Soldati-Favre, D. (2017). Myosin-dependent cell-cell communication controls synchronicity of division in acute and chronic stages of Toxoplasma gondii. *Nature Communications*, 8, 1–18. Available from: <https://doi.org/10.1038/ncomms15710>
- Frénal, K., Krishnan, A. & Soldati-Favre, D. (2020). The actomyosin systems in Apicomplexa. *Advances in Experimental Medicine and Biology*, 1239, 331–354. Available from: https://doi.org/10.1007/978-3-030-38062-5_14
- Frénal, K., Polonais, V., Marq, J.-B., Stratmann, R., Limenitakis, J. & Soldati-Favre, D. (2010). Functional dissection of the apicomplexan glideosome molecular architecture. *Cell Host & Microbe*, 8, 343–357. Available from: <https://doi.org/10.1016/j.chom.2010.09.002>
- Freyvogel, T.A. (1966). Shape, movement in situ and locomotion of plasmodial ookinetes. *Acta Tropica*, 23, 201–222.
- Fukuda, S. & Ando, T. (2021). Faster high-speed atomic force microscopy for imaging of biomolecular processes. *Review of Scientific Instruments*, 92, 033705. Available from: <https://doi.org/10.1063/5.0032948>
- Gaskins, E., Gilk, S., DeVore, N., Mann, T., Ward, G. & Beckers, C. (2004). Identification of the membrane receptor of a class XIV myosin in Toxoplasma gondii. *Journal of Cell Biology*, 165, 383–393. Available from: <https://doi.org/10.1083/jcb.200311137>
- Green, J.L., Wall, R.J., Vahokoski, J., Yusuf, N.A., Ridzuan, M.A.M., Stanway, R.R. et al. (2017). Compositional and expression analyses of the glideosome during the Plasmodium life cycle reveal an additional myosin light chain required for maximum motility. *Journal of Biological Chemistry*, 292, 17857–17875. Available from: <https://doi.org/10.1074/jbc.M117.802769>
- Gubbels, M.-J., Wieffer, M. & Striepen, B. (2004). Fluorescent protein tagging in Toxoplasma gondii: identification of a novel inner membrane complex component conserved among Apicomplexa. *Molecular and Biochemical Parasitology*, 137, 99–110. Available from: <https://doi.org/10.1016/j.molbiopara.2004.05.007>
- Guck, J., Ananthakrishnan, R., Mahmood, H., Moon, T.J., Cunningham, C.C. & Käs, J. (2001). The optical stretcher: a novel laser tool to micromanipulate cells. *Biophysical Journal*, 81, 767–784.
- Guillaume-Gentil, O., Potthoff, E., Ossola, D., Franz, C.M., Zambelli, T. & Vorholt, J.A. (2014). Force-controlled manipulation of single cells: from AFM to FluidFM. *Trends in Biotechnology*, 32, 381–388. Available from: <https://doi.org/10.1016/j.tibtech.2014.04.008>
- Håkansson, S., Morisaki, H., Heuser, J. & Sibley, L. D. (1999). Time-lapse video microscopy of gliding motility in toxoplasma gondii reveals a novel, biphasic mechanism of cell locomotion. *Molecular Biology of the Cell*, 10, 9.
- Harding, C.R. & Frischknecht, F. (2020). The riveting cellular structures of apicomplexan parasites. *Trends in Parasitology*, 36, 979–991. Available from: <https://doi.org/10.1016/j.pt.2020.09.001>
- Heaslip, A.T., Nishi, M., Stein, B. & Hu, K. (2011). The motility of a human parasite, Toxoplasma gondii, is regulated by a novel lysine methyltransferase. *PLoS Pathogens*, 7, e1002201. Available from: <https://doi.org/10.1371/journal.ppat.1002201>
- Hegge, S., Uhrig, K., Streichfuss, M., Kynast-Wolf, G., Matuschewski, K., Spatz, J.P. et al. (2012). Direct manipulation of malaria parasites with optical tweezers reveals distinct functions of plasmodium surface proteins. *ACS Nano*, 6, 4648–4662. Available from: <https://doi.org/10.1021/nn203616u>
- Heintzelman, M.B. (2015). Gliding motility in apicomplexan parasites. *Seminars in Cell & Developmental Biology*, 46, 135–142. Available from: <https://doi.org/10.1016/j.semcd.2015.09.020>
- Helms, G., Dasanna, A.K., Schwarz, U.S. & Lanzer, M. (2016). Modeling cytoadhesion of Plasmodium falciparum-infected erythrocytes and leukocytes—common principles and distinctive features. *FEBS Letters*, 590, 1955–1971. Available from: <https://doi.org/10.1002/1873-3468.12142>
- Hosseini, S.M. & Feng, J.J. (2011). Pressure boundary conditions for computing incompressible flows with SPH. *Journal of Computational Physics*, 230, 7473–7487. Available from: <https://doi.org/10.1016/j.jcp.2011.06.013>
- Hung, Y.-F., Chen, Q., Pires, I., Rosenthal, P.B. & Kursula, I. (2022). Structure of Toxoplasma gondii glideosome-associated connector suggests a role as an elastic element in actomyosin force generation for gliding motility. *bioRxiv*, 2022, 12.09519741. Available from: <https://doi.org/10.1101/2022.12.09.519741>
- Jacot, D., Tosetti, N., Pires, I., Stock, J., Graindorge, A., Hung, Y.-F. et al. (2016). An Apicomplexan actin-binding protein serves as a connector and lipid sensor to coordinate motility and invasion. *Cell Host*

- & *Microbe*, 20, 731–743. Available from: <https://doi.org/10.1016/j.chom.2016.10.020>
- Jensen, A.R., Adams, Y. & Hviid, L. (2020). Cerebral Plasmodium falciparum malaria: the role of PfEMP1 in its pathogenesis and immunity, and PfEMP1-based vaccines to prevent it. *Immunological Reviews*, 293, 230–252. Available from: <https://doi.org/10.1111/imr.12807>
- Kim, K. & Weiss, L.M. (2004). Toxoplasma gondii: the model apicomplexan. *International Journal for Parasitology*, 34, 423–432. Available from: <https://doi.org/10.1016/j.ijpara.2003.12.009>
- Kirkman, L.A. & Deitsch, K.W. (2020). Vive la différence: exploiting the differences between rodent and human malaras. *Trends in Parasitology*, 36, 504–511. Available from: <https://doi.org/10.1016/j.pt.2020.03.008>
- Leung, J.M., Rould, M.A., Konradt, C., Hunter, C.A. & Ward, G.E. (2014a). Disruption of TgPHIL1 alters specific parameters of toxoplasma gondii motility measured in a quantitative, three-dimensional live motility assay. *PLoS ONE*, 9, e85763. Available from: <https://doi.org/10.1371/journal.pone.0085763>
- Leung, J.M., Tran, F., Pathak, R.B., Poupard, S., Heaslip, A.T., Ballif, B.A. et al. (2014b). Identification of T. gondii myosin light chain-1 as a direct target of TachypleglinA-2, a small-molecule inhibitor of parasite motility and invasion. *PLoS ONE*, 9, e98056. Available from: <https://doi.org/10.1371/journal.pone.0098056>
- Liu, H.-C., Li, Y., Chen, R., Jung, H. & Shung, K.K. (2017). Single-beam acoustic trapping of red blood cells and polystyrene microspheres in flowing red blood cell saline and plasma suspensions. *Ultrasound in Medicine & Biology*, 43, 852–859. Available from: <https://doi.org/10.1016/j.ultrasmedbio.2016.12.005>
- Looker, O., Blanch, A.J., Liu, B., Nunez-Iglesias, J., McMillan, P.J., Tilley, L. et al. (2019). The knob protein KAHRP assembles into a ring-shaped structure that underpins virulence complex assembly. *PLoS Pathogens*, 15, e1007761. Available from: <https://doi.org/10.1371/journal.ppat.1007761>
- McGrath, J.S., Quist, J., Seddon, J.R.T., Lai, S. C.S., Lemay, S.G. & Bridle, H.L. (2016). Deformability assessment of waterborne protozoa using a microfluidic-enabled force microscopy probe. *PLoS ONE*, 11, e0150438. Available from: <https://doi.org/10.1371/journal.pone.0150438>
- Meister, A., Gabi, M., Behr, P., Studer, P., Vörös, J., Niedermann, P. et al. (2009). FluidFM: combining atomic force microscopy and nanofluidics in a universal liquid delivery system for single cell applications and beyond. *Nano Letters*, 9, 2501–2507. Available from: <https://doi.org/10.1021/nl901384x>
- Messina, V., Valtieri, M., Rubio, M., Falchi, M., Mancini, F., Mayor, A. et al. (2018). Gametocytes of the malaria parasite plasmodium falciparum interact with and stimulate bone marrow mesenchymal cells to secrete angiogenic factors. *Frontiers in Cellular and Infection Microbiology*, 8. Available from: <https://www.frontiersin.org/articles/10.3389/fcimb.2018.00050> [Accessed 15th February 2023].
- Moussaoui, D., Robblee, J.P., Auguin, D., Kremntsova, E.B., Haase, S., Blake, T.C. et al. (2020). Full-length Plasmodium falciparum myosin A and essential light chain PfELC structures provide new anti-malarial targets. *eLife*, 9, e60581. Available from: <https://doi.org/10.7554/eLife.60581>
- Nash, G.B., Cooke, B.M., Marsh, K., Berendt, A., Newbold, C. & Stuart, J. (1992). Rheological analysis of the adhesive interactions of red blood cells parasitized by Plasmodium falciparum. *Blood*, 79, 798–807.
- Nash, G.B., O'Brien, E., Gordon-Smith, E.C. & Dormandy, J.A. (1989). Abnormalities in the mechanical properties of red blood cells caused by Plasmodium falciparum. *Blood*, 74, 855–861.
- Neuman, K.C. & Nagy, A. (2008). Single-molecule force spectroscopy: optical tweezers, magnetic tweezers and atomic force microscopy. *Nature Methods*, 5, 491–505. Available from: <https://doi.org/10.1038/nmeth.1218>
- Neveu, G. & Lavazec, C. (2019). Erythrocyte membrane makeover by Plasmodium falciparum gametocytes. *Frontiers in Microbiology*, 10, 2652. Available from: <https://doi.org/10.3389/fmicb.2019.02652>
- Opitz, C. & Soldati, D. (2002). “The glideosome”: a dynamic complex powering gliding motion and host cell invasion by Toxoplasma gondii. *Molecular Microbiology*, 45, 597–604. Available from: <https://doi.org/10.1046/j.1365-2958.2002.03056.x>
- Patra, P., Beyer, K., Jaiswal, A., Battista, A., Rohr, K., Frischknecht, F. et al. (2022). Collective migration reveals mechanical flexibility of malaria parasites. *Nature Physics*, 18, 586–594. Available from: <https://doi.org/10.1038/s41567-022-01583-2>
- Paul, A., Ramdani, G., Tatu, U., Langsley, G. & Natarajan, V. (2019). Studying the rigidity of red blood cells induced by Plasmodium falciparum infection. *Scientific Reports*, 9, 6336. Available from: <https://doi.org/10.1038/s41598-019-42721-w>
- Pavlou, G., Touquet, B., Vigetti, L., Renesto, P., Bougdour, A., Debarre, D., et al. (2020). Coupling polar adhesion with traction, spring and torque forces allows high speed helical migration of the protozoan parasite toxoplasma. *ACS Nano*, 14, 7121–7139. Available from: <https://doi.org/10.1021/acsnano.0c01893>
- Pazicky, S., Dhamotharan, K., Kaszuba, K., Mertens, H.D.T., Gilberger, T., Svergun, D. et al. (2020). Structural role of essential light chains in the apicomplexan glideosome. *Communications Biology*, 3, 1–14. Available from: <https://doi.org/10.1038/s42003-020-01283-8>
- Powell, C.J., Jenkins, M.L., Parker, M.L., Ramaswamy, R., Kelsen, A., Warsaw, D.M. et al. (2017a). Dissecting the molecular assembly of the Toxoplasma gondii MyoA motility complex. *Journal of Biological Chemistry*, 292, 19469–19477. Available from: <https://doi.org/10.1074/jbc.M117.809632>
- Powell, C.J., Jenkins, M.L., Parker, M.L., Ramaswamy, R., Kelsen, A., Warsaw, D.M. et al. (2017b). Dissecting the molecular assembly of the Toxoplasma gondii MyoA motility complex. *Journal of Biological Chemistry*, 292, 19469–19477. Available from: <https://doi.org/10.1074/jbc.M117.809632>
- Quadt, K.A., Barfod, L., Andersen, D., Bruun, J., Gyan, B., Hassenkam, T. et al. (2012). The density of knobs on plasmodium falciparum-infected erythrocytes depends on developmental age and varies among isolates. *PLoS ONE*, 7, e45658. Available from: <https://doi.org/10.1371/journal.pone.0045658>
- Quadt, K.A., Streichfuss, M., Moreau, C.A., Spatz, J. P. & Frischknecht, F. (2016). Coupling of retrograde flow to force production during malaria parasite migration. *ACS Nano*, 10, 2091–2102. Available from: <https://doi.org/10.1021/acsnano.5b06417>
- Ripp, J., Smyrnakou, X., Neuhoff, M.-T., Hentzschel, F. & Frischknecht, F. (2022). Phosphorylation of myosin A regulates gliding motility and is essential for Plasmodium transmission. *EMBO Reports*, 23, e54857. Available from: <https://doi.org/10.15252/embr.202254857>
- Risco-Castillo, V., Topçu, S., Marinach, C., Manzoni, G., Bigorgne, A.E., Briquet, S. et al. (2015). Malaria sporozoites traverse host cells within transient vacuoles. *Cell Host & Microbe*, 18, 593–603. Available from: <https://doi.org/10.1016/j.chom.2015.10.006>
- Robert-Paganin, J., Robblee, J.P., Auguin, D., Blake, T.C.A., Bookwalter, C.S., Kremntsova, E.B. et al. (2019). Plasmodium myosin A drives parasite invasion by an atypical force generating mechanism. *Nature Communications*, 10, 3286. Available from: <https://doi.org/10.1038/s41467-019-11120-0>
- Rompikuntal, P.K., Kent, R.S., Foe, I.T., Deng, B., Bogoyo, M. & Ward, G.E. (2021). Blocking palmitoylation of Toxoplasma gondii myosin light chain 1 disrupts glideosome composition but has little impact on parasite motility. *mSphere*, 6, 15.
- Rug, M., Prescott, S.W., Fernandez, K.M., Cooke, B.M. & Cowman, A.F. (2006). The role of KAHRP domains in knob formation and cytoadherence of P falciparum-infected human erythrocytes. *Blood*, 108, 370–378. Available from: <https://doi.org/10.1182/blood-2005-11-4624>
- Russell, B.M. & Cooke, B.M. (2017). The Rheopathobiology of Plasmodium vivax and other important primate malaria parasites.

- Trends in Parasitology*, 33, 321–334. Available from: <https://doi.org/10.1016/j.pt.2016.11.009>
- Sanchez, C.P., Patra, P., Chang, S.-Y.S., Karathanasis, C., Hanebutte, L., Kilian, N. et al. (2022). KAHRP dynamically relocalizes to remodeled actin junctions and associates with knob spirals in *Plasmodium falciparum*-infected erythrocytes. *Molecular Microbiology*, 117, 274–292. Available from: <https://doi.org/10.1111/mmi.14811>
- Sancho, A., Vandersmissen, I., Craps, S., Luttun, A. & Groll, J. (2017). A new strategy to measure intercellular adhesion forces in mature cell-cell contacts. *Scientific Reports*, 7, 46152. Available from: <https://doi.org/10.1038/srep46152>
- Sarkar, R. & Rybenkov, V.V. (2016). A guide to magnetic tweezers and their applications. *Frontiers in Physics*, 4. Available from: <https://www.frontiersin.org/articles/10.3389/fphy.2016.00048> [Accessed 21st February 2023].
- Sidik, S.M., Huet, D., Ganesan, S.M., Huynh, M.-H., Wang, T., Nasamu, A.S. et al. (2016). A genome-wide CRISPR screen in *Toxoplasma* identifies essential Apicomplexan genes. *Cell*, 166, 1423–1435.e12. Available from: <https://doi.org/10.1016/j.cell.2016.08.019>
- Silvestrini, F., Tibúrcio, M., Bertuccini, L. & Alano, P. (2012). Differential adhesive properties of sequestered asexual and sexual stages of *Plasmodium falciparum* on human endothelial cells are tissue independent. *PLoS ONE*, 7, e31567. Available from: <https://doi.org/10.1371/journal.pone.0031567>
- Stadler, R.V., Nelson, S.R., Warshaw, D.M. & Ward, G.E. (2022). A circular zone of attachment to the extracellular matrix provides directionality to the motility of *Toxoplasma gondii* in 3D. *eLife*, 11, e85171. Available from: <https://doi.org/10.7554/eLife.85171>
- Stadler, R.V., White, L.A., Hu, K., Helmke, B.P. & Guilford, W.H. (2017). Direct measurement of cortical force generation and polarization in a living parasite. *Molecular Biology of the Cell*, 28, 1912–1923. Available from: <https://doi.org/10.1091/mbc.e16-07-0518>
- Stellamanns, E., Uppaluri, S., Hochstetter, A., Heddergott, N., Engstler, M. & Pfohl, T. (2014). Optical trapping reveals propulsion forces, power generation and motility efficiency of the unicellular parasites *Trypanosoma brucei*. *Scientific Reports*, 4, 6515. Available from: <https://doi.org/10.1038/srep06515>
- Stelzer, S., Basso, W., Benavides Silván, J., Ortega-Mora, L.M., Maksimov, P., Gethmann, J. et al. (2019). *Toxoplasma gondii* infection and toxoplasmosis in farm animals: risk factors and economic impact. *Food and Waterborne Parasitology*, 15, e00037. Available from: <https://doi.org/10.1016/j.fawpar.2019.e00037>
- Stewart, M.J. & Vanderberg, J.P. (1988). Malaria sporozoites leave behind trails of circumsporozoite protein during gliding motility. *Journal of Protozoology*, 35, 389–393. Available from: <https://doi.org/10.1111/j.1550-7408.1988.tb04115.x>
- Sturm, A., Amino, R., van de Sand, C., Regen, T., Retzlaff, S., Rennenberg, A. et al. (2006). Manipulation of host hepatocytes by the malaria parasite for delivery into liver sinusoids. *Science*, 313, 1287–1290. Available from: <https://doi.org/10.1126/science.1129720>
- Tang, Q., Andenmatten, N., Hortua Triana, M.A., Deng, B., Meissner, M., Moreno, S.N.J. et al. (2014). Calcium-dependent phosphorylation alters class XIVa myosin function in the protozoan parasite *Toxoplasma gondii*. *Molecular Biology of the Cell*, 25, 2579–2591. Available from: <https://doi.org/10.1091/mbc.E13-11-0648>
- Tardieux, I. & Baum, J. (2016). Reassessing the mechanics of parasite motility and host-cell invasion. *Journal of Cell Biology*, 214, 507–515. Available from: <https://doi.org/10.1083/jcb.201605100>
- Thiberge, S., Blazquez, S., Baldacci, P., Renaud, O., Shorte, S., Ménard, R. et al. (2007). In vivo imaging of malaria parasites in the murine liver. *Nature Protocols*, 2, 1811–1818. Available from: <https://doi.org/10.1038/nprot.2007.257>
- Tolić, I.M. & Tardieux, I. (2022). The power of parasite collectives. *Nature Physics*, 18, 491–492. Available from: <https://doi.org/10.1038/s41567-022-01554-7>
- Tomaiuolo, G. (2014). Biomechanical properties of red blood cells in health and disease towards microfluidics. *Biomicrofluidics*, 8, 051501. Available from: <https://doi.org/10.1063/1.4895755>
- Tosetti, N., Dos Santos Pacheco, N., Soldati-Favre, D. & Jacot, D. (2019). Three F-actin assembly centers regulate organelle inheritance, cell-cell communication and motility in *Toxoplasma gondii*. *eLife*, 8, e42669. Available from: <https://doi.org/10.7554/eLife.42669>
- Totino, P.R. & Lopes, S.C. (2017). Insights into the cytoadherence phenomenon of *Plasmodium vivax*: the putative role of phosphatidylserine. *Frontiers in Immunology*, 8. Available from: <https://www.frontiersin.org/articles/10.3389/fimmu.2017.01148> [Accessed 15th February 2023].
- Trecek, M., Sanders, J.L., Elias, J.E. & Boothroyd, J. C. (2011). The phosphoproteomes of *Plasmodium falciparum* and *Toxoplasma gondii* reveal unusual adaptations within and beyond the parasites' boundaries. *Cell Host & Microbe*, 10, 410–419. Available from: <https://doi.org/10.1016/j.chom.2011.09.004>
- Udeinya, I.J., Schmidt, J.A., Aikawa, M., Miller, L. H. & Green, I. (1981). *Falciparum* malaria-infected erythrocytes specifically bind to cultured human endothelial cells. *Science*, 213, 555–557. Available from: <https://doi.org/10.1126/science.7017935>
- Vanderberg, J.P. (1974). Studies on the motility of *Plasmodium* sporozoites. *Journal of Protozoology*, 21, 527–537. Available from: <https://doi.org/10.1111/j.1550-7408.1974.tb03693.x>
- Watermeyer, J.M., Hale, V.L., Hackett, F., Clare, D.K., Cutts, E.E., Vakonakis, I. et al. (2016). A spiral scaffold underlies cytoadherent knobs in *Plasmodium falciparum*-infected erythrocytes. *Blood*, 127, 343–351. Available from: <https://doi.org/10.1182/blood-2015-10-674002>
- Wells, M.B. & Andrew, D.J. (2019). Anopheles salivary gland architecture shapes *Plasmodium* sporozoite availability for transmission. *mBio*, 10, e01238-19. Available from: <https://doi.org/10.1128/mBio.01238-19>
- Wichers, J.S., Scholz, J.A.M., Strauss, J., Witt, S., Lill, A., Ehnold, L.-I., et al. (2019). Dissecting the gene expression, localization, membrane topology, and function of the *Plasmodium falciparum* STEVOR protein family. *mBio*, 10, e01500-19. Available from: <https://doi.org/10.1128/mBio.01500-19>
- Williams, M.J., Alonso, H., Enciso, M., Egarter, S., Sheiner, L., Meissner, M. et al. (2015). Two essential light chains regulate the myosin lever arm to promote *Toxoplasma* gliding motility. *mBio*, 6, e00845-15. Available from: <https://doi.org/10.1128/mBio.00845-15>
- World Health Organization. (2021). Available from: <https://www.who.int/health-topics/malaria> [Accessed 15th February 2023].
- Yahata, K., Hart, M.N., Davies, H., Asada, M., Wassmer, S.C., Templeton, T.J. et al. (2021). Gliding motility of *Plasmodium* merozoites. *Proceedings of the National Academy of Sciences of the United States of America*, 118, e2114442118. Available from: <https://doi.org/10.1073/pnas.2114442118>
- Yang, T., Bragheri, F. & Minzioni, P. (2016). A comprehensive review of optical stretcher for cell mechanical characterization at single-cell level. *Micromachines*, 7, 90. Available from: <https://doi.org/10.3390/mi7050090>
- Yoeli, M. (1964). Movement of the sporozoites of *Plasmodium berghei* (Vincke et Lips, 1948). *Nature*, 201, 1344–1345. Available from: <https://doi.org/10.1038/2011344a0>
- Zhang, M., Gallego-Delgado, J., Fernandez-Arias, C., Waters, N.C., Rodriguez, A., Tsuji, M. et al. (2017). Inhibiting the *Plasmodium* eIF2 α kinase PK4 prevents artemisinin-induced latency. *Cell Host & Microbe*, 22, 766–776.e4. Available from: <https://doi.org/10.1016/j.chom.2017.11.005>
- Zhang, Y., Min, C., Dou, X., Wang, X., Urbach, H. P., Somekh, M.G. et al. (2021). Plasmonic tweezers: for nanoscale optical trapping

and beyond. *Light: Science & Applications*, 10, 59. Available from: <https://doi.org/10.1038/s41377-021-00474-0>

Zhao, X., Zhao, N., Shi, Y., Xin, H. & Li, B. (2020). Optical fiber tweezers: a versatile tool for optical trapping and manipulation. *Micromachines*, 11, 114. Available from: <https://doi.org/10.3390/mi11020114>

How to cite this article: Vigetti, L. & Tardieux, I. (2023) Fostering innovation to solve the biomechanics of microbe–host interactions: Focus on the adhesive forces underlying Apicomplexa parasite biology. *Biology of the Cell*, 1–17. <https://doi.org/10.1111/boc.202300016>

3. Highlighting the apico-basal bipolarity of the *T. gondii* tachyzoite

During the first chapter of the thesis, we report on technical development and assays to gain knowledge on how the tachyzoite builds a contact with a surface that supports the generation of a traction force compatible with helical propelling. In one side, we could demonstrate that the parasite needs to only attach through the two poles to engage in motion while the rest of its elliptical body does not contribute to movement with respect to the linear distance travelled. Once the posteriorly attached parasite engages apically with the substrate, it can build an adhesive platform which remains stable in the substrate throughout the time the parasite takes to move over, and this until its posterior sticks on it. When there, the tachyzoite sitting on its base rotates to end the 360° helical twist and be ideally prepared for the next helical path. On the other side, we brought evidence that this adhesion requirement can be fulfilled if extracellular GAGs are presented to the parasite with increasing motile activity correlating with increased GAG molecules.

Although the motile process does involve the two poles of the parasite, the apex stays the leader since it controls the directionality of helical gliding through the release of adhesins that bridge extracellular ligands with the internal actomyosin engine during helical propelling. Being filled by two types of organelles, not only releasing adhesins during gliding and cell invasion but also effectors during invasion, and structurally organized around a retractile conic-shaped appendage, the apex has received much attention in the last decades. In contrast on the opposing side of the cell, the basal pole has only started to be looked at in particular during the endodyogeny process. The basal pole progressively buildup as the new progeny inside the mother's body (Hu, 2008). While recent studies have made significant progress in annotating the different components of the basal pole, the understanding on the functional properties of these players remains largely unknown. At the frontier of the cytoskeleton structure, and encompassing three different kinds of myosin motors (TgMyoC, TgMyoJ and TgMyoI) and enriched in actin filaments, recent studies have shown that the basal pole may harbor more functions than being restricted to an architectural purpose (B. Anderson-White et al., 2012; Gubbels et al., 2022; Periz et al., 2017; Roumégous et al., 2022). In this functional scenario, there is the possibility that the basal pole structure could offer resistance to the mechanical

stress encountered by the tachyzoites during the invasion. Indeed a peculiar structure has to withstand the torques that impose the twisting motion which signs both for the complex twirling motile behavior that prevails in 2D conditions, but for entry into the host cell within a growth-permissive parasitophorous vacuole (Pavlou et al., 2018).

In this context, **Chapter 2** of the thesis focuses on the fine *in situ* description of a 500 kDa protein termed BCC7 that we report to be located at the distal border of the internal membrane scaffold where it possibly also interact with myosin motors.

4. Chapter 2

Towards a better understanding of the *Toxoplasma gondii* tachyzoite basal pole

4.1 Rationale and main objectives of the study

In **Chapter 1**, we put a focus on the bipolarity of the tachyzoite highlighting that the two polar compartments display dynamic surface binding properties to the substrate that coordinate to promote parasite gliding skills. In this second chapter, we characterize in detail a high molecular weight protein, specific to Coccidia which first identification as **BCC7** through dedicated proteomic studies indicated it could be a specific basal pole component. Taking into account our expertise in live and nanoscale-resolution imaging together with approaches combining molecular genetics and biochemistry, we chose to verify *in situ* if and how BCC7 contributes to assemble a functional tachyzoite basal pole, with respect to molecular partner candidates. These questions led us to explore BCC7 in the context of the tachyzoite biogenesis, therefore during endodyogeny when the bipolarity of nascent daughter cells sets up, but also once the mature tachyzoite has egressed from the host cell and gain motile and invasive capacities. In particular, our first dataset led us to further examine the relationships between BCC7 and the IMC posterior border as well as with specific myosins since the latter could contribute to typical torques that likely power the zoite twirling behavior and possibly helical motility (*Section 2.2.2.2*).

Therefore, this work had for objectives to:

- Apply live and super resolution microscopy to provide a dynamic and *in situ* picture of BCC7 and its positioning with respect to basal pole components such as (i) myosin motors and (ii) IMC members.
- Use molecular genetics and phenotypic analysis to assay the BCC7 impact on the parasite viability.

- Combining co-immunoprecipitation assays coupled to mass spectrometry (MS)-based proteomics and *in silico* analysis to identify protein candidates that would interact with BCC7, further characterized through molecular genetics and imaging.

4.2 Context and state-of-the-art

This section intends to provide the reader with useful information on (i) the peculiar mode of division of the *T. gondii* tachyzoite that gives rise to two polarized daughter cells within the mother, (ii) the structural mosaic organization of the tachyzoite cell surface that contributes to the typical tri-layered membranous pellicle of Apicomplexa zoites, and (iii) the biogenesis of a basal compartment that culminates in mature tachyzoites ready to egress the host cell.

4.2.1 The *Toxoplasma gondii* tachyzoite division

The tachyzoite reproduces asexually by endodyogeny, a process during which two daughter cells are assembled inside a mother's cell after each round of DNA replication. This replicative cycle lasts approximately 6-7 hours at 37°C, and is divided into the G1 (growth), S (DNA replication), M (mitosis), and C (cytokinesis) phases; as many other apicomplexans and unlike other unicellular eukaryotes, tachyzoites do not display a G2 period (Radke et al., 2001). The division of the tachyzoites starts with a rather long G1 phase compared to other eukaryotes, with an increase in cell size to accommodate the two-budding progeny; the G1 checkpoint commits the cell to division and prepares for DNA replication (**Figure 15**). The scaffold structure of the daughter cell begins while the DNA is still being synthesized, with the microtubule organizing center (MTOC) acting as a polarity reference along the process (White & Suvorova, 2018). The endodyogeny process starts with the duplication of the centrosome, leading to the alignment and insertion of TgIMC15 to scaffold the nascent daughter cells. (B. R. Anderson-White et al., 2011). This is followed by the accommodation of TgAC1 and TgAC5, two apical cap proteins, and ISP1 (A. L. Chen et al., 2015). Progressive assembly of the two daughter cells occurs with the growth of the 22 subpellicular spiraled microtubules (MTs) and the alveolar network (Hu et al., 2002).

Regarding the replication or distribution of organelles in the nascent daughter cells, the first one to be allocated is the apicoplast (Striepen et al., 2000), followed by the full division of the

nucleus, and the partition of the ER and the mitochondrion into the budding daughters (Nishi et al., 2008). Secretory organelles (*i.e.* rhoptries, micronemes, and dense granules) are synthesized *de novo* at each division cycle (Nishi et al., 2008) whereas at the end of the process, the mother's cytoskeleton is disassembled, and the remaining PM recycled into the one of newly formed daughters. Of note, the glideosome components are also assembled between the PM and the IMC at this stage (Fréchal et al., 2010).

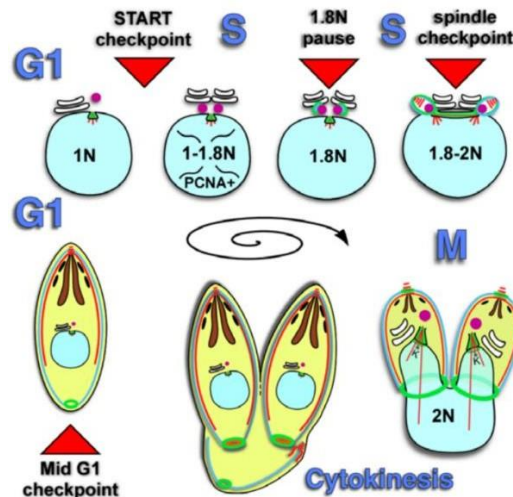


Figure 15 – Schematic of the tachyzoite endodyogeny production of daughter cells as the cell cycle progresses. The tachyzoite division goes from the G1 phase (top left) to the cytokinesis (bottom right), with the checkpoints noted as red triangles. Different organelles are shown in the division process, as primarily the nucleus (cyan), microtubules (red), inner membrane complex (IMC – in light blue), membrane occupation and recognition nexus protein 1 (MORN1, green), centrosome (purple spot), centrin2 protein (orange), rhoptries (brown), micronemes (black) and Golgi apparatus (white). Adapted from (Gubbels et al., 2008)

Several division rounds create an organization of tachyzoites known as rosette, with their apical pole aligned peripherally and their basal poles attached at the center of the rosette. The tachyzoite division ends when the two daughter cells are individualized, sometimes still attached by a small membrane from the mother's cell called residual body: at this stage, each cell contains a nucleus and all separate organelles (*i.e.* Golgi, mitochondrion, apicoplast, rhoptries) that are synthesized during the process (Striepen et al., 2007). Restricted to the residual body, TgMyoI is present in the last common structure of the mother's body in the tachyzoite division process, and could associate with the bundles of F-actin that form a network

shown to be crucial for intravacuolar cell-cell communication during endodyogeny (Frénal et al., 2017; Periz et al., 2017; Tosetti et al., 2019).

4.2.2 The IMC system assembles as the core of the tri-layered pellicle that delineates the tachyzoite and compartmentalize specific glideosomes

Despite its diversity in terms of members and accordingly lifestyles, Apicomplexans are still characterized by a set of structures in common. The first of them is the alveoli sacs that define the Alveolata infrakingdom, which aside from Apicomplexa gather the Dinoflagellates and Ciliates, and is known for former as the Inner Membrane Complex (IMC) (Kono et al., 2013). The IMC with the outer plasma membrane forms a tri-laminar structure qualified as the pellicle. Beneath the IMC, on the cytoplasmic side, there are filaments referred to as the subpellicular network (SPN) which is composed of alveolins, a family of proteins typifying the Alveolata (Gould et al., 2008).

Specifically, the *T. gondii* IMC alveolar structure consists of several flattened membrane sacs called alveoli that demarcate jointed plates along the parasite's body. There is a single cone-shaped plate in the apical region (the apical cap), and then the next plaque distribution continues along longitudinally with 3 or 4 rows of rectangular-like areas; the juxtaposed connections between plates are called the sutures (Porchet & Torpier, 1977). As such, the composite IMC runs along the entire length of the tachyzoite stage of *T. gondii*, with opening at the apical conoid and basal poles. The IMC proteins goes through dynamic changes during the endodyogeny process being cytoplasmic before associated as a network but also derived either from (i) *de novo* synthesis during endodyogeny, or (ii) recycling of maternal IMC (Choi et al., 2019; Ouologuem & Roos, 2014).

To briefly summarize the complex choreography of IMCs' integration into nascent cells, let's start when the centrosome replicates (*i.e.*, at the onset of endodyogeny), which coincides with the time during which TgIMC15 aligns and inserts at the scaffold of the forming progeny (B. R. Anderson-White et al., 2011). Several groups of IMC are then progressively incorporated into the scaffold with the one containing IMC1, IMC3, IMC4, IMC6 and IM10 guiding the way (B. Anderson-White et al., 2012). As this group elongates giving shape to the daughter's

cell, it also associates with the integration of GAP40 and GAP50 (Frénal et al., 2010). Indeed, as presented in **Chapter 1** (*Section 2.2.2.2, The glideosome*), the IMC serves as a scaffold for the glideosome motor machinery (Gaskins et al., 2004; Soldati et al., 2004). A second group consisting of IMC5, IMC8, IMC9 and IMC13 are assembled and then distributed from the initial position to the basal end, finishing with a ring structure that can be colocalized with the canonical basal marker MORN1 (Hu, 2008) presented in the next paragraph. The last IMC proteins to be inserted, IMC7, IMC12 and IMC14 are recycled from the mother's cell and added at the end of the division process (B. R. Anderson-White et al., 2011) (**Figure 16**).



Figure 16 - Schematic of dynamics of IMC proteins along the endodyogeny process. Adapted from B. R. Anderson-White et al., 2011.

Associated to the IMC network are proteins that can be grouped according to their structural and functional activity (B. Anderson-White et al., 2012; Harding & Meissner, 2014). First, the IMC sub-compartment proteins (ISPs) which play an important role in the coordination of daughter cells assembly (Beck et al., 2010). ISPs are regionally restricted on the tachyzoite body since ISP1 occupies only the apical cap region while ISP2 takes the relay on the central part and ISP3 is expressed in both the central and basal compartments. This compartmentalization also partially superimposes with the distribution of GAPs that feature distinct glideosomes in mature tachyzoites (**Figure 17**) (see **Chapter 1**). For instance, the GAP 40-45-50 are all anchored to the IMC and forms the canonical MyoA-based glideosome, while GAP70 and GAP80 which are closely related to GAP45 locate exclusively at the apical and most basal IMC compartments, respectively (Frénal et al., 2010). While the GAP70 relates to the MyoH glideosome, the GAP80 forms a ring and recruits Myosin C although it was also reported to minimally associate with MyoA (Frénal et al., 2010). MyoC is a class XIV myosin which is formed from the differential splicing of the myosinB/C gene, and designs a ring shaped

structure at the upper basal pole, and is both involved in gliding and host cell invasion (Fréchal et al., 2014). The MyoC motor is associated with both IMC-associated protein 1 (TgIAP1) and TgGAP80. The class VI TgMyoJ is more basally located than MyoC, and it is also shaped in a ring-like structure, that can be seen more clearly when the daughter cells are developing, as it is active during constriction of the budding at the final step of the endodyogeny process (Fréchal et al., 2017). When the division process is complete, the ring structure is less noticeable as is constricted in the posterior cup part of the parasite (Hu, 2008).

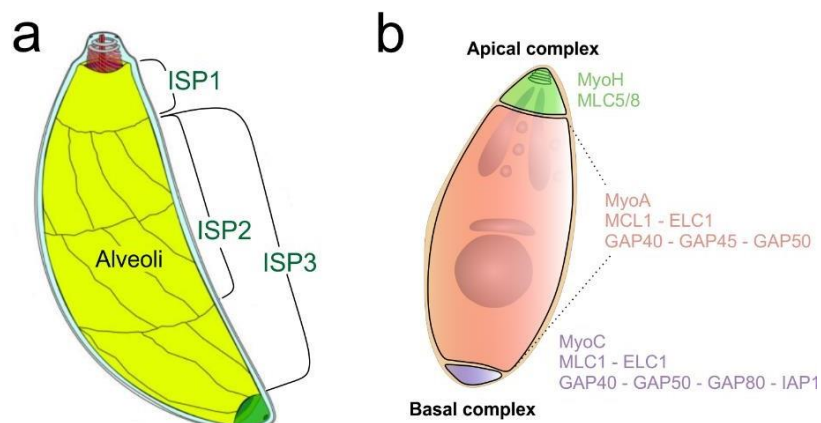


Figure 17 - (a) Schematic representation of the structures under the PPM, with the alveolar vesicles shown in yellow. There is a single alveolar vesicle in the apical cap, and there are three bands filling the remainder of the IMC. It is also shown the localization of the three ISPs. (b) Schematic representation of the localization of the apical MyoH on top, with its myosin light chains associated (MLCs), the MyoA glideosome present in the majority of the tachyzoite's body with its MLCs and GAPs, and the MyoC at the basal pole. Adapted from (B. Anderson-White et al., 2012; Fréchal et al., 2014).

Finally, the articulins-like proteins which are named alveolins in *T. gondii* also home at the IMC. Having a structural homology with the intermediate filament proteins of mammals (B. R. Anderson-White et al., 2011) these proteins are in close contact with the cortical microtubule cytoskeleton, and a sub-group of them are in restricted to the basal cytoskeleton or basal complex.

4.2.3 A basal pole dynamically assembles below the IMC during endodyogeny with the recruitment of specific components including myosin motors

Once endodyogeny terminates, there are three different regions in the basal complex, as (i) the basal inner collar (BIC), delimited by the presence of MORN1, IMCs9/12/15 and MyoC (Gubbels et al., 2006); (ii) the basal inner ring (BIR), with IMCs5/8; and (iii) a more distal group, the posterior cup, that corresponds to the presence of CEN2 and IMCs5/8 and MyoJ (Hu et al., 2006) (**Figure 18**).

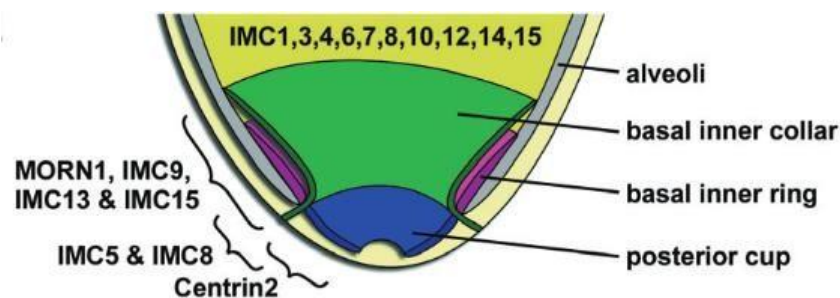


Figure 18 – Representation of the basal pole complex. A first layer, known as the basal inner collar, is delimited by the presence of MORN1 and IMC9/12/15. The more basal tip corresponds to the posterior cup, where CEN2 and IM5/8. Most of the other IMC proteins are not present in the basal pole (yellow area). Adapted from B. R. Anderson-White et al., 2011.

The main function of the basal pole during endodyogeny is to act as a ring that contracts to separate the two daughter cells: failure to do so by depletion of MORN1 for example, is lethal in the long-term, as tachyzoites are able to undergo several budding rounds but still joint at the basal end (Lorestani et al., 2010). Specifically, MORN1 is synthesized very early on the endodyogeny process, and is detected close to the centrosome, while it moves towards the basal pole where it forms a ring-like shape as the IMC elongates (Gubbels et al., 2006). MyoC was reported to colocalize with MORN1 using epifluorescence microscopy (xy resolution ~ 250 nm), both in ring-shaped structures at the basal pole (Gubbels et al., 2006).

Building the posterior cup, the CEN2 is a calmodulin-like protein, which at epifluorescence microscopy (xy resolution ~ 250 nm) appears to colocalize with MyoJ (Frénal et al., 2017). When MyoJ is not present, the tachyzoite basal pole is enlarged and there is also a loss of CEN2 signal. Furthermore, CEN2 deletion has an impact on the basal pole constriction and presents the same basal widening (Frénal et al., 2017). It has been proposed that CEN2 acts as a myosin light chain for TgMyoJ, yet evidence is still missing.

Recent studies (Engelberg et al., 2022; Roumégous et al., 2022) show that there are a plethora of other components, named Basal Complex Components 0 to 11. These components were

found using BioID approach with baits corresponding to different compartments of the basal pole: MORN1 for the upper part, IMC8 for the middle section, and CEN2 and MyoJ for the lower part. Interestingly, BCC4 showed a MORN1-like behavior when depleted, being required for the correct structural integrity of the pole.

4.3 Implemented techniques to study the basal pole candidate BCC7 protein

4.3.1 Bioinformatic analysis

The first step into characterizing this new protein was acquiring its sequence from the open-source database ToxoDB (Amos et al., 2022) ; complementing from previous subcellular proteome classification (Barylyuk et al., 2020), BCC7 is annotated as a IMC-related protein. Briefly, several techniques were combined for obtaining more information of the sequence:

- For predicting the transmembrane helix, we used TMHMM-2.0 server (*Services*, 2022).
- The PEST motif identification were retrieved using EMBOSS program ePESTfind tool (*EMBOSS: Epestfind*, 2022)
- The amino acid composition for each region was recovered using Expasy ProtParam (*ExPASy - ProtParam Tool*, 2022)
- The phosphorylation sites were regained using the ToxoDB database according to previous *T. gondii* phosphoproteomic studies (Treeck et al., 2011).

4.3.2 Engineering of tachyzoite lines expressing different reporters of interest

T. gondii is a very amenable working biological model since the discovery of the first methodologies that allow genetic manipulation and the introduction of transgenic reporters some 30 years ago (Donald & Roos, 1993). Nowadays, one of the most common strategies for transgenic work involves the Ligation Independent Cloning (LIC) strategy, which allows the localization and purification of proteins by adding an short epitope tag, a fluorescent marker or an enzyme reporter (Huynh & Carruthers, 2009). Briefly, this methodology works by targeting the modification of the genomic locus of the gene by homologous recombination using a

plasmid that contains a part of the sequence derived from genomic DNA to target the recombination site, and the tag and antibiotic resistance of choice. To eliminate the possibility of non-homologous recombination, a mutant strain knock-out of the *ku80* recombinase is normally used, favoring the homologous recombination on the transfected cells. This strategy was used in our study for the generation of transgenic lines expressing simple epitope tags (*i.e.* HA, Myc, FLAG - short sequences that are fused to proteins for antibody recognition) for immunofluorescence localization and co-immunoprecipitation, and fluorescent markers (*i.e.* mCherry, Emerald) for live videomicroscopy (**Figure 19a**).

Furthermore, to assess the impact of BCC7 on (i) extracellular lifestyle (*i.e.* motility) and (ii) intracellular lifestyle (*i.e.* vacuole organization and growth rate), we generated a conditional knock-down (cKD) transgenic line. Before our studies, in a genome-wide knock out screen fitness score attributed in (Sidik et al., 2016), this protein is dispensable for the tachyzoite overall fitness. To generate our cKD, we used a different cloning strategy, based on the auxin-inducible degron (mAID) system (K. Brown et al., 2018). In this method, the base transgenic line expresses a plant auxin receptor named transport inhibitor response 1 (TIR1) on a *ku80* transgenic line; on this parasitic line we transfect a plasmid of our gene of interest (*i.e.* BCC7) followed by an AID tag. As such, in normal conditions the small AID tag doesn't impact on the protein function, but when we add auxin (3-indolacetic acid, IAA) to the culture medium, TIR1 changes conformation and recruits a complex that ubiquitinates the AID tag of the protein, signaling for proteasomal degradation (**Figure 19b**). As a result, after ~1 hour, the protein expression diminishes, resulting in a fast and efficient way to eliminate the desired protein.

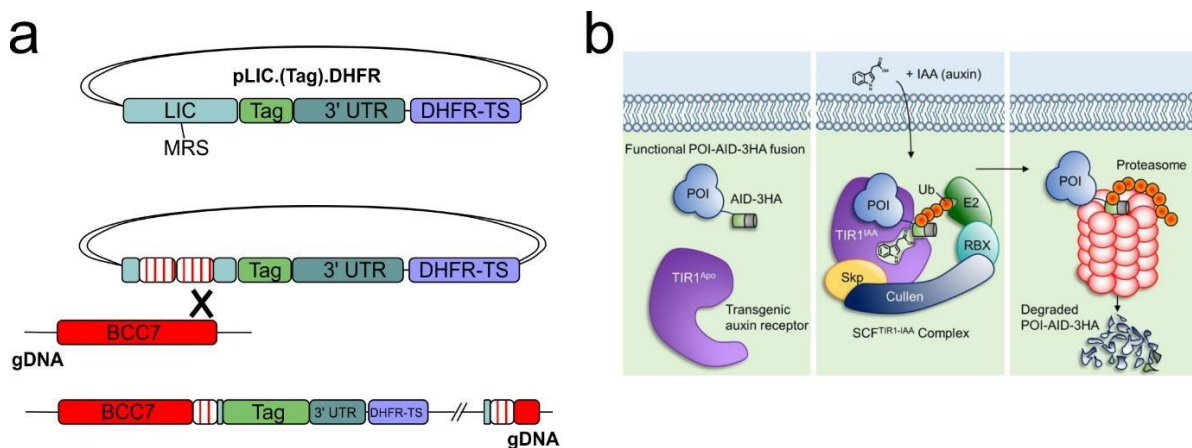


Figure 19 – (a) The LIC endogenous gene tagging consists on a pLIC plasmid vector containing a sequence with multiple resistance (MRS) for restriction enzymes fused in frame with a tag sequence (e.g. HA, c-Myc), followed by a 3' untranslated region (UTR) and a drug resistance cassette for selection. Later, a PCR product containing part of the sequence of the gene of interest (e.g. BCC7) is inserted into the vector. When tachyzoites are transfected with this plasmid, a single crossover integration occurs and the sequence is added to the genomic DNA. Adapted from (Huynh & Carruthers, 2009). (b) Model for conditional knock-down strategy using auxin inducible-degron system. The protein of interest (POI, *i.e.* BCC7) is tagged with an AID and HA tags, which doesn't affect its function. When there is no auxin (IAA) in the medium, the TIR1 protein is inactive. At the addition of IAA, TIR1 assembles into an ubiquitin ligase complex that recognizes and polyubiquitinates the AID tag in the protein, targeting it for proteasomal degradation. Adapted from (K. Brown et al., 2018).

4.3.3 Biochemical characterization

To perform the biochemical characterization of the BCC7 protein, which was annotated as a potentially membrane spanning and IMC-related protein, we performed its isolation by sub-fractionation assays. As a protein that is membrane related, it would most likely be in a hydrophobic environment, which is key for its stability and function. As such, for its purification is important an extraction using amphipathic molecules like detergents, to later disperse the protein in aqueous conditions and at the same time keeping its conformation. Nevertheless, not all detergents are suitable for solubilizing all proteins, as they present different hydrophobicity, charge and micelle concentration, interacting in a different way with the desired protein and affecting the solubilization efficiency. As a result, we tested different types of detergent conditions, listed as follows:

- BC500: lysis buffer containing NP40 (0.05% v/v): this buffer contains a high salt concentration and is supplemented with NP40, a non-ionic surfactant, with a low critical micelle concentration (CMC – 0.29 mM). As such, it provides gentle conditions for protein solubilization.
- BC500 supplemented with n-Dodecyl- β -D-maltopyranoside (0.1% w/v): This buffer was composed with NP-40 as the one before, complemented with DDM, a maltoside based non-ionic detergent which improves the hydrophobic protein solubilization.
- Empigen BB (1% v/v): this detergent is of zwitterionic nature, meaning it can work as an anionic, non-ionic or cationic surfactant. It presents a higher critical micelle

concentration compared with NP-40, and its usually used to preserve the antigenicity of solubilized proteins (Lowthert et al., 1995).

- N-lauroyl sarcosine (0.1% w/v): a gentle anionic surfactant.
- Sulfobetaine 3–14 (n-Tetradecyl-N, N-dimethyl-3-ammonio-1-propanesulfonate) (1% w/v): a zwitterionic detergent with a low CMC.
- Triton X-100 (0.1% v/v): a non-ionic surfactant, which is slightly more hydrophilic than the other detergents from the list, and widely used for cell lysis extraction. For this particular detergent, we confirmed previous results that did not mention BCC7 as a TX-100 soluble cytoskeleton protein (Gómez de León et al., 2014)

4.3.4 Mass-spectrometry based proteomics

To further characterize BCC7, we aimed to identify its putative interacting partners; to do so, we coupled co-immunoprecipitation with mass spectrometry (MS)-based proteomics. Briefly, MS-based proteomics is a quantitative approach for the collection of proteins present in a sample, by measuring the ion mass-to-charge values and signal intensities of the peptides present in the specimen. In our experimental setup, we first generate a tachyzoite line expressing a FLAG tag to purify the protein, as described on *Section 4.2.2*. Next, to recover a BCC7-HA-FLAG enriched extract, we performed two lysis steps, the first one using TX-100 to remove cytoskeleton proteins, and as BCC7 is insoluble in this detergent, a second one using Empigen BB, where the extract containing our protein was immunoprecipitated using anti-FLAG agarose beads; the presence of BCC7 in the final elution was assessed by SDS-PAGE. Three replicates of the co-immunoprecipitation were performed, with the BCC7-HA-FLAG expressing *T. gondii* line and the parental RH Δ ku80 line as control. The proteins were digested using trypsin, and next analyzed using liquid chromatography coupled to MS/MS. Comparative statistical analysis allowed retrieving thirteen enriched *Toxoplasma* proteins in the BCC7-HA-FLAG pool, and the identity of those proteins were assigned using ToxoDB (Amos et al., 2022), with the subcellular localization was evaluated with the HyperLopit approach (Barylyuk et al., 2020). All the MS-based proteomics were performed in collaboration with Dr. Yohann Couté (CEA, Grenoble, France). A schematic synthesizing the MS-based proteomics is shown on **Figure 20**.

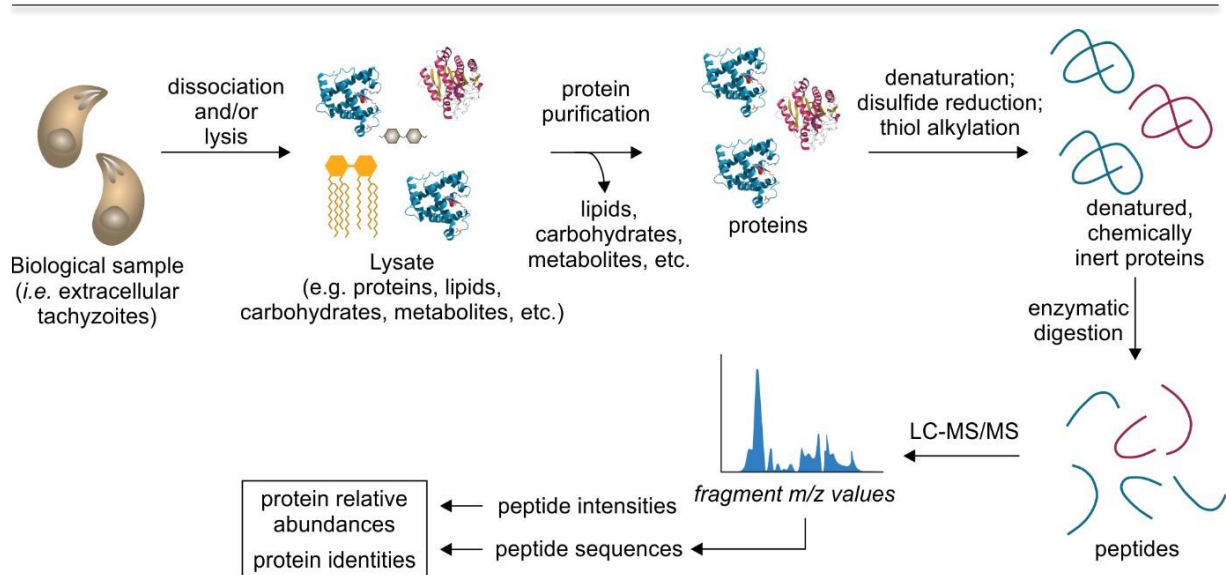


Figure 20 – Schematic representation of the sample preparation workflow for MS-based proteomics. First, cells are lysed and the proteins are separated from other components by precipitation. Then, the proteins are denatured using a detergent solution. The denatured proteins can be rendered chemically inert by disulfide bond reduction, generally with a dithiothreitol (DTT) treatment. The resulting peptides are then hydrolyzed by proteolysis, typically using trypsin. After protease treatment, the peptides can be separated by liquid chromatography and inserted into a mass spectrometer. The MS analyses the peptide’s mass-to-charge (m/z) values and also the relative abundance as the signal intensity. Both variables are used to identify the peptide’s sequences and abundance. Adapted from Shuken, 2023.

4.3.5 Scanning Electron Microscopy

Furthermore, we aimed to assess if the deletion of BCC7 determined any differences at the structure of the basal pole, as it is the biggest protein characterized so far and in the interface between cytoskeleton components. To do so, we collected in collaboration with Prof. Isabelle Florent (Muséum National d’Histoire Naturelle, Paris) Scanning Electron Microscopy (SEM) images on the conditional knock-down transgenic tachyzoite line, expressing or not the BCC7 protein. Briefly, SEM produces high-resolution images as a result of using high-energy (2-40 keV) electron beam instead of a light wavelength illuminating the sample like in fluorescence microscopy. As the electron beam interacts with the sample, it generates the excitement of secondary and backscattered electrons of the specimen’s surface, which are collected by different detectors to generate the image. As a result of the electron beam not traversing through the sample, SEM provides information about the surface topography at a ~ 1 -20 nm resolution (Vernon-Parry, 2000).

First, we used a fixation solution with glutaraldehyde to crosslink the proteins as a more potent agent compared to formaldehyde, while using sodium cacodylate to precisely control the solution pH. Next, the fixed samples were dehydrated by incubating them in ethanol, to gently remove water that can cause breakages on the cell's membrane. The ethanol was subsequently dried to avoid artefacts, and next the samples were coated with a 5 nm platinum layer to create a conductive coating and avoid charge buildup on the surface while imaging.

4.3.6 Coupling microfluidics and micropattern for long-recording videomicroscopy

After generating the fluorescently tagged versions of the BCC7 protein, we pursued the videorecording of the entire division process to follow the dynamics in cycling tachyzoites at high resolution. Several basal pole proteins migrate during endodyogeny (*i.e.* TgMORN1, TgCEN2), as they are generated near the apical pole of the nascent daughters and later progress to the basal pole as the division progresses. The entire recording process was long (~ 48 hours) in order to capture the entire process from the first division to egress, and as such there were several challenges to address:

- i. As a result of the long duration of the recording, host cells were drifting or moving considerably along the xy axis, displacing the focus of the intracellular vacuole.
- ii. As the setting with the host cells and the dividing vacuoles was kept for the entire process in the microscope chamber with limited volume of cell culture medium, we needed to explore a strategy to replenish with fresh medium along the recording.
- iii. Maintaining focus of the vacuole along the long recording process.
- iv. Setting the correct recording parameters to avoid photobleaching and phototoxicity for both host cells and tachyzoites.

All these points were successfully worked out by the combination of a microfluidics setting in our confocal microscope, and coupling a fine tuning of recording conditions:

- i. We stabilized the host cells by seeding them on top of micropatterned rectangle surfaces. We used fibronectin rectangle areas of 120 μm of length by 40 μm of width separated between each other by the anti-adhesive PLL-PEG. This design was used to include several cells inside and avoid death of isolated cells by loss of cell-cell

interactions. Also, the host cells had restricted their movement along the xy axis while recording, by being unable to move towards the anti-adhesive PLL-PEG areas. If during that time they divided or moved, they would still be inside the microscope frame and the vacuole would be always correctly recorded.

- ii. Host cells need nutrients (*i.e.* glucose, glutamine, sodium pyruvate, and salts) and a balanced pH (obtained through sodium bicarbonate buffer) in order to maintain good viability, and thus optimum vacuole division. In order to replenish the microscope chamber with fresh medium, we installed a microfluidic system to control the injection of liquid inside the receptacle at the same time that it aspirates the exhausted medium. The injection valve was in the coverslip level to get in contact with the seeded cells, restoring the needed nutrients; the outlet was located in the top of the chamber to aspirate the depleted medium and also act as a safe valve to avoid leakage by excess (**Figure 21**).
- iii. For maintaining the focus along the recording, the microscope was equipped with a piezo objective to calibrate tightly the Z-plane change. The Perfect Focus System (PFS) was set to maintain the focus on the fluorescent signal of the BCC7 protein, to keep the fluorescent intensity equal and at focus at all time.
- iv. Three wavelengths were used for the recordings: brightfield (for imaging the host-cell and the vacuole), green (for BCC7 tagged with Emerald) and red (for the corresponding partner tagged with mCherry). As tachyzoites divide every 6 hours approximately, it was not necessary to take many consecutive images and thus avoiding phototoxicity. As a result, we chose to image 1 frame every 7 minutes, giving a good detail of the vacuole conformation and minimizing the laser exposure on the cells, to surpass photobleaching also.

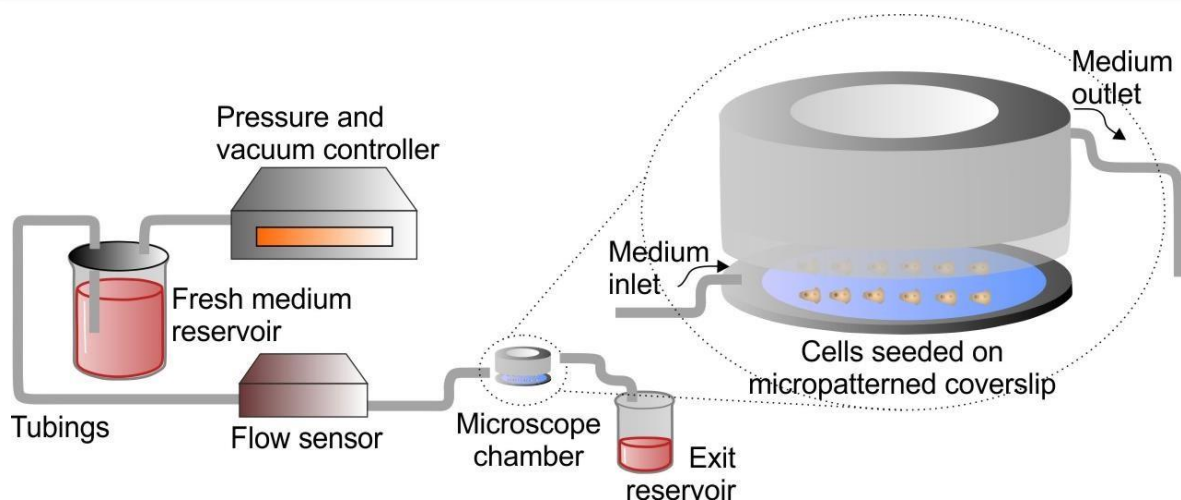


Figure 21 – The microfluidics setting was built using an OB1 Microfluidic flow controller (Elveflow Systems), equipped with a MS4 flow sensor to calibrate the amount of liquid entering the microscope chamber between 2 to 100 $\mu\text{l}/\text{min}$. The inlet located at the base of the chamber allowed refreshing the medium in contact with the cells, and the outlet at the top of the chamber withdraws the exhausted medium.

4.4 Main highlights of the study

In the main collaborative publication of this chapter, we applied conventional biochemistry, advanced proteomics, and *in silico* protein domain prediction analysis in conjunction with live and super-resolution microscopy of transgenic fluorescent tachyzoites to (i) localize the BCC7 protein *in situ*, (ii) identify potential partners and validate the interaction, (iii) assess its functional contribution to the lytic cycle. Specifically, the following are our study highlights:

- Bioinformatic analysis indicates that BCC7 is a *Coccidia*-restricted 500 kDa protein, with no structural homology or predicted functional association with any known proteins.
- *In situ* BCC7 is seen as a ribbed ring that marks the basal pole of the *T. gondii* tachyzoite, both in mature intracellular and extracellular tachyzoites.
- Dynamic imaging of intracellular diving tachyzoites shows that *de novo* BCC7 traffics in an anterograde path as protein patches which eventually merges with the maternal-derived material to form a complete basal ring.

- Imaging BCC7 and MyoC at a 25 nm resolution scale reveals that the former lies close on top of the latter and likely forms homo-multimers.
- The BCC7 protein is dispensable for the tachyzoite lytic cycle in vitro, and its loss does not impact the ultrastructural organization of the basal pole surface assessed by scanning electron microscopy.
- Biochemistry coupled to mass spectrometry-based proteomics indicates that BCC7 may have 13 putative partners encompassing a majority of IMC proteins, including two new ones named IMC35 and IMC36.

4.5 Vigetti et al., *Int. J. Mol. Sci.*, 2022

Publication

Vigetti L, Labouré T, Roumégous C, Cannella D, Touquet B, Mayer C, Couté Y, Frénel K, Tardieux I, Renesto P. The BCC7 Protein Contributes to the *Toxoplasma* Basal Pole by Interfacing between the MyoC Motor and the IMC Membrane Network. *International Journal of Molecular Sciences*. 2022; 23(11):5995. <https://doi.org/10.3390/ijms23115995>



Article

The BCC7 Protein Contributes to the *Toxoplasma* Basal Pole by Interfacing between the MyoC Motor and the IMC Membrane Network

Luis Vigetti ^{1,†}, Tatiana Labouré ^{1,†}, Chloé Roumégous ², Dominique Cannella ³, Bastien Touquet ¹, Claudine Mayer ^{4,5}, Yohann Couté ⁶, Karine Frénel ², Isabelle Tardieux ^{1,*} and Patricia Renesto ^{1,*}

- ¹ IAB, Team Biomechanics of Host-Apicomplexa Parasite, INSERM U1209, CNRS UMR5309, Grenoble Alpes University, 38700 Grenoble, France; luis.vigetti@univ-grenoble-alpes.fr (L.V.); tlaboure1998@gmail.com (T.L.); bastien.touquet@univ-grenoble-alpes.fr (B.T.)
- ² Université de Bordeaux, Team Microbiologie Fondamentale et Pathogénicité, CNRS UMR 5234, 33000 Bordeaux, France; roumegouschloe@gmail.com (C.R.); karine.frenel@u-bordeaux.fr (K.F.)
- ³ IAB, Team Host-Pathogen Interactions & Immunity to Infection, INSERM U1209, CNRS UMR5309, Grenoble Alpes University, 38700 Grenoble, France; dominique.cannella@univ-grenoble-alpes.fr
- ⁴ Université Paris Cité, 75013 Paris, France; claudine.mayer@unistra.fr
- ⁵ ICube-UMR7357, CSTB, Centre de Recherche en Biomédecine de Strasbourg, 67084 Strasbourg, France
- ⁶ INSERM, University of Grenoble Alpes, CEA, UMR BioSanté U1292, CNRS, CEA, FR2048, 38000 Grenoble, France; yohann.coute@cea.fr
- * Correspondence: isabelle.tardieux@inserm.fr (I.T.); patricia.renesto@univ-grenoble-alpes.fr (P.R.)
- † These authors contributed equally to this work.



Citation: Vigetti, L.; Labouré, T.; Roumégous, C.; Cannella, D.; Touquet, B.; Mayer, C.; Couté, Y.; Frénel, K.; Tardieux, I.; Renesto, P. The BCC7 Protein Contributes to the *Toxoplasma* Basal Pole by Interfacing between the MyoC Motor and the IMC Membrane Network. *Int. J. Mol. Sci.* **2022**, *23*, 5995. <https://doi.org/10.3390/ijms23115995>

Academic Editor: John Lucoq

Received: 21 April 2022

Accepted: 24 May 2022

Published: 26 May 2022

Publisher's Note: MDPI stays neutral with regard to jurisdictional claims in published maps and institutional affiliations.



Copyright: © 2022 by the authors. Licensee MDPI, Basel, Switzerland. This article is an open access article distributed under the terms and conditions of the Creative Commons Attribution (CC BY) license (<https://creativecommons.org/licenses/by/4.0/>).

Abstract: *T. gondii* is a eukaryotic parasite that has evolved a stage called tachyzoite which multiplies in host cells by producing two daughter cells internally. These nascent tachyzoites bud off their mother and repeat the division process until the expanding progenies escape to settle and multiply in other host cells. Over these intra- and extra-cellular phases, the tachyzoite maintains an essential apicobasal polarity that emerges through a unique bidirectional budding process of the elongating cells. This process requires the assembly of several molecular complexes that, at the nascent pole, encompass structural and myosin motor elements. To characterize a recently identified basal pole marker named BCC7 with respect to the posterior myosin J and myosin C motors, we used conventional biochemistry as well as advanced proteomic and in silico analysis in conjunction with live and super resolution microscopy of transgenic fluorescent tachyzoites. We document that BCC7 forms a ribbed ring below which myosin C motor entities distribute regularly. In addition, we identified—among 13 BCC7 putative partners—two novel and five known members of the inner membrane complex (IMC) family which ends at the apical side of the ring. Therefore, BCC7 could assist the stabilization of the IMC plaques and contribute to the parasite biomechanical properties.

Keywords: Apicomplexa parasites; *Toxoplasma gondii*; cell biogenesis; cell polarity; cytoskeleton; basal pole complex; inner membrane complex; myosin C; myosin J; proteomics; expansion microscopy; STED microscopy

1. Introduction

Toxoplasma gondii is an obligate intracellular protozoan parasite of a wide range of homeotherm animals worldwide. Following ingestion of host-to-host transmissible developmental stages called zoites, *T. gondii* reproduces asexually as either fast cycling and tissue-damaging tachyzoites, or as slow cycling and clinically quasi-silent bradyzoites in multiple cell lineages. Because of its ability to reversibly differentiate under tachyzoites and bradyzoites in deep and vital tissues of its hosts, *T. gondii* poses a significant health threat. In humans, ocular and cerebral toxoplasmosis are common recurrent and possibly life-threatening diseases of mostly—but not exclusively—immune-weakened individuals [1] while both also typifying congenital infection.

T. gondii belongs to the ancient phylum of Apicomplexa and shares with the other companion groups from the Alveolata infrakingdom, featuring a tri-lamellar pellicle outlining the cell [2] while a permanent apicobasal polarity also characterizes the *T. gondii* zoites. In addition to the plasma membrane bilayer, the pellicle encompasses the underneath inner membrane complex (IMC) [3] derived from flattened and fused vesicles identified as alveoli and made of a IMC and IMC-like protein's repertoire, yet to complete. In close juxtaposition to this pellicle is the sub-pellicular alveolin-rich cytoskeleton which lies on a basket of 22 strikingly stable but flexible subpellicular microtubules [4,5]. While the microtubule network emerges apically from an atypical microtubule organizing center termed polar ring and extends over the two-thirds of the cell length, the IMC starts with an apical cone-shaped plate and follows with a patchwork of longitudinally aligned plates down to near the posterior edge [6,7]. Therefore, neither the apical nor the basal conic poles are outlined by the multilayer cortex. Importantly, all these structural membranous and cytoskeletal elements maintain complex molecular interactions between each other and with associated proteins, and jointly, they provide enhanced mechanical strength and flexibility to the elliptical zoite [8].

Beyond the long-lasting interest for the structural organization and functional contribution of the zoite apical complex to the motile and invasive behaviors of extracellular zoites [9,10], an increasing number of studies have started to highlight the specific composition and architecture of the basal pole and to model its progressive fabrication during the development of new zoites inside the host cells [7,11–13]. Zoites multiply by endodyogeny, a process through which two daughter cells assemble their cortex and cytoskeleton *de novo* inside an intact mother prior to cytokinesis. The progenies eventually bud out of the mother cell by recycling material from the mother plasma membrane while they complete cytokinesis. Successive rounds of division lead to typical rosettes of polarized tachyzoites whose basal poles are centripetally clustered around the maternal residual body through which they continue to connect to each other. Early studies have pointed out a spatial and temporal coincident biogenesis of the two poles in the daughter cells which subsequently elongate in an apical-to-basal direction [2,9]. A combination of advanced proteomics and cell imaging has recently allowed not only arguing for a bi-directional rather than unidirectional daughter cell budding process, but also discriminating four protein complexes with selective sub-cellular localization and assembly kinetics at the basal pole.

T. gondii expresses 11 myosins that distribute across five classes of the myosin super-families (i.e., class VI, XIV, XXII, XXIII, XXIV) [14], for which specific subcellular location and functional contribution have been resolved in large part. The basal pole of tachyzoites contains the class VI MyoJ and the class XIV MyoC which arises from differential splicing of the myosinB/C gene, and both delineate rings whereas the class XXIV MyoI was shown to accumulate behind at the residual body center of mature rosettes. Using gene invalidation strategies, MyoJ has been assigned a dispensable and actin-dependent role in the otherwise critical late constriction step of the daughter cell basal pole; a process that folds the basal cap post-cytokinesis whereas MyoI was involved in preserving communication between daughter cells, a prerequisite for cell division synchronicity [15].

Therefore, the assembly of basal pole components—myosin motors included—directs the biogenesis of the posterior cup in the two polarized daughter cells while it ensures proper rosette organization. Yet, in free tachyzoites, the structural arrangement of these components must be compatible with the generation of biological forces, in particular related to contraction and torque. As such, one can think of the peculiar twisting motion executed by the free tachyzoite to terminate invasion within an intracellular growth permissive vacuole [16]. Given that myosin motors can twirl actin in both left-handed and right-handed helical paths in mammalian systems, one can hypothesize that the invading tachyzoite generates an actomyosin-based torque to power the twisting motion. In the same line, torques are frequently observed when the free tachyzoites twirl upright against the 2D surface being posteriorly attached to it. Active exit of posteriorly constricted mature tachyzoites out of the host cells is also associated with a torque applied on the maternal

residual body to free from it and individually undergo egress. Periodic contraction of the basal pole is also required for efficient traction force at the front to drive the typical tachyzoite helical motility [5]. Therefore, integrating how the myosin motors present at the basal pole could be efficiently anchored to scaffolding pieces of the basal pole—allowing the development of lateral forces or torques—would add to the understanding of the tachyzoite extracellular and intracellular life.

A proteomic analysis carried on a detergent-extracted subpellicular cytoskeleton fraction allowed identifying a 500 kDa protein encoded by TGGT1_311230 [17] which was subsequently selected in a Yeast two-hybrid (Y2H) screen with MORN1 as a bait [18] and therefore possibly involved in the shaping of the basal pole. We also identified this protein in a screen for *Toxoplasma* tachyzoite Histone Deacetylase 3 (HDAC3) substrate candidates and further invalidated its HDAC3 substrate potential, but we noticed the striking posterior localization of an epitope-tagged version of the protein. This *in situ* observation prompted us to map the protein position with respect to the posteriorly located myosins. In the course of our study, a BioID-based map of the basal complex (BC) proteome also picked up this protein as a basal complex component and named it as BCC7 [12,13]. Using a combination of biochemistry, co-immunoprecipitation coupled to mass spectrometry (MS)-based proteomics, and live and super resolution laser scanning microscopy, we now bring evidence for BCC7 positioned at the interface between a set of IMC proteins including two newly identified herein, and the MyoC motor. Similar to MyoC and the majority of IMCs studied so far, BCC7 was found dispensable for the tachyzoite lytic cycle, and in the same vein, the ultrastructural organization of the basal pole was not impacted in either resting or motile parasites lacking BCC7.

2. Results

2.1. BCC7, a Coccidia Restricted Protein with a Ring-Shaped Architecture Marking the Basal Pole of the *T. gondii* Tachyzoite

As indicated in ToxoDB [19], the TGGT1_311230 encodes a 4603 AA hypothetical protein of 494.8 kDa with a pI of 4.54 that harbors a N-terminal transmembrane domain. Identified as BCC7 in a previous proteomic analysis, this protein specifies the Coccidia within the Apicomplexa phylum but shows no structural homology or predicted functional association with any known proteins. However, the subcellular atlas of *T. gondii* tachyzoite proteins presumably assigned BCC7 to an IMC compartment based on a recent hyperLOPIT-based study [20]. We have now refined the amino acid sequence analysis by combining sequence composition analyses with Blast searches, which allowed highlighting 13 regions (Figure 1a). Each region was characterized by BLAST-hits, biased amino-acid composition, and degree of order/disorder. Two glutamic acid (E)-rich and a mix E/arginine (R)-rich (>25%) zones were identified. Four regions display significant BLAST hits for *T. gondii* sequences exclusively (residues 80–500) or for other Sarcocystidae including the *Neospora* and *Besnoitia* genera (residues 2530–3260 and 3260–3660). Interestingly, BCC7 appears intrinsically disordered except for a 730 aa in length domain (2530–3260) which is predicted as mainly ordered and might thus be folded. Bioinformatic analysis of BCC7 amino acid sequence also pointed out two VPV repeats (3340–3342; 3348–3350), the sequence of which is considered as a second repeat element that hallmarks alveolin proteins [21]. In addition, 129 phosphorylated amino-acid residues have been detected by phospho-proteomic analysis and the large majority (86%) of target serine in the C-terminal region along with four ubiquitin-binding sites that cluster at the extreme C-terminus of BCC7 (positions 4048, 4339, 4507, and 4461) (Table S1).

To biochemically characterize this potentially membrane spanning and IMC-related BCC7 product, we conducted a series of sub-fractionation assays taking advantage of the tachyzoite line expressing a BCC7-HA-FLAG chimera at the endogenous locus. We first confirmed the Triton X-100 (TX-100) insoluble property of the BCC7 fusion protein in agreement with what has been described for the endogenous protein [17]. We then refined the extraction conditions to optimize protein recovery. Because proteins embedded

in the IMC network to which BCC7 has been associated [20] were described as highly resistant to the detergents commonly used for membrane protein extraction [9,22,23], we analyzed the partitioning of BCC7-HA-FLAG under different solubilization conditions using Western blot and anti-HA antibodies. BCC7-HA-FLAG was found fully insoluble in the high salt BC500 lysis buffer containing NP40 (0.05% *v/v*) or in BC500 supplemented with DDM (0.1% *w/v*). In contrast, a significant amount of protein was recovered in the soluble fraction using the zwitterionic neutral Empigen BB (1% *v/v*) or sulfobetaine 3–14 (n-Tetradecyl-N,N-dimethyl-3-ammonio-1-propanesulfonate) (1% *w/v*) as well as the anionic N-lauryl sarcoside (0.1% *w/v*). It is worth noting that the Empigen-BB was the most efficient at solubilizing BCC7-HA-FLAG (Figure 1b). Although the migration in SDS-PAGE 4–12% gradient gels of BCC7 did not seem to depend on the detergent used and the solubility or insolubility status (Figure S4), we observed some variability in the migration pattern between experiments with products migrating faster but only one band was always observed arguing for a full-length product.

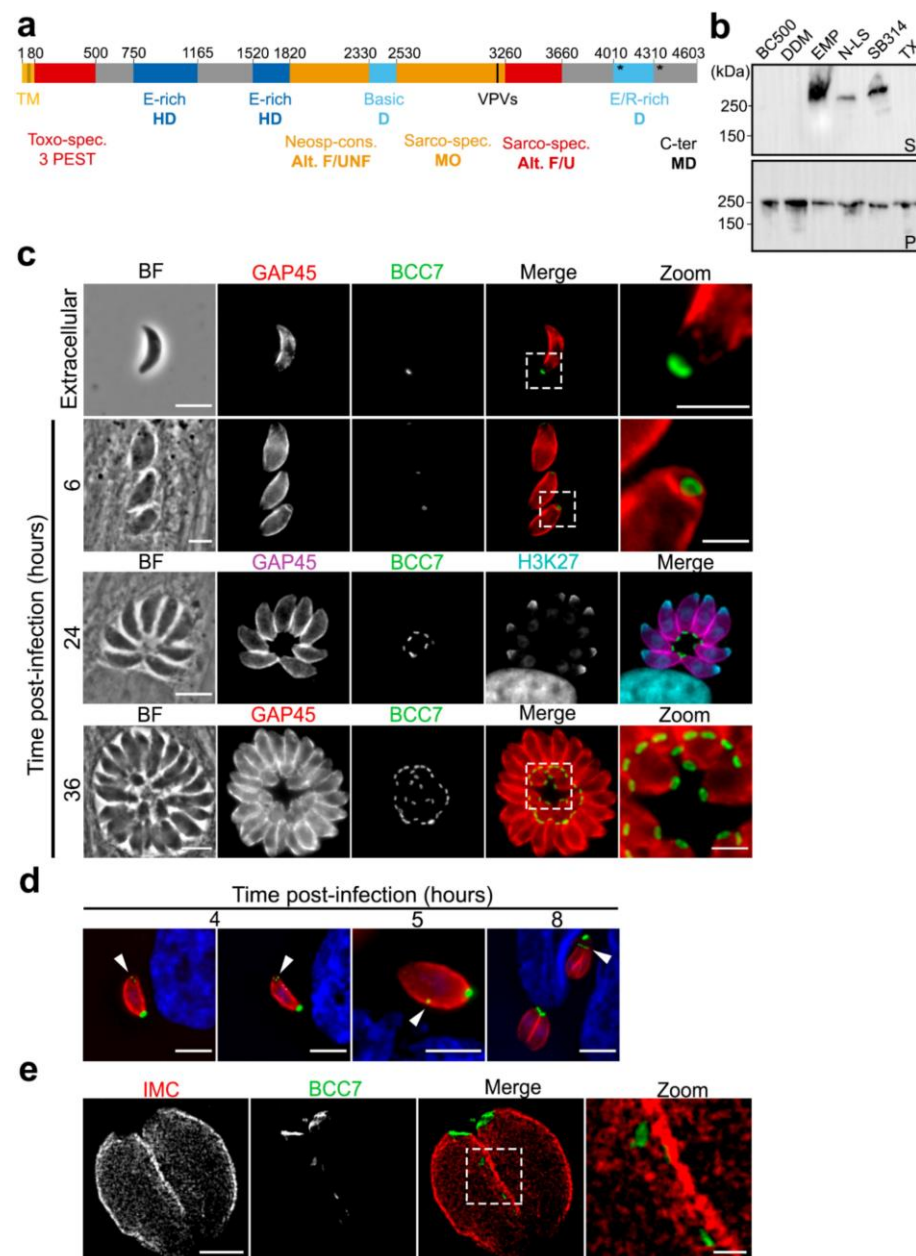


Figure 1. Main features of the *T. gondii* BCC7 protein. (a) Schematic representation of the BCC7 primary

sequence based on predictive analysis. Thirteen regions were discriminated. TM, predicted transmembrane helix (residues 35–57); PEST, proline (P), glutamic acid (E), serine (S), and threonine (T) residues. In blue, regions with biased composition; in red and orange, regions conserved in *Toxoplasma* or other *Sarcocystidae* and which could be partially folded; in grey, other regions. Toxo-spec: *T. gondii* specific domain; Neosp-cons.: Neospora conserved domain; Sarco-spec: Sarcocystidae specific domain. Alt. F/UNF, Alternated Folded/UNFolded; D, Disordered; HD, highly disordered; MO, mainly ordered domains. Glutamic acid represents 26.8% of the amino-acids in the (750–1165) E-rich region and 26.3% in the (1520–1820) region. Arginine and lysine together account for 23.8% of the amino-acids of the (2330–2530) basic region while arginine and glutamic acid account for 26.6% of the E/R-rich region. The sarco-specific region includes an aromatic-rich region, and the black bar denotes 2 VPV (3340–3342 and 3348–3350) (V: valine, P: proline) repeats. * denotes ubiquitin sites at positions 4048, 4339, 4461 and 4507. (b) Analysis of the BCC7-HA-FLAG solubility from transgenic tachyzoites under different detergent conditions. BC500: control lysis buffer containing NP40 (0.05% v/v); DDM: BC500 supplemented with n-Dodecyl- β -D-maltopyranoside (0.1% w/v); EMP: Empigen BB (1% v/v); N-LS: N-lauryl sarcoside (0.1% w/v); SB314: sulfobetaine 3–14 (n-Tetradecyl-N,N-dimethyl-3-ammonio-1-propanesulfonate) (1% w/v); TX: Triton X-100 (0.1% v/v). Soluble (S, upper panel) and insoluble fractions (P, lower panel) from each lysate were resolved on SDS-PAGE and analyzed by Western blot using monoclonal rabbit anti-HA antibodies. The molecular weights are indicated in kiloDaltons (kDa). This figure is representative of two distinct experiments. (c) In situ fluorescence-based detection of BCC7-mEm in transgenic extracellular and intracellular dividing tachyzoites reveals a ring-like organization at the basal pole. The glideosome protein GAP45 is immunostained (red or purple) to visualize the parasite periphery; the apical pole and nucleus were visualized by immunostaining of tri-methylated H3K27 residues (blue) that mark the nucleus and apical cap of the parasites [24]. Scale bars: 5 μ m; for zoomed areas: 2 μ m. (d) In situ fluorescence-based detection of BCC7-mEm highlights the apical pools (4 h post invasion), lateral peripheral pools (5 h post invasion) and the enrichment at the growing end of daughter cells together with the basal pool of the mother cell (white arrowhead). The tachyzoite GAP45 is immunolabeled (red). Scale bar: 5 μ m. (e) STED imaging of transgenic tachyzoites co-expressing BCC7-mEm and IMC-mC after immunostaining with anti-GFP antibodies (secondary antibodies conjugated to STAR Orange, green), anti-mC antibodies (secondary antibodies conjugated to STAR Red, red). Note the BCC7-mEm small pools along the IMC network and at the ring at the basal pole of dividing parasites. Movie S2 corresponds to the 3D reconstruction of this sequence. Scale bar: 2 μ m; for zoomed area: 500 nm.

Next, in order to obtain in situ insights on the BCC7 distribution in tachyzoites, we generated parasites stably expressing various fluorescent- and epitope-tagged versions of BCC7 after insertion at the endogenous locus. The BCC7-mEmerald (mEm) expressing tachyzoites unambiguously delineated a ring that positioned near the edge of the basal pole of both intracellular and extracellular samples (Figure 1c). The same posterior location and circular shape were observed for tachyzoites expressing a BCC7-mCherry (mC) version or when using anti-HA antibodies to detect the chimeric BCC7-HA-FLAG protein (Figure S1). To document the dynamics of fluorescent BCC7 in cycling tachyzoites at a high spatial resolution, HFF cells were infected with BCC7-mEm tachyzoites which provided the brightest direct fluorescent BCC7 signal. Following a 30 min period of contact between freshly egressed tachyzoites and HFF monolayers, the non-internalized parasites were removed and the development of the internalized ones was further monitored. Within two to four hours post invasion, we observed newly synthesized BCC7-mEm pools at the very front of the tachyzoite where the IMC emerges with a symmetrical pair or triad dot pattern. With time, BCC7-mEm pools were detected slightly more posteriorly, shaping peripheral successive dots or elongated spots (e.g., possibly merging dots) along the cell edge nearby the IMC, a pattern suggesting trafficking features (Figure 1d, see arrows). This multiple dot-like localization recalls the one reported for the canonical marker of the posterior cup at the extreme basis of mature tachyzoites, namely centrin2 (CEN2) which was also detected at the polar ring and peripheral annuli during the interphase [9,11]. Similar to CEN2 but also

to MORN1, another canonical marker of the basal complex, we occasionally detected BCC7-mEm in close juxtaposition of the nucleus apical side but we did not see signals nearby the duplicated centriole as typically observed for CEN2 [11]. When each budding daughter cell has then synchronously extended their IMC posteriorly, BCC7-mEm pools were detected as forming individual rings at the nascent basal pole of each progeny similarly to what is known for MORN1, and these rings progressively gained in signal intensity suggesting addition of material (Figure 1c). To reach better resolution of BCC7-mEm in intracellular tachyzoites, we used STimulated Emission Depletion (STED) microscopy and confirmed the travelling of BCC7 pools along the peripheral IMC network at a 25 nm resolution, as well as their integration in the basal pole of each daughter cell (Figure 1e). Next, to monitor in live the dynamics of the BCC7 trafficking during endodyogeny, we video-recorded BCC7-mEm signal with respect to the tachyzoite nucleus over several rounds of cell cycle, which highlights the BCC7 apicobasal trafficking. Live imaging also indicated that the two BCC7-mEm de novo pools which assemble into rings at the cytoskeleton base of the budding daughters can integrate some maternal BCC7 product at the latest step, thereby suggesting that both de novo synthesis and recycling could contribute to the BCC7 found at the basal cap of mature tachyzoites (Figure 1d and Movie S1).

2.2. Super Resolution Microscopy Highlights the Close Proximity between MyoC and BCC7

To assess the position of BCC7 with respect to actomyosin motors known to assemble as a ring at the basal complex, namely MyoC and MyoJ, we imaged tachyzoites co-expressing either BCC7 HA-Flag and MyoC-YFP, BCC7-mC and MyoC-YFP, or BCC7- HA-Flag and MyoJ-mC. Using widefield fluorescence microscopy coupled to structured illumination through the Apotome module, we observed for both extracellular and intracellular tachyzoites that the MyoC-YFP signals were overlapping those from either the immuno-fluorescently labeled BCC7-HA-Flag or the fluorescent BCC7-mC products (Figure 2a and Figure S2a). By contrast, the 4.54 pixel size of the camera allowed detecting two apposed but separate fluorescent signals when BCC7-HA-Flag was co-detected with MyoJ-mC (Figure S2b). To better map the relative position of the BCC7 and MyoC proteins, we embedded samples in swellable hydrogels and processed them for an isotropic mechanical expansion following recently developed protocols of the so-called expansion microscopy (proExM) [25]. Under these isotropic expansion conditions (which allowed a linear estimated 4X expansion), and using a 6.5 μm pixel size CMOS Prime camera, we increased the resolution up to about 70 nm and were indeed able to discriminate the two molecular species, hence to position MyoC just below the BCC7 ring as attested by the more central nucleus location (Figure 2b). Moreover, when we applied the Airyscan technique to improve signal to noise ration and resolution on the proExM gel sample, we gained descriptive information with a regular distribution of MyoC elements around the continuous circular BCC7 signal (Figure 2c). This in-depth imaging analysis argues for a close physical partnership between the motor and BCC7. Of note, well-defined rings of MyoC were detected in the assembling daughter cells coinciding with BCC7 signals, in line with a spatially co-assembly process (Figure 2a bottom panel, Figure 2d).

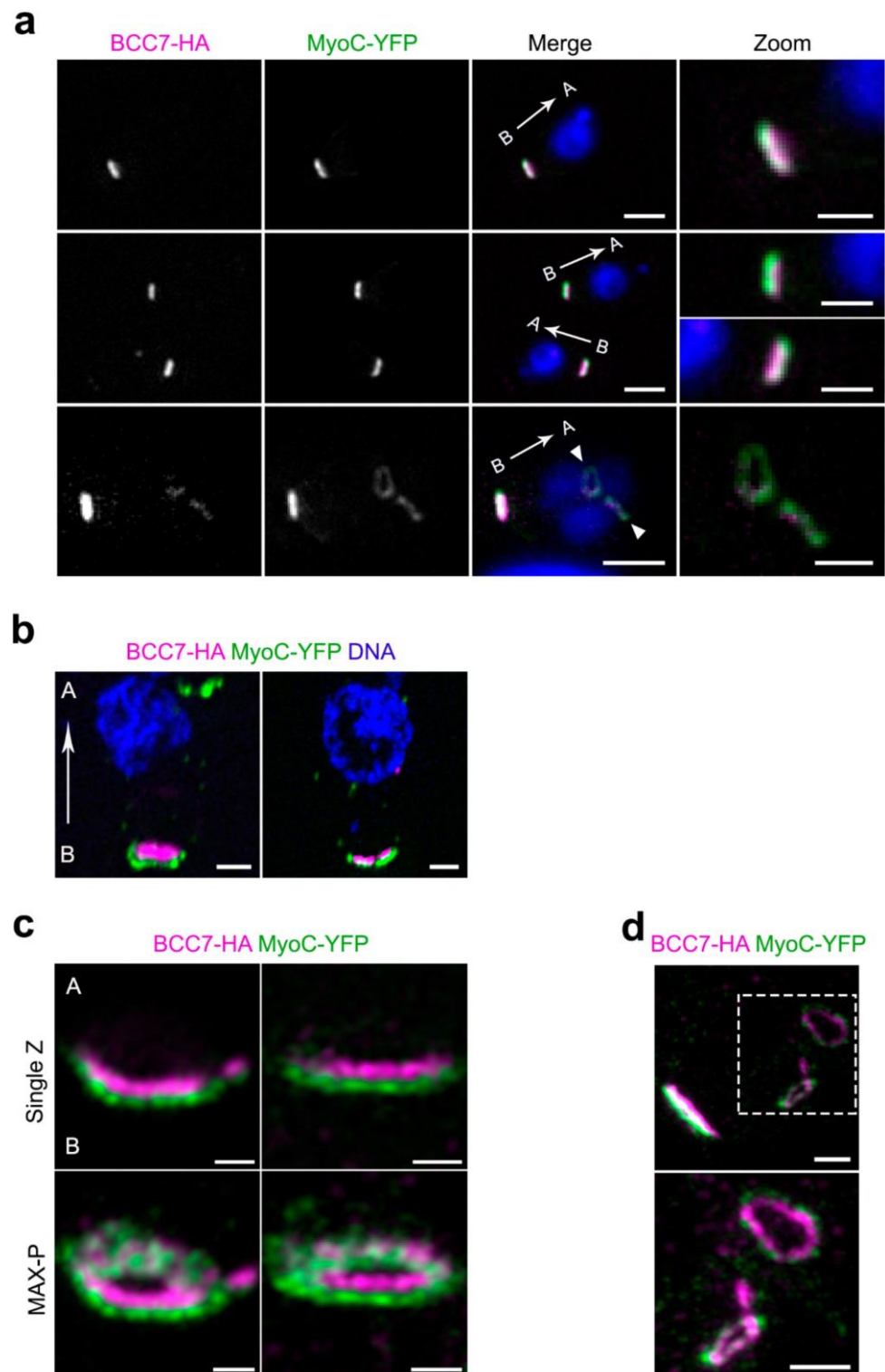


Figure 2. Localization of BCC7 with respect of the actomyosin motor MyoC. (a) HFF monolayers were infected with tachyzoites expressing BCC7-HA (magenta) and MyoC-YFP (green) tagged proteins. Following immuno-(anti-HA) and DAPI (blue) staining, image were acquired (Zeiss ApoTome.2 microscope). At this resolution, the signal from each proteins quasi overlap. White arrows show apicobasal orientation. White arrowheads mark the progeny (bottom panel). A: apex, B: base. Scale bar: 2 μ m, zoom 1 μ m. (b) Extracellular parasites expressing BCC7-HA (magenta) and MyoC-YFP

(green) tagged proteins. Cells were immunostained and expanded using proExM before image acquisition (Eclipse Ti inverted confocal microscope). Note that BCC7 and MyoC can be distinguished from each other. White arrow shows apicobasal orientation. A: apex, B: base. Scale bar: 0.2 μm . **(c)** HFF monolayers were infected with tachyzoites expressing BCC7-HA (magenta) and MyoC-YFP (green) tagged proteins. Images from proExM-treated samples were acquired using Zeiss AxioImager M2 with Airyscan detector. Note the gain in resolution for the relative localization of MyoC and BCC7 in the basal pole. A: apex; B: base. Maximal projections (MAX-P) are shown in the bottom panels. Scale bar: 0.2 μm . **(d)** Dividing tachyzoites in samples from (c) show presence of MyoC and BCC7 ring-shaped signals in the budding daughter cells. Zoom is shown in bottom panel. Scale bars: 0.5 μm .

2.3. The BCC7 Protein Is Dispensable for the Tachyzoite Extracellular and Intracellular Lifestyle

Considering the large size and the position of BCC7 relative to the MyoJ and MyoC motors, we wanted to check whether mutants devoid of BCC7 would have impaired actomyosin-dependent critical behaviors (e.g., motile, replicative, and invasive abilities). To this end, we generated an inducible mutant of BCC7 using the auxin-inducible degron (AID) system proved to drive the specific and conditional depletion of a target protein in presence of auxin (indoleacetic acid, IAA) [26] (Figure S3). Indeed, when the HFF monolayer was loaded with BCC7-mAID-3HA mutants and further incubated with IAA for 40 h, the BCC7-HA tag became undetectable under IF conditions, arguing for an efficient depletion of BCC7. It is noteworthy that the BCC7 altered neither the daughter cell assembly process including its polar orientation nor the development of rosette-like structures (Figure 3a). Using real time confocal microscopy, we next monitored the motile behavior of both wild-type and mutant tachyzoite populations. The tachyzoites for which BCC7 was undetectable remained typically organized in rosettes within a parasitophorous vacuole which dismantled upon active egress of the BCC7-depleted progenies, this with indistinguishable features from the sequences recorded with BCC7 expressing tachyzoites. Similarly, newly egressed BCC7 mutants displayed typical wild-type circular and helical gliding modes of motility as well as twirling behavior (Figure 3b, Movies S3 and S4). The absence of apparent defects of motile, replicative, and invasive behaviors in vitro was recapitulated by the similar surface of HFF destruction as a result of the wild-type and mutant tachyzoite 'lytic cycle' using typical plaque assays over a 7-day period (Figure 3c). To then check for any ultrastructural change at the cell surface in particular at the basal pole that would be driven by the lack of BCC7, we applied scanning electron microscopy on wild-type and mutant tachyzoite samples. Focusing on resting (e.g., conoid retracted) but also gliding tachyzoites (e.g., as attested by both the apical flexure [5] and the trail left behind), we could appreciate the significant stretching of the basal pole that elongates as a thin elastic cone in gliding tachyzoites when compared to no gliding ones, but this occurred regardless of BCC7 expression (Figure 3d,e). Collectively, despite the large size of BCC7, these results argue for a dispensable BCC7 contribution to the biogenesis of a functional basal pole and consequently for the perpetuation of tachyzoites in vitro, in line with the fitness score retrieved in a genome-wide knock out CRISPR screen [27].

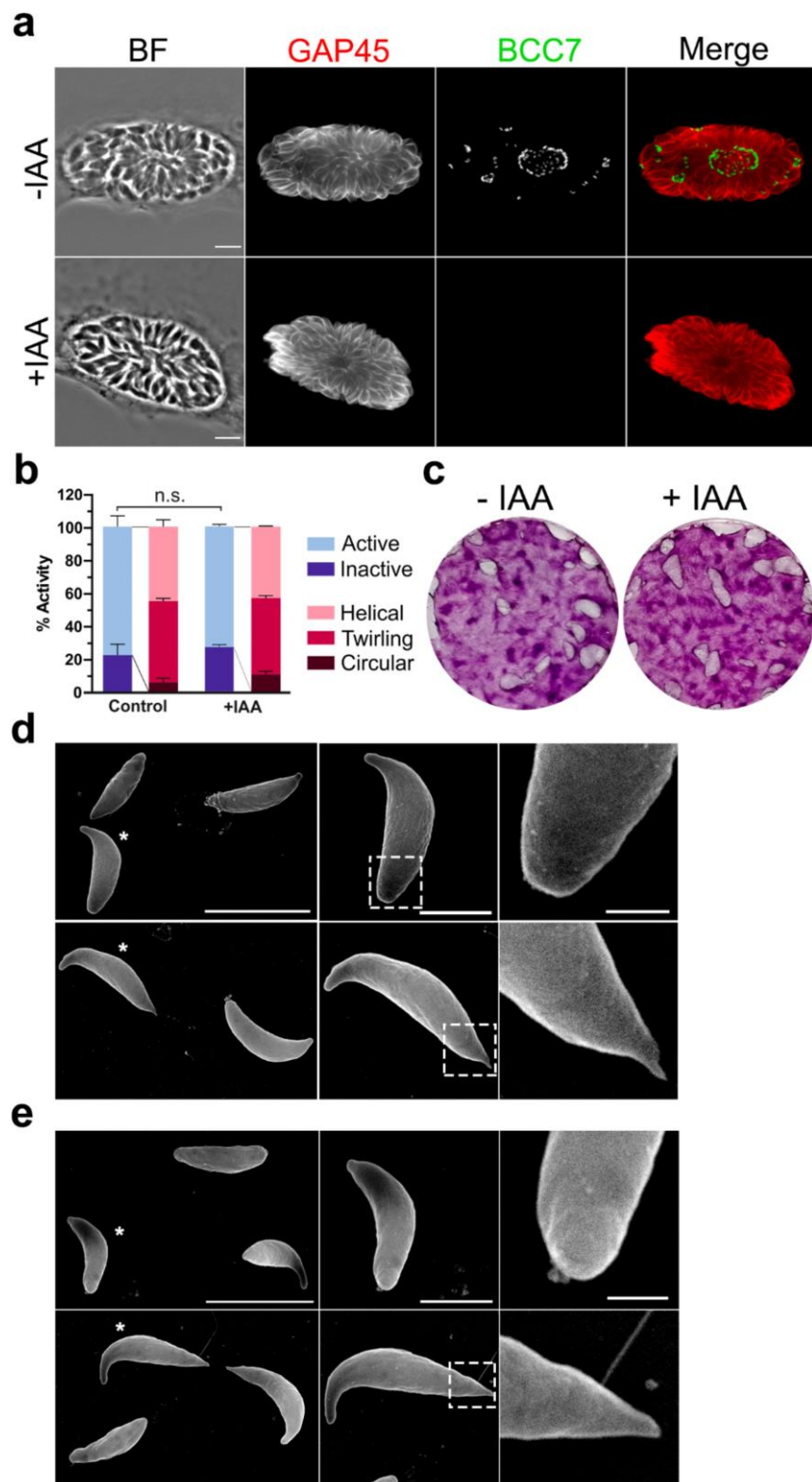


Figure 3. BCC7 is dispensable for the tachyzoite lytic cycle in vitro and does not impact on the ultrastructural organization of the basal pole surface. (a) RH_BCC7-mAID-3HA/MyoJ-2TY parasites grown in HFF cells for 48 h ± 500 μM IAA and fixed just before egress (see Movies S3 and S4). BCC7 depletion was evidenced by HA-immunostaining. No differences in the rate of progeny growing or organization as assessed by GAP45 immunostaining (red), and nuclei DAPI stain in BCC7 wild-type and BCC7-depleted parasites. Scale bar: 5 μm. (b) Graph showing no significant differences in the

percentage of active and/or gliding BCC7 wild-type and depleted tachyzoite upon egress from the vacuole. Quantification was performed on the Movies S3 and S4 (mean \pm Standard Error of the Mean (SEM), unpaired *t*-test followed by Holm–Sidak comparisons method, *n* = 166–313 parasites from 2–3 separate experiments, n.s.: non-significant, *p*-value = 0.622399). (c) Plaque formation in HFF monolayers over a 7-day infection. Relative size of the plaques showed no significant differences between BCC7 wild-type and BCC7 depleted parasites. These images are representatives of three different experiments. (d,e) Scanning Electron Microscopy (SEM) images of RH_BCC7-mAID-3HA. BCC7 expressing (d) or BCC7-depleted (e) extracellular tachyzoites did not show major ultrastructural differences of their basal pole regardless of their resting tachyzoites or acting status. SEM field overview on the left, zoom on the parasite selected with an asterisk (middle column), and a second zoom on the parasite's basal pole (pointed square, right column). Scale bars: left: 5 μ m; middle: 2 μ m; right: 500 nm.

2.4. Identification of Putative BCC7-Interacting Partners by Co-Immunoprecipitation Coupled to Mass Spectrometry Analysis

Considering the highest yield of BCC7-HA-FLAG recovered with Empigen BB and the capacity of this zwitterionic detergent to preserve antigenicity of solubilized proteins [28], the latter was subsequently used for co-immunoprecipitation experiments. To obtain a BCC7-HA-FLAG enriched extract, a two-step subcellular fractionation method based on sequential lysis was applied. A first lysis step was carried with the non-ionic detergent TX-100 (1%, *v/v*), and allowed the release of many cytosolic proteins including a significant fraction of the MyoA motor known to be mainly housed within the pellicle space [29]. As expected, these conditions did not allow solubilizing BCC7-HA-FLAG (Figure 1b and Figure S4a), and we applied a second extraction step by adding Empigen BB (at the concentration defined previously, see Figure 1b) to the BCC7-HA-FLAG positive TX-100 insoluble fraction. After clarification of the lysate, the soluble extract was enriched in BCC7-HA-FLAG and could therefore be subjected to immunoprecipitation with anti-FLAG[®] M2 antibodies covalently linked to agarose beads. While the solubilized BCC7-HA-FLAG pool was entirely immobilized on the anti-FLAG agarose under the experimental conditions, it was subsequently recovered in the two first eluate fractions collected after competitive elution with FLAG peptides (Figure S4b). Having set the right conditions to capture BCC7-HA-FLAG from tachyzoite extracts, we could upscale the assays in order to identify putative partners of BCC7-HA-FLAG. To this end, three replicates of this co-immunoprecipitation procedure were performed using in parallel the BCC7-HA-FLAG-expressing *T. gondii* line and the parental one (RH Δ ku80) which served as control. For both types, the eluate samples were pooled and processed for MS-based quantitative proteomics. Comparative statistical analysis allowed ranking of 13 *Toxoplasma* proteins that were significantly enriched (four-fold) in the BCC7-HA-FLAG eluates as compared to controls, among which several IMC proteins (Table 1). Aside from the already identified IMC7, IMC10, IMC12, IMC18, and IMC24, three other proteins annotated as hypothetical proteins and encoded by TGGT1_230160 (Partner 8), TGGT1_236950 (Partner 9), and TGGT1_231160 (Partner 13 untagged) have been captured in our screen and have previously been putatively assigned to the IMC subcellular compartment after their endogenous tagging [20]. The list also includes the SAG-Related Sequence SRS29A protein (TGGT1_233450), a surface-exposed protein from the SAG glycoprotein superfamily [30] and TgZFP2 (TGGT1_212260; Partner 6). TgZFP2 is zinc-finger protein with features of a cytoskeleton-associated protein which has been reported essential for parasite survival [31]. Two additional putative BCC7-HA-FLAG partners were identified as a 155 kDa protein of unknown function and localization (TGGT1_230940; Partner 3), and a nuclear FUSE-binding protein 2 (TGGT1_216670; Partner 7), both proteins being predicted a high contribution to parasite fitness [27]. The last BCC7-HA-FLAG partner candidate is one hypothetical protein that has not yet been assigned to any sub-cellular compartment (TGGT1_315610; Partner 12).

Table 1. List of putative BCC7-binding proteins identified by co-IP coupled to MS-based proteomics. Identity of proteins was assigned by ToxoDB [19] unless specified (*) and their subcellular location was determined by Hyper Lopit approach [20]. Parasite fitness during the lytic cycle was evaluated from the genome-wide CRISPR screen [27].

| Partner | TGGT1 Accession Number | Description | MW (kDa) | Proteomic Data | | Subcellular Location | Phenotype Score |
|---------|---------------------------|-----------------------------|-------------|----------------|-----------------------|-----------------------|--------------------|
| | | | | Log2FC | p-Value | | |
| - | 311230 | BCC7 | 494.8 | 8.71 | 2.68×10^{-7} | unknown | 0.74 |
| 1 | 222220 | IMC7 | 46.8 | 3.44 | 1.96×10^{-3} | IMC | -0.64 |
| 2 | 258470 | IMC24 [32] | 31.7 | 3.26 | 1.10×10^{-3} | IMC | 2.12 |
| 3 | 230940 | hypothetical protein | 155.2 | 2.95 | 7.63×10^{-3} | unknown | -4.92 |
| 4 | 233450 | SAG-related sequence SRS29A | 44.2 | 2.71 | 4.61×10^{-4} | PM-peripheral 1 | 2.42 |
| 5 | 248700 | IMC12 | 29.8 | 2.38 | 6.88×10^{-3} | IMC | -0.17 |
| 6 | 212260 | TgZFP2 [33] | 38 | 2.47 | 4.11×10^{-2} | unknown | -4.5 |
| 7 | 216670 | FUSE-binding protein 2 | 100 | 2.19 | 4.86×10^{-2} | nucleus-non chromatin | -3.31 |
| 8 | 230160 | hypothetical protein | 15.8 | 2.19 | 1.54×10^{-2} | IMC | 2.11 |
| 9 | 236950 | hypothetical protein | 12.5 | 2.13 | 1.07×10^{-2} | IMC | 0.96 |
| 10 | 230210 | IMC10 | 61.2 | 2.05 | 1.19×10^{-2} | IMC | -4.7 |
| 11 | 295360 | IMC18 [32] | 29.6 | 2.00 | 1.45×10^{-2} | IMC | 1.13 |
| 12 | 315610 | hypothetical protein | 15.9 | 2.67 | 8.17×10^{-4} | unknown | 1.33 |
| 13 | 231160 | hypothetical protein | 18.3 | 2.41 | 3.11×10^{-3} | IMC | -1.6 |

2.5. A Majority of IMC Proteins, Including Two New Ones Were Identified in the BCC7-Binding Protein Screen

To characterize the putative BCC7-HA-FLAG partners in situ, we engineered a series of lines that co-express BCC7-mEm and a mCherry(mC)- or myc-tagged given target in the RHΔku80 background strain. As observed in Figure 4, the five IMC-mC fusion proteins (e.g., IMC7, IMC10, IMC12, IMC18, and IMC24) showed a typical IMC peripheric sub-membranous distribution [32,34], thereby attesting to the functionality of the given fusion protein. It is worth noting that, while these IMC-mC fusions ran up to just above the BCC7 ring, only the IMC10 was detected into the growing cytoskeletons of nascent daughter cells (Figure 4, Movie S5). Outside from the IMCs, the TgZFP2 zinc finger protein (Partner 6) reported to critically assist daughter cell budding through a partnership with the cytoskeleton [33], shows a punctate cytoplasmic distribution intracellular tachyzoites (Figure S5). Notably, previous attempts to identify putative molecular partners of this protein have remained unsuccessful [33]. In contrast with a predicted nuclear localization, the protein encoded by TGGT1_216670 (Partner 7) and annotated as FUSE-binding protein 2/KH-type splicing regulatory protein was observed dispersed in the tachyzoite cytoplasm when expressed as a chimera with the mCherry protein (Figure S5). Partner 3 is a protein of unknown function with no current assignment to any compartment, and while we failed to generate a mCherry fusion version of the protein, we succeeded in producing tachyzoites stably expressing the myc-tagged Partner 3. Using anti-myc antibodies, we detected a cytoplasmic localization with a patchy distribution (Figure S5). Finally, the Partner 12 (TGGT1_315610) without assigned sub-localization, was found to be nucleus associated when tachyzoites expressed either mCherry or HA tags (Figure S5). We remained unsuccessful at generating a transgenic parasite line expressing the endogenously SRS29A-tagged SAG-Related Sequence protein which, given its high immunogenicity [30] and predicted localization [20], is likely to be exposed at the tachyzoite plasma membrane.

Specific attention has been given to two other BCC7-putative partners, namely Partners 8 (TGGT1_230160) and 9 (TGGT1_236950) that are conserved across the phylum of Apicomplexa and have been classified as dispensable [27]. Both displayed an IMC-like localization when expressed as mCherry fluorescent versions (Figure 5a,b), in agreement with their predictive assignment as IMC proteins [20]. To the best of our knowledge, the last IMC protein identified in *T. gondii* is IMC34 [35]. Accordingly, we propose to name Partner 8 and Partner 9 as IMC35 and IMC36, respectively. When image resolution reached 25 nm owing to STED microscopy, we could visualize not only the relative position of the IMC35 with respect to the underlying microtubule regular network with the IMC35 grid-like signal distribution, but also the very close proximity between the BCC7-mEm ring and IMC35

(Figure 5c). Remarkably, with this resolution, the BCC7 ring appears ribbed with grooves while small claws of BCC7 material could be seen facing up the IMCs, here exemplified with the IMC35 and IMC18, and these could possibly contribute to the firm attachment of the IMC basal plaques (Figure 5c,d). Finally, to gain some insights on the dynamics of these novel IMC proteins, we monitored their expression pattern using high-resolution live-cell imaging. We observed that expression and localization of both IMC35 and IMC36 are cell cycle regulated, which fits with the typical transcriptional [36] and protein expression profiles [3,37,38] of several IMCs. Periodic fluctuations in the fluorescent signal intensity of both IMC35-mC and IMC36-mC-expressing tachyzoites were observed during intracellular multiplication with a progressive increase in expression and in pellicle association, along with the late steps of daughter cell formation. Indeed, no labeling of budding progeny that would sign for an early integration of the protein into the nascent cytoskeleton of the daughter cells has been detected. In addition, the IMC35-mC and IMC36-mC kept a strong fluorescent IMC pattern in extracellular parasites as observed post egress using live and static microscopy (Movies S6 and S7; Figure 5).

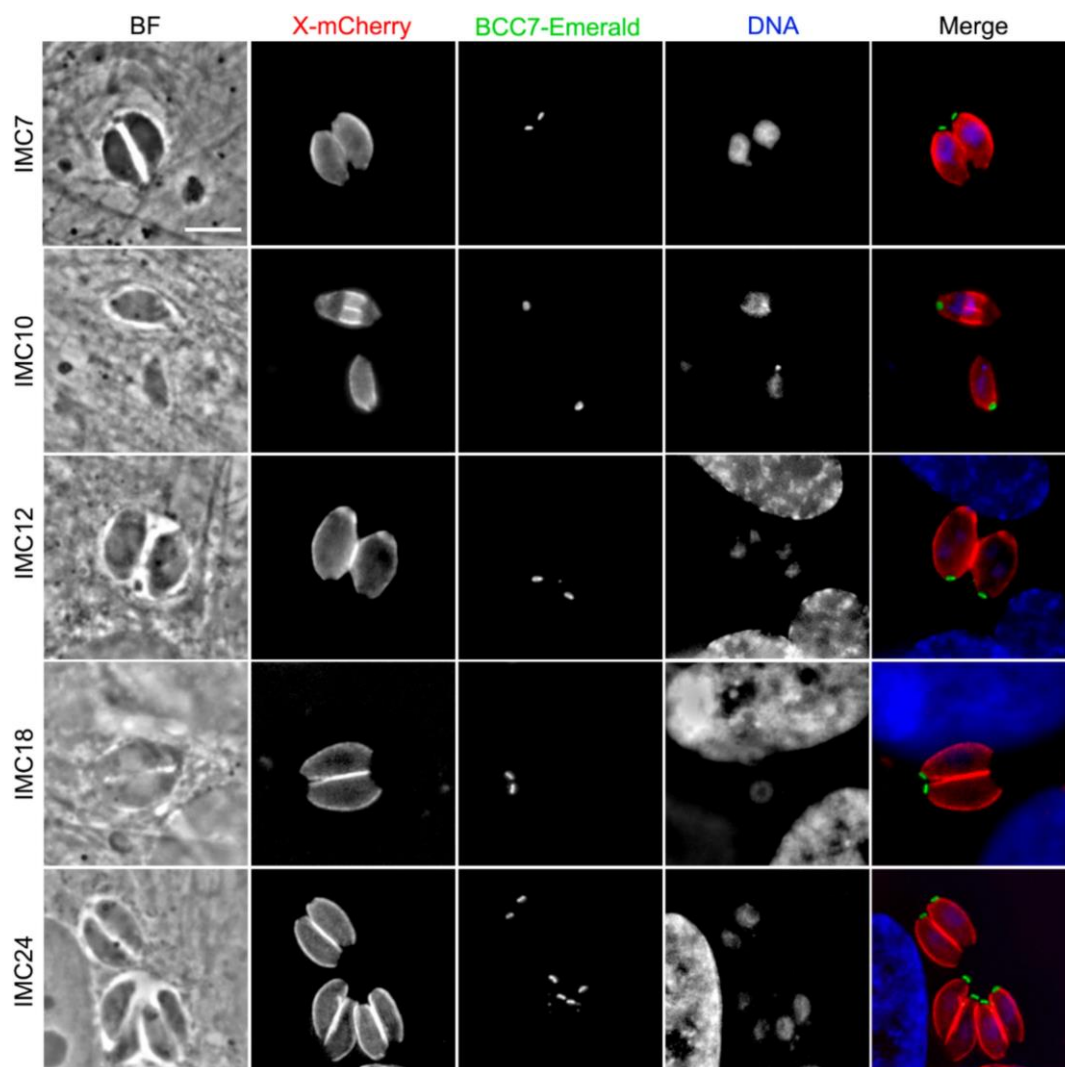


Figure 4. Images of IMC proteins identified in this study as putative BCC7-binding proteins. HFF monolayers were infected with freshly egressed parasites expressing endogenously fused BCC7-mEm (green) and IMC-mC tagged proteins (red). Samples were fixed and stained with DAPI (blue) before image acquisition (ZEISS ApoTome.2 microscope). The elongating IMC from the budding progeny contains IMC10. Scale bar, 5 μ m.

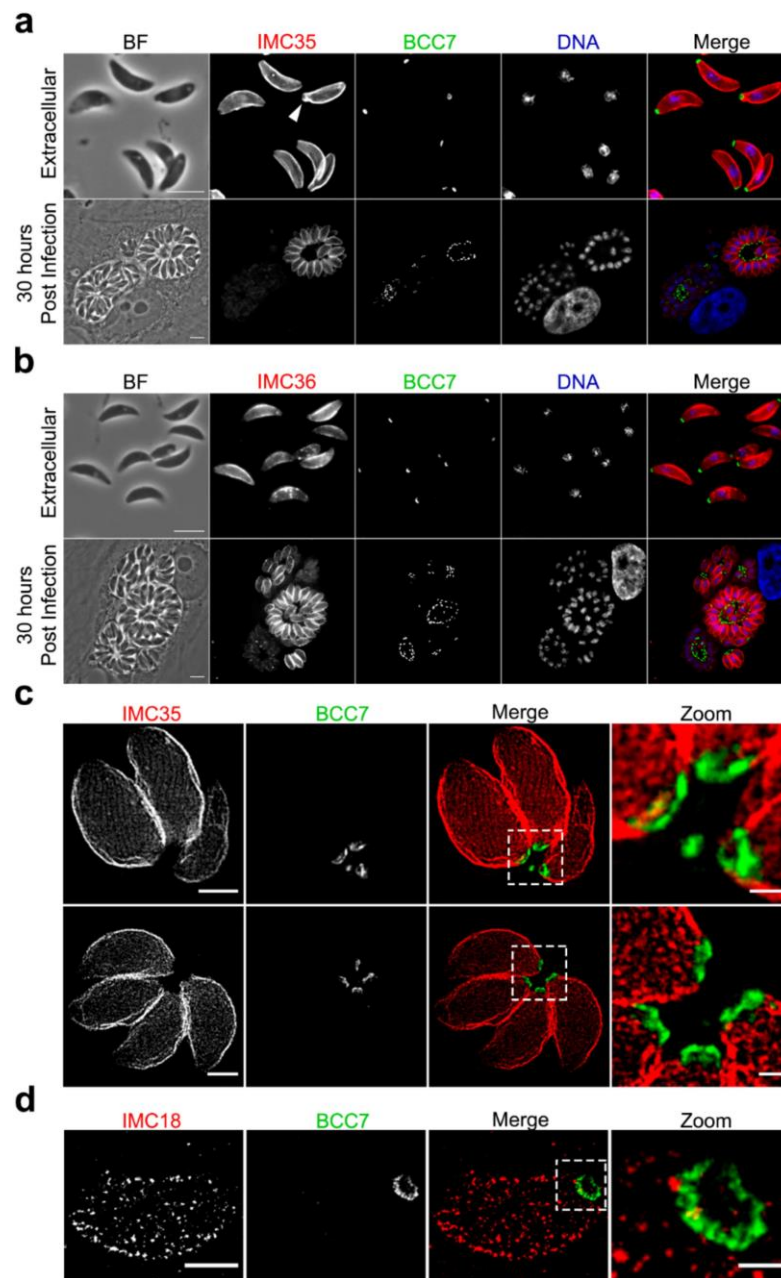


Figure 5. Cell-cycle-dependent expression of IMC35 and IMC36. Parasites expressing endogenously fused BCC7-mEm (green) and IMC35-mC (a) or IMC36-mC (b) proteins (red) were fixed and stained with DAPI (blue) before images acquisition (ZEISS ApoTome.2 microscope). Different steps of the division process were observed as indicated. IMC35 showed a continuity with the BCC7 ring structure on extracellular parasites (white arrowhead). Scale bars: 5 μ m. (c) STED imaging of tachyzoites co-expressing BCC7-mEm and IMC35-mC and immunostained with anti-GFP and anti-mCherry antibodies respectively. Appropriate secondary antibodies conjugated to either Abberior STAR Orange (BCC7-mEm, green) or Abberior STAR Red (IMC35-mC, red) were used. Note the pattern alignment of IMC35 with the microtubule basket orientation and the spatial proximity between IMC35-mC and BCC7-mEm at the basal pole. (d) STED imaging of a rosette of intracellular parasites expressing endogenously fused BCC7-mEm and IMC36-mC using the same staining as in (c). Scale bars for (c,d): 2 μ m; for zoomed areas: 500 nm.

3. Discussion

Toxoplasma zoites acquire a typical polar architecture as early as it assembles within a mother cell while undergoing a peculiar mode of division referred as to endodyogeny. Most of our knowledge concerning how polar ends form in nascent progenies has been gained on the *T. gondii* tachyzoite developmental stage taking advantage of both its fast-cycling properties in most mammalian host cells and its genetic tractability. Indeed, pioneering studies have uncovered that the daughter cells emerge with the simultaneous de novo building of the apical and basal complexes nearby the duplicated centriole at the apical side of the mother nucleus [9,11]. In this study, we focused on the basal complex known as a dynamic structure made of several ring-like protein arrangements that caps posteriorly, thereby limiting the elongating daughter cells. An essential myosin-J dependent constriction of the basal complex allows shaping of the definitive basal compartment of the mature progenies [15]. While significant progress has been made in the inventory and in situ relative mapping of main molecular elements of the basal complex, a comprehensive understanding of the basal pole functional properties is still uncompleted. How do the endodyogeny mechanisms lead to the emergence of progenies of roughly the same size from generation to generation inside the expanding intracellular vacuole remain mysterious. Moreover, free from the subpellicular microtubule scaffold but enriched in actin filaments and myosin motors, the basal pole of mature tachyzoites has shown great elasticity, a property that supports the periodic extension and contraction cycles of the basal pole requested to glide out of the cell and throughout extracellular matrices [5].

With the imaging at a few tens of nanometers of the BCC7 protein recently identified [12,13] but not yet resolved in situ, we now document that this remarkably large protein of about 500 kDa organizes as a ribbed ring around the conic basal pole. Interestingly, one can distinguish some kind of claws that extend from the ring-like base and could promote better stabilization of the molecular pieces lying on top for optimal biomechanical coordination. On the other hand, super-resolution and live imaging brought evidence for the BCC7 apicobasal trafficking with clusters of proteins running peripherally at the pellicle vicinity. Finally, the conjunction of biochemical assays, live and static imaging has pinpointed the close apposition of the IMCs—in particular, IMC35 with BCC7—but also the quite close partnership with MyoC seen in this study as discrete entities distributed just below the BCC7 ring. Of note, similar to BCC7, MyoC was also reported to partition with the subpellicular cytoskeleton TX-100-insoluble fraction [17] and to display an overlapping transcriptional profile with a peak of expression during mitosis (M)/cytokinesis (C) phases of the cell cycle [36]. MyoC has been reported to co-localize with MORN1, both forming rings at the base of nascent daughter cells [39], and BCC7 was picked up both in the Y2H screen with MORN1 as a bait [18] and a BioID CEN2 screen [13]. Future investigations should clarify the in situ partnership between the three players.

BCC7 is a much larger protein than the canonical markers of the basal pole such as CEN2 and MORN1, and despite an accurate in silico analysis, no evidence for predictive functional domains was found. However, specific features and signature motifs could assist future characterization. First, given the enrichment of the BCC7 amino acid sequence in glutamic acid, the most common disorder-promoting amino acid, one can speculate on the BCC7 capacity to interact with several unrelated binding partners and to consequently impact on the 3D architecture [40]. Similarly, intermolecular partnerships could be favored through the large E and E/R-rich sequence repeats often involved in the regulation of protein–protein interactions [40,41]. The two BCC7 VPV repeats argue for a structural proximity with alveolin proteins [21,23]. These observations fit with a bioinformatic analysis, showing that 21% of the putative pellicular proteins contain highly repetitive regions with strong amino-acid biases for particular residues including glutamic acid [42]. Another striking BCC7 sequence feature is the high number of phosphorylation/dephosphorylation sites (Table S1). As described for glutamic acid enrichment, protein phosphorylation/dephosphorylation events are major regulatory processes for protein activities by affecting protein structure, stability, subcellular localization, as well as

interaction with other biomolecules, and not surprisingly, these post-translational modifications (PTMs) critically control many steps along the tachyzoite lytic cycle [43]. Another BCC7 predicted PTM is ubiquitination, which would be restricted to the BCC7 extreme C-terminus while it usually characterizes cytoskeletal and IMC proteins of *T. gondii*, many of which contribute to the cell division and host cell invasion processes [44]. By targeting proteins to the proteasome, polyubiquitination directs their proteolytic degradation. Notably, turnover of proteins can also depend on additional degradation signals in particular the phosphorylation of PEST sequences rich in proline (P), glutamic acid (E), serine (S), and threonine (T) residues [40]. Interestingly, three PEST motifs were detected but these are located at the BCC7 N-terminus. Collectively, the large repertoire of predictive PTMs on BCC7 amino-acid residues suggests that ubiquitination and phosphorylation could interplay to fine tune BCC7 properties, as already proposed for the complex regulatory mechanisms underlying tachyzoite endodyogeny [44]. However, that BCC7 was found dispensable in vitro for *T. gondii* tachyzoite perpetuation based on plaque formation capacity was surprising. A detailed study by Gubbels et al. published in the course of our manuscript evaluation [12] points out the subtle effect of BCC7 loss following gene knock out strategy on the rosette organization of the progeny within vacuole which appears to be less consistent than in wild type, and which do not impact on the general in vitro fitness score. This defect suggests that BCC7 could assist in the formation and maintenance of the cytoplasmic bridge between progeny after division within the parasitophorous vacuole which would translate into a rosette disorganization. It is also worth noting that other BC components identified in the Gubbels et al. study were found to separately affect the parasite alignment in rosette to various extents, indicating that *T. gondii* has likely evolved a versatile multi-component process that introduces molecular plasticity in the shaping of mature cell upon the final step of division.

In conclusion, BCC7 is the largest protein identified so far in the *T. gondii* basal pole of the nascent and mature tachyzoites that we found to closely interface between the IMC network and the myosin C motor which has not been assigned a highly specific functional contribution so far. Future investigations regarding the structural determinants of BCC7 oligomerization that result in the formation of ordered ring structures could now be envisaged using cryoEM for example. A better knowledge of the spatial architecture of BCC7 in the context of the whole set of structural players—also including the actin cytoskeleton and the myosin motors—should improve our understanding of the structural and functional peculiarities of the early designed basal pole cell compartment of *T. gondii* tachyzoite.

4. Materials and Methods

4.1. Parasites and Host Cells

Unless specified all reagents used for cell culture were from Gibco-Life Technologies. *T. gondii* strains (RH and RH- $\Delta ku80$ and derivatives) were propagated in human foreskin fibroblasts (HFFs, ATCC CCL-171) cultured at 37 °C under 5% CO₂ atmosphere in Dulbecco's modified Eagle's medium (DMEM) supplemented with 10% heat-inactivated fetal bovine serum (Invitrogen), 10 mM HEPES buffer pH 7.2, 2 mM L-Glutamine, 100 U/mL penicillin, and 50 µg/mL streptomycin.

4.2. Generation of Transgenic Parasites Expressing Endogenously Tagged Proteins

Endogenous gene tagging was carried out using primers and plasmids listed Table S2. Briefly, the C-terminus coding sequences of genes of interest were amplified with specific forward and reverse primers and using RH $\Delta ku80$ *T. gondii* strain genomic DNA as template. The resulting PCR products were inserted into various pLIC vectors following the ligation-independent cloning protocol [45]. The BCC7-mEmerald fusion protein was generated via overlapping PCRs of TGGT1-311230 and of EmGFP-SUN2, amplified from genomic DNA and synthetic TUB8-EmGFP-SUN2 gene (Genscript), respectively. The reverse primer of the whole amplicon was engineered to add a STOP codon downstream the Emerald coding sequence. The correctness of the fusion was confirmed by DNA sequencing and

the PCR product was incorporated in pLIC-HA-FLAG-HX vector (Gift of M.-A. Hakimi). For transfection, 10^7 of freshly egressed RH Δ ku80 parasites washed then re-suspended in 800 μ L of cytomix (10 mM K₂HPO₄, 10 mM KH₂PO₄, 120 mM KCl, 0.15 mM CaCl₂, 5 mM MgCl₂, 25 mM HEPES, 2 mM EGTA) were electroporated with 10–15 μ g DNA in 2 mm gap cuvettes and using a BTX ECM 630 machine (Harvard Apparatus) at 1100 V, 25 Ω , and 25 F. Transgenic parasite populations were enriched using mycophenolic acid (25 μ g/mL; Sigma-Aldrich) and xanthine (50 μ g/mL; Sigma-Aldrich) for HXGPRT selection or pyrimethamine (3 μ M) for DHFR selection, and individual clones were isolated by limiting dilution in 96-well plates.

4.3. Bioinformatic Analyses

Sequence of BCC7 was retrieved from ToxoDB [19]. Several sequence analyses tools were combined to Blast searches. A transmembrane helix has been predicted by TMHMM-2.0 webserver [46]. PEST motif identification was performed using the EMBOSS program ePESTfind tool using the standard setting. Three potential PEST motifs (224–258, 313–347, 427–475)—with PEST scores of 6.2, 8.9, and 5.5 respectively—have been identified [47]. Composition in amino acids of each region has been recovered with the ProtParam tool of Expasy [48]. Ordered and disordered regions have been predicted using the FoldIndex webserver [49]. Predicted phosphorylation sites were retrieved from ToxoDB documented based on the phosphoproteomic studies on *Toxoplasma* and *Plasmodium* zoites [50].

4.4. Auxin-Inducible Degron Plasmid Construction

The BCC7-mAID-3HA cell line was generated using the pU6-Cas9-sgRNA-BCC7 plasmid, which targets the 3' end of the gene, near the stop codon, for the double strand break and a PCR product generated with the Q5 High-Fidelity DNA Polymerase (NEB) using the pTUB1:YFP-mAID-3HA, DHFR-TS:HXGPRT vector as template [51] and the primers 1875/1876 to repair (Table S2). The pU6-Cas9-sgRNA-BCC7 plasmid was generated by annealing primers 1873 and 1874 and ligating them in the BsaI-digested pU6-Universal vector (gift from Sebastian Lourido [52]). The PCR product containing 33 bp homology to BCC7 and the pU6-Cas9-sgRNA-BCC7 were co-transfected in the RH TIR1-3FLAG cell line allowing integration and selection using mycophenolic acid and xanthine as described in Section 4.2. Downregulation of BCC7 was performed by incubation with a final concentration of 500 μ M of IAA (Sigma).

4.5. Plaque Assays

Freshly egressed parasites were collected, counted, and seeded to invade confluent HFF monolayers grown on 24-well plates. Parasites were allowed to invade overnight before treatment with 500 μ M IAA or vehicle for 7 days. Monolayers were later methanol fixed and 0.1% crystal violet (Sigma) stained for plaque formation assessment.

4.6. BCC7 Solubilization Assays

RH Δ ku80_BCC7-HA-FLAG parasites were pelleted ($900 \times g$ for 7 min) and washed in cold PBS supplemented with complete protease inhibitor cocktail EDTA free (Roche Diagnostics) and 1 mM Phenylmethylsulfonyl fluoride (PMSF). The pelleted parasites were resuspended at a density of 1×10^9 cell per mL of ice-cold lysis buffer (20 mM Tris-HCl pH 7.9–500 mM KCl—1.5 mM MgCl₂—0.2 mM EDTA—0.05% NP-40—20% glycerol containing 1 mM PMSF and protease inhibitor cocktail). Parasites were then disrupted by 15 strokes in a Dounce homogenizer and 100 μ L aliquots of the cell homogenate were distributed in Eppendorf tubes in presence of various detergents (BC500: control lysis buffer containing NP40 (0.05% v/v); BC500 supplemented with *n*-Dodecyl- β -D-maltopyranoside (0.1% w/v); Empigen BB (1% v/v); N-lauryl sarcoside (0.1% w/v); sulfobetaine 3–14 (n-Tetradecyl-N,N-dimethyl-3-ammonio-1-propanesulfonate) (1% w/v); Triton X-100 (0.1% v/v). Following a 90 min incubation on a rotating shaker, soluble and insoluble fractions were separated by

centrifugation (12,000× *g* for 30 min, 4 °C) and further analyzed by Western blot. All of the purification steps have been carried out at 4 °C.

4.7. Immunoprecipitation Procedure

Freshly egressed parasites collected from 20 T180 flasks ($1.3\text{--}1.5 \times 10^{10}$ tachyzoites) were washed as described above and resuspended in 5 mL PBS supplemented with TX-100 1% (*v/v*). All lysis steps were performed at 4 °C in presence of antiproteases (Complete, Roche) and 1 mM PMSF. A mechanical lysis step was performed with Dounce homogenization of parasites followed by 1 h incubation on rotating shaker. The insoluble fraction collected after centrifugation (16,000× *g* for 20 min) was resuspended in lysis buffer (1×10^9 tachyzoites/mL) supplemented with 1% Empigen BB (Sigma-Aldrich) and 1 μL Benzonase (Sigma-Aldrich). This BCC7 enriched fraction was further submitted to a second step of mechanical Dounce homogenization and 1 h incubation on rotating shaker. The soluble lysate obtained after centrifugation (20,000× *g* for 45 min) was diluted half in lysis buffer without detergent and incubated with 1 mL anti-FLAG M2 affinity beads (Sigma-Aldrich). After 1 h incubation, unbound material was washed away from the beads with 30 mL PBS and elution was carried out with 150 mg/mL FLAG peptide. The presence of HA-FLAG-tagged proteins in the elution fractions was assessed by immunoblot analysis after SDS-PAGE. Experiments were conducted in triplicate with both RHΔku80_BCC7-HA-FLAG, and wild-type parasites were used as controls.

4.8. Western Blots

The samples were resolved by SDS-PAGE (NuPAGE™ 4–12% Bis-Tris Gel; Thermo Fisher Scientific) at 130 V using NuPAGE™ MOPS SDS running buffer before transfer on PVDF membranes (2 h, 100 V) using NuPAGE™ transfer buffer supplemented with 0.05% (*w/v*) SDS in order to ease the transfer of large proteins such as BCC7. Following a saturation step with PBS—Tween 20 (0.2% *v/v*)—nonfat milk (5% *w/v*), membranes were incubated with a rabbit monoclonal anti-HA antibody (C29F4; 1:1000; Cell Signaling) and a rabbit secondary antibody coupled to peroxidase (1:10,000; Jackson ImmunoResearch, Baltimore, PA, USA). After extensive washes with PBS-Tween, Western blot were revealed using Clarity Western ECL substrate (Bio-Rad) using ChemiDoc™ XRS+ with image Lab™ Software.

4.9. Mass Spectrometry-Based Quantitative Proteomic Analyses

Eluted proteins were solubilized in Laemmli buffer and stacked in the top of a 4–12% NuPAGE gel (Invitrogen). After staining with R-250 Coomassie Blue (Biorad), proteins were digested in gel using trypsin (modified, sequencing purity, Promega), as previously described [53]. The resulting peptides were analyzed by online nanoliquid chromatography coupled to MS/MS (Ultimate 3000 RSLCnano and Q-Exactive HF, Thermo Fisher Scientific) using a 140 min gradient. For this purpose, the peptides were sampled on a precolumn (300 μm particle size × 5 mm length PepMap C18, Thermo Scientific) and further separated in a 75 μm × 250 mm C18 column (Reprosil-Pur 120 C18-AQ, 1.9 μm, Dr. Maisch). The MS and MS/MS data were acquired by Xcalibur (Thermo Fisher Scientific). Peptides and proteins were identified by Mascot (version 2.7.0.1, Matrix Science) through concomitant searches against the *T. gondii* database (ME49 taxonomy, v.30, downloaded from ToxoDB), the Uniprot database (*Homo sapiens* taxonomy, October 2020-10 version), and a homemade database containing the sequences of classical contaminant proteins found in proteomic analyses (bovine albumin, keratins, trypsin, etc.). Trypsin/P was chosen as the enzyme for protein digestion and two missed cleavages were allowed. Precursor and fragment mass error tolerances were set at respectively at 10 and 20 ppm. Peptide modifications allowed during the search were: carbamidomethyl (C, fixed), acetyl (Protein N-term, variable), and oxidation (M, variable). The Proline software [54] was used for the compilation, grouping, and filtering of the results (conservation of rank 1 peptides, peptide length ≥ 6, PSM score ≥ 25, false discovery rate of peptide-spectrum-match identifications <1% as

calculated on peptide-spectrum-match scores by employing the reverse database strategy, and a minimum of 1 specific peptide per identified protein group. Proline was then used to perform a MS1 quantification of the identified protein groups, based on razor and specific peptides.

Statistical analysis was then performed using the ProStaR software [55]. Proteins identified in the contaminant database, proteins identified by MS/MS in less than two replicates of BCC7-HA-FLAG eluates, and proteins detected in less than three replicates of one condition were discarded. After log₂ transformation, abundance values were normalized by median centering, before missing value imputation (salsa algorithm for partially observed values in the condition and DetQuantile algorithm for totally absent values in the condition). Statistical testing was then conducted using limma, whereby differentially expressed proteins were sorted out using a log₂(fold change) cut-off of 2 and a *p*-value cut-off of 0.05, leading to FDR below 2% according to the adjusted Benjamini–Hochberg (abh) estimator.

4.10. Immunofluorescence Microscopy

Intracellular (in HFF cells) or extracellular tachyzoites were fixed for 20 min at room temperature with 4% paraformaldehyde (PFA) diluted in PHEM pH 7.5 and dH₂O then treated 10 min with 50 mM NH₄Cl to quench free aldehyde groups before TX-100 permeabilization (0.1% *v/v*; 10 min). Following a 20 min non-specific site saturation step in PBS-BSA 2% (*w/v*) the cells were incubated with antibodies (Table S3) and nucleic acids were stained for 10 min at room temperature with DAPI (500 nM from 14.3 mM stock; 10 min RT). Coverslips were mounted with Mowiol mounting medium, and images were acquired with the Zeiss AxioImager M2 fluorescence upright microscope equipped with ApoTome 2 module (Carl Zeiss, Inc., Oberkochen, Germany). For confocal images, immunostained samples were imaged using a 63×Plan-Apotome oil immersion objective (1.46 NA, Zeiss) in a Zeiss LSM 170 inverted microscope coupled with Airyscan detector. For stimulated emission depletion (STED) microscopy, image acquisition was performed using a 100× Plan-Apotome oil immersion objective (1.46 NA, Zeiss) in an Abberior 2D-STEDYCON module on an upright Zeiss Axio Observer Z1 confocal microscope.

4.11. Video Microscopy

Time-lapse video microscopy was conducted as previously described [5]. Briefly, HFFs loaded with tachyzoites were plated on 18 mm diameter coverslips coated with poly-L-Lysine (PLL 150–300 kDa, Sigma-Aldrich) and inserted in a Chamlide chambers (LCI Corp., Seoul, Korea). This magnetic cell culture chamber where temperature and CO₂ (37 °C, 5%) are tightly controlled, was installed on an Eclipse Ti inverted confocal microscope (Nikon France Instruments, Champigny sur Marne, France) coupled to a CMOS Prime camera (Photometrics, Tucson, AZ, USA) and a CSU X1 spinning disk (Yokogawa, Roper Scientific, Lisses, France). Images were captured with a 60× Plan-neofluar objective (NA: 1.46).

4.12. Tachyzoite Egress and Motility Assays

HFFs were seeded on 18 mm diameter glass coverslips precoated with poly-L-lysine (150–300 kDa, 50 µg/mL in PBS, Sigma) 24 h prior to assay. They were infected with active extracellular tachyzoites in a 1 h-time window before most if not all extracellular parasites were removed with energetic cold PBS washes. Cells were cultured for 40 h at 37 °C, 5% CO₂, and then placed on the appropriate Chamlide chamber (Live Cell Instrument) in the confocal microscope under similar conditions. Intravacuolar parasite growth, parasite egress, and subsequent motility were monitored and recorded at 1.07451 s/ frame.

4.13. Expansion Microscopy

Expansion microscopy (proExM) was achieved according to the protocol described in [56]. Briefly, samples were prepared on 12 mm diameter glass coverslip, PFA fixed, TX-100 permeabilized and subsequently immunolabeled (Table S3). Next, they were

subjected to 0.1 mg/mL (6-((acryloyl) amino) hexanoic acid, succinimidyl ester) -Acryloyl X- diluted in PBS for 2 h at room temperature. Gelation (1 h) was completed on parafilm with the sample facing down before a 1 h incubation period in a humidified oven at 37 °C. The gel was immersed for 3 h at room temperature in digestion buffer containing 8 units/ml of proteinase K (Biolabs) and subsequently rinsed twice in PBS. A piece of digested gel was cut and expanded in a Petri dish filled with dH₂O. During the first bath, nuclear staining with DAPI (1 µg/mL, Sigma) was performed. The gel was immobilized on a poly-L-lysine coated coverslip prior to image acquisition with either a Zeiss LSM 170 inverted microscope (Airyscan module) or a spinning disk coupled Nikon EclipseTi inverted microscope (see Section 4.11).

4.14. Scanning Electron Microscopy (SEM)

HFF monolayers were infected with RH_BCC7mAID x3HA_MyoJ x2Ty Tir1 tachyzoites and incubated with either 500 µM IAA or vehicle for 24 h under routine culture conditions. Freshly egressed tachyzoites were collected, filtered through a 5 µm pore size polycarbonate membrane filter (Cytiva Whatman Cyclopore 7062-2513, Fisher Scientific), and deposited on a fibronectin-pre-coated glass coverslip for 15 min. The samples were fixed with 2.5% high grade glutaraldehyde (Electron Microscopy Sciences) diluted immediately before use in 0.1 M cacodylate buffer (pH 7.2, Electron Microscopy Sciences) for 1 h at 4 °C. Samples were subsequently washed in 0.1M cacodylate buffer and left overnight at 4 °C before being transferred in PBS. Samples were ethanol dehydrated and critical point dried under CO₂ atmosphere using a Leica EM CPD 300 apparatus prior to be coated with a 5 nm fine-grained and conductive platinum layer using the Leica high vacuum sputter coater EM ACE600. Images were captured with the Scanning Electron Microscope SU3500 (Hitachi, Tokyo, Japan). Digital images were recorded and further processed as described below.

4.15. Image Processing

All samples processed were randomly selected by researchers that were not blinded during the study. MetaMorph [57], ImageJ [58] and Icy [59] software were used to process the raw images from x,y,z,t stacks for events of interest. Photocompositions were realized with ImageJ and Photoshop software. 3D reconstructions were performed using 3D Slicer [60]. All images shown in the manuscript are representative of multiple independent biological replicates.

4.16. Statistical Analysis

Data were statistically analyzed and plots were made using GraphPad Prism 8.0 software for Windows (La Jolla, CA, USA). Data are presented as mean ± standard deviation if not indicated otherwise. Figure legends include the statistical test and resulting comparison when appropriate. For Figure 3c, an unpaired *t*-test followed by Holm–Sidak comparisons was used, with significance being represented as a *p*-value < 0.05, and the *n* indicated represents the parasite sample size.

Supplementary Materials: The following are available online at <https://www.mdpi.com/article/10.3390/ijms23115995/s1>.

Author Contributions: Conceptualization and design of the project: P.R. and I.T. Contribution to reagents, materials, and analysis tools: Y.C., K.F., P.R. and I.T. Bioinformatic analysis: C.M. and P.R. Biochemical investigation: D.C. and P.R. Mass spectrometry experiments and data analysis: Y.C. Design and cloning of *T. gondii* mutants D.C., T.L., K.F., C.R., P.R. and L.V. Image acquisition and analysis: T.L., P.R., B.T., L.V. and I.T. Writing draft: P.R. and I.T. Composing figures and writing legends: L.V. Editing: K.F., C.M., Y.C. and L.V. All authors have read and agreed to the published version of the manuscript.

Funding: The project was co-funded by the I.T. grants (Inserm and CNRS dotations, ANR-19-CE13-0034-01) and K.F. grants (CNRS dotation, Preciput SBM and ParaFrap Young Investigator grant). The

proteomic experiments were partially supported by the Agence Nationale de la Recherche under projects ProFI (Proteomics French Infrastructure, ANR-10-INBS-08) and GRAL, a program from the Chemistry Biology Health (CBH) Graduate School of University Grenoble Alpes (ANR-17-EURE-0003). L. Vigetti is a recipient of the University Grenoble Alpes Ph.D. fellowship under I.T. supervision and T. Labouré has performed a master internship supported by I.T. grant under P.R. supervision. C. Roumégous is a recipient of the University of Bordeaux Ph.D. fellowship.

Institutional Review Board Statement: Not applicable.

Informed Consent Statement: Not applicable.

Data Availability Statement: The mass spectrometry proteomics data have been deposited to the ProteomeXchange Consortium via the PRIDE (PMID: 34723319) partner repository with the dataset identifier PXD032362.

Acknowledgments: The authors thank M.-A. Hakimi and A. Bougdour (IAB, Team Host-Pathogen Interactions & Immunity to Infection, INSERM U1209, CNRS UMR5309, UGA, Grenoble, France) for support in transgenic *T. gondii* engineering. We are also grateful to I. Florent, L. Raveendran, and G. Toutirais (Molécules de Communication et Adaptation des Micro-organismes et (GT) Plateau Technique de Microscopie Electronique, Museum National d'Histoire Naturelle, Paris) for their assistance with SEM. We thank M. Khamitova for her assistance in immunofluorescence staining of intracellular and extracellular tachyzoites along her master internship in IT team. We would also like to thank C. Uwizeye for her contribution to 3D image reconstruction of BCC7-HA-Flag expressing tachyzoites processed for STED microscopy.

Conflicts of Interest: The authors declare no conflict of interest.

References

1. Carme, B.; Demar, M.; Ajzenberg, D.; Dardé, M.L. Severe Acquired Toxoplasmosis Caused by Wild Cycle of *Toxoplasma gondii*, French Guiana. *Emerg. Infect. Dis.* **2009**, *15*, 656–658. [[CrossRef](#)] [[PubMed](#)]
2. Anderson-White, B.; Beck, J.R.; Chen, C.-T.; Meissner, M.; Bradley, P.J.; Gubbels, M.-J. Cytoskeleton Assembly in *Toxoplasma gondii* Cell Division. In *International Review of Cell and Molecular Biology*; Elsevier: Amsterdam, The Netherlands, 2012; Volume 298, pp. 1–31. ISBN 978-0-12-394309-5.
3. Mann, T.; Gaskins, E.; Beckers, C. Proteolytic Processing of TgIMC1 during Maturation of the Membrane Skeleton of *Toxoplasma gondii*. *J. Biol. Chem.* **2002**, *277*, 41240–41246. [[CrossRef](#)] [[PubMed](#)]
4. Morrissette, N.S.; Sibley, L.D. Cytoskeleton of Apicomplexan Parasites. *Microbiol. Mol. Biol. Rev.* **2002**, *66*, 21–38. [[CrossRef](#)] [[PubMed](#)]
5. Pavlou, G.; Touquet, B.; Vigetti, L.; Renesto, P.; Bougdour, A.; Debarre, D.; Balland, M.; Tardieux, I. Coupling Polar Adhesion with Traction, Spring, and Torque Forces Allows High-Speed Helical Migration of the Protozoan Parasite *Toxoplasma*. *ACS Nano* **2020**, *14*, 7121–7139. [[CrossRef](#)]
6. Beck, J.R.; Rodriguez-Fernandez, I.A.; Cruz de Leon, J.; Huynh, M.-H.; Carruthers, V.B.; Morrissette, N.S.; Bradley, P.J. A Novel Family of *Toxoplasma* IMC Proteins Displays a Hierarchical Organization and Functions in Coordinating Parasite Division. *PLoS Pathog.* **2010**, *6*, e1001094. [[CrossRef](#)] [[PubMed](#)]
7. Lentini, G.; Kong-Hap, M.; El Hajj, H.; Francia, M.; Claudet, C.; Striepen, B.; Dubremetz, J.-F.; Lebrun, M. Identification and Characterization of *Toxoplasma* SIP, a Conserved Apicomplexan Cytoskeleton Protein Involved in Maintaining the Shape, Motility and Virulence of the Parasite: Cytoskeleton Protein Associated with the IMC Edges. *Cell. Microbiol.* **2015**, *17*, 62–78. [[CrossRef](#)]
8. Harding, C.R.; Gow, M.; Kang, J.H.; Shortt, E.; Manalis, S.R.; Meissner, M.; Lourido, S. Alveolar Proteins Stabilize Cortical Microtubules in *Toxoplasma gondii*. *Nat. Commun.* **2019**, *10*, 401. [[CrossRef](#)]
9. Hu, K.; Johnson, J.; Florens, L.; Fraunholz, M.; Suravajjala, S.; DiLullo, C.; Yates, J.; Roos, D.S.; Murray, J.M. Cytoskeletal Components of an Invasion Machine—The Apical Complex of *Toxoplasma gondii*. *PLoS Pathog.* **2006**, *2*, e13. [[CrossRef](#)]
10. Dos Santos Pacheco, N.; Tosetti, N.; Koreny, L.; Waller, R.F.; Soldati-Favre, D. Evolution, Composition, Assembly, and Function of the Conoid in Apicomplexa. *Trends Parasitol.* **2020**, *36*, 688–704. [[CrossRef](#)]
11. Hu, K. Organizational Changes of the Daughter Basal Complex during the Parasite Replication of *Toxoplasma gondii*. *PLoS Pathog.* **2008**, *4*, e10. [[CrossRef](#)]
12. Gubbels, M.-J.; Ferguson, D.J.P.; Saha, S.; Romano, J.D.; Chavan, S.; Primo, V.A.; Michaud, C.; Coppens, I.; Engelberg, K. *Toxoplasma gondii*'s Basal Complex: The Other Apicomplexan Business End Is Multifunctional. *Front. Cell. Infect. Microbiol.* **2022**, *12*, 882166. [[CrossRef](#)]
13. Engelberg, K.; Bechtel, T.; Michaud, C.; Weerapana, E.; Gubbels, M.-J. A More Complex Basal Complex: Novel Components Mapped to the *Toxoplasma gondii* Cytokinesis Machinery Portray an Expanded Hierarchy of Its Assembly and Function. *bioRxiv* **2021**. [[CrossRef](#)]

14. Frénal, K.; Krishnan, A.; Soldati-Favre, D. The Actomyosin Systems in Apicomplexa. In *Myosins*; Coluccio, L.M., Ed.; Advances in Experimental Medicine and Biology; Springer International Publishing: Cham, Switzerland, 2020; Volume 1239, pp. 331–354. ISBN 978-3-030-38061-8.
15. Frénal, K.; Jacot, D.; Hammoudi, P.-M.; Graindorge, A.; Maco, B.; Soldati-Favre, D. Myosin-Dependent Cell-Cell Communication Controls Synchronicity of Division in Acute and Chronic Stages of *Toxoplasma gondii*. *Nat. Commun.* **2017**, *8*, 15710. [[CrossRef](#)] [[PubMed](#)]
16. Pavlou, G.; Biesaga, M.; Touquet, B.; Lagal, V.; Bolland, M.; Dufour, A.; Hakimi, M.; Tardieux, I. *Toxoplasma* Parasite Twisting Motion Mechanically Induces Host Cell Membrane Fission to Complete Invasion within a Protective Vacuole. *Cell Host Microbe* **2018**, *24*, 81–96.e5. [[CrossRef](#)] [[PubMed](#)]
17. Gómez de León, C.T.; Díaz Martín, R.D.; Mendoza Hernández, G.; González Pozos, S.; Ambrosio, J.R.; Mondragón Flores, R. Proteomic Characterization of the Subpellicular Cytoskeleton of *Toxoplasma Gondii* Tachyzoites. *J. Proteom.* **2014**, *111*, 86–99. [[CrossRef](#)]
18. Engelberg, K.; Ivey, F.D.; Lin, A.; Kono, M.; Lorestani, A.; Faugno-Fusci, D.; Gilberger, T.-W.; White, M.; Gubbels, M.-J. A MORN1-Associated HAD Phosphatase in the Basal Complex Is Essential for *Toxoplasma Gondii* Daughter Budding. *Cell. Microbiol.* **2016**, *18*, 1153–1171. [[CrossRef](#)]
19. Amos, B.; Aurrecochea, C.; Barba, M.; Barreto, A.; Basenko, E.Y.; Bažant, W.; Belnap, R.; Blevins, A.S.; Böhme, U.; Brestelli, J.; et al. VEuPathDB: The Eukaryotic Pathogen, Vector and Host Bioinformatics Resource Center. *Nucleic Acids Res.* **2022**, *50*, D898–D911. [[CrossRef](#)]
20. Barylyuk, K.; Koreny, L.; Ke, H.; Butterworth, S.; Crook, O.M.; Lassadi, I.; Gupta, V.; Tromer, E.; Mourier, T.; Stevens, T.J.; et al. A Subcellular Atlas of *Toxoplasma* Reveals the Functional Context of the Proteome. *Cell Biol.* **2020**, *28*, 752–766.e9.
21. Gould, S.B.; Tham, W.-H.; Cowman, A.F.; McFadden, G.I.; Waller, R.F. Alveolins, a New Family of Cortical Proteins That Define the Protist Infrakingdom Alveolata. *Mol. Biol. Evol.* **2008**, *25*, 1219–1230. [[CrossRef](#)]
22. Gubbels, M.-J.; Wieffer, M.; Striepen, B. Fluorescent Protein Tagging in *Toxoplasma gondii*: Identification of a Novel Inner Membrane Complex Component Conserved among Apicomplexa. *Mol. Biochem. Parasitol.* **2004**, *137*, 99–110. [[CrossRef](#)]
23. Mann, T. Characterization of the Subpellicular Network, a Filamentous Membrane Skeletal Component in the Parasite *Toxoplasma gondii*. *Mol. Biochem. Parasitol.* **2001**, *115*, 257–268. [[CrossRef](#)]
24. Heaslip, A.T.; Leung, J.M.; Carey, K.L.; Catti, F.; Warshaw, D.M.; Westwood, N.J.; Ballif, B.A.; Ward, G.E. A Small-Molecule Inhibitor of *T. Gondii* Motility Induces the Posttranslational Modification of Myosin Light Chain-1 and Inhibits Myosin Motor Activity. *PLoS Pathog.* **2010**, *6*, e1000720. [[CrossRef](#)] [[PubMed](#)]
25. Wassie, A.T.; Zhao, Y.; Boyden, E.S. Expansion Microscopy: Principles and Uses in Biological Research. *Nat. Methods* **2019**, *16*, 33–41. [[CrossRef](#)]
26. Brown, K.; Long, S.; Sibley, L. Conditional Knockdown of Proteins Using Auxin-Inducible Degron (AID) Fusions in *Toxoplasma gondii*. *Bio-Protocol* **2018**, *8*, e2728. [[CrossRef](#)]
27. Sidik, S.M.; Huet, D.; Ganesan, S.M.; Huynh, M.-H.; Wang, T.; Nasamu, A.S.; Thiru, P.; Saeij, J.P.J.; Carruthers, V.B.; Niles, J.C.; et al. A Genome-Wide CRISPR Screen in *Toxoplasma* Identifies Essential Apicomplexan Genes. *Cell* **2016**, *166*, 1423–1435.e12. [[CrossRef](#)] [[PubMed](#)]
28. Lowthert, L.A.; Ku, N.O.; Liao, J.; Coulombe, P.A.; Omary, M.B. Empigen BB: A Useful Detergent for Solubilization and Biochemical Analysis of Keratins. *Biochem. Biophys. Res. Commun.* **1995**, *206*, 370–379. [[CrossRef](#)] [[PubMed](#)]
29. Hettmann, C.; Herm, A.; Geiter, A.; Frank, B.; Schwarz, E.; Soldati, T.; Soldati, D. A Dibasic Motif in the Tail of a Class XIV Apicomplexan Myosin Is an Essential Determinant of Plasma Membrane Localization. *Mol. Biol. Cell* **2000**, *11*, 1385–1400. [[CrossRef](#)] [[PubMed](#)]
30. Döşkaya, M.; Liang, L.; Jain, A.; Can, H.; Gülçe İz, S.; Felgner, P.L.; Değirmenci Döşkaya, A.; Davies, D.H.; Gürüz, A.Y. Discovery of New *Toxoplasma gondii* Antigenic Proteins Using a High Throughput Protein Microarray Approach Screening Sera of Murine Model Infected Orally with Oocysts and Tissue Cysts. *Parasit. Vectors* **2018**, *11*, 393. [[CrossRef](#)]
31. Besteiro, S.; Michelin, A.; Poncet, J.; Dubremetz, J.-F.; Lebrun, M. Export of a *Toxoplasma gondii* Rhoptry Neck Protein Complex at the Host Cell Membrane to Form the Moving Junction during Invasion. *PLoS Pathog.* **2009**, *5*, e1000309. [[CrossRef](#)]
32. Chen, A.L.; Kim, E.W.; Toh, J.Y.; Vashisht, A.A.; Rashoff, A.Q.; Van, C.; Huang, A.S.; Moon, A.S.; Bell, H.N.; Bentolila, L.A.; et al. Novel Components of the *Toxoplasma* Inner Membrane Complex Revealed by BioID. *mBio* **2015**, *6*, e02357-14. [[CrossRef](#)]
33. Semenovskaya, K.; Lévêque, M.F.; Berry, L.; Bordat, Y.; Dubremetz, J.; Lebrun, M.; Besteiro, S. TgZFP2 Is a Novel Zinc Finger Protein Involved in Coordinating Mitosis and Budding in *Toxoplasma*. *Cell. Microbiol.* **2020**, *22*, e13120. [[CrossRef](#)] [[PubMed](#)]
34. Anderson-White, B.R.; Ivey, F.D.; Cheng, K.; Szatanek, T.; Lorestani, A.; Beckers, C.J.; Ferguson, D.J.P.; Sahoo, N.; Gubbels, M.-J. A Family of Intermediate Filament-like Proteins Is Sequentially Assembled into the Cytoskeleton of *Toxoplasma gondii*: IMC Proteins in *Toxoplasma* Cell Division. *Cell. Microbiol.* **2011**, *13*, 18–31. [[CrossRef](#)]
35. Dos Santos Pacheco, N.; Tosetti, N.; Krishnan, A.; Haase, R.; Maco, B.; Suarez, C.; Ren, B.; Soldati-Favre, D. Revisiting the Role of *Toxoplasma Gondii* ERK7 in the Maintenance and Stability of the Apical Complex. *mBio* **2021**, *12*, e02057-21. [[CrossRef](#)]
36. Behnke, M.S.; Wootton, J.C.; Lehmann, M.M.; Radke, J.B.; Lucas, O.; Nawas, J.; Sibley, L.D.; White, M.W. Coordinated Progression through Two Subtranscriptomes Underlies the Tachyzoite Cycle of *Toxoplasma gondii*. *PLoS ONE* **2010**, *5*, e12354. [[CrossRef](#)] [[PubMed](#)]

37. Striepen, B.; Jordan, C.N.; Reiff, S.; van Dooren, G.G. Building the Perfect Parasite: Cell Division in Apicomplexa. *PLoS Pathog.* **2007**, *3*, e78. [CrossRef] [PubMed]
38. Ouologuem, D.T.; Roos, D.S. Dynamics of the *Toxoplasma gondii* Inner Membrane Complex. *J. Cell Sci.* **2014**, *127*, 3320–3330. [CrossRef]
39. Gubbels, M.-J.; Vaishnav, S.; Boot, N.; Dubremetz, J.-F.; Striepen, B. A MORN-Repeat Protein Is a Dynamic Component of the *Toxoplasma gondii* Cell Division Apparatus. *J. Cell Sci.* **2006**, *119*, 2236–2245. [CrossRef]
40. Uversky, V.N. The Alphabet of Intrinsic Disorder: II. Various Roles of Glutamic Acid in Ordered and Intrinsically Disordered Proteins. *Intrinsically Disord. Proteins* **2013**, *1*, e24684. [CrossRef]
41. McBride, A.E.; Conboy, A.K.; Brown, S.P.; Ariyachet, C.; Rutledge, K.L. Specific Sequences within Arginine-Glycine-Rich Domains Affect mRNA-Binding Protein Function. *Nucleic Acids Res.* **2009**, *37*, 4322–4330. [CrossRef]
42. Gould, S.B.; Kraft, L.G.K.; van Dooren, G.G.; Goodman, C.D.; Ford, K.L.; Cassin, A.M.; Bacic, A.; McFadden, G.I.; Waller, R.F. Ciliate Pellicular Proteome Identifies Novel Protein Families with Characteristic Repeat Motifs That Are Common to Alveolates. *Mol. Biol. Evol.* **2011**, *28*, 1319–1331. [CrossRef]
43. He, C.; Xu, M.; Pan, S.; Wang, H.; Peng, H.; Liu, Z. ITRAQ-Based Phosphoproteomic Analysis of *Toxoplasma gondii* Tachyzoites Provides Insight Into the Role of Phosphorylation for Its Invasion and Egress. *Front. Cell. Infect. Microbiol.* **2020**, *10*, 586466. [CrossRef] [PubMed]
44. Silmon de Monerri, N.C.; Yakubu, R.R.; Chen, A.L.; Bradley, P.J.; Nieves, E.; Weiss, L.M.; Kim, K. The Ubiquitin Proteome of *Toxoplasma gondii* Reveals Roles for Protein Ubiquitination in Cell-Cycle Transitions. *Cell Host Microbe* **2015**, *18*, 621–633. [CrossRef]
45. Huynh, M.-H.; Carruthers, V.B. Tagging of Endogenous Genes in a *Toxoplasma gondii* Strain Lacking Ku80. *Eukaryot. Cell* **2009**, *8*, 530–539. [CrossRef] [PubMed]
46. Services. Available online: <https://services.healthtech.dtu.dk> (accessed on 8 April 2022).
47. EMBOSS: Epestfind. Available online: <https://emboss.bioinformatics.nl/cgi-bin/emboss/epestfind/> (accessed on 8 April 2022).
48. ExPASy-ProtParam Tool. Available online: <https://web.expasy.org/protparam/> (accessed on 8 April 2022).
49. FoldIndex(c). Available online: <https://fold.proteopedia.org/cgi-bin/findex> (accessed on 8 April 2022).
50. Treeck, M.; Sanders, J.L.; Elias, J.E.; Boothroyd, J.C. The Phosphoproteomes of Plasmodium Falciparum and *Toxoplasma gondii* Reveal Unusual Adaptations within and beyond the Parasites' Boundaries. *Cell Host Microbe* **2011**, *10*, 410–419. [CrossRef] [PubMed]
51. Brown, K.M.; Long, S.; Sibley, L.D. Plasma Membrane Association by N-Acylation Governs PKG Function in *Toxoplasma gondii*. *mBio* **2017**, *8*, e00375-17. [CrossRef]
52. Sidik, S.M.; Hackett, C.G.; Tran, F.; Westwood, N.J.; Lourido, S. Efficient Genome Engineering of *Toxoplasma gondii* Using CRISPR/Cas9. *PLoS ONE* **2014**, *9*, e100450. [CrossRef]
53. Casabona, M.G.; Vandenbrouck, Y.; Attree, I.; Couté, Y. Proteomic Characterization of Pseudomonas Aeruginosa PAO1 Inner Membrane. *Proteomics* **2013**, *13*, 2419–2423. [CrossRef]
54. Bouyssié, D.; Hesse, A.-M.; Mouton-Barbosa, E.; Rompais, M.; Macron, C.; Carapito, C.; Gonzalez de Peredo, A.; Couté, Y.; Dupierris, V.; Burel, A.; et al. Proline: An Efficient and User-Friendly Software Suite for Large-Scale Proteomics. *Bioinformatics* **2020**, *36*, 3148–3155. [CrossRef]
55. Wieczorek, S.; Combes, F.; Lazar, C.; Giai Gianetto, Q.; Gatto, L.; Dorffer, A.; Hesse, A.-M.; Couté, Y.; Ferro, M.; Bruley, C.; et al. DAPAR & ProStar: Software to Perform Statistical Analyses in Quantitative Discovery Proteomics. *Bioinformatics* **2017**, *33*, 135–136. [CrossRef]
56. Asano, S.M.; Gao, R.; Wassie, A.T.; Tillberg, P.W.; Chen, F.; Boyden, E.S. Expansion Microscopy: Protocols for Imaging Proteins and RNA in Cells and Tissues. *Curr. Protoc. Cell Biol.* **2018**, *80*, e56. [CrossRef]
57. Molecular Devices. Available online: <https://www.moleculardevices.com> (accessed on 8 April 2022).
58. Schneider, C.A.; Rasband, W.S.; Eliceiri, K.W. NIH Image to ImageJ: 25 Years of Image Analysis. *Nat. Methods* **2012**, *9*, 671–675. [CrossRef] [PubMed]
59. de Chaumont, F.; Dallongeville, S.; Chenouard, N.; Hervé, N.; Pop, S.; Provoost, T.; Meas-Yedid, V.; Pankajakshan, P.; Lecomte, T.; Le Montagner, Y.; et al. Icy: An Open Bioimage Informatics Platform for Extended Reproducible Research. *Nat. Methods* **2012**, *9*, 690–696. [CrossRef] [PubMed]
60. Fedorov, A.; Beichel, R.; Kalpathy-Cramer, J.; Finet, J.; Fillion-Robin, J.-C.; Pujol, S.; Bauer, C.; Jennings, D.; Fennessy, F.; Sonka, M.; et al. 3D Slicer as an Image Computing Platform for the Quantitative Imaging Network. *Magn. Reson. Imaging* **2012**, *30*, 1323–1341. [CrossRef] [PubMed]

4.6 Discussion and perspectives

In this study, our focus was set on the basal pole, a composite compartment that assembles during endodyogeny and must be structurally and functionally completed in parasites about to egress out of the host cells thereby being fit for their motile and cell-invasive needs. The typical cone-shaped basal pole is structurally organized in a series of rings -each made of a specific protein and that pile up from below the limit of the IMCs up to the basal tip. While advanced biochemistry and molecular genetics have recently allowed significant progress to map the different ring elements and start defining their functional properties, which has led to discriminate the basal complex and the posterior cup compartments, the overall picture still remains incomplete. In particular how these rings may articulate with each other and provide the right balance between rigidity (as a scaffold) and flexibility in a body area *quasi* deprived of IMC and microtubules, but that is a crucial dynamic attachment site for motility (see Chapter 2) and force development, is far from being understood.

Chronologically, the BCC7 protein was first identified in a screen for *Toxoplasma* tachyzoite Histone Deacetylase 3 (HDAC3) substrate candidates carried out by the Hakimi's lab which further invalidated its HDAC3 substrate potential. However, being close collaborators of the team, we noticed the striking posterior localization, much below the nucleus of an epitope-tagged version of the protein when imaging mature intracellular and extracellular tachyzoites. Because of our interest in understanding how twisting force(s) can be generated during cell invasion (Pavlou et al., 2018) or during twirling and helical motility (Pavlou et al., 2020), this in situ observation prompted us to map the protein position in particular with respect to the posteriorly located myosins. Of note, in the course of our study, a BioID-based map of the basal complex (BC) proteome also picked up this protein as a basal complex component and named it as BCC7 (Engelberg et al., 2022; Gubbels et al., 2022).

To gain insight on how BCC7 could organize as a basal ring, we first engineered a line expressing a fluorescent version of BCC7 with either a mCherry or an Emerald tag that were amenable to long-live imaging. Because our data also pointed to several IMC proteins as potential BCC7 partners among others, we also wanted to co-monitor in real time the IMC of interest and the BCC7 proteins, hence generating parasites lines with dual fluorescent markers.

Long-time live-imaging covering several rounds of tachyzoite endodyogeny allowed detecting first BCC7 at the apical nascent daughter and its subsequent traffic in an apicobasal direction as clusters, running most probably in conjunction with other IMC or IMC like proteins at the pellicle. This could also explain the presence of several cytoplasmic (TgZFP2 and hypothetical protein TGGT1_230940) and even nuclear proteins (FUSE-binding protein 2 and hypothetical protein TGGT1_315610) in the co-immunoprecipitation assay. These interactions that may not seem straightforward at first but could be due to the several glutamic acid-rich regions revealed in the *in silico* analysis, which causes protein disorganization and could impact the binding with several non-related partners (Uversky, 2013).

In parallel, when we performed super-resolution static imaging using Stimulated Emission Depletion (STED) microscopy with the STEDYCON that does not permit optimal 3D reconstruction, the proximity between patches of BCC7 and IMC35 was confirmed. In addition, these few tens' resolution scale brought evidence that the BCC7 structure is not a perfect ring, as we observed 'claws-like' structures that extended towards the end of the IMC, possibly to uphold a better stabilization of the molecular components for optimal biomechanical coordination. As a result, it was not surprising to see that most of the interacting partner candidates were identified as IMC or membrane proteins (IMC7, IMC10, IMC12, IMC18 and IMC24, with the addition of the SAG-related sequence SRS29A). From the unidentified pool of partner candidates, further characterization allowed us to pinpoint two more as the newly named IMC35 and IMC36, which are conserved across the Apicomplexa phylum; the expression pattern we retrieved on the ToxoDB coincides with the typical IMC profiles (Ouologuem & Roos, 2014), with peaks at the daughter budding stage and a decay afterwards. Recently, a study by the Bradley lab found by BioID that IMC29 also interacts with BCC7 (Back et al., 2023), although we didn't observe this IMC in our studies. IMC29 also presents a peak in expression at the endodyogeny division process. We also observed the same peak in expression for IMC10, an interacting partner of BCC7, delimiting the daughter during endodyogeny process and later diminishing its expression as the cycle progresses.

We also applied Ultrastructure Expansion Microscopy that allows 3D reconstruction and focused on the topological relationship between BCC7 and MyoC. We were able to resolve that both proteins, which assemble as ring-shaped structures, are closely juxtaposed, as MyoC is located slightly basally with respect to BCC7. As BCC7, MyoC is also reported to be a part of the detergent-insoluble cytoskeleton fraction (Gómez de León et al., 2014). MyoC and

BCC7 share a similar transcriptional profile, with an expression peak during mitosis and cytokinesis (Behnke et al., 2010). This overlapping in expression could relate BCC7 to the stabilization of the basal complex during division, as MyoC plays a role in cell shape cohesion during endodyogeny (Delbac et al., 2001). Furthermore, MyoC and MORN1, a classical *T. gondii* basal pole marker, are reported to colocalize (Gubbels et al., 2006), which is probably the explanation for the BCC7 collection in a yeast-two-hybrid screen using MORN1 as a bait (Engelberg et al., 2016). A somewhat similar result occurs with another well-known basal pole marker, TgCEN2. Indeed, on a CEN2 BioID screen BCC7 was picked up (Engelberg et al., 2021), but the opposite was not seen in our studies. One question still to be resolved is the interaction between these proteins, including the possibility that BCC7 form a stabilization scaffolding complex during some part of the cycle.

The BCC7 sequence contains also a high number of phosphorylation/dephosphorylation sites, a post-translational modification (PTMs) that regulates several checkpoints in the lytic cycle (He et al., 2020). This PTM is a sign of potential regulatory function, as it affects not only the protein structure, but also its subcellular localization and interaction with other biomolecules. Moreover, the large E and E/R rich (glutamate and arginine) regions present in the sequence sustains this idea, as these repeats are known to be involved in regulating protein-protein interactions (McBride et al., 2009). There is also a VPV region on BCC7, a common hallmark for IMC proteins (Gould et al., 2008) and would explain why it was annotated as this category according to the HyperLOPIT approach (Barylyuk et al., 2020). Another PTM in the predicted structure of BCC7 is ubiquitination sites restricted to the C-terminus, a characteristic of cytoskeletal and IMC proteins in *T. gondii* (Silmon de Monerri et al., 2015). As ubiquitylation contributes to cell division and host cell invasion by inducing proteasome-degradation protein turnover, if we combine both PTM results together, we could enforce the idea of BCC7 as being a regulatory partner in endodyogeny besides its structural function.

Taking in consideration the possible structural and regulatory possible functions, as well as its big size and strategic localization at the end of most IMC complex and before myosin motors, it was a surprising result the *in vitro* dispensable phenotype observed based on plaque formation capacity and motile activity, coinciding with its fitness score (Sidik et al., 2016). Nevertheless, our approach in this study was at the level of protein elimination; a recent work by the Gubbels lab (Gubbels et al., 2022) show that BCC7 gene knock-out causes a slightly disorganized vacuole compared to the wild type. This could be due to subtle defects in the formation and

maintenance of the cytoplasmic bridges between progeny, as the same phenotype was observed by MyoI knock-out.

However, several points regarding the relationships between BCC7 and the IMC network since BCC7 localizes at the limit of the latter could be addressed in the future with the main questions listed below:

- How is the oligomerization of BCC7 formed, resulting in the ordered ring structure? Cryo EM analysis could shed light on the atomic 3D structure of BCC7 but also on the ring structures and provide few clues on the function of the claw-like structures observed that point towards the IMC.
- What is the contribution of BCC7 for the actin cytoskeleton stabilization and network organization? BCC7 is at the interface of the organization of MyoC, possibly interacting due to its position with basal pole actin, which could play a role in motility (*i.e.* during twirling), invasion (*i.e.* for the host-cell penetration and constriction) and with reported activity in intravacuolar communication during budding (Periz et al., 2017). As the subpellicular cortical microtubules don't reach to the basal pole, another scaffold could play the cytoskeleton stabilization role, and BCC7 could be a player in that organization.
- Can we define how MyoC and possibly other Myosins (*e.g.* MyoI) anchor to a permit force transmission? Would BCC7 and other potential scaffolding components be involved during twirling and twisting-associated force development? As the knock-out phenotypic analysis suggests, there could also be a possible link between BCC7 and MyoI for vacuole communication.

5. Conclusion

Concluding this three-year (and a bit more) journey that led into the intricate and particular world of *Toxoplasma gondii*'s biomechanics is not an easy task, but now in hindsight, I can have a better picture of the impact that the two projects presented in this manuscript carry. Both comprise a high amount of originality in the combination of biochemistry, biophysics and cell biology techniques that added an extra challenge to the already remarkable mechanic properties of the *T. gondii* tachyzoite.

For the project described on Chapter 1, we provided a step forward in providing a thorough quantitative analysis on the bio-physicochemical requirements relying on tachyzoite-substrate adhesion and motility. We uncovered that the tachyzoite only attaches through the two poles to generate the traction necessary for its helical gliding, and we illuminated the critical role of GAG species for productive motility. Furthermore, the technical toolkit presented, with the combination of micropattern, QCM-D and tunable surface PEG/SAv-biotin layers, has the potential application on characterization of interfaces (*i.e.* cell-ligands, cell-cell and cell-substrate interactions) that goes beyond *T. gondii* or the Apicomplexan field. Overall, our findings not only refined the understanding the tachyzoite gliding's mechanics but also provided a new perspective on how cellular adhesion intertwine in the context of motility.

Going further into the cellular landscape, the second chapter directed our focus towards the basal pole, introducing the 500 kDa protein BCC7 that occupies a pivotal position in the architecture of the tachyzoite's basal pole between the Inner Membrane Complex and myosin motors. We showed its anteroposterior trafficking process while describing its role as scaffold structure. Although the project is framed in a fundamental scientific research, in the long term in a clinical perspective, a detailed understanding of the molecular players in the basal pole should provide targets for therapeutic applications, especially in the current advancements in myosin inhibitors for *Toxoplasma*.

In conclusion, the work performed during this Ph.D. enriches the understanding of *Toxoplasma gondii*'s tachyzoite biomechanics and molecular interactions, while also providing a diverse toolkit that can be applicable to study the complexities of host-pathogen interactions in the

CONCLUSIONS

future. As we bring this adventure to a close, I still feel that several interesting questions remain unexplored, as we are adding pieces to a puzzle that the scientific community will take and collaborate into.

6. Annex

In the period before formally starting the Ph.D. thesis, there were two participations in publications which are related to the main projects described in the first two chapters. As such, in this section we will briefly overview their context, our contributions to them and the main highlights of the results obtained.

6.1 Broncel et al., *eLife*, 2020

6.1.1 Context and questions

The experiments performed for this publication are a result of a planned collaborative program with the Dr. Moritz Treeck laboratory at Francis Crick Institute, UK. They were performed with the aim to complement their investigation line with state-of-the-art videomicroscopy techniques and quantitative image analysis.

The main goal of the study relates to the identification of myristoylated and glycosylphosphatidylinositolated (GPI) anchored proteins, present in *T. gondii* and also in its close relative *P. falciparum*. To this end, the Treeck team has combined several chemoproteomic tools. Among the myristoylated proteins and novel substrates across the “invasion-replication-egress lytic cycle” they were able to detect, they identified a myristoylation modification of the microneme protein 7 (MIC7). MIC7 has been previously identified as a type I transmembrane protein, composed of an N-terminal signal peptide, five EGF-like domains, a membrane spanning region and a short cytoplasmic tail (Meissner, Reiss, et al., 2002). The remarkable characteristic of MIC7 is that it seems it follows the secretory pathway with the myristoylated N-terminus facing the lumen of the micronemes. Because previously this protein has been suggested to be expressed in the bradyzoite stage of the *T. gondii* development (Meissner, Reiss, et al., 2002), this research was the first piece of evidence that MIC7 is expressed in the tachyzoite stage, based on genome annotation and high-confidence proteome comparison between both stages. Since the functional contribution of the MIC7 was yet to be known, my contribution to the research was to assess the consequences of MIC7 loss on the tachyzoite motile and invasive behavior as a direct way to pin down MIC7 contribution to the processes.

To achieve these objectives, we could count on four transgenic lines of parasites engineered by the Treeck laboratory. First we had an inducible knock-out (iKO) *T. gondii* line which carried the dimerizable recombinase DiCre/LoxP system (Andenmatten et al., 2013) in a parental type 1 RH Δ ku80 background strain (Huynh & Carruthers, 2009). To obtain such iKO, the wild type (WT) *mic7* coding sequence was replaced by a recodoned version, flanked at each end with two LoxP regions and tagged with a C-terminally positioned HA-Flag double epitopes. The Cre recombinase (DiCre) is used to mediate the excision and loss of loxP-flanked DNA sequences in a rapamycin controlled manner, thereby allowing generating *mic7* KO parasites. In addition, two more lines were constructed. The first consists of a complementation to the iKO line with the introduction of a Ty tagged WT *mic7* copy at the *uprt* locus. The second carries a mutated copy of the *mic7* gene at the *uprt* locus (called cMut) in the iKO background, which differs from the WT sequence in its inability to be myristoylated and is in fusion with the N-terminally positioned Ty epitope tag.

6.1.2 Contributions to the publication

For this jointed collaboration, we dissected the motile and invasive behaviors of tachyzoite expressing or not MIC7, or expressing a mutated myristoylated version of MIC7. We performed high-speed high-resolution live imaging to monitor the locomotive behavior and detect potential failure in invasion events, including abnormal formation of the entry vesicle and parasitophorous vacuole, using as a target host a Human Bone OsteoSarcoma cells (U2OS) that stably expressed the GFP-GPI plasma membrane fluorescent reporter.

The resulting videosequences were subsequently qualitatively and statistically validated by applying complementary 2D gliding experiments and large-scale invasion assays to provide relevant statistical analysis for the invasive capabilities of all the described MIC7 lines.

6.1.3 Main highlights of the study

- The libraries of myristoylated- and glycosylphosphatidylinositol- anchored *T. gondii* tachyzoite proteins were obtained by a combination of metabolic labeling using myristic acid analogs and small-molecule NMT inhibition.
- MIC7 is a microneme protein included in the newly described myristoylated proteins.

- MIC7 possesses an important role in tachyzoite fitness-conferring abilities such as invasion and cell attachment. Nevertheless, MIC7 is not essential for a correct lytic cycle.
- The myristoylation of MIC7 is necessary for host cell invasion. The depletion of MIC7 complemented with a wild-type or mutant version of the protein does not restore full-invasive phenotypes. Nevertheless, it has no impact on the tachyzoite's motility.

6.1.4 Publication

Broncel M, Dominicus C, Vignetti L, Nofal SD, Bartlett EJ, Touquet B, Hunt A, Wallbank BA, Federico S, Matthews S, Young JC, Tate EW, Tardieux I, Treeck M. Profiling of myristoylation in *Toxoplasma gondii* reveals an *N*-myristoylated protein important for host cell penetration. *Elife*. 2020 Jul 3;9:e57861. doi: 10.7554/eLife.57861. PMID: 32618271; PMCID: PMC7373427.

Profiling of myristoylation in *Toxoplasma gondii* reveals an *N*-myristoylated protein important for host cell penetration

Malgorzata Broncel¹, Caia Dominicus¹, Luis Vigetti², Stephanie D Nofal¹, Edward J Bartlett³, Bastien Touquet², Alex Hunt¹, Bethan A Wallbank¹, Stefania Federico⁴, Stephen Matthews⁵, Joanna C Young¹, Edward W Tate³, Isabelle Tardieux², Moritz Treeck^{1*}

¹Signalling in Apicomplexan Parasites Laboratory, The Francis Crick Institute, London, United Kingdom; ²Institute for Advanced Biosciences, Team Membrane Dynamics of Parasite-Host Cell Interactions, CNRS UMR5309, INSERM U1209, Université Grenoble Alpes, Grenoble, France; ³Department of Chemistry, Imperial College London, Molecular Sciences Research Hub, White City Campus, London, United Kingdom; ⁴The Peptide Chemistry STP, The Francis Crick Institute, London, United Kingdom; ⁵Department of Life Sciences, Imperial College London, South Kensington, London, United Kingdom

Abstract *N*-myristoylation is a ubiquitous class of protein lipidation across eukaryotes and *N*-myristoyl transferase (NMT) has been proposed as an attractive drug target in several pathogens. Myristoylation often primes for subsequent palmitoylation and stable membrane attachment, however, growing evidence suggests additional regulatory roles for myristoylation on proteins. Here we describe the myristoylated proteome of *Toxoplasma gondii* using chemoproteomic methods and show that a small-molecule NMT inhibitor developed against related *Plasmodium* spp. is also functional in *Toxoplasma*. We identify myristoylation on a transmembrane protein, the microneme protein 7 (MIC7), which enters the secretory pathway in an unconventional fashion with the myristoylated N-terminus facing the lumen of the micronemes. MIC7 and its myristoylation play a crucial role in the initial steps of invasion, likely during the interaction with and penetration of the host cell. Myristoylation of secreted eukaryotic proteins represents a substantial expansion of the functional repertoire of this co-translational modification.

*For correspondence: moritz.treeck@crick.ac.uk

Competing interest: See page 32

Funding: See page 32

Received: 14 April 2020

Accepted: 27 June 2020

Published: 03 July 2020

Reviewing editor: Dominique Soldati-Favre, University of Geneva, Switzerland

© Copyright Broncel et al. This article is distributed under the terms of the [Creative Commons Attribution License](https://creativecommons.org/licenses/by/4.0/), which permits unrestricted use and redistribution provided that the original author and source are credited.

Introduction

Toxoplasmosis currently affects approximately one third of the world's population (*Robert-Gangneux and Dardé, 2012*). It is caused by the obligate protozoan parasite *Toxoplasma gondii* originating from the phylum Apicomplexa. While the majority of human infections are asymptomatic, the disease manifests its severity in immunocompromised individuals, such as those receiving chemotherapy and transplants or in HIV/AIDS patients (*Montoya and Liesenfeld, 2004*). Key steps in the successful propagation of *Toxoplasma* infection in the acute phase are orchestrated cycles of invasion and egress of tachyzoites from host cells (*Black and Boothroyd, 2000*). These crucial processes are regulated by several post-translational modifications (PTMs), such as phosphorylation (*Gaji et al., 2015; Jacot and Soldati-Favre, 2012; Lourido et al., 2010; Treeck et al., 2014*), ubiquitination (*Silmon de Monerri et al., 2015*), and also protein lipidation, such as palmitoylation and myristoylation (*Alonso et al., 2012; Fréchal et al., 2014*).

While the extent of protein palmitoylation in *Toxoplasma* has been investigated (*Caballero et al., 2016; Foe et al., 2015*), the myristoylated proteome remains largely uncharacterised. *N*-

eLife digest A microscopic parasite known as *Toxoplasma gondii* infects around 30% of the human population. Most infections remain asymptomatic, but in people with a compromised immune system, developing fetuses and people infected with particular virulent strains of the parasite, infection can be fatal. *T. gondii* is closely related to other parasites that also infect humans, including the one that causes malaria. These parasites have complex lifecycles that involve successive rounds of invading the cells of their hosts, growing and then exiting these cells. Signaling proteins found at specific locations within parasite cells regulate the ability of the parasites to interact with and invade host cells. Sometimes these signaling proteins are attached to membranes using lipid anchors, for example through a molecule called myristic acid.

An enzyme called NMT can attach myristic acid to one end of its target proteins. The myristic acid tag can influence the ability of target proteins to bind to other proteins, or to membranes. Previous studies have found that drugs that inhibit the NMT enzyme prevent the malaria parasite from successfully invading and growing inside host cells. The NMT enzyme from *T. gondii* is very similar to that of the malaria parasite. Broncel et al. have shown that the drug developed against *P. falciparum* also inhibits the ability of *T. gondii* to grow. These findings suggest that drugs against the NMT enzyme may be useful to treat diseases caused by *T. gondii* and other closely-related parasites.

Broncel et al. also identified 65 proteins in *T. gondii* that contain a myristic acid tag using an approach called proteomics. One of the unexpected 'myristoylated' proteins identified in the experiments is known as MIC7. This protein was found to be transported onto the surface of *T. gondii* parasites and is required in its myristoylated form for the parasite to successfully invade host cells. This was surprising as myristoylated proteins are generally thought to not enter the pathway that brings proteins to the outside of cell.

These findings suggest that myristic acid on proteins that are secreted can facilitate interactions between cells, maybe by inserting the myristic acid into the cell membrane.

myristoylation is an irreversible, predominantly co-translational covalent addition of myristic acid to an N-terminal glycine (Boutin, 1997; Gordon et al., 1991). Functionally, myristoylation often primes proteins for subsequent palmitoylation and a stable protein-membrane association (Martin et al., 2011; Wright et al., 2010), however, it has also been shown to facilitate protein-protein interactions (PPIs) (Chow et al., 1987; Mousnier et al., 2018), affect protein activity (Zhu et al., 2019) as well as structure and stability (Zheng et al., 1993). It is catalysed by *N*-myristoyl transferase (NMT), which is conserved across many organisms, including *Toxoplasma*, and has been reported to be a prominent drug target in fungal (Devadas et al., 1995; Nagarajan et al., 1997), *Trypanosome* (Frearson et al., 2010; Wright et al., 2016) and *Leishmania* infections (Hutton et al., 2014; Wright et al., 2015). In *Plasmodium falciparum* (the major causative agent of malaria), inhibition of NMT leads to severe pleiotropic consequences affecting parasite development (Schlott et al., 2019; Wright et al., 2014), highlighting the importance of myristoylation for parasite survival and progression.

An N-terminal glycine (MG motif) is a requirement, but not a predictor of myristoylation. Approximately 6% of all gene products in *Toxoplasma* contain an N-terminal glycine and an in silico prediction of myristoylation suggests that ~ 1.8% of all *T. gondii* gene products are modified (Alonso et al., 2019). The functional significance of myristoylation has been described for only a few *T. gondii* proteins, and mainly in conjunction with adjacent palmitoylation that promotes stable membrane attachment. These proteins include key signal mediators in parasite egress and invasion, for example CDPK3 (Garrison et al., 2012; McCoy et al., 2012), PKG (Brown et al., 2017), PKAr (Jia et al., 2017b; Uboldi et al., 2018); proteins involved in invasion, for example IMP1 (Jia et al., 2017a); parasite gliding, for example GAP45 and GAP70 (Fréchal et al., 2010); division, for example F-box protein 1 and ISP1, 2, 3 (Baptista et al., 2019; Beck et al., 2010); and correct rhoptry positioning required for invasion, for example ARO (Cabrerá et al., 2012; Mueller et al., 2013). Collectively, these studies show key roles for myristoylation throughout the parasite's lytic cycle, but the function of myristoylation in the absence of palmitoylation and its relationship to other PTMs remains poorly described.

By combining several chemoproteomic tools for substrate identification with a small-molecule NMT inhibitor, we provide experimentally-validated libraries of myristoylated as well as glycosylphosphatidylinositol (GPI) anchored proteins in *T. gondii*. We identify all the previously reported myristoylated proteins, as well as novel substrates with heterogeneous localisations and variable functions across the lytic cycle. Furthermore, by analysing substrate orthology in other Apicomplexans we provide new clues to the identity of previously uncharacterized myristoylated proteomes across the phylum. We validate the presence and elucidate the functional importance of myristoylation for the microneme protein MIC7, a predicted type I transmembrane protein. Utilizing conditional substrate depletion and complementation with wild-type (cWT) and myristoylation mutant (cMut) versions, we demonstrate that myristoylation of MIC7 is functionally important in host cell invasion. Taken together, our study identifies a large proportion of the *Toxoplasma* myristoylated proteome and points to unexpected and novel functions of myristoylation in *Toxoplasma* that extend beyond priming for palmitoylation and stable membrane attachment.

Results

Metabolic labelling allows for enrichment and visualisation of myristoylated and GPI-anchored proteins in *Toxoplasma*

To visualise the extent of myristoylation in *Toxoplasma*, we adapted a metabolic labelling approach that has previously been applied to mammalian cells (Broncel *et al.*, 2015; Thion *et al.*, 2014) and protozoan parasites (Wright *et al.*, 2014; Wright *et al.*, 2016; Wright *et al.*, 2015). In this workflow, a myristic acid (Myr) analogue containing a terminal alkyne group (YnMyr) is added to cell culture upon infection with *Toxoplasma* tachyzoites (Figure 1A). The hydrophobic nature of YnMyr allows for optimal biomimicry of myristate and conversion into the active co-substrate YnMyr-CoA in situ, while the alkyne tag allows for NMT-mediated metabolic labelling of both host and parasite substrate proteins. Upon cell lysis, labelled proteins are liberated and conjugated to azide-bearing multifunctional capture reagents by a click reaction (Heal *et al.*, 2012). The conjugation process introduces secondary labels, like biotin and fluorophores, allowing for substrate enrichment on streptavidin beads and visualisation via in-gel fluorescence (igFL), respectively. To investigate the extent of YnMyr incorporation, intracellular tachyzoites were treated with either Myr or increasing concentrations of YnMyr for 16 hr. Within this timeframe protein labelling in vivo did not appear to exert any toxic effects on *Toxoplasma* parasites. Labelled proteins were then conjugated to a capture reagent and resolved by SDS-PAGE. As visualised by igFL, the labelling was concentration-dependent with only negligible background (Figure 1—figure supplement 1A). In addition, the extent of labelling did not seem to depend on parasite localisation inside or outside the host cell, and was efficiently out-competed by excess myristate, indicating that YnMyr is an effective mimic of myristate in *Toxoplasma* parasites (Figure 1—figure supplement 1B). To estimate the efficiency of substrate enrichment, we took advantage of the biotin moiety that enables a streptavidin-based pull down. Using igFL as readout we observed robust enrichment of protein substrates in a YnMyr-dependent manner, and detected very little background in controls (Figure 1—figure supplement 1C).

It has been reported that in *Plasmodium* parasites, YnMyr can be incorporated not only at N-terminal glycines via amide bonds, but also through ester-linked incorporation of myristate into GPI anchors (Wright *et al.*, 2014). These two distinct types of labelling can be readily distinguished by their different sensitivity to base treatment; amide bonds are stable in basic conditions, whereas ester bonds are hydrolysed. To visualise the extent of YnMyr incorporation into GPI anchors in *Toxoplasma*, we performed base treatment prior to enrichment of substrate proteins and observed a reduction of igFL signal for selected enriched bands (Figure 1B). To further validate the base treatment approach, we probed known *N*-myristoylated and GPI-anchored *Toxoplasma* proteins, GAP45 and SAG1, for their ability to be enriched in a base-dependent manner. In the absence of treatment, both proteins were robustly pulled down with YnMyr, while upon base treatment, only GAP45 remained enriched, confirming that it is a true myristoylation substrate (Figure 1C). Collectively, we confirmed that YnMyr is a robust and high-fidelity myristate analogue and demonstrated that it can be applied to profile both *N*-myristoylated and GPI-anchored proteins in live *T. gondii*.

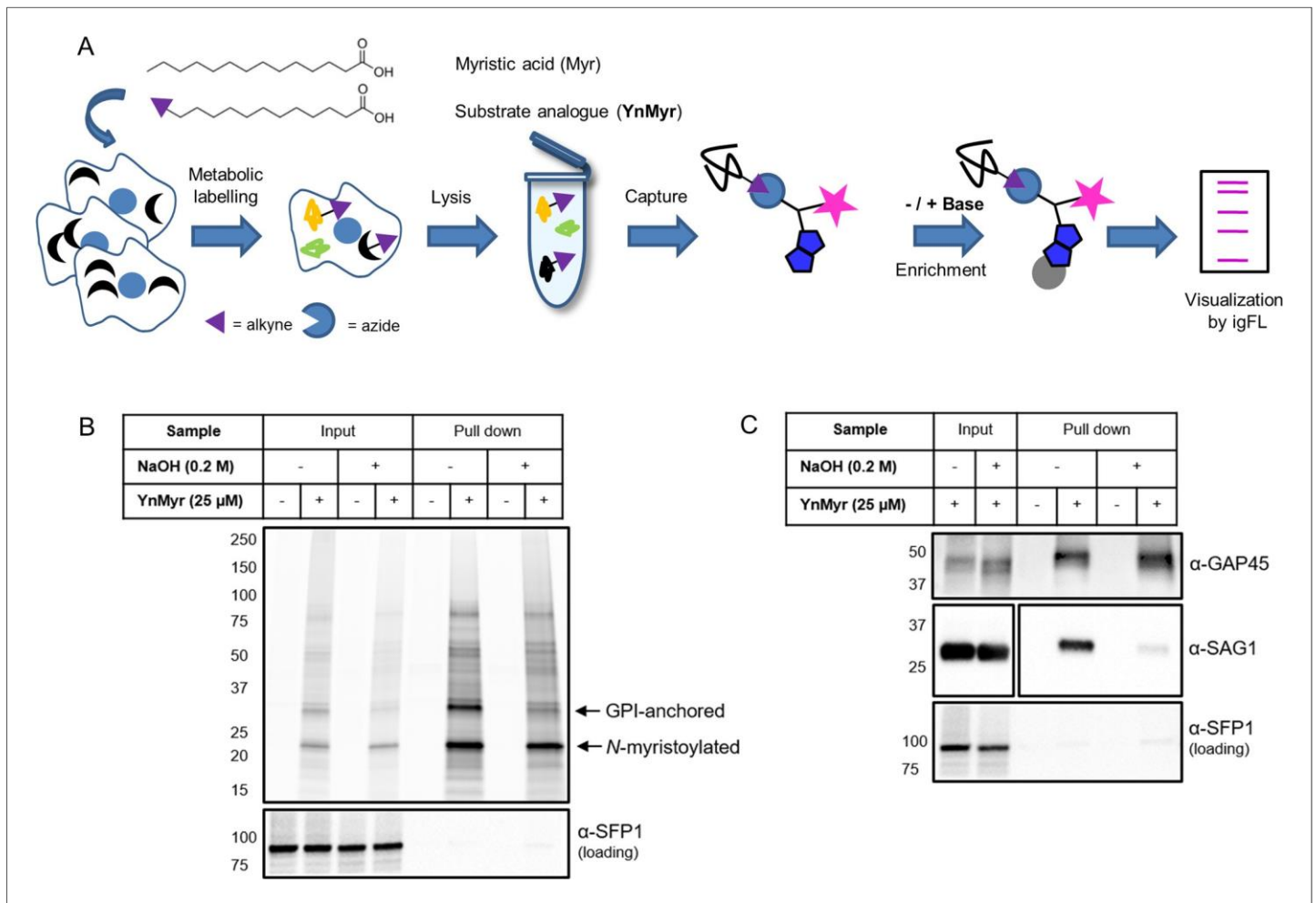


Figure 1. Metabolic labelling allows for enrichment and visualisation of myristoylated and GPI-anchored proteins in *T. gondii*. (A) Metabolic labelling workflow. (B) In gel fluorescence visualisation of YnMyr-dependent enrichment without and with the base treatment (top) and western blot with α -SFP1 (TGGT1_289540) showing the loading control (bottom). (C) Western blot analysis of YnMyr-dependent pull down for known myristoylated and GPI-anchored proteins GAP45 and SAG1, respectively. White space was used to indicate where gel lanes were not contiguous. See also *Figure 1—figure supplement 1*.

The online version of this article includes the following figure supplement(s) for figure 1:

Figure supplement 1. Metabolic labelling optimisation.

Proteomic identification of YnMyr-enriched proteins in *T. gondii*

To confidently identify YnMyr-labelled proteins in *Toxoplasma*, we applied state-of-the-art mass spectrometry (MS)-based proteomics combined with validated chemical tools (*Figure 2—figure supplement 1A*); (Broncel *et al.*, 2015; Speers and Cravatt, 2005; Thinon *et al.*, 2014; Wright *et al.*, 2014). We started with a small-scale pilot experiment to test our workflow and differentiate between N-myristoylation-based enrichment and GPI-anchored substrates. We metabolically labelled intracellular tachyzoites of the RH strain (Huynh and Carruthers, 2009) with either YnMyr or Myr each at 25 mM for 16 hr. We then lysed the infected cell monolayers and performed the click reaction with the azido biotin capture reagent (reagent 1) to facilitate YnMyr-dependent enrichment of labelled proteins. To distinguish myristoylated from GPI-anchored substrates, we applied base treatment prior to the streptavidin-based pull down. Following trypsin digestion, we analysed samples by LC-MS/MS and performed label free quantification (LFQ) of enriched proteins. We quantified 2363 human and *Toxoplasma* proteins, 349 of which were parasite proteins with YnMyr intensities irrespective of base treatment (*Supplementary file 1*). To identify GPI-anchored proteins, we calculated log₂ fold changes between base-treated and untreated samples. To threshold we utilised the

least extreme negative value (\log_2 fold change < -1) quantified from all Surface Antigen Proteins (SAGs) detected in our study, which are known to be GPI-anchored (Figure 2—figure supplement 1B). This selection strategy yielded 52 substrates, that included known and predicted GPI-anchored proteins (Supplementary file 1). To identify myristoylated proteins we utilised a stringent selection method based on three criteria: a) robust YnMyr/Myr enrichment (\log_2 fold change > 2) with threshold selected based on known myristoylated proteins (Figure 2—figure supplement 1C), b) the presence of an MG motif and c) insensitivity to base treatment. 56 proteins met these criteria, including those previously reported as myristoylated (Supplementary file 1). Analysis of post enrichment supernatants did not reveal any substantial changes between proteomes of the YnMyr- and Myr-treated samples, confirming that the observed enrichment is not due to globally altered protein abundance (Figure 2—figure supplement 1D and Supplementary file 1).

After successful testing of the metabolic labelling workflow, we performed a more elaborate MS experiment using cleavable capture reagents bearing either trypsin (reagent 2) or TEV (reagent 3) cleavable linkers (Figure 2—figure supplement 1A). In contrast to a non-cleavable reagent (e.g. reagent 1) that provides only indirect proof of substrate myristoylation, cleavable reagents allow for detection of myristoylated peptides in addition to peptides that originate from the enriched proteins (Figure 2A). This additional layer of confidence in MS-based substrate identification is especially important given the high level of non-myristoylation dependent background reported for metabolic labelling with YnMyr (Broncel et al., 2015; Wright et al., 2016; Wright et al., 2015). While reagent 2 has been validated as a tool for myristoylated protein and peptide discovery (Broncel et al., 2015), reagent 3 (Speers and Cravatt, 2005), which is expected to produce less background and improve myristoylated peptide discovery, has not previously been applied to study protein myristoylation. We therefore first tested reagent 3 in terms of YnMyr-dependent protein enrichment and observed robust pull down of potential NMT substrates (Figure 2—figure supplement 1E). We next generated samples for the MS workflow as described above but, instead of conjugating reagent 1, we conjugated either 2 or 3, each in biological triplicate, to labelled proteins via click reaction to enable myristoylation-dependent pull down. As depicted in Figure 2A, reagent 2 requires only a single trypsin digestion step to liberate both unmodified and myristoylated peptides in one pool. By contrast, reagent 3 requires both trypsin and TEV protease digestion and, depending on the enzyme combination, releases unmodified and myristoylated peptides in either one (TEV I) or two (TEV II) separate fractions (Figure 2A). In the TEV I strategy TEV protease is used to cleave proteins from beads followed by trypsin digestion of proteins into peptides. The cleavage will only occur for proteins bound via the TEV linker and not for the non-specifically bound ones, which should significantly reduce background. In the TEV II strategy, trypsin is used first to remove most proteins from the beads, only retaining the captured myristoylated peptides. These are then specifically released using TEV protease cleavage resulting in much reduced sample complexity, which increases the myristoylated peptide discovery by MS. Following digestion, all samples were subjected to LC-MS/MS, and LFQ was performed to identify proteins robustly enriched in YnMyr-dependent manner. This yielded 206 human and 117 *T. gondii* proteins bearing an N-terminal MG motif (Supplementary file 2). Within the parasite protein pool, we obtained statistically significant (FDR 1%, \log_2 fold change > 2) enrichment in YnMyr over Myr controls for 72 potential substrates using reagent 2 (Supplementary file 2). For reagent 3, which was used in two different scenarios (TEV I and TEV II) resulting in larger variability between replicates, we utilised a fold change based threshold (\log_2 fold change > 2) and obtained 48 robustly enriched proteins (Supplementary file 2). Reassuringly, we observed a ~ 5 and ~ 8 fold reduction in background in TEV I vs TEV II and TEV I vs reagent 2, respectively, as shown by the number of proteins quantified in Myr controls (Supplementary file 2). Collectively we identified 76 significantly YnMyr-enriched proteins utilizing reagents 2 and 3 with an overlap of 60% (Figure 2B, Supplementary file 2) which provides substantial confidence to the accuracy of our results. Application of the same selection criteria to 206 human MG proteins identified in our study yielded 102 potential substrates. 84 of these proteins have previously been reported as myristoylated (Broncel et al., 2015; Castrec et al., 2018; Thimon et al., 2014), which further strengthens our substrate identification strategy.

We next focused on the identification of myristoylated peptides in samples processed with reagents 2 and 3. Using stringent criteria for the unbiased identification of the myristoylation adduct, as well as manual validation of the acquired MS/MS spectra, we identified 31 myristoylated peptides (Supplementary file 2), 24 of which were detected using reagent 2, and 20 using reagent 3

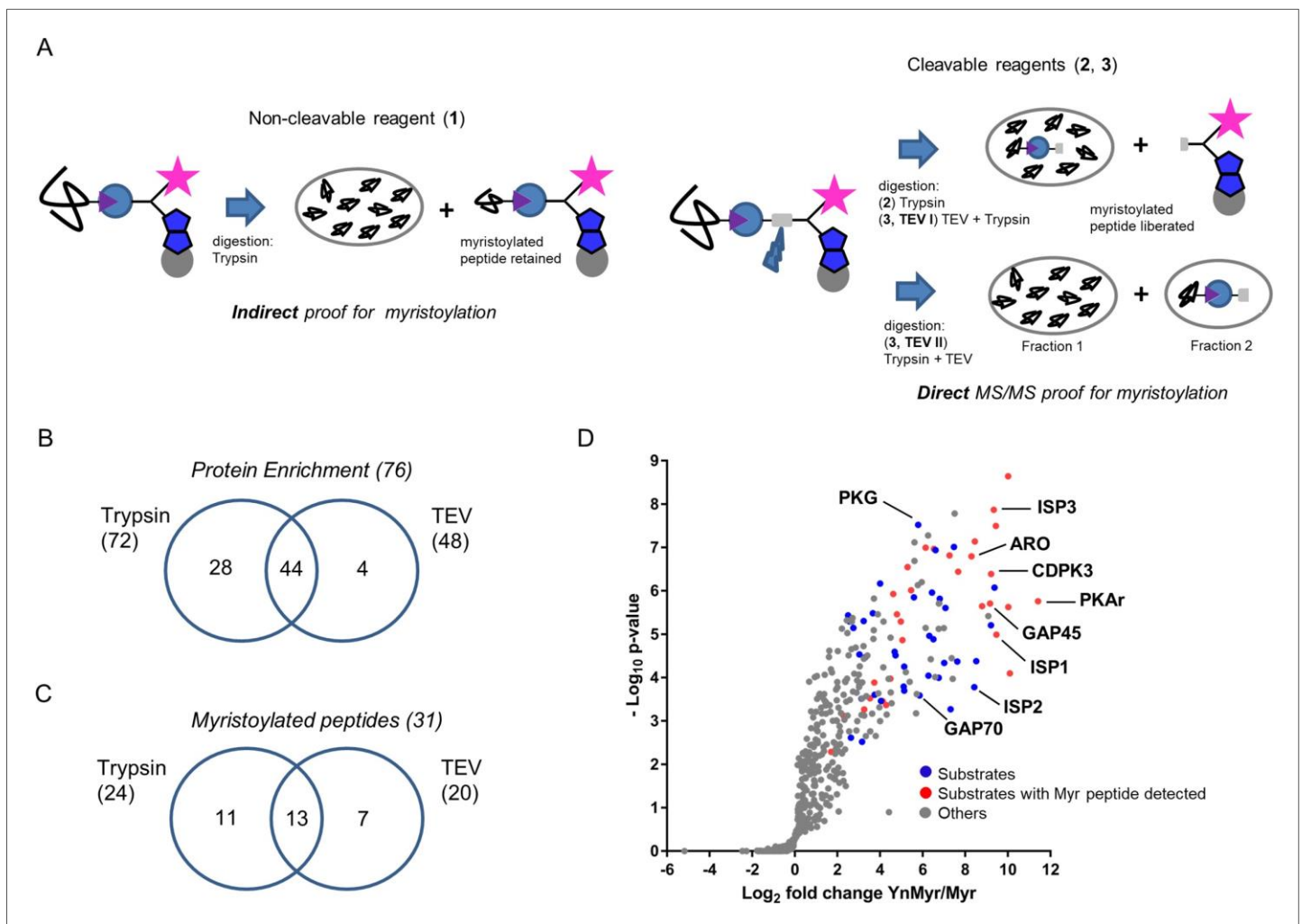


Figure 2. Identification of the YnMyr-enriched proteome in *T. gondii*. (A) Schematic representation of the MS workflow using non-cleavable and cleavable capture reagents. (B) Venn diagram illustrating the overlap between significantly YnMyr-enriched proteins identified with capture reagents 2 and 3. The number of significantly enriched proteins per reagent and in total is given in parenthesis. (C) Venn diagram showing the overlap in myristoylated peptide discovery between the two cleavable capture reagents used in this study. The number of modified peptides identified with each reagent and in total is given in parenthesis. (D) Label free quantification of the \log_2 fold changes in YnMyr enrichment over the Myr control plotted against the statistical significance for all parasite proteins detected in this study using reagent 2. Proteins with N-terminal glycine and significant, base-insensitive enrichment with at least two capture reagents are highlighted in blue and red subject to the presence of a myristoylated peptide. All other identified proteins (YnMyr-enriched with only one reagent, background and GPI-anchors) are represented in grey. See also [Figure 2—figure supplement 1](#), [Supplementary file 1](#) and [Supplementary file 2](#).

The online version of this article includes the following figure supplement(s) for figure 2:

Figure supplement 1. Identification of the YnMyr-enriched proteome in *T. gondii*.

([Figure 2C](#)). None of these peptides were detected in Myr controls, and the myristoylation adduct was not identified on cysteine residues. Despite almost equal numbers of peptides detected by the two reagents, the overlap was only 40% ([Figure 2C](#)), confirming the added value of orthogonal methods for modified peptide detection. As envisioned in our design strategy, we obtained an increase in myristoylated peptide discovery in TEV II (17) vs TEV I (12) workflow ([Figure 2—figure supplement 1F](#)).

Finally, to summarise our global proteomic study, we combined our results on both protein enrichment and the modified peptide levels. We filtered for proteins identified with at least two of three capture reagents or proteins for which we detected a lipid modified peptide. This resulted in

65 proteins, of which 48% have direct MS/MS evidence for protein myristoylation (Supplementary file 2, Figure 2D).

Chemical inhibition of *Tg*NMT

Given that our global proteomic screen provided direct proof for substrate myristoylation for approximately 50% of selected proteins, we sought for an alternative strategy for substrate validation using NMT inhibitors (NMTi). Here, parasites are treated with NMTi to specifically reduce the incorporation of YnMyr into nascent proteins, which can be quantified by MS (Thinon *et al.*, 2014; Wright *et al.*, 2014; Wright *et al.*, 2016; Wright *et al.*, 2015). In the absence of a dedicated *Tg*NMTi, we used IMP-1002, a compound recently shown to inhibit NMT of *Plasmodium falciparum* (Schlott *et al.*, 2019) which is related to *Toxoplasma*. Homology modelling (SWISS-MODEL, [Waterhouse *et al.*, 2018]) of the *Tg*NMT sequence onto the available *Plasmodium vivax* (another important malaria causing *Plasmodium spp.*) NMT crystal structure with bound IMP-1002 (PDB: 6MB1, [Schlott *et al.*, 2019]) revealed high sequence identity (57%) and showed that all residues directly involved in compound binding are conserved within the *Tg*NMT active site and therefore predicted to adopt an identical structural arrangement (Figure 3A). We therefore reasoned that IMP-1002 should also inhibit *Tg*NMT. To test this, we co-treated intracellular parasites 16 hr post invasion with YnMyr and increasing concentrations of the inhibitor for 5 hr and analysed the effects on YnMyr labelling of *Toxoplasma* proteins. A dose-dependent drop in igFL labelling of most protein bands was observed and further confirmed by specifically probing for CDPK1, a substrate identified herein (Figure 3B). Consistent with *Tg*NMT inhibition, CDPK1 pull down was reduced with increasing inhibitor concentrations. This was not a general reduction of protein levels as shown by anti-*Toxoplasma* antibodies. Plaque assays in the presence of inhibitor showed dose-dependent killing of parasites, suggesting that treatment with IMP-1002 has severe consequences for the *in vitro* expansion of the tachyzoite population but not for the host cells which appeared unaffected (Figure 3C).

Having confirmed target engagement with IMP-1002, we next performed a large-scale MS-based inhibitor response analysis. Intracellular parasites were fed with 25 mM YnMyr alone or co-incubated with 0.05 mM and 0.5 mM NMTi in biological triplicates. Samples were then clicked, pulled down and the level of protein myristoylation in response to IMP-1002 quantified by MS and LFQ. No major effect was observed for the lower concentration of the inhibitor, therefore we performed statistical analysis between triplicate samples treated with either only YnMyr, or YnMyr + 0.5 mM NMTi. We identified a statistically significant (FDR 5%, log₂ fold change > 0.5) response for 56 proteins (Figure 3D, Supplementary file 3). Analysis of total proteomes from inhibited samples confirmed that the observed substrate response was not due to the altered protein abundance (Figure 3—figure supplement 1, Supplementary file 3). 49 significant responders contained the MG motif with 47 of these being significantly enriched in our previous experiment, while two proteins were not quantified. Specific dose-responses were plotted for selected proteins identified previously as significantly YnMyr-enriched (Figure 3E). While most showed a robust response to the highest concentration of inhibitor, CDPK3 and PKG did not, despite substantial literature evidence for myristoylation (Brown *et al.*, 2017; Garrison *et al.*, 2012; McCoy *et al.*, 2012), including the presence of a myristoylated peptide in case of CDPK3 (Supplementary file 2). In fact, a total of 7 proteins for which the myristoylated peptide was detected did not respond robustly to NMT inhibition (Supplementary file 3). This behaviour is surprising, however a similar observation has been described for other organisms (Thinon *et al.*, 2014; Wright *et al.*, 2014; Wright *et al.*, 2016; Wright *et al.*, 2015) and could be due to low protein turnover, higher affinity for NMT, or potential interference from other modifications, such as protein S-acylation for example. A further seven proteins for which we obtained myristoylated peptides were not quantified at the highest concentration of IMP-1002 (Supplementary file 3), suggesting that their myristoylation state, and therefore enrichment, is most affected by NMT inhibition.

A significant response to NMTi was also observed for seven proteins that did not contain the MG motif (Figure 3D, Supplementary file 3). This could be due to post-translational myristoylation where proteolysis results in formation of N-terminal glycine (Martin *et al.*, 2011; Thinon *et al.*, 2014), a tight association in complex with an NMT substrate (Thinon *et al.*, 2014), potential protein mis-annotation or an off-target effect of the inhibitor which was originally designed for *Pf*NMT. Importantly, all non MG proteins previously assigned as sensitive to base treatment, including all

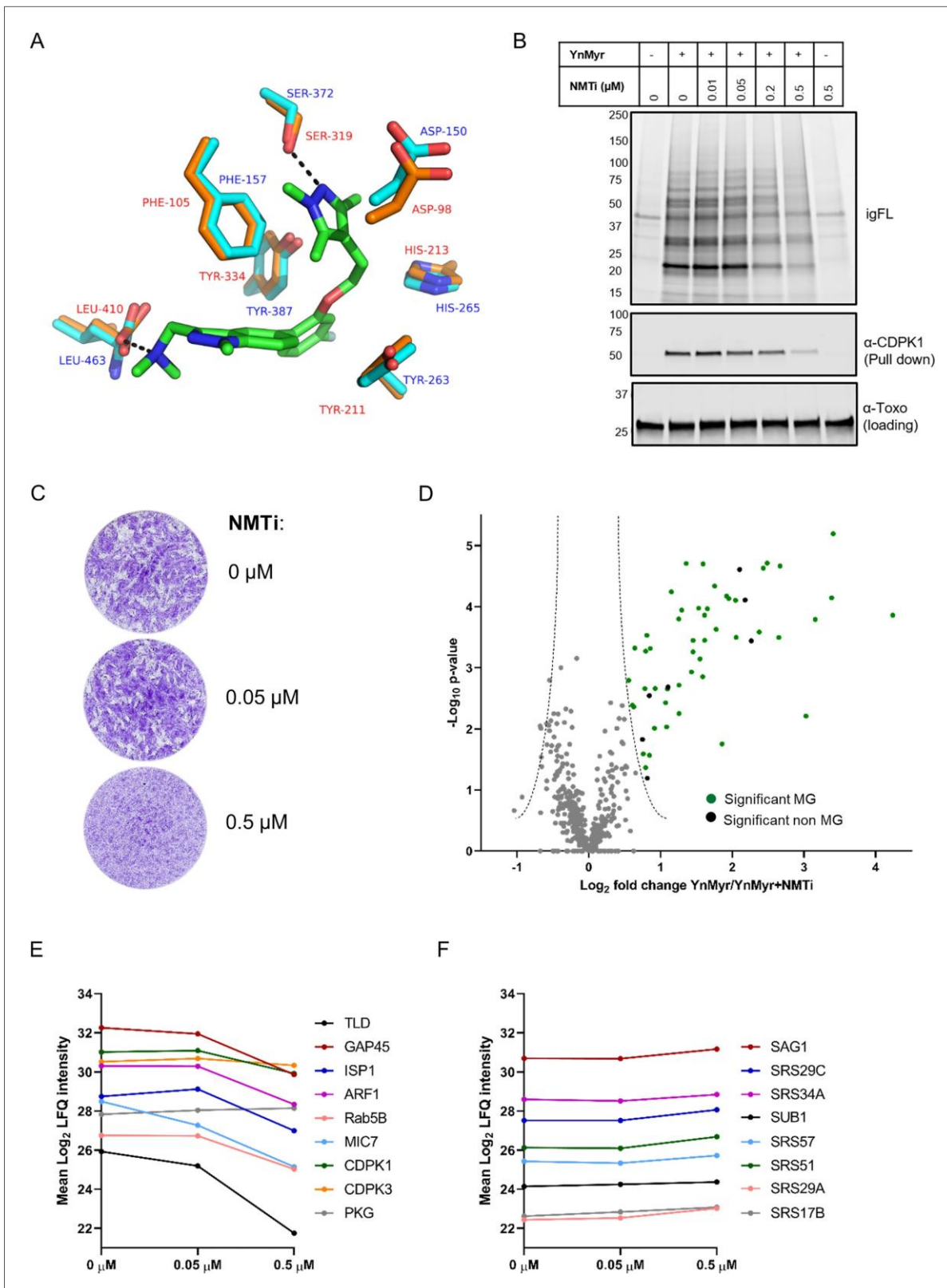


Figure 3. Chemical inhibition of *TgNMT* and substrate response. (A) Prediction of IMP-1002 interaction with *TgNMT* based on the *PvNMT* crystal structure. Crystal structure of the *PvNMT* (PDB: 6MB1, *Schlott et al., 2019*) active site (orange, red text) with IMP-1002 inhibitor bound, overlaid with a *TgNMT* model (cyan, blue text). Hydrogen bonds between key *PvNMT* residues (Serine and Leucine) and IMP-1002 are shown as black dashes. (B) Analysis of the dose response to IMP-1002 via igFL and by western blotting with CDPK1 – a substrate identified in this study. (C) Plaque assay
 Figure 3 continued on next page

Figure 3 continued

illustrating differential killing of parasites and the host cells. The assay was performed for 5 days in three biological replicates, each in technical triplicate, representative images are shown. (D) Label free quantification of the YnMyr label incorporation into proteins in the presence of NMTi (0.5 mM) plotted against the statistical significance for all parasite proteins detected in this study. Proteins with a significant response and N-terminal glycine (MG) are highlighted in green, those without MG highlighted in black. (E) Dose response to NMTi plotted for selected proteins with significant YnMyr enrichment. (F) Dose response to NMTi plotted for selected SAG proteins assigned previously as base sensitive. See also *Figure 3—figure supplement 1* and *Supplementary file 3*.

The online version of this article includes the following figure supplement(s) for figure 3:

Figure supplement 1. Chemical inhibition of TgNMT.

SAG proteins, showed no significant response to inhibitor (*Supplementary file 3, Figure 3F*) thus validating base sensitivity as a means to distinguish YnMyr incorporation at N-terminal glycines or GPI anchors.

Finally, despite no apparent effect on host cells in plaque assays (*Figure 3C*), we also observed a certain level of response to IMP-1002 for host proteins (*Supplementary file 3*). This suggests that human NMT is also targeted by this compound, however, without visible impact on the integrity of the monolayer of host cells.

The myristoylated proteome of *Toxoplasma*

To generate a comprehensive list of myristoylated proteins in *Toxoplasma*, we combined YnMyr enrichment with the substrate response to NMT inhibition and the myristoylated peptide discovery. This stringent selection strategy yielded 65 substrates that were further split based on the confidence level (*Supplementary file 4*). 42 substrates were classified as high confidence (the presence of myristoylated peptide and/or robust response to NMT inhibition with YnMyr enrichment \geq two capture reagents) while 19 were classified as medium confidence (the presence of myristoylated peptide or response to NMT inhibition with YnMyr enrichment with one capture reagent). Finally, PKG and PPM5C that did not pass our confidence criteria, yet have been reported as myristoylated by others (*Brown et al., 2017; Yang et al., 2019*), as well as two proteins that responded to NMT inhibition, yet were not present in our global enrichment analysis, were classified as lower confidence hits (*Supplementary file 4*). Our substrate list includes all proteins previously reported as myristoylated, which validates our approach and indicates that this analysis covers a large fraction of the myristoylated proteome in *Toxoplasma*. Notably, in silico prediction for myristoylation (*Alonso et al., 2019*) disagreed with 11 of our high and medium confidence substrates (*Supplementary file 4*). This is not necessarily surprising, given that the prediction was based on a consensus myristoylation sequence derived from other organisms (*Martin et al., 2011*), and highlights the importance of experimental validation of NMT substrates.

90% of our substrate pool represent novel substrates of TgNMT. Several of these proteins have previously been shown to play important functions across the lytic cycle, for example CDPK1 (egress/invasion; [*Lourido et al., 2010*]); PPM5C (attachment; [*Yang et al., 2019*]); ARF1 and Rab5B (trafficking; [*Kremer et al., 2013; Liendo et al., 2001*]). Others, for which the precise function has yet to be discovered, were assigned by gene ontology into key functional classes, like kinases, phosphatases, hydrolases and protein binding (*Supplementary file 4*). We did not obtain any evidence for myristoylation on known secreted *Toxoplasma* proteins, such as rhoptry or dense granule proteins, indicating that these are not substrates of host NMT after secretion. Approximately one third of the reported substrates are uncharacterized proteins, indicating that a large amount of myristoylation-related biology is still to be uncovered.

As expected, the identified substrates showed heterogeneous localisation (*Figure 4A*). Utilizing the localisation of organelle proteins by isotope tagging (LOPIT) prediction (*Barylyuk et al., 2020*) within ToxoDB (*Gajria et al., 2008*), we found proteins from key cellular organelles, including the nucleus, mitochondrion, proteasome and micronemes. In agreement with the functional relevance of myristoylation, we found 50% substrates with known or predicted localisation at the plasma membrane (PM), as well as membrane-bound compartments (e.g. inner membrane complex (IMC), endoplasmic reticulum (ER), and Golgi apparatus). Stable attachment at membranes may require a double acylation, that is both myristoylation and palmitoylation (*Wright et al., 2010*), however, only

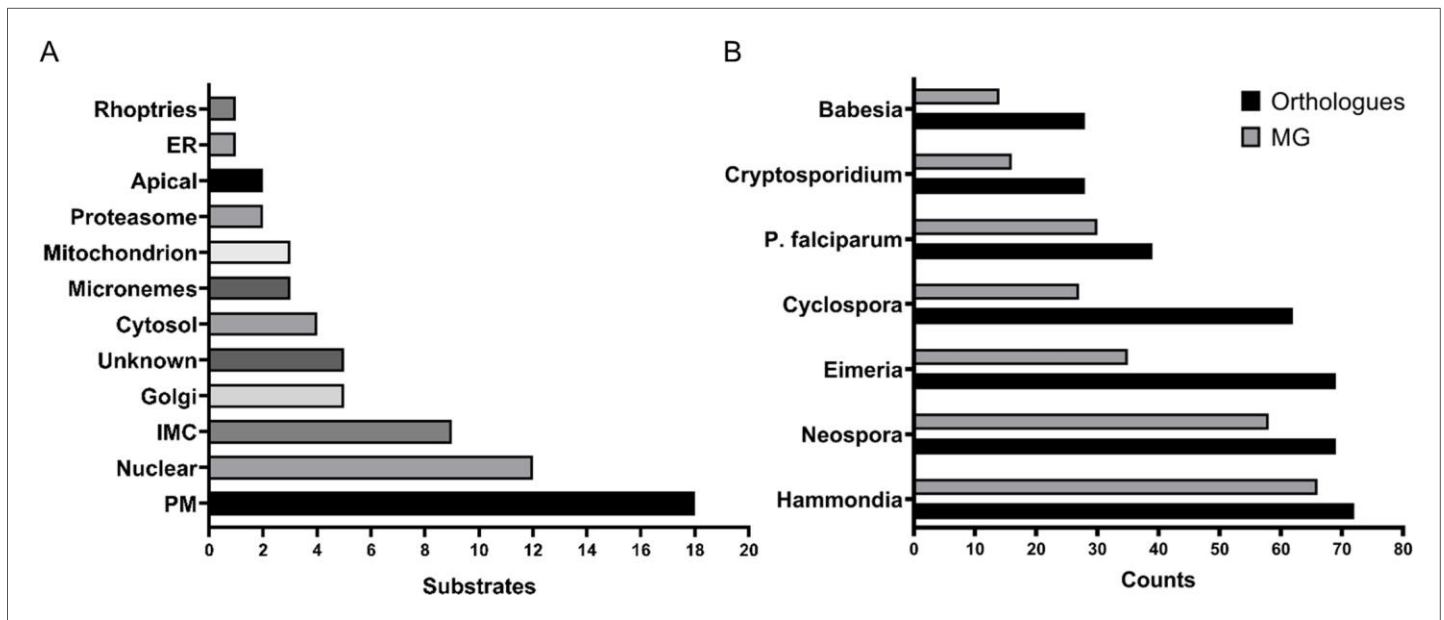


Figure 4. The myristoylated proteome of *Toxoplasma gondii*. (A) Distribution of the subcellular localisation across our substrate list. Analysis performed using ToxoDB and the build in LOPIT predictor. (B) Substrate orthology within selected Apicomplexans. Analysis was performed using EuPathDB. See also *Figure 4—figure supplement 1* and *Supplementary file 4*.

The online version of this article includes the following figure supplement(s) for figure 4:

Figure supplement 1. The myristoylated proteome of *Toxoplasma gondii*.

30% of our substrates were previously reported to be palmitoylated (*Caballero et al., 2016; Foe et al., 2015*) and *Supplementary file 4*). Since palmitoylation is frequently enriched at the protein N-terminus, in close proximity to the myristate, we analysed the first 20 amino acid sequences of our substrates (*Figure 4—figure supplement 1A*) and found that approximately half possessed cysteine residues (sites of palmitoylation) and, hence, the potential for double acylation. This number correlated well with the 54% palmitoylation prediction (*Ren et al., 2008*) for our substrate pool (*Supplementary file 4*). The reported and predicted palmitoylation data suggested that 12 of the 18 PM substrates likely utilise double acylation for stable membrane attachment while the remaining six may be targeted to the PM via alternative mechanisms. Of the 9 IMC localised substrates, 8 are reported or predicted as palmitoylated as well as 4 of the 5 Golgi-localised ones. This indicates that double acylation is a strong predictor for membrane targeting, albeit to different localisations within the cell, suggesting that further signals are required for their definitive subcellular localisation.

Although the absence of palmitoylation cannot exclude the presence of other secondary signals, such as polybasic regions and PPI sites, which could still aid in PM attachment, we predict that about half of the substrates we identified are likely only myristoylated at the N-terminus. Consistent with this, all cytosolic and proteasome localised substrates were deprived of any palmitoylation and only 3 of the 12 nuclear proteins were shown to be palmitoylated. Within this varied group were CDPK1 (*Ojo et al., 2010; Pomel et al., 2008*), the two phosphatases PPM2A and PPM2B (*Yang et al., 2019*) and, surprisingly, the microneme protein MIC7 (*Meissner et al., 2002*). For these proteins myristoylation is likely to serve a distinct function beyond just a simple PM anchor.

The availability of the myristoylated proteomes of *Toxoplasma* and the related *P. falciparum* (*Wright et al., 2014*) allowed us to investigate conserved and non-conserved features of myristoylation across the Apicomplexa. First, we compared both myristoylated proteomes by converting *Plasmodium* myristoylated proteins into *Toxoplasma* orthologues using EuPathDB (*Aurrecochea et al., 2017*) and compared the overlap of both species. This yielded 24 shared substrates, which corresponds to 37% of the *Toxoplasma* and 63% of the *P. falciparum* experimentally validated myristoylated proteome (*Figure 4—figure supplement 1B*). 39 substrates from the *Toxoplasma* dataset have orthologues in *P. falciparum* and 30 of them contain the MG motif, hinting towards potentially

unexplored PfNMT substrates (*Supplementary file 4*). We also investigated substrate orthology with other Apicomplexans (*Figure 4B, Supplementary file 4*). This analysis showed that the lowest level of substrate conservation is present in *Babesia* and *Cryptosporidium* (28 orthologues), followed by *Plasmodium* (39), *Cyclospora* (62), *Eimeria* and *Neospora* (69) and finally *Hammondia* (72). Probing these species-specific orthologues for the presence of the MG motif indicates that between 14 (*Babesia*) and 66 (*Hammondia*) proteins could be potential substrates of NMT (*Figure 4B, Supplementary file 4*) and therefore could also be myristoylated in these species. 13 proteins, including CDPK3, PKG, PKAr and ARO, were present in all analysed species, suggesting that their myristoylation may be essential across the phylum (*Supplementary file 4*).

MIC7 is myristoylated and is important for *Toxoplasma* fitness in vitro

Within our substrate list three proteins were classified as micronemal by LOPIT prediction (*Figure 4A*). TGGT1_249970 was recently described as a protein on the microneme surface where dual acylation is important for its anchoring into the membrane (*Bullen et al., 2016*). The second protein (TGGT1_309990) is annotated as a multi-pass transmembrane protein of unknown function. The third, and perhaps the most interesting, was the microneme protein MIC7 (TGGT1_261780). MIC7 has been reported to be a putative type I transmembrane protein, comprising an N-terminal signal peptide, five EGF-like domains, a membrane-spanning region, and a short cytoplasmic tail (*Meissner et al., 2002*). As MIC signal peptides are typically co-translationally cleaved upon entry into the ER (*Soldati et al., 2001*), the presence of a myristate within the classical signal sequence of MIC7 was unusual. In addition, MIC7 has been suggested to be predominantly expressed in bradyzoites (*Meissner et al., 2002*), the lifecycle stage responsible for the chronic phase of *T. gondii* infection. As our experiments were performed exclusively in tachyzoites, the stage responsible for acute infection, the presence of MIC7 within our dataset could represent a potential false positive identification. To exclude this possibility, we mined MS-based quantification data from an experiment comparing bradyzoite and tachyzoite proteomes (*Young et al., 2020; PXD019729*). The log₂ fold changes in protein abundance for MIC7 and the bradyzoite-specific marker MAG1 (*Tu et al., 2019; Figure 5A, Supplementary file 5*) revealed that in contrast to MAG1, MIC7 is expressed in tachyzoites, supporting the MS and transcriptional evidence in ToxoDB. We next aimed to directly validate protein myristoylation using ectopically expressed HA-tagged MIC7 WT and myristoylation mutant (Mut, G2G3 > KA) under control of either the endogenous or the strong tubulin promoter. We metabolically labelled parasites with YnMyr and performed a myristoylation-dependent pull down on lysates. Only WT but not the Mut was enriched in this manner (*Figure 5B*), confirming that MIC7 is indeed myristoylated.

To investigate the functional relevance of MIC7 and its myristoylation, we created an inducible knock-out (iKO) line using the DiCre/loxP system (*Andenmatten et al., 2013*) that we recently optimised in RHDku80 parasites (*Hunt et al., 2019*). The *Mic7* coding sequence was replaced with a floxed, HA-tagged copy of the gene, hereafter called MIC7^{HA}, that could be excised upon rapamycin (RAPA) treatment (*Figure 5C*). We verified correct integration at the endogenous locus and confirmed RAPA-induced excision by PCR (*Figure 5—figure supplement 1*). At the protein level, MIC7^{HA} was efficiently depleted 24 hr post RAPA treatment (*Figure 5D*). Correct trafficking of MIC7^{HA} to micronemes was verified by the co-localisation with the micronemal marker MIC2 (*Figure 5E*). Upon deletion of *Mic7*, parasites no longer formed detectable plaques in host cell monolayers after 5 days in culture, but we could observe very small plaques emerging after 7 days (*Figure 5F*). Collectively these results demonstrate an important, but non-essential, role for MIC7 in the lytic cycle.

Myristoylation of MIC7 appears important for host cell invasion

To investigate where in the lytic cycle MIC7 plays a role, and test the functional relevance of N-terminal myristoylation, we complemented the iKO line by introducing Ty1-tagged WT or myristoylation defective mutant (hereafter called cWT and cMut, respectively) copies of *Mic7* into the *Uprt* locus (*Figure 6A*). Both inserts were correctly integrated and both complemented lines retained efficient RAPA-induced *Mic7* excision (*Figure 6—figure supplement 1*) and depletion of MIC7^{HA} (*Figure 6B*). After confirming equivalent and RAPA-insensitive expression of cWT and cMut (*Figure 6B*), we validated both lines in terms of their myristoylation-dependent enrichment and

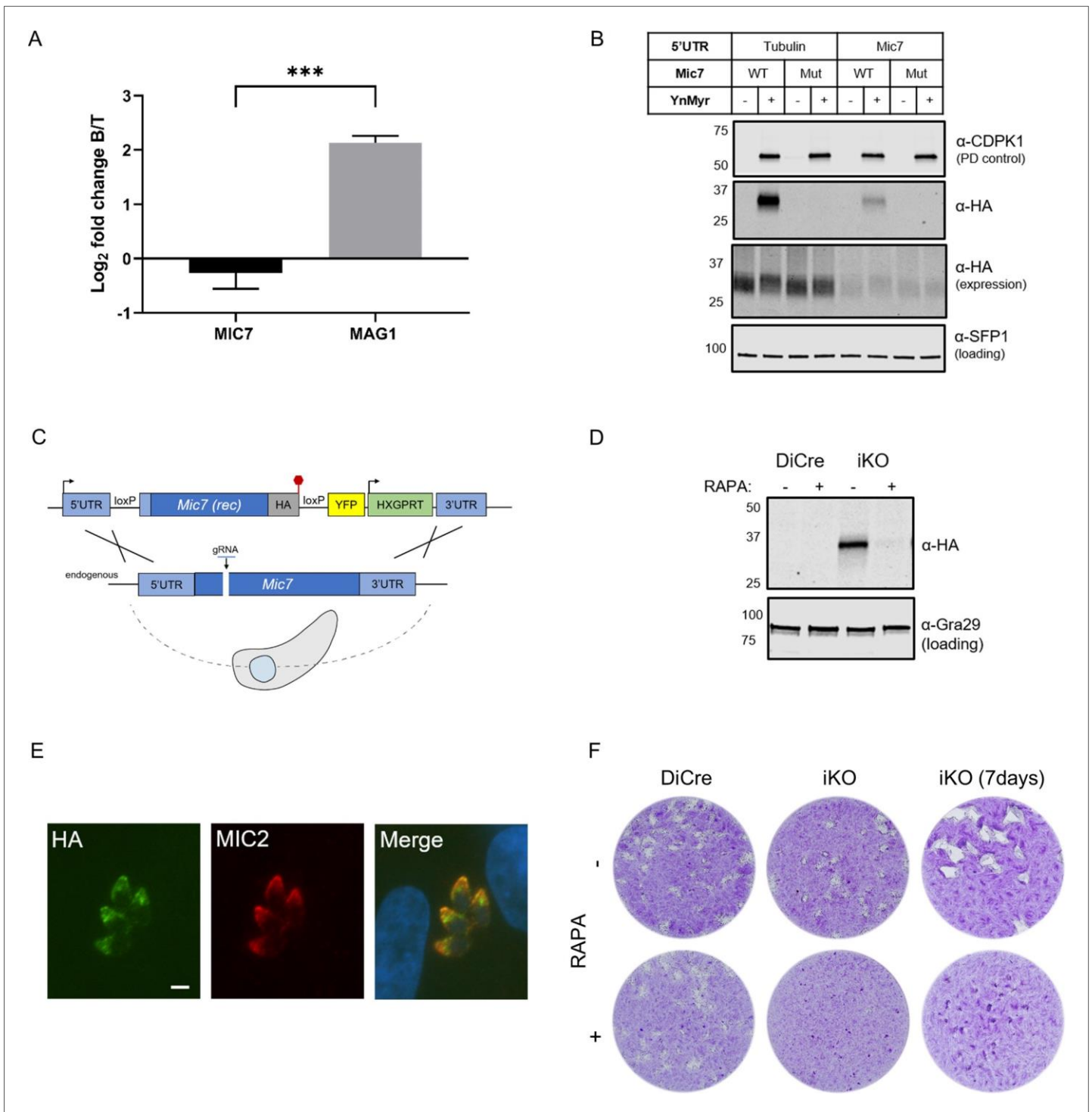


Figure 5. MIC7 is myristoylated and is important for *T. gondii* lytic cycle. (A) MS-based quantification of MIC7 and MAG1 abundance in tachyzoites [T] and bradyzoites [B] of *T. gondii*. Significance calculated using two-tailed Student's t-test, ***p=0.0002, N = 3, error bars represent standard deviation. (B) MIC7 is myristoylated as shown by YnMyr-dependent pull down and western blotting with α -HA antibody. CDPK1 and SFP1 (TGGT1_289540) are used as enrichment and loading controls, respectively. (C) Schematic representation of the DiCre/loxP-based iKO strategy used for the conditional depletion of *Mic7*. Red hexagon represents STOP codon, rec - recodonized. (D) Validation of RAPA-dependent depletion of MIC7^{HA} in the iKO line illustrated by western blotting with α -HA antibody. Gra29 was used as loading control. (E) Co-localisation of MIC7^{HA} (green) with the micronemal marker MIC2 (red) in the iKO line by immunofluorescence analysis. Scale bar: 3 mm. (F) Plaque assays illustrating that MIC7 is important, but not essential for the intracellular growth of *Toxoplasma*. Assay was performed for 5 days (where not indicated) in three biological replicates, each in technical triplicate, representative images are shown. See also *Figure 5—figure supplement 1*.

Figure 5 continued on next page

Figure 5 continued

The online version of this article includes the following source data and figure supplement(s) for figure 5:

Source data 1. Numerical data of the graph presented in Figure 5A.

Figure supplement 1. Inducible knock-out of MIC7.

showed that only the cWT was selectively pulled down after metabolic labelling with YnMyc (Figure 6C). In the next step, we investigated the co-localisation of MIC7^{HA} with cWT and cMut (Figure 6D). Both complementation isoforms localised to the micronemes, indicating that the myristate is not required for the trafficking of MIC7 to this organelle.

We next sought to evaluate the role of MIC7 myristoylation in the parasite lytic cycle. While cWT rescued the iKO phenotype upon RAPA treatment, cMut parasites formed substantially smaller plaques under equivalent conditions (Figure 6E). This demonstrates that myristoylation indeed plays a key role in MIC7 function. Given the well-established role of microneme proteins in facilitating host cell penetration, we explored whether myristoylation of MIC7 may be important for invasion. We treated iKO, cWT and cMut parasites with RAPA and performed a red/green assay (Huynh *et al.*, 2003) which can distinguish invaded from attached parasites. As shown in Figure 6F, we observed efficient invasion of host cells by the cWT parasites. This was not the case in the iKO and cMut lines, where invasion was reduced by 57% and 32%, respectively. Compared to the cWT line, we also observed a consistent 61% drop in the total number of iKO parasites (Figure 6G), which suggests a defect in the attachment to host cells. A modest but non-significant reduction of 15% in attachment was observed in the cMut strain. Collectively, these results indicate that MIC7 plays an important role in *Toxoplasma* propagation by facilitating parasite attachment and subsequent entry into host cells. Furthermore, myristoylation is not required for sorting MIC7 to the micronemes but appears to be important for its function in invasion of host cells.

Generation of double tagged MIC7 lines for in depth characterisation of MIC7 myristoylation

To monitor MIC7 N-terminus, and thus the fate of the myristate, we generated double tagged MIC7 variants bearing a Myc tag in the ectodomain and a Ty1 tag at the C-terminus. Placing a Myc tag in the region between the MIC7 transmembrane (TM) domain and the last predicted EGF domain (EGF5) yielded non-functional protein (Figure 7—figure supplement 1A). To select a likely suitable position for the tag, we resorted to structural predictions. The region between EGF5 and the TM domain (EGF5-TM, residues 230-284) possesses two pairs of cysteine residues and may represent either an extension of EGF5, or a non-canonical/truncated EGF6. This could explain the inability to place an epitope tag in this region and yield functional MIC7. We also excluded EGF3 and EGF4, that possess the strongest signatures for calcium-binding motifs (PFAM database domain entry PF07645), which normally imparts a rigid domain arrangement with its neighbours. Finally, we considered possible locations (Figure 7A) where some degree of structural flexibility would be most likely. The loop between the last two cysteine residues is variable amongst EGF domains, therefore locations were chosen between C38 and C53 of EGF1 and between C86 and C97 of EGF2 as well as within the linker between EGF1 and EGF2. Using ectopic expression, we tested all these positions in terms of protein expression and localisation. All three double tagged protein variants localised to micronemes (Figure 7—figure supplement 1B), but the most abundant protein levels were observed when the Myc tag was placed within the EGF2 (Figure 7—figure supplement 1C). This indicated that the tag is well tolerated in this position, readily detected by western blot and could be used for further experiments. Myc tagged cWT and cMut (hereafter called ^{Myc}cWT and ^{Myc}cMut, respectively) were then inserted into the *Uprt* locus of the iKO line. Both inserts correctly integrated, the new lines retained efficient RAPA-induced *Mic7* excision and depletion of MIC7^{HA} (Figure 7—figure supplement 1D–F). After verifying equivalent and RAPA independent expression of the ^{Myc}cWT and ^{Myc}cMut (Figure 7—figure supplement 1F), we confirmed their micronemal localisation by IFA (Figure 7—figure supplement 1G). Several microneme proteins have been shown to dimerise (Cérède *et al.*, 2002), which harbours the potential that any additional copy of a protein in a merodiploid strain, even when lacking trafficking information, could piggy back as a heterodimer into the micronemes. Indeed, when testing co-IPs in the absence of RAPA, we observed that both

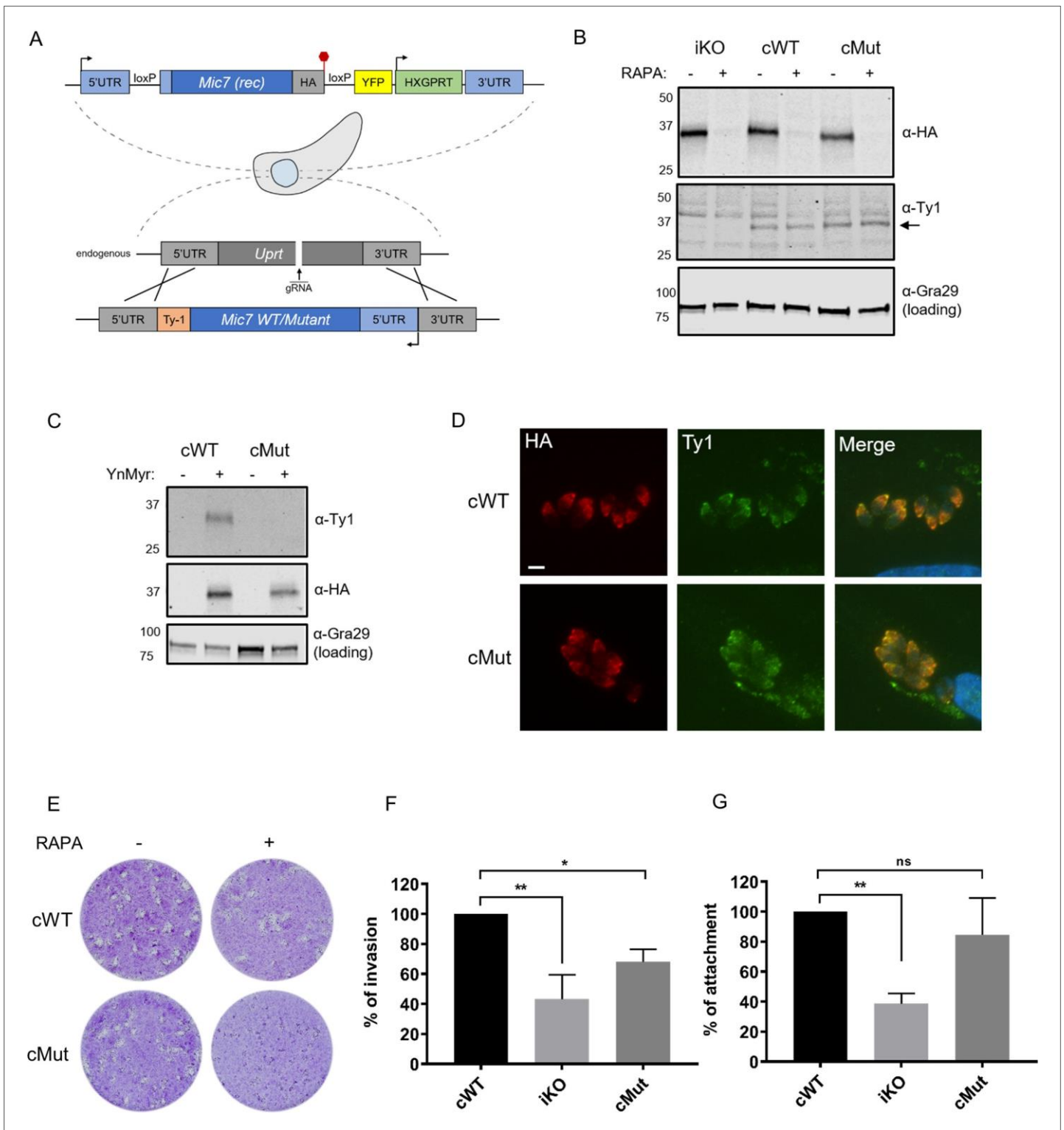


Figure 6. Myristoylation of MIC7 plays a role in the invasion of host cells. (A) Complementation strategy used to evaluate the functional importance of MIC7 myristoylation. The orientation of cWT and cMut is reversed in the *Uprt* locus with the Ty1 tag at the C-terminus. Red hexagon represents STOP codon, rec – recodized. (B) Western blot analysis demonstrating the RAPA-dependent depletion of MIC7^{HA} in the iKO, cWT and cMut lines (α -HA) as well as equivalent and RAPA-independent expression of the complements (α -Ty1). Gra29 was used as loading control. (C) Biochemical validation of complemented lines by YnMyr-dependent pull down. Enrichment of WT and Mut copy of MIC7 was evaluated by western blotting with α -Ty1 antibody. MIC7^{HA} (α -HA) and Gra29 were used as enrichment and loading controls, respectively. (D) Co-localisation of MIC7^{HA} (red) with the cWT and cMut (green) by immunofluorescence analysis. Scale bar: 5 μ m. (E) Plaque assay demonstrating that myristoylation of MIC7 is important in the intracellular invasion of host cells. **Figure 6 continued on next page**

Figure 6 continued

growth of *Toxoplasma*. Assay performed for 5 days in three biological replicates, each in technical triplicate, representative images are shown. (F) Quantification of invasion efficiency in the RAPA-treated cWT, iKO and cMut lines. Figure shows the average of three biological replicates, each in technical duplicate, error bars represent standard deviation. Significance calculated using 1-way ANOVA with Dunnett's multiple comparison test, ** $p=0.001$, * $p=0.018$. (G) Quantification of attachment efficiency in the RAPA-treated cWT, iKO and cMut lines. Figure shows the average of three biological replicates, each in technical duplicate, error bars represent standard deviation. Significance calculated using 1-way ANOVA with Dunnett's multiple comparison test, ** $p=0.004$, ns = not significant. See also *Figure 6—figure supplement 1*.

The online version of this article includes the following source data and figure supplement(s) for figure 6:

Source data 1. Numerical data of the graphs presented in *Figure 6F and G*.

Figure supplement 1. Complementation of the MIC7 iKO line.

complements can co-IP with MIC7^{HA} (*Figure 7B*), which is independent of the myristate. We therefore repeated the localisation experiments in the presence of RAPA to delete MIC7^{HA}. As shown in *Figure 7—figure supplement 1H*, both ^{Myc}cWT and ^{Myc}cMut localise to the micronemes in RAPA-treated parasites, confirming that the myristate is not necessary for MIC7 sorting.

Plaque assays of RAPA-treated complementation lines showed the expected defect in plaque formation for ^{Myc}cMut, however, we also observed a small reduction of plaque size for ^{Myc}cWT expressing parasites as compared to the DMSO control (*Figure 7C*). This slightly reduced ability to form plaques is likely due to the effect of Myc tag insertion on the MIC7 function. However, since the tag is present in both complemented lines and the ability to form plaques was substantially more impeded in the ^{Myc}cMut parasites, these lines are still suitable to investigate the specific function of MIC7 myristoylation.

MIC7 and its myristoylation are important for the initiation of host cell invasion

In order to shed some light on MIC7 topology within the micronemes as well as the fate of its N-terminal myristate, we performed proteinase K protection assays (*Figure 7D*). In these experiments, proteins/domains that are accessible to proteinase K after digitonin-mediated plasma membrane permeabilisation are digested, while those retained within organelles, such as the micronemes, are protected from this proteolytic digest. We treated tachyzoites from both ^{Myc}cWT and ^{Myc}cMut lines with RAPA to deplete MIC7^{HA} and fed with YnMyr to allow for myristoylation-dependent pull down of the complements. We then subjected parasites to digitonin and proteinase K treatment, followed by detection of Myc and Ty1 tags. As a control we used antibodies against the ectodomain of MIC2, as it should be protected (*Bullen et al., 2016*). Under these conditions the MIC7 C-terminus was digested, while the N-terminus was protected as visualised by the Ty1 and the Myc antibodies, respectively. As the parasites were treated with YnMyr prior to the experiment, we could use a YnMyr-dependent pull down to demonstrate that the protected N-terminus of MIC7 remains myristoylated (*Figure 7D*). These results strongly suggest that MIC7 is indeed a transmembrane protein with a myristoylated N-terminus facing the microneme lumen and a short C-terminal cytoplasmic tail that faces the parasite cytoplasm.

Having established the presence of MIC7 N-terminal myristoylation within the micronemes, we aimed to perform a more detailed characterisation of its function. First, we repeated invasion assays in large scale as described in *Touquet et al., 2018*. We performed three independent experiments with a total of 15 replicates per tested parasite line (*Figure 7E*). Taking into account the phenotypic effect for the Myc tag insertion in complemented parasite lines we used untreated iKO parasites as a parental control. Parasites that no longer expressed MIC7^{HA} displayed a 78% decrease in invasiveness when compared to the control. Complementation with ^{Myc}cWT copy can restore the invasiveness to 61%, while ^{Myc}cMut reach only 30% invasion capacity. These results are largely consistent with our previous observations (*Figure 6F*) and further confirm the critical role for MIC7 and its myristoylation in the invasion process.

To gain a better understanding of the function of MIC7 during host cell penetration, we filmed invasion of the DMSO and RAPA-treated iKO and the complemented lines into GFP-GPI expressing host cells (*Figure 7—videos 1-4*). We calculated times of successful and failed invasions for each genetic background and observed that despite different success rates between lines, the parasites that did enter the host cell proceed with a similar speed as the control (*Figure 7F, Figure 7—videos*

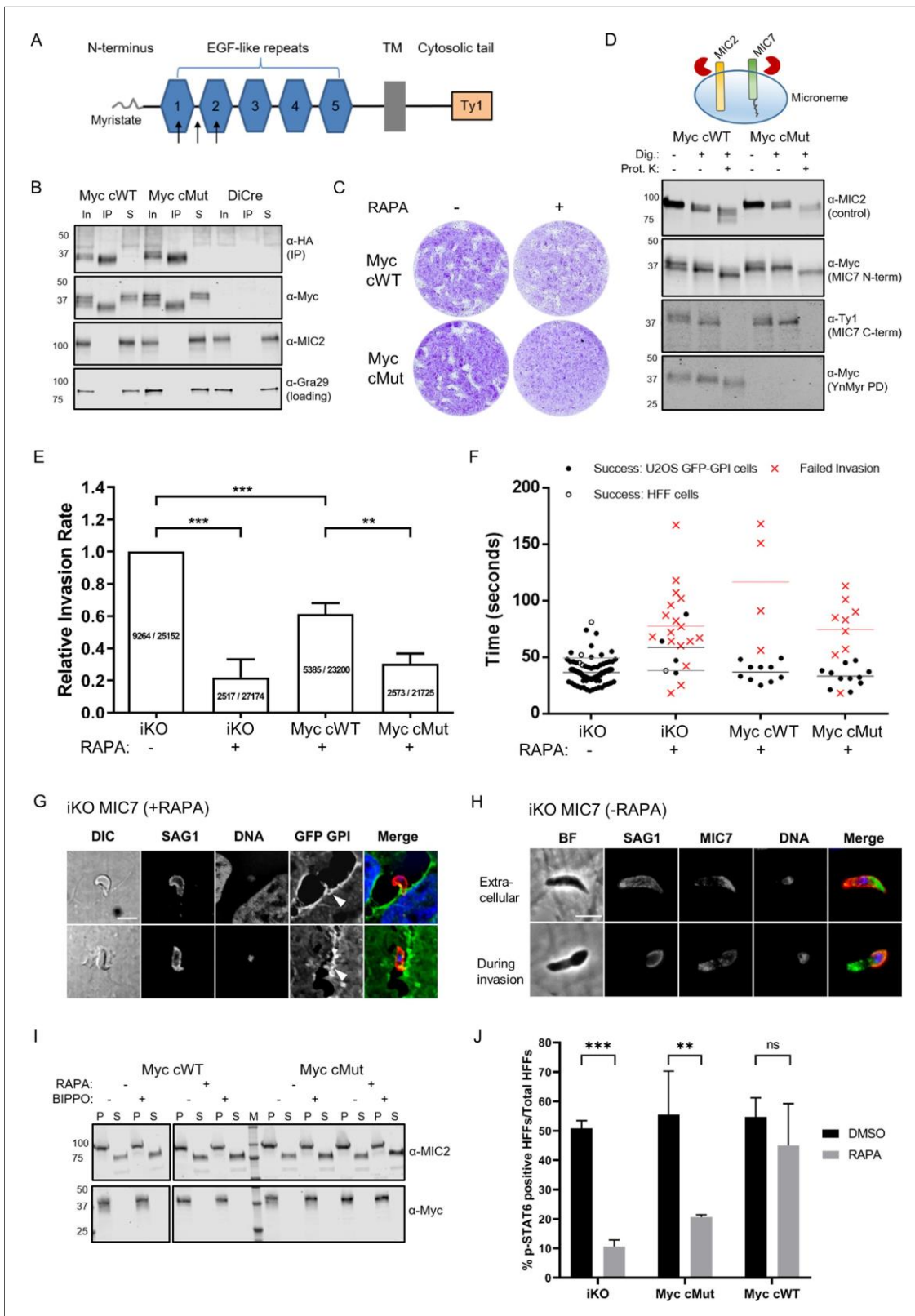


Figure 7. Functional analysis of MIC7 and its myristoylation in double tagged MIC7 lines. (A) Schematic representation of MIC7 domain structure with evaluated Myc tag positions indicated by arrows. (B) Western blot analysis showing co-immunoprecipitation of ^{Myc}cWT and ^{Myc}cMut (α -Myc) with MIC7^{HA} (α -HA). MIC2 and Gra29 were used as controls for microneme solubilisation and equal loading, respectively; In = input, IP = immunoprecipitate, S = supernatant after IP. (C) Plaque assay confirming that myristoylation of MIC7 is important in the intracellular growth of *Figure 7 continued on next page*

Figure 7 continued

Toxoplasma in the newly generated lines. Assay performed for 5 days in three biological replicates, each in technical triplicate, representative images are shown. (D) Proteinase K protection assay demonstrating that the N-terminus of MIC7 is myristoylated and protected (α -Myc) while the C-terminus is digested (α -Ty1) upon permeabilisation and protease treatment. MIC2 was used as a known control where the ectodomain is protected under similar conditions. Dig. = digitonin, Prot.K = proteinase K. (E) Quantitative large scale invasion assay. Results show the relative invasion rate as mean \pm standard deviation calculated from three independent assays, each performed with five replicates. The total number of intracellular tachyzoites and human cells are indicated in each column. Two-tailed Student's t-test was performed for two-group comparisons, *** $p < 0.0006$, ** $p = 0.0044$. (F) Distribution of the successful/failed invasion times for each of the four genetic backgrounds. Mean invasion time is displayed for both HFF and U2OS host cells. (G) Representative immunofluorescence images ($n = 45/68$) demonstrating the characteristic bending of the conoid in extracellular RAPA-treated iKO parasites stained against the surface protein SAG1 (marking extracellular parasites and the extracellular part of invading tachyzoites only). It is also possible to observe the U2OS GFP-GPI membrane invagination at the vicinity of the extracellular parasites (white arrowheads). Scale bar: 5 μ m. (H) Representative immunofluorescence images of untreated (-RAPA) iKO parasites while extracellular ($n = 63$) and during invasion ($n = 22$). Parasites were stained against SAG1 (marking extracellular parasites and the extracellular part of invading tachyzoites only) and α -HA to stain MIC7. Scale bar: 5 μ m. (I) Analysis of MIC7 secretion upon stimulation with BIPPO. No shedding of MIC7 was observed (α -Myc) in contrast to MIC2 which was used as a control. P - pellet, S - supernatant containing the excreted secreted antigens, M - molecular weight marker. White space was used to indicate where gel lanes were not contiguous. (J) Immunofluorescence based quantification of pSTAT6 as a reporter for ROP16 secretion in all tested lines with and without RAPA treatment. Figure shows the average of three biological replicates, error bars represent standard deviation. Significance calculated using 2-way ANOVA with Sidak's multiple comparison test, *** $p = 0.0004$, ** $p = 0.0013$, ns = not significant. See also Figure 7—figure supplements 1 and 2. The online version of this article includes the following video, source data, and figure supplement(s) for figure 7:

Source data 1. Numerical data of the graph presented in Figure 7E.

Source data 2. Numerical data of the graph presented in Figure 7F.

Source data 3. Numerical data of the graph presented in Figure 7J.

Figure supplement 1. Generation of doubly-tagged MIC7 lines.

Figure supplement 2. Functional analysis of MIC7 and its myristoylation.

Figure 7—video 1. Related to Figure 7F.

<https://elifesciences.org/articles/57861#fig7video1>

Figure 7—video 2. Related to Figure 7F.

<https://elifesciences.org/articles/57861#fig7video2>

Figure 7—video 3. Related to Figure 7F.

<https://elifesciences.org/articles/57861#fig7video3>

Figure 7—video 4. Related to Figure 7F.

<https://elifesciences.org/articles/57861#fig7video4>

1-4). This suggests a potential failure to initiate invasion. In several failed invasion events we also observed a notable membrane invagination (Figure 7—figure supplement 2A, Figure 7—videos 2 and 4), which normally occurs after secretion of the rhoptry neck components required for the formation of the tachyzoite-host cell junction (Bichet et al., 2016). It is worth noting, that the immunofluorescent analysis of likely aborted invasion events in the RAPA treated iKO line revealed more than half of extracellular parasites (45 of 68) show a strong arch-shaped morphology while associated with a host cell (Figure 7G). This is indicative of MIC7 KO parasites exerting force during the attempt to invade, possibly leading to the zoite deformation.

The inability to initiate invasion in the iKO and ^{Myc}cMut lines could be caused by a general defect in gliding motility or a failure to secrete micronemes. However, both circular and helical trails were detected with no obvious differences between parasites (Figure 7—videos 1-4, Figure 7—figure supplement 2B). We also observed no reduction in microneme secretion, as shown by efficient MIC2 processing in MIC7 KO parasites, even in the presence of 5-benzyl-3-isopropyl-1H-pyrazolo [4,3-d]pyrimidin-7(6H)-one (BIPPO), a phosphodiesterase inhibitor that triggers signalling pathways leading to increased parasite motility and microneme secretion (Figure 7—figure supplement 2C).

To get a better understanding of MIC7 distribution in parasites before and during invasion, we co-localised MIC7 with SAG1, a well characterized surface marker, which can be used to delineate the intra- and extracellular part of invading parasites. This revealed that MIC7 partially redistributes around the periphery of extracellular and invading parasites, but appears absent from the tachyzoite-host cell junction (Figure 7H), a constriction through which the parasite moves as it enters the host cell (Pavlou et al., 2018; Tyler et al., 2011). This redistribution suggests, but is not proof, that MIC7, as many other microneme proteins, is secreted onto the parasite surface during or after egress from the host cell. Most transmembrane microneme proteins undergo proteolytic maturation

near or within the transmembrane domain after egress and during invasion (Soldati *et al.*, 2001). This process is facilitated by subtilisin or rhomboid proteases and is thought to relieve the high affinity interactions between the parasite and host cell receptors (Carruthers, 2006; Dowse and Soldati, 2005). We analysed if MIC7 could undergo similar processing and found that while MIC2 was efficiently cleaved and released into the culture supernatant, this was not the case for MIC7, even in the presence of BIPPO (Figure 7). We also tested whether MIC7 could be shed during invasion by analysing the culture supernatant as well as parasite and host material of freshly invaded cells. Again, no MIC7 shedding was observed (Figure 7—figure supplement 2D). These results are in agreement with previously reported observations (Meissner *et al.*, 2002), and confirm that MIC7 is not subject to a proteolytic cleavage.

MIC7 and its myristoylation may be important for efficient secretion of rhoptry contents into the host cell

The live imaging data of the iKO parasites suggested that MIC7 plays an important role in the onset of invasion, potentially after the establishment of the tachyzoite-host cell junction. In one instance we could observe a membrane swirl formation at the apex of the parasite attempting invasion, suggesting that rhoptry contents may have been secreted (Figure 7—video 2). Rhoptries are apical organelles which contain a number of kinases the parasite injects into the host cell upon invasion. These effector kinases modulate many important functions in host-microbe interaction (Boothroyd and Dubremetz, 2008). One of these kinases, the rhoptry kinase 16 (ROP16) acts as a JAK mimetic leading to rapid and direct phosphorylation of STAT6 (Ong *et al.*, 2010; Saeij *et al.*, 2007). Accordingly, we used STAT6 phosphorylation as a reporter for efficient rhoptry secretion and ROP16 translocation into the host cell (Figure 7J). RAPA-treated ^{Myc}cWT parasites showed 45% pSTAT6 positive nuclei. RAPA-treated iKO and ^{Myc}cMut parasites showed a significant reduction of pSTAT6 positive nuclei (11% and 21%, respectively). No significant differences in pSTAT6 positive cells between tested parasite lines were observed when treated with DMSO. This indicates that iKO and ^{Myc}cMut parasites can still secrete ROP16 into the host cell and induce STAT6 phosphorylation, although at significantly reduced levels.

Discussion

Our understanding of myristoylation and its functional consequences in *Toxoplasma* is hampered by the limited knowledge of NMT substrates. Using an integrated MS-approach we describe here the first experimentally validated myristoylated proteome in *T. gondii*. We combine two orthogonal chemoproteomic techniques, that is quantitative response to NMT inhibition with direct MS/MS evidence for substrate modification, which allows for high confidence in substrate identification as well as substantial substrate coverage. Despite the complex nature of our samples, consisting of both human and parasite proteins, our discovery includes all proteins previously reported to be myristoylated in *Toxoplasma* as well as novel and unexpected *Tg*NMT substrates. The fact that these proteins are functionally diverse, and involved in all steps of the lytic cycle highlights the importance of myristoylation in *Toxoplasma* biology. Consistent with this, treatment with NMTi resulted in dose dependent parasite killing. Although we cannot exclude small off-target effects of IMP-1002 that was originally designed for *Plasmodium spp.*, we predict that this severe phenotype was largely due to pleiotropic effects of *Tg*NMT inhibition on the *Toxoplasma* lytic cycle. Potent and selective *Tg*NMT inhibitors are yet to be reported, however extensive work in other protozoan parasites (Ritzefeld *et al.*, 2018) demonstrates that selective NMT inhibition could provide an attractive strategy to combat infection. Moreover, results presented here indicate that related parasites, with high structural conservation of their NMTs, could be inhibited by a single compound, which may allow for the development of a pan-parasite inhibitor in the future.

Our substrates showed heterogeneous localisation with ca. 50% localised to PM or membrane bound compartments. Palmitoylation analysis confirmed that for the majority of these substrates stable attachment to membranes is likely driven by double acylation. Although we cannot exclude the presence of other secondary signals which could aid in PM targeting within our substrate pool, such as polybasic regions and PPI sites, our analysis and the predicted localisation suggest that many of our substrates may be myristoylated only, indicating that their myristoylation can serve more discrete functions than just a priming site for the palmitate. Such alternate functions could include reversible

membrane binding by the conformation regulated exposure of the myristate as shown for mammalian ARF1 (Goldberg, 1998), regulation of protein activity as demonstrated for GPAT4 during glycerolipid synthesis (Zhu *et al.*, 2019), or involvement in PPIs, as shown for the viral capsid assembly (Chow *et al.*, 1987; Mousnier *et al.*, 2018).

Here we identified unexpected myristoylation of the *Toxoplasma* microneme protein 7 (MIC7). Microneme proteins are key factors in *Toxoplasma* propagation involved in parasite egress, motility and host cell invasion. They are trafficked into the secretory pathway by virtue of an N-terminal signal peptide that is cleaved during ER import (Soldati *et al.*, 2001). We show that MIC7 is an important, yet not essential protein and we unequivocally demonstrate that MIC7 is myristoylated at its N-terminus, excluding the existence of an N-terminal signal sequence. While it is known that proteins can enter the secretory pathway by virtue of a recessed signal or leader peptide, this has not been reported for microneme proteins. Furthermore, many known microneme proteins are type I transmembrane proteins, where an N-terminal PPI or carbohydrate binding domain faces the microneme lumen and a short cytoplasmic domain faces the parasite cytosol. Upon microneme secretion the protein is transferred to the parasite PM, with the interacting domain exposed to bind to host cell receptors. Because MIC7 lacks a signal peptide but otherwise mimics this domain structure, it most likely enters the secretory pathway as a type III transmembrane protein (Goder and Spiess, 2001). Although we have not specifically tested this here, this is supported by several features in the MIC7 primary amino acid sequence. That is: a transmembrane domain of > 20 amino acids in length (22 in MIC7) and positive charges on the C-terminal side of the transmembrane domain.

We demonstrated that MIC7 and its myristoylation are important in host cell invasion. Live imaging of the invasion process further revealed a potential defect in initiating invasion in the MIC7 KO and myristoylation defective parasites. This phenomenon was not caused by a fault in microneme secretion itself or parasite gliding. The live video analysis suggests that the parasites may be able to initiate the tachyzoite-host cell junction (supported by some rhoptry content secretion as measured by STAT6 phosphorylation), but then fail to progress beyond the initiation. This phenotype is similar to *Toxoplasma* Myosin A knockout parasites, that are also able to initiate invasion, but then fail to invade given the lack of a functional actin-myosin system. However, the strong arch-shaped deformation of extracellular MIC7 KO parasites in live invasion assays is substantially different from the MyoA knockouts (Bichet *et al.*, 2016). While we could not unequivocally show that MIC7 is secreted to the zoite surface to engage with host cell receptors via its EGF domains, the fact that it redistributes around the periphery of the cell shortly after egress and during invasion supports this scenario. When secreted, the myristate could contribute to specific PPIs with other surface proteins or potentially host ligands to support attachment and initiate invasion.

It is also tempting to speculate that alternatively, the myristate could be inserted into the lipid bilayer of the host cell. It has been shown that HBV viruses can utilise a myristoylated protein on their surface to enter host cells (Maurer-Stroh and Eisenhaber, 2004). In *Toxoplasma* this mechanism could contribute to host cell attachment, for which we observed a measurable defect upon MIC7 deletion, but also to the earliest events of invasion, that is rhoptry secretion or host-cell penetration. This is reminiscent of MIC8, another microneme protein, that has been implicated in a signalling cascade leading to rhoptry discharge (Kessler *et al.*, 2008). Our experiments to probe secretion of ROP16, which rapidly phosphorylates STAT6 (Ong *et al.*, 2010; Saeij *et al.*, 2007), indicate that rhoptry secretion per se is not affected upon MIC7 deletion, but reduced ROP16 mediated STAT6 phosphorylation is observed. We cannot currently distinguish whether the decrease in ROP16 injected cells is due to decreased invasion efficiency of MIC7 KO and ^{Myc}Mut lines, or whether equal amounts of cells have been attempted to be invaded but ROP16 has not been efficiently transferred. However, the attachment phenotype observed for MIC7 myristoylation mutants is less profound than the reduction of pSTAT6 induction, suggesting that the major cause of the rhoptry secretion phenotype is independent of attachment and most likely due to an inefficient translocation of rhoptry contents into the host cell. Whether the failure to progress beyond the initiation of the tachyzoite-host cell junction lies in a failure to properly secrete rhoptry contents, or to form the junction itself remains to be clarified.

In summary we provide a useful resource of experimentally validated myristoylated and GPI-anchored proteins, as well as first clues to the identity of so far uncharacterized myristoylated proteomes across the phylum. We show that an NMT inhibitor that was generated against *Plasmodium* spp. also inhibits *Toxoplasma* growth. The presence of several essential N-myristoylated proteins

conserved across many Apicomplexa indicates that NMT inhibition by a single compound may be a viable strategy to target several pathogens. We have identified N-terminal myristoylation on a *Toxoplasma* protein that uses an unconventional mode of trafficking to the parasite secretory pathway and the micronemes, and displays a novel use of myristoylation in parasite biology. This unexpected discovery, which can likely be found in other organisms, demonstrates how our dataset can serve as a tool in target-specific investigations that can ultimately help to unravel the exciting biology of host-microbe or more broadly, cell-cell interactions.

Materials and methods

Key resources table

| Reagent type (species) or resource | Designation | Source or reference | Identifiers | Additional information |
|---|--|-----------------------------------|--|---|
| Synthetic Gene (<i>Toxoplasma gondii</i>) | Microneme protein 7 (MIC7) | GeneArt, Life Technologies | TGGT1_261780 (http://toxodb.org) | Floxed and HA tagged sequence |
| Cell line (<i>Homo sapiens</i>) | Human foreskin fibroblasts (HFFs) | ATCC | Cat# SCRC-1041, RRID:CVCL_3285 | The cell line is available from the American Type Culture Collection (ATCC) |
| Cell line (<i>Toxoplasma gondii</i>) | RH <i>Dku80 Dhxgprt</i> | <i>Huynh and Carruthers, 2009</i> | | Used in all mass spectrometry experiments |
| Cell line (<i>Toxoplasma gondii</i>) | RH DiCre <i>Dku80 Dhxgprt</i> | <i>Hunt et al., 2019</i> | | The second-generation DiCre-expressing cell line in <i>Toxoplasma gondii</i> |
| Cell line (<i>Toxoplasma gondii</i>) | iKO MIC7; RH DiCre <i>Dku80 Dhxgprt_LoxMic7_HA</i> | This paper | | The endogenous <i>Mic7</i> gene was replaced with a floxed and HA-tagged <i>Mic7</i> gene |
| Cell line (<i>Toxoplasma gondii</i>) | cWT MIC7 | This paper | | As described for the iKO MIC7 line, however a <i>Mic7-Ty1</i> expressing construct was integrated into the <i>UPRT</i> locus. |
| Cell line (<i>Toxoplasma gondii</i>) | cMut MIC7 | This paper | | As described for the iKO MIC7 line, however a <i>Mic7(G2K/G3A)-Ty1</i> expressing construct was integrated into the <i>UPRT</i> locus. |
| Cell line (<i>Toxoplasma gondii</i>) | Myc cWT MIC7 | This paper | | As described for the cWT MIC7 line, however a <i>Myc-Mic7-Ty1</i> expressing construct was integrated into the <i>UPRT</i> locus. |
| Cell line (<i>Toxoplasma gondii</i>) | Myc cMut MIC7 | This paper | | As described for the cMut MIC7 line, however a <i>Myc-Mic7(G2K/G3A)-Ty1</i> expressing construct was integrated into the <i>UPRT</i> locus. |
| Antibody | Rat anti-HA monoclonal clone 3F10 | Roche | Cat# 11867423001 RRID:AB_390919 | WB (1:1000) IFA (1:1000) |
| Antibody | Mouse anti-Myc monoclonal clone 4A6 | Millipore | Cat# 05-724 RRID:AB_11211891 | WB (1:1000) IFA (1:1000) |

Continued on next page

Continued

| Reagent type (species) or resource | Designation | Source or reference | Identifiers | Additional information |
|------------------------------------|--|---------------------------------|-----------------------------------|--|
| Antibody | Mouse anti-Ty1 monoclonal clone BB2 | Thermo Fisher | Cat# MA5-23513 RRID:AB_2610644 | WB (1:2000) IFA (1:500) |
| Antibody | Mouse anti- <i>Toxoplasma</i> monoclonal clone TP3 | Abcam | Cat# ab8313 RRID:AB_306466 | WB (1:1000) |
| Antibody | Mouse anti-MIC2 monoclonal clone 6D10 | other | | Provided by Vernon Carruthers Lab WB (1:1000) |
| Antibody | Rabbit anti-MIC2 polyclonal | other | | Provided by Vernon Carruthers Lab WB (1:500) IFA (1:5000) |
| Antibody | Rabbit anti-TgCAP polyclonal | <i>Hunt et al., 2019</i> | | WB (1:2000) |
| Antibody | Rabbit anti-Gra29 polyclonal | <i>Young et al., 2020</i> | | WB (1:1000) |
| Antibody | Rabbit anti-SFP1 polyclonal | <i>Young et al., 2020</i> | | WB (1:1000) |
| Antibody | Mouse anti-CDPK1 polyclonal | other | | Provided by Matthew Child and Matt Bogyo WB (1:3000) |
| Antibody | Rabbit anti-SAG1 monoclonal | other | | Provided by John Boothroyd Lab WB (1:10,000) |
| Antibody | Rabbit anti-GAP45 polyclonal | other | | Provided by Peter Bradley Lab WB (1:1000) |
| Antibody | Rabbit anti-phospho-Stat6 polyclonal | Cell Signaling | Cat# 9361 RRID:AB_331595 | IFA (1:600) |
| Chemical compound | Myristic acid (Myr) | Tokyo Chemical Industry | Cat# M0476 | |
| Chemical compound | Alkyne-myristic acid (YnMyr) | Iris Biotech | Cat# RL-2055 | |
| Chemical compound | Azide-PEG3-biotin (N3-biotin) | Sigma-Aldrich | Cat# 762024 | Capture reagent 1 |
| Chemical compound | Trypsin cleavable reagent | <i>Broncel et al., 2015</i> | | The reagent used here was synthesised in-house by the Peptide Chemistry science technology platform, The Francis Crick Institute |
| Chemical compound | TEV cleavable reagent | <i>Speers and Cravatt, 2005</i> | | The reagent used here was synthesised in-house by the Peptide Chemistry science technology platform, The Francis Crick Institute |
| Chemical compound | IMP-1002 | <i>Schlott et al., 2019</i> | | The reagent used here was synthesised by the Tate Laboratory, Imperial College London |
| Chemical compound | Rapamycin | Sigma-Aldrich | Cat# R8781 | |

Continued on next page

Continued

| Reagent type (species) or resource | Designation | Source or reference | Identifiers | Additional information |
|------------------------------------|--|-----------------------------|-----------------|--|
| Chemical compound | 5-Benzyl-3-isopropyl-1H-pyrazolo[4,3-d]pyrimidin-7(6H)-one (BIPPO) | <i>Howard et al., 2015</i> | | The reagent used here was synthesised in-house by the Peptide Chemistry science technology platform, The Francis Crick Institute |
| Software, algorithm | MaxQuant (version 1.5.0.25 and 1.5.2.8) | <i>Cox and Mann, 2008</i> | RRID:SCR_014485 | Free software for searching of mass spectrometry acquisition files |
| Software, algorithm | Perseus (version 1.5.0.9) | <i>Tyanova et al., 2016</i> | RRID:SCR_015753 | Free software for processing of MaxQuant output files |
| Software, algorithm | PyMOL (version 1.3r1) | Schrodinger LLC | RRID:SCR_000305 | Commercial software for molecular visualisation |
| Software, algorithm | Prism 8 (version 8.1.1) | GraphPad Software, Inc | RRID:SCR_002798 | Commercial software for statistical analysis |

General

Reagents: CuSO₄, TCEP, TBTA, buffer salts, DTT, iodoacetamide, DMSO, BSA, Triton-X100 and Tween-20 were from Sigma-Aldrich. Azide-PEG3-biotin was from Sigma-Aldrich. Peptide synthesis coupling reagents HATU and HCTU were from Fluorochem and Merck, respectively. MS-grade water, acetonitrile, methanol, TFA and formic acid were from Thermo Scientific. IMP-1002 was synthesised as described in *Schlott et al., 2019*. BIPPO was synthesised as described in *Howard et al., 2015*.

Plasmid generation

Primers used throughout this study are listed in *Supplementary file 6*. Plasmid sequences were confirmed by Sanger sequencing (Eurofins Genomics).

To generate the *Mic7* iKO plasmid, pG140_MIC7_HA_iKO_loxP100, the *Mic7* 5'UTR with a *loxP* site inserted 100 bp upstream of the *Mic7* start codon, and a recodonised *Mic7* cDNA-HA sequence, were synthesized (GeneArt strings, Life Technologies). These DNA fragments were Gibson cloned into the *Apal/Pacl* digested parental vector p5RT70loxPKillerRedloxPYFP-HX (*Andenmatten et al., 2013*) to generate an intermediate plasmid. The *Mic7* 3'UTR was subsequently amplified from genomic DNA using primers 1 and 2, while *mCherry* flanked by *Gra* gene UTRs was amplified from pTKO2C (*Caffaro et al., 2013*) using primer pair 3/4. The resulting fragments were Gibson cloned into the *SacI*-digested intermediate plasmid to generate pG140_MIC7_HA_iKO_loxP100.

To generate the complementation construct pUPRT_MIC7_Ty1, the *Mic7* sequence flanked by its 5'UTR was amplified from genomic DNA using primer pair 5/6. In parallel, the *Uprt* targeting vector pUPRT_HA (*Reese et al., 2011*) was amplified by inverse PCR using primers 7 and 8. The resulting PCR amplicons were Gibson cloned to generate pUPRT_MIC7_Ty1. Primers 5 and 8 comprise overhangs to facilitate introduction of a Ty1 tag 3' of the *Mic7* sequence.

To generate the complementation construct pUPRT_MIC7(G2K/G3A)_Ty1, the *Mic7* 5'UTR and *Mic7* endogenous sequence were amplified using primer pairs 9/10 and 5/11, respectively. In parallel, the *Uprt* targeting vector pUPRT_HA (*Reese et al., 2011*) was amplified by inverse PCR using primers 7 and 8. The resulting PCR amplicons were Gibson cloned to generate pUPRT_MIC7(G2K/G3A)_Ty1. Primers 9 and 11 comprise overhangs that introduce point mutations G2K and G3A, while primers 5 and 8 introduce a Ty1 tag 3' of the *Mic7* sequence.

To generate the complementation construct pUPRT_Myc_MIC7_Ty1, the Myc tag coding sequence was introduced within pUPRT_MIC7_Ty1 plasmid by inverse PCR using primers 12 and 13. The resulting linear fragment was circularized using KLD reaction buffer (NEB) as per manufacturer's instructions.

To generate the complementation construct pUPRT_Myc_MIC7(G2K/G3A)_Ty1, the Myc tag coding sequence was introduced within pUPRT_MIC7(G2K/G3A)_Ty1 plasmid by inverse PCR using primers 12 and 13. The resulting linear fragment was circularized using KLD reaction buffer (NEB) as per manufacturer's instructions.

To generate pSag1_Cas9-U6_sgMIC7, the pSag1_Cas9-U6_sgUPRT (Shen *et al.*, 2014; Addgene plasmid # 54467) vector was amplified by inverse PCR using primers 14 and 15. Primer 15 comprises a sequence extension that replaces the *Uprt*-targeting sgRNA with a sgRNA sequence targeting *Mic7*. The resulting linear fragment was circularized using KLD reaction buffer (NEB) as per manufacturer's instructions.

To generate pGra_5'UTRMIC7_MIC7_HA, the 5'UTR of *Mic7* was amplified from gDNA using primer pair 30/31, and recodonised *Mic7* sequence was amplified from pG140_MIC7_HA_iKO_loxP100 using primers 32 and 33. In parallel, the vector pGra_ApiAT5-3_HA (Wallbank *et al.*, 2019) was amplified by inverse PCR using primer pair 34/35. The three resulting PCR amplicons were Gibson assembled to generate pGra_5'UTRMIC7_MIC7_HA.

To generate pGra_5'UTRMIC7_MIC7(G2K/G3A)_HA, the 5'UTR of *Mic7* was amplified from gDNA using primer pair 30/31, and recodonised *Mic7*(G2K/G3A) sequence was amplified from pG140_MIC7_HA_iKO_loxP100 using primers 36 and 33. Primer 36 was used to introduce the point mutations G2K and G3A into the *Mic7* recodonised sequence. In parallel, the vector pGra_ApiAT5-3_HA (Wallbank *et al.*, 2019) was amplified by inverse PCR using primer pair 34/35. The three resulting PCR amplicons were Gibson assembled to generate pGra_5'UTRMIC7_MIC7(G2K/G3A)_HA.

To generate pGra_5'UTRTUB_MIC7_HA, the *Tub* 5'UTR was amplified from gDNA using primer pair 37/38, and recodonised *Mic7* sequence was amplified from pG140_MIC7_HA_iKO_loxP100 using primers 39 and 33. In parallel, the vector pGra_ApiAT5-3_HA (Wallbank *et al.*, 2019) sequence was amplified by inverse PCR using primer pair 34/40. The three resulting PCR amplicons were Gibson assembled to generate pGra_5'UTRTUB_MIC7_HA.

To generate pGra_5'UTRTUB_MIC7(G2K/G3A)_HA, the *Tub* 5'UTR was amplified from gDNA using primer pair 37/38, and recodonised *Mic7*(G2K/G3A) sequence was amplified from pG140_MIC7_HA_iKO_loxP100 using primers 41 and 33. Primer 41 was used to introduce the point mutations G2K and G3A into the *Mic7* recodonised sequence. In parallel, the vector pGra_ApiAT5-3_HA (Wallbank *et al.*, 2019) was amplified by inverse PCR using primer pair 34/40. The three resulting PCR amplicons were Gibson assembled to generate pGra_5'UTRTUB_MIC7(G2K/G3A)_HA.

To generate pGra_5'UTRMIC7_Myc1_MIC7_HA, pGra_5'UTRMIC7_Myc1/2_MIC7_HA and pGra_5'UTRMIC7_Myc2_MIC7_HA, the Myc tag coding sequence was introduced at different positions within pGra_5'UTRMIC7_MIC7_HA plasmid by inverse PCR using primers 42 and 43 (Myc1), 44 and 45 (Myc1/2), and 46 and 47 (Myc2). The resulting linear fragments were circularized using KLD reaction buffer (NEB) as per manufacturer's instructions.

Parasite line generation

Freshly harvested parasites were transfected by electroporation (1500 V) using the Gene Pulser Xcell system (Bio-Rad) as previously described (Soldati and Boothroyd, 1993).

To generate the inducible MIC7 knock-out line (RH DiCreDku80Dhxpgrt_loxPMIC7_HA, referred to here as iKO MIC7), the plasmid pG140_MIC7_HA_iKO_loxP100 was linearized using *PciI* and co-transfected with pSag1_Cas9-U6_sgMIC7 into the RH DiCreDku80Dhxpgrt line (Hunt *et al.*, 2019). Recombinant parasites were selected 24 hr post transfection by addition of mycophenolic acid (MPA; 25 mg/mL) and xanthine (XAN; 50 mg/mL) to culture medium. Resistant non-fluorescent parasites were cloned, and successful 5' and 3' integration at the *Mic7* locus was confirmed using primer pairs 16/17 and 18/19, respectively. Absence of the endogenous *Mic7* locus was confirmed using primers 24 and 25. Rapamycin-induced excision of the *loxPMic7* sequence was confirmed using primer pair 26/27.

To complement the iKO MIC7 line with MIC7-expressing constructs, pUPRT_MIC7_Ty1 and pUPRT_MIC7(G2K/G3A)_Ty1 or pUPRT_Myc_MIC7_Ty1 and pUPRT_Myc_MIC7(G2K/G3A)_Ty1 plasmids were linearized with *Scal* and individually co-transfected with pSAG1_Cas9-U6_sgUPRT. Transgenic parasites were subjected to 5'-fluo-2'-deoxyuridine (FUdR) selection (5 mM) 24 hr post transfection. Resistant parasites were cloned, and successful 5' and 3' integration was confirmed

using primer pairs 20/21 and 22/23. Disruption of the endogenous *Uprt* locus was confirmed using primer pair 28/29.

To generate lines that express WT and myristoylation mutant (G2K/G3A) MIC7 ectopically, plasmids pGra_5'UTRMIC7_MIC7_HA, pGra_5'UTRMIC7_MIC7(G2K/G3A)_HA, pGra_5'UTRTUB_MIC7_HA, and pGra_5'UTRTUB_MIC7(G2K/G3A)_HA were linearized using NotI and individually transfected into the RH *Dhxp* strain. Recombinant parasites were selected 24 hr post transfection by addition of mycophenolic acid (MPA; 25 mg/mL) and xanthine (XAN; 50 mg/mL) to culture medium.

To generate lines that ectopically express MIC7 with Myc tag within the EGF1, EGF1/2 or EGF2 domains, plasmids pGra_5'UTRMIC7_Myc1_MIC7_HA, pGra_5'UTRMIC7_Myc1/2_MIC7_HA and pGra_5'UTRMIC7_Myc2_MIC7_HA were linearized using NotI and individually transfected into the RH *Dhxp* strain. Recombinant parasites were selected 24 hr post transfection by addition of mycophenolic acid (MPA; 25 mg/mL) and xanthine (XAN; 50 mg/mL) to culture medium.

Cell culture

Parasites of the RH strain were cultured in Human foreskin fibroblasts (HFFs) monolayers in Dulbecco's Modified Eagle Medium (DMEM), GlutaMAX (Thermo Fisher) supplemented with 10% heat-inactivated foetal bovine serum (FBS; Life technologies), at 37°C and 5% CO₂. All strains and host cell lines tested negative for the presence of mycoplasma.

Metabolic labelling and cell lysis

Upon infection of HFF monolayers the medium was removed and replaced by fresh culture medium supplemented with 25 mM YnMyr (Iris Biotech) or Myr (Tokyo Chemical Industry). The parasites were then incubated for 16 hr, washed with PBS (2x) and lysed on ice using a lysis buffer (PBS, 0.1% SDS, 1% Triton X-100, EDTA-free complete protease inhibitor (Roche Diagnostics)). Lysates were kept on ice for 20 min and centrifuged at 17,000 × g for 20 min to remove insoluble material. Supernatants were collected and protein concentration was determined using a BCA protein assay kit (Pierce).

Click reaction and pull down

Lysates were thawed on ice. Proteins (100–300 mg) were taken and diluted to 1 mg/mL using the lysis buffer. A click mixture was prepared by adding reagents in the following order and by vortexing between the addition of each reagent: a capture reagent (stock solution 10 mM in water, final concentration 0.1 mM), CuSO₄ (stock solution 50 mM in water, final concentration 1 mM), TCEP (stock solution 50 mM in water, final concentration 1 mM), TBTA (stock solution 10 mM in DMSO, final concentration 0.1 mM). Following the addition of the click mixture the samples were vortexed (room temperature, 1 hr), and the reaction was stopped by addition of EDTA (final concentration 10 mM). Subsequently, proteins were precipitated (chloroform/methanol, 0.25:1, relative to the sample volume), the precipitates isolated by centrifugation (17,000 × g, 10 min), washed with methanol (1 × 400 mL) and air dried (10 min). The pellets were then resuspended (final concentration 1 mg/mL, PBS, 0.4% SDS) and the precipitation step was repeated to remove excess of the capture reagent. Next, samples were added to 15 mL of pre-washed (0.2% SDS in PBS (3 × 500 mL)) Dynabeads MyOne Streptavidin C1 (Invitrogen) and gently vortexed for 90 min. The supernatant was removed and the beads were washed with 0.2% SDS in PBS (3 × 500 mL).

SDS-PAGE, in gel fluorescence and western blotting

Beads were supplemented with 2% SDS in PBS (20 mL) and 4x SLB (Invitrogen), boiled (95°C, 10 min), centrifuged (1000 × g, 2 min) and loaded on 10% or 4–20% SDS-PAGE gel (Bio-Rad). Following electrophoresis (60 min, 160V), gels were washed with water (3x). In-gel fluorescence was detected using a Pharos FX Plus Imager (Bio-Rad) and the protein loading was checked by Coomassie staining. For western blotting proteins were transferred (25 V, 1.3 A, 7 min) onto nitrocellulose membranes (Bio-Rad) using Bio-Rad Trans Blot Turbo transfer system. After a brief wash with PBS-T (PBS, 0.1% Tween-20) membranes were blocked (5% milk, TBS-T, 1 hr) and incubated with primary antibodies (5% milk, TBS-T, overnight, 4°C) at the following dilutions: rat anti-HA (1:1000; Roche Diagnostics), mouse anti-Myc (1:1000; Millipore), mouse anti-Ty1 (1:2000; Thermo Fisher), rabbit anti-Gra29 (1:1000; [Young *et al.*, 2020]), rabbit anti-SFP1 (1:1000; [Young *et al.*, 2020]), mouse anti-

Toxoplasma (1:1000; Abcam), mouse anti-CDPK1 (1:3000; Matt Bogyo Lab), rabbit anti-SAG1 (1:10,000; John Boothroyd Lab), rabbit anti-GAP45 (1:1000; Peter Bradley Lab), rabbit anti-TgCAP (1:2000; [Hunt et al., 2019]), rabbit anti-MIC2 (1:500; Vernon Carruthers Lab), and mouse anti-MIC2 (6D10) (1:1000; Vernon Carruthers Lab). Following washing (TBS-T, 3x) membranes were incubated with IR dye-conjugated secondary antibodies from LI-COR Biosciences (1:10,000, 5% milk, TBS-T, 1 hr), and after a final washing step imaged on a LiCOR Odyssey imaging system (LI-COR Biosciences). In case of a biotin western blot, membranes were blocked with 3% BSA and incubated with Streptavidin-HRP (1:4000; Thermo Scientific) in 0.3% BSA, PBS-T for 1 hr. ECL western blotting Detection Reagent (GE Healthcare) was then used for chemiluminescence based imaging on a ChemiDoc MP Imaging System (Bio-Rad).

Synthesis of capture reagents

TEV reagent: Solid phase synthesis took place on a CF peptide synthesizer (Intavis) using a Rink Amide LL resin (100 mmol; Merck) and *N*(α)-Fmoc amino acids, including Fmoc-Lys(N₃)-OH (Fluorochem) and Fmoc-Gly-(Dmb)Gly-OH (Merck). HCTU was used as the coupling reagent with 5-fold excess of amino acids. Fmoc-Lys(Biotin)-OH (four eq; Merck) in 6 mL DMSO:NMP (1:1) was coupled manually after automated assembly of the rest of the chain. DIPEA (four eq) was added, followed by HOBt (1 M, four eq) in NMP. After 3 min DIC (four eq) was added, then after 30 min the solution was added to the resin and allowed to react overnight. The resin was washed with DCM and DMF prior to manual Fmoc removal and acetylation. The peptide was cleaved from the resin and protecting groups removed by addition of a cleavage solution (95% TFA, 2.5% H₂O, 2.5% TIS). After 2 hr, the resin was removed by filtration and peptides were precipitated with diethyl ether on ice. The peptide was isolated by centrifugation, then dissolved in H₂O and freeze dried overnight. After dissolving in methanol, portions of the peptide were purified on a C8 reverse phase HPLC column (Agilent PrepHT Zorbax 300 SB-C8, 21.2 × 250 mm, 7 m) using a linear solvent gradient of 13-50% MeCN (0.08% TFA) in H₂O (0.08% TFA) over 40 min at a flow rate of 8 mL/min. The peak fraction was analysed by LC-MS on an Agilent 1100 LC-MSD. The calculated molecular weight of the peptide was in agreement with the mass found. Calculated MW: 1804.08, actual mass: 1803.87.

Trypsin reagent: Solid phase synthesis took place on a CF peptide synthesizer (Intavis) using a Fmoc-PEG-Biotin NovaTag resin (100 mmol; Merck), 2-Azidoacetic acid (Fluorochem) and *N*(α)-Fmoc amino acids, including Fmoc-Lys(MMT)-OH (Merck). HATU was used as the coupling reagent with 5-fold excess of amino acids. Following chain assembly, the MMT protecting group was removed from the peptidyl-resin by treatment with 1% TFA in DCM (10 mL for 2 min × 8) and the resin washed with DCM and DMF. Next 5-TAMRA (four eq; Anaspec) was dissolved in 1 mL DMSO:NMP (1:1). DIPEA (four eq) was added, followed by HOBt (1 M, four eq) in NMP. After 3 min DIC (four eq) was added, then after 30 min the solution was added to the resin and allowed to react overnight. After washing the resin with DMF and DCM, the peptide was cleaved from the resin and protecting groups removed by addition of a cleavage solution (95% TFA, 2.5% H₂O, 2.5% TIS). After 2 hr, the resin was removed by filtration and peptides were precipitated with diethyl ether on ice. The peptide was isolated by centrifugation, then dissolved in H₂O and freeze dried overnight. After dissolving in MeCN:H₂O (1:1), portions of the peptide were purified on a C8 reverse phase HPLC column (Agilent PrepHT Zorbax 300 SB-C8, 21.2 × 250 mm, 7 m) using a linear solvent gradient of 10-50% MeCN (0.08% TFA) in H₂O (0.08% TFA) over 40 min at a flow rate of 8 mL/min. The peak fraction was analysed by LC-MS on an Agilent 1100 LC-MSD. The calculated molecular weight of the peptide was in agreement with the mass found. Calculated MW: 1396.31, actual mass: 1395.60.

Sample preparation for MS-based proteomics

Click reaction - Reagent 1 and 2: lysates were thawed on ice and the click reaction was carried out with 1 mg of proteins at 2 mg/mL. Proteins were captured by adding a mixture of respective capture reagent (final concentration 0.1 mM), CuSO₄ (final concentration 1 mM), TCEP (final concentration 1 mM) and TBTA (final concentration 0.1 mM). The samples were vortex-mixed (room temperature, 1 hr) before the addition of EDTA (final concentration 10 mM), methanol (four volumes), chloroform (1 vol), and water (three volumes). The samples were vortex-mixed briefly, centrifuged (10,000 × g, 20 min) and the resulting pellets were either washed with methanol (four volumes) and dried (reagent 1) or resuspended (at 2 mg/mL, 1% SDS in PBS) after which the precipitation step was repeated and

the resulting pellets washed with methanol (four volumes) and dried (reagent 2). Reagent 3: lysates were thawed on ice and the click reaction was carried out with 1 mg of proteins at 2 mg/mL. Proteins were captured by sequential addition of the capture reagent (final concentration 0.1 mM), TCEP (final concentration 1 mM), TBTA (stock in DMSO:t-Butanol 1:4, final concentration 0.1 mM) and CuSO₄ (final concentration 1 mM) with mixing between each step. The samples were incubated at room temperature for 1 hr before the addition of EDTA (final concentration 10 mM), methanol (four volumes), chloroform (1 vol), and water (three volumes). The samples were vortex-mixed briefly, centrifuged (10,000 × g, 20 min) and the resulting pellets were washed with methanol (four volumes) and dried. Subsequently, the dried pellets were resuspended in 2% SDS in PBS and, once completely dissolved, PBS was added (final concentration 0.8% SDS, 2 mg/mL). For samples treated with base, NaOH was added (final concentration 0.2 M, 1 hr) followed by neutralisation with equivalent amount of HCl. Base-treated and untreated samples were then diluted (1 mg/mL, 0.4% SDS, 1 mM DTT) before pull down.

Pull down, reduction and alkylation - NeutrAvidin agarose resin (Thermo Scientific) was washed with 0.2% SDS in PBS (3x). Typically, 50 mL of bead slurry was used for 1 mg of lysate. The samples were added to beads and the enrichment was carried out with gentle mixing (2 hr, room temperature). Following the removal of supernatants, the beads were sequentially washed with 1% SDS in PBS (3x), 4 M urea in PBS (2x) and 50 mM ammonium bicarbonate (3x). The samples were reduced (5 mM DTT, 56°C, 30 min) and cysteines alkylated (10 mM iodoacetamide, room temperature, 30 min) in the dark with washing the beads (2x, 50 mM ammonium bicarbonate) after each step.

Protein digestion - for samples processed with reagent 1 and 2 as well as for supernatants (proteomes) MS grade trypsin (Promega) was used at 1:1000 w/w protease:protein, and samples were incubated overnight at 37°C. For reagent 3 two digestion strategies were used. TEV I: beads were washed (2x) with water followed by TEV buffer (50 mM TrisHCl, 0.5 mM EDTA, 1 mM DTT, pH 8.0) and the TEV protease (50 units; Invitrogen) was added. Samples were incubated overnight at 30°C. Supernatant was then removed and beads washed with TEV buffer (1x, 50 mL). The wash fraction was combined with the supernatant and stored at 4°C. A fresh portion of TEV protease (20 units) was then added to beads which were incubated for additional 6 hr at 30°C. The supernatant and wash were combined with the first TEV elution. MS grade trypsin was subsequently added at 1:1000 w/w protease:protein, and samples were incubated overnight at 37°C. TEV II: samples were incubated overnight at 37°C with MS grade trypsin at 1:1000 w/w protease:protein. The supernatant was removed (fraction 1) and beads washed with water and TEV buffer (2x each). The TEV protease was then added (50 units) and beads incubated overnight at 30°C (fraction 2).

Stage tip - samples were desalted prior to LC-MS/MS using Empore C18 discs (3M). Each stage tip was packed with one C18 disc, conditioned with 100 mL of 100% methanol, followed by 200 mL of 1% TFA. The samples were loaded in 1% TFA, washed 3 times with 200 mL of 1% TFA and eluted with 50 mL of 50% acetonitrile, 5% TFA. Desalted peptides were vacuum dried in preparation for LC-MS/MS analysis.

Chemical inhibition of TgNMT

HFFs were infected with *Toxoplasma* and cultured for 16 hr. The medium was then replaced and intracellular parasites co-treated with 25 mM YnMyr and the indicated concentrations of IMP-1002 for 5 hr. Following PBS wash (2x) the cells were lysed on ice using the lysis buffer and further processed exactly as described above. The click reaction, pull down on NeutrAvidin beads and the MS sample prep were performed as described above for reagent 1 and 2.

LC-MS/MS

Samples were resuspended in 0.1% TFA and loaded on a 50 cm Easy Spray PepMap column (75 mm inner diameter, 2 mm particle size, Thermo Fisher Scientific) equipped with an integrated electrospray emitter. Reverse phase chromatography was performed using the RSLC nano U3000 (Thermo Fisher Scientific) with a binary buffer system (solvent A: 0.1% formic acid, 5% DMSO; solvent B: 80% acetonitrile, 0.1% formic acid, 5% DMSO) at a flow rate of 250 nL/min. Samples processed with reagent 1 were run on a linear gradient of 2-35% B in 90 min with a total run time of 120 min including column conditioning. Samples processed with reagents 2 and 3 were run on a linear gradient of 2-40% B or 2-55% B (TEV II myristoylated peptide fraction) in 155 min with a total run time of 180

min including column conditioning. The nanoLC was coupled to a Q Exactive mass spectrometer using an EasySpray nano source (both Thermo Fisher Scientific). The Q Exactive was operated in data-dependent mode, acquiring HCD MS/MS scans ($R = 17,500$) after an MS1 survey scan ($R = 70,000$) on the 10 most abundant ions using MS1 target of $1E6$ ions, and MS2 target of $5E4$ ions. The maximum ion injection time utilised for MS2 scans was 120 ms, the HCD normalised collision energy was set at 28 and the dynamic exclusion was set at 30 s. The peptide match and isotope exclusion functions were enabled. NMTi samples were run on a linear gradient of 2–20% B in 55 min, followed by 20–40% B in 35 min and 40–60% B in 5 min with a total run time of 120 min including column conditioning. The nanoLC was coupled to a Orbitrap Lumos mass spectrometer using an EasySpray nano source (both Thermo Fisher Scientific). The Orbitrap Lumos was operated in data-dependent mode (3 s cycle time), acquiring IT HCD MS/MS scans in rapid mode after an MS1 survey scan ($R = 120,000$). The MS1 target was $4E5$ ions whereas the MS2 target was $2E3$ ions. The maximum ion injection time utilised for MS2 scans was 300 ms, the HCD normalised collision energy was set at 32 and the dynamic exclusion was set at 30 s.

Data analysis

Acquired raw files were processed with MaxQuant, versions 1.5.0.25 and 1.5.2.8 (Cox and Mann, 2008). Peptides were identified from the MS/MS spectra searched against *Toxoplasma gondii* (combined TG1, ME49 and VEG proteomes, ToxoDB) and *Homo sapiens* (UniProt) proteomes using Andromeda (Cox et al., 2011) search engine. Cysteine carbamidomethylation was selected as a fixed modification and methionine oxidation was selected as a variable modification. The enzyme specificity was set to trypsin with a maximum of 2 missed cleavages. The precursor mass tolerance was set to 20 ppm for the first search (used for mass re-calibration) and to 4.5 ppm for the main search. The datasets were filtered on posterior error probability (PEP) to achieve a 1% false discovery rate on protein, peptide and site level. Other parameters were used as pre-set in the software. 'Unique and razor peptides' mode was selected to allow identification and quantification of proteins in groups (razor peptides are uniquely assigned to protein groups and not to individual proteins). Label-free quantification (LFQ) in MaxQuant was performed using a built-in label-free quantification algorithm (Cox and Mann, 2008) enabling the 'Match between runs' option (time window 0.7 min) within replicates. Each experiment comprised of replicates treated with YnMyr and the same number of replicates treated with Myr control or NMTi. The LFQ is based on intensities of proteins calculated by MaxQuant from peak intensities and based on the ion currents carried by peptides whose sequences match a specific protein or a protein group to provide an approximation of abundance.

Myristoylated peptide search in MaxQuant was performed as described above applying the following variable modifications: cysteine carbamidomethylation, +463.2907 (reagent 2) and +491.3220 (reagent 3) at any peptide N-terminus and cysteine residues. In addition, the minimum peptide length was reduced to six amino acids and the 'Match between runs' option was disabled. MaxQuant utilises a scoring algorithm when matching experimental MS/MS spectra with a library of theoretical spectra generated from the in silico digestion of proteins within databases selected for the search. The algorithm is used to evaluate the quality of peptide-spectrum matches (PSMs). To each PSM, MaxQuant also attributes a delta score, which is a difference between scores associated with the match to the best peptide candidate and the second best match within the database. The higher the score and the delta score, the more reliable the identification. In order to reduce a possibility for a false peptide sequence assignment even further, we applied relatively high delta score thresholds (20 vs 6 pre-set as default) for all myristoylated peptides in our analysis. MaxQuant output files were processed with Perseus, version 1.5.0.9 (Tyanova et al., 2016) as described in the Results section and in *Supplementary files 1–3*. The mass spectrometry proteomics data have been deposited to the ProteomeXchange Consortium via the PRIDE (Perez-Riverol et al., 2019) partner repository with the dataset identifier PXD019677.

Homology modelling of TgNMT onto PvNMT crystal structure

The model of TgNMT was generated using SWISS-MODEL (Waterhouse et al., 2018), and aligned with a crystal structure of PvNMT bound to NMT inhibitor IMP-1002 (PDB: 6MB1). The structural image was generated using PyMOL (Schrodinger LLC (2010), The PyMOL Molecular Graphics System, Version 1.3r1).

MIC7 expression in tachyzoites and bradyzoites

HFF monolayers were infected with Pru Dhxgprt parasites in triplicate. For tachyzoite samples an MOI of 1 was used for a 27 hr infection. For bradyzoite samples monolayers were infected at an MOI of 0.8 for 3.5 hr, washed and grown in switch conditions (RPMI, 1% FBS, pH 8.1, ambient CO₂) for 3 days. Triplicate samples were lysed in 2 mL ice cold lysis buffer (50 mM Tris-HCl, 75 mM NaCl, 8 M urea, pH 8.2), supplemented with protease (Roche Diagnostics) and phosphatase (Phos Stop, Roche Diagnostics) inhibitors. Lysis was followed by sonication to reduce sample viscosity (30% duty cycle, 3 × 30 s bursts, on ice). Protein concentration was measured using a BCA protein assay kit (Pierce). Lysates (1 mg per condition) were subsequently processed for mass spectrometry as described (Young *et al.*, 2020) and data analysis performed as explained in *Supplementary file 5*. For full dataset please see Young *et al.*, 2020 and PXD019729.

Depletion of *Mic7*

Parasites were allowed to invade HFFs for 2 hr and then treated with 50 nM rapamycin (Sigma-Aldrich) or an equivalent volume of vehicle (DMSO) for 4 hr. The medium was then replaced and the parasites allowed to grow for at least 24 hr prior to PCR and western blot analysis.

Parasite preparation for large scale invasion assay/live microscopy/gliding:

HFF monolayers in T25 flasks were infected in culture conditions (37°C and 5% CO₂) with recently egressed tachyzoites to achieve a one to two-per-cell parasite infection. Non-internalized parasites were removed with PBS, and the infected monolayers were cultivated for about 2 hr in complete culture medium (DMEM supplemented with 10% FCS, 10 mM HEPES, 100 units/mL penicillin, and 100 mg/mL streptomycin). After 2 hr incubation the parasites were treated with 50 nM rapamycin or vehicle. Following a 14 hr incubation the medium was replaced with the complete medium and tachyzoites were used within 2 to 5 hr post-egress.

Plaque assays

Parasites were harvested by syringe lysis, counted, and 400 parasites were seeded on confluent HFF monolayers grown in 24-well plates (Falcon). Parasites were allowed to invade overnight prior to treatment with 50 nM rapamycin or vehicle (DMSO) for 4 hr. Following medium replacement to standard culture medium, plaques were allowed to form for 5 days. iKO MIC7 line: Parasites were harvested by syringe lysis, counted, and 100 parasites were seeded on confluent HFF monolayers grown in 24-well plates (Falcon). Parasites were allowed to invade overnight prior to treatment with 50 nM rapamycin or vehicle (DMSO) for 4 hr. Following medium replacement to standard culture medium, plaques were allowed to form for 7 days. NMTi: Parasites were harvested by syringe lysis, counted, and 200 parasites were seeded on confluent HFF monolayers grown in the presence of IMP-1002 for 5 days.

Plaque formation was assessed by inspecting the methanol fixed and 0.1% crystal violet stained HFF monolayers.

Immunofluorescence analysis

Parasite-infected HFF monolayers grown on glass coverslips were fixed with 3% formaldehyde for 15 min prior to washing with PBS. Fixed cells were then permeabilised (0.2% Triton X-100/PBS, 10 min), blocked (3% BSA/PBS, 1 hr) and stained for 1 hr with primary antibodies at the following dilutions: rat anti-HA (1:1000; Roche), mouse anti-Myc (1:1000; Millipore), mouse anti-Ty1 (1:500; Thermo Fisher), rabbit anti-MIC2 (1:5000; Vernon Carruthers Lab). Labelled proteins were visualised with Alexa Fluor-conjugated secondary goat antibodies (1:2000, 1 hr; Life Technologies). Nuclei were visualised with the DNA stain DAPI (5 mg/mL; Sigma) supplemented with the secondary antibody. Stained coverslips were mounted on glass slides with Slowfade (Life Technologies) and imaged on a Nikon Eclipse Ti-U inverted fluorescent microscope using 100x oil objective. Images were analysed using Nikon NIS-Elements imaging software.

Invasion assay

Parasites were treated with 50 nM rapamycin for 4 hr and after replacing the medium allowed to grow for 24 hr. Red/green invasion assays were then performed. Parasites were lysed in an invasion non-permissive buffer, Endo buffer (44.7 mM K₂SO₄, 10 mM MgSO₄, 106 mM sucrose, 5 mM

glucose, 20 mM Tris-H₂SO₄, 3.5 mg/mL BSA, pH 8.2). 250 mL of 8E5 parasites/mL in Endo buffer were added to each well of a 24-well flat-bottom plate (Falcon) containing a coverslip with a confluent HFF monolayer. The plates were spun at 129 x g for 1 min at 37°C to deposit parasites onto the monolayer. The Endo buffer was gently removed and replaced with invasion permissive medium (1% FBS/DMEM). Parasites were allowed to invade for 15 min at 37°C, after which the monolayer was gently washed with PBS and fixed with 3% formaldehyde for 15 min at room temperature. Extracellular (attached) parasites were stained with mouse anti-*Toxoplasma* (TP3) (1:1000; Abcam) and goat anti-mouse Alexa Fluor 488 before permeabilisation (0.2% Triton X-100/PBS) and detection of intracellular (invaded) parasites with rabbit anti-*Tg*CAP (1:2000; [Hunt *et al.*, 2019]) and goat anti-rabbit Alexa Fluor 594. For each replicate, at least five random fields were imaged with a 40x objective. Three independent experiments were performed in duplicate. The number of intracellular (594+/488-) and extracellular (594+/488+) parasites was determined by counting, in a blinded fashion, at least 275 parasites per strain. The parasite counts in the MIC7 iKO and cMut lines were normalised to the cWT, and results were statistically tested with a one-way ANOVA with Dunnett's multiple comparison test in GraphPad Prism 8. The data are presented as mean ± SD. For estimation of the parasite attachment efficiency, the number of all (594+) parasites was used and the results were statistically tested as above.

Large scale automated invasion assay

Cell Invasion - HFFs were seeded at a density of 2E4 cells per well into 96-well plate and cultivated in complete medium at 37°C and 5% CO₂ for 24 hr to allow for sub-confluence. 5E6 to E7 parasites were collected upon spontaneous egress from synchronously infected HFF monolayers. The supernatant was centrifuged at higher speed (900 x g, 7 min) to collect parasites that were gently suspended in 2 mL of complete medium before counting. 2.5E5 parasites were added to each well. To synchronize invasion, the 96-well plate was centrifuged (300 x g, 3 min) and incubated for 30 min at 37°C and 5% CO₂. After gentle aspiration, invasion was stopped by addition of 3.2% paraformaldehyde (PFA) in PBS, pH 7.5 (20 min).

Parasite staining - immunostaining was performed first under conditions that did not permeabilise the HFF cells to allow discriminating between the extracellular and intracellular parasites. Fixed cell samples were incubated in 2%BSA/PBS as a blocking buffer (BB) for 20 min. Extracellular tachyzoites were selectively stained using mouse anti-*Tg*SAG1(TP3) (1 mg/mL stock, 1:600, 40 min; Novocastra) followed by Alexa Fluor 488-conjugated highly cross-adsorbed (HCA) anti-mouse antibody (2 mg/mL stock, 1:800, 1 hr). The excess of reagents was washed off with PBS and cells were permeabilised (0.2% Triton X-100/PBS, 10 min) prior to incubation in BB and the second staining step using anti-*Tg*SAG1 (1 mg/mL stock, 1:600, 1 hr) but followed by Alexa Fluor 594-conjugated HCA anti-mouse antibody (2 mg /ml stock, 1:800, 1 hr). Cell nuclei were stained with 500 nM DAPI and the 96 well plates were automatically scanned to quantify the average number of cells per well. The nuclei of parasites are detected by blue fluorescence whereas the intracellular tachyzoites by red fluorescence and the extracellular ones by yellow fluorescence (as the result of green and red fluorescence).

Quantification - samples were automatically scanned at a magnification of 20x under an Olympus ScanR automated inverted microscope. Images were acquired for five wells per parasite strain for each invasion assay, with 16 randomly scanned fields per well and further processed with ScanR software. ScanRAnalysis includes algorithms to provide automated cell nuclei segmentation following signal-to-noise ratio optimisation and accurate cell surface mask definition. To identify intracellular (red) over extracellular (yellow) parasites, image subtraction from each channel was automatically obtained. Data collected allowed determining the total number of intracellular tachyzoites over the total number of host cells for each well. Three independent assays were carried out, and data were statistically analysed using a two-tailed Student's t-test in GraphPad Prism 8. The data are presented as mean ± SD.

Invasion video microscopy

Preparation of human cells - HFF and Human Bone OsteoSarcoma cells (U2OS) that stably expressed the GFP-GPI plasma membrane reporter, were seeded at a density of 3E5 cells per 18 mm glass coverslip, previously coated with poly-L-lysine (50 mg/mL). Cells were cultivated in complete medium at

37°C and 5% CO₂ for 24 hr to allow for 80% confluence. Coverslips were placed in Chamide chambers (LCI Corp.) and covered with a minimal volume (i.e. 100 mL) of motility buffer (see below).

Preparation of parasites – 2E5 to 4E5 parasites were typically collected upon spontaneous egress from synchronously infected HFF monolayers. 150 mL of this suspension were mixed with 5 mL of Hanks' Balanced Salt Solution (HBSS) supplemented with 0.2% FCS. After centrifugation (900 x g, 7 min), parasites were resuspended in 200 mL of motility buffer (HBSS supplemented with 1% FCS and 0.5 mM CaCl₂ to reach about 1.6 mM CaCl₂ final). Typically, 30 to 40 mL of the suspension were added to the cells on the coverslip immobilized in the chamber, to avoid parasite overcrowding during recording.

Video recording of the tachyzoite behaviour - the recording chamber that accommodates the coverslips was installed on an Eclipse Ti inverted confocal microscope (Nikon) to perform time-lapse video microscopy, with a temperature and CO₂-controlled stage (LCI Corp.). The microscope was also equipped with a CMOS camera and a CSU X1 spinning disk (Yokogawa, Roper Scientific). The microscope was piloted using MetaMorph software (Universal Imaging Corporation, Roper Scientific). Similar parameters for image acquisition were used throughout each independent experiment. Time of invasion was estimated for each tachyzoite using MetaMorph time scale between the moment of contact between parasite apex (i.e. conoid) and host cell membrane until the tachyzoite has fully passed through the cell-zoite junction. Time of failed invasion was quantified using the same software, once again between the time of apical contact to those of body withdrawal and detachment, or the moment the tachyzoite did not perform any movement.

Gliding assays

Freshly egressed parasites of each genetic background were prepared as for the video recording assays. About 2 to 4E5 tachyzoites in 300 mL of motility buffer were deposited on 12 mm glass coverslip, previously coated with poly-L-lysine (as above) and placed in a 24 well plate. Parasites were gently centrifuged (200 x g, 3 min) to ensure rapid contact with the coverslip and then allowed to glide for 10-15 min at 37°C and 5% CO₂. Motile activity was checked under microscope after a few first minutes. At the end of this period, the samples were fixed after gentle aspiration of the liquid by the addition of 3.2% PFA in PHEM pH 7.5 (20 min). Trails left by gliding parasites and parasite surface were stained after a blocking step (2% BSA/PBS, 30 min) with mouse anti-*TgSAG1* antibody (1 mg/mL stock, 1:600, 2 hr) and Alexa Fluor 488-conjugated HCA anti-mouse antibody (2 mg/mL stock, 1:800, 2 hr). Cell nuclei were stained with 500 nM DAPI and mounted in Mowiol. Images of trails and tachyzoites were captured under the fluorescent ApoTome two microscope (Zeiss) using appropriate set of filters, the Zen software (Zeiss) and a z step of 0.3 mm. Image stacks were further processed with FIJI (*Schindelin et al., 2012*) and Photoshop.

Immunofluorescence of successful and failed invasions

MIC7 iKO parasites were treated with DMSO or rapamycin and were prepared as described for the video recording assays. Approximately 8E5 tachyzoites in 300 mL of motility buffer were deposited on 12 mm glass coverslip previously coated with poly-L-lysine (as above) and placed in a 24 well plate. Tachyzoites were gently centrifuged (300 x g, 3 min) to ensure rapid contact with the host cell (non-fluorescent HFF and GFP-GPI expressing U2OS cells) and allowed to invade for 2 to 4 min periods at 37°C and 5% CO₂. Samples were immediately fixed in 3.2% PFA in PHEM pH 7.5 (20 min) prior to be processed for IFA. Blocking step and anti-*TgSAG1* staining were performed as for the gliding assay except that the incubation with SAG1 primary antibody and Alexa Fluor 633-conjugated secondary antibody was reduced to 30 min. After SAG1 staining, the HFF-tachyzoite samples were permeabilised with (0.2% Triton X-100/PBS, 5 min) prior to a second step of blocking. MIC7 labelling was performed using rabbit anti-HA (clone C29F4), (1:800, 2 hr; Cell Signaling) followed by Alexa Fluor 488-conjugated HCA anti-rabbit antibody (2 mg/mL stock, 1:800, 2 hr).

MIC7 dimerisation

HFF monolayers infected with parasites from the DiCre, ^{Myc}WT and ^{Myc}Mut lines were washed with cold PBS and lysed in IP buffer (50 mM Tris, 150 mM NaCl, 0.2% Triton-X100, pH7.5) supplemented with protease inhibitors (Roche Diagnostics) for 30 min on ice. The lysates were then centrifuged (5000 x g, 20 min, 4°C), the supernatants collected and incubated with 20 mL of *a*-HA-

conjugated agarose beads (Millipore) on a rotating wheel at 4°C. After 3 hr the supernatant was removed and beads washed 3x with IP buffer. Protein elution from beads was performed with SDS sample loading buffer and boiling at 95°C for 10 min. Input, IP and supernatant samples for each tested parasite line were then analysed by SDS-PAGE and western blotting.

Microneme secretion assay

Parasites from MIC7 iKO line were treated with DMSO or rapamycin (50 nM, 4 hr). After 24 hr incubation parasites were syringe lysed in DMEM at room temperature and collected by centrifugation (800 x g, 4°C, 10 min). Pellets were resuspended in Ringer's buffer (155 mM NaCl, 3 mM KCl, 2 mM CaCl₂, 1 mM MgCl₂, 3 mM NaH₂PO₄, 10 mM HEPES, 10 mM glucose) supplemented with BIPPO (50 mM) or vehicle and microneme secretion was induced at 37°C for 20 min. Following this incubation step the parasites were placed on ice and pelleted (1000 x g, 5 min, 4°C). The pellet was kept on ice while the supernatant was re-pelleted (2000 x g, 5 min, 4°C). The final supernatant, containing the excreted secreted antigens, and pellet fractions were resuspended in sample loading buffer prior to SDS-PAGE and western blotting.

Shedding assays

Shedding tests during egress for ^{Myc}cWT and ^{Myc}cMut lines were performed exactly as described in microneme secretion assay.

To test for MIC7 shedding upon invasion, parasites from the iKO, ^{Myc}cWT and ^{Myc}cMut lines were treated with DMSO or rapamycin (50 nM, 4 hr). After 24 hr incubation parasites were syringe lysed in cold DMEM and spun (300 x g, 3 min, 4°C) onto PBS washed HFF monolayers in a 6-well plate (Falcon). The plate was then incubated at 37°C to facilitate invasion. After 1 hr the plate was placed on ice, the supernatant was gently aspirated off and spun down (700 x g, 10 min, 4°C) to remove any aspirated parasites. Proteins were precipitated out by the addition of cold trichloroacetic acid (10% v/v) on ice (30 min). Samples were centrifuged (17,000 x g, 20 min, 4°C), washed with 300 mL of cold acetone and air dried. The infected monolayers were scraped in 0.5 mL cold PBS and collected by centrifugation (17,000 x g, 20 min, 4°C). Both pellet and supernatant samples were resuspended in sample loading buffer prior to SDS-PAGE and western blotting.

Proteinase K protection assay

Parasites from ^{Myc}cWT and ^{Myc}cMut lines were treated with rapamycin (50 nM, 4 hr) followed by YnMyr (25 mM, 16 hr). Parasites were then syringe lysed in DMEM at room temperature and collected by centrifugation (800 x g, 10 min, 4°C). Pellets were resuspended in 1.7 mL cold SoTE buffer (0.6 M sorbitol, 20 mM Tris-HCl (pH 7.5), and 2 mM EDTA) and split into three tubes (0.5 mL each) per tested parasite line. Tubes 2 and 3 were permeabilised with 0.01% cold Digitonin (Sigma-Aldrich) in SoTE. Samples were carefully mixed by inversion and incubated on ice (10 min) prior to centrifugation (1000 x g, 10 min, 4°C). Supernatant was discarded. Pellets were resuspended in 0.5 mL cold SoTE and 8 mg of Proteinase K (Sigma-Aldrich) were added to tube 3. All tubes were gently inverted and incubated on ice (30 min). Proteinase K was inactivated by addition of ice cold trichloroacetic acid to a final concentration of 10% v/v on ice (30 min). Samples were centrifuged (17,000 x g, 20 min, 4°C), washed with 300 mL of cold acetone and air dried prior to SDS-PAGE and western blotting.

Rhoptry secretion assay

Parasites from iKO, ^{Myc}cWT and ^{Myc}cMut lines were treated with 50 nM rapamycin or an equivalent volume of vehicle (DMSO) for 4 hr after which the medium was replaced and the parasites allowed to grow for 24 hr. Parasites were harvested by syringe lysis, counted, and treated with 1 mM Cytochalasin D (Sigma) for 10 min at room temperature. 500,000 parasites from each condition were seeded onto confluent HFF monolayers grown in chambered coverslip slides (ibidi) and allowed to settle for 10 min on ice. The slides were spun down (250 x g, 1 min, 4°C) then transferred to a 37°C water bath for 20 min to initiate rhoptry secretion. The chambers were washed 3x with PBS then fixed with ice-cold methanol at -20°C for 8 min and washed 3x with PBS. Fixed cells were permeabilised with 0.1% Triton X-100 in PBS for 15 min then blocked with 3% BSA in PBS for 1 hr. Cells were then incubated with rabbit anti-phospho-Stat6 (1:600; Cell Signaling) and mouse anti-*Toxoplasma*

(TP3) (1:1000; Abcam) primary antibodies for 1 hr. After 3x washes with PBS, cells were incubated with goat anti-rabbit Alexa Fluor 594 (1:2000; Life Technologies) and goat anti-mouse Alexa Fluor 488 (1:2,000; Life Technologies) secondary antibodies and 5 mg/mL DAPI (Sigma) for 1 hr followed by 3x washes with PBS. Images were obtained using a Nikon Eclipse Ti-U inverted fluorescent microscope using a 20x objective and analysed using FIJI software. ≥ 5 fields of view per condition were analysed in three independent experiments. The number of pSTAT6 positive HFFs was normalised to the total number of HFFs, and results were statistically tested with a two-way ANOVA with Sidak's multiple comparison test in GraphPad Prism 8. The data are presented as mean \pm SD.

Acknowledgements

We would like to thank Peter Bradley, Matt Bogyo, Vern Carruthers, and John Boothroyd for sharing reagents as well as the teams from EupathDB and ToxoDB for their valuable contributions to the community. We also thank members of the Proteomics and Peptide Synthesis Science Technology platforms at The Francis Crick Institute. This work was supported by funding from The Francis Crick Institute (<https://www.crick.ac.uk/>), which receives its core funding from Cancer Research UK (FC001189; FC001999), the UK Medical Research Council (FC001189; FC001999) and the Wellcome Trust (FC001189; FC001999) as well as the National Institute of Health grant (NIH-R01AI123457). SM was supported by the Leverhulme Trust (RPG-2018-107), IT by the internal grant from the Prevention and Therapy of Chronic Diseases call at the IAB, and EWT by the Cancer Research UK Programme Foundation Award C29637/A20183.

Additional information

Competing interests

Edward W Tate: EWT is a founder, shareholder and Director of Myricx Pharma Ltd. The other authors declare that no competing interests exist.

Funding

| Funder | Grant reference number | Author |
|------------------------------------|--|--|
| Francis Crick Institute | FC001189 | Malgorzata Broncel Caia Dominicus Stephanie D Nofal Alex Hunt Bethan A Wallbank Joanna C Young Moritz Treeck |
| NIH Office of the Director | R01AI123457 | Malgorzata Broncel Caia Dominicus Moritz Treeck |
| Leverhulme Trust | RPG-2018-107 | Stephen Matthews |
| Cancer Research UK | C29637/A20183 | Edward J Bartlett Edward W Tate |
| Francis Crick Institute | FC001999 | Stefania Federico Joanna C Young Moritz Treeck |
| Institute for Advanced Biosciences | Prevention and Therapy of Chronic Diseases grant | Isabelle Tardieux |

The funders had no role in study design, data collection and interpretation, or the decision to submit the work for publication.

Author contributions

Malgorzata Broncel, Conceptualisation, Data curation, Validation, Investigation, Visualisation, Methodology, Writing - original draft, Writing - review and editing; Caia Dominicus, Investigation, Methodology, Writing - review and editing; Luis Vigetti, Stephanie D Nofal, Investigation, Visualisation,

Writing - review and editing; Edward J Bartlett, Alex Hunt, Investigation, Visualisation; Bastien Touquet, Bethan A Wallbank, Investigation; Stefania Federico, Resources; Stephen Matthews, Joanna C Young, Investigation, Writing - review and editing; Edward W Tate, Resources, Writing - review and editing; Isabelle Tardieux, Visualisation, Writing - review and editing; Moritz Treeck, Conceptualisation, Supervision, Funding acquisition, Methodology, Writing - original draft, Writing - review and editing

Author ORCIDs

Malgorzata Broncel  <https://orcid.org/0000-0003-2991-3500>

Luis Vigetti  <https://orcid.org/0000-0001-9733-2770>

Stephanie D Nofal  <https://orcid.org/0000-0003-1415-3369>

Alex Hunt  <http://orcid.org/0000-0001-7431-7156>

Bethan A Wallbank  <https://orcid.org/0000-0002-6432-2135>

Stephen Matthews  <http://orcid.org/0000-0003-0676-0927>

Isabelle Tardieux  <https://orcid.org/0000-0002-5677-7463>

Moritz Treeck  <https://orcid.org/0000-0002-9727-6657>

Decision letter and Author response

Decision letter <https://doi.org/10.7554/eLife.57861.sa1>

Author response <https://doi.org/10.7554/eLife.57861.sa2>

Additional files

Supplementary files

- Supplementary file 1. related to *Figure 2*. Identification of base-dependent YnMyr enrichment in *T. gondii*. Sheet 1: *Toxoplasma* proteins with YnMyr intensities quantified irrespective of base treatment. Sheet 2: Proteins with base-sensitive enrichment. Sheet 3: MG proteins insensitive to base treatment and robustly enriched in a YnMyr-dependent manner with N₃-biotin reagent (1). Sheet 4: Analysis of proteomes (supernatants post enrichment).
- Supplementary file 2. related to *Figure 2*. Identification of myristoylated proteins and myristoylated peptides in *T. gondii*. Sheet 1: *Toxoplasma* proteins bearing the MG motif. Sheet 2: Substrates significantly enriched with Trypsin reagent (2). Sheet 3: Substrates selected based on fold change in YnMyr/Myr enrichment with TEV reagent (3). Sheet 4: Myristoylated peptides found with Trypsin reagent (2). Sheet 5: Myristoylated peptides found with TEV reagent (3). Sheet 6: Human proteins bearing the MG motif. Sheet 7: Human substrates significantly enriched with Trypsin and TEV reagents.
- Supplementary file 3. related to *Figure 3*. Chemical inhibition of TgNMT. Sheet 1: Response of YnMyr enriched *Toxoplasma* proteins to NMTi. Sheet 2: NMTi does not significantly affect *Toxoplasma* proteome. Sheet 3: Response of base-sensitive *Toxoplasma* proteins to NMTi. Sheet 4: Response of YnMyr enriched Human proteins to NMTi. Sheet 5: NMTi does not significantly affect Human proteome.
- Supplementary file 4. related to *Figure 4*. Myristoylated proteome of *T. gondii*. Sheet 1: Substrate list and annotation. Sheet 2: Myristoylated proteins in *P. falciparum* and their orthologues in *Toxoplasma*. Sheets 3-9: Substrate orthologues in selected Apicomplexans.
- Supplementary file 5. related to *Figure 5*. MIC7 expression in tachyzoites and bradyzoites.
- Supplementary file 6. Primers used for plasmid and parasite lines generation.
- Transparent reporting form

Data availability

All data generated or analysed during this study are included in the manuscript and supporting files. Source data files have been provided for Figures 5, 6 and 7. Source data for mass spectrometry proteomics results can be found in Supplementary files 1-4. The mass spectrometry proteomics data

have been deposited to the ProteomeXchange Consortium via the PRIDE (Perez-Riverol et al., 2019) partner repository with the dataset identifier PXD019677.

The following dataset was generated:

| Author(s) | Year | Dataset title | Dataset URL | Database and Identifier |
|---|------|--|---|----------------------------|
| Broncel M, Dominicus C, Vigetti L, Nofal SD, Bartlett EJ, Touquet B, Hunt A, Wallbank BA, Federico S, Matthews S, Young JC, Tate EW, Tardieux I, Treeck M | 2020 | Global profiling of myristoylation in <i>Toxoplasma gondii</i> . | http://proteomecentral.proteomexchange.org/cgi/GetDataset?ID=PX019677 | ProteomeXchange, PXD019677 |

The following previously published datasets were used:

| Author(s) | Year | Dataset title | Dataset URL | Database and Identifier |
|---|------|--|---|----------------------------|
| Koreny L, Ke H, Butterworth S, Crook OM, Lassadi I, Gupta V, Tromer E, Mourier T, Stevens TJ, Breckels LM, Pain A, Lilley KS, Waller RF | 2020 | Hyper LOPIT Global mapping of protein subcellular location. | https://toxodb.org/toxo/app/record/dataset/DS_eda79f81b5 | ToxoDB, DS_eda79f81b5 |
| Young J, Broncel M, Teague H, Russell M, McGovern O, Renshaw M, Frith D, Snijders B, Collinson L, Carruthers V, Ewald S, Treeck M | 2020 | Differential protein phosphorylation during stage conversion in <i>Toxoplasma gondii</i> | http://proteomecentral.proteomexchange.org/cgi/GetDataset?ID=PX019729 | ProteomeXchange, PXD019729 |

References

- Alonso AM, Coceres VM, De Napoli MG, Nieto Guil AF, Angel SO, Corvi MM. 2012. Protein palmitoylation inhibition by 2-bromopalmitate alters gliding, host cell invasion and parasite morphology in *Toxoplasma gondii*. *Molecular and Biochemical Parasitology* 184:39-43. DOI: <https://doi.org/10.1016/j.molbiopara.2012.03.006>, PMID: 22484029
- Alonso AM, Turowski VR, Ruiz DM, Orelo BD, Moresco JJ, Yates JR, Corvi MM. 2019. Exploring protein myristoylation in *Toxoplasma gondii*. *Experimental Parasitology* 203:8-18. DOI: <https://doi.org/10.1016/j.exppara.2019.05.007>, PMID: 31150653
- Andenmatten N, Egarter S, Jackson AJ, Jullien N, Herman J-P, Meissner M. 2013. Conditional genome engineering in *Toxoplasma gondii* uncovers alternative invasion mechanisms. *Nature Methods* 10:125-127. DOI: <https://doi.org/10.1038/nmeth.2301>
- Aurrecochea C, Barreto A, Basenko EY, Brestelli J, Brunk BP, Cade S, Crouch K, Doherty R, Falke D, Fischer S, Gajria B, Harb OS, Heiges M, Hertz-Fowler C, Hu S, Iodice J, Kissinger JC, Lawrence C, Li W, Pinney DF, et al. 2017. EuPathDB: the eukaryotic pathogen genomics database resource. *Nucleic Acids Research* 45:D581-D591. DOI: <https://doi.org/10.1093/nar/gkw1105>, PMID: 27903906
- Baptista CG, Lis A, Deng B, Gas-Pascual E, Dittmar A, Sigurdson W, West CM, Blader IJ. 2019. *Toxoplasma* F-box protein 1 is required for daughter cell scaffold function during parasite replication. *PLoS Pathogens* 15:e1007946. DOI: <https://doi.org/10.1371/journal.ppat.1007946>, PMID: 31348812
- Barylyuk K, Koreny L, Ke H, Butterworth S, Crook OM, Lassadi I, Gupta V, Tromer E, Mourier T, Stevens TJ, Breckels LM, Pain A, Lilley KS, Waller RF. 2020. A subcellular atlas of *Toxoplasma* reveals the functional context of the proteome. *bioRxiv*. DOI: <https://doi.org/10.1101/2020.04.23.057125>
- Beck JR, Rodriguez-Fernandez IA, de Leon JC, Huynh MH, Carruthers VB, Morrissette NS, Bradley PJ. 2010. A novel family of *Toxoplasma* IMC proteins displays a hierarchical organization and functions in coordinating parasite division. *PLoS Pathogens* 6:e1001094. DOI: <https://doi.org/10.1371/journal.ppat.1001094>, PMID: 20844581
- Bichet M, Touquet B, Gonzalez V, Florent I, Meissner M, Tardieux I. 2016. Genetic impairment of parasite myosin motors uncovers the contribution of host cell membrane dynamics to *Toxoplasma* invasion forces. *BMC Biology* 14:97. DOI: <https://doi.org/10.1186/s12915-016-0316-8>, PMID: 27829452

- Black MW, Boothroyd JC. 2000. Lytic cycle of *Toxoplasma gondii*. *Microbiology and Molecular Biology Reviews* 64:607-623. DOI: <https://doi.org/10.1128/MMBR.64.3.607-623.2000>, PMID: 10974128
- Boothroyd JC, Dubremetz JF. 2008. Kiss and spit: the dual roles of *Toxoplasma* rhoptries. *Nature Reviews Microbiology* 6:79-88. DOI: <https://doi.org/10.1038/nrmicro1800>, PMID: 18059289
- Boutin JA. 1997. Myristoylation. *Cellular Signalling* 9:15-35. DOI: [https://doi.org/10.1016/S0898-6568\(96\)00100-3](https://doi.org/10.1016/S0898-6568(96)00100-3), PMID: 9067626
- Broncel M, Serwa RA, Ciepla P, Krause E, Dallman MJ, Magee AI, Tate EW. 2015. Multifunctional reagents for quantitative Proteome-Wide analysis of protein modification in human cells and dynamic profiling of protein lipidation during vertebrate development. *Angewandte Chemie International Edition* 54:5948-5951. DOI: <https://doi.org/10.1002/anie.201500342>
- Brown KM, Long S, Sibley LD. 2017. Plasma membrane association by N-Acylation governs PKG function in *Toxoplasma gondii*. *mBio* 8:e00375-17. DOI: <https://doi.org/10.1128/mBio.00375-17>, PMID: 28465425
- Bullen HE, Jia Y, Yamaro-Boite´ Y, Bisio H, Zhang O, Jemelin NK, Marq JB, Carruthers V, Boite´ CY, Soldati-Favre D. 2016. Phosphatidic Acid-Mediated signaling regulates microneme secretion in *Toxoplasma*. *Cell Host & Microbe* 19:349-360. DOI: <https://doi.org/10.1016/j.chom.2016.02.006>, PMID: 26962945
- Caballero MC, Alonso AM, Deng B, Attias M, de Souza W, Corvi MM. 2016. Identification of new palmitoylated proteins in *Toxoplasma gondii*. *Biochimica Et Biophysica Acta (BBA) - Proteins and Proteomics* 1864:400-408. DOI: <https://doi.org/10.1016/j.bbapap.2016.01.010>
- Cabrera A, Herrmann S, Warszta D, Santos JM, John Peter AT, Kono M, Debrouver S, Jacobs T, Spielmann T, Ungermann C, Soldati-Favre D, Gilberger TW. 2012. Dissection of minimal sequence requirements for rhoptry membrane targeting in the malaria parasite. *Traffic* 13:1335-1350. DOI: <https://doi.org/10.1111/j.1600-0854.2012.01394.x>, PMID: 22759070
- Caffaro CE, Koshy AA, Liu L, Zeiner GM, Hirschberg CB, Boothroyd JC. 2013. A nucleotide sugar transporter involved in glycosylation of the *Toxoplasma* tissue cyst wall is required for efficient persistence of bradyzoites. *PLOS Pathogens* 9:e1003331. DOI: <https://doi.org/10.1371/journal.ppat.1003331>, PMID: 23658519
- Carruthers VB. 2006. Proteolysis and toxoplasma invasion. *International Journal for Parasitology* 36:595-600. DOI: <https://doi.org/10.1016/j.ijpara.2006.02.008>, PMID: 16600244
- Castrec B, Dian C, Ciccone S, Ebert CL, Bienvenut WV, Le Caer JP, Steyaert JM, Giglione C, Meinzel T. 2018. Structural and genomic decoding of human and plant myristoylomes reveals a definitive recognition pattern. *Nature Chemical Biology* 14:671-679. DOI: <https://doi.org/10.1038/s41589-018-0077-5>, PMID: 29892081
- Cérède O, Dubremetz JF, Bout D, Lebrun M. 2002. The *Toxoplasma gondii* protein MIC3 requires pro-peptide cleavage and dimerization to function as adhesin. *The EMBO Journal* 21:2526-2536. DOI: <https://doi.org/10.1093/emboj/21.11.2526>, PMID: 12032066
- Chow M, Newman JFE, Filman D, Hogle JM, Rowlands DJ, Brown F. 1987. Myristylation of Picornavirus capsid protein VP4 and its structural significance. *Nature* 327:482-486. DOI: <https://doi.org/10.1038/327482a0>
- Cox J, Neuhauser N, Michalski A, Scheltema RA, Olsen JV, Mann M. 2011. Andromeda: a peptide search engine integrated into the MaxQuant environment. *Journal of Proteome Research* 10:1794-1805. DOI: <https://doi.org/10.1021/pr101065j>, PMID: 21254760
- Cox J, Mann M. 2008. MaxQuant enables high peptide identification rates, individualized p.p.b.-range mass accuracies and proteome-wide protein quantification. *Nature Biotechnology* 26:1367-1372. DOI: <https://doi.org/10.1038/nbt.1511>, PMID: 19029910
- Devadas B, Zupec ME, Freeman SK, Brown DL, Nagarajan S, Sikorski JA, McWherter CA, Getman DP, Gordon JL. 1995. Design and syntheses of potent and selective dipeptide inhibitors of candida albicans myristoyl-CoA: protein N-myristoyltransferase. *Journal of Medicinal Chemistry* 38:1837-1840. DOI: <https://doi.org/10.1021/jm00011a001>, PMID: 7783114
- Dowse TJ, Soldati D. 2005. Rhomboid-like proteins in apicomplexa: phylogeny and nomenclature. *Trends in Parasitology* 21:254-258. DOI: <https://doi.org/10.1016/j.pt.2005.04.009>, PMID: 15922242
- Foe IT, Child MA, Majmudar JD, Krishnamurthy S, van der Linden WA, Ward GE, Martin BR, Bogyo M. 2015. Global analysis of palmitoylated proteins in *Toxoplasma gondii*. *Cell Host & Microbe* 18:501-511. DOI: <https://doi.org/10.1016/j.chom.2015.09.006>, PMID: 26468752
- Frearson JA, Brand S, McElroy SP, Cleghorn LA, Smid O, Stojanovski L, Price HP, Guther ML, Torrie LS, Robinson DA, Hallyburton I, Mpamhanga CP, Brannigan JA, Wilkinson AJ, Hodgkinson M, Hui R, Qiu W, Raimi OG, van Aalten DM, Brenk R, et al. 2010. N-myristoyltransferase inhibitors as new leads to treat sleeping sickness. *Nature* 464:728-732. DOI: <https://doi.org/10.1038/nature08893>, PMID: 20360736
- Frénal K, Polonais V, Marq JB, Stratmann R, Limenitakis J, Soldati-Favre D. 2010. Functional dissection of the apicomplexan glideosome molecular architecture. *Cell Host & Microbe* 8:343-357. DOI: <https://doi.org/10.1016/j.chom.2010.09.002>, PMID: 20951968
- Frénal K, Kemp LE, Soldati-Favre D. 2014. Emerging roles for protein S-palmitoylation in *Toxoplasma* biology. *International Journal for Parasitology* 44:121-131. DOI: <https://doi.org/10.1016/j.ijpara.2013.09.004>, PMID: 24184909
- Gaji RY, Johnson DE, Treeck M, Wang M, Hudmon A, Arrizabalaga G. 2015. Phosphorylation of a myosin motor by TgCDPK3 facilitates rapid initiation of motility during *Toxoplasma gondii* egress. *PLOS Pathogens* 11:e1005268. DOI: <https://doi.org/10.1371/journal.ppat.1005268>, PMID: 26544049
- Gajria B, Bahl A, Brestelli J, Dommer J, Fischer S, Gao X, Heiges M, Iodice J, Kissingner JC, Mackey AJ, Pinney DF, Roos DS, Stoeckert CJ, Wang H, Brunk BP. 2008. ToxoDB: an integrated *Toxoplasma gondii* database resource. *Nucleic Acids Research* 36:D553-D556. DOI: <https://doi.org/10.1093/nar/gkm981>, PMID: 18003657

- Garrison E, Treeck M, Ehret E, Butz H, Garbuz T, Oswald BP, Settles M, Boothroyd J, Arrizabalaga G. 2012. A forward genetic screen reveals that calcium-dependent protein kinase 3 regulates egress in *Toxoplasma*. *PLOS Pathogens* 8:e1003049. DOI: <https://doi.org/10.1371/journal.ppat.1003049>, PMID: 23209419
- Goder V, Spiess M. 2001. Topogenesis of membrane proteins: determinants and dynamics. *FEBS Letters* 504: 87-93. DOI: [https://doi.org/10.1016/S0014-5793\(01\)02712-0](https://doi.org/10.1016/S0014-5793(01)02712-0), PMID: 11532438
- Goldberg J. 1998. Structural basis for activation of ARF GTPase: mechanisms of guanine nucleotide exchange and GTP-myristoyl switching. *Cell* 95:237-248. DOI: [https://doi.org/10.1016/s0092-8674\(00\)81754-7](https://doi.org/10.1016/s0092-8674(00)81754-7), PMID: 9790530
- Gordon JI, Duronio RJ, Rudnick DA, Adams SP, Gokel GW. 1991. Protein N-myristoylation. *The Journal of Biological Chemistry* 266:8647-8650. PMID: 2026581
- Heal WP, Wright MH, Thion E, Tate EW. 2012. Multifunctional protein labeling via enzymatic N-terminal tagging and elaboration by click chemistry. *Nature Protocols* 7:105-117. DOI: <https://doi.org/10.1038/nprot.2011.425>
- Howard BL, Harvey KL, Stewart RJ, Azevedo MF, Crabb BS, Jennings IG, Sanders PR, Manallack DT, Thompson PE, Tonkin CJ, Gilson PR. 2015. Identification of potent phosphodiesterase inhibitors that demonstrate cyclic nucleotide-dependent functions in apicomplexan parasites. *ACS Chemical Biology* 10:1145-1154. DOI: <https://doi.org/10.1021/cb501004q>, PMID: 25555060
- Hunt A, Russell MRG, Wagener J, Kent R, Carmelle R, Peddie CJ, Collinson L, Heaslip A, Ward GE, Treeck M. 2019. Differential requirements for cyclase-associated protein (CAP) in actin-dependent processes of *Toxoplasma gondii*. *eLife* 8:e50598. DOI: <https://doi.org/10.7554/eLife.50598>, PMID: 31577230
- Hutton JA, Goncalves V, Brannigan JA, Paape D, Wright MH, Waugh TM, Roberts SM, Bell AS, Wilkinson AJ, Smith DF, Leatherbarrow RJ, Tate EW. 2014. Structure-based design of potent and selective leishmania N-myristoyltransferase inhibitors. *Journal of Medicinal Chemistry* 57:8664-8670. DOI: <https://doi.org/10.1021/jm5011397>, PMID: 25238611
- Huynh MH, Rabenau KE, Harper JM, Beatty WL, Sibley LD, Carruthers VB. 2003. Rapid invasion of host cells by *Toxoplasma* requires secretion of the MIC2-M2AP adhesive protein complex. *The EMBO Journal* 22:2082-2090. DOI: <https://doi.org/10.1093/emboj/cdg217>, PMID: 12727875
- Huynh MH, Carruthers VB. 2009. Tagging of endogenous genes in a *Toxoplasma gondii* strain lacking Ku80. *Eukaryotic Cell* 8:530-539. DOI: <https://doi.org/10.1128/EC.00358-08>, PMID: 19218426
- Jacot D, Soldati-Favre D. 2012. Does protein phosphorylation govern host cell entry and egress by the apicomplexa? *International Journal of Medical Microbiology* 302:195-202. DOI: <https://doi.org/10.1016/j.ijmm.2012.07.012>
- Jia Y, Benjamin S, Liu Q, Xu Y, Dogga SK, Liu J, Matthews S, Soldati-Favre D. 2017a. *Toxoplasma gondii* immune mapped protein 1 is anchored to the inner leaflet of the plasma membrane and adopts a novel protein fold. *Biochimica Et Biophysica Acta (BBA) - Proteins and Proteomics* 1865:208-219. DOI: <https://doi.org/10.1016/j.bbapap.2016.11.010>
- Jia Y, Marq JB, Bisio H, Jacot D, Mueller C, Yu L, Choudhary J, Brochet M, Soldati-Favre D. 2017b. Crosstalk between PKA and PKG controls pH-dependent host cell egress of *Toxoplasma gondii*. *The EMBO Journal* 36: 3250-3267. DOI: <https://doi.org/10.15252/embj.201796794>, PMID: 29030485
- Kessler H, Herm-Götz A, Hegge S, Rauch M, Soldati-Favre D, Frischknecht F, Meissner M. 2008. Microneme protein 8-a new essential invasion factor in *Toxoplasma gondii*. *Journal of Cell Science* 121:947-956. DOI: <https://doi.org/10.1242/jcs.022350>, PMID: 18319299
- Kremer K, Kamin D, Rittweger E, Wilkes J, Flammer H, Mahler S, Heng J, Tonkin CJ, Langsley G, Hell SW, Carruthers VB, Ferguson DJP, Meissner M. 2013. An overexpression screen of *Toxoplasma gondii* Rab-GTPases reveals distinct transport routes to the micronemes. *PLOS Pathogens* 9:e1003213. DOI: <https://doi.org/10.1371/journal.ppat.1003213>
- Liendo A, Stedman TT, Ngo HM, Chaturvedi S, Hoppe HC, Joiner KA. 2001. *Toxoplasma gondii* ADP-ribosylation factor 1 mediates enhanced release of constitutively secreted dense granule proteins. *Journal of Biological Chemistry* 276:18272-18281. DOI: <https://doi.org/10.1074/jbc.M008352200>, PMID: 11278405
- Lourido S, Shuman J, Zhang C, Shokat KM, Hui R, Sibley LD. 2010. Calcium-dependent protein kinase 1 is an essential regulator of exocytosis in *Toxoplasma*. *Nature* 465:359-362. DOI: <https://doi.org/10.1038/nature09022>, PMID: 20485436
- Martin DD, Beauchamp E, Berthiaume LG. 2011. Post-translational myristoylation: fat matters in cellular life and death. *Biochimie* 93:18-31. DOI: <https://doi.org/10.1016/j.biochi.2010.10.018>, PMID: 21056615
- Maurer-Stroh S, Eisenhaber F. 2004. Myristoylation of viral and bacterial proteins. *Trends in Microbiology* 12: 178-185. DOI: <https://doi.org/10.1016/j.tim.2004.02.006>, PMID: 15051068
- McCoy JM, Whitehead L, van Dooren GG, Tonkin CJ. 2012. TgCDPK3 regulates calcium-dependent egress of *Toxoplasma gondii* from host cells. *PLOS Pathogens* 8:e1003066. DOI: <https://doi.org/10.1371/journal.ppat.1003066>, PMID: 23226109
- Meissner M, Reiss M, Viebig N, Carruthers VB, Tourse C, Tomavo S, Ajioka JW, Soldati D. 2002. A family of transmembrane microneme proteins of *Toxoplasma gondii* contain EGF-like domains and function as escorters. *Journal of Cell Science* 115:563-574. PMID: 11861763
- Montoya JG, Liesenfeld O. 2004. Toxoplasmosis. *The Lancet* 363:1965-1976. DOI: [https://doi.org/10.1016/S0140-6736\(04\)16412-X](https://doi.org/10.1016/S0140-6736(04)16412-X)
- Mousnier A, Bell AS, Swieboda DP, Morales-Sanfrutos J, Pe' rez-Dorado I, Brannigan JA, Newman J, Ritzefeld M, Hutton JA, Gueda'n A, Asfor AS, Robinson SW, Hopkins-Navratilova I, Wilkinson AJ, Johnston SL, Leatherbarrow RJ, Tuthill TJ, Solari R, Tate EW. 2018. Fragment-derived inhibitors of human

- N-myristoyltransferase block capsid assembly and replication of the common cold virus. *Nature Chemistry* 10: 599-606. DOI: <https://doi.org/10.1038/s41557-018-0039-2>, PMID: 29760414
- Mueller C, Klages N, Jacot D, Santos JM, Cabrera A, Gilberger TW, Dubremetz JF, Soldati-Favre D. 2013. The Toxoplasma protein ARO mediates the apical positioning of Rhoptry Organelles, a prerequisite for host cell invasion. *Cell Host & Microbe* 13:289-301. DOI: <https://doi.org/10.1016/j.chom.2013.02.001>, PMID: 23498954
- Nagarajan SR, Devadas B, Zupec ME, Freeman SK, Brown DL, Lu HF, Mehta PP, Kishore NS, McWherter CA, Getman DP, Gordon JI, Sikorski JA. 1997. Conformationally constrained [p-(omega-aminoalkyl)phenacetyl]-L-seryl-L-lysyl dipeptide amides as potent peptidomimetic inhibitors of *Candida Albicans* and human myristoyl-CoA:protein N-myristoyl transferase. *Journal of Medicinal Chemistry* 40:1422-1438. DOI: <https://doi.org/10.1021/jm9608671>, PMID: 9154965
- Ojo KK, Larson ET, Keyloun KR, Castaneda LJ, Derocher AE, Inampudi KK, Kim JE, Arakaki TL, Murphy RC, Zhang L, Napuli AJ, Maly DJ, Verlinde CL, Buckner FS, Parsons M, Hol WG, Merritt EA, Van Voorhis WC. 2010. Toxoplasma gondii calcium-dependent protein kinase 1 is a target for selective kinase inhibitors. *Nature Structural & Molecular Biology* 17:602-607. DOI: <https://doi.org/10.1038/nsmb.1818>, PMID: 20436472
- Ong YC, Reese ML, Boothroyd JC. 2010. Toxoplasma rhoptry protein 16 (ROP16) subverts host function by direct tyrosine phosphorylation of STAT6. *Journal of Biological Chemistry* 285:28731-28740. DOI: <https://doi.org/10.1074/jbc.M110.112359>, PMID: 20624917
- Pavlou G, Biesaga M, Touquet B, Lagal V, Balland M, Dufour A, Hakimi MA, Tardieux I. 2018. Toxoplasma parasite twisting motion mechanically induces host cell membrane fission to complete invasion within a protective vacuole. *Cell Host & Microbe* 24:81-96. DOI: <https://doi.org/10.1016/j.chom.2018.06.003>, PMID: 30008293
- Perez-Riverol Y, Csordas A, Bai J, Bernal-Llinares M, Hewapathirana S, Kundu DJ, Inuganti A, Griss J, Mayer G, Eisenacher M, Pe' rez E, Uszkoreit J, Pfeuffer J, Sachsenberg T, Yilmaz S, Tiwary S, Cox J, Audain E, Walzer M, Jarnuczak AF, et al. 2019. The PRIDE database and related tools and resources in 2019: improving support for quantification data. *Nucleic Acids Research* 47:D442-D450. DOI: <https://doi.org/10.1093/nar/gky1106>, PMID: 30395289
- Pomel S, Luk FC, Beckers CJ. 2008. Host cell egress and invasion induce marked relocations of glycolytic enzymes in Toxoplasma gondii tachyzoites. *PLOS Pathogens* 4:e1000188. DOI: <https://doi.org/10.1371/journal.ppat.1000188>, PMID: 18949028
- Reese ML, Zeiner GM, Saeij JP, Boothroyd JC, Boyle JP. 2011. Polymorphic family of injected pseudokinases is paramount in Toxoplasma virulence. *PNAS* 108:9625-9630. DOI: <https://doi.org/10.1073/pnas.1015980108>, PMID: 21436047
- Ren J, Wen L, Gao X, Jin C, Xue Y, Yao X. 2008. CSS-Palm 2.0: an updated software for palmitoylation sites prediction. *Protein Engineering Design and Selection* 21:639-644. DOI: <https://doi.org/10.1093/protein/gzn039>
- Ritzefeld M, Wright MH, Tate EW. 2018. New developments in probing and targeting protein acylation in malaria, leishmaniasis and african sleeping sickness. *Parasitology* 145:157-174. DOI: <https://doi.org/10.1017/S0031182017000282>, PMID: 28270257
- Robert-Gangneux F, Dardé ML. 2012. Epidemiology of and diagnostic strategies for toxoplasmosis. *Clinical Microbiology Reviews* 25:264-296. DOI: <https://doi.org/10.1128/CMR.05013-11>, PMID: 22491772
- Saeij JP, Collier S, Boyle JP, Jerome ME, White MW, Boothroyd JC. 2007. Toxoplasma co-opts host gene expression by injection of a polymorphic kinase homologue. *Nature* 445:324-327. DOI: <https://doi.org/10.1038/nature05395>, PMID: 17183270
- Schindelin J, Arganda-Carreras I, Frise E, Kaynig V, Longair M, Pietzsch T, Preibisch S, Rueden C, Saalfeld S, Schmid B, Tinevez J-Y, White DJ, Hartenstein V, Eliceiri K, Tomancak P, Cardona A. 2012. Fiji: an open-source platform for biological-image analysis. *Nature Methods* 9:676-682. DOI: <https://doi.org/10.1038/nmeth.2019>
- Schlott AC, Mayclin S, Reers AR, Coburn-Flynn O, Bell AS, Green J, Knuepfer E, Charter D, Bonnert R, Campo B, Burrows J, Lyons-Abbott S, Staker BL, Chung CW, Myler PJ, Fidock DA, Tate EW, Holder AA. 2019. Structure-Guided identification of resistance breaking antimalarial nmyristoyltransferase inhibitors. *Cell Chemical Biology* 26:991-1000. DOI: <https://doi.org/10.1016/j.chembiol.2019.03.015>, PMID: 31080074
- Shen B, Brown KM, Lee TD, Sibley LD. 2014. Efficient gene disruption in diverse strains of Toxoplasma gondii using CRISPR/CAS9. *mBio* 5:e01114. DOI: <https://doi.org/10.1128/mBio.01114-14>, PMID: 24825012
- Silmon de Monerri NC, Yakubu RR, Chen AL, Bradley PJ, Nieves E, Weiss LM, Kim K. 2015. The ubiquitin proteome of Toxoplasma gondii reveals roles for protein ubiquitination in Cell-Cycle transitions. *Cell Host & Microbe* 18:621-633. DOI: <https://doi.org/10.1016/j.chom.2015.10.014>, PMID: 26567513
- Soldati D, Dubremetz JF, Lebrun M. 2001. Microneme proteins: structural and functional requirements to promote adhesion and invasion by the apicomplexan parasite Toxoplasma gondii. *International Journal for Parasitology* 31:1293-1302. DOI: [https://doi.org/10.1016/S0020-7519\(01\)00257-0](https://doi.org/10.1016/S0020-7519(01)00257-0), PMID: 11566297
- Soldati D, Boothroyd JC. 1993. Transient transfection and expression in the obligate intracellular parasite Toxoplasma gondii. *Science* 260:349-352. DOI: <https://doi.org/10.1126/science.8469986>, PMID: 8469986
- Speers AE, Cravatt BF. 2005. A tandem orthogonal proteolysis strategy for high-content chemical proteomics. *Journal of the American Chemical Society* 127:10018-10019. DOI: <https://doi.org/10.1021/ja0532842>, PMID: 16011363
- Thinon E, Serwa RA, Broncel M, Brannigan JA, Brassat U, Wright MH, Heal WP, Wilkinson AJ, Mann DJ, Tate EW. 2014. Global profiling of co- and post-translationally N-myristoylated proteomes in human cells. *Nature Communications* 5:4919. DOI: <https://doi.org/10.1038/ncomms5919>, PMID: 25255805

- Touquet B, Pelissier L, Cavailles P, Yi W, Bellini V, Mercier C, Cesbron-Delauw MF, Boumendjel A, Aldebert D. 2018. High-content imaging assay to evaluate *Toxoplasma gondii* infection and proliferation: a multiparametric assay to screen new compounds. *PLOS ONE* 13:e0201678. DOI: <https://doi.org/10.1371/journal.pone.0201678>, PMID: 30157171
- Treeck M, Sanders JL, Gaji RY, LaFavers KA, Child MA, Arrizabalaga G, Elias JE, Boothroyd JC. 2014. The calcium-dependent protein kinase 3 of *Toxoplasma* influences basal calcium levels and functions beyond egress as revealed by quantitative phosphoproteome analysis. *PLOS Pathogens* 10:e1004197. DOI: <https://doi.org/10.1371/journal.ppat.1004197>, PMID: 24945436
- Tu V, Mayoral J, Sugi T, Tomita T, Han B, Ma YF, Weiss LM. 2019. Enrichment and proteomic characterization of the cyst wall from *In Vitro* *Toxoplasma gondii* Cysts. *mBio* 10:e00469-19. DOI: <https://doi.org/10.1128/mBio.00469-19>, PMID: 31040239
- Tyanova S, Temu T, Sinitcyn P, Carlson A, Hein MY, Geiger T, Mann M, Cox J. 2016. The perseus computational platform for comprehensive analysis of (prote)omics data. *Nature Methods* 13:731-740. DOI: <https://doi.org/10.1038/nmeth.3901>, PMID: 27348712
- Tyler JS, Treeck M, Boothroyd JC. 2011. Focus on the ringleader: the role of AMA1 in apicomplexan invasion and replication. *Trends in Parasitology* 27:410-420. DOI: <https://doi.org/10.1016/j.pt.2011.04.002>, PMID: 21659001
- Uboldi AD, Wilde ML, McRae EA, Stewart RJ, Dagley LF, Yang L, Katris NJ, Hapuarachchi SV, Coffey MJ, Lehane AM, Botte CY, Waller RF, Webb AI, McConville MJ, Tonkin CJ. 2018. Protein kinase A negatively regulates Ca²⁺ + signalling in *Toxoplasma gondii*. *PLOS Biology* 16:e2005642. DOI: <https://doi.org/10.1371/journal.pbio.2005642>, PMID: 30208022
- Wallbank BA, Dominicus CS, Broncel M, Legrave N, Kelly G, MacRae JI, Staines HM, Treeck M. 2019. Characterisation of the *Toxoplasma gondii* tyrosine transporter and its phosphorylation by the calcium-dependent protein kinase 3. *Molecular Microbiology* 111:1167-1181. DOI: <https://doi.org/10.1111/mmi.14156>, PMID: 30402958
- Waterhouse A, Bertoni M, Bienert S, Studer G, Tauriello G, Gumienny R, Heer FT, de Beer TAP, Rempfer C, Bordoli L, Lepore R, Schwede T. 2018. SWISS-MODEL: homology modelling of protein structures and complexes. *Nucleic Acids Research* 46:W296-W303. DOI: <https://doi.org/10.1093/nar/gky427>, PMID: 29788355
- Wright MH, Heal WP, Mann DJ, Tate EW. 2010. Protein myristoylation in health and disease. *Journal of Chemical Biology* 3:19-35. DOI: <https://doi.org/10.1007/s12154-009-0032-8>, PMID: 19898886
- Wright MH, Clough B, Rackham MD, Rangachari K, Brannigan JA, Grainger M, Moss DK, Bottrill AR, Heal WP, Broncel M, Serwa RA, Brady D, Mann DJ, Leatherbarrow RJ, Tewari R, Wilkinson AJ, Holder AA, Tate EW. 2014. Validation of N-myristoyltransferase as an antimalarial drug target using an integrated chemical biology approach. *Nature Chemistry* 6:112-121. DOI: <https://doi.org/10.1038/nchem.1830>, PMID: 24451586
- Wright MH, Paape D, Storck EM, Serwa RA, Smith DF, Tate EW. 2015. Global analysis of protein N-myristoylation and exploration of N-myristoyltransferase as a drug target in the neglected human pathogen *leishmania donovani*. *Chemistry & Biology* 22:342-354. DOI: <https://doi.org/10.1016/j.chembiol.2015.01.003>, PMID: 25728269
- Wright MH, Paape D, Price HP, Smith DF, Tate EW. 2016. Global profiling and inhibition of protein lipidation in vector and host stages of the sleeping sickness parasite *Trypanosoma brucei*. *ACS Infectious Diseases* 2:427-441. DOI: <https://doi.org/10.1021/acsinfecdis.6b00034>, PMID: 27331140
- Yang C, Broncel M, Dominicus C, Sampson E, Blakely WJ, Treeck M, Arrizabalaga G. 2019. A plasma membrane localized protein phosphatase in *Toxoplasma gondii*, PPM5C, regulates attachment to host cells. *Scientific Reports* 9:5924. DOI: <https://doi.org/10.1038/s41598-019-42441-1>, PMID: 30976120
- Young J, Broncel M, Teague H, Russell M, McGovern O, Renshaw M, Frith D, Snijders B, Collinson L, Carruthers V, Ewald S, Treeck M. 2020. Differential protein phosphorylation affects the localisation of two secreted *Toxoplasma* proteins and is widespread during stage conversion. *bioRxiv*. DOI: <https://doi.org/10.1101/2020.04.09.035279>
- Zheng J, Knighton DR, Xiong NH, Taylor SS, Sowadski JM, Ten Eyck LF. 1993. Crystal structures of the myristylated catalytic subunit of cAMP-dependent protein kinase reveal open and closed conformations. *Protein Science* 2:1559-1573. DOI: <https://doi.org/10.1002/pro.5560021003>, PMID: 8251932
- Zhu XG, Nicholson Puthenveedu S, Shen Y, La K, Ozlu C, Wang T, Klompstra D, Gultekin Y, Chi J, Fidelin J, Peng T, Molina H, Hang HC, Min W, Birsoy K. 2019. CHP1 regulates compartmentalized glycerolipid synthesis by activating GPAT4. *Molecular Cell* 74:45-58. DOI: <https://doi.org/10.1016/j.molcel.2019.01.037>

6.2 Pavlou et al., *ACS Nano*, 2020

6.2.1 Context and questions

The technical innovations and experiments of this collaboration were performed in the frame of the project of the Ph.D. project of the member of the laboratory Georgios Pavlou. As referred in Section 2.1.1, while it is currently known under 2D conditions that circular and helical gliding facilitate access to the target cells, it is yet not fully understood how the coordination of force generation and tachyzoite-substrate adhesion coordinate during helical gliding. As a consequence, the project's main objective was to unravel the tachyzoite's force generation required for locomotion and pinpoint each pole's adhesive contribution. To accomplish these objectives, the lab used biophysical techniques such as Reflection Interference Contrast Microscopy (RICM) and Traction Force Microscopy (TFM) both combined with quantitative image analysis to map at a submicron and millisecond spatiotemporal resolution the sequence of parasite adhesion to the surface during helical progression. TFM was applied in order to retrieve the adhesion site associated with specific traction force transmission. We then developed a set of micropattern and functionalized bead-based assays to directly probe the essentiality of the adhesion events mapped, including their turn-over (adhesion-deadhesion cycles), along the helical gliding sequence. We found that the tachyzoite must build an apical adhesion with the substrate from which it initiates a traction force that pulls the body forward only if the rear pole timely disengages from the substrate. Both apical adhesion and basal retraction are strictly required and are tightly coupled during gliding. Cell pulling results in the lift of the apical pole which drives the progression of the body up following transient interaction with the substrate at the exact site where the tachyzoite first engages apically. Furthermore, to control whether this pulling strategy could occur in a complex 3D environment, we proposed to use a combination of experimental settings mimicking the physiological microenvironments the free parasite faces *in vivo* when it navigates within tissue and targets a host cell, using fibrillary matrices.

6.2.2 Contributions to the publication: technical set up and application

To differentiate from the previous approaches using commercially available Matrigel gels (Leung et al., 2014), we chose to use collagen-1, a prominent member of the collagen family and major component of the ECM in the dermis of the skin, bone, tendon and other areas. The collagen-1 fibrils aggregate to form thick bundles of 2–10 μm in diameter and provide the

connective tissue high tensile strength (500–1000 kg/cm²). We prepared rat tail collagen 1 to specifically visualize collagen fibers during gliding assays, we took advantage of a tool-box made of fusion proteins that carry at the C-terminal end of a given fluorescent protein sequence (*i.e.* eGFP, mCherry), the *Staphylococcus*-derived sequence of the collagen binding CNA35 protein (Aper et al., 2014). CNA35 recognizes the collagen triple helix forming fibrils of several collagens (type I, II and IV) but does not bind to other common and abundant ECM matrix proteins such as laminin, elastin and fibronectin.

First, we purified the collagen-binding recombinant CNA35 protein in combination with five different fluorescent proteins (*i.e.* eGFP, mCherry, Turquoise, mAmetrine, dTomato), and we analyzed the specificity of the CNA 35 emission at different incitement wavelengths of our confocal microscope to select the fluorophore with a more efficient signal-to-noise ratio with our lasers. Once we selected the most appropriate fluorophores, we prepared the fibrillary collagen matrices at a final concentration of 2 mg/ml to mimic the concentration on interstitial tissues and stained them with the probes.

Once the setting up of the fibrillary matrices was mastered, we relied on high-speed high-resolution live imaging and image processing to dissect the changes in the shape of the tachyzoite cell once it was gliding inside this 3D environment. We also studied the fibrils behavior to conclude on the points of adhesion the tachyzoite creates as it glides. Depending on fibril density in the matrix, parasites could be transiently or sustainably halted in their progression or slowed down, a very interesting setting since they allow a precise examination of the motile cell sequence.

6.2.3 Main highlights of the study

- Tachyzoite helical gliding in 3D fibrillary environments is initiated by pulling of the fibers, followed by an acceleration of the helical motion and propulsion forward.
- Apical adhesion is necessary for creating an anchoring point on which to build a traction force with specific acto-myosin requirements, and essential to change between the non-productive twirling to the productive helical type of movement.

- This site of force transmission corresponds to a local apical deformation of the parasite referred to as a kink which release coincides with the maximal acceleration in forward helical gliding.
- Apical adhesion and basal deadhesion are tightly coupled in time. While the former event is strictly required for enabling helical progression, the latter is equally crucial since when it is artificially prevented, the parasite over-contracts, swells and literally lysed with loss of pellicle and MT integrity.
- The subpellicular cortical microtubules could act as a spring-like force for the tachyzoite motility, bending during the kink process, storing energy loaded by the apical actoMyoA-based traction force, which is released in the forward movement.

6.2.4 Publication

Pavlou G, Touquet B, Vigetti L, Renesto P, Bougdour A, Debarre D, Balland M, Tardieux I. Coupling Polar Adhesion with Traction, Spring, and Torque Forces Allows High-Speed Helical Migration of the Protozoan Parasite *Toxoplasma*. ACS Nano. 2020 Jun 23;14(6):7121-7139. doi: 10.1021/acsnano.0c01893. Epub 2020 Jun 1. PMID: 32432851.

Coupling Polar Adhesion with Traction, Spring, and Torque Forces Allows High-Speed Helical Migration of the Protozoan Parasite *Toxoplasma*

Georgios Pavlou, Bastien Touquet, Luis Vigetti, Patricia Renesto, Alexandre Bougdour, Delphine Debarre, Martial Balland, and Isabelle Tardieux*

Cite This: <https://dx.doi.org/10.1021/acsnano.0c01893>

Read Online

ACCESS |

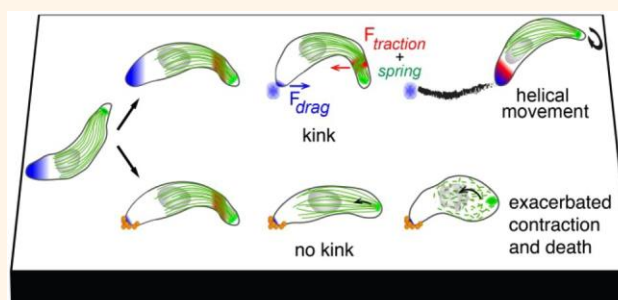
Metrics & More

Article Recommendations

* Supporting Information

ABSTRACT: Among the eukaryotic cells that navigate through fully developed metazoan tissues, protozoans from the Apicomplexa phylum have evolved motile developmental stages that move much faster than the fastest crawling cells owing to a peculiar substrate-dependent type of motility, known as gliding. Best-studied models are the *Plasmodium* sporozoite and the *Toxoplasma* tachyzoite polarized cells for which motility is vital to achieve their developmental programs in the metazoan hosts. The gliding machinery is shared between the two parasites and is largely characterized. Localized beneath the cell surface, it includes actin filaments, unconventional myosin motors housed within a multimember glideosome unit, and apically secreted transmembrane adhesins. In contrast, less is known about the force mechanisms powering cell movement. Pioneered biophysical studies on the sporozoite and phenotypic analysis of tachyzoite actin-related mutants have added complexity to the general view that force production for parasite forward movement directly results from the myosin-driven rearward motion of the actin-coupled adhesion sites. Here, we have interrogated how forces and substrate adhesion–de-adhesion cycles operate and coordinate to allow the typical left-handed helical gliding mode of the tachyzoite. By combining quantitative traction force and reflection interference microscopy with micropatterning and expansion microscopy, we unveil at the millisecond and nanometer scales the integration of a critical apical anchoring adhesion with specific traction and spring-like forces. We propose that the acto-myosin motor directs the traction force which allows transient energy storage by the microtubule cytoskeleton and therefore sets the thrust force required for *T. gondii* tachyzoite vital helical gliding capacity.

KEYWORDS: cell migration, cell focal contact, 3D collagen, *Toxoplasma*, traction force microscopy, reflection interference contrast microscopy, expansion microscopy



Across eukaryotic phyla, cell migration is an evolutionary conserved function which appears vital for both free living protozoans and metazoans.¹ In metazoans, cells such as fibroblasts and leukocytes use a wide spectrum of adhesion-dependent motility modes conjointly defined as crawling and primarily driven by the dynamics of the cell actin–myosin cytoskeleton.^{2,3} These cells crawl with the help of dynamic actin-powered membrane protrusions that fold at the leading edge as a flat lamellipodium or as a variety of pseudopodia-like membrane projections. Firmly attached to the substrate upon coordinated assembly of integrin-driven adhesive platforms, the lamellipodium is a hallmark of the mesenchymal cell migration mode in 2D and 3D micro-

environments. These anchoring multimolecular platforms allow the development of actomyosin bundles that tune contractile forces between the front and trailing margins and eventually lead to the release of trailing adhesions, hence allowing cell forward translocation.^{4,5} Likewise, metazoan cells as well as large free-living protozoans can display a

Received: March 4, 2020

Accepted: May 20, 2020

Published: May 20, 2020

49 more versatile motility mode and cope with heterogeneous 3D
50 microenvironments. In addition to the lamellipodium style,
51 they can adopt diversified pseudopodia mechanisms that,
52 combined with a range of relative cell-matrix adhesion and
53 actomyosin contractility, account for the rapid amoeboid type
54 of motility (~ 10 to $20 \mu\text{m}/\text{min}$ versus less than $1 \mu\text{m}/\text{min}$ for
55 the lamellipodia mode).⁶ Alternatively, fibroblasts can utilize
56 an amoeboid–mesenchymal hybrid type of 3D migration
57 called lopotodial during which a pressure-driven bleb-like
58 membrane protrusion stems at the leading margin from the
59 piston-like forward movement of the nucleus itself driven by
60 the cortical actomyosin contractility.⁷ Biophysical studies have
61 proved instrumental in mapping and measuring the develop-
62 ment of forces in cells, and they brought insights on how cells
63 differentially regulate the adhesion–contractile balance to
64 spatiotemporally control the adhesion assembly/deassembly
65 cycle and achieve productive forward movement in different
66 contexts.⁸

67 Intriguingly, unicellular eukaryotic parasites from the ancient
68 phylum of Apicomplexa have evolved an adhesion- and actin-
69 dependent motility mode that differs from the mesenchymal,
70 amoeboid, lopotodial repertoire and enables the microbes to
71 glide within host tissues and across barriers to follow their
72 complex stepwise developmental program. The several
73 thousand members of the Apicomplexa phylum include
74 among the world's most pre-eminent mammal-invasive
75 protozoan parasites. In humans, *Plasmodium* spp. are
76 inoculated in the vascularized dermis/extracellular matrix
77 (ECM) by a blood-feeding mosquito which hosts parasites in
78 salivary glands. *Plasmodium* displays a prolonged asexual
79 developmental phase in red blood cells, which results in a
80 range of clinical outcomes known as malaria, impacting human
81 populations in tropical and subtropical regions of the Earth. Its
82 relative *Toxoplasma gondii* is present in a large assortment of
83 endotherm metazoans worldwide. Being ingested with
84 contaminated food and water, *T. gondii* is hosted quasi-silently
85 by possibly up to a third of the human population in tissues
86 such as the brain, retina, and heart and skeletal muscles.
87 However, in case of immune dysfunction, *T. gondii* can re-
88 emerge from these tissues and proliferate, causing life-
89 threatening or debilitating complications.⁹

90 Throughout their life cycle in their respective hosts, both
91 *Plasmodium* and *T. gondii* ensure their perpetuation by
92 undergoing multiple cell differentiation events that give rise
93 to specific developmental stages with sizes of several microns,
94 harboring a crescent shape and endowed with high motility
95 skills.¹⁰ Best studied are the *Plasmodium* slender mature
96 sporozoite inoculated in the host skin and the *T. gondii* bulky
97 highly replicative tachyzoite stages that glide 10 times faster
98 than the amoeboid cells without folding any of the crawling-
99 associated protrusions.^{10–12} Instead, they share a robust
100 longitudinal apico-basal polarity which persists during the
101 generally unidirectional motile activity with the apex leading.¹³
102 Whereas the *Plasmodium* sporozoite moves on a circular path
103 in either counterclockwise (CCW) or clockwise (CW)
104 directions with an irregular stop and go kinetics,¹³ it can also
105 occasionally adopt a random motion or a corkscrew-like
106 pattern *in vivo*.^{14,15} Instead a left-handed helix characterizes the
107 path the mosquito-restricted ookinete *Plasmodium* stage used
108 to move in Matrigel-based 3D matrices.¹⁶ The *Toxoplasma*
109 tachyzoite can similarly glide CCW on a circular path under
110 2D *in vitro* settings but often uses a CCW helical trajectory or a
111 succession of the two mechanisms over the same gliding

sequence.^{11,17} Another intermittent 2D movement termed
112 twirling accounts for the stationary CW rotation executed by
113 the upright-positioned tachyzoite around its posterior end.¹⁸
114 The corkscrew-like mode of gliding, which is the obligate
115 mechanism in 3D reconstituted or *in vivo* environments was
116 proposed to relate to the 2D helical mode of gliding.¹⁹ The
117 latter typically starts with a CW short motion, follows with a
118 180° twist; meanwhile, the body flattens on the substrate
119 before twisting up and flipping on the side, which allows
120 starting another helical cycle.^{11,18} 121

To initiate and sustain all types of gliding activity, both the
122 sporozoite and tachyzoite rely on the regulated secretion of
123 adhesive protein oligomers at the cell surface^{20,21} that, once
124 delivered at the apical tip, can coengage with ECM proteins
125 and short cortical actin filaments organized beneath the plasma
126 membrane. Force production driving parasite movement has
127 long been considered to directly translate from the apico-basal
128 translocation of the ECM-bound adhesins coupled to the
129 flowing actin filaments and their enzymatic-mediated release of
130 these adhesins at the trailing edge.^{22,23} It is the Apicomplexa
131 specific, fast, nonprocessive, single-headed motor myosin A
132 (MyoA) that was assigned an essential powering role in pulling
133 backward the apically initiated actin filaments and the captured
134 adhesins.^{24,25} Upstream from MyoA however, the *T. gondii*
135 tachyzoite additionally requires myosin H (MyoH) to propel
136 actin filaments from the parasite apical tip formed by the
137 conoid,²⁶ a retractile appendage missing in *Plasmodium*. Both
138 MyoA and MyoH molecules function within a multisubunit
139 complex identified as glideosome²² that also comprises several
140 regulatory subunits and scaffolding partners.^{27–29} Specifically
141 for MyoA, the glideosome associated proteins (GAPs) anchor
142 the motor machinery to the plasma membrane and the lining
143 internal bilayered membrane complex (IMC) which underside
144 is tethered to a cytoplasmic array of cortical microtubules
145 (cMTs), the number and arrangement of which typify each
146 Apicomplexa species and developmental stage.^{27,30} 147

However, the recent introduction of force microscopy,
148 reflection interference contrast microscopy (RICM) and
149 optical tweezers in conjunction with molecular genetics in
150 the *Plasmodium* field has added more complexity to the
151 prevalent force production model.³¹ A key observation is the
152 discrepancy between the speed of the retrograde flow of
153 optically trapped microbeads on the apical surface of the
154 sporozoite and the speed achieved during typical circular
155 gliding, the former being up to 50% faster than the latter.³¹ In
156 addition, several distinct areas of contact between the moving
157 sporozoite and the substrate were uncovered at the apex, base,
158 and center over the circular path and were shown to display
159 specific on–off dynamics,¹³ whereas the genetic loss of a
160 surface-exposed adhesin reported to function during motility
161 was found to trigger a speed increase in the retrograde flow and
162

a concomitant decrease in force production.³¹ Collectively,
163 these studies bring compelling evidence for the assembly of
164 distinct force-generating adhesive structures which differ-
165 entially control production of the force required for migration.
166

By contrast, how forces and dynamic adhesions coordinate
167 in space and time and integrate with the impressive high-speed
168 helical path that features the *T. gondii* tachyzoite gliding
169 mechanism has been much less investigated. Intriguingly, the
170 rearward capping of nanobeads bound to the tachyzoite surface
171 was shown not to require an intact actomyosin system but
172 rather a polarized secretory–endocytic cycle that would locally
173 drive membrane tension.³² On the other hand, qualitative 174

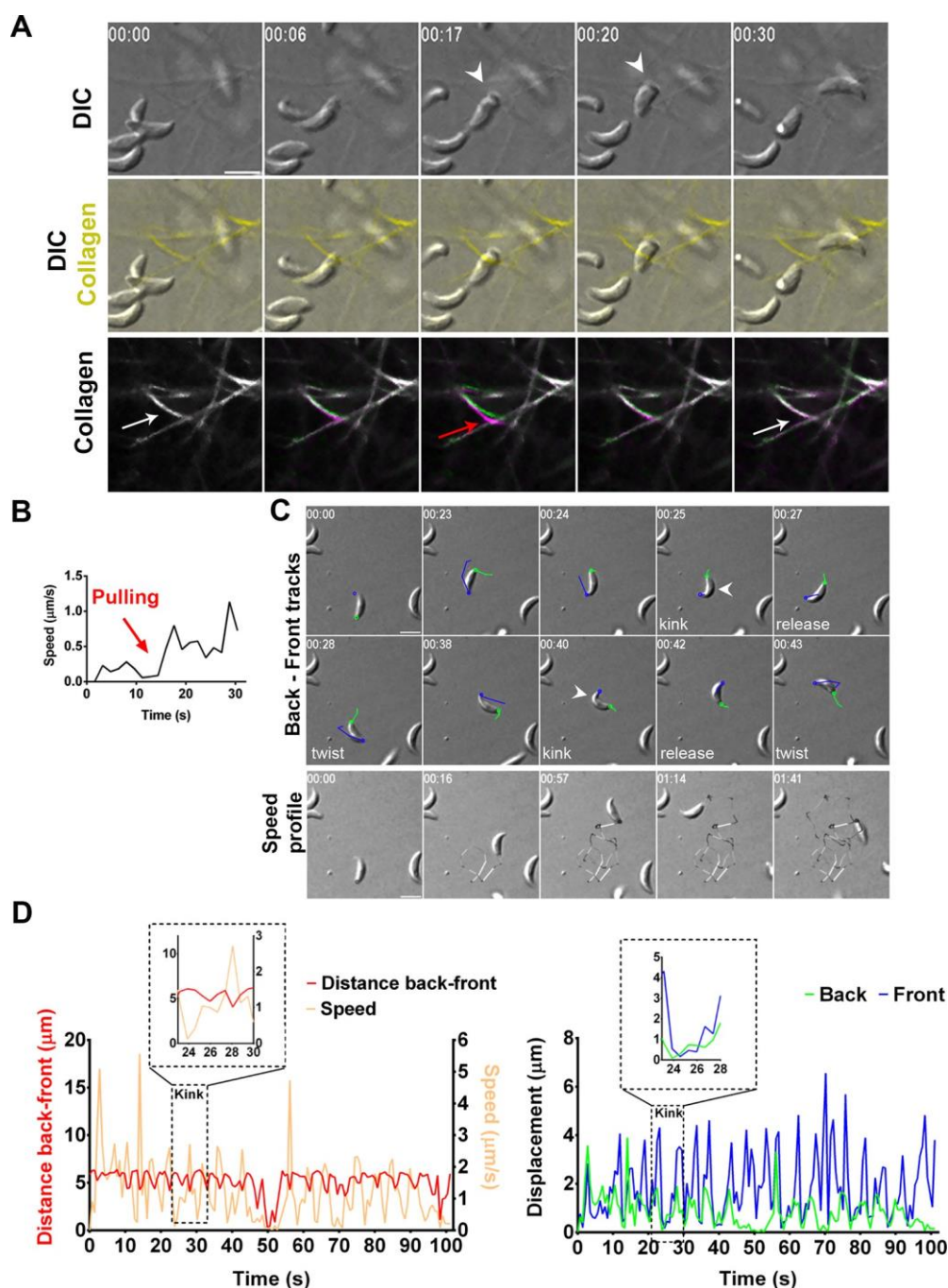


Figure 1. Tachyzoite pulls on the collagen fibers prior to helical acceleration. (A) Successive images from a time lapse of a tachyzoite navigating within a 3D-meshwork of rat collagen1 fibers pre-labeled with the CNA35-GFP collagen chimeric probe. Panels show images of (top) DIC, (middle) DIC-GFP over, giving yellow-colored fibers, (bottom) the fiber initial (t_0 , green) and over time (t_x , magenta) positions when encountered by the moving tachyzoite. The overimposition of the green and magenta signals comes as white (white arrows) when the fiber maintains the t_0 position, whereas the separation between the green (t_0) and magenta (t_x) signals attests two distinct positions overtime. The backward displacement indicates the parasite pulls on the fiber (red arrow), whereas the graph (B) documents that this pulling coincides with the parasite low speed. Next the acceleration step coincides with the merge back of the green and magenta signals that signs for the release of fiber tension post motion. (C) Successive DIC images from a time lapse of a tachyzoite undergoing helical gliding on fibronectin-coated glass. (Top) back (green) and front (blue) tracks over three last frames (t_{x-2} to t_x) are shown, (bottom) speed profile is shown from black to white scaling with increasing speeds. All white arrowheads point to the kink, all scale bars: $5 \mu\text{m}$, time is in minutes/seconds. (D) Graph (left) plots the tachyzoite back–front distance (red line) and the speed based on the back tracking (light orange); note that the value close to zero corresponds to the time the tachyzoite twirls, hence the apex is out of focus and the back-front distance not measurable (right) the xy displacement for both the back (green) and front (blue) sites over the helical sequence. Zoomed of a typical kink step for both graphs shown as inlays.

175 R1CM allowed identifying an early tachyzoite contact with the
176 substrate at the cell front and its rearward translocation which

was assumed to directly power the force-producing parasite 177
movement.³³ In this study, we revisited the mechanisms 178

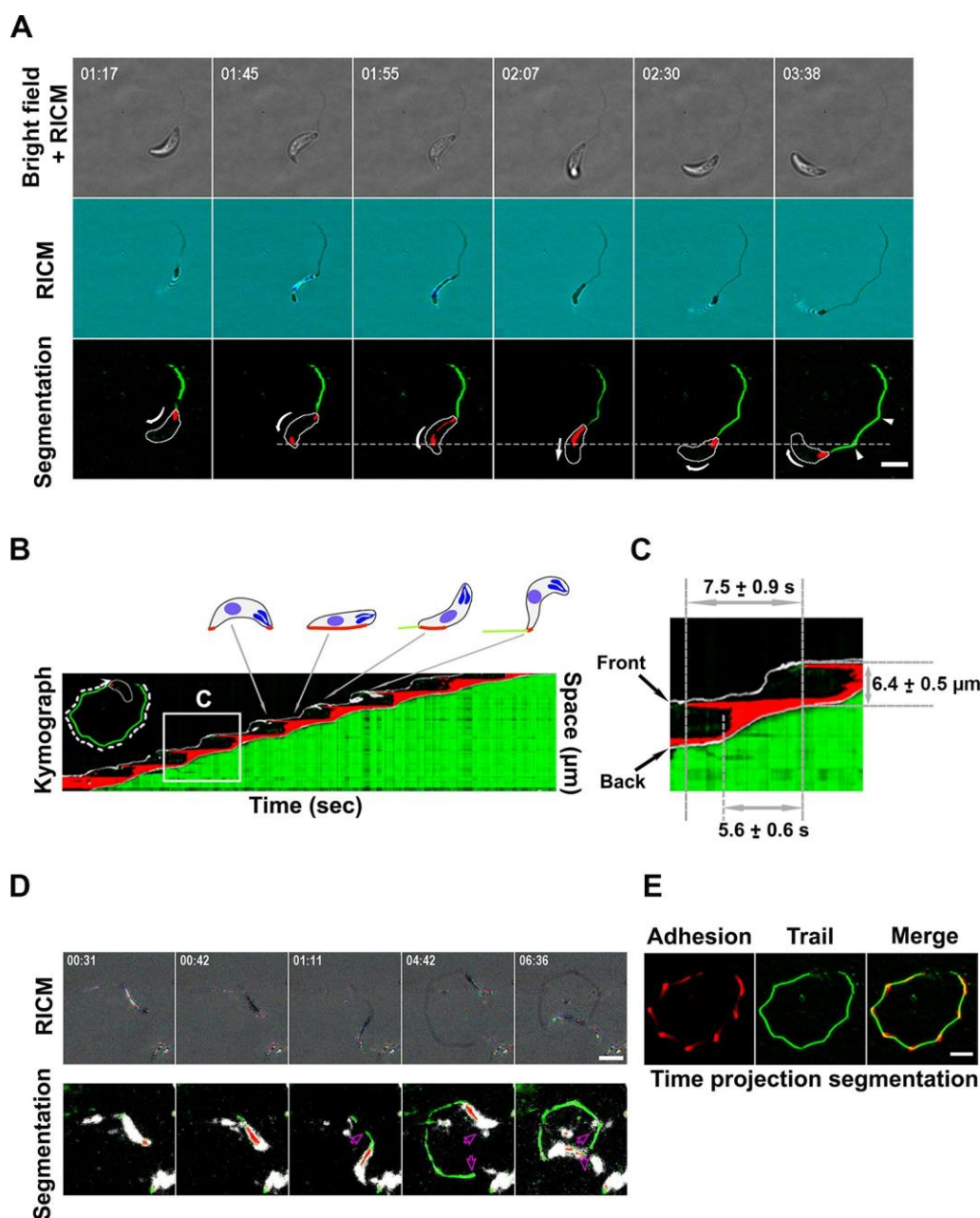


Figure 2. Helical cycle starts with an apical site of adhesion that constraints sliding of both the parasite and the parasite posteriorly shed trail. (A) Successive RICM images from a time lapse of a tachyzoite undergoing helical motion on a glass coverslip. Panels show (top) simultaneous bright-field (BF) and RICM images, (middle) blue and green RICM images superimposed and displayed as RGB, (bottom) segmentation of BF and RICM images showing the parasite outline (white), areas of close contact between the glass and the moving parasite (red), and material shed behind as trail (green). White arrows indicate the direction of the parasite movement. The dotted line marks the position of the initial contact over one helical cycle and delineates the trajectory angular point. (B,C) Kymograph of the whole gliding sequence from (A) and for a single zoomed helical cycle (C) shows the evolution of the close contact area along the trajectory over time. (D) Successive three-color RICM images (shown as RGB) from a time lapse of a tachyzoite undergoing helical motion on a poly-L-lysine-coated glass coverslip (top) and corresponding segmentation with the Weka Fiji plugin (bottom). The pink arrows indicate that over time the tachyzoite pulls on the trail that slides without breaking but follows the polygonal trajectory imposed by the initial anchoring sites. (E) Time projection of the segmented close contact areas over the gliding sequence on which (left) the longest-lived attachment points are brightest, (middle) the trails are green, and (right) adhesion and trails are overimposed. Note that angles in the polygonal path coincide with both the long-lived close contacts and the kinks. All scale bars: 5 μm ; time is in minutes/seconds.

179 underpinning the helical gliding of *T. gondii* by combining
 180 quantitative live imaging with traction force microscopy,
 181 quantitative RICM, micropatterning and expansion micros-
 182 copy. We provided evidence for a spatiotemporal coordination
 183 of an actoMyoA-based traction force produced at a stable
 184 apical adhesion site and a spring-like force which, driven by the

left-handed cMT spiral orientation, directs straightening and 185
 helical propelling of the *T. gondii* tachyzoite. 186

RESULTS/DISCUSSION 187

Tachyzoite Pulls on the Collagen Fibers in a 3D 188
 Meshwork Prior to Accelerating with a Helical Motion. 189

Pioneering work on *T. gondii* 3D *in vitro* motility has relied on Matrigel-based matrices under rather elastic and homogeneous conditions.¹⁹ However, *in vivo*, most ECM microenvironments are enriched in a nonlinear, anisotropic, and dynamic fibril-rich meshwork. Because collagens are dominant ECM components that form multiscale fibrils withstanding tensile forces,³⁴ we analyzed how the *T. gondii* tachyzoite moves within a confined collagen fibril-based matrix. Whereas the tachyzoite squeezed its body to pass through the meshwork, it first paused and bent, showing an apical deviation as it next accelerated, possibly with a rotation around its main axis, to escape from the collagen fibrils (Figure 1A,B and Supporting Information Figure S1, Movie 1, and Movie 2). Using a fluorescent probe selectively associated with collagen fibrils,³⁵ we applied a temporal color-code (green and magenta) and identified fibers encountered by the motile tachyzoite that shifted backward before returning to initial position as the parasite propelled forward (Figure 1A, Supporting Information Movie 1). This fiber backward displacement was seen in all cases of moving tachyzoites encountering a fiber ($n = 10$), and qualitatively indicated that the parasite exerted pulling forces on the surrounding fibers.

To get more mechanistic insights on the front-rear spatiotemporal coordination over the helical gliding cycle, we further analyzed the changes in the tachyzoite shape with high spatiotemporal acuity using a 2D setting. We observed a yet undefined apical inward bending immediately post the initial clockwise arc motion and concomitant with the parasite pause (Figure 1C). Indeed, tracking the front and back revealed a shortening of the parasite that coincided with an apical flexure and thus an increased curvature, resembling the observation made within the fibrous 3D matrix, and which we defined as the kink step. Associating with the apical pole arrest we detected the contraction of the cell body and retraction of the posterior pole. Next the apex re-extended and lifted up, a phase defined as the kink release, while the tachyzoite straightened and slid to further twisted in the typical CCW motion (Figure 1C, Supporting Information Movie 3a and Movie 3b, slow motion). Accordingly, not only the instantaneous speed was about null during the kink step and reached maximal value as the latter relaxed back (Figure 1D), resulting in the characteristic periodic speed fluctuations documented under 3D conditions.¹⁹ No such pattern was detected when the parasite performed the 2D-restricted CCW circular trajectory (Supporting Information Figure S1B,C and Movie 4). Of note, high temporal resolution live imaging of *Plasmodium* sporozoites also reveals alternating periods of rapid movement in which they travel up to one body length and periods of slow movement in which they more firmly adhere to the substrate, thereby indicating that distinct adhesion types operate during motility.¹³ Although such kinetics was associated with the sporozoite body stretching upon firm adhesion of its polar and center regions to the substrate and the subsequent thrust in speed,¹³ no peculiar apical deformation that could resemble a kink has been observed to initiate movement. We proposed that the kink deformation and the subsequent body extension might reflect the tension built in the tachyzoite cytoskeleton to achieve the thrust force required for the helical twisting motion.

Apical Focal Adhesion Behaves as a Firm Long-Lived Anchor That Constrains Sliding of the Parasite Body. Because the apical kink suggests the assembly of a specific contact between the parasite front and the substrate, which

would be appropriate for building up tension in the *T. gondii* cytoskeleton, we first used qRICM to monitor the parasite-substrate distance. In contrast to a recent study,³³ we used high-speed (30 frames/s), multicolor RICM with simultaneous transmitted-light imaging coupled with machine-learning-based image processing to achieve a precise segmentation of close contact regions between the parasite and the substrate at high temporal resolution (33 ms) over thousands of frames (Figure 2 and Supporting Information Movie 5 and Movie 6). In addition to the low-distance patches detected between the parasite basal pole and the substrate even in absence of movement, we found that at the onset of a helical cycle, the membrane of the tachyzoite apex came in contact with the glass surface. Because these RICM-detected signals coexisted with motion, we assumed they accounted for two polar parasite-substrate adhesive areas in agreement with Tosetti and collaborators³³ and similarly to what was found for the *Plasmodium* sporozoite.¹³ Crucially, the apical contact remained static over the full length of the helical cycle (7.5 ± 0.9 s), and the posterior contact progressively expanded to account for $\sim 80\%$ of the tachyzoite length along its major axis (Figure 2A–C, see kymographs, Supporting Information Movie 5). Upon release of the kink, the parasite propelled forward and shifted orientation before it started a new front attachment. For each helical cycle, the kink step could be a posteriori inferred through the mix of parasite-derived membrane hydrophobic droplets and surface-exposed proteins/glycoproteins left as a complex trail behind the cell edge onto the substrate, a common feature of Apicomplexa motile stages (Figure 2A,D,E).^{11,36} Quantitative modeling of the RICM signal provides transverse dimensions for these trails of ~ 70 nm (isotropic) or 100 nm (width) and 40–60 nm (height). By comonitoring the parasite helical motion and the trail assembly in real time, we were able to uncover that the tachyzoite not only slid on the adhesive tracks it built itself but could also pull these, an observation that has not been reported for the RICM data collected on *Plasmodium*.¹³ These observations suggest a continuous nature of the shed material that remained close but not firmly fixed on the substrate (Figure 2D and Supporting Information Movie 6), which would agree with membrane components including lipids as previously deduced from the analysis of fixed samples.¹¹ Importantly, the sliding trajectories of the shed material once pulled by the moving tachyzoite appeared constraint by the periodically distributed firm anchors, which could occasionally be stripped off from the substrate (Supporting Information Movie 6). In further support of these periodic stable anchors, the time projection of the trail trajectory postimage segmentation allowed positioning the longest-lived parasite-substrate contacts at each angular point of the trajectory, matching the initial apical anchoring sites (Figure 2E). The relative homogeneity in the trail observed at our RICM resolution cannot inform on a specific distribution or arrangement in proteins and lipids upon specific secretory events or/and due to local physical constraints that would compose the periodic anchors. The microneme-stored MIC2 is seen as the adhesion prototype that bridges the parasite motor system and ECM ligands during motility. Indeed partial or full silencing of the *mic2* expression significantly impairs both the helical and twirling motions.^{37,38} This double default argues more for a MIC2 contribution to the posterior adhesion force,³⁷ hence *mic2* KO parasites show a reduced capacity to bind to host cells and collagen-coated surfaces.³⁸ Consistently, 315

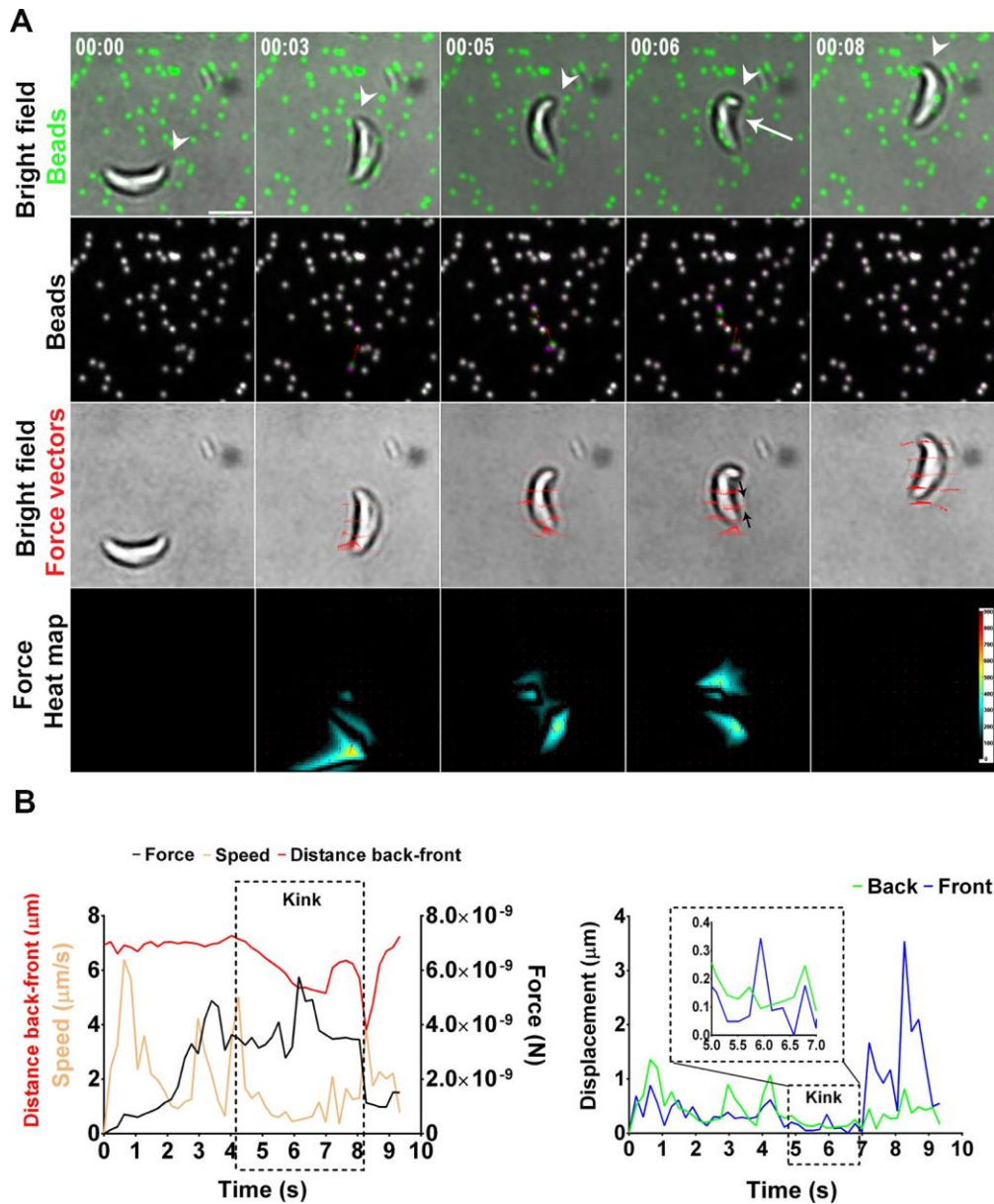


Figure 3. Helical motion includes the development of apical traction at the kink site and basal dragging forces. (A) Traction force microscopy (TFM) images were taken at the time a parasite glides on a 2 kPa PAA gel in which fluorescent TFM beads are embedded underneath the gel surface itself coated with fibronectin (20 $\mu\text{g}/\text{mL}$). Panels show (top) bright-field (BF) and TFM beads composite images; white arrowheads indicate the apex of the tachyzoite, and white arrow marks the kink, (second row) BF with force vectors computed by the MATLAB TFM code. Red arrows indicate the force direction and value; black arrows have been manually added to ease visualization of the two longitudinal forces and their orientation, (bottom) force heat map computed MATLAB TFM code. Scale bar: 5 μm , time is in minutes/seconds; au for force heat map. (B) (Left) Speed (light orange line), the back to front body distance (red line) and the traction force applied by the parasite over time (black line) are shown with a zoomed inlay (black dotted line) at the kink step time, and (right) the back and front displacement (green and blue trajectories, respectively) are shown with a zoomed inlay (black dotted line) at the kink time.

316 when the *T. gondii* tachyzoite expresses only residual levels of
 317 the rhomboid protease (ROM4) in charge of cleaving the
 318 surface-exposed MIC2, MIC2 molecules accumulate at the
 319 surface of the parasite that can no longer glide forward but
 320 instead shows enhanced twirling motility.³⁹ Similarly, when
 321 *Plasmodium berghei* sporozoites express a mutant version of the
 322 MIC2 homologue TRAP that cannot be processed by the
 323 rhomboid protease, the parasite can no longer disengage its
 324 posterior pole from the substrate and move forward.³⁶
 325 Whereas we detected both SAG1 and MIC2 proteins in
 326 patches over successive segments of the helical trails

postfixation and immunolabeling, we did not find MIC2- 327
 specific enrichment at the angular adhesion regions that were 328
 accurately identified using the RICM live sequences as 329
 recognition pattern (Supporting Information Figure S2). 330
 Therefore, it is possible that another unknown adhesin(s), 331
 which would not integrate the retrograde flow, might modulate 332
 force production at the parasite apex in line with the turnover- 333
 specific adhesion sites built by the *Plasmodium* sporozoite 334
 during circular gliding.¹³ In addition, monitoring the apico- 335
 basal flow of optically trapped beads pinned out that specific 336
 adhesions do not integrate the apico-basal capping process, yet 337

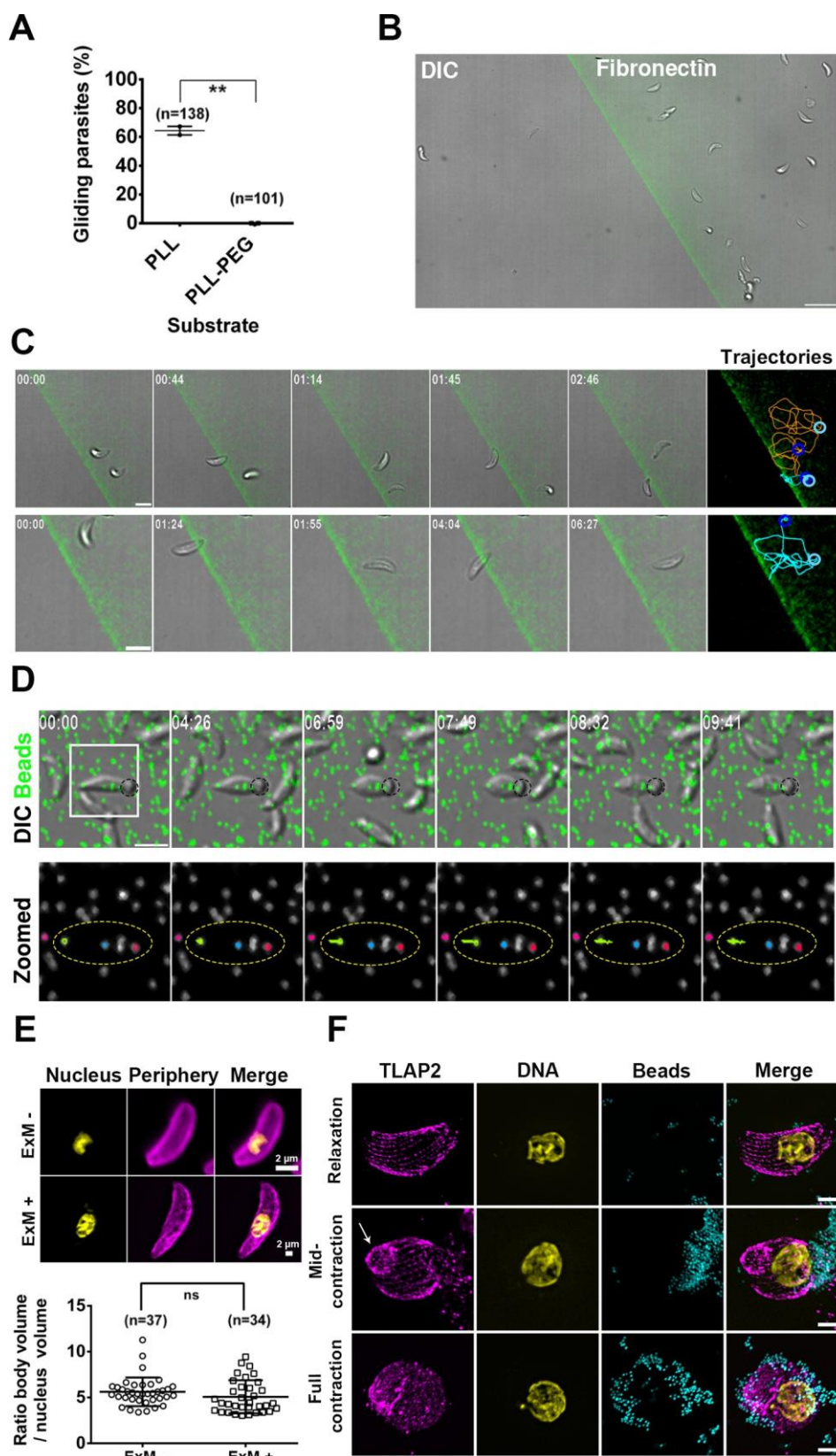


Figure 4. Front adhesion to and back disengagement from the substrate are both required for kink formation and traction force development. (A) Percentage of tachyzoites that moved by at least one body length displacement over a 20 min period post contact with poly-L-lysine (PLL) or poly(ethylene glycol) (PEG) chains grafted on PLL coating, unpaired *t* test, $**p = 0.021$. (B) Large view of the poly-L-lysine PEG–fibronectin composite micropattern shows that tachyzoites are selectively retained in the fibronectin area, which is fluorescently labeled by fibrinogen-Alexa647, scale bar: 15 μm . (C) Images from a sequence of two (top) or one (bottom) representative gliding tachyzoite(s) that fail to pass over the fibronectin–PLL–PEG demarcation line being incapable of interacting apically with PEG. Instead they elicit twirling around their posterior end bound to fibronectin and regain helical motion once apically sensing fibronectin. Blue and

Figure 4. continued

cyan circles in the trajectories window indicate the initial and the final position of the tachyzoite over the several-minute gliding sequence. Trajectories were reconstituted by tracking the tachyzoite base, which unlike the apex stays in focus even during twisting and twirling motions. (D) TFM on a tachyzoite posteriorly immobilized on fibronectin through carboxylated microbeads (black circle). (Top) Selective inward displacement of TFM beads (green) beneath the apex of the immobilized parasite occurs during sustained contraction, whereas the beads relax back to initial position upon parasite relaxation, (bottom) zoomed white square from top, showing the colored trajectories; note the large yellow trajectory that attests significant bead inward displacement, the yellow dotted ellipsoid delineates the tachyzoite. (E) Confocal images showing a representative tachyzoite immunolabeled for the GAP45 protein (pink) that delineates the parasite periphery and PI stained for DNA (yellow) prior ExM (ExM−) and after ExM (ExM+), maximal projection intensity are presented, compare the scale bars that attests the physical magnification of the ExM specimens. The graph shows the ratio of the body and nucleus volumes after 3D reconstruction prior (ExM−) and after ExM (ExM+), Kruskal–Wallis test, NS, $p = 0.17$. (F) ExM on tachyzoites posteriorly immobilized on beads (cyan) and immunolabeled for the cortical MT-associated TLAP2 protein (pink) and PI stained for DNA (yellow), (top) no contraction has yet started, (middle) contraction has started, note the apical humpy deformation in the cMT cytoskeleton indicated with a white arrow, (bottom) cMT disruption at a latest time of tachyzoite sustained contraction. Scale bars: 5 μm unless indicated, time is in minutes/seconds. The ExM allowed reaching about a 70 nM xy resolution thanks to a ~ 3 –5-fold increase in the biological sample size.

338 they can optimize force production. Accordingly, the trap-like
339 protein (TLP) was proposed to promote firmer adhesion to
340 the substrate by enabling specific actin remodeling underneath
341 the plasma membrane. Such function would explain why TLP
342 causes specific slowdown of the actin-dependent flow.³¹ With
343 these in mind, we next interrogated whether the firm stable
344 apical anchor formed by the moving tachyzoite and localized at
345 the kink could indeed serve as a platform for force transmission
346 by using traction force microscopy (TFM). These assays also
347 allowed testing whether the kink-induced cell shortening could
348 be associated with tension stored in the parasite that would be
349 released to promote the thrust required for productive helical
350 movement.

351 Traction force Spatiotemporally Associates with the
352 Kink and Coincides with Body Dragging. To design the
353 TFM assay, we first identified a substrate in which the stiffness
354 was sufficient to allow helical gliding while being elastic enough
355 to measure substrate deformations via a displacement field
356 analysis performed using fluorescent beads embedded into the
357 polyacrylamide (PAA) hydrogel. Particle image velocity (PIV)
358 combined with single-particle tracking allowed analyzing
359 substrate deformation with a spatial resolution in the range
360 of tenth of nanometers. Tracking in space and time the
361 tachyzoite posterior pole and scoring as motile those that
362 performed at least one body length displacement, we found
363 that stiffer substrates such as glass ($n = 73$) and 40 kPa PAA (n
364 = 55) correlated with optimal gliding skills, whereas lowering
365 stiffness gradually decreased the frequency and duration of the
366 motile behavior. Yet, the tachyzoites retained a short-lasting
367 ability to perform helical motion on the soft 2 kPa PAA
368 substrate ($n = 103$) (Supporting Information Figure S3).
369 Applying TFM⁴⁰ to parasites gliding on 2 kPa fibronectin–
370 PAA substrate, we obtained a traction vector map and
371 identified an early inward-oriented traction force stemming
372 at the cell front and exerted longitudinally in line with the
373 backward displacement of the in-gel beads (i.e., TFM beads)
374 underneath the apical part of the parasite (Figure 3A and
375 Supporting Information Movie 7a and Movie 7b, slow
376 motion). As the force progressively increased, concomitant
377 dragging of the parasite body occurred and accounted for the
378 TFM bead's displacement underneath the posterior pole in the
379 direction of the parasite motion, in line with the previous
380 detection of trails being pulled by the tachyzoite (Supporting
381 Information Movie 6). Relaxation of the TFM beads back to
382 their initial position was recorded immediately after the kink
383 release and the parasite forward acceleration (Figure 3A,B).
384 Pioneering TFM on the *Plasmodium* sporozoite has allowed

uncovering two longitudinal forces applied at each pole during 385
circular gliding, alike what we found for the *T. gondii* tachyzoite 386
undergoing helical gliding. A large force localized at the 387
posterior adhesion site peaked just prior sporozoite de- 388
adhesion, whereas a lower pulling traction force at the apex 389
pointed toward the center. In contrast to what we detected for 390
the tachyzoite, large forces were also found to point 391
orthogonally toward the sporozoite center,¹³ where they 392
promote body stretching and thus favor close contact of the 393
whole cell with the substrate—an obligate requirement for 394
circular gliding without contributing to force production.⁴¹ 395
Therefore, although both the tachyzoite and sporozoite likely 396
use a stalling force at the back, which upon rupture of the 397
adhesive contact contributes to a thrust force, the spatiotem- 398
poral distribution and intensity of the forces during their 399
specific gliding cycle (i.e., helical versus circular) likely differ. 400
Accordingly, the overall force during the helical cycle was 401
computed to a few nanoNewtons (~ 1 to 4 nN, $n = 10$) with an 402
increment over the kink step, therefore significantly higher 403
than the 100–200 pN range inferred for cortical forces using 404
laser trap on nongliding *T. gondii* tachyzoites⁴² or gliding 405
Plasmodium sporozoites.³¹ By comparison, the nanoNewton 406
range characterize forces applied by both bacteria and 407
mammalian cells on their surroundings.⁴³ 408

Toxoplasma Apical Focal Adhesion Is Essential to 409
Switch from Nonproductive Twirling to Productive 410
Helical Motion. To demonstrate the functional contribution 411
of the apical body adhesion to the subsequent helical gliding, 412
we sought interfering with the parasite adhesive step at the 413
apical traction force site. First, we screened for substrates not 414
permissive to parasite adhesion using several chemicals of 415
distinct charge and wettability properties. We found that 416
tachyzoites were unable to stabilize and glide on the densely 417
packed polymeric poly(ethylene glycol) (PEG) brushes grafted 418
on poly-L-lysine (PLL) (Figure 4A) similarly to what was 419 f4
reported for *Plasmodium* sporozoites.⁴⁴ Therefore, composite 420
substrate was photopatterned: the parasites underwent 421
energetic gliding on the fibronectin-coated area when 422
approaching the demarcation line between the fibronectin 423
and PLL–PEG-juxtaposed areas. The tachyzoites stopped 424
when facing PEG, sometimes sliding on it prior to stepping 425
back in a reverse motion while still posteriorly bound to 426
fibronectin (Figure 4B,C and Supporting Information Movie 8 427
and Movie 9). They responded to the exclusive basal 428
attachment by spinning around the main axis in a typical 429
twirling nonproductive motion¹⁸ until the front region was 430
eventually caught again in an interaction with fibronectin, 431

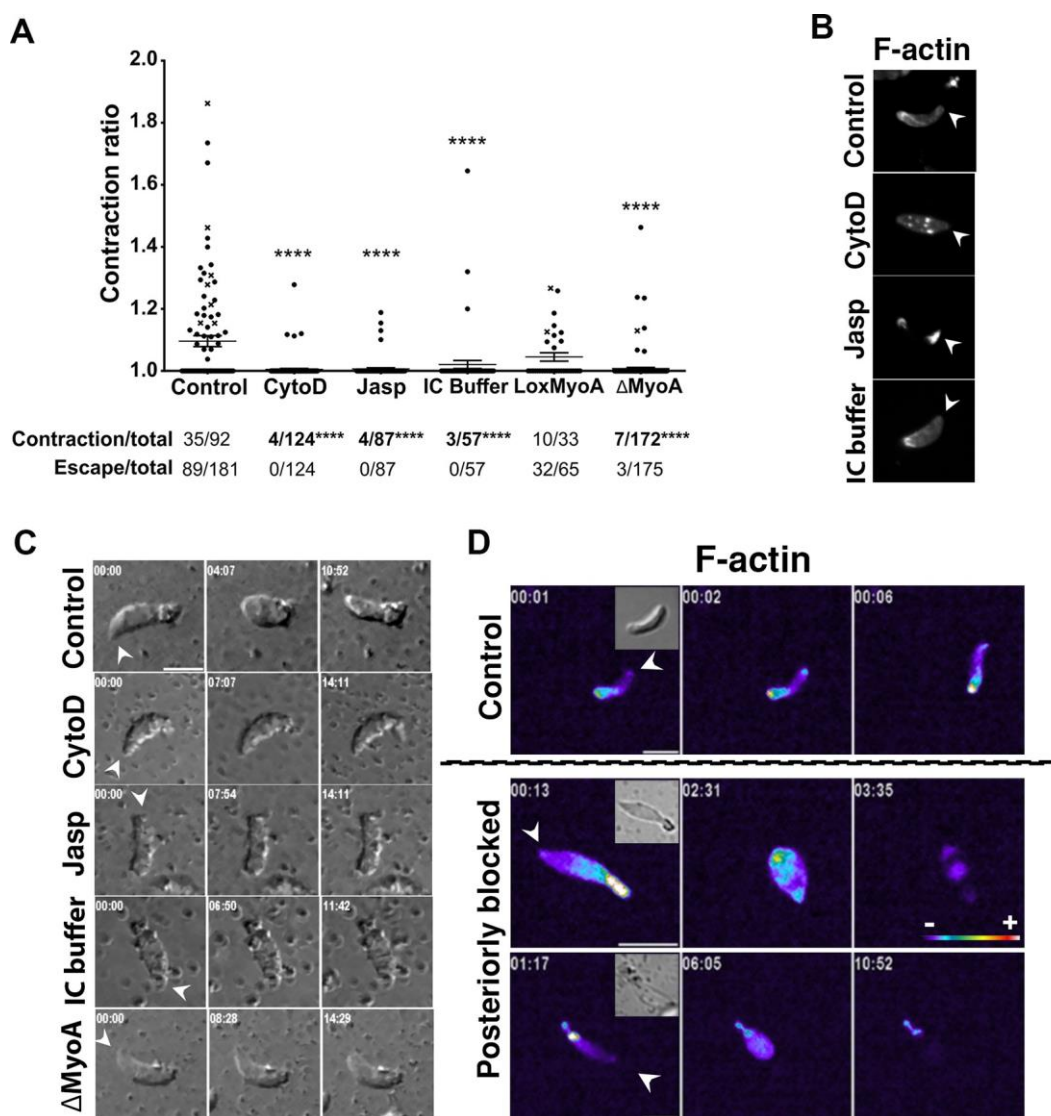


Figure 5. Prolonged and exacerbated tachyzoite contraction relies on intact actin filaments and MyoA motor. (A) Graph shows the contraction ratio after posterior immobilization on beads over a 20 min period for (i) wild-type control tachyzoites expressing the F-actin chromobody-Emerald (Acb-E) and incubated in EC buffer supplemented or not with 1 μ M cytochalasin D or 1 μ M jasplakinolide actin poisons or in IC buffer, and (ii) for tachyzoites before (LoxMyoA) and after (Δ MyoA) Cre-mediated excision of the *myoA* gene. Kruskal–Wallis test, **** p < 0.001 Dunn's multiple comparisons with the control genotype. Table below the graph shows (i) proportions of number of parasites contracted over the total and (ii) proportions of number of parasites that escape over the total. For both, chi square test, **** p < 0.001 Fisher's exact test with the control. (B) Confocal images of tachyzoites showing F-actin prior to record the contractile behavior. Maximal projection intensities are presented. (C) Representative DIC images of tachyzoites posteriorly immobilized to monitor both contractile behavior and bead-capping ability under each setting over a 20 min period ($57 > n > 181$ depending on the actin poison used and $65 > n > 165$ for *myoA* KO, 3 independent assays). (D) Representative fluorescent images of F-actin dynamics in tachyzoites expressing the Ach-E undergoing helical gliding (top panel) or sustained contraction upon posterior immobilization (middle and bottom panels); DIC images are presented as inlays for each sample. Heat map intensity is presented in arbitrary units.

432 hence restoring the tachyzoite ability to perform helical
 433 trajectory. These data reinforce the view that the tachyzoite
 434 builds an apical stable adhesion site with the substrate that is
 435 compatible with the development of traction force. As we
 436 showed that both adhesion and force spatiotemporally
 437 coincide with the kink-like deformation, we expected then
 438 that the thrust productive force would be at least partly driven
 439 by the relaxation of the kink, which drives the slight lift of the
 440 parasite apex. Of note, this thrust force might also require
 441 some contribution from the parasite basal contact which
 442 loosens when traction operates allowing both dragging and
 443 retraction of the body. Given that tachyzoites must overcome

the resistance of the 3D nonlinear meshwork to navigate in
 physiological microenvironments, the acceleration induced
 upon the kink release should provide the right thrust to pass
 through the meshwork of fibers they pulled on. Accordingly,
 we next addressed how the contact and dragging force at the
 cell back identified by, respectively, RICM and TFM
 contribute to the helical gliding mode of the tachyzoite.

Adhesion–De-adhesion Coupling at Both Poles
 Drives the *Toxoplasma* Apical Kink and Its Release, in
 Turn Promoting the Helical Thrust Force. We designed
 another TFM assay in which the tachyzoite would be unable to
 disengage its posterior pole from the substrate using submicron

456 sticky beads. As already reported in the context of membrane
457 flow or cortical forces studies,^{32,42} the beads deposited on the
458 tachyzoite surface underwent apico-basal translocation. How-
459 ever, because in our setting the bead's surface engaged covalent
460 interactions not only with the parasite but also with the
461 fibronectin layer in a configuration that forced the former to
462 stay posteriorly immobilized on the latter, the cell forward
463 progression could be hindered (Figure 4D). Such posteriorly
464 constraint tachyzoites never formed the apical kink ($n = 0/92$)
465 and, instead, underwent a directional, minute time scale and
466 repetitive inward-oriented contraction visualized by the whole
467 body rounding (Figure 4D and Supporting Information Movie
468 10). The TFM captured the displacement of in-gel beads
469 suitably positioned underneath the apex of the immobilized
470 parasite consistent with a sustained apical traction force, and
471 therefore a sustained adhesion between the parasite front and
472 the substrate (Figure 4D, zoomed panel, yellow bead and
473 trajectory). The prolonged force application induced pro-
474 nounced shrinkage of the cell body along the longitudinal axis
475 and eventually led to membrane damages to the extent the
476 tachyzoite was likely wounded beyond repair. Meanwhile, we
477 observed that the in-gel beads shifted back to almost the initial
478 position, which we assumed to relate to the sudden relaxation
479 of the cell "ghost" when internal tension fell (Figure 4D and
480 Supporting Information Movie 10). Strong evidence for the
481 rupture of the plasma membrane upon excessive contraction of
482 the YFP-expressing tachyzoite was provided by the acute loss
483 of fluorescence that occurred immediately after maximal cell
484 rounding and concomitantly with the relaxation of the cell
485 (Supporting Information Figure S4). The relaxed tachyzoite
486 cell looked mis-shapen for the rest of the recording time as
487 expected for a cell ghost, therefore attesting that the
488 exacerbated and sustained contraction induced cell death. To
489 next visualize the deleterious effect of the long-lasting
490 contraction on internal cytoskeletal structures at the nanoscale
491 resolution, we applied the expansion microscopy technique
492 (ExM)⁴⁵ and first validated the isotropic expansion of the
493 specimen with the 3D co-reconstruction of the tachyzoite body
494 and nucleus prior and after expansion (Figure 4E). We then
495 analyzed a tachyzoite line engineered to express a fluorescent
496 version of TLAP2, a protein aligned with the 22 cMTs,³⁰ and
497 confirmed that during the prolonged contraction period, the
498 capped beads accumulated posteriorly while the spiral cMTs
499 deformed. We first observed an apical hump in the cMT
500 network (Figure 4F, middle panel), and eventually, the latter
501 fell apart while the capped beads were redistributed over the
502 damaged surface (Figure 4F, bottom panel). Overall, these
503 data support that the kink rose from the interplay between the
504 apical adhesion/base de-adhesion and the forces generated at
505 both poles rather than from the apical traction force only. They
506 also highlight that creating unbalance between the front and
507 back responses can result in a contractile force that imposes a
508 mechanical compression to the cMT network to which it
509 cannot resist. The need for a balanced myosin-A-based
510 contractile activity that stems at the tachyzoite apex and
511 promotes disengagement of the posterior pole can explain why
512 the genetically myosinA-deficient tachyzoites, which retain
513 only residual motility, do not any longer undergo helical
514 gliding.^{37,32}

515 Tachyzoite Apico-Basal Contraction Requires Intact
516 Actin Filaments and Myosin A Motor and Correlates
517 Only Partially with the Requirements for Rearward
518 Membrane Flow. Apart from the prolonged contraction and

fatal outcome described earlier, we also observed that the
tachyzoites, which were posteriorly immobilized, could either
rotate on the beads, slightly contract, and move forward, hence
those escaped (Supporting Information Movie 11) or remain
inactive, hence those showed no contraction and stayed
attached. To verify whether actin dynamics and MyoA motor
the function of which are required for motility^{25,46} would also
contribute to the apically driven exacerbated contraction, we
first defined a quantitative readout for measuring the
contraction extend over time. Using the ratio between the
resting body length (*i.e.*, no contraction) and the minimal body
length (*i.e.*, maximum contraction) as a contraction indicator,
we found that nearly half of the wild-type (WT) control
parasites were able to escape from the immobilization setting,
therefore attesting to the energetically active status of the
specimens under study. Approximately 40% of the second half
($n = 35/92$) contracted over a wide range of amplitude,
whereas 20% of this contracting population actually showed
signs of irreversible damages ($n = 7/35$) (Figure 5A). Blocking
actin dynamics with cytochalasin D (0.5 and 1 μM) or
jasplakinolide (1 μM) that work through different mecha-
nisms^{47,48} almost abolished both the escape (*i.e.*, motile) and
contractile behaviors. Of note, the few (less than 5%)
tachyzoites that displayed contraction never reached the
stage of high and sustained body compression, hence none
of them died (Figure 5A). We confirmed the cytochalasin and
jasplakinolide potency on tachyzoite actin as parasites
expressing the fluorescent chromobody actin-Emerald (Acb-
E)⁴⁹ displayed the typical drug-induced redistribution of actin
filaments as, respectively, cytoplasmic aggregates and apical
acrosome-like.⁵⁰ With the same readout, we also compared the
contractile behavior of parasites following or not MyoA gene
silencing using the well-characterized DiCre Lox MyoA
strains.²⁴ We observed that loss of MyoA (ΔMyoA)
significantly altered the contractile capability of tachyzoites
immobilized on their base when compared to the MyoA-
expressing parental line (LoxMyoA) ($\Delta\text{MyoA} = 175$, $p < 0.001$)
(Figure 5A). Finally, we checked if the contractile
activity was specific for tachyzoites metabolically ready for
initiating motility by measuring the contraction of WT control
tachyzoites kept in the Endo buffer which mimics the
intracellular buffer (hereafter referred to as IC buffer) and is
known to drastically decrease microneme secretion (*i.e.*,
adhesin delivery on the tachyzoite surface) and consequently
motility.²⁰ Those tachyzoites showed the typical actin posterior
network of intracellular tachyzoites⁵¹ and were significantly
inefficient at contracting under the posterior microbead setting
($n\text{IC} = 57$, $p < 0.001$) (Figure 5A–C and Supporting
Information Movie 12). Finally, we monitored actin filaments
in real time in Acb-E-expressing tachyzoites undergoing either
helical gliding or forced contraction during the immobilization
phase. The F-actin apical focus detected at the onset of the
helical cycle remained discrete and rapidly resolved into the
large stable basal F-actin pool, as reported^{33,51} and in line with
our force mapping assays. In contrast, an increasing F-actin
signal was detected within the whole body, in particular, in the
cell front upon prolonged contraction of the immobilized and
rounding tachyzoites (Figure 5D and Supporting Information
Movie 13). Eventually, the F-actin signal vanished, which fits
with the loss of fluorescence observed with YFP-expressing
tachyzoite artificially immobilized on the substrate through
their basal pole (Supporting Information Figure S4), thereby
confirming that the membrane had ruptured upon excessive

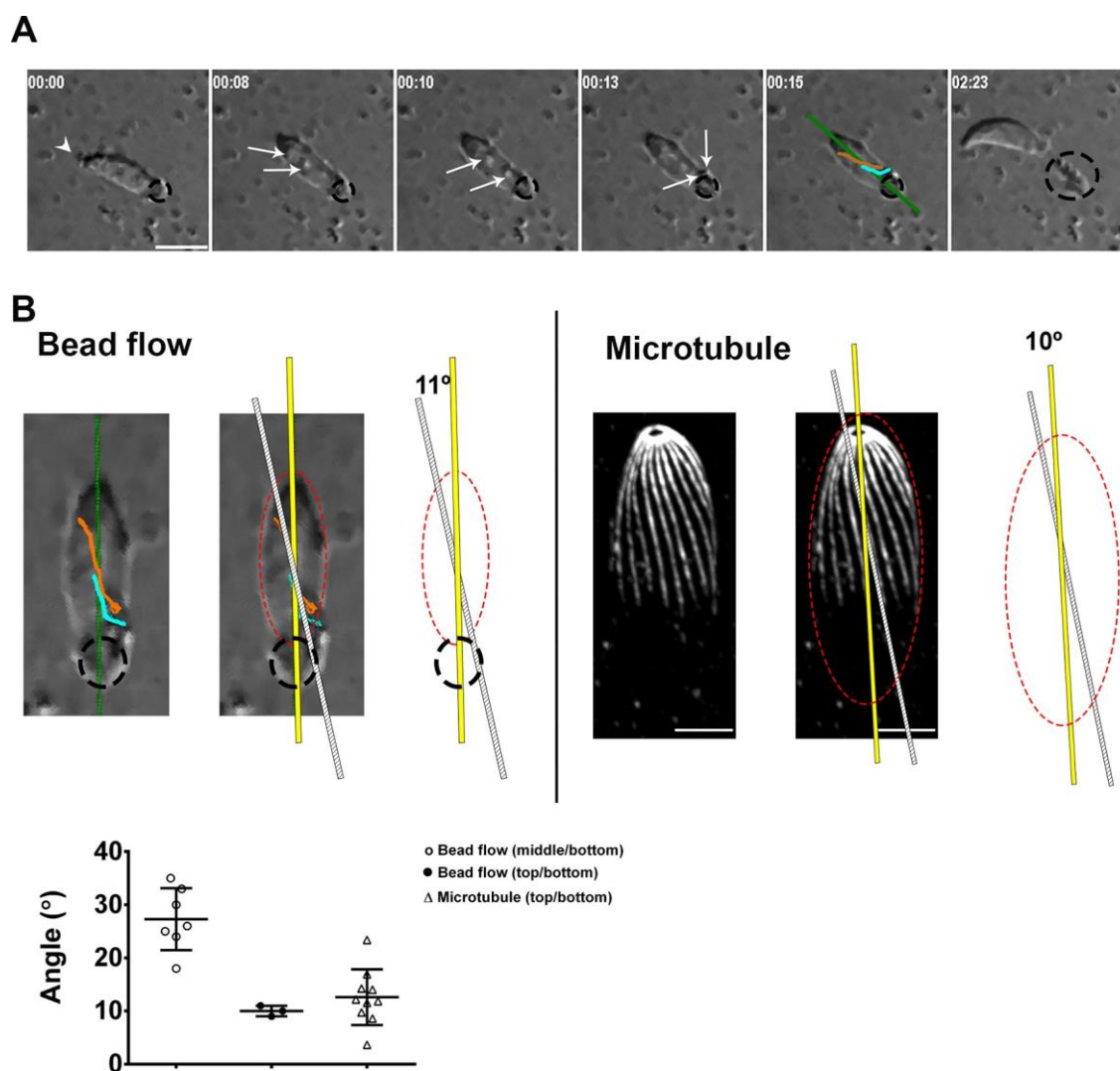


Figure 6. Apico-basal translocation of surface-bound microbeads follows a helical path that approximates the spiral direction of the tachyzoite cMTs. (A) Representative images of apico-basal bead capping monitored in real time for tachyzoites posteriorly immobilized on beads encircled with the dotted black line. The two surface-bound beads are indicated with white arrows, and their trajectory depicted in orange and cyan lines is shown on the fifth panel, before active escape of the tachyzoite from the immobilizing setting. In all panels, white arrowheads mark the tachyzoite apex; all scale bars: 5 μm , time is in minutes/seconds. (B) Zoomed panels show images and schematics for (left) trajectory of two beads over the capping time taken from the sequence shown in A, which deviates from the body main axis (yellow line) of about a 11° angle, while (right) the spiral cMTs visualized on an extracellular tachyzoite treated for U-ExM and stained with antipolyglutamylated tubulin show about a 10° angle. (Bottom) Plot of the different angles calculated for the cMTs; the mean with SD is shown for each group ($n = 10$ tachyzoites, mean of 4 cMTs per tachyzoite) and for the capping bead flow ($n = 9$ tachyzoites). Please note the larger variability shown by the bead angles, which depends on the bead position at the initial time of capture and tracking.

582 contractile activity, leaving a tachyzoite ghost, the apex of
583 which no longer attached to the substrate.

584 As the retrograde membrane flow process has been shown to
585 operate in *T. gondii* tachyzoites in absence of the actomyosin
586 system,³² we analyzed how this process would operate for
587 tachyzoites artificially immobilized on their base. Unlike
588 previously,³² we monitored in real time the bead-capping
589 process and found that the loss of contractility driven by actin
590 poisons and IC conditions did correlate with the inhibition of
591 the rearward bead capping along the parasite surface ($57 > n >$
592 181 depending on the condition) (Figure 5C and Figure 6A
593 and Supporting Information Movie 14), thus recapitulating the
594 phenotype of formin 1(FRM1)-deficient tachyzoites³³ and
595 consistent with the need of apically initiated actin filaments.
596 However, on loss of myosinA,⁴⁶ whereas the tachyzoites
597 showed almost no ability to contract (Figure 5A), they

intriguingly maintained a bead-capping activity almost as
598 efficient as tachyzoites from the parental line ($65 > n > 165$)
599 (Figure 5C and Supporting Information Movie 12), in
600 agreement with a MyoA contribution to force transmission
601 rather than production.³² Furthermore, along with these bead-
602 translocation assays we observed in WT tachyzoites that the
603 bead-capping process could precede productive helical move-
604 ment (Figure 6A and Supporting Information Movie 14), and
605 that the bead apico-basal motion could follow the cMT helical
606 trajectory. To confirm this observation, we applied ExM with a
607 recently refined near-native expansion microscopy (U-ExM)
608 protocol,⁵² and labeled the α,β -tubulin dimer that forms the
609 cMT polymers taking advantage of the polyglutamylation post-
610 translational modification of these isoforms.⁵³ With this level of
611 resolution, we could measure the angle with the longitudinal
612 axis made by the cMTs when they emanate at the apical polar
613

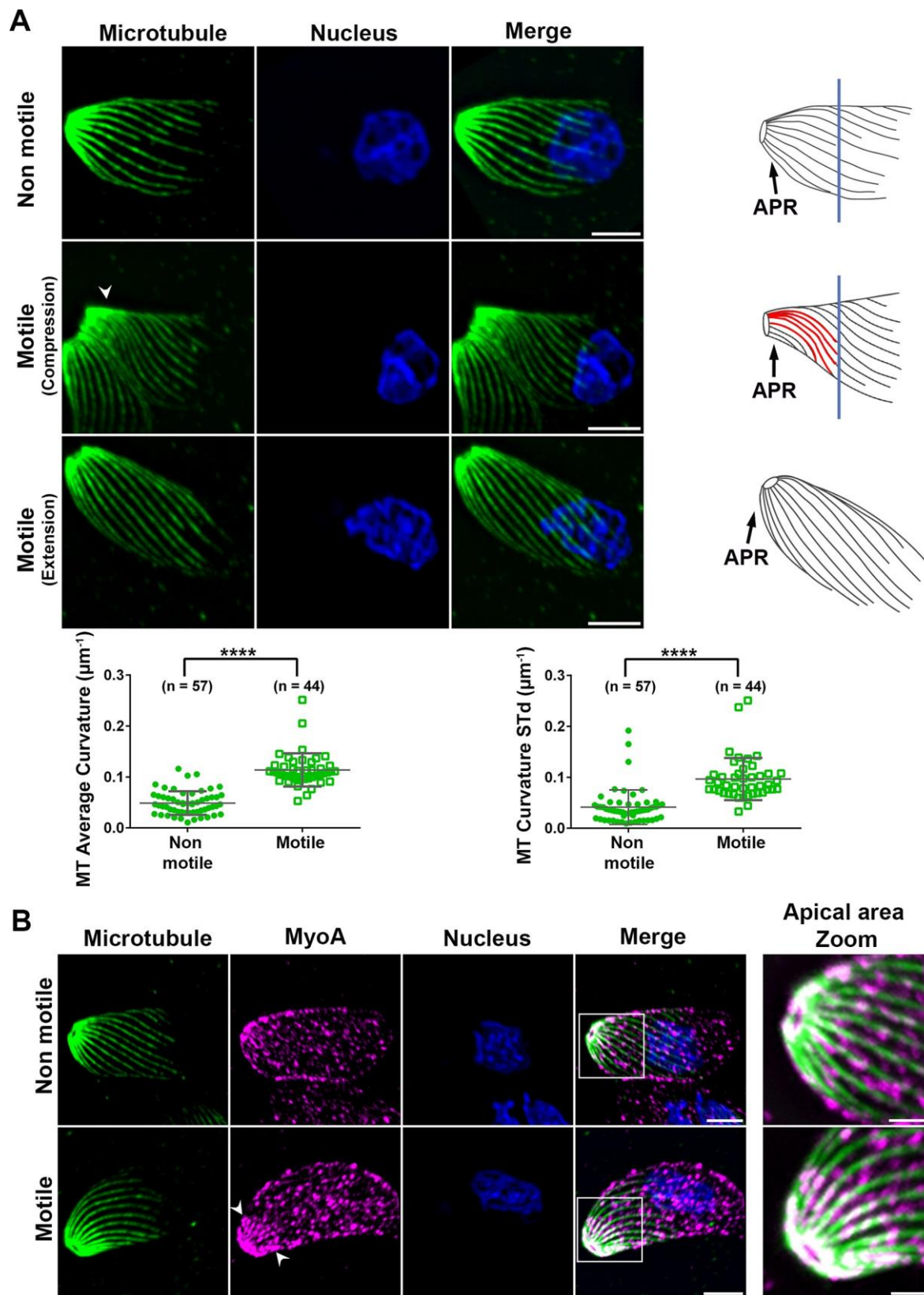


Figure 7. Curvature of cortical microtubules changes during helical gliding suggesting a spring-like mechanism apically driven by myosin-based contractile forces. (A,B) Confocal images representative of extracellular tachyzoites following U-ExM and immunofluorescence co-staining of (A) tachyzoite cMTs using antipolyglutamylated tubulin antibodies (green) and nucleus (blue). Maximal projection intensities of the cMTs from the tachyzoite ventral side are shown for (top) a nonmotile tachyzoite, (middle and bottom) two motile tachyzoites. Note the pronounced torsion and compression (white arrowhead, middle panel) and the extension (white arrowhead, bottom panel) that likely account for the spring like force underlying helical gliding. Right: Schematics of the cMTs for each stage show the highly curved cMTs at the apical region of the motile tachyzoites, drawn in red. (Bottom) Graph on the left shows a significant increase in mean curvature of the cMTs

Figure 7. continued

for the motile tachyzoites in torsion, unpaired *t* test, *** $p < 0.0001$ $n = 44$, when compared to the nonmotile ($n = 57$); graph on the right shows enhanced curvature amplitude over the length of single cMT for motile tachyzoites during the compression step ($n = 47$) when compared to nonmotile ($n = 57$) tachyzoites, unpaired *t* test, *** $p < 0.0001$. (B) Co-staining of the cMTs (green) and MyoA-HA tagged using anti-HA antibodies (purple) and the nucleus (blue). (Top) Nonmotile tachyzoite, (bottom) motile tachyzoite are shown. Note the clear MyoA signal enrichment at the apex of the motile parasite indicated with white arrowheads, which co-aligns with the MT signal. The right frames show zoomed areas delineated in the merge frames with a white square. All scale bars: $5 \mu\text{m}$ except for the B zoomed frames: $2 \mu\text{m}$. The U-ExM protocol gave a 3–5-fold increase of the tachyzoite size and provided a $\sim 70 \text{ nm}$ xy resolution. APR: Apical polar ring.

614 ring while approximating the angle made by the microbeads
615 monitored over the capping process (Figure 6B and
616 Supporting Information Movie 14). Although we observed
617 for some beads that the angles were off the range of those
618 made by the well-resolved cMTs, it is worth noting that these
619 gaps mainly correspond to situations where the microbeads
620 were tracked while they had already reached the minor axis
621 plane of the ellipsoid tachyzoite. While traveling toward the
622 posterior pole, the beads approached an area devoid of cMTs
623 and often collided with the substrate before reaching the
624 posterior pole, an observation already reported when
625 monitoring the apico-basal trajectory of $0.6 \mu\text{m}$ beads delivered
626 by laser trap to the surface of resting (*i.e.*, nonmotile)
627 tachyzoites.⁴² Collectively, these data indicate that the
628 actomyosin system mobilized during the rearward bead
629 translocation process has aligned with the longitudinal cMT
630 network, this independently of the apical adhesion and thus
631 before the apical traction force operates.

632 Curvature of Cortical Microtubules Significantly
633 Changes during Helical Gliding, Suggesting a Spring-
634 like Mechanism Apically Driven by Myosin-Based
635 Contractile Forces. Triggered upon relaxation of the apical
636 kink, the extension of the tachyzoite body coincided with the
637 thrust force while the parasite rotated with an orientation
638 dictated by the MTs' helical architecture (Figure 1C and
639 Figure 3A and Supporting Information Movie 3a). In
640 metazoans, the general ability of MTs to bear compressive
641 loads imposed by contractile forces translates into a
642 coordinated bending of MTs and to drive a spring-like force
643 mechanism as exemplified with the rhythmically contracting
644 cardiac myocytes.⁵⁴ To interrogate whether the cMTs could
645 transiently store energy upon actomyosin activation and acts as
646 a torsional spring to promote the required thrust for helical
647 propelling, we analyzed the behavior of cMTs during helical
648 motion. Whereas the U-ExM allows nanoscale resolution, it
649 does not permit to affirm that the tachyzoites under
650 observation were actually caught in motion. As under pro-
651 gliding conditions, the tachyzoites displayed a statistically
652 significant elongation of the nucleus as compared to the
653 samples of either extracellular tachyzoites left in IC buffer or
654 tachyzoites which had just invaded host cells ($n > 75$ for each
655 condition, Supporting Information Figure S5A), we used the
656 nucleus sphericity as first criterion. We next selected for
657 tachyzoites associated with helical trails using the surface-
658 exposed glycoprotein SAG1 known as robust trail marker,¹¹
659 which also bore an elongated nucleus ($p < 0.0001$, $n = 12$
660 motile helical and $n = 15$ intracellular) (Supporting
661 Information Figure S5B). To analyze whether individual
662 cMTs could display a specific compression, relaxation and
663 torsion behavior in motile tachyzoites, we applied U-ExM and
664 used both acetylated α -tubulin and antipolyglutamylated
665 α , β -tubulin antibodies which have been widely used for labeling
666 *T. gondii* cMTs.⁵³ When quantifying the curvature of the cMTs

in nonmotile extracellular (Figure 7A, top panel) or nonmotile
intracellular (Supporting Information Figure S5C, top panel)
and motile parasites (Figure 7A, middle panel; Supporting
Information Figure S5C, bottom panel), we observed for the
motile specimens, a highly significant increase in the mean
curvature of the MTs as compared to the nonmotile ones
(Figure 7A, polyglutamylated tubulin, $p < 0.0001$, $n = 57$
nonmotile and $n = 44$ motile parasites) (Supporting
Information Figure S5B,C, acetylated tubulin, $p < 0.0001$, n
 $= 24$ nonmotile and $n = 22$ motile tachyzoites). Importantly,
the curvature amplitude over the length of a single MT was
also significantly enhanced in gliding when compared to
intracellular parasites as assessed by the standard deviation
values of the curvature profile over the full length MTs
(Figure 7A, polyglutamylated tubulin, $p < 0.0001$, Supporting
Information Figure S5B,C, acetylated tubulin, $p < 0.0001$).
The decreased interdistance between single cMT nearby the
apical ring (APR) from where they emanate together with the
observed nonuniform bending over the cMT length strongly
argue for a specific compression occurring at the tachyzoite
apex during cell movement. In addition, situations where the
cMTs straightened at the apical region likely corresponded to
the time of the thrust force occurring upon kink release
(Figure 7A, bottom panel; see also schematics on the right). To further
test the hypothesis of cooperation between the actoMyoA-
based and the cMT-based cytoskeletons could contribute to
force production at the kink, we performed U-ExM imaging of
MyoA and cMTs simultaneously on either motile or nonmotile
tachyzoites. To this end, we used a tachyzoite line that
expresses a chimeric MyoA-HA protein under the endogenous
promoter and anti-HA antibodies. A clear co-alignment of the
MyoA and the cMTs was detected in the apical region of
motile tachyzoites together with a local enrichment in MyoA
when compared to nonmotile parasites (Figure 7B). Although
it is not possible to ascertain that this situation reflects the kink
step, the alignment between the MyoA and the cMTs makes
plausible an indirect connection and thus argue for an energy
transfer between the two cytoskeletons. In addition, this co-
alignment is consistent with the helical path taken by the beads
undergoing actin-based rearward capping. In metazoans cells, it
was found that the MTs were embedded in a viscoelastic
material provided by the surrounding medium and MT-
associated proteins—in particular, kinesin motors⁵⁵ that
influence the MT ability to buckle and bear energy load.⁵⁴
Therefore, it would be worth investigating whether some MT
or/and IMC protein partners - including the APR-associated
kinesin,⁵⁶ proteins that coat the cMT length and alveoli
positioned at the apical flexure site could behave as pro-elastic
elements and thus optimize a cMT driven spring-like reaction.
Of note the intrinsic stable left-handed curvature of
resting cMTs already sign for their ability to withstand
large forces within the cytoplasm in agreement with their
contribution to shape maintenance.^{30,57} As the activation of

720 the actomyosin system translates into force-powering motility,
721 it is plausible that the significant local increase in cMT
722 curvature of motile tachyzoites accounts for higher compres-
723 sive loads on the cMTs in response to the increased
724 contractility. Indeed, when the tachyzoite underwent exacer-
725 bated actomyosin-driven contraction (Figure 4F) in a failed
726 attempt to disengage its base from the adhesion site, the cMT
727 cytoskeleton overcame its bending capacity and eventually
728 broke up.

729 CONCLUSIONS

730 In this study, by combining surface sensitive biophysical
731 techniques with high resolution-high speed 2D and 3D live
732 imaging and expansion microscopy, we provided insights on
733 how the *T. gondii* parasite couples cycles of adhesion–de-
734 adhesion to the substrate with traction and spring-like force
735 generation to achieve helical gliding, a function which is
736 required for perpetuating *T. gondii* populations in the
737 homeothermic hosts. Owing to its persistent structural polarity
738 over the intracellular/extracellular cycles, the tachyzoite
739 bypasses the canonical symmetry break most eukaryotic cells
740 must undergo to start migrating.⁵⁸ In addition, although
741 lacking the typical actomyosin II motor commonly used to
742 generate traction in eukaryotes, *Toxoplasma* has evolved an
743 Apicomplexa-restricted unconventional myosinA motor that,
744 immobilized within the glideosome unit and between the
745 membrane layers forming the pellicle at the cell surface, works
746 on noncanonical actin filaments to activate motility.²⁹ The
747 pellicle and the subtending twisted 22 microtubules provide
748 the tachyzoite with a peculiar crescent shape and flexibility,
749 which has proposed to act as the primary driver of the helical
750 motion. We now demonstrate that the *T. gondii* tachyzoite
751 must engage its apical region in a specific stable adhesion with
752 the substrate that is compatible with the development of a
753 balanced traction force and drives, in turn, the loosening of the
754 posterior contact point, allowing retraction of the parasite base
755 and dragging force. Therefore, similarly to what was found for
756 the *Plasmodium* motile sporozoite, real time analysis of
757 adhesion dynamics and force mapping supported by recently
758 refined high spatiotemporal resolution imaging approaches and
759 biophysics characterization applied to the *Toxoplasma* motile
760 tachyzoite have challenged the classic model of Apicomplexa
761 gliding motility. In addition to the backward capping of
762 adhesion proteins at the cell surface, both parasite rely on a
763 distinct class of adhesive contact that do not enter the rearward
764 flow but directly contribute to build tension in the parasite
765 cytoskeleton and produce force by strengthening anchors
766 points with a specific on–off dynamics, hence regulating the
767 motile process. Although these studies confirm the need to
768 shift paradigm for a comprehensive mechanistic understanding
769 of Apicomplexa gliding motility, they raised key questions on
770 the nanoscale architecture of the singular adhesive platforms
771 including the adhesin ligand identities on the extracellular side,
772 the actin filament organization on the cytoplasmic side, but
773 also how they would transmit tensional forces from the
774 cytoskeleton to the ECM with the yet to clarify contribution of
775 the MyoA motor, and eventually, it would be worth
776 investigating their putative contribution for mechanotransduc-
777 tion. Providing indication of a spatiotemporally regulated
778 cooperation between the tachyzoite actomyoA-based contrac-
779 tile activity and the helical flexible cMT ability to build tension,
780 this study gives credit to pioneered kinematic analysis.¹⁸ These
781 results also highlight the necessity to delve deeper into the

compressive, torsional, and tensile strengths of *Toxoplasma* 782
tachyzoite and also *Plasmodium* sporozoite cMTs as some 783
differences between the two stages could in part account for 784
their specific motile behavior. 785

METHODS/EXPERIMENTAL

Parasite Strain Maintenance and Preparation for All 787
Motility Live Assays. All media and products used for cell culture 788
were from Gibco-Life Technologies (St Aubin, France) unless 789
specified. *T. gondii* strains were propagated on Mycoplasma-free 790
human foreskin fibroblast monolayers (HFFs) and grown in 791
Dulbecco's modified Eagle medium (DMEM) supplemented with 792
glutamax, 10% heat-inactivated fetal calf serum (FCS), penicillin (100 793
U/mL), and streptomycin (100 µg/mL) at 37 °C and 5% CO₂. The 794
laboratory type 1 RH strain was used as well as the YFP-expressing 795
RH¹⁷ and the mutant deleted for the KU80 protein⁵⁹ (gift from V. 796
Carruthers, Michigan University, USA; see Molecular Cloning 797
section). The RH Δku80: DiCre/lox MyoA, RH Δku80: DiCre/ 798
ΔMyoA,⁶⁰ and the RH cbactinEmFP⁴⁹ expressing strains were given 799
by M. Meissner (MLU Munich University, Germany) and hereafter 800
designated LoxMyoA, ΔMyoA, or Ach-E, respectively. For most 801
motility assays, tachyzoites were collected within a few hours 802
following spontaneous egress from the HFF monolayers, and ~10⁵ 803
cells were centrifuged in HBSS⁺⁺ supplemented with 0.2% FCS (0.2% 804
HBSS). The pellet containing parasites was resuspended in 150 µL of 805
1% FCS HBSS (1% HBSS) and adjusted at 1.6 mM of CaCl₂ (1% 806
HBSS-Ca²⁺). Typically, when using the 18 mm diameter glass 807
coverslip fitting chamber, 50 µL of the tachyzoite suspension was 808
added to 100 µL of 1% FCS HBSS-Ca²⁺ covering the coverslip. The 809
amounts of FCS, CaCl₂, and pharmacological reagents were adjusted 810
upon need as described in each appropriate section. 811

Molecular Cloning. A mCherry (mC) tag was fused in frame with 812
the C-terminus of TLAP2 gene (ToxoDb.org, TGGT1_232130) in 813
the Δku80 strain using the ligation independent cloning strategy.⁵⁹ A 814
1.5 kb fragment corresponding to the 3' end of the TLAP2 excluding 815
the stop codon was amplified by PCR with the forward primer 5'- 816
GCGCCCTCCTTCAGTGTTC-3' and reverse primer 5'- 817
TGACCCTGCGGCACCGGCAG-3'. The PCR fragment and 818
vector p-LIC-mCherry-HXG were digested with T4 DNA polymerase 819
and annealed, yielding plasmid pTLAP2mCherry-LIC-DHFR. Freshly 820
egressed Δku80 tachyzoites from a 1/2 T25 flask were transfected 821
with 15 µg of the EcoRV-linearized plasmid. After one cycle without 822
drug, Δku80/TLAP2-mC transformants were selected with 2 µg/mL 823
pyrimethamine and single-cell cloned by limiting dilution. 824

Endogenous tagging of MyoA with HA-tag was achieved using the 825
pLIC-MyoA-HA-HXGPRT vector. To construct this plasmid the 826
coding sequence of MyoA was amplified using primers 5'- 827
TACTTCCAATCCAATTTAGCAAAGCAGCAAAGTCCCA- 828 GCGAAG-
3' and 5'-TCCTCCACTTCCAATTTTAGC- 829
GAACGCCGGTGAACAGTCGCGGG-3' and RH Δku80 genomic 830
DNA as template. The PCR product was cloned to pLIC-mAID-HA- 831
HXGPRT vector using the LIC cloning method as described above.⁶¹ 832
RHku80 OsTir1-(Ty)3 parasites were electroporated with BstBI- 833
linearized plasmid, and recombinant parasites were selected with 834
mycophenolic acid (25 µg/mL) and xanthine (50 µg/mL). Stable 835
transgenic parasites were single-cell cloned by limiting dilution. 836

Video Microscopy. Time-lapse video microscopy was conducted 837
in Chamlide chambers (LCI Corp., Seoul, Korea) accommodating 18 838
mm diameter coverslips or 35 mm MatTek glass bottom dishes 839
(Matek corporation) installed on an Eclipse Ti inverted confocal 840
microscope (Nikon France Instruments, Champigny sur Marne, 841
France) set up with a temperature and CO₂-controlled stage and 842
chamber (LCI Corp., Seoul, Korea). The microscope was equipped 843
with the sCMOS prime camera (Photometrics), a 60× objective, and 844
a CSU X1 spinning disk (Yokogawa, Roper Scientific, Lisses, France). 845
MetaMorph software was used for controlling the microscope 846
(Universal Imaging Corporation, Roper Scientific, Lisses, France). 847
All live microscopy was performed at 37 °C and 5% CO₂. 848

849 Image Processing. For image processing, we combined the use of
850 ImageJ, Icy, MATLAB, ChimeraX, and Amira-Avizo (Thermo-Fisher)
851 software. Details of image processing are included in the appropriate
852 protocol sections. Slow motion videos were created using Adobe
853 Premiere with the optical flow module.

854 Motility Assays in Collagen1 Fibrous Matrices. Collagen gels
855 were made using rat tail type I collagen (CellSystems). Nine parts of
856 collagen dissolved in acidic medium were mixed with 1 part of
857 neutralization solution to reach the concentration of 4 mg/mL and
858 promote matrix formation. All solutions were kept in 4 °C during
859 preparation. Then dilution of the gel at a concentration of 2 mg/mL
860 in HBSS⁺⁺ supplemented with 1% FCS was rapidly spread in the
861 middle of a MatTek glass bottom dish and incubated for 30 min at 37
862 °C and 5% CO₂. Labeling of the collagen fibers was achieved with the
863 recombinant CNA35-EGFP produced in *Escherichia coli* (BL21-DE3
864 strain) used at 2 μM final concentration according to the protocol.³⁵
865 A 50 μL volume of the tachyzoite suspension prepared in 1% FCS
866 HBSS-Ca²⁺ was deposited on top of the gel prior to being transferred
867 in the microscopy stage for video microscopy. Once tachyzoites had
868 penetrated within the mesh, images were captured at 1 frame/s. For
869 tracking the fibers during parasite navigation, we used Icy and
870 visualized with green the initial position of the fibers at $t = 0$ s while
871 we duplicated this frame as many times as the number of the time-
872 lapse frames. Then we merged this “time zero” stack with the original
873 time lapse in which the fibers were colored in magenta. The whitish
874 color accounts for the green and magenta overlay and indicates no
875 displacement, whereas the detection of the green and magenta reveals
876 the fiber displacement during the sequence.

877 Tachyzoite 2D Gliding Assays. Parasites were prepared as
878 described above, and assays were carried on 18 mm plasma-activated
879 glass coverslips coated with either fibronectin (20–50 μg/mL in
880 phosphate-buffered saline (PBS)) or poly-L-lysine (150–300 kDa
881 PLL, 50 μg/mL in PBS). Image analysis included tracking the
882 tachyzoite back and front parts over the gliding time by using Icy as
883 described.⁶² “Manual tracking” and “Motion profiler” plugins were
884 used to extract the $x-y$ position of the back and front spots over time.
885 Having tracked the $x-y$ positions over time, we used the “Distance
886 profiler” plugin to calculate the distance between the two positions
887 (back and front) over time.

888 Reflection Interference Contrast Microscopy. RICM images
889 were acquired on an inverted microscope (IX71, Olympus) on which
890 a white-light source (HPLS 345, Thorlabs) was coupled using a
891 home-built illumination arm incorporating a diaphragm (SM1D12C,
892 Thorlabs) controlling the illumination numerical aperture (NA = 0.46
893 in all experiments shown here) and a triple-band spectral filter (FF01-
894 457/530/628-25, Semrock) as described.⁶³ The usual fluorescence
895 cube in the microscope turret was replaced by polarization optics,
896 allowing separation of the incoming and reflected light (polarizer
897 WP25M-VIS, Thorlabs), polarizing beamsplitter cube (PBS251,
898 Thorlabs), and achromatic imaging flat quarter waveplate (QWP;
899 custom-made, Fichou, France). The sample was imaged with an oil-
900 immersion objective (60XO UPLSApo, Olympus, Japan) onto a
901 sCMOS camera (Orca Flash 4 v2, Hamamatsu) after passing through
902 an autofocus device (CRISP system, ASI imaging, USA) and a home-
903 built image-splitting setup incorporating a variable slit (VA100/M,
904 Thorlabs), achromatic relay lenses (ITL200, Thorlabs), imaging flat
905 dichroic mirrors (FF484-FDi01-25X36 and FF560-FDi01-25X36,
906 Semrock) gently held through curable silicon paste (Sugru, Form-
907 Form, UK), silver mirrors (PFSQ10-03-P01, Thorlabs) and
908 dichroic filters (blue: Semrock FF01-452/45-25; green: FF01-531/46-
909 25; red: FF01-629/56-25, Semrock). In addition, for bright-field (BF)
910 imaging, a red colored glass filter (FGL610S, Thorlabs) was used to
911 filter the light for the microscope illumination arm that was
912 subsequently focused by a long-distance 0.3 NA condenser (all
913 Olympus, Japan). BF and RICM images were acquired simulta-
914 neously, in the red channel, and thus show a dim RICM image
915 superimposed. Finally, a custom-built thermostated box (Digital Pixel,
916 UK) enclosing most of the microscope was used to control the
917 temperature at the sample. Image processing was done using ImageJ.
918 Blue, green, and red stacks of images were first manually registered.

RICM images were subsequently filtered using the “FFT band-pass 919
filter” plugin (1–100 pixels) to remove high-frequency noise and 920
uneven illumination background. The two (in the case of 921
simultaneous BF/RICM imaging) or three (in the case of only 922
RICM imaging) RICM images were then superimposed and 923
converted into a RGB image. BF images and RGB RICM images 924
were then segmented using the “trainable Weka segmentation” 925
plugin.⁶⁴ For BF images, the classifier was trained to segment the 926
whole parasite, and the outline of the resulting binary image was 927
extracted subsequently. For RICM images, the algorithm was used to 928
separate the “close contact” area defined by the first dark RICM fringe 929
on the parasite surface, the trail (when relevant), the rest of the RICM 930
signal coming from the parasite (when no BF image was present), and 931
the rest of the image. Because the classifier could detect the second 932
dark RICM fringe manual correction of the segmented images was 933
performed afterward to remove incorrect areas classified as “close 934
contact”. A binary image was obtained for the “close contact” area, 935
whereas an 8-bit probability image was extracted for the trail. Analysis 936
of the processed images was also performed using ImageJ. The 937
kymograph was obtained using the plugin “KymoResliceWide”. For 938
measuring the speed of the parasite back end, the corresponding white 939
line on the kymograph was isolated and the positions of the pixels 940
were exported to Origin. After smoothing, the position curve was 941
derived to obtain the velocity of the back end over time. 942

943 Traction Force Microscopy. TFM setting was adapted from ref 944
65. The 2 kPa PAA gels were made and mixed with TFM beads 945
(FluoSpheres carboxylate-modified microspheres, ThermoFisher 946
Scientific, 0.2 μm dark red fluorescent, λ: 660/680, 2% solid). The 947
gel was top-coated with fibronectin (20 μg/mL, 30 min, 23 °C) 948
diluted in sodium bicarbonate pH 8.3 (100 mM). Typical samples 949
were made from stocks of 0.7 μL beads mixed in 165 μL of gel 950
supplemented with 1 μL of both tetramethylethylenediamine 951
(TEMED) and ammonium persulfate (APS) 10% using 20 μL of 952
bead-gel suspension for an 18 mm diameter silanized glass coverslip. 953
A 50 μL volume of the tachyzoite suspension prepared in 1% HBSS- 954
Ca²⁺ (see above) was deposited on top of the fibronectin-coated PAA 955
gel already filled with 100 μL of 1% HBSS-Ca²⁺ in the appropriate 956
chamber and video recording started upon tachyzoite contact with the 957
substrate. MetaMorph streaming option was used for fast recording 958
(<1 frame/s) in both the DIC and far-red channels. Analysis of the 959
TFM beads displacement for extracting the force values carried out 960
using MATLAB. The TFM bead displacement was assessed using as a 961
reference bead position, the frame with a gel area free of parasite (*i.e.*, 962
relaxed position of the gel). Then using the frames taken over time, 963
the bead's displacement was tracked from their initial relaxed position. 964
To check the tachyzoite gliding behavior on a substrate of different 965
stiffness, gels of different PAA concentration and coated with a layer 966
of fibronectin were made using the same protocol, omitting the bead 967
addition step, and the stiffness was controlled by atomic force 968
microscopy. 969

970 Micropatterned Devices. Micropatterned PEG-fibronectin 971
composite coverslips were engineered by Alveole using the PRIMO 972
patterning with specific area coated with a mix of fibronectin (100 μg/ 973
mL) and AlexaFluor647-coupled fibrinogen (10 μg/mL) and other 974
coated with PLL-PEG. Fifty microliters of the tachyzoite suspension 975
prepared in 1% HBSS-Ca²⁺ was deposited on top of the fibronectin- 976
coated glass coverslip placed in the chamber and pre-filled with 100 μL 977
of buffer prior to video microscopy. 978

979 Rear-Blocked Parasite Assay. The 0.2 μm diameter beads 980
(FluoSpheres carboxylate-modified microspheres, ThermoFisher 981
Scientific F8807, λ: 660/680, 2% solid) were activated using the 982
microsphere coupling—two-step EDC/Sulfo NHS covalent coupling 983
procedure for Estapor carboxyl-modified dyed microspheres protocol 984
(MerckMillipore). Fifty microliters of the stock-activated bead 985
solution was diluted in 150 μL of MES buffer (50 mM, pH 6.0). 986
Then 30 μL of the bead solution was added to 120 μL of the 987
tachyzoite suspension in 0.15% FCS HBSS⁺⁺ (0.15% HBSS). Fifty 988
microliters of the parasite suspension (from either the RHΔKu80, 989
ΔMyoA, RHΔKu80AcB-E, or YFP tachyzoite lines) was deposited on 990
the (50 μg/mL) fibronectin-coated glass coverslips in the microscopy 991
992

989 chamber, which was already filled with 200 μL of 0.15% HBSS⁺⁺. In
990 some experiments, parasites were preincubated for 10 min with 0.5 or
991 1 μM of either jasplakinolide or cytochalasin D (Sigma) and video-
992 recorded in the presence of the compounds. For the intracellular
993 mimicking conditions, tachyzoites collected by centrifugation in
994 0.15% HBSS⁺⁺ were rinsed in ENDO buffer referred to here as IC
995 buffer (145 mM KCl; 5 mM NaCl; 1 mM MgCl_2 ; 15 mM MES; 15
996 mM HEPES; pH 8.3)⁶⁶ before use, and the activated beads were
997 prepared in IC buffer. The mixture prepared as mentioned above was
998 deposited on the microscopy chamber, which was pre-filled with 200
999 μL of IC buffer. Images were acquired at 1 s intervals for 20 min. To
1000 describe the contractile potential of tachyzoites under each
1001 experimental condition, we calculated the contraction ratio by
1002 measuring two times the length of the parasite body starting from
1003 the back until its farther apical point but excluding the conoid to avoid
1004 false measurements in case of fluctuating extrusion. The first measure
1005 corresponded to the relaxed position and the second to the maximal
1006 contraction. Division of the relaxed versus the contracted length
1007 provided the contraction ratio. When needed, both DIC and
1008 fluorescence channels were recorded at ~ 1 frame/s.

1009 **Bead Flow Assays.** The assay was performed similarly to the rear
1010 blocked parasite assay. For tracking the beads, visualizing their tracks
1011 and extracting their speed, "Spot detector" and "Track manager"
1012 plugins (Icy) were used.

1013 **Expansion Microscopy.** To analyze gliding tachyzoites, we
1014 collected the parasites in either in prewarmed 1% FCS HBSS-Ca²⁺
1015 or IC buffer, which were centrifuged at low speed to synchronize their
1016 sedimentation and left to glide for 10 min on PLL (50 $\mu\text{g}/\text{mL}$)-coated
1017 plasma-activated glass coverslips (37 $^\circ\text{C}$, 5% CO_2). Gliding was
1018 stopped by addition of paraformaldehyde (PFA, 3.2%, 15 min). The
1019 tachyzoite surface and trails were immunolabeled with anti-TgPSAG1
1020 antibodies (mAb, clone TP3), and the chimeric TLAP2 protein was
1021 detected using the rabbit anti-mCherry antibodies (Institut Curie,
1022 TAb-IP Paris, France) directed against the mC tag after cell
1023 permeabilization with TritonX-100 (0.1% in PBS, 5 min). The
1024 samples were next incubated with appropriate secondary highly cross-
1025 adsorbed antibodies (4 $\mu\text{g}/\text{mL}$, 2h). The ExM protocol was adapted
1026 from ref 45. Briefly Acryloyl-X was used at 0.1 mg/mL PBS for 2 h at
1027 23 $^\circ\text{C}$ prior to the gelation step, which was performed by placing the
1028 gelation solution (80 μL) on parafilm and the coverslip with the cell
1029 sample face down on top of it. Gelation was allowed to proceed at 37
1030 $^\circ\text{C}$ for 1 h followed by the digestion step (0.5% Triton X-100, 8 units/
1031 mL Proteinase K) carried out overnight at 23 $^\circ\text{C}$. A 4 mm diameter gel
1032 core sample was collected with a puncher and immersed in 5 mL of
1033 ddH₂O in a 50 mm diameter Petri dish to promote expansion, while
1034 PI staining was concomitantly performed (2.5 μM in PBS). H₂O was
1035 exchanged every 20 min until maximal expansion. The piece of gel
1036 was next gently transferred onto a PLL-coated glass coverslip in the
1037 minimal liquid volume to avoid gel drift. The 0.2 μm Z-image stacks
1038 of parasites in stages were captured using a spinning disk confocal
1039 Eclipse-ti Nikon microscope.

1040 **Ultrastructure Expansion Microscopy.** Gliding assays were
1041 performed with RH Δ Ku80MyoA-HA similarly to that for ExM.
1042 Additionally, for the invasion assay, HFF cells were plated on a poly-L-
1043 lysine-coated glass coverslip to obtain 80% cell confluence on the
1044 following day. Parasites were settled on top of the cells by gentle
1045 centrifugation (2 min, 250g) and left to invade for 1 h (37 $^\circ\text{C}$, 5%
1046 CO_2). For U-ExM, we followed the protocol developed by the
1047 Guichard laboratory,⁵² but to optimally preserve both free and
1048 intracellular tachyzoite shapes, we found it better to fix the samples
1049 before expansion in a solution made of 0.7% formaldehyde and 1%
1050 acrylamide in PBS (4–5 h, 37 $^\circ\text{C}$). Next, similar to the ExM protocol,
1051 gelation was carried out for 1 h (37 $^\circ\text{C}$). Coverslips with gels were
1052 then transferred into ~ 2 mL of the denaturation buffer in a 6-well
1053 plate for 15 min (23 $^\circ\text{C}$). Gels were removed from the coverslips with
1054 tweezers and transferred to a 35 mm diameter glass Petri dish filled
1055 fresh denaturation buffer for a 60 min incubation at 95 $^\circ\text{C}$. After
1056 denaturation, gels were placed in a 150 mm diameter glass Petri dish
1057 filled with ddH₂O for the first expansion. Water was exchanged at
1058 least twice every 30 min at room temperature, and gels were

incubated overnight in ddH₂O. After limited shrinkage in PBS, several
1059 4 mm diameter pieces of gel were collected and deposited on 24-well
1060 plates. Gels were then incubated for 3 h at 37 $^\circ\text{C}$ under shaking in
1061 primary antibodies (antiacetylated α -tubulin, mAb, clone 6-11B-1) or
1062 rabbit α -polyglutamylated (mAb, clone GT335) and rat anti-HA
1063 antibodies (mAb, clone 3F10). Gels were washed in PBS-Tween 0.1%
1064 prior to incubation with appropriate secondary highly cross-adsorbed
1065 antibodies (4 $\mu\text{g}/\text{mL}$) for 150 min at 37 $^\circ\text{C}$ and washed again in PBS-
1066 Tween 0.1%. Expansion was achieved by controlled immersion in
1067 ddH₂O. The PI staining, final ddH₂O wash, and gel mounting steps
1068 were all performed as mentioned for ExM. 1069

1070 **ExM and U-ExM Image Processing.** 3D reconstruction was
1071 achieved with the UCSF ChimeraX software from the raw data (*i.e.*,
1072 xyz files) processed with ImageJ to first crop the region of interest and
1073 then to apply the "Iterative Deconvolve 3D" plugin for each channel.
1074 We used the ImageJ "3D Object counter" plugin to check for the
1075 isotropic physical expansion of the specimen by comparing the ratio
1076 of the parasite (SAG1 staining) and the nucleus (PI staining) volumes
1077 in controlled and expanded extracellular tachyzoite samples. The
1078 nucleus sphericity index of motile, nonmotile, and intracellular
1079 tachyzoites was compared by thresholding each image object to create
1080 3D binary images, whereas the "3D Object counter" plugin was next
1081 used to segment Z-stack binary images and retrieve the volume and
1082 surface of the 3D objects (*i.e.*, parasite nucleus and whole body). The
1083 sphericity index was calculated using the formula where V is the
1084 volume and S the surface:

$$\text{sphericity } \Psi = \frac{(36\pi V^2)^{1/3}}{S}$$

The nucleus roundness was obtained by thresholding a Z-Max
1085 projection from the Z-stack images and using the "Particle analysis"
1086 plugin. 1087

1088 For the tubulin curvature analysis in expanded specimens, we used
1089 the "Kappa" plugin in Fiji on the Z-Max projection from Z-stack
1090 images of the tachyzoite ventral cMTs (*i.e.*, facing the substrate),
1091 which allowed tracing each MT shape and retrieving the mean
1092 curvature of each cMT as well as the curvature amplitude over the
1093 cMT length (standard deviation). 1093

1094 **MIC2 and SAG1 Analysis in Helical Trail.** Extracellular
1095 tachyzoites were let to glide for 15 min prior to be fixed with PFA
1096 as described in the ExM section. A double immunolabeling was
1097 performed sequentially using the anti-TgSAG1 protein (clone TP3,
1098 30 min, 23 $^\circ\text{C}$) and the anti-TgMIC2 (clone 6D10, overnight, 4 $^\circ\text{C}$)
1099 as primary antibodies, each followed by incubation with appropriate
1100 secondary highly cross-adsorbed antibodies (4 $\mu\text{g}/\text{mL}$, 2 h). Images
1101 were acquired on the Axio Imager Z1 Zeiss microscope using the
1102 Zeiss imaging software ZEN before being processed using Fiji
1103 software. 1103

1104 To determine the size and position of the adhesion point formed at
1105 the early step of the helical cycle (*i.e.*, coinciding with the kink) on the
1106 MIC2/SAG1 immunolabeled trails, we used the machine-learning-
1107 based segmentation of the real-time RICM sequence as a template.
1108 The region of interest for the trail trajectory, the angular area, and the
1109 parasite apical adhesion area were defined manually with Fiji: the
1110 distance between the center of adhesion point and the angle point was
1111 measured for six angles over a sequence of successive helical cycles,
1112 which allowed positioning the apical adhesion at about +0.170 μm
1113 downstream the angle point, and the size of the adhesion point was
1114 estimated around 0.5 μm . Applying these values on the MIC2/SAG1
1115 labeled trails, it was possible to accurately identify the adhesion and
1116 angle area over the profiles of fluorescence intensity measured for the
1117 whole trails trajectories that in total defined 40 helical cycles
1118 performed by eight tachyzoites. The fluorescence intensity is given as
1119 a ratio by normalizing on the mean intensity value. 1119

1120 **Quantification and Statistical Analysis.** Data were statistically
1121 analyzed, and plots were made using GraphPad Prism 6.0 software for
1122 Windows (La Jolla, CA, USA). Data are presented as mean \pm
1123 standard error of mean if not indicated otherwise. Figure legends
1124 include the statistical test and resulting comparison when appropriate. 1124

1125 For Figure 4A, Figure 7A, and Figures S3A and S5B,C, an unpaired *t*
 1126 test was used with significance being represented as a *p* value <0.05,
 1127 and the *n* indicated represents the parasite sample size or the number
 1128 of individual microtubules analyzed. For Figure 4E, Figure 5A, and
 1129 Figure S5A, an unpaired Kruskal–Wallis test was performed, and the
 1130 *n* indicates the sample size. For the table in Figure 5A, a chi-square
 1131 test followed by Fisher's exact test was used, with the *n* showing the
 1132 proportions analyzed.

1133 ASSOCIATED CONTENT

1134 [✉] Supporting Information

1135 The Supporting Information is available free of charge at
 1136 <https://pubs.acs.org/doi/10.1021/acsnano.0c01893>.

1137 Helical and circular gliding by *T. gondii* tachyzoites;
 1138 tachyzoite apical adhesion site is not enriched in MIC2
 1139 and SAG1 proteins; frequency and duration of *T. gondii*
 1140 tachyzoite gliding behavior depends on the substrate
 1141 stiffness; prolonged and exacerbated contraction induced
 1142 upon tachyzoite posterior immobilization leads to
 1143 membrane leakage; expansion microscopy allows un-
 1144 covering cMT local selective compression and torsion in
 1145 gliding tachyzoites (PDF)
 1146 Movie 1: Parasite moving in 3D collagen fibers1 (AVI)
 1147 Movie 2: Parasite moving 3D collagen fibers2 (AVI)
 1148 Movie 3a: Parasite helical gliding in 2D (AVI)
 1149 Movie 3b: Slow motion but same as movie 3a (AVI)
 1150 Movie 4: Parasite circular gliding in 2D (AVI)
 1151 Movie 5: RICM analysis of parasite helical gliding (AVI)
 1152 Movie 6: RICM-pulling on or breaking the trail (AVI)
 1153 Movie 7a: TFM analysis of parasite helical gliding (AVI)
 1154 Movie 7b: Slow motion but same as movie 7a (AVI)
 1155 Movie 8: Parasite helical gliding on micropattern
 1156 Alveole1 (AVI)
 1157 Movie 9: Parasite helical gliding micropattern Alveole2
 1158 (AVI)
 1159 Movie 10: Parasite base blocked by microbeads (AVI)
 1160 Movie 11: Bead release from the base of a moving
 1161 parasite (AVI)
 1162 Movie 12: Parasite contraction in the presence of drugs
 1163 (AVI)
 1164 Movie 13: Actin dynamics in gliding or immobilized
 1165 parasites (AVI)
 1166 Movie 14: Bead flow and bead release in tachyzoites
 1167 (AVI)

1168 AUTHOR INFORMATION

1169 Corresponding Author

1170 Isabelle Tardieux – *Institute for Advanced Biosciences (IAB),*
 1171 *Team Membrane Dynamics of Parasite–Host Cell Interactions,*
 1172 *CNRS UMR5309, INSERM U1209, Université Grenoble*
 1173 *Alpes, 38700 Grenoble, France;* [orcid.org/0000-0002-](https://orcid.org/0000-0002-5677-7463)
 1174 [5677-7463](https://orcid.org/0000-0002-5677-7463); Email: isabelle.tardieux@inserm.fr

1175 Authors

1176 Georgios Pavlou – *Institute for Advanced Biosciences (IAB),*
 1177 *Team Membrane Dynamics of Parasite–Host Cell Interactions,*
 1178 *CNRS UMR5309, INSERM U1209, Université Grenoble*
 1179 *Alpes, 38700 Grenoble, France*
 1180 Bastien Touquet – *Institute for Advanced Biosciences (IAB),*
 1181 *Team Membrane Dynamics of Parasite–Host Cell Interactions,*
 1182 *CNRS UMR5309, INSERM U1209, Université Grenoble*
 1183 *Alpes, 38700 Grenoble, France*

Luis Vigetti – *Institute for Advanced Biosciences (IAB), Team* 1184
Membrane Dynamics of Parasite–Host Cell Interactions, CNRS 1185
UMR5309, INSERM U1209, Université Grenoble Alpes, 1186
38700 Grenoble, France 1187
 Patricia Renesto – *Institute for Advanced Biosciences (IAB),* 1188
Team Membrane Dynamics of Parasite–Host Cell Interactions, 1189

CNRS UMR5309, INSERM U1209, Université Grenoble 1190
Alpes, 38700 Grenoble, France; TIMC-IMAG UMR 5525 - 1191
UGA CNRS, 38700 Grenoble, France 1192

Alexandre Bougdour – *Institute for Advanced Biosciences* 1193
(IAB), Team Host–Pathogen Interactions & Immunity to 1194
Infections, CNRS UMR5309, INSERM U1209, Université 1195
Grenoble Alpes, 38700 Grenoble, France 1196

Delphine Debarre – *Laboratoire Interdisciplinaire de Physique,* 1197
UMR CNRS, 5588, Université Grenoble Alpes, Grenoble 1198
38402, France 1199

Martial Balland – *Laboratoire Interdisciplinaire de Physique,* 1200
UMR CNRS, 5588, Université Grenoble Alpes, Grenoble 1201
38402, France 1202

Complete contact information is available at: 1203
<https://pubs.acs.org/doi/10.1021/acsnano.0c01893> 1204

Author Contributions

Conceptualization, I.T., M.B, G.P; Software, M.B., D.D, G.P.; 1205
 Formal Analysis, G.P., B.T., D.D, L.V.; Funding acquisition, 1206
 I.T.; Investigation; G.P., B.T., I.T., V.L., D.D., P.R., A.B.; 1207
 Methodology, I.T., G.P., B.T., A.B.; Project administration, 1208
 I.T.; Supervision, I.T., M.B., P.R.; Validation, I.T., G.P., M.B., 1209
 D.D.; Visualization, G.P., B.T., L.V.; Writing—original draft, 1210
 I.T. Writing—review and editing, I.T., G.P., P.R., A.B., M.B., 1211
 D.D. 1212

Funding

This work has been funded by the IAB department 1215
 “Prevention and Therapy of Chronic Diseases (Grenoble, 1216
 France) with an internal grant. The University Grenoble-Alpes 1217
 and the Fondation pour la Recherche Médicale (FRM 1218
 FDT201904008408) awarded to G.P. with a 3 year Ph.D. 1219
 fellowship and 6 month Ph.D. extension fellowship, respec- 1220
 tively. 1221

Notes

The authors declare no competing financial interest. 1222

ACKNOWLEDGMENTS

We thank T. Boudou for help with the collagen gels, T. 1225
 Andersen, V. Petrolli, and A. Ruppel for help in setting and 1226
 analyzing the TFM assays. They all belong to the Laboratoire 1227
 Interdisciplinaire de Physique, UMR CNRS, 5588, Université 1228
 Grenoble Alpes, France. We thank C. Guilluy for the AFM 1229
 assays to probe gels, M. Bogeda for help in micropatterning 1230
 (IAB, Grenoble), and the Alveole team for providing the 1231
 composite micropatterns. We thank the therapeutic antibodies 1232
 (Tab-IP) and recombinant antibodies platform from the Curie 1233
 Institute, Paris, France for providing the anti-mCherry 1234
 antibodies. 1235

REFERENCES

- 1236 (1) Scarpa, E.; Mayor, R. Collective Cell Migration in Development. 1237
J. Cell Biol. 2016, 212, 143–155. 1238
- 1239 (2) Friedl, P.; Weigelin, B. Interstitial Leukocyte Migration and 1239
 Immune Function. *Nat. Immunol.* 2008, 9, 960–969. 1240
- 1241 (3) Tschumperlin, D. J. Fibroblasts and the Ground They Walk On. 1241
Physiology 2013, 28, 380–390. 1242

- 1243 (4) Raftopoulos, M.; Hall, A. Cell Migration: Rho GTPases Lead
1244 the Way. *Dev. Biol.* 2004, *265*, 23–32.
- 1245 (5) Gardel, M. L.; Schneider, I. C.; Aratyn-Schaus, Y.; Waterman, C.
1246 M. Mechanical Integration of Actin and Adhesion Dynamics in Cell
1247 Migration. *Annu. Rev. Cell Dev. Biol.* 2010, *26*, 315–333.
- 1248 (6) Yamada, K. M.; Sixt, M. Mechanisms of 3D Cell Migration. *Nat.*
1249 *Rev. Mol. Cell Biol.* 2019, *20*, 738–752.
- 1250 (7) Petrie, R. J.; Koo, H.; Yamada, K. M. Generation of
1251 Compartmentalized Pressure by a Nuclear Piston Governs Cell
1252 Motility in a 3D Matrix. *Science* 2014, *345*, 1062–1065.
- 1253 (8) Copos, C. A.; Walcott, S.; del Álamo, J. C.; Bastounis, E.;
1254 Mogilner, A.; Guy, R. D. Mechanosensitive Adhesion Explains
1255 Stepping Motility in Amoeboid Cells. *Biophys. J.* 2017, *112*, 2672–
1256 2682.
- 1257 (9) Robert-Gangneux, F.; Darde, M.-L. Epidemiology of and
1258 Diagnostic Strategies for Toxoplasmosis. *Clin. Microbiol. Rev.* 2012,
1259 *25*, 264–296.
- 1260 (10) Tardieux, I.; Baum, J. Reassessing the Mechanics of Parasite
1261 Motility and Host-Cell Invasion. *J. Cell Biol.* 2016, *214*, 507–515.
- 1262 (11) Håkansson, S.; Morisaki, H.; Heuser, J.; Sibley, L. D. Time-
1263 Lapse Video Microscopy of Gliding Motility in *Toxoplasma Gondii*
1264 Reveals a Novel, Biphasic Mechanism of Cell Locomotion. *Mol. Biol.*
1265 *Cell* 1999, *10*, 3539–3547.
- 1266 (12) Amino, R.; Thiberge, S.; Martin, B.; Celli, S.; Shorte, S.;
1267 Frischknecht, F.; Mearl, R. Quantitative Imaging of *Plasmodium*
1268 Transmission from Mosquito to Mammal. *Nat. Med.* 2006, *12*, 220–
1269 224.
- 1270 (13) Münter, S.; Sabass, B.; Selhuber-Unkel, C.; Kudryashev, M.;
1271 Hegge, S.; Engel, U.; Spatz, J. P.; Matuschewski, K.; Schwarz, U. S.;
1272 Frischknecht, F. *Plasmodium* Sporozoite Motility Is Modulated by the
1273 Turnover of Discrete Adhesion Sites. *Cell Host Microbe* 2009, *6*, 551–
1274 562.
- 1275 (14) Frischknecht, F.; Matuschewski, K. *Plasmodium* Sporozoite
1276 Biology. *Cold Spring Harbor Perspect. Med.* 2017, *7*, a025478.
- 1277 (15) Amino, R.; Giovannini, D.; Thiberge, S.; Gueirard, P.; Boisson,
1278 B.; Dubremetz, J.-F.; Prévost, M.-C.; Ishino, T.; Yuda, M.; Mearl, R.
1279 Host Cell Traversal Is Important for Progression of the Malaria
1280 Parasite through the Dermis to the Liver. *Cell Host Microbe* 2008, *3*,
1281 88–96.
- 1282 (16) Kan, A.; Tan, Y.-H.; Angrisano, F.; Hanssen, E.; Rogers, K. L.;
1283 Whitehead, L.; Mollard, V. P.; Cozijnsen, A.; Delves, M. J.; Crawford,
1284 S.; Sinden, R. E.; McFadden, G. I.; Leckie, C.; Bailey, J.; Baum, J.
1285 Quantitative Analysis of *Plasmodium* Ookinete Motion in Three
1286 Dimensions Suggests a Critical Role for Cell Shape in the
1287 Biomechanics of Malaria Parasite Gliding Motility. *Cell. Microbiol.*
1288 2014, *16*, 734–750.
- 1289 (17) Bichet, M.; Joly, C.; Hadj Henni, A.; Guilbert, T.; Xemard, M.;
1290 Tafani, V.; Lagal, V.; Charras, G.; Tardieux, I. The *Toxoplasma*-Host
1291 Cell Junction Is Anchored to the Cell Cortex to Sustain Parasite
1292 Invasive Force. *BMC Biol.* 2014, *12*, 773.
- 1293 (18) Frixione, E.; Mondragón, R.; Meza, I. Kinematic Analysis of
1294 *Toxoplasma Gondii* Motility. *Cell Motil. Cytoskeleton* 1996, *34*, 152–
1295 163.
- 1296 (19) Leung, J. M.; Rould, M. A.; Konradt, C.; Hunter, C. A.; Ward,
1297 G. E. Disruption of TgPHIL1 Alters Specific Parameters of
1298 *Toxoplasma Gondii* Motility Measured in a Quantitative, Three-
1299 Dimensional Live Motility Assay. *PLoS One* 2014, *9*, No. e85763.
- 1300 (20) Carruthers, V. B.; Tomley, F. M. Receptor-Ligand Interaction
1301 and Invasion: Microneme Proteins in Apicomplexans. *Subcell Biochem*
1302 2008, *47*, 33–45.
- 1303 (21) Lagal, V.; Binder, E. M.; Huynh, M.-H.; Kafsack, B. F. C.;
1304 Harris, P. K.; Diez, R.; Chen, D.; Cole, R. N.; Carruthers, V. B.; Kim,
1305 K. *Toxoplasma Gondii* Protease TgSUB1 Is Required for Cell Surface
1306 Processing of Micronemal Adhesive Complexes and Efficient
1307 Adhesion of Tachyzoites: TgSUB1 Microneme Protein Processing.
1308 *Cell. Microbiol.* 2010, *12*, 1792–1808.
- 1309 (22) Opitz, C.; Soldati, D. The Glideosome: A Dynamic Complex
1310 Powering Gliding Motion and Host Cell Invasion by *Toxoplasma*
1311 *Gondii*. *Mol. Microbiol.* 2002, *45*, 597–604.
- (23) Fréal, K.; Dubremetz, J.-F.; Lebrun, M.; Soldati-Favre, D. 1312
Gliding Motility Powers Invasion and Egress in Apicomplexa. *Nat.* 1313
Rev. Microbiol. 2017, *15*, 645–660. 1314
- (24) Andenmatten, N.; Egarter, S.; Jackson, A. J.; Jullien, N.; 1315
Herman, J.-P.; Meissner, M. Conditional Genome Engineering in 1316
Toxoplasma Gondii Uncovers Alternative Invasion Mechanisms. *Nat.* 1317
Methods 2013, *10*, 125–127. 1318
- (25) Bichet, M.; Touquet, B.; Gonzalez, V.; Florent, I.; Meissner, 1319
M.; Tardieux, I. Genetic Impairment of Parasite Myosin Motors 1320
Uncovers the Contribution of Host Cell Membrane Dynamics to 1321
Toxoplasma Invasion Forces. *BMC Biol.* 2016, *14*, 97. 1322
- (26) Graindorge, A.; Fréal, K.; Jacot, D.; Salamun, J.; Marq, J. B.; 1323
Soldati-Favre, D. The Conoid Associated Motor MyoH Is 1324
Indispensable for *Toxoplasma Gondii* Entry and Exit from Host 1325
Cells. *PLoS Pathog.* 2016, *12*, No. e1005388. 1326
- (27) Morrisette, N. S.; Sibley, L. D. Cytoskeleton of Apicomplexan 1327
Parasites. *Microbiol. Mol. Biol. Rev.* 2002, *66*, 21–38. 1328
- (28) Fréal, K.; Polonais, V.; Marq, J.-B.; Stratmann, R.; Limenitakis, 1329
J.; Soldati-Favre, D. Functional Dissection of the Apicomplexan 1330
Glideosome Molecular Architecture. *Cell Host Microbe* 2010, *8*, 343– 1331
357. 1332
- (29) Mueller, C.; Graindorge, A.; Soldati-Favre, D. Functions of 1333
Myosin Motors Tailored for Parasitism. *Curr. Opin. Microbiol.* 2017, 1334
40, 113–122. 1335
- (30) Liu, J.; He, Y.; Benmerzouga, I.; Sullivan, W. J.; Morrisette, N. 1336
S.; Murray, J. M.; Hu, K. An Ensemble of Specifically Targeted 1337
Proteins Stabilizes Cortical Microtubules in the Human Parasite 1338
Toxoplasma Gondii. *Mol. Biol. Cell* 2016, *27*, 549–571. 1339
- (31) Quadt, K. A.; Streichfuss, M.; Moreau, C. A.; Spatz, J. P.; 1340
Frischknecht, F. Coupling of Retrograde Flow to Force Production 1341
During Malaria Parasite Migration. *ACS Nano* 2016, *10*, 2091–2102. 1342
- (32) Whitelaw, J. A.; Latorre-Barragan, F.; Gras, S.; Pall, G. S.; 1343
Leung, J. M.; Heaslip, A.; Egarter, S.; Andenmatten, N.; Nelson, S. R.; 1344
Warshaw, D. M.; Ward, G. E.; Meissner, M. Surface Attachment, 1345
Promoted by the Actomyosin System of *Toxoplasma Gondii* Is 1346
Important for Efficient Gliding Motility and Invasion. *BMC Biol.* 1347
2017, *15*, 1. 1348
- (33) Tosetti, N.; Dos Santos Pacheco, N.; Soldati-Favre, D.; Jacot, 1349
D. Three F-Actin Assembly Centers Regulate Organelle Inheritance, 1350
Cell-Cell Communication and Motility in *Toxoplasma gondii*. *eLife* 1351
2019, *8*, e42669. 1352
- (34) Mouw, J. K.; Ou, G.; Weaver, V. M. Extracellular Matrix 1353
Assembly: A Multiscale Deconstruction. *Nat. Rev. Mol. Cell Biol.* 2014, 1354
15, 771–785. 1355
- (35) Aper, S. J. A.; van Spreeuwel, A. C. C.; van Turnhout, M. C.; 1356
van der Linden, A. J.; Pieters, P. A.; van der Zon, N. L. L.; de la 1357
Rambelje, S. L.; Bouten, C. V. C.; Merckx, M. Colorful Protein-Based 1358
Fluorescent Probes for Collagen Imaging. *PLoS One* 2014, *9*, 1359
No. e114983. 1360
- (36) Ejigiri, I.; Ragheb, D. R. T.; Pino, P.; Coppi, A.; Bennett, B. L.; 1361
Soldati-Favre, D.; Sinnis, P. Shedding of TRAP by a Rhomboid 1362
Protease from the Malaria Sporozoite Surface Is Essential for Gliding 1363
Motility and Sporozoite Infectivity. *PLoS Pathog.* 2012, *8*, 1364
No. e1002725. 1365
- (37) Huynh, M.-H.; Carruthers, V. B. *Toxoplasma* MIC2 Is a Major 1366
Determinant of Invasion and Virulence. *PLoS Pathog.* 2006, *2*, 1367
No. e84. 1368
- (38) Gras, S.; Jackson, A.; Woods, S.; Pall, G.; Whitelaw, J.; Leung, J. 1369
M.; Ward, G. E.; Roberts, C. W.; Meissner, M. Parasites Lacking the 1370
Micronemal Protein MIC2 Are Deficient in Surface Attachment and 1371
Host Cell Egress, but Remain Virulent *In Vivo*. *Wellcome Open Res.* 1372
2017, *2*, 32. 1373
- (39) Buguliskis, J. S.; Brossier, F.; Shuman, J.; Sibley, L. D. 1374
Rhomboid 4 (ROM4) Affects the Processing of Surface Adhesins and 1375
Facilitates Host Cell Invasion by *Toxoplasma Gondii*. *PLoS Pathog.* 1376
2010, *6*, No. e1000858. 1377
- (40) Martiel, J.-L.; Leal, A.; Kurzawa, L.; Bolland, M.; Wang, I.; 1378
Vignaud, T.; Tseng, Q.; Théry, M. Measurement of Cell Traction 1379
Forces with Image. *Methods Cell Biol.* 2015, *125*, 269–287. 1380

- 1381 (41) Hegge, S.; Uhrig, K.; Streichfuss, M.; Kynast-Wolf, G.;
1382 Matuschewski, K.; Spatz, J. P.; Frischknecht, F. Direct Manipulation
1383 of Malaria Parasites with Optical Tweezers Reveals Distinct Functions
1384 of *Plasmodium* Surface Proteins. *ACS Nano* 2012, 6, 4648–4662.
- 1385 (42) Stadler, R. V.; White, L. A.; Hu, K.; Helmke, B. P.; Guilford, W.
1386 H. Direct Measurement of Cortical Force Generation and Polar-
1387 ization in a Living Parasite. *Mol. Biol. Cell* 2017, 28, 1912–1923.
- 1388 (43) Biais, N.; Higashi, D. L.; Brujic, J.; So, M.; Sheetz, M. P. Force-
1389 Dependent Polymorphism in Type IV Pili Reveals Hidden Epitopes.
1390 *Proc. Natl. Acad. Sci. U. S. A.* 2010, 107, 11358–11363.
- 1391 (44) Perschmann, N.; Hellmann, J. K.; Frischknecht, F.; Spatz, J. P.
1392 Induction of Malaria Parasite Migration by Synthetically Tunable
1393 Microenvironments. *Nano Lett.* 2011, 11, 4468–4474.
- 1394 (45) Asano, S. M.; Gao, R.; Wassie, A. T.; Tillberg, P. W.; Chen, F.;
1395 Boyden, E. S. Expansion Microscopy: Protocols for Imaging Proteins
1396 and RNA in Cells and Tissues. *Curr. Protoc. Cell Biol.* 2018, 80,
1397 No. e56.
- 1398 (46) Egarter, S.; Andenmatten, N.; Jackson, A. J.; Whitelaw, J. A.;
1399 Pall, G.; Black, J. A.; Ferguson, D. J. P.; Tardieux, I.; Mogilner, A.;
1400 Meissner, M. The *Toxoplasma* Acto-MyoA Motor Complex Is
1401 Important but Not Essential for Gliding Motility and Host Cell
1402 Invasion. *PLoS One* 2014, 9, No. e91819.
- 1403 (47) Bubb, M. R.; Spector, I.; Beyer, B. B.; Fosen, K. M. Effects of
1404 Jasplakinolide on the Kinetics of Actin Polymerization. An
1405 Explanation for Certain *In Vivo* Observations. *J. Biol. Chem.* 2000,
1406 275, 5163–5170.
- 1407 (48) Sampath, P.; Pollard, T. D. Effects of Cytochalasin, Phalloidin,
1408 and PH on the Elongation of Actin Filaments. *Biochemistry* 1991, 30,
1409 1973–1980.
- 1410 (49) Periz, J.; Whitelaw, J.; Harding, C.; Gras, S.; Del Rosario
1411 Minina, M. I.; Latorre-Barragan, F.; Lemgruber, L.; Reimer, M. A.;
1412 Insall, R.; Heaslip, A.; Meissner, M. *Toxoplasma Gondii* F-Actin Forms
1413 an Extensive Filamentous Network Required for Material Exchange
1414 and Parasite Maturation. *eLife* 2017, 6, e24119.
- 1415 (50) Shaw, M. K.; Tilney, L. G. Induction of an Acrosomal Process
1416 in *Toxoplasma Gondii*: Visualization of Actin Filaments in a Protozoan
1417 Parasite. *Proc. Natl. Acad. Sci. U. S. A.* 1999, 96, 9095–9099.
- 1418 (51) Del Rosario, M.; Periz, J.; Pavlou, G.; Lyth, O.; Latorre-
1419 Barragan, F.; Das, S.; Pall, G. S.; Stortz, J. F.; Lemgruber, L.;
1420 Whitelaw, J. A.; Baum, J.; Tardieux, I.; Meissner, M. Apicomplexan F-
1421 Actin Is Required for Efficient Nuclear Entry during Host Cell
1422 Invasion. *EMBO Rep.* 2019, 20, e48896.
- 1423 (52) Gambarotto, D.; Zwettler, F. U.; Le Guennec, M.; Schmidt-
1424 Cernohorska, M.; Fortun, D.; Borgers, S.; Heine, J.; Schloetel, J.-G.;
1425 Reuss, M.; Unser, M.; Boyden, E. S.; Sauer, M.; Hamel, V.; Guichard,
1426 P. Imaging Cellular Ultrastructures Using Expansion Microscopy (U-
1427 ExM). *Nat. Methods* 2019, 16, 71–74.
- 1428 (53) Plessmann, U.; Reiter-Owona, I.; Lechtreck, K.-F. Posttransla-
1429 tional Modifications of α -Tubulin of *Toxoplasma Gondii*. *Parasitol.*
1430 *Res.* 2004, 94, 386–389.
- 1431 (54) Brangwynne, C. P.; MacKintosh, F. C.; Kumar, S.; Geisse, N.
1432 A.; Talbot, J.; Mahadevan, L.; Parker, K. K.; Ingber, D. E.; Weitz, D.
1433 A. Microtubules Can Bear Enhanced Compressive Loads in Living
1434 Cells Because of Lateral Reinforcement. *J. Cell Biol.* 2006, 173, 733–
1435 741.
- 1436 (55) Kabir, A. Md. R.; Inoue, D.; Afrin, T.; Mayama, H.; Sada, K.;
1437 Kakugo, A. Buckling of Microtubules on a 2D Elastic Medium. *Sci.*
1438 *Rep.* 2015, 5, 17222.
- 1439 (56) Leung, J. M.; He, Y.; Zhang, F.; Hwang, Y.-C.; Nagayasu, E.;
1440 Liu, J.; Murray, J. M.; Hu, K. Stability and Function of a Putative
1441 Microtubule-Organizing Center in the Human Parasite *Toxoplasma*
1442 *Gondii*. *Mol. Biol. Cell* 2017, 28, 1361–1378.
- 1443 (57) Harding, C. R.; Gow, M.; Kang, J. H.; Shortt, E.; Manalis, S. R.;
1444 Meissner, M.; Lourido, S. Alveolar Proteins Stabilize Cortical
1445 Microtubules in *Toxoplasma Gondii*. *Nat. Commun.* 2019, 10, 401.
- 1446 (58) Cramer, L. P. Forming the Cell Rear First: Breaking Cell
1447 Symmetry to Trigger Directed Cell Migration. *Nat. Cell Biol.* 2010,
1448 12, 628–632.
- (59) Huynh, M.-H.; Carruthers, V. B. Tagging of Endogenous Genes
in a *Toxoplasma Gondii* Strain Lacking Ku80. *Eukaryotic Cell* 2009, 8,
530–539. 1451
- (60) Andenmatten, N.; Egarter, S.; Jackson, A. J.; Jullien, N.;
Herman, J.-P.; Meissner, M. Conditional Genome Engineering in
Toxoplasma Gondii Uncovers Alternative Invasion Mechanisms. *Nat.*
Methods 2013, 10, 125–127. 1455
- (61) Farhat, D. C.; Swale, C.; Dard, C.; Cannella, D.; Ortet, P.;
Barakat, M.; Sindikubwabo, F.; Belmudes, L.; De Bock, P.-J.; Couté,
Y.; Bougdour, A.; Hakimi, M.-A. A MORC-Driven Transcriptional
Switch Controls *Toxoplasma* Developmental Trajectories and Sexual
Commitment. *Nat. Microbiol.* 2020, 5, 570–583. 1460
- (62) Pavlou, G.; Tardieux, I. Phenotyping *Toxoplasma* Invasive Skills
by Fast Live Cell Imaging. *Methods Mol. Biol.* 2020, 2071, 209–220.
1462
- (63) Davies, H. S.; Baranova, N. S.; El Amri, N.; Coche-Guéfente,
L.; Verdier, C.; Bureau, L.; Richter, R. P.; Débère, D. An Integrated
Assay to Probe Endothelial Glycocalyx-Blood Cell Interactions under
Flow in Mechanically and Biochemically Well-Defined Environments.
Matrix Biol. 2019, 78–79, 47–59. 1467
- (64) Arganda-Carreras, I.; Kaynig, V.; Rueden, C.; Eliceiri, K. W.;
Schindelin, J.; Cardona, A.; Sebastian Seung, H. Trainable Weka
Segmentation: A Machine Learning Tool for Microscopy Pixel
Classification. *Bioinformatics* 2017, 33, 2424–2426. 1471
- (65) Martiel, J.-L.; Leal, A.; Kurzawa, L.; Balland, M.; Wang, I.;
Vignaud, T.; Tseng, Q.; Théry, M. Measurement of Cell Traction
Forces with ImageJ. *Methods Cell Biol.* 2015, 125, 269–287. 1474
- (66) Moudy, R.; Manning, T. J.; Beckers, C. J. The Loss of
Cytoplasmic Potassium upon Host Cell Breakdown Triggers Egress of
Toxoplasma Gondii. *J. Biol. Chem.* 2001, 276, 41492–41501. 1477

7. References

- Abrahamsen, M. S., Templeton, T. J., Enomoto, S., Abrahante, J. E., Zhu, G., Lancto, C. A., Deng, M., Liu, C., Widmer, G., Tzipori, S., Buck, G. A., Xu, P., Bankier, A. T., Dear, P. H., Konfortov, B. A., Spriggs, H. F., Iyer, L., Anantharaman, V., Aravind, L., & Kapur, V. (2004). Complete genome sequence of the apicomplexan, *Cryptosporidium parvum*. *Science (New York, N.Y.)*, *304*(5669), 441–445. <https://doi.org/10.1126/science.1094786>
- Adl, S. M., Bass, D., Lane, C. E., Lukeš, J., Schoch, C. L., Smirnov, A., Agatha, S., Berney, C., Brown, M. W., Burki, F., Cárdenas, P., Čepička, I., Chistyakova, L., del Campo, J., Dunthorn, M., Edvardsen, B., Eglit, Y., Guillou, L., Hampl, V., ... Zhang, Q. (2019). Revisions to the Classification, Nomenclature, and Diversity of Eukaryotes. *The Journal of Eukaryotic Microbiology*, *66*(1), 4–119. <https://doi.org/10.1111/jeu.12691>
- Akaki, M., Nakano, Y., Nagayasu, E., Nagakura, K., Kawai, S., & Aikawa, M. (2001). Invasive forms of *Toxoplasma gondii*, *Leishmania amazonensis* and *Trypanosoma cruzi* have a positive charge at their contact site with host cells. *Parasitology Research*, *87*(3), 193–197. <https://doi.org/10.1007/pl00008574>
- Amino, R., Thiberge, S., Martin, B., Celli, S., Shorte, S., Frischknecht, F., & Ménard, R. (2006). Quantitative imaging of *Plasmodium* transmission from mosquito to mammal. *Nature Medicine*, *12*(2), 220–224. <https://doi.org/10.1038/nm1350>
- Amos, B., Aurrecochea, C., Barba, M., Barreto, A., Basenko, E. Y., Bažant, W., Belnap, R., Blevins, A. S., Böhme, U., Brestelli, J., Brunk, B. P., Caddick, M., Callan, D., Campbell, L., Christensen, M. B., Christophides, G. K., Crouch, K., Davis, K., DeBarry, J., ... Zheng, J. (2022). VEuPathDB: The eukaryotic pathogen, vector and host bioinformatics resource center. *Nucleic Acids Research*, *50*(D1), D898–D911. <https://doi.org/10.1093/nar/gkab929>
- Andenmatten, N., Egarter, S., Jackson, A. J., Jullien, N., Herman, J.-P., & Meissner, M. (2013). Conditional genome engineering in *Toxoplasma gondii* uncovers alternative invasion mechanisms. *Nature Methods*, *10*(2), 125–127. <https://doi.org/10.1038/nmeth.2301>
- Anderson-White, B., Beck, J. R., Chen, C.-T., Meissner, M., Bradley, P. J., & Gubbels, M.-J. (2012). Cytoskeleton Assembly in *Toxoplasma gondii* Cell Division. In *International Review of Cell and Molecular Biology* (Vol. 298, pp. 1–31). Elsevier. <https://doi.org/10.1016/B978-0-12-394309-5.00001-8>
- Anderson-White, B. R., Ivey, F. D., Cheng, K., Szatanek, T., Lorestani, A., Beckers, C. J., Ferguson, D. J. P., Sahoo, N., & Gubbels, M.-J. (2011). A family of intermediate filament-like proteins is sequentially assembled into the cytoskeleton of *Toxoplasma gondii*. *Cellular Microbiology*, *13*(1), 18–31. <https://doi.org/10.1111/j.1462-5822.2010.01514.x>
- Aper, S. J. A., van Spreuwel, A. C. C., van Turnhout, M. C., van der Linden, A. J., Pieters, P. A., van der Zon, N. L. L., de la Rambelje, S. L., Bouten, C. V. C., & Merks, M. (2014). Colorful Protein-Based Fluorescent Probes for Collagen Imaging. *PLoS ONE*, *9*(12), e114983. <https://doi.org/10.1371/journal.pone.0114983>
- Arrizabalaga, G., & Boothroyd, J. C. (2004). Role of calcium during *Toxoplasma gondii* invasion and egress. *International Journal for Parasitology*, *34*(3), 361–368. <https://doi.org/10.1016/j.ijpara.2003.11.017>
- Attias, M., Teixeira, D. E., Benchimol, M., Vommaro, R. C., Crepaldi, P. H., & De Souza, W. (2020). The life-cycle of *Toxoplasma gondii* reviewed using animations. *Parasites & Vectors*, *13*(1), 588. <https://doi.org/10.1186/s13071-020-04445-z>

REFERENCES

- Azioune, A., Carpi, N., Tseng, Q., Théry, M., & Piel, M. (2010). Protein Micropatterns. In *Methods in Cell Biology* (Vol. 97, pp. 133–146). Elsevier. [https://doi.org/10.1016/S0091-679X\(10\)97008-8](https://doi.org/10.1016/S0091-679X(10)97008-8)
- Back, P. S., Moon, A. S., Pasquarelli, R. R., Bell, H. N., Torres, J. A., Chen, A. L., Sha, J., Vashisht, A. A., Wohlschlegel, J. A., & Bradley, P. J. (2023). IMC29 Plays an Important Role in Toxoplasma Endodyogeny and Reveals New Components of the Daughter-Enriched IMC Proteome. *MBio*, *14*(1), e03042-22. <https://doi.org/10.1128/mbio.03042-22>
- Barkhuff, W. D., Gilk, S. D., Whitmarsh, R., Tilley, L. D., Hunter, C., & Ward, G. E. (2011). Targeted Disruption of TgPhIL1 in Toxoplasma gondii Results in Altered Parasite Morphology and Fitness. *PLoS ONE*, *6*(8), e23977. <https://doi.org/10.1371/journal.pone.0023977>
- Barragan, A., Brossier, F., & Sibley, L. D. (2005). Transepithelial migration of Toxoplasma gondii involves an interaction of intercellular adhesion molecule 1 (ICAM-1) with the parasite adhesin MIC2. *Cellular Microbiology*, *7*(4), 561–568. <https://doi.org/10.1111/j.1462-5822.2005.00486.x>
- Barylyuk, K., Koreny, L., Ke, H., Butterworth, S., Crook, O. M., Lassadi, I., Gupta, V., Tromer, E., Mourier, T., Stevens, T. J., Breckels, L. M., Pain, A., Lilley, K. S., & Waller, R. F. (2020). A subcellular atlas of Toxoplasma reveals the functional context of the proteome [Preprint]. *Cell Biology*. <https://doi.org/10.1101/2020.04.23.057125>
- Beck, J. R., Rodriguez-Fernandez, I. A., Cruz de Leon, J., Huynh, M.-H., Carruthers, V. B., Morrissette, N. S., & Bradley, P. J. (2010). A Novel Family of Toxoplasma IMC Proteins Displays a Hierarchical Organization and Functions in Coordinating Parasite Division. *PLoS Pathogens*, *6*(9), Article 9. <https://doi.org/10.1371/journal.ppat.1001094>
- Behnke, M. S., Wootton, J. C., Lehmann, M. M., Radke, J. B., Lucas, O., Nawas, J., Sibley, L. D., & White, M. W. (2010). Coordinated Progression through Two Subtranscriptomes Underlies the Tachyzoite Cycle of Toxoplasma gondii. *PLoS ONE*, *5*(8), Article 8. <https://doi.org/10.1371/journal.pone.0012354>
- Bershady, A. D., & Kozlov, M. M. (2011). Crawling cell locomotion revisited. *Proceedings of the National Academy of Sciences*, *108*(51), 20275–20276. <https://doi.org/10.1073/pnas.1116814108>
- Bichet, M., Joly, C., Hadj Henni, A., Guilbert, T., Xémard, M., Tafani, V., Lagal, V., Charras, G., & Tardieux, I. (2014). The toxoplasma-host cell junction is anchored to the cell cortex to sustain parasite invasive force. *BMC Biology*, *12*(1), 773. <https://doi.org/10.1186/s12915-014-0108-y>
- Bichet, M., Touquet, B., Gonzalez, V., Florent, I., Meissner, M., & Tardieux, I. (2016). Genetic impairment of parasite myosin motors uncovers the contribution of host cell membrane dynamics to Toxoplasma invasion forces. *BMC Biology*, *14*(1), 97. <https://doi.org/10.1186/s12915-016-0316-8>
- Blader, I., Coleman, B., Chen, C.-T., & Gubbels, M.-J. (2015). The lytic cycle of Toxoplasma gondii: 15 years later. *Annual Review of Microbiology*, *69*, 463–485. <https://doi.org/10.1146/annurev-micro-091014-104100>
- Bonhomme, A., Pingret, L., & Pinon, J. M. (1992). Review: Toxoplasma gondii cellular invasion. *Parassitologia*, *34*(1–3), 31–43.
- Bookwalter, C. S., Kelsen, A., Leung, J. M., Ward, G. E., & Trybus, K. M. (2014). A Toxoplasma gondii class XIV myosin, expressed in Sf9 cells with a parasite co-chaperone, requires two light chains for fast motility. *The Journal of Biological Chemistry*, *289*(44), 30832–30841. <https://doi.org/10.1074/jbc.M114.572453>
- Brown, K., Long, S., & Sibley, L. (2018). Conditional Knockdown of Proteins Using Auxin-inducible Degron (AID) Fusions in Toxoplasma gondii. *BIO-PROTOCOL*, *8*(4), Article 4. <https://doi.org/10.21769/BioProtoc.2728>
- Brown, K. M., Lourido, S., & Sibley, L. D. (2016). Serum Albumin Stimulates Protein Kinase G-dependent Microneme Secretion in Toxoplasma gondii. *The Journal of Biological Chemistry*, *291*(18), 9554–9565. <https://doi.org/10.1074/jbc.M115.700518>

REFERENCES

- Brückner, D. B., Arlt, N., Fink, A., Ronceray, P., Rädler, J. O., & Broedersz, C. P. (2021). Learning the dynamics of cell-cell interactions in confined cell migration. *Proceedings of the National Academy of Sciences of the United States of America*, *118*(7), e2016602118. <https://doi.org/10.1073/pnas.2016602118>
- Buguliskis, J. S., Brossier, F., Shuman, J., & Sibley, L. D. (2010). Rhomboid 4 (ROM4) Affects the Processing of Surface Adhesins and Facilitates Host Cell Invasion by *Toxoplasma gondii*. *PLoS Pathogens*, *6*(4), e1000858. <https://doi.org/10.1371/journal.ppat.1000858>
- Bullen, H. E., Bisio, H., & Soldati-Favre, D. (2019). The triumvirate of signaling molecules controlling *Toxoplasma* microneme exocytosis: Cyclic GMP, calcium, and phosphatidic acid. *PLoS Pathogens*, *15*(5), e1007670. <https://doi.org/10.1371/journal.ppat.1007670>
- Cady, W. G. (1946). *Piezoelectricity: An introduction to the theory and applications of electromechanical phenomena in crystals* (1st ed). McGraw-Hill Book Company, Inc.
- Callan-Jones, A., Albarran Arriagada, O. E., Massiera, G., Lorman, V., & Abkarian, M. (2012). Red Blood Cell Membrane Dynamics during Malaria Parasite Egress. *Biophysical Journal*, *103*(12), 2475–2483. <https://doi.org/10.1016/j.bpj.2012.11.008>
- Carey, K. L., Westwood, N. J., Mitchison, T. J., & Ward, G. E. (2004). A small-molecule approach to studying invasive mechanisms of *Toxoplasma gondii*. *Proceedings of the National Academy of Sciences*, *101*(19), 7433–7438. <https://doi.org/10.1073/pnas.0307769101>
- Carruthers, V. B., Hakansson, S., Giddings, O. K., & Sibley, L. D. (2000). *Toxoplasma gondii* Uses Sulfated Proteoglycans for Substrate and Host Cell Attachment. *Infection and Immunity*, *68*(7), 4005–4011. <https://doi.org/10.1128/IAI.68.7.4005-4011.2000>
- Carruthers, V. B., Moreno, S. N., & Sibley, L. D. (1999). Ethanol and acetaldehyde elevate intracellular [Ca²⁺] and stimulate microneme discharge in *Toxoplasma gondii*. *Biochemical Journal*, *342*(Pt 2), 379–386.
- Carruthers, V. B., & Sibley, L. D. (1999). Mobilization of intracellular calcium stimulates microneme discharge in *Toxoplasma gondii*. *Molecular Microbiology*, *31*(2), 421–428. <https://doi.org/10.1046/j.1365-2958.1999.01174.x>
- Carruthers, V. B., & Tomley, F. M. (2008). Microneme proteins in apicomplexans. *Sub-Cellular Biochemistry*, *47*, 33–45. https://doi.org/10.1007/978-0-387-78267-6_2
- Cavalier-Smith, T. (1999). Principles of protein and lipid targeting in secondary symbiogenesis: Euglenoid, dinoflagellate, and sporozoan plastid origins and the eukaryote family tree. *The Journal of Eukaryotic Microbiology*, *46*(4), 347–366. <https://doi.org/10.1111/j.1550-7408.1999.tb04614.x>
- CDC - *Toxoplasmosis*. (2021, January 15). <https://www.cdc.gov/parasites/toxoplasmosis/index.html>
- Chandramohanadas, R., Davis, P. H., Beiting, D. P., Harbut, M. B., Darling, C., Velmourougane, G., Lee, M. Y., Greer, P. A., Roos, D. S., & Greenbaum, D. C. (2009). Apicomplexan Parasites Co-Opt Host Calpains to Facilitate Their Escape from Infected Cells. *Science (New York, N.y.)*, *324*(5928), 794–797. <https://doi.org/10.1126/science.1171085>
- Chen, A. L., Kim, E. W., Toh, J. Y., Vashisht, A. A., Rashoff, A. Q., Van, C., Huang, A. S., Moon, A. S., Bell, H. N., Bentolila, L. A., Wohlschlegel, J. A., & Bradley, P. J. (2015). Novel components of the *Toxoplasma* inner membrane complex revealed by BioID. *MBio*, *6*(1), e02357-02314. <https://doi.org/10.1128/mBio.02357-14>
- Chen, F., Tillberg, P. W., & Boyden, E. S. (2015). Expansion microscopy. *Science*, *347*(6221), 543–548. <https://doi.org/10.1126/science.1260088>
- Choi, C. P., Moon, A. S., Back, P. S., Jami-Alahmadi, Y., Vashisht, A. A., Wohlschlegel, J. A., & Bradley, P. J. (2019). A photoactivatable crosslinking system reveals protein interactions in the *Toxoplasma gondii* inner membrane complex. *PLOS Biology*, *17*(10), e3000475. <https://doi.org/10.1371/journal.pbio.3000475>

REFERENCES

- Chozinski, T. J., Halpern, A. R., Okawa, H., Kim, H.-J., Tremel, G. J., Wong, R. O. L., & Vaughan, J. C. (2016). Expansion microscopy with conventional antibodies and fluorescent proteins. *Nature Methods*, *13*(6), 485–488. <https://doi.org/10.1038/nmeth.3833>
- Courret, N., Darce, S., Sonigo, P., Milon, G., Buzoni-Gâtél, D., & Tardieux, I. (2006). CD11c- and CD11b-expressing mouse leukocytes transport single *Toxoplasma gondii* tachyzoites to the brain. *Blood*, *107*(1), 309–316. <https://doi.org/10.1182/blood-2005-02-0666>
- Daher, W., Klages, N., Carlier, M.-F., & Soldati-Favre, D. (2012). Molecular characterization of *Toxoplasma gondii* formin 3, an actin nucleator dispensable for tachyzoite growth and motility. *Eukaryotic Cell*, *11*(3), 343–352. <https://doi.org/10.1128/EC.05192-11>
- Daher, W., Plattner, F., Carlier, M.-F., & Soldati-Favre, D. (2010). Concerted Action of Two Formins in Gliding Motility and Host Cell Invasion by *Toxoplasma gondii*. *PLoS Pathogens*, *6*(10), e1001132. <https://doi.org/10.1371/journal.ppat.1001132>
- Damstra, H. G. J., Mohar, B., Eddison, M., Akhmanova, A., Kapitein, L. C., & Tillberg, P. W. (2022). Visualizing cellular and tissue ultrastructure using Ten-fold Robust Expansion Microscopy (TREx). *ELife*, *11*, e73775. <https://doi.org/10.7554/eLife.73775>
- Damstra, H. G. J., Passmore, J. B., Serweta, A. K., Koutlas, I., Burute, M., Meye, F. J., Akhmanova, A., & Kapitein, L. C. (2022). *GelMap: Intrinsic calibration and deformation mapping for expansion microscopy* [Preprint]. Cell Biology. <https://doi.org/10.1101/2022.12.21.521394>
- de Chaumont, F., Dallongeville, S., Chenouard, N., Hervé, N., Pop, S., Provoost, T., Meas-Yedid, V., Pankajakshan, P., Lecomte, T., Le Montagner, Y., Lagache, T., Dufour, A., & Olivo-Marin, J.-C. (2012). Icy: An open bioimage informatics platform for extended reproducible research. *Nature Methods*, *9*(7), Article 7. <https://doi.org/10.1038/nmeth.2075>
- De Niz, M., Burda, P.-C., Kaiser, G., Del Portillo, H. A., Spielmann, T., Frischknecht, F., & Heussler, V. T. (2017). Progress in imaging methods: Insights gained into Plasmodium biology. *Nature Reviews. Microbiology*, *15*(1), 37–54. <https://doi.org/10.1038/nrmicro.2016.158>
- Delbac, F., Sängler, A., Neuhaus, E. M., Stratmann, R., Ajioka, J. W., Toursel, C., Herm-Götz, A., Tomavo, S., Soldati, T., & Soldati, D. (2001). *Toxoplasma gondii* myosins B/C. *Journal of Cell Biology*, *155*(4), Article 4. <https://doi.org/10.1083/jcb.200012116>
- Delorme-Walker, V., Abrivard, M., Lagal, V., Anderson, K., Perazzi, A., Gonzalez, V., Page, C., Chauvet, J., Ochoa, W., Volkmann, N., Hanein, D., & Tardieux, I. (2012). Toxofilin upregulates the host cortical actin cytoskeleton dynamics, facilitating *Toxoplasma* invasion. *Journal of Cell Science*, *125*(Pt 18), 4333–4342. <https://doi.org/10.1242/jcs.103648>
- Dobrowolski, J. M., Carruthers, V. B., & Sibley, L. D. (1997). Participation of myosin in gliding motility and host cell invasion by *Toxoplasma gondii*. *Molecular Microbiology*, *26*(1), 163–173. <https://doi.org/10.1046/j.1365-2958.1997.5671913.x>
- Dobrowolski, J. M., Niesman, I. R., & Sibley, L. D. (1997). Actin in the parasite *Toxoplasma gondii* is encoded by a single copy gene, ACT1 and exists primarily in a globular form. *Cell Motility and the Cytoskeleton*, *37*(3), 253–262. [https://doi.org/10.1002/\(SICI\)1097-0169\(1997\)37:3<253::AID-CM7>3.0.CO;2-7](https://doi.org/10.1002/(SICI)1097-0169(1997)37:3<253::AID-CM7>3.0.CO;2-7)
- Dobrowolski, J. M., & Sibley, L. D. (1996). *Toxoplasma* invasion of mammalian cells is powered by the actin cytoskeleton of the parasite. *Cell*, *84*(6), 933–939. [https://doi.org/10.1016/s0092-8674\(00\)81071-5](https://doi.org/10.1016/s0092-8674(00)81071-5)
- Domack, A., Prucker, O., Rühle, J., & Johannsmann, D. (1997). Swelling of a polymer brush probed with a quartz crystal resonator. *Physical Review E*, *56*(1), 680–689. <https://doi.org/10.1103/PhysRevE.56.680>
- Donald, R. G., & Roos, D. S. (1993). Stable molecular transformation of *Toxoplasma gondii*: A selectable dihydrofolate reductase-thymidylate synthase marker based on drug-resistance mutations in

REFERENCES

- malaria. *Proceedings of the National Academy of Sciences of the United States of America*, 90(24), 11703–11707. <https://doi.org/10.1073/pnas.90.24.11703>
- Dow, L. P., Gaietta, G., Kaufman, Y., Swift, M. F., Lemos, M., Lane, K., Hopcroft, M., Bezault, A., Sauvanet, C., Volkmann, N., Pruitt, B. L., & Hanein, D. (2022). Morphological control enables nanometer-scale dissection of cell-cell signaling complexes. *Nature Communications*, 13(1), Article 1. <https://doi.org/10.1038/s41467-022-35409-9>
- Dowse, T. J., & Soldati, D. (2005). Rhomboid-like proteins in Apicomplexa: Phylogeny and nomenclature. *Trends in Parasitology*, 21(6), 254–258. <https://doi.org/10.1016/j.pt.2005.04.009>
- Dubacheva, G. V., Araya-Callis, C., Geert Volbeda, A., Fairhead, M., Codée, J., Howarth, M., & Richter, R. P. (2017). Controlling Multivalent Binding through Surface Chemistry: Model Study on Streptavidin. *Journal of the American Chemical Society*, 139(11), 4157–4167. <https://doi.org/10.1021/jacs.7b00540>
- Dubey, J. P. (1997). Bradyzoite-induced murine toxoplasmosis: Stage conversion, pathogenesis, and tissue cyst formation in mice fed bradyzoites of different strains of *Toxoplasma gondii*. *The Journal of Eukaryotic Microbiology*, 44(6), 592–602. <https://doi.org/10.1111/j.1550-7408.1997.tb05965.x>
- Dubey, J. P. (1998). Advances in the life cycle of *Toxoplasma gondii*. *International Journal for Parasitology*, 28(7), Article 7. [https://doi.org/10.1016/S0020-7519\(98\)00023-X](https://doi.org/10.1016/S0020-7519(98)00023-X)
- Dubey, J. P., & Frenkel, J. K. (1972). Cyst-induced toxoplasmosis in cats. *The Journal of Protozoology*, 19(1), 155–177. <https://doi.org/10.1111/j.1550-7408.1972.tb03431.x>
- Dubey, J. P., & Frenkel, J. K. (1973). Experimental toxoplasma infection in mice with strains producing oocysts. *The Journal of Parasitology*, 59(3), 505–512.
- Dubois, D. J., & Soldati-Favre, D. (2019). Biogenesis and secretion of micronemes in *Toxoplasma gondii*. *Cellular Microbiology*, 21(5), e13018. <https://doi.org/10.1111/cmi.13018>
- Dupré, L., Houmadi, R., Tang, C., & Rey-Barroso, J. (2015). T Lymphocyte Migration: An Action Movie Starring the Actin and Associated Actors. *Frontiers in Immunology*, 6. <https://www.frontiersin.org/articles/10.3389/fimmu.2015.00586>
- Egarter, S., Andenmatten, N., Jackson, A. J., Whitelaw, J. A., Pall, G., Black, J. A., Ferguson, D. J. P., Tardieux, I., Mogilner, A., & Meissner, M. (2014). The *Toxoplasma* Acto-MyoA Motor Complex Is Important but Not Essential for Gliding Motility and Host Cell Invasion. *PLOS ONE*, 9(3), e91819. <https://doi.org/10.1371/journal.pone.0091819>
- Eisele, N. B., Andersson, F. I., Frey, S., & Richter, R. P. (2012). Viscoelasticity of thin biomolecular films: A case study on nucleoporin phenylalanine-glycine repeats grafted to a histidine-tag capturing QCM-D sensor. *Biomacromolecules*, 13(8), 2322–2332. <https://doi.org/10.1021/bm300577s>
- EMBOSS: epestfind*. (2022, April 8). <https://emboss.bioinformatics.nl/cgi-bin/emboss/epestfind/>
- Engel, L., Gaietta, G., Dow, L. P., Swif, M. F., Pardon, G., Volkmann, N., Weis, W. I., Hanein, D., & Pruitt, B. L. (2019). Extracellular matrix micropatterning technology for whole cell cryogenic electron microscopy studies. *Journal of Micromechanics and Microengineering*, 29(11), 115018. <https://doi.org/10.1088/1361-6439/ab419a>
- Engelberg, K., Bechtel, T., Michaud, C., Weerapana, E., & Gubbels, M.-J. (2021). A more complex basal complex: Novel components mapped to the *Toxoplasma gondii* cytokinesis machinery portray an expanded hierarchy of its assembly and function (<https://doi.org/10.1101/2021.10.14.464364>; p. <https://doi.org/10.1101/2021.10.14.464364>). bioRxiv. <https://doi.org/10.1101/2021.10.14.464364>
- Engelberg, K., Bechtel, T., Michaud, C., Weerapana, E., & Gubbels, M.-J. (2022). Proteomic characterization of the *Toxoplasma gondii* cytokinesis machinery portrays an expanded hierarchy of its assembly and function. *Nature Communications*, 13(1), 4644. <https://doi.org/10.1038/s41467-022-32151-0>

REFERENCES

- Engelberg, K., Ivey, F. D., Lin, A., Kono, M., Lorestani, A., Faugno-Fusci, D., Gilberger, T.-W., White, M., & Gubbels, M.-J. (2016). A MORN1-associated HAD phosphatase in the basal complex is essential for *Toxoplasma gondii* daughter budding: *Toxoplasma basal complex HAD phosphatase*. *Cellular Microbiology*, *18*(8), Article 8. <https://doi.org/10.1111/cmi.12574>
- Ermis, M., Antmen, E., & Hasirci, V. (2018). Micro and Nanofabrication methods to control cell-substrate interactions and cell behavior: A review from the tissue engineering perspective. *Bioactive Materials*, *3*(3), 355–369. <https://doi.org/10.1016/j.bioactmat.2018.05.005>
- ExPASy—ProtParam tool. (2022, April 8). <https://web.expasy.org/protparam/>
- Ferguson, D. J., Hutchison, W. M., Dunachie, J. F., & Siim, J. C. (1974). Ultrastructural study of early stages of asexual multiplication and microgametogony of *Toxoplasma gondii* in the small intestine of the cat. *Acta Pathologica Et Microbiologica Scandinavica. Section B: Microbiology and Immunology*, *82*(2), 167–181. <https://doi.org/10.1111/j.1699-0463.1974.tb02309.x>
- Ferguson, D. J. P., Bowker, C., Jeffery, K. J. M., Chamberlain, P., & Squier, W. (2013). Congenital toxoplasmosis: Continued parasite proliferation in the fetal brain despite maternal immunological control in other tissues. *Clinical Infectious Diseases: An Official Publication of the Infectious Diseases Society of America*, *56*(2), 204–208. <https://doi.org/10.1093/cid/cis882>
- Fichera, M. E., & Roos, D. S. (1997). A plastid organelle as a drug target in apicomplexan parasites. *Nature*, *390*(6658), 407–409. <https://doi.org/10.1038/37132>
- Folch, A., & Toner, M. (2000). Microengineering of cellular interactions. *Annual Review of Biomedical Engineering*, *2*, 227–256. <https://doi.org/10.1146/annurev.bioeng.2.1.227>
- Frénal, K., Jacot, D., Hammoudi, P.-M., Graindorge, A., Maco, B., & Soldati-Favre, D. (2017). Myosin-dependent cell-cell communication controls synchronicity of division in acute and chronic stages of *Toxoplasma gondii*. *Nature Communications*, *8*(1), Article 1. <https://doi.org/10.1038/ncomms15710>
- Frénal, K., Marq, J.-B., Jacot, D., Polonais, V., & Soldati-Favre, D. (2014). Plasticity between MyoC- and MyoA-Glideosomes: An Example of Functional Compensation in *Toxoplasma gondii* Invasion. *PLoS Pathogens*, *10*(11), e1004504. <https://doi.org/10.1371/journal.ppat.1004504>
- Frénal, K., Polonais, V., Marq, J.-B., Stratmann, R., Limenitakis, J., & Soldati-Favre, D. (2010). Functional dissection of the apicomplexan glideosome molecular architecture. *Cell Host and Microbe*, *8*(4), 343–357. <https://doi.org/10.1016/j.chom.2010.09.002>
- Frevert, U., Engelmann, S., Zougbedé, S., Stange, J., Ng, B., Matuschewski, K., Liebes, L., & Yee, H. (2005). Intravital observation of *Plasmodium berghei* sporozoite infection of the liver. *PLoS Biology*, *3*(6), e192. <https://doi.org/10.1371/journal.pbio.0030192>
- Frixione, E., Mondragón, R., & Meza, I. (1996). Kinematic analysis of *Toxoplasma gondii* motility. *Cell Motility and the Cytoskeleton*, *34*(2), 152–163. [https://doi.org/10.1002/\(SICI\)1097-0169\(1996\)34:2<152::AID-CM6>3.0.CO;2-D](https://doi.org/10.1002/(SICI)1097-0169(1996)34:2<152::AID-CM6>3.0.CO;2-D)
- Furtado, G. C., Slowik, M., Kleinman, H. K., & Joiner, K. A. (1992). Laminin enhances binding of *Toxoplasma gondii* tachyzoites to J774 murine macrophage cells. *Infection and Immunity*, *60*(6), 2337–2342. <https://doi.org/10.1128/iai.60.6.2337-2342.1992>
- Gambarotto, D., Zwettler, F. U., Le Guennec, M., Schmidt-Cernohorska, M., Fortun, D., Borgers, S., Heine, J., Schloetel, J. G., Reuss, M., Unser, M., Boyden, E. S., Sauer, M., Hamel, V., & Guichard, P. (2019). Imaging cellular ultrastructures using expansion microscopy (U-ExM). *Nature Methods*, *16*(1), 71–74. <https://doi.org/10.1038/s41592-018-0238-1>
- Gaskins, E., Gilk, S., DeVore, N., Mann, T., Ward, G., & Beckers, C. (2004). Identification of the membrane receptor of a class XIV myosin in *Toxoplasma gondii*. *The Journal of Cell Biology*, *165*(3), 383–393. <https://doi.org/10.1083/jcb.200311137>

REFERENCES

- Ghosh, I., Singh, R. K., Mishra, M., Kapoor, S., & Jana, S. S. (2021). Switching between blebbing and lamellipodia depends on the degree of non-muscle myosin II activity. *Journal of Cell Science*, *134*(1), jcs248732. <https://doi.org/10.1242/jcs.248732>
- Gomes, L. C., & Mergulhão, F. J. M. (2021). A Selection of Platforms to Evaluate Surface Adhesion and Biofilm Formation in Controlled Hydrodynamic Conditions. *Microorganisms*, *9*(9), 1993. <https://doi.org/10.3390/microorganisms9091993>
- Gómez de León, C. T., Díaz Martín, R. D., Mendoza Hernández, G., González Pozos, S., Ambrosio, J. R., & Mondragón Flores, R. (2014). Proteomic characterization of the subpellicular cytoskeleton of *Toxoplasma gondii* tachyzoites. *Journal of Proteomics*, *111*, 86–99. <https://doi.org/10.1016/j.jprot.2014.03.008>
- Gonzalez, V., Combe, A., David, V., Malmquist, N. A., Delorme, V., Leroy, C., Blazquez, S., Ménard, R., & Tardieux, I. (2009). Host cell entry by apicomplexa parasites requires actin polymerization in the host cell. *Cell Host & Microbe*, *5*(3), 259–272. <https://doi.org/10.1016/j.chom.2009.01.011>
- Gould, S. B., Tham, W.-H., Cowman, A. F., McFadden, G. I., & Waller, R. F. (2008). Alveolins, a New Family of Cortical Proteins that Define the Protist Infrakingdom Alveolata. *Molecular Biology and Evolution*, *25*(6), Article 6. <https://doi.org/10.1093/molbev/msn070>
- Graindorge, A., Frénal, K., Jacot, D., Salamun, J., Marq, J. B., & Soldati-Favre, D. (2016). The Conoid Associated Motor MyoH Is Indispensable for *Toxoplasma gondii* Entry and Exit from Host Cells. *PLOS Pathogens*, *12*(1), e1005388. <https://doi.org/10.1371/journal.ppat.1005388>
- Gras, S., Jackson, A., Woods, S., Pall, G., Whitelaw, J., Leung, J. M., Ward, G. E., Roberts, C. W., & Meissner, M. (2017). Parasites lacking the micronemal protein MIC2 are deficient in surface attachment and host cell egress, but remain virulent in vivo. *Wellcome Open Research*, *2*, 32. <https://doi.org/10.12688/wellcomeopenres.11594.2>
- Gras, S., Jimenez-Ruiz, E., Klinger, C. M., Schneider, K., Klingl, A., Lemgruber, L., & Meissner, M. (2019). An endocytic-secretory cycle participates in *Toxoplasma gondii* in motility. *PLoS Biology*, *17*(6), e3000060. <https://doi.org/10.1371/journal.pbio.3000060>
- Gubbels, M.-J., Ferguson, D. J. P., Saha, S., Romano, J. D., Chavan, S., Primo, V. A., Michaud, C., Coppens, I., & Engelberg, K. (2022). *Toxoplasma gondii*'s Basal Complex: The Other Apicomplexan Business End Is Multifunctional. *Frontiers in Cellular and Infection Microbiology*, *12*, 882166. <https://doi.org/10.3389/fcimb.2022.882166>
- Gubbels, M.-J., Vaishnav, S., Boot, N., Dubremetz, J.-F., & Striepen, B. (2006). A MORN-repeat protein is a dynamic component of the *Toxoplasma gondii* cell division apparatus. *Journal of Cell Science*, *119*(11), Article 11. <https://doi.org/10.1242/jcs.02949>
- Gubbels, M.-J., White, M., & Szatanek, T. (2008). The cell cycle and *Toxoplasma gondii* cell division: Tightly knit or loosely stitched? *International Journal for Parasitology*, *38*(12), 1343–1358. <https://doi.org/10.1016/j.ijpara.2008.06.004>
- Gupta, M., Doss, B., Lim, C. T., Voituriez, R., & Ladoux, B. (2016). Single cell rigidity sensing: A complex relationship between focal adhesion dynamics and large-scale actin cytoskeleton remodeling. *Cell Adhesion & Migration*, *10*(5), 554–567. <https://doi.org/10.1080/19336918.2016.1173800>
- Håkansson, S., Morisaki, H., Heuser, J., & Sibley, L. D. (1999). Time-Lapse Video Microscopy of Gliding Motility in *Toxoplasma gondii* Reveals a Novel, Biphasic Mechanism of Cell Locomotion. *Molecular Biology of the Cell*, *10*, 9.
- Harding, C. R., & Frischknecht, F. (2020). The Riveting Cellular Structures of Apicomplexan Parasites. *Trends in Parasitology*, *36*(12), 979–991. <https://doi.org/10.1016/j.pt.2020.09.001>

REFERENCES

- Harding, C. R., Gow, M., Kang, J. H., Shortt, E., Manalis, S. R., Meissner, M., & Lourido, S. (2019). Alveolar proteins stabilize cortical microtubules in *Toxoplasma gondii*. *Nature Communications*, *10*(1), Article 1. <https://doi.org/10.1038/s41467-019-08318-7>
- Harding, C. R., & Meissner, M. (2014). The inner membrane complex through development of *Toxoplasma gondii* and *Plasmodium*. *Cellular Microbiology*, *16*(5), 632–641. <https://doi.org/10.1111/cmi.12285>
- Harper, J. M., Hoff, E. F., & Carruthers, V. B. (2004). Multimerization of the *Toxoplasma gondii* MIC2 integrin-like A-domain is required for binding to heparin and human cells. *Molecular and Biochemical Parasitology*, *134*(2), 201–212. <https://doi.org/10.1016/j.molbiopara.2003.12.001>
- He, C., Xu, M., Pan, S., Wang, H., Peng, H., & Liu, Z. (2020). ITRAQ-Based Phosphoproteomic Analysis of *Toxoplasma gondii* Tachyzoites Provides Insight Into the Role of Phosphorylation for its Invasion and Egress. *Frontiers in Cellular and Infection Microbiology*, *10*, 586466. <https://doi.org/10.3389/fcimb.2020.586466>
- Hegge, S., Munter, S., Steinbüchel, M., Heiss, K., Engel, U., Matuschewski, K., & Frischknecht, F. (2010). Multistep adhesion of *Plasmodium* sporozoites. *The FASEB Journal*, *24*(7), 2222–2234. <https://doi.org/10.1096/fj.09-148700>
- Herm-Götz, A., Weiss, S., Stratmann, R., Fujita-Becker, S., Ruff, C., Meyhöfer, E., Soldati, T., Manstein, D. J., Geeves, M. A., & Soldati, D. (2002). *Toxoplasma gondii* myosin A and its light chain: A fast, single-headed, plus-end-directed motor. *The EMBO Journal*, *21*(9), 2149–2158. <https://doi.org/10.1093/emboj/21.9.2149>
- Hoang, A. N., Jones, C. N., Dimisko, L., Hamza, B., Martel, J., Kojic, N., & Irimia, D. (2013). Measuring neutrophil speed and directionality during chemotaxis, directly from a droplet of whole blood. *Technology*, *1*(1), 49. <https://doi.org/10.1142/S2339547813500040>
- Hu, K. (2008). Organizational Changes of the Daughter Basal Complex during the Parasite Replication of *Toxoplasma gondii*. *PLoS Pathogens*, *4*(1), Article 1. <https://doi.org/10.1371/journal.ppat.0040010>
- Hu, K., Johnson, J., Florens, L., Fraunholz, M., Suravajjala, S., DiLullo, C., Yates, J., Roos, D. S., & Murray, J. M. (2006). Cytoskeletal components of an invasion machine—The apical complex of *Toxoplasma gondii*. *PLoS Pathogens*, *2*(2), e13. <https://doi.org/10.1371/journal.ppat.0020013>
- Hu, K., Mann, T., Striepen, B., Beckers, C. J. M., Roos, D. S., & Murray, J. M. (2002). Daughter cell assembly in the protozoan parasite *Toxoplasma gondii*. *Molecular Biology of the Cell*, *13*(2), 593–606. <https://doi.org/10.1091/mbc.01-06-0309>
- Hunter, C. A., & Sibley, L. D. (2012). Modulation of innate immunity by *Toxoplasma gondii* virulence effectors. *Nature Reviews. Microbiology*, *10*(11), 766–778. <https://doi.org/10.1038/nrmicro2858>
- Huynh, M.-H., & Carruthers, V. B. (2006). *Toxoplasma* MIC2 Is a Major Determinant of Invasion and Virulence. *PLOS Pathogens*, *2*(8), e84. <https://doi.org/10.1371/journal.ppat.0020084>
- Huynh, M.-H., & Carruthers, V. B. (2009). Tagging of endogenous genes in a *Toxoplasma gondii* strain lacking Ku80. *Eukaryotic Cell*, *8*(4), 530–539. <https://doi.org/10.1128/EC.00358-08>
- Huynh, M.-H., Liu, B., Henry, M., Liew, L., Matthews, S. J., & Carruthers, V. B. (2015). Structural Basis of *Toxoplasma gondii* MIC2-associated Protein Interaction with MIC2. *The Journal of Biological Chemistry*, *290*(3), 1432–1441. <https://doi.org/10.1074/jbc.M114.613646>
- Jacot, D., Daher, W., & Soldati-Favre, D. (2013). *Toxoplasma gondii* myosin F, an essential motor for centrosomes positioning and apicoplast inheritance. *The EMBO Journal*, *32*(12), 1702–1716. <https://doi.org/10.1038/emboj.2013.113>
- Jacot, D., Tosetti, N., Pires, I., Stock, J., Graindorge, A., Hung, Y.-F., Han, H., Tewari, R., Kursula, I., & Soldati-Favre, D. (2016). An Apicomplexan Actin-Binding Protein Serves as a Connector and

REFERENCES

- Lipid Sensor to Coordinate Motility and Invasion. *Cell Host & Microbe*, 20(6), 731–743. <https://doi.org/10.1016/j.chom.2016.10.020>
- Jacquet, A., Coulon, L., De Nève, J., Daminet, V., Haumont, M., Garcia, L., Bollen, A., Jurado, M., & Biemans, R. (2001). The surface antigen SAG3 mediates the attachment of *Toxoplasma gondii* to cell-surface proteoglycans. *Molecular and Biochemical Parasitology*, 116(1), 35–44. [https://doi.org/10.1016/S0166-6851\(01\)00297-3](https://doi.org/10.1016/S0166-6851(01)00297-3)
- Jones, J. L., & Dubey, J. P. (2012). Foodborne toxoplasmosis. *Clinical Infectious Diseases: An Official Publication of the Infectious Diseases Society of America*, 55(6), 845–851. <https://doi.org/10.1093/cid/cis508>
- Jones, J., Lopez, A., & Wilson, M. (2003). Congenital toxoplasmosis. *American Family Physician*, 67(10), 2131–2138.
- Kafsack, B. F. C., Pena, J. D. O., Coppens, I., Ravindran, S., Boothroyd, J. C., & Carruthers, V. B. (2009). Rapid membrane disruption by a perforin-like protein facilitates parasite exit from host cells. *Science (New York, N.Y.)*, 323(5913), 530–533. <https://doi.org/10.1126/science.1165740>
- Kelsen, A., Kent, R. S., Snyder, A. K., Wehri, E., Bishop, S. J., Stadler, R. V., Powell, C., Genova, B. M. di, Rompikuntal, P. K., Boulanger, M. J., Warshaw, D. M., Westwood, N. J., Schaletzky, J., & Ward, G. E. (2023). The class XIV myosin of *Toxoplasma gondii*, TgMyoA, is druggable in an animal model of infection (p. 2022.09.09.507210). bioRxiv. <https://doi.org/10.1101/2022.09.09.507210>
- Khan, E. S., Sankaran, S., Paez, J. I., Muth, C., Han, M. K. L., & Del Campo, A. (2019). Photoactivatable Hsp47: A Tool to Regulate Collagen Secretion and Assembly. *Advanced Science (Weinheim, Baden-Wuerttemberg, Germany)*, 6(9), 1801982. <https://doi.org/10.1002/advs.201801982>
- Kono, M., Prusty, D., Parkinson, J., & Gilberger, T. W. (2013). The apicomplexan inner membrane complex. *Frontiers in Bioscience (Landmark Edition)*, 18(3), 982–992. <https://doi.org/10.2741/4157>
- Konradt, C., Ueno, N., Christian, D. A., Delong, J. H., Pritchard, G. H., Herz, J., Bzik, D. J., Koshy, A. A., McGavern, D. B., Lodoen, M. B., & Hunter, C. A. (2016). Endothelial cells are a replicative niche for entry of *Toxoplasma gondii* to the central nervous system. *Nature Microbiology*, 1, 16001. <https://doi.org/10.1038/nmicrobiol.2016.1>
- Koreny, L., Mercado-Saavedra, B. N., Klinger, C. M., Barylyuk, K., Butterworth, S., Hirst, J., Rivera-Cuevas, Y., Zaccai, N. R., Holzer, V. J. C., Klingl, A., Dacks, J. B., Carruthers, V. B., Robinson, M. S., Gras, S., & Waller, R. F. (2023). Stable endocytic structures navigate the complex pellicle of apicomplexan parasites. *Nature Communications*, 14, 2167. <https://doi.org/10.1038/s41467-023-37431-x>
- Kretschmer, M., Schüßler, C. A., & Lieleg, O. (2021). Biofilm Adhesion to Surfaces is Modulated by Biofilm Wettability and Stiffness. *Advanced Materials Interfaces*, 8(5), 2001658. <https://doi.org/10.1002/admi.202001658>
- Kumar, A., Vadas, O., Dos Santos Pacheco, N., Zhang, X., Chao, K., Darvill, N., Rasmussen, H. Ø., Xu, Y., Lin, G. M.-H., Stylianou, F. A., Pedersen, J. S., Rouse, S. L., Morgan, M. L., Soldati-Favre, D., & Matthews, S. (2023). Structural and regulatory insights into the glideosome-associated connector from *Toxoplasma gondii*. *ELife*, 12, e86049. <https://doi.org/10.7554/eLife.86049>
- Lämmermann, T., & Sixt, M. (2009). Mechanical modes of ‘amoeboid’ cell migration. *Current Opinion in Cell Biology*, 21(5), 636–644. <https://doi.org/10.1016/j.ceb.2009.05.003>
- Leander, B. S. (2008). Marine gregarines: Evolutionary prelude to the apicomplexan radiation? *Trends in Parasitology*, 24(2), 60–67. <https://doi.org/10.1016/j.pt.2007.11.005>
- Leung, J. M., Rould, M. A., Konradt, C., Hunter, C. A., & Ward, G. E. (2014). Disruption of TgPHIL1 Alters Specific Parameters of *Toxoplasma gondii* Motility Measured in a Quantitative, Three-Dimensional Live Motility Assay. *PLoS ONE*, 9(1), e85763. <https://doi.org/10.1371/journal.pone.0085763>

REFERENCES

- Levine, N. D. (1971). Uniform Terminology for the Protozoan Subphylum Apicomplexa*. *The Journal of Protozoology*, 18(2), 352–355. <https://doi.org/10.1111/j.1550-7408.1971.tb03330.x>
- Levine, N. D. (1988). Progress in taxonomy of the Apicomplexan protozoa. *The Journal of Protozoology*, 35(4), 518–520. <https://doi.org/10.1111/j.1550-7408.1988.tb04141.x>
- Liu, J., He, Y., Benmerzouga, I., Sullivan, W. J., Morrisette, N. S., Murray, J. M., & Hu, K. (2016). An ensemble of specifically targeted proteins stabilizes cortical microtubules in the human parasite *Toxoplasma gondii*. *Molecular Biology of the Cell*, 27(3), 549–571. <https://doi.org/10.1091/mbc.E15-11-0754>
- Long, S., Brown, K. M., Drewry, L. L., Anthony, B., Phan, I. Q. H., & Sibley, L. D. (2017). Calmodulin-like proteins localized to the conoid regulate motility and cell invasion by *Toxoplasma gondii*. *PLoS Pathogens*, 13(5), e1006379. <https://doi.org/10.1371/journal.ppat.1006379>
- Lorestani, A., Sheiner, L., Yang, K., Robertson, S. D., Sahoo, N., Brooks, C. F., Ferguson, D. J. P., Striepen, B., & Gubbels, M.-J. (2010). A *Toxoplasma* MORN1 null mutant undergoes repeated divisions but is defective in basal assembly, apicoplast division and cytokinesis. *PloS One*, 5(8), e12302. <https://doi.org/10.1371/journal.pone.0012302>
- Lowthert, L. A., Ku, N. O., Liao, J., Coulombe, P. A., & Omary, M. B. (1995). Empigen BB: A Useful Detergent for Solubilization and Biochemical Analysis of Keratins. *Biochemical and Biophysical Research Communications*, 206(1), Article 1. <https://doi.org/10.1006/bbrc.1995.1051>
- Luft, B. J., & Remington, J. S. (1992). Toxoplasmic encephalitis in AIDS. *Clinical Infectious Diseases: An Official Publication of the Infectious Diseases Society of America*, 15(2), 211–222. <https://doi.org/10.1093/clinids/15.2.211>
- Mageswaran, S. K., Guérin, A., Theveny, L. M., Chen, W. D., Martinez, M., Lebrun, M., Striepen, B., & Chang, Y.-W. (2021). In situ ultrastructures of two evolutionarily distant apicomplexan rhoptry secretion systems. *Nature Communications*, 12, 4983. <https://doi.org/10.1038/s41467-021-25309-9>
- Marx, K. A. (2003). Quartz Crystal Microbalance: A Useful Tool for Studying Thin Polymer Films and Complex Biomolecular Systems at the Solution–Surface Interface. *Biomacromolecules*, 4(5), 1099–1120. <https://doi.org/10.1021/bm020116i>
- McBride, A. E., Conboy, A. K., Brown, S. P., Ariyachet, C., & Rutledge, K. L. (2009). Specific sequences within arginine-glycine-rich domains affect mRNA-binding protein function. *Nucleic Acids Research*, 37(13), Article 13. <https://doi.org/10.1093/nar/gkp349>
- McCourt, R. (2016). Archaeplastida: Diversification of Red Algae and the Green Plant Lineage. In R. M. Kliman (Ed.), *Encyclopedia of Evolutionary Biology* (pp. 101–106). Academic Press. <https://doi.org/10.1016/B978-0-12-800049-6.00254-7>
- McFadden, G. I., & Yeh, E. (2017). The apicoplast: Now you see it, now you don't. *International Journal for Parasitology*, 47(2–3), 137–144. <https://doi.org/10.1016/j.ijpara.2016.08.005>
- Meissner, M., Reiss, M., Viebig, N., Carruthers, V. B., Toursel, C., Tomavo, S., Ajioka, J. W., & Soldati, D. (2002). A family of transmembrane microneme proteins of *Toxoplasma gondii* contain EGF-like domains and function as escorts. *Journal of Cell Science*, 115(Pt 3), 563–574.
- Meissner, M., Schlüter, D., & Soldati, D. (2002). Role of *Toxoplasma gondii* myosin A in powering parasite gliding and host cell invasion. *Science (New York, N.Y.)*, 298(5594), Article 5594. <https://doi.org/10.1126/science.1074553>
- Monteiro, V. G., Soares, C. P., & de Souza, W. (1998). Host cell surface sialic acid residues are involved on the process of penetration of *Toxoplasma gondii* into mammalian cells. *FEMS Microbiology Letters*.
- Montoya, J. G., & Remington, J. S. (2008). Management of *Toxoplasma gondii* infection during pregnancy. *Clinical Infectious Diseases: An Official Publication of the Infectious Diseases Society of America*, 47(4), 554–566. <https://doi.org/10.1086/590149>

REFERENCES

- Moudy, R., Manning, T. J., & Beckers, C. J. (2001). The loss of cytoplasmic potassium upon host cell breakdown triggers egress of *Toxoplasma gondii*. *The Journal of Biological Chemistry*, 276(44), 41492–41501. <https://doi.org/10.1074/jbc.M106154200>
- M'Saad, O., & Bewersdorf, J. (2020). Light microscopy of proteins in their ultrastructural context. *Nature Communications*, 11(1), Article 1. <https://doi.org/10.1038/s41467-020-17523-8>
- Mueller, C., Graindorge, A., & Soldati-Favre, D. (2017). Functions of myosin motors tailored for parasitism. *Current Opinion in Microbiology*, 40, 113–122. <https://doi.org/10.1016/j.mib.2017.11.003>
- Münter, S., Sabass, B., Selhuber-Unkel, C., Kudryashev, M., Hegge, S., Engel, U., Spatz, J. P., Matuschewski, K., Schwarz, U. S., & Frischknecht, F. (2009). Plasmodium Sporozoite Motility Is Modulated by the Turnover of Discrete Adhesion Sites. *Cell Host & Microbe*, 6(6), 551–562. <https://doi.org/10.1016/j.chom.2009.11.007>
- Nanda, J. S., & Lorsch, J. R. (2014). Chapter Eight—Labeling a Protein with Fluorophores Using NHS Ester Derivatization. In J. Lorsch (Ed.), *Methods in Enzymology* (Vol. 536, pp. 87–94). Academic Press. <https://doi.org/10.1016/B978-0-12-420070-8.00008-8>
- Nicolle, C., & Manceaux, L. H. (1909). *Sur un protozoaire nouveau du gondi, Toxoplasma*. 2, 97–103.
- Nicolle, C., & Manceaux, L. H. (2009). On a leishman body infection (or related organisms) of the gondi. 1908. *International Journal for Parasitology*, 39(8), 863–864. <https://doi.org/10.1016/j.ijpara.2009.02.001>
- Nishi, M., Hu, K., Murray, J. M., & Roos, D. S. (2008). Organellar dynamics during the cell cycle of *Toxoplasma gondii*. *Journal of Cell Science*, 121(9), Article 9. <https://doi.org/10.1242/jcs.021089>
- Ortega-Barria, E., & Boothroyd, J. C. (1999). A *Toxoplasma* lectin-like activity specific for sulfated polysaccharides is involved in host cell infection. *The Journal of Biological Chemistry*, 274(3), 1267–1276. <https://doi.org/10.1074/jbc.274.3.1267>
- Ouologuem, D. T., & Roos, D. S. (2014). Dynamics of the *Toxoplasma gondii* inner membrane complex. *Journal of Cell Science*, 127(15), 3320–3330. <https://doi.org/10.1242/jcs.147736>
- Paluch, E. K., & Raz, E. (2013). The role and regulation of blebs in cell migration. *Current Opinion in Cell Biology*, 25(5), 582–590. <https://doi.org/10.1016/j.ceb.2013.05.005>
- Pappas, G., Roussos, N., & Falagas, M. E. (2009). Toxoplasmosis snapshots: Global status of *Toxoplasma gondii* seroprevalence and implications for pregnancy and congenital toxoplasmosis. *International Journal for Parasitology*, 39(12), 1385–1394. <https://doi.org/10.1016/j.ijpara.2009.04.003>
- Park, Y. S., & Ito, Y. (2000). Micropattern-immobilization of heparin to regulate cell growth with fibroblast growth factor. *Cytotechnology*, 33(1–3), 117–122. <https://doi.org/10.1023/A:1008154326954>
- Pasturel, A., Strale, P.-O., & Studer, V. (2020). Tailoring Common Hydrogels into 3D Cell Culture Templates. *Advanced Healthcare Materials*, 9(18), e2000519. <https://doi.org/10.1002/adhm.202000519>
- Pavlou, G., Biesaga, M., Touquet, B., Lagal, V., Balland, M., Dufour, A., Hakimi, M., & Tardieux, I. (2018). *Toxoplasma* Parasite Twisting Motion Mechanically Induces Host Cell Membrane Fission to Complete Invasion within a Protective Vacuole. *Cell Host & Microbe*, 24(1), 81–96.e5. <https://doi.org/10.1016/j.chom.2018.06.003>
- Pavlou, G., Touquet, B., Vigetti, L., Renesto, P., Bougdour, A., Debarre, D., Balland, M., & Tardieux, I. (2020). Coupling Polar Adhesion with Traction, Spring and Torque Forces Allows High Speed Helical Migration of the Protozoan Parasite *Toxoplasma*. *ACS Nano*. <https://doi.org/10.1021/acsnano.0c01893>
- Periz, J., Whitelaw, J., Harding, C., Gras, S., Del Rosario Minina, M. I., Latorre-Barragan, F., Lemgruber, L., Reimer, M. A., Insall, R., Heaslip, A., & Meissner, M. (2017). *Toxoplasma gondii* F-

REFERENCES

- actin forms an extensive filamentous network required for material exchange and parasite maturation. *ELife*, 6, e24119. <https://doi.org/10.7554/eLife.24119>
- Petrie, R. J., Doyle, A. D., & Yamada, K. M. (2009). Random versus directionally persistent cell migration. *Nature Reviews. Molecular Cell Biology*, 10(8), 538–549. <https://doi.org/10.1038/nrm2729>
- Phillips, M. A., Burrows, J. N., Manyando, C., van Huijsduijnen, R. H., Van Voorhis, W. C., & Wells, T. N. C. (2017). Malaria. *Nature Reviews Disease Primers*, 3(1), Article 1. <https://doi.org/10.1038/nrdp.2017.50>
- Pollard, T. D. (2016). Actin and Actin-Binding Proteins. *Cold Spring Harbor Perspectives in Biology*, 8(8), a018226. <https://doi.org/10.1101/cshperspect.a018226>
- Porchet, E., & Torpier, G. (1977). [Freeze fracture study of *Toxoplasma* and *Sarcocystis* infective stages (author's transl)]. *Zeitschrift Fur Parasitenkunde (Berlin, Germany)*, 54(2), 101–124. <https://doi.org/10.1007/BF00380795>
- Portman, N., & Šlapeta, J. (2014). The flagellar contribution to the apical complex: A new tool for the eukaryotic Swiss Army knife? *Trends in Parasitology*, 30(2), 58–64. <https://doi.org/10.1016/j.pt.2013.12.006>
- Poupel, O., Boleti, H., Axisa, S., Couture-Tosi, E., & Tardieux, I. (2000). Toxofilin, a Novel Actin-binding Protein from *Toxoplasma gondii*, Sequesters Actin Monomers and Caps Actin Filaments. *Molecular Biology of the Cell*, 11(1), 355–368.
- Prandovszky, E., Gaskell, E., Martin, H., Dubey, J. P., Webster, J. P., & McConkey, G. A. (2011). The Neurotropic Parasite *Toxoplasma Gondii* Increases Dopamine Metabolism. *PLoS ONE*, 6(9), e23866. <https://doi.org/10.1371/journal.pone.0023866>
- Quadt, K. A., Streichfuss, M., Moreau, C. A., Spatz, J. P., & Frischknecht, F. (2016). Coupling of Retrograde Flow to Force Production During Malaria Parasite Migration. *ACS Nano*, 10(2), 2091–2102. <https://doi.org/10.1021/acsnano.5b06417>
- Radke, J. R., Striepen, B., Guerini, M. N., Jerome, M. E., Roos, D. S., & White, M. W. (2001). Defining the cell cycle for the tachyzoite stage of *Toxoplasma gondii*. *Molecular and Biochemical Parasitology*, 115(2), 165–175. [https://doi.org/10.1016/s0166-6851\(01\)00284-5](https://doi.org/10.1016/s0166-6851(01)00284-5)
- Reig, G., Pulgar, E., & Concha, M. L. (2014). Cell migration: From tissue culture to embryos. *Development*, 141(10), 1999–2013. <https://doi.org/10.1242/dev.101451>
- Rim, N.-G., Yih, A., Hsi, P., Wang, Y., Zhang, Y., & Wong, J. Y. (2018). Micropatterned cell sheets as structural building blocks for biomimetic vascular patches. *Biomaterials*, 181, 126–139. <https://doi.org/10.1016/j.biomaterials.2018.07.047>
- Robert-Gangneux, F., & Darde, M.-L. (2012). Epidemiology of and Diagnostic Strategies for Toxoplasmosis. *Clinical Microbiology Reviews*, 25(2), 264–296. <https://doi.org/10.1128/CMR.05013-11>
- Rodahl, M., Höök, F., Krozer, A., Brzezinski, P., & Kasemo, B. (1995). Quartz crystal microbalance setup for frequency and Q-factor measurements in gaseous and liquid environments. *Review of Scientific Instruments*, 66(7), 3924–3930. <https://doi.org/10.1063/1.1145396>
- Roiko, M. S., Svezhova, N., & Carruthers, V. B. (2014). Acidification Activates *Toxoplasma gondii* Motility and Egress by Enhancing Protein Secretion and Cytolytic Activity. *PLoS Pathogens*, 10(11), e1004488. <https://doi.org/10.1371/journal.ppat.1004488>
- Roumégous, C., Abou Hammoud, A., Fuster, D., Dupuy, J.-W., Blancard, C., Salin, B., Robinson, D. R., Renesto, P., Tardieux, I., & Fréchal, K. (2022). Identification of new components of the basal pole of *Toxoplasma gondii* provides novel insights into its molecular organization and functions. *Frontiers in Cellular and Infection Microbiology*, 12, 1010038. <https://doi.org/10.3389/fcimb.2022.1010038>
- Sahoo, N., Beatty, W., Heuser, J., Sept, D., & Sibley, L. D. (2006). Unusual kinetic and structural properties control rapid assembly and turnover of actin in the parasite *Toxoplasma gondii*. *Molecular Biology of the Cell*, 17(2), 895–906. <https://doi.org/10.1091/mbc.e05-06-0512>

REFERENCES

- Salamun, J., Kallio, J. P., Daher, W., Soldati-Favre, D., & Kursula, I. (2014). Structure of *Toxoplasma gondii* coronin, an actin-binding protein that relocalizes to the posterior pole of invasive parasites and contributes to invasion and egress. *FASEB Journal: Official Publication of the Federation of American Societies for Experimental Biology*, 28(11), 4729–4747. <https://doi.org/10.1096/fj.14-252569>
- Sanchez, S. G., Bassot, E., Cerutti, A., Mai Nguyen, H., Aïda, A., Blanchard, N., & Besteiro, S. (2023). The apicoplast is important for the viability and persistence of *Toxoplasma gondii* bradyzoites. *Proceedings of the National Academy of Sciences*, 120(34), e2309043120. <https://doi.org/10.1073/pnas.2309043120>
- Sawers, L., Wallon, M., Mandelbrot, L., Villena, I., Stillwaggon, E., & Kieffer, F. (2022). Prevention of congenital toxoplasmosis in France using prenatal screening: A decision-analytic economic model. *PLOS ONE*, 17(11), e0273781. <https://doi.org/10.1371/journal.pone.0273781>
- Schneider, C. A., Rasband, W. S., & Eliceiri, K. W. (2012). NIH Image to ImageJ: 25 years of image analysis. *Nature Methods*, 9(7), Article 7. <https://doi.org/10.1038/nmeth.2089>
- Schumacher, R. (1990). The Quartz Microbalance: A Novel Approach to the In-Situ Investigation of Interfacial Phenomena at the Solid/Liquid Junction [New Analytical Methods (40)]. *Angewandte Chemie International Edition in English*, 29(4), 329–343. <https://doi.org/10.1002/anie.199003293>
- Sena, F., Cancela, S., Bollati-Fogolin, M., Pagotto, R., & Francia, M. E. (2023). Exploring *Toxoplasma gondii*'s Biology within the Intestinal Epithelium: Intestinal-derived models to unravel sexual differentiation. *Frontiers in Cellular and Infection Microbiology*, 13. <https://www.frontiersin.org/articles/10.3389/fcimb.2023.1134471>
- Services. (2022, April 8). <https://www.healthtech.dtu.dk>. <https://services.healthtech.dtu.dk>
- Shen, B., Buguliskis, J. S., Lee, T. D., & Sibley, L. D. (2014). Functional analysis of rhomboid proteases during *Toxoplasma* invasion. *MBio*, 5(5), e01795-01714. <https://doi.org/10.1128/mBio.01795-14>
- Shuken, S. R. (2023). An Introduction to Mass Spectrometry-Based Proteomics. *Journal of Proteome Research*, 22(7), 2151–2171. <https://doi.org/10.1021/acs.jproteome.2c00838>
- Sidik, S. M., Huet, D., Ganesan, S. M., Huynh, M.-H., Wang, T., Nasamu, A. S., Thiru, P., Saeij, J. P. J., Carruthers, V. B., Niles, J. C., & Lourido, S. (2016). A Genome-wide CRISPR Screen in *Toxoplasma* Identifies Essential Apicomplexan Genes. *Cell*, 166(6), Article 6. <https://doi.org/10.1016/j.cell.2016.08.019>
- Silmon de Monerri, N. C., Yakubu, R. R., Chen, A. L., Bradley, P. J., Nieves, E., Weiss, L. M., & Kim, K. (2015). The Ubiquitin Proteome of *Toxoplasma gondii* Reveals Roles for Protein Ubiquitination in Cell-Cycle Transitions. *Cell Host & Microbe*, 18(5), Article 5. <https://doi.org/10.1016/j.chom.2015.10.014>
- Skillman, K. M., Ma, C. I., Fremont, D. H., Diraviyam, K., Cooper, J. A., Sept, D., & Sibley, L. D. (2013). The unusual dynamics of parasite actin result from isodesmic polymerization. *Nature Communications*, 4, 2285. <https://doi.org/10.1038/ncomms3285>
- Smulders, M. M. J., Nieuwenhuizen, M. M. L., de Greef, T. F. A., van der Schoot, P., Schenning, A. P. H. J., & Meijer, E. W. (2010). How to distinguish isodesmic from cooperative supramolecular polymerisation. *Chemistry (Weinheim an Der Bergstrasse, Germany)*, 16(1), 362–367. <https://doi.org/10.1002/chem.200902415>
- Soldati, D., Foth, B. J., & Cowman, A. F. (2004). Molecular and functional aspects of parasite invasion. *Trends in Parasitology*, 20(12), 567–574. <https://doi.org/10.1016/j.pt.2004.09.009>
- Splendore, A. (1909). *Sur un nouveau protozoaire parasite du lapin, deuxième note préliminaire*. https://scholar.google.com/scholar_lookup?journal=Bull+Soc+Pathol+Exot&title=Sur+un+nouveau+protozoaire+parasite+du+lapin,+deuxi%C3%A8me+note+pr%C3%A9liminaire&author=A+Splendore&volume=2&publication_year=1909&pages=462-465&

REFERENCES

- Stadler, R. V., Nelson, S. R., Warshaw, D. M., & Ward, G. E. (2022). A circular zone of attachment to the extracellular matrix provides directionality to the motility of *Toxoplasma gondii* in 3D. *ELife*, *11*, e85171. <https://doi.org/10.7554/eLife.85171>
- Strale, P.-O., Azioune, A., Bugnicourt, G., Lecomte, Y., Chahid, M., & Studer, V. (2016). Multiprotein Printing by Light-Induced Molecular Adsorption. *Advanced Materials (Deerfield Beach, Fla.)*, *28*(10), 2024–2029. <https://doi.org/10.1002/adma.201504154>
- Striepen, B., Crawford, M. J., Shaw, M. K., Tilney, L. G., Seeber, F., & Roos, D. S. (2000). The Plastid of *Toxoplasma gondii* Is Divided by Association with the Centrosomes. *The Journal of Cell Biology*, *151*(7), 1423–1434.
- Striepen, B., Jordan, C. N., Reiff, S., & van Dooren, G. G. (2007). Building the Perfect Parasite: Cell Division in Apicomplexa. *PLoS Pathogens*, *3*(6), Article 6. <https://doi.org/10.1371/journal.ppat.0030078>
- Tanaka, M., Kikuchi, T., Uno, H., Okita, K., Kitanishi-Yumura, T., & Yumura, S. (2017). Turnover and flow of the cell membrane for cell migration. *Scientific Reports*, *7*, 12970. <https://doi.org/10.1038/s41598-017-13438-5>
- Théry, M. (2010). Micropatterning as a tool to decipher cell morphogenesis and functions. *Journal of Cell Science*, *123*(24), 4201–4213. <https://doi.org/10.1242/jcs.075150>
- Théry, M., Jiménez-Dalmaroni, A., Racine, V., Bornens, M., & Jülicher, F. (2007). Experimental and theoretical study of mitotic spindle orientation. *Nature*, *447*, 493–496. <https://doi.org/10.1038/nature05786>
- Tonkin, M. L., Roques, M., Lamarque, M. H., Pugnière, M., Douguet, D., Crawford, J., Lebrun, M., & Boulanger, M. J. (2011). Host cell invasion by apicomplexan parasites: Insights from the co-structure of AMA1 with a RON2 peptide. *Science (New York, N.Y.)*, *333*(6041), 463–467. <https://doi.org/10.1126/science.1204988>
- Torgerson, P. R., & Mastroiacovo, P. (2013). The global burden of congenital toxoplasmosis: A systematic review. *Bulletin of the World Health Organization*, *91*(7), 501–508. <https://doi.org/10.2471/BLT.12.111732>
- Tosetti, N., Dos Santos Pacheco, N., Soldati-Favre, D., & Jacot, D. (2019). Three F-actin assembly centers regulate organelle inheritance, cell-cell communication and motility in *Toxoplasma gondii*. *ELife*, *8*, e42669. <https://doi.org/10.7554/eLife.42669>
- Trecek, M., Sanders, J. L., Elias, J. E., & Boothroyd, J. C. (2011). The phosphoproteomes of *Plasmodium falciparum* and *Toxoplasma gondii* reveal unusual adaptations within and beyond the parasites' boundaries. *Cell Host & Microbe*, *10*(4), 410–419. <https://doi.org/10.1016/j.chom.2011.09.004>
- Trivedi, D., Karabina, A., Bergnes, G., Racca, A., Wander, H., Jung, S., Mittal, N., Huijs, T., Ouchida, S., Ruijgrok, P., Song, D., Wittlin, S., Mukherjee, P., Chakraborty, A., Winzeler, E., Burrows, J., Laleu, B., Spudich, A., Ruppel, K., & Spudich, J. (2022). A small-molecule myosin inhibitor as a targeted multi-stage antimalarial. <https://doi.org/10.1101/2022.09.09.507317>
- Uversky, V. N. (2013). The alphabet of intrinsic disorder: II. Various roles of glutamic acid in ordered and intrinsically disordered proteins. *Intrinsically Disordered Proteins*, *1*(1), Article 1. <https://doi.org/10.4161/idp.24684>
- Vanderberg, J. P. (1974). Studies on the motility of *Plasmodium* sporozoites. *The Journal of Protozoology*, *21*(4), 527–537. <https://doi.org/10.1111/j.1550-7408.1974.tb03693.x>
- Vernon-Parry, K. D. (2000). Scanning electron microscopy: An introduction. *III-Vs Review*, *13*(4), 40–44. [https://doi.org/10.1016/S0961-1290\(00\)80006-X](https://doi.org/10.1016/S0961-1290(00)80006-X)
- Vigetti, L., & Tardieux, I. (2023). Fostering Innovation to solve the biomechanics of Microbe-Host Interactions: Focus on the adhesive forces underlying Apicomplexa parasite biology. *Biology of the Cell*. <https://doi.org/10.1111/boc.202300016>

REFERENCES

- Wang, Z.-D., Wang, S.-C., Liu, H.-H., Ma, H.-Y., Li, Z.-Y., Wei, F., Zhu, X.-Q., & Liu, Q. (2017). Prevalence and burden of *Toxoplasma gondii* infection in HIV-infected people: A systematic review and meta-analysis. *The Lancet. HIV*, 4(4), e177–e188. [https://doi.org/10.1016/S2352-3018\(17\)30005-X](https://doi.org/10.1016/S2352-3018(17)30005-X)
- Ward, M. D., & Buttry, D. A. (1990). In situ interfacial mass detection with piezoelectric transducers. *Science (New York, N.Y.)*, 249(4972), 1000–1007. <https://doi.org/10.1126/science.249.4972.1000>
- Wassie, A. T., Zhao, Y., & Boyden, E. S. (2019). Expansion microscopy: Principles and uses in biological research. *Nature Methods*, 16(1), 33–41. <https://doi.org/10.1038/s41592-018-0219-4>
- Weiss, L. M., & Dubey, J. P. (2009). Toxoplasmosis: A history of clinical observations. *International Journal for Parasitology*, 39(8), 895–901. <https://doi.org/10.1016/j.ijpara.2009.02.004>
- Wesseling, J. G., Smits, M. A., & Schoenmakers, J. G. (1988). Extremely diverged actin proteins in *Plasmodium falciparum*. *Molecular and Biochemical Parasitology*, 30(2), 143–153. [https://doi.org/10.1016/0166-6851\(88\)90107-7](https://doi.org/10.1016/0166-6851(88)90107-7)
- White, M. W., & Suvorova, E. S. (2018). Apicomplexa Cell Cycles: Something Old, Borrowed, Lost, and New: (Trends in Parasitology 34, 759-771; 2018). *Trends in Parasitology*, 34(11), 1012–1013. <https://doi.org/10.1016/j.pt.2018.09.002>
- Williams, M. J., Alonso, H., Enciso, M., Egarter, S., Sheiner, L., Meissner, M., Striepen, B., Smith, B. J., & Tonkin, C. J. (2015). Two Essential Light Chains Regulate the MyoA Lever Arm To Promote *Toxoplasma* Gliding Motility. *MBio*, 6(5), e00845-15. <https://doi.org/10.1128/mBio.00845-15>
- Wolf, A., & Cowen, D. (1937). Granulomatous encephalomyelitis due to an encephalitozoon (encephalitozoic encephalomyelitis). A new protozoan disease of man. *Bull. Neurol. Inst. N.Y.*, 6, 306–371.
- World Health Organization Malaria Report. (2022). <https://www.who.int/teams/global-malaria-programme/reports/world-malaria-report-2022>
- Yamada, K. M., & Sixt, M. (2019). Mechanisms of 3D cell migration. *Nature Reviews. Molecular Cell Biology*, 20(12), 738–752. <https://doi.org/10.1038/s41580-019-0172-9>
- Yoeli, M. (1964). Movement of the Sporozoites of *Plasmodium berghei* (Vincke et Lips, 1948). *Nature*, 201(4926), 1344–1345. <https://doi.org/10.1038/2011344a0>
- Zhang, Y., De Mets, R., Monzel, C., Acharya, V., Toh, P., Chin, J. F. L., Van Hul, N., Ng, I. C., Yu, H., Ng, S. S., Tamir Rashid, S., & Viasnoff, V. (2020). Biomimetic niches reveal the minimal cues to trigger apical lumen formation in single hepatocytes. *Nature Materials*, 19(9), 1026–1035. <https://doi.org/10.1038/s41563-020-0662-3>

8. Acknowledgements

Everything I do in life will be first dedicated to my family. Without their support, none of the work along the different paths traveled would had been possible.

Furthermore, I would like to thank all the people who, in different ways, contributed to this work.

My PhD supervisor, Isabelle Tardieux, who opened me the doors of the lab back in October 2018. It has been five years under her guidance and support filled with scientific discussions and hard work, always striving to get a better research.

I am also grateful to Patricia Renesto for her continuous support along the last years, scientifically and personally. I would like to give a big thanks to Georgios Pavlou and Bastien Touquet for all the help and advices since day one, and also to all the past and present members of the lab: Tatiana Labouré, Antony Sarraf, Sevan Belian, Loic Engels and Clarisse Uwizeye.

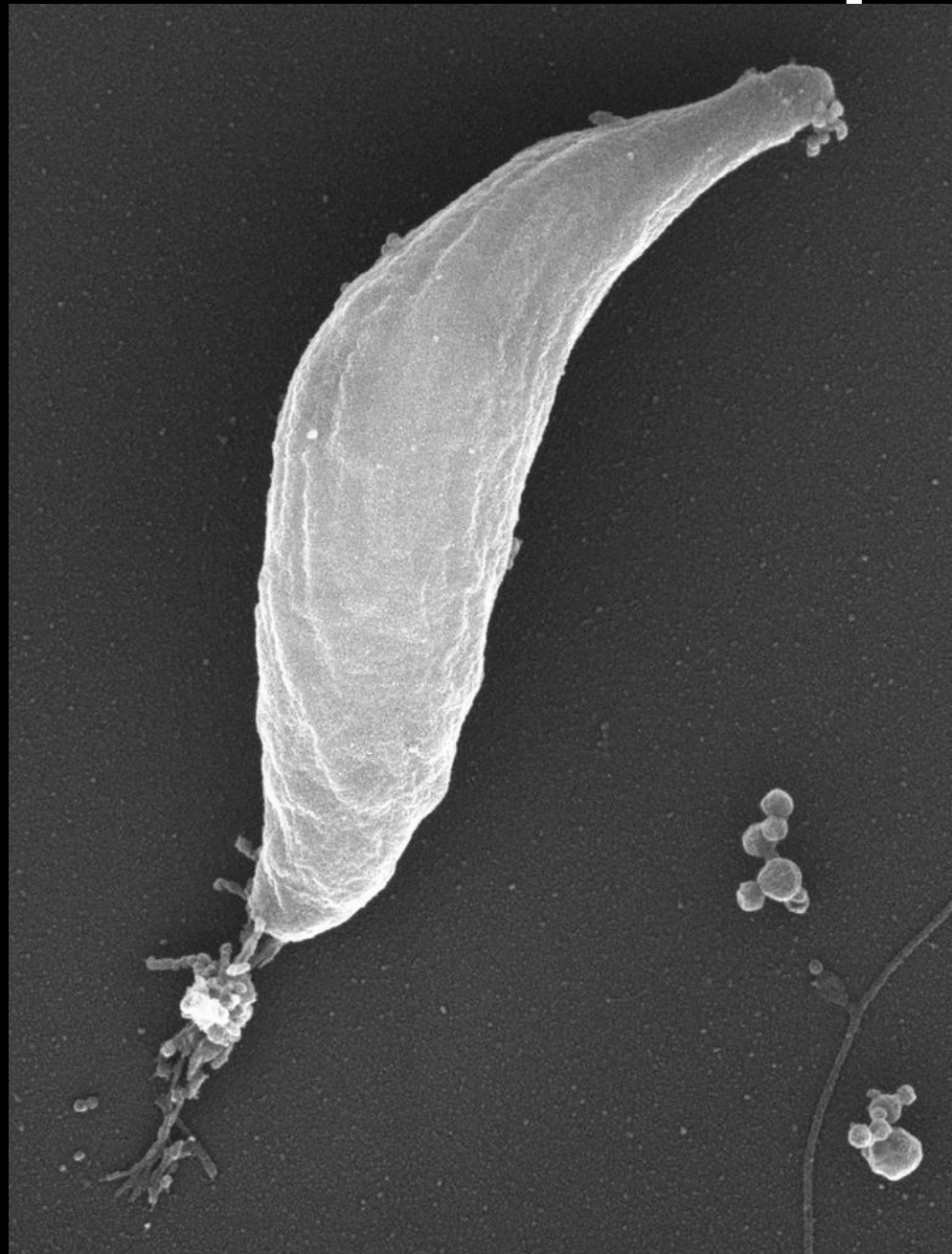
I would like to thank Galina Dubacheva, always encouraging for doing good and thoughtful research. A huge thanks to Mohamed-Ali Hakimi for his support along the thesis, and to his group for all the valuable help and feedback during meetings. Big thanks to Belén Pachano for all the teas, mates, talks, and discussions, and to Martina Shahinas and Silvia Díaz for their support; the trip to Boston was a perfect way to wrap up the Ph.D. Special thanks to Sarah Charital for all the pause cafés along the way.

I would also like to thank the members of the Liphy lab that helped setting several techniques in the first steps on the Ph.D., Martial Balland, Artur Ruppel and Maxime Bonnefoy.

The jury members – Delphine Delacour, Catharine Lavazec, Markus Meissner, Isabelle Florent and Guy Royal – for accepting the invitation and being open for discussion in order to close this journey.

To the École Doctorale Chimie et Sciences du Vivant for the scholarship that made possible my Ph.D. work.

To all of them, thank you very much!



Luis Vigetti
Ph.D. Thesis

2023